Alma Mater Studiorum – Università di Bologna
in cotutela con Università di Orléans

DOTTORATO DI RICERCA IN

Scienze della Terra, Vita ed Ambiente (STVA)

Ciclo XXXII

Settore Concorsuale: 04/A2

Settore Scientifico Disciplinare: GEO01

COUPLING INSTRUMENTATION AND METHODOLOGY IN THE SEARCH FOR TRACES OF LIFE ON THE EARLY EARTH AND MARS

Presentata da: Keyron Hickman-Lewis

Coordinatore Dottorato

Prof. Giulio Viola

Supervisore

Dr Barbara Cavalazzi

Supervisore

Dr Frances Westall

Esame finale anno 2019

One can easily forgive a child who is afraid of the dark; the real tragedy of life is when men are afraid of the light.

Plato

Contents

Chapter I – Traces of early life on Earth and the search for life on Mars

Much of the content of this chapter was published in:

Westall, F., **Hickman-Lewis, K.**, Hinman, N., Gautret, P., Campbell, K.A., Bréhéret, J.-G., Foucher, F., Hubert, A., Sorieul, S., Kee, T.P., Dass, A.V., Georgelin, T., Brack, A., 2018 A hydrothermal-sedimentary context for the origin for life. Astrobiology **18**, 259–293.

Some of the remainder of the content of this chapter was published in:

Westall, F., **Hickman-Lewis, K.**, 2018. Fossilisation of bacteria and implications for the search for early life on Earth and astrobiology missions to Mars. In Handbook of Astrobiology (Ed. Kolb, V.). CSC Press, pp. 609–631.

Westall, F., **Hickman-Lewis, K.**, Cavalazzi, B., 2018. Biosignatures in deep time. In Biosignatures for Astrobiology (Eds. Cavalazzi, B., Westall, F.). Springer pp. 145–164.

Ollivier, B., Zeyen, N., Gales, G., **Hickman-Lewis, K.**, Gaboyer, F., Benzerara, K., Westall, F., 2019. Importance of prokaryotes in the functioning and evolution of the present and past geosphere and biosphere. In Bertrand, J.-C., Normand, P., Ollivier, B., Sime-Ngando, T., (Eds.) Prokaryotes and Evolution, Springer, pp. 57–129.

Introduction

This opening chapter illustrates the broad planetary and regional environmental context of the earliest traces of life on Earth, the characteristics of the earliest ecosystems when observed at 'low resolution', placing them within the palaeobiological record of Archaean biosignatures. It concludes with a discussion of the philosophical and scientific rationale for the use of Archaean biosignatures as an informative framework for the type of life that may have arisen on Mars during its habitable early periods.

The early Earth and early Mars are considered to have had many similarities in geodynamics, palaeoenvironment and habitability. After around 4-3.5 Ga, their trajectories of planetary evolution diverged. The smaller Mars underwent more rapid cooling, the loss of its atmosphere, and the loss of its surface oceans, becoming seemingly uninhabitable at the surface during the Hesperian. The Earth, by contrast, became increasingly more habitable during the same period of several hundred million years and saw the advent of more complex geodynamics, more diverse surface environments, and an increasingly impactful and consequential biosphere colonising most available niches. The earliest history of the two planets reflects the moment in time at which the most apposite comparisons may be made between them. This period, spanning the Hadean to Palaeoarchaean on Earth and the Noachian to Early Hesperian on Mars, represents when both planets were habitable and may have shared biospheric characteristics, at least at the scale of microbial habitability. For astrobiology, the geological records of the early Earth and early Mars share a plenitude of characteristics of astrobiological relevance, and each of these planets may assist the interpretation of the early history of the other.

The characterisation of the environments and biosphere of the early Earth are thus the objective of this thesis, and the application of these findings to the search for life on Mars, both *in situ* using rovers and following Mars Sample Return, are its implications. The structure of this thesis is presented at the conclusion of this chapter.

1. Geological environment of the early Earth

When studying the early evolution of life, one must contextualise its record within the constraints placed on the environment of the primitive Earth at planetary, regional, local and microbial scales (Fig. 1). Efforts to parameterise the environment of the Earth through the first two billion years of its history have been numerous, but leave many constraints poorly resolved (e.g. Nisbet and Fowler, 1999; Nisbet and Sleep, 2001; Arndt and Nisbet, 2012). The lack of preserved Hadean crust (4.5–3.85 Ga) crust entails that our understanding of the Hadean environment – i.e., the hundreds of millions of years preceding the oldest well-preserved crust – is extremely incomplete and limited to only a small number of highly metamorphosed supracrustal sequences, largely distributed across Greenland and Canada. The lack of Hadean crust has been attributed to i) post-Hadean plate tectonics, ii) destruction and resurfacing during the period of the hypothesised Late Heavy Bombardment, around 4.1-3.85 Ga (Bottke et al., 2012), when the inner planets were subjected to intense and deleterious impacting (Kemp et al., 2010; Marchi et al., 2014), and iii) hypothesised catastrophic recycling of the early crust, possibly entailing the collapse of a single lithospheric covering the early Earth (the stagnant lid) along with episodic, short-lived plate tectonics (Debaille et al., 2013; Griffin et al., 2014). The consequences of this lack of record are that we do not have direct evidence of the origin and earliest evolutionary stages of life, which is predicted to have emerged on Earth at some consequential moment between 4.5 and 3.8 Ga (Fig. 1) irrespective of whether astrophysical constraints, such as accretion and planetary differentiation phenomena, or biological constraints, such as molecular clocks, are applied (Pearce et al., 2018; Sleep, 2018; Betts et al., 2018). The well-preserved sedimentary sequences of the Palaeoarchaean are therefore the oldest fragments of the rock record from which we can garner an understanding of the co-evolution of ecosystems and environments on the early Earth. Of these sequences, the East Pilbara terrane of Western Australia and the Barberton greenstone belt of southern Africa are the most extensively and intensively studied, and will form much of the subject matter of this thesis. In terms of the constraints that can be placed upon planetary habitability by virtue of the study of these sequences, there are also expected to be differences between the global-scale condition of the Earth and the microscopic- to local-scale environments in which early life evolved. This scale-dependent variation of characteristics necessitates that all conclusions regarding the nature of the lithologies and palaeoenvironments reflected in this most ancient rock record must be made according to multi-scalar approaches.

1.1. Palaeoenvironments of the earliest ecosystems

1.1.1. Temperature

Despite the relative lack of geological record, remnant geochemical signatures in preserved Eoarchaean-Paleoarchaean cratons (Rosing, 1999; Wilde et al., 2001; Fedo and Whitehouse, 2002; Kamber et al., 2003; Harrison, 2009; Cawood et al., 2018) throw some light on the evolution of early Earth environments (Fig. 1). It is possible that, even this early in Earth history, the planet was already characterised by a crustal dichotomy between the continents and oceans (Armstrong, 1981; Rosing, 1999; Wilde et al., 2001), although the picture has gradually changed to a more drawn-out crust-building process lasting until the Neoarchaean (see review in Cawood et al., 2018). Temperatures at the surface of the early Earth remain a subject of debate, especially when considering the "Faint Young Sun" hypothesis (Sagan and

Mullen, 1972) that gives credence to climate models predicting cold or temperate surface temperatures early in Earth history (e.g. Charnay et al., 2017). Recent work taking into account i) the absence of plant life through the Precambrian resulting in the lack of biologically induced cloud condensation nuclei and ii) the reduced surface albedo as a result of limited exposed continental crust prior to around 2.7 Ga has suggested, however, that no climate paradox ever existed due to the "Faint Young Sun" (Rosing et al., 2010), and thus that the Earth was clement to life very early in its history, irrespective of the concentrations of greenhouse gases. Indeed, although Walker (1985) and Kasting (1993) modelled a high pCO_2, mildly reducing atmosphere, this extreme atmospheric condition has been moderated with time and reflection (see Shaw, 2014). Although high greenhouse gas concentrations favour sustained water bodies under the "Faint Young Sun", much mineralogical data from the Archaean, for example, the presence of mixed valence iron oxides in Archaean sedimentary sequences is inconsistent with such gases as dominant atmospheric constituents (Rosing et al., 2010).

Of specific relevance to early ecosystems, the temperatures of the early oceans in which life originated and evolved have been estimated using oxygen, silicon, and hydrogen isotopic fractionations preserved in cherts dating back to 3.5 Ga. These analyses concur that seawater temperatures were above freezing, at least at the sediment-seawater layer. Cooler temperatures of ~26°C were deduced by Hren et al. (2009) and Blake et al. (2010), whereas warmer temperatures (in excess of 50-60°C) have been estimated from the Si and O isotopic studies of Knauth (2005), van den Boorn et al. (2010), Marin-Carbonne et al. (2014), and Tartèse et al. (2017). Studies estimating higher temperatures note the influence of hydrothermal fluids on ambient seafloor temperatures. This raises an important and essentially undiscussed quandary in the application of isotope geochemistry to the physical oceanography of the early Earth: which waters are being measured by isotopic analyses? The sample choice in such studies is rarely well-documented in detail, but in cases of careful sample characterisation, the influence of hydrothermal activity is usually clear (Tartèse et al., 2017). This may skew estimated temperatures toward higher values. On the other hand, if indeed the studied samples – hydrothermally influenced marine sediments – represent the most common environments for life, the calculated values may nonetheless by highly informative of the palaeoenvironments of early life. This sustains the prevailing hypothesis that early life was thermophilic (e.g. Nisbet and Fowler, 1999; Gaucher et al., 2010) and was adapted to metal-rich conditions that defined the balance of metabolisms in the ecosystem (Williams and Fraústo da Silva, 2003; Robbins et al., 2016; Moore et al., 2017) (Figs. 2-3).

1.1.2. Catastrophes and palaeoenvironmental stability

Potentially catastrophic impacts continued to impact the surface of the Earth until the Mesoarchaean (Koeberl, 2006) and may have played a role in the change of tectonic regimes during the first billion years of Earth history (Decker et al., 2015). These regionally catastrophic events would have had significant influence on the spatial distribution of early life. In recent re-evaluations of the models pertaining to asteroid bombardment during the Hadean, however, Sleep (2016) and Zellner (2017) estimated that most large impacts would have been relatively benign to surface environments and that there would not have been more than one impact severe enough to act to the global detriment of early life. The surface environments of the Earth may thus, contrary to traditional expectations, have been relatively constant over millions of years. Thermal, tectonic, and isostatic constraints suggest that, at least

during the Archaean (3.85 to ~2.5Ga), stable and regionally important oceans contained up to several kilometres of water, and that the incipient continents were somewhat submerged and thus characterised by shallow-water sediment sequences across much of their areal extent (de Wit and Hart, 1993; Kamber et al., 2015; Nijman et al., 2017; Cawood et al., 2018).

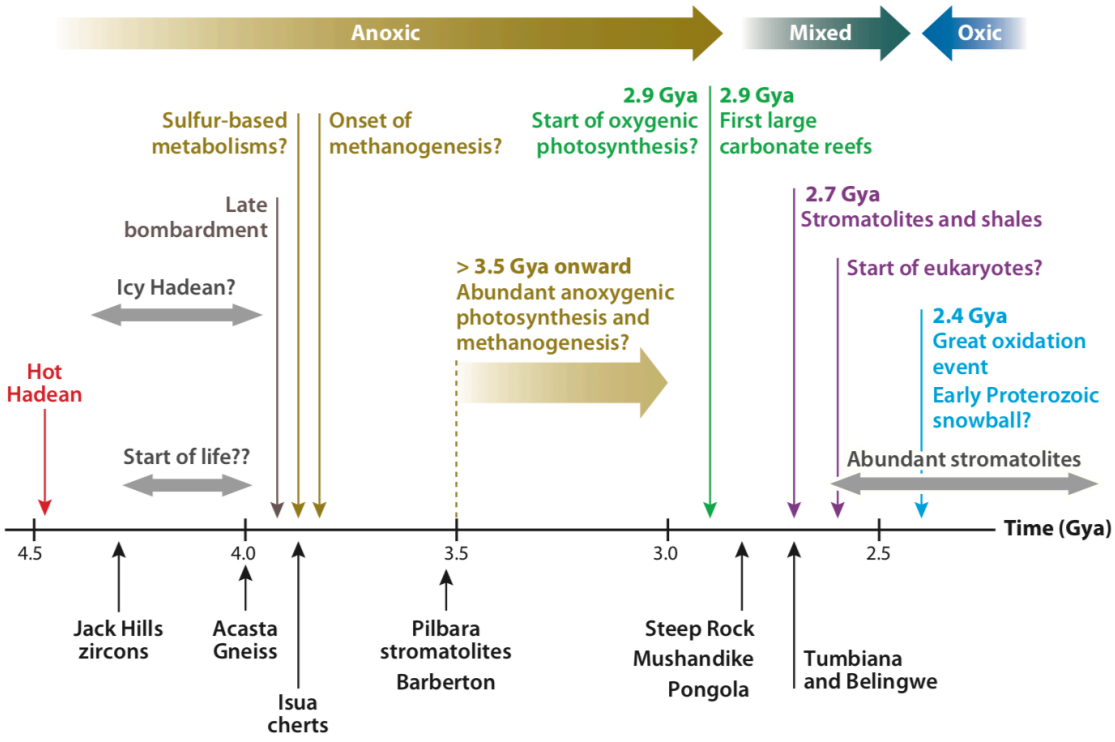

Fig. 1. Defining events in the co-evolution of Earth and Life throughout the Hadean and Archaean. All Archaean samples studied herein come from the period between the onset of abundant anoxygenic photosynthesis and the proposed origins of oxygenic photosynthesis. From Arndt and Nisbet (2012).

1.1.3. Hydrospheric, sedimentary and biogeochemical characteristics

Aside from the isotopic record, sedimentological and mineralogical data from Palaeoarchaean marine deposits provide constraints on physical oceanographic parameters. Sediments from the Onverwacht Group of the Barberton greenstone belt document typical marine sedimentary sequences (Tice and Lowe, 2004; de Vries et al., 2010; Ledevin et al., 2014; Westall et al., 2015). Some shallow-water sediments record tidal environments in the form of oscillatory ripple marks (de Vries et al. 2010; Allwood et al., 2010; Westall et al., 2015), evaporitic minerals (Lowe and Fisher Worrell, 1999; Van Kranendonk, 2007), and desiccation cracks associated with evaporitic mineral suites (Westall et al., 2006). These structures and mineralogies suggest formation in a relatively warm environment. Many early sedimentary horizons show evidence for carbonate precipitation (Altermann, 2002; Van Kranendonk, 2007; Westall et al., 2011; Allwood et al., 2010; Hickman-Lewis et al., 2018) and further geological evidence suggestive of warmer atmospheres comes from mineralogies indicating relatively high concentrations of atmospheric CO_2 in contact with warm oceans, for example siderite (Hessler et al., 2004; Westall et al., 2018) and nahcolite (Tice and Lowe, 2006). It is important to note that some finely laminated sediments in the Barberton greenstone belt have been interpreted as glacial diamictites (de Wit and Furnes, 2016), which is consistent

with the proposed cool temperatures at the surface of the Earth by climate models (see above), however, these sediments are also similar to other finely laminated lithologies from the Onverwacht Group that were deposited in shallow, wind-driven, quiescent environments (e.g. Lowe and Knauth, 1977; Trower and Lowe, 2016). If, as suggested by de Wit and Furnes (2016), these glacial deposits are associated with hydrothermal fields, it becomes necessary to consider very fine-scale palaeoenvironmental variations within single horizons.

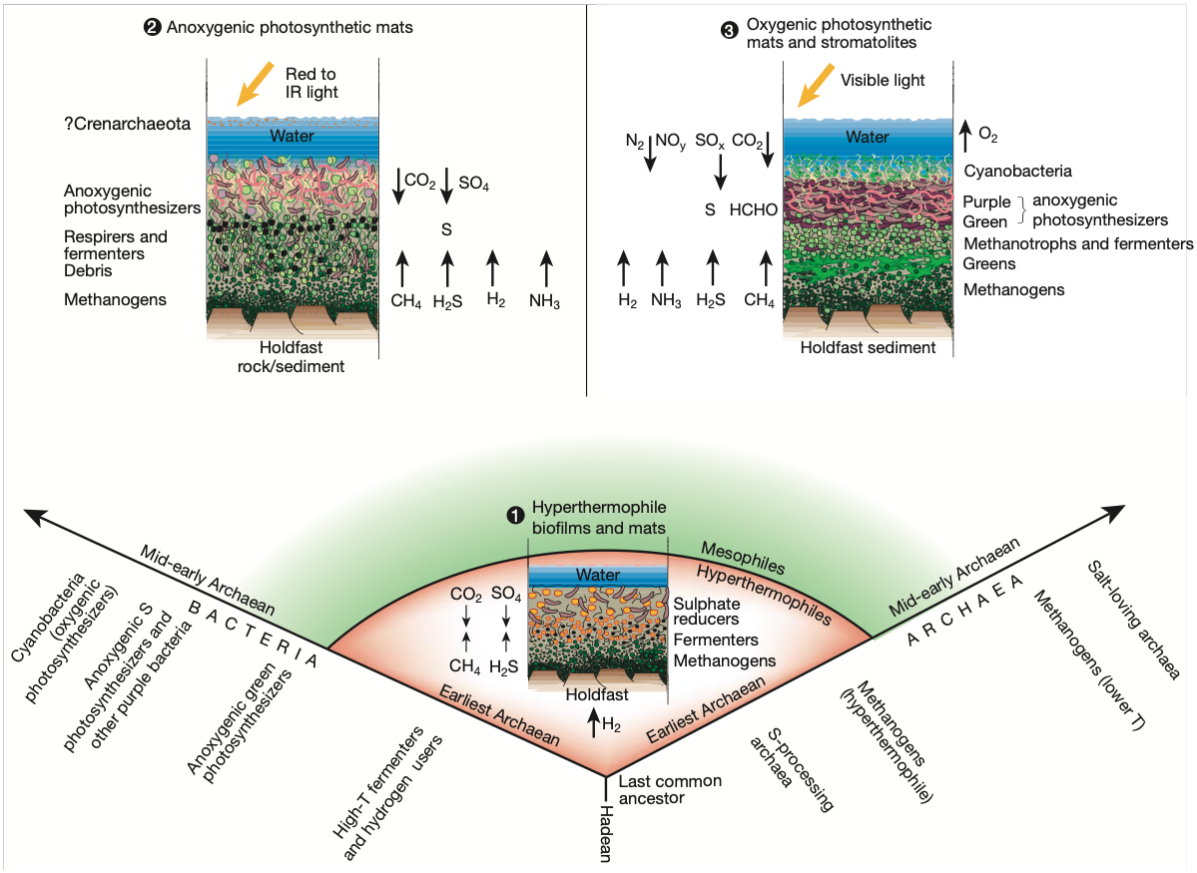

Fig. 2. Evolution of microbial communities – in terms of metabolism and microbial stratigraphy – throughout the Archaean Eon. The Early Archaean, i.e., the Eoarchaean to Palaeoarchaean is expected to be characterised by (1) hyperthermophile communities based on sulphur and methane cycling metabolisms and (2) thermophilic-mesophilic anoxygenic communities based on anoxygenic photosynthesis (termed *Chloroflexus*-like by Nisbet and Fowler, 1999), sulphur, methane and nitrogen cycling. The later Archaean, i.e., the Mesoarchaean to Neoarchaean, saw the rise of oxygenic photosynthesis performed by cyanobacteria (3), and the development of oxygenic-anoxygenic interface consortia and highly stratified mat consortia that continue to play a major role in marine primary productivity and biogeochemical cycling at present. Adapted from Nisbet and Sleep (2001), based on Nisbet and Fowler (1999).

Rare earth element plus yttrium (REE+Y) systematics have been proven as a reliable method by which certain hydrospheric parameters of the palaeoenvironment can be decoded. For more than twenty-five years, the influences of marine and hydrothermal fluids on Archaean hydrogeneous sedimentation have been well-known and studied in ever increasing detail (Danielson et al., 1992; Kamber and Webb, 2001; Van Kranendonk et al., 2003; Gourcerol et al., 2016). This has led to a view of the Archaean Earth that is dominated by hydrothermal input into highly saline, anoxic oceans (Kamber et al., 2001; Hofmann, 2011; Westall et al.,

2018), with the implication that hydrothermal effluence was so significant that its signal had been advected into even the shallow oceans (Kamber et al., 2001), i.e., hydrothermal fluids were an important constituent of the Archaean oceans and exerted control over their elemental budgets (Fig. 4-5). Indeed, geochemical evidence suggests hydrothermal influence over even shallow water environments (e.g., Hofmann, 2011; Westall et al., 2018). Most chert horizons are underlain by progressive silicification zones through volcanic sequences (Hofmann and Bolhar, 2007; Hofmann and Wilson, 2007; Hofmann and Harris, 2008), suggesting that hydrothermal effusions were widespread and that the palaeoenvironments of many early ecosystems were consequently thermophilic and metal- and nutrient-rich (Nisbet and Fowler, 1996; Hofmann and Bolhar, 2007; Westall et al., 2018) (cf. Figs. 3-5).

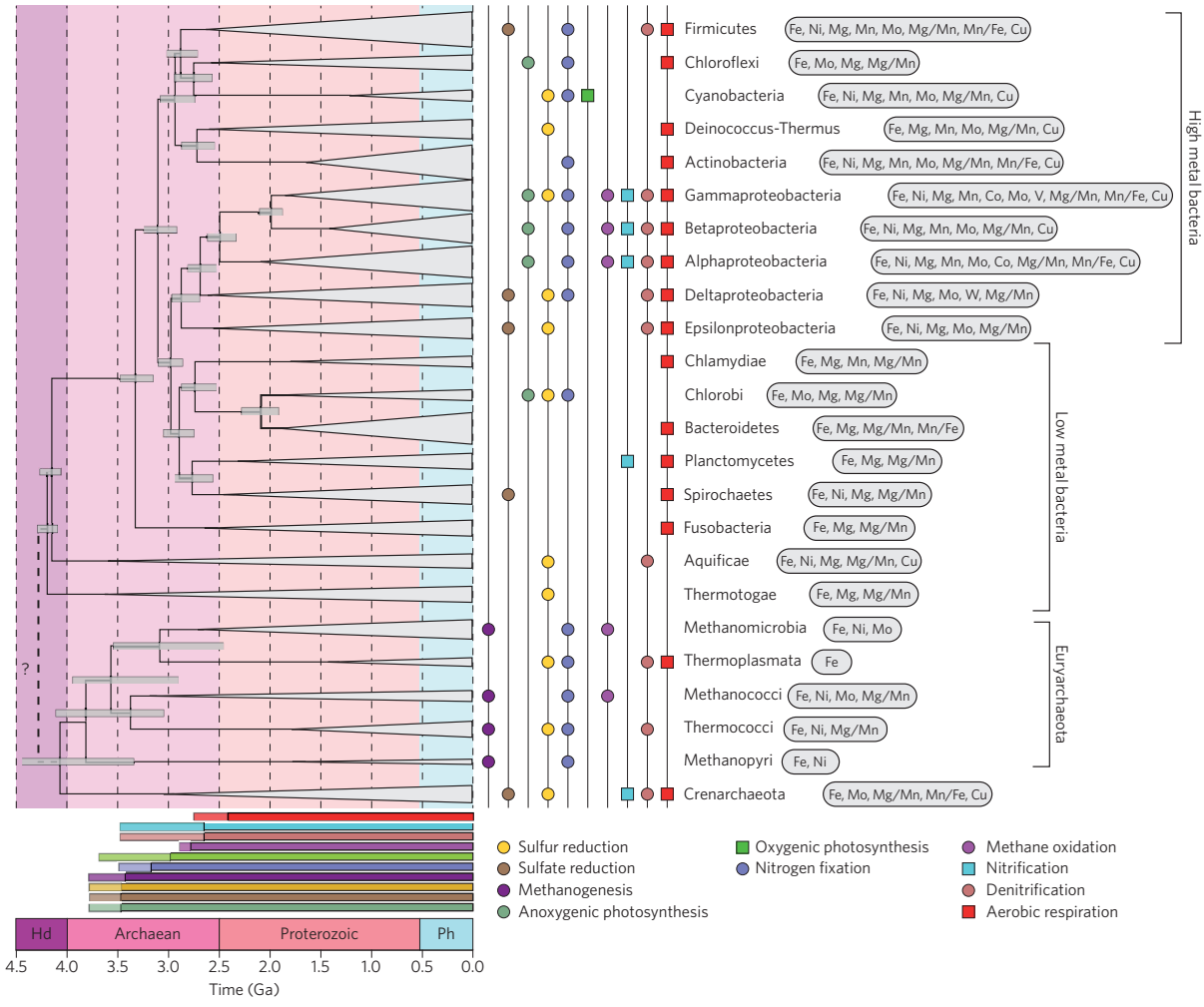

Fig. 3. Expanding network of metal use by microbes throughout Earth history. Note that groups of organisms with earlier divergence times are linked to more limited suites of metals that nonetheless correspond to the proposed metal-rich compositions of the Hadean-Palaeoarchaean oceans (Nisbet and Fowler, 1996; Fraústo da Silva and Williams, 2001). Metal incorporation into oxidoreductase metallocofactors increases significantly following the oxygenation of the atmosphere. This trajectory of metal use is consistent with thermophilic early life that gradually expands into niches of lower temperature (Gaucher et al., 2010). From Moore et al. (2017).

Thermophilic palaeoenvironments appear to have developed at the interface between volcano-hydrothermal effluent and seawater (Hofmann and Bolhar, 2007). Gradients in pH

would have varied from alkaline to acidic, depending upon the input of hydrothermal fluids mixing with seawater and modifying the pH of pore waters during the alteration of volcanic particles (Oelkers and Gíslaison, 2001; Wolff-Boenisch et al., 2006). The fluid dynamics in these environments would have been locally variable, but disruptive, permeating intrusions had the potential to mix lithological and hydrogenous components of the system together on short and longer timescales (Westall et al., 2018) (Fig. 4-5). The ionic strength of these sedimentary environments would thus have been high, with a plenitude of bio-essential and bio-functional ions sourced from seawater, hydrothermal fluids, and the alteration of volcanic particles and culminating in high trace and REE contents associated with ambient oxyhydroxide particles (cf. Shibuya et al., 2010; Jeandel and Oelkers, 2015). Aside from solar flux, energy sources would have been provided to the early biomes by heat from hydrothermal vents and fluids, as well as by ubiquitous, exothermic redox reactions occurring during the aqueous alteration of the surfaces of the volcanic basement, the diverse mineralogy of which consisted predominantly of volcanic glass, pyroxene, plagioclase, olivine, and their secondary alteration minerals, together with phyllosilicates, anatase, tourmaline, and other accessory phases. Secondary minerals included Fe carbonate, pyrite, and barite (Van Kranendonk, 2006; Westall et al., 2018), together with zeolites after the alteration of felsic rocks (Brasier et al., 2011). A meteoritic component, whether significant or reduced, would also have been expected long after the cessation of the Late Heavy Bombardment (cf. Lowe et al., 2003; Maurette and Brack, 2006; Koeberl, 2006; Decker et al., 2015; Gourier et al., 2019), delivering a wide of elements dependent upon the composition of the impactor (stony, iron, or carbonaceous, for example).

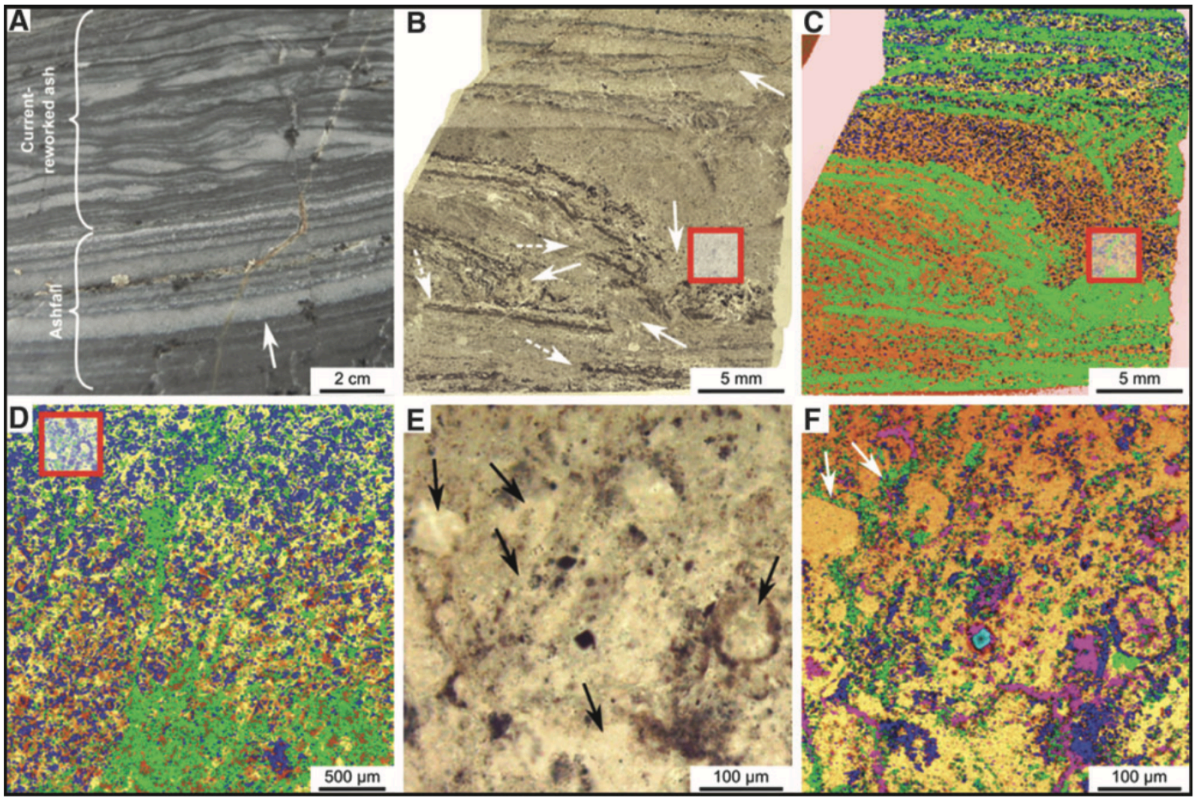

Fig. 4. Early Archaean laminated, shallow marine, volcanogenic sediments interacting with pervasive hydrothermal effluent from the 3.33 Ga Josefsdal Chert. **A**) Field photograph of alternating ash (light) and carbonaceous (dark) layers. **B**) Photomicrograph showing a thin section from the same material documenting

layers disrupted, through soft sediment deformation, by stratiform and discordant hydrothermal fluid perfusion (arrowed). Red box outlines detail in D. **C**) Raman map of thin section B, showing carbon (green), the silicified matrix (orange, quartz), and anatase (blue) representing altered volcanic clasts. Red box outlines detail in D. **D**) Raman map (red boxes in B-C showing carbon (green) intermixed with volcanic particles (represented by alteration phases: anatase, blue; muscovite, pink); the quartz matrix (yellow/orange) represents the silica precipitated by hydrothermal fluids. **E-F**) Photomicrograph (E) and Raman map (F) showing detail of the red box in D. Carbon (green) occurs as a coating on volcanic particles (arrowed), which have been replaced by muscovite (pink), anatase (blue), and quartz (yellow/orange). Additional minerals: magnetite, light blue; rutile, red.

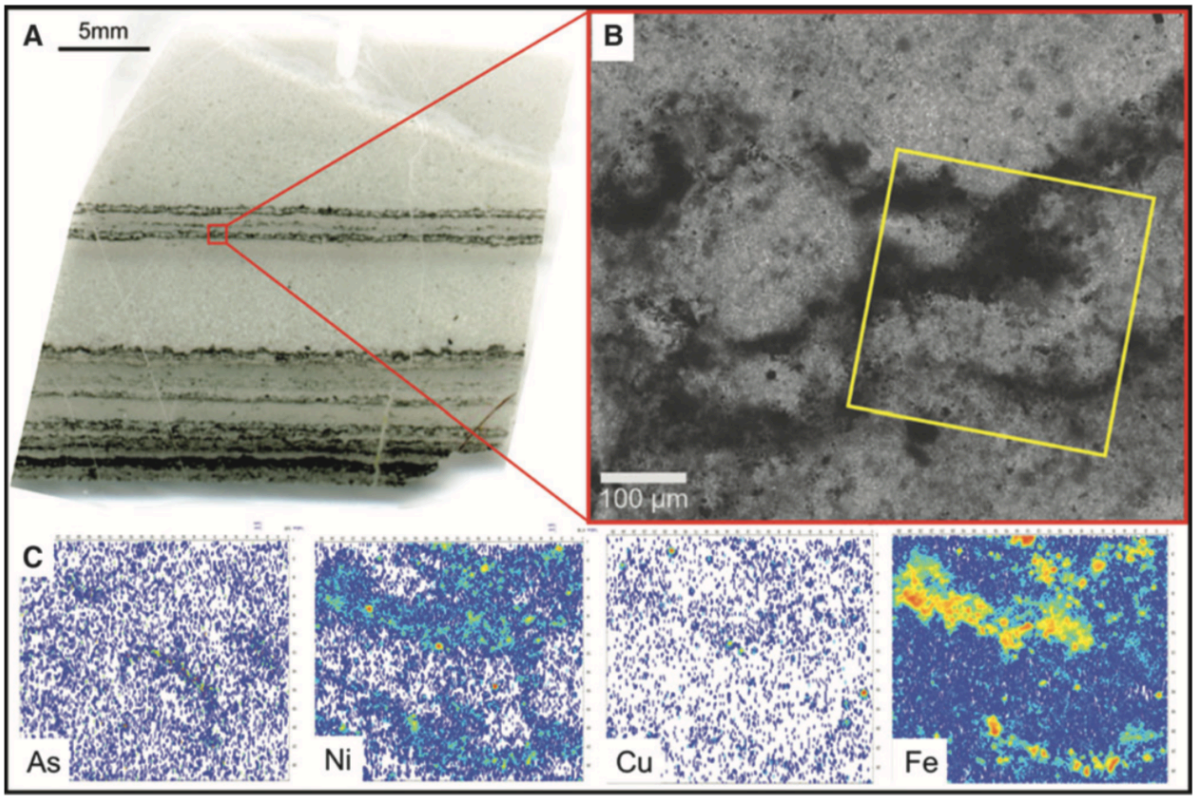

Fig. 5. Organic material associated with an elemental signature derived from hydrothermal effluent. **A**) Thin section of laminated volcanogenic sediments (black-grey-white chert); dark horizons are carbonaceous microbial laminations that concentrate volcanic particles due to trapping and binding by microbial biofilms. **B**) Optical photomicrograph of pseudomorphed volcanic particles. Yellow box denotes the area of the regions analysed in C. **C**) µPIXE elemental maps showing the distribution of Fe, As, Ni, and Cu, trace elements of probable hydrothermal genesis that co-occur with organic material. Acquisition parameters: beam size: 2 µm; map size: 300 x 300 mm; resolution: 256 x 256 pixels; duration of acquisition 3.5 h.

As will be highlighted in Chapter II, Manuscript III, widespread biomes – the set of environmental and organismal parameters common to and governing a set of ecosystems – may have existed on the Archaean Earth and may assist in the reconstruction of Archaean microbial habitability (Nisbet, 1995; Nisbet and Fowler, 1999; Hickman-Lewis et al., in review). The characteristics, occurrence and the potential metabolic networks that they represent are considered key to the interpretation of the possible biosignatures that may be found during *in situ* astrobiology mission at the surface of Mars (see Westall et al., 2015).

2. Challenges inherent to the proof of biogenicity

Putative biosignatures in early Earth environments must meet three benchmark criteria: i) they should possess features or signatures consistent with biology; ii) they should be syngenetic with their host rock; and iii) the host rock should evidence a geological setting consistent with habitability. The order in which this assessment is made is of little consequence to proposing a biosignature, since failure to meet even one of the three criteria is sufficient to preclude a feature being adjudged of palaeobiological significance.

Having been submitted to several billion years of processes capable of changing them beyond recognition, the identification and analysis of Archaean biosignatures can be fraught with difficulties. The first task is to determine whether the purported biogenic signature is truly of biogenic origin and not an abiotic look-alike (biomorph) or an artefact. Microbial structures and constructs, both macroscopic and microscopic, often have very simple shapes that can be imitated by abiotic processes: spheroidal microfossils may be easily confused with spheroidal mineral precipitates, such as silica, while a sheet-like concentration of abiotic organic material could superficially resemble a biofilm. Disseminated organic matter in ancient sediments, especially when significantly degraded, needs to be distinguished from abiotic organic matter of hydrothermal or other origin. A noteworthy case study of controversial biogenicity is presented by the pseudofossils of the 3.46 Ga "Apex Chert," Western Australia. Although initially interpreted as organisms with a cyanobacterial affinity (Schopf and Packer, 1987; Schopf, 1992), later studies of the same material gradually unravelled this case for their biogenicity (Brasier et al., 2002, 2005, 2006; Wacey et al., 2016). Although of superficially microfossil-like morphology (filamentous, apparently septate), high-resolution FIB-SEM work demonstrated that this morphology results from aluminous clay minerals onto which carbon had become fortuitously adhered (Brasier et al., 2015; Wacey et al., 2016). With recent isotopic studies (Schopf et al., 2017), this particular controversy is ongoing. Such cases of controversial or mistaken biogenicity plague biosignatures of all sizes, up to and including stromatolites. A famous (admittedly extreme) example thereof is the "Taylor stromatolite," a complex laminar-domical structure closely resembling modern stromatolites but having been created by coincidence during paint spraying in the mid-Twentieth Century. Similar supposed abiological examples are known from the geological record, and especially ancient stromatolitic occurrences, such as the 3.481 Ga Dresser Formation and 3.43 Ga Strelley Pool Formation stromatolites, have been rountinely subject to strong criticism (Lowe, 1994; Lindsay et al., 2005) in spite of bearing many biological charactristics (Van Kranendonk, 2007; Hickman-Lewis et al., 2016, 2019).

Having established the biogenicity of the feature, the second task is to establish its syngenicity with the host rock. Microbes infiltrate cracks and fissures in rocks of various ages (as chasmoliths or endoliths) and can even become fossilised in their endo-/chasmolithic habitats. Westall and Folk (2003) described silicified endolithic cyanobacteria (< 8000 years old) that had previously been considered syngenetic within rocks of ~3.8 Ga from the Isua complex in Greenland. Without conducting tests for syngenicity, younger microorganisms could be mistaken for ancient fossils and, indeed, have been (Pflug and Jaeschke-Boyer, 1979).

The third, governing consideration in biogneicity is the environment of formation, i.e., does the purported biosignature occur in a geological context consistent microbial habitability? For example, while cyanobacteria can be thermophilic and are found around hot springs (Campbell

et al., 2015), they do not occur within low-temperature (< 100˚C) hydrothermal veins, a niche that is instead colonised mostly by chemolithoautotrophs. As a further example, organotrophs require direct access to a carbon source and would fail to dominate an oligotrophic, carbon-poor environment, whereas lithotrophs and phototrophs may do so.

The challenges inherent in biogenicity will be considered out of necessity in great detail in Chapters II and III, for each studied sample. This brief background for the rationale of biogenicity criteria will be built upon throughout the thesis, and we will not dwell further on this topic here.

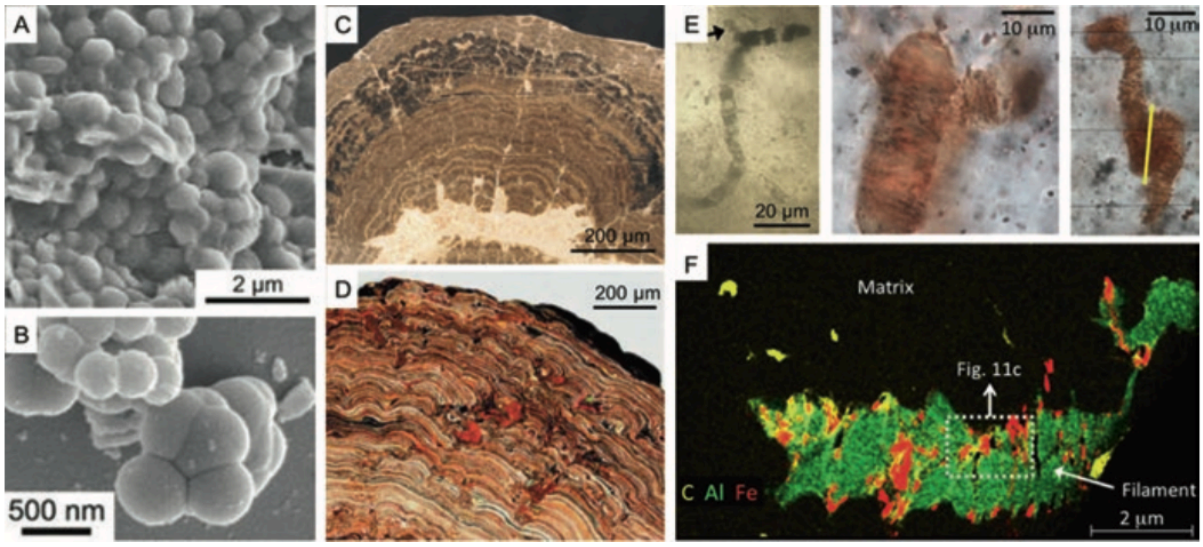

Fig. 6. Fossil, pseudofossil, or non-fossil? Biomorphs and false-positive detections of biosignatures from the rock record. **A**) Colony of coccoidal cells forming a biofilm on a volcanic grain, from Kitty's Gap Chert, Pilbara. **B**) Agglomerated silica spheres, a crystalline biomorph for coccoidal cells, which even bear hallmarks such as pseudo-division. **C**) Biogenic stromatolite from an ancient carbonate platform of the Tumbiana Formation. **D**) The infamous "Taylor Stromatolite," texturally similar to the biological conical-domical stromatolites but formed abiotically during a paint-spraying process. **E**) Three examples of filamentous, pseudoseptate microfossil-like objects from the 3.46 Ga Apex Basalt. Arrow indicates a side branch (a feature deemed incompatible with prokaryotic morphology); yellow line indicates plane of the FIB-SEM image in F). **F**) FIB-SEM element map showing the dominantly aluminosilicate composition of the fossil-like object. Green = Al (proxy for aluminous phyllosilicate); yellow = C (adhered to the outermost extremities); red = Fe. A-B from Westall et al. (2011); D from McLoughlin et al. (2008); E-F from Schopf, 1993 and Wacey et al. (2016).

3. The early Earth as an "analogue" for Martian astrobiology

3.1. Why search for life elsewhere?

It is hypothesised that if carbon-bearing molecules, water, rocks, energy and other essential elements (HNOPS and transition metals) are associated in a suitable geological setting for a sufficient amount of time, life should appear as a consequence of favourable prebiotic chemistry merging into biology (Russell et al., 2010; Stüeken et al., 2013; Westall et al., 2018). This is a simplified view, of course, and details of the process are much debated. Nonetheless, it is the basis of our understanding that life could have emerged on other planets and satellites in the Solar System, as well as elsewhere in the Universe (de Duve, 1991, 1995; Morowitz, 2002). The principal criteria for the emergence of life is nonetheless "habitability", i.e., the existence of an environment capable of hosting life. Lammer et al. (2009) gave a

comprehensive assessment of the relevance of the idea of habitability in the Solar System, concluding that Mars, Enceladus and Europa constitute the prime targets for near-Earth astrobiology in the coming decades. Since the type of habitable conditions necessary for the emergence of life are not equivalent to those for hosting well-established cellular life or slow-growing or dormant life, the types of life that might exist or have existed on extraterrestrial bodies need to be considered on a body-by-body basis.

In such a framework, the biological communities of the early Earth are relevant for the search for life elsewhere in the Solar System for several reasons. On regional and microbial scales, the anaerobic environment of the early Earth was similar to that of the other telluric planets, particularly Venus and Mars, in the early phases of their development. The environments of the early Earth and Mars bear several salient similitudes: anaerobic, volcanically and hydrothermally active, and with atmospheres defined by the outgassing of volcanism (Fig. 7). Unlike Venus, the geological record of Mars remains accessible to planetary exploration. Energy on the early planets would have been sourced largely from internal processes, including the decay of now-extinct radionuclides of Al, Hf and Pu, and the latent heat of planetary accretion (Turcotte and Pflugrath, 1985). C-bearing molecules originated from both endogenous (atmosphere, subsurface hydrothermal) and exogenous (carbonaceous chondrites, micrometeorites) sources. In brief, the implication is thus that life could have emerged on any such telluric planet (de Duve, 1995). In contrast to Earth, Mars has seemingly always been a landlocked planet characterised by isolated pockets of habitable areas of variable sizes (Head et al., 2019, and references therein). Way et al. (2016) considered that such planets with only a moderate amount of water, such as early Mars and Venus, could even have had a higher habitability than mostly oceanic worlds, such as the early Earth. This is consistent with both chemolithoautotrophy and organotrophy associated with hydrothermal serpentinising systems and photosynthetic consortia including photoferrotrophs and anaerobic photosynthesisers in shallow-water environments being important in the early habitable realm.

Mars started to become uninhabitable at the surface between 4 and 3.8 Ga (Fig. 8), but its subsurface potentially remained habitable, and may be habitable to this day (Boston et al., 1992; Des Marais et al., 2008). Furthermore, unlike Earth, Mars has never been either permanently habitable or consistently habitable (Westall et al., 2015; Cabrol, 2018), and the degree of habitability present throughout its geological history remains questioned. There is evidence for a significant amount of water at the surface of the planet during its early history but not for a global ocean, whereas the later history of Mars is characterised by a gradual decrease in habitability, punctuated by sporadic and localised peaks in aqueous activity during the Hesperian (e.g., the catastrophic outflow channels), before reaching essentially dry desert conditions from the Late Hesperian and throughout the Amazonian (Carr and Head, 2010; Head et al., 2019). With a decrease of internal heat flow and the demise of the dynamo that created a radiation shield protecting the atmosphere and volatiles from erosion by the solar wind and specific solar events, Mars was left unprotected and essentially devoid of an atmosphere (Jakosky et al., 2015). The habitability of Mars has changed drastically through time, and habitats were not necessarily co-located in time or space. This was termed “punctuated habitability” by Westall et al. (2015), corroborating the notion of “uninhabited habitats” (Cockell et al., 2012). These considerations, together with the trade-offs between science, cost and remote operability are crucial considerations in any astrobiology mission (see discussions in Foing et al., 2011; Martins et al., 2017).

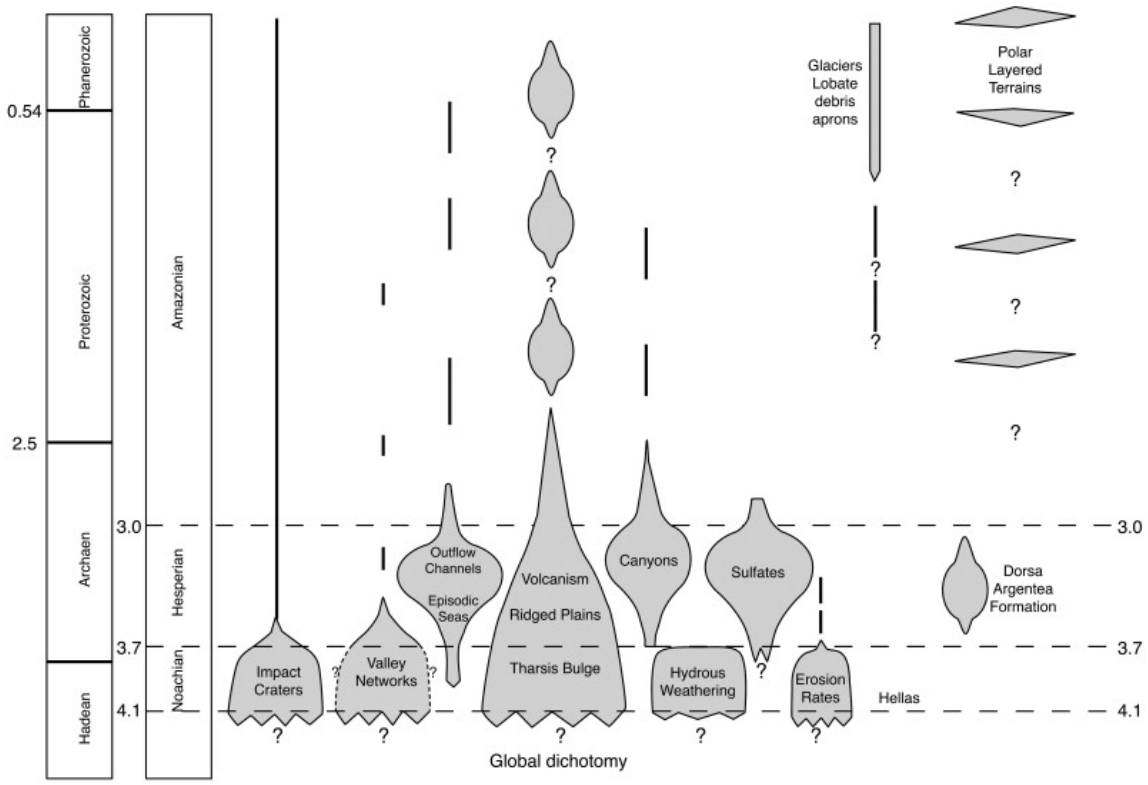

Fig. 7. Geological processes controlling the geomorphology and surface processes of Mars, including those relevant to the generation of habitable conditions. The hydrosphere is significant until 3.7-3.5 Ga, after which only significant outflow channels and potential volcano-hydrothermal hydrospheric activity (and later glaciers) would have been recurrent throughout the Mid-Hesperian into the Amazonian. Volcanism co-occurs with hydrospheric activity early in Mars history (mostly in the Noachian), suggesting that habitable conditions at the surface of Mars would have borne similarities to the volcanism-dominated geomorphology of the Archaean Earth. A comparison with the geological timescale of Earth is given at the left. From Carr and Head (2010).

3.2. Rover astrobiology on Mars

Punctuated habitability means that a potentially habitable body is not necessarily globally habitable, and much of the potential active biomass may be either hidden from view, for example, in the subsurface, or simply not have produced detectable biosignatures, for instance, biolaminations, microbially induced sedimentary structures, and stromatolites. Failing to find traces of life does not mean that life did not exist on the planet. Finding traces of past life on Mars will require serendipitous landing in the perfect location, hampered by limitations to the resolution of correlative geomorphology and composition that can be achieved from orbit. Rover surface operations permit the closest examination of Martian lithologies and thus the highest probability of unambiguous life detection.

3.2.1. Mars Exploration Rover mission

The Mars Exploration Rover (MER) mission involved two rovers, landing on Mars in 2003, with the search for and analyse rocks and sediments evidencing the past Martian hydrosphere. The *Opportunity* rover landed in Meridiani Planum and *Spirit* in Gusev Crater. *Opportunity* found nodules of haematite in layered, jarosite-rich seidments, indicating the evaporation of a saline water body (Squyres et al., 2006). *Spirit* provided evidence for limited aqueous alteration of a basaltic precursor lithology in a debris-filled crater (Arvidson et al.,

2004; McSween et al., 2004) after which its investigation of the Columbia Hills area found increased evidence of water alteration and the formation of clay minerals, as well as sulphates and jarosite (Ming et al., 2006) and digitate, nodular deposits at Home Plate (Ruff and Farmer, 2016) that resemble hot spring deposits (Barbieri and Cavalazzi, 2014).

3.2.2. Mars Science Laboratory mission

The Mars Science Laboratory (MSL) mission involved a single rover, *Curiosity*, which has provided abundant evidence for previously habitable conditions in Gale Crater (e.g., Williams et al., 2013; Grotzinger et al. 2014; Noffke et al., 2015; Rubin et al., 2016; Nachon et al., 2017). This evidence includes sediments deposited in fluvio-lacustrine conditions and detailed evidence of aqueous alteration of volcanic detrital deposits. The goals of this ongoing mission are to determine the role of water in this palaeoenvironment and to study Martian climate through changes in the deposits infilling Gale Crater. This location was chosen because of the extensive diversity of diverse sediments infilling the crater coupled with its potential habitability (Golombek at al., 2012). Well-preserved sedimentary structures, combined with mineralogy, have allowed the most detailed analysis and discussion of habitability and environmental changes in any one location on Mars by virtue of an instrumental payload capable of making elemental, mineralogical, and organogeochemical analyses (Grotzinger et al. 2014; Schieber et al., 2017; Nachon et al., 2017). The MSL mission also has goals of relevance to astrobiology: (i) studying the inventory of organic carbon compounds; (ii) investigating the distribution of CHNOPS; and (iii) identifying potential biosignatures. The Sample Analysis at Mars (SAM) instrument has detected indigenous Martian organics in the form of aromatic and aliphatic hydrocarbons (Freissinet et al. 2015; Eigenbrode et al., 2018).

3.2.3. ExoMars 2020 and Mars 2020

The two upcoming endeavours whose primary goal is to find traces of life on Mars are the ESA-Roscosmos ExoMars 2020 mission (Vago et al., 2017) and the NASA Mars 2020 mission (Williford et al., 2018). Both missions aim to uncover traces of primarily past life (without excluding the possibility of extant life) within their geological contexts at, respectively, Oxia Planum and Jezero Crater. The ExoMars rover is uniquely equipped with a 2 m drill in order to obtain sediments and potential constituent organics from the subsurface, i.e., in a zone protected from surface radiation. ExoMars 2020 will land in Oxia Planum, which has been characterised, by orbital mapping, to have diverse clay mineralogy at the surface, the supposed evidence of changing environmental conditions at the end of the Noachian (Quantin et al., 2016; Bishop et al. 2018; Quantin-Nataf et al., 2019). The NASA Mars 2020 mission will cache selected samples in the first step toward Mars Sample Return. It has sophisticated instrumentation for mapping the elemental and mineralogical compositions of sample surfaces in the form of the Planetary Instrument for X-ray Lithochemistry (PIXL) and Scanning Habitable Environments with Raman and Luminescence for Organics and Chemicals (SHERLOC) instruments. During both missions, morphological and chemical biosignatures would be sought.

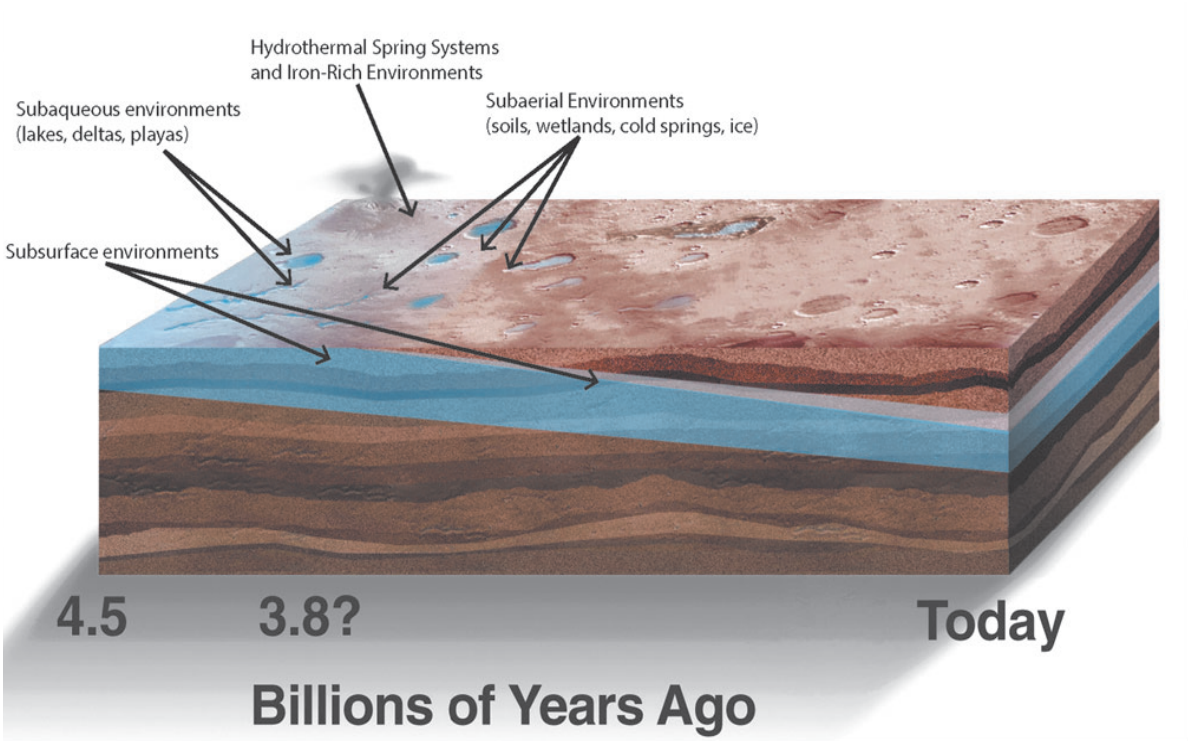

Fig. 8. The changing face of Martian habitability. During the first several hundred billion years, persistent surface water may have opened multiple habitable niches, five groups of which – hydrothermal spring systems, iron-rich environments, subaerial environments, submarine/subaqueous environment and subsurface environment (categorisation of Hays et al., 2017) – are considered plausible for biosignature searches on Mars. After 4.0-3.8 Ga, habitability appears to have ceased at the surface and moved to depth, where it may endure even at present. From Hays et al. (2017), adapted from Des Marais et al. (2008).

3.3. What type of life to search for?

Life, if it emerged on Mars, would most likely have remained in a primitive, prokaryotic stage demanding polyextremophily (Cavalazzi et al., 2019). Although liquid could have re-appeared at the surface either after impact-driven mobilisation of the subsurface cryosphere or through the melting of subsurface ice at the poles during obliquity changes (Mars' axis of rotation is not stabilised by a large moon, as is the case for Earth), these features are considered Mars special regions, and are not yet rover exploration targets. It remains possible that extant life endures in the Martian subsurface (Boston et al., 1992; Cockell, 2014), and that viable cells preserved in the cryosphere could rapidly colonise short-lived habitats, however, the upcoming Mars astrobiology missions ExoMars 2020 and Mars 2020 will more likely analyse terranes in which only fossil organisms could be found.

Primitive, anaerobic, photosynthetic and chemosynthetic prokaryotic biomass represents the kind of life that could plausibly have existed within the habitability constraints on the early Mars. The habitats of these organisms, as decoded from the geological record (Nisbet and Fowler, 1999; Westall et al., 2015) or observed in modern-day Mars analogue environments (Hays et al., 2017; Cavalazzi et al., 2019), and their modes of preservation are critical indications for how microbial life on Mars could have been preserved. The analogy is naturally limited because potential life on Mars may have inhabited a wider range of anaerobic environmental systems, including frozen deserts, ice, hyperarid, hypersaline environments, and

the subsurface, not all of which are represented in either the fossil record or the modern Earth. Where similar environments are found on Earth today with the presence of oxygen, these extreme localities are nonetheless relevant to the search for life on Mars (Martins et al., 2017; Cavalazzi et al., 2019). The early Earth remains, however, the only truly anaerobic analogue for life on the Noachian Mars.

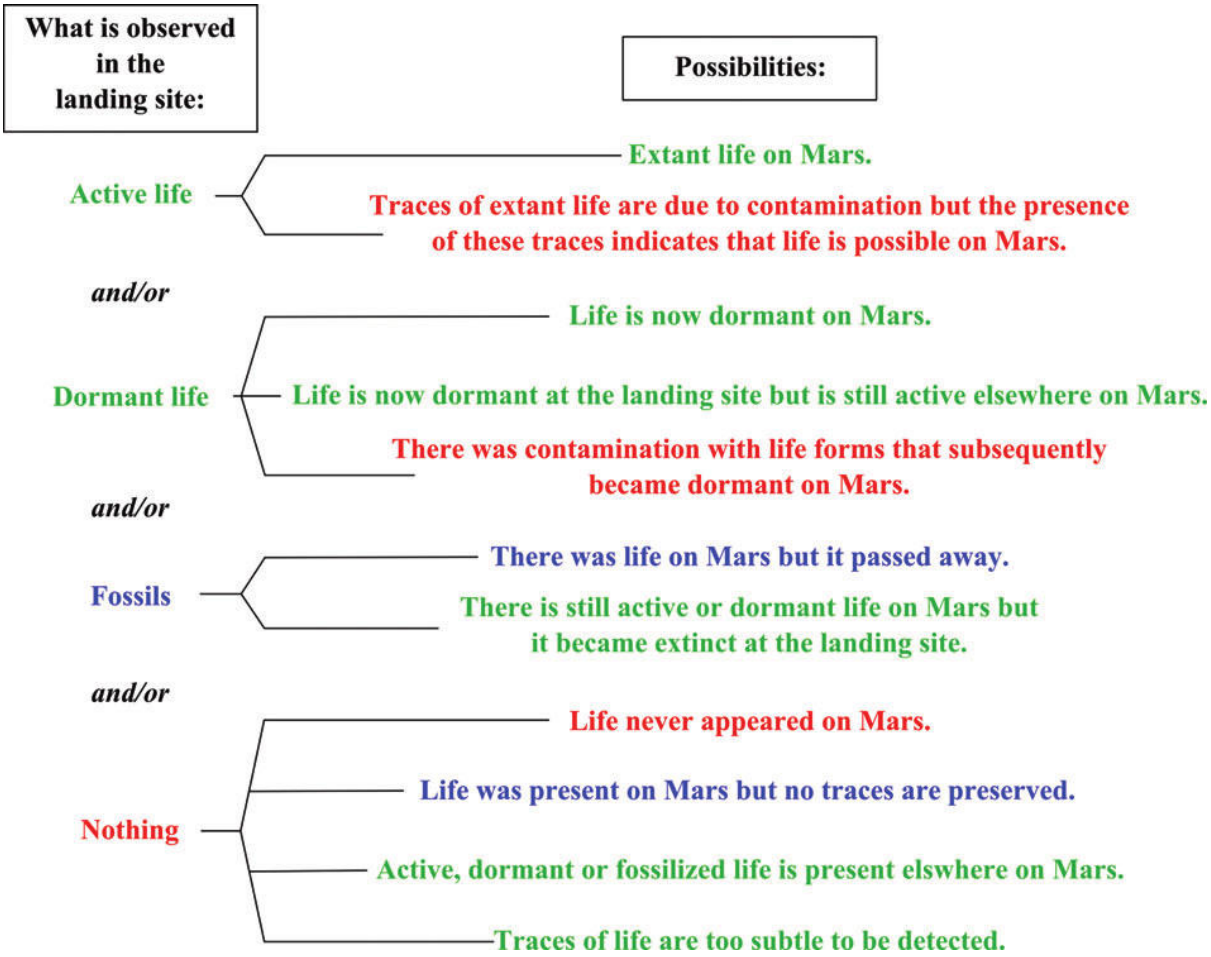

Fig. 9. Possible outcomes of a biosignature search on Mars. It is possible that both false positive and false negative detections could influence the interpretation of the potential fossil record at the landing site. Importantly, failure to detect a biosignature is not incompatible with the presence of traces of life.

3.4. The relevance of the early Earth to Martian astrobiology

Primitive life on the early Earth was mostly anaerobic, extremotolerant and extremophilic (Bosak et al., 2007; Knoll et al., 2016) and thus provides an appropriate framework for understanding the potential nature and distribution of contemporaneous life on the rocky planets and satellites, most notably Mars (Westall et al,. 2015; Vago et al., 2017). Specifically, it represents a maximum of evolution theoretically possible in the equivalent environments to which we have access. Many of the rocky planets of the Solar System may have been habitable during their earliest periods, but have become less so, even to the point of being uninhabitable, over time (Lammer et al., 2009; Westall et al., 2015). Early life on Earth has the potential to inform us about the nature of extinct Martian life, how it could be preserved,

how to search for it and, in the contentious cases for which no unambiguous biomolecules are identified, how its biogenic origin might be confirmed or disproven. Precambrian palaeontology has set the benchmark of stringency against which the biogenicity of potential extraterrestrial biosignatures will need to be tested. As a philosophical Mars analogue, the early Earth delineates the level of scrutiny that must be applied to any putative Martian biosignature and the characterisation required to demonstrate its origin.

The range of widely accepted, well-described, and comprehensively understood signatures of early life (see Chapter II, Manuscript I) represent "exceptions", and not the "rule" for ancient fossils. The majority of modern-day biomass does not enter into the fossil record due to recombination, consumption or degradation, and this would also have been the case prior to the advent of bioturbation at ~540-580 Ma. Many Early Archaean biosignatures have been proposed based on weak geological and geochemical foundations, and many more have been misinterpreted, despite having been subjected to the efforts of the most exacting techniques, by virtue of their enigmatic, ambiguous, and obfuscated geological-geochemical signals. The assessment of potential biosignatures *in situ* on Mars would present new, and greater, challenges. The lessons from the Allan Hills 84001 meteorite (McKay et al., 1996), in which Martian fossils were proposed and subsequently disproven, underline the caveats involved in assessing biosignatures, even using terrestrial laboratories with sophisticated instrumentation. Since some researchers have already started to postulate comparisons between sedimentary fabrics on Earth and Mars – i) strata resembling microbially induced sedimentary structures in the Gillespie Lake Member, Gale Crater (Noffke, 2015); and ii) digitate structures resembling biogenic hot spring deposits in Columbia Hills, Gusev Crater (Ruff and Farmer, 2016) – caution, consideration, multidisciplinary consensus, correlative multi-scalar approaches, and conscious, prudent circumspection in biosignature interpretation are of utmost importance.

We live in interesting times for Martian astrobiology, and both upcoming rover missions and the prospect of Mars Samples Return heralds the advent of ever-flourishing technological and methodological advances, with the eventual goal of studying material brought back from the Red Planet.

4. Presentation of this thesis

This thesis will seek to address multiple topics of relevance to the co-evolution of Earth and Life based on the Palaeoarchaean fossil record throughout Chapters II and III. In Chapter IV, these considerations will be applied to the search for traces of life on Mars with a specific focus on the payload capabilities of the ExoMars 2020 rover *Rosalind Franklin*.

Chapter II, entitled "Multimodal characterisation of the occurrence, nature and biome organisation of Palaeoarchaean microbial life" presents four manuscripts assessing the nature and distribution of life on the Archaean Earth, with a focus on anoxygenic photsynthetic ecosystems. The manuscripts seek to answer the following questions:

- What is the nature of the full range of evidence for palaeobiology throughout the stratigraphy of the Barberton greenstone belt?

- How robust is this evidence and in what ways can it inform us regarding metabolic networks of the Archaean?
- What is the petrological context and sedimentary association of the microbial mats that represent the earliest traces of life in the Barberton greenstone belt and what is their morphological diversity?
- If chertified horizons with microbial mat fabrics reflect examples of common Archaean biomes, what are the prevailing palaeoenvironmental characteristics of these biomes, and are these characteristics consistent through space and time?
- If the palaeoenvironment controls the occurrence and morphology of the organisms within, can detectable morphogenetic biosignatures in macro- and meso-scale bio-structures provide proof of the processes involved in their biogenic origin?
- Is it possible to move from an understanding of Archaean life based only on individual microfossils and advance our understanding of the Archaean biosphere to the scale of biomes and their constituent ecosystems?

At the time of writing, the first two manuscripts have been published, respectively in the Second Edition of *Earth's Oldest Rocks* and in *Precambrian Research*. The fourth manuscript has been published in *Geosciences* and the third manuscript is under review with *Geochimica et Cosmochimica Acta*.

Chapter III, entitled "Biosignatures in the absence of obvious cellular preservation: nano-structural characterisation of putative biomass and palaeo-metallomic trace element biosignatures" presents two manuscripts that aim to deduce the origins of enigmatic carbonaceous material forming clotted structures that potentially represent degraded cellular remains. Clots are a common occurrence of carbonaceous material in Barberton cherts. The manuscripts seek to answer the following questions:

- Are carbonaceous clots of biological origin and, if so, how can their biogenesis be proven in the absence of obvious cellular preservation?
- What information can be garnered regarding the origin of clots from their nanostructure and isotopic and trace element compositions?
- Can trace element compositions associated with carbonaceous material be used as a palaeo-metallomic biosignature that indicated the metabolism of the precursor biomass?
- Can trace element concentration within carbonaceous material decode aspects of the utilisation of metals and metalloids in the environments of early life?

At the time of writing, both manuscripts are in the final stages of preparation for submission.

Chapter IV, entitled "Geological-geochemical-geobiological testing of the ExoMars 2020 rover payload instrumentation" seeks to conduct similar geological-biogeochemical assessments as in Chapters II and III taking into the limited instrumentation capabilities of Mars rovers. Focussing on the scientific protocol of the ExoMars 2020 rover, the two manuscripts within seek to answer the following questions:

- To what extent can rover instrumentation alone be used to provide constraints of geological environment and petrological context?
- How does the unique ExoMars 2020 payload suite and protocol compare to standard geological fieldwork and sample analyses as conducted on Earth, and how should the key differences be incorporated into a successful analytical strategy?
- What are the limitations inherent in making geological-biogeochemical interpretations on core samples, i.e., samples of limited dimensions and pre-defined morphologies that may hinder observation, and how should this be mitigated during the ExoMars mission?
- If given astrobiologically relevant analogue samples, to what extent can a complete characterisation of the nature of the organic material and its context be interpreted by the ExoMars 2020 Pasteur payload?
- Can the ExoMars 2020 payload distinguish unambiguously biological organic material from ambient organic material of unspecified origins?

At the time of writing, the first manuscript is in revision with *Planetary and Space Science* and the second manuscript is in preparation for submission.

Chapter V presents a summary of the conclusions drawn from each of the research chapter, highlights the advancements made and ideas raised throughout the course of the thesis, and provides a range of perspectives for furthering these studies in the future.

Chapter II – Multimodal characterisation of the occurrence, nature and biome organisation of Palaeoarchaean microbial life

This chapter contains work published in the following articles:

Hickman-Lewis, K., Westall, F., Cavalazzi, B., 2018. Trace of early life from the Barberton greenstone belt. In *Earth's Oldest Rocks*, Second Edition (Eds. Van Kranendonk, M.J., Bennett, V.C., Hofmann, J.E.). Elsevier, pp. 1029–1058.

Hickman-Lewis, K., Cavalazzi, B., Foucher, F., Westall, F., 2018. Most ancient evidence for life in the Barberton greenstone belt: microbial mats and biofabrics of the ~3.47 Ga Middle Marker horizon. *Precambrian Research* **312***,* 45–67.

Hickman-Lewis, K., Gautret, P., Arbaret, L., Sorieul, S., De Wit, R., Foucher, F., Cavalazzi, B., Westall, F. Mechanistic morphogenesis of organo-sedimentary structures growing under geochemically stressed conditions: keystone to the interpretation of some Archaean stromatolites? In press, *Geosciences Special Edition "Microbialites"*.

This chapter also includes the work contained in the following submitted manuscript:

Hickman-Lewis, K., Gourcerol, B., Westall, F., Manzini, D., Cavalazzi, B. Reconstructing Archaean microbial biomes using trace and rare earth element systematics. Under review, *Geochimica et Cosmochimica Acta*.

Introduction

The Barberton greenstone belt (BGB) is one of the two well-preserved Early Archaean (~3.6 to 3.2 Ga) successions – together with the East Pilbara of Western Australia – from which most convincing evidence for early life has been described. Understanding the geology and fossil record of this sequence is therefore of paramount importance in constraining both the palaeoenvironments of the earliest biomes and the metabolic networks of the earliest ecosystems. If the fossiliferous horizons of the BGB are to be used as Earth-based examples of the primitive life that might have colonised a Noachian Martian biosphere, it is further critical to develop and demonstrate a fossil-calibrated understanding of the occurrence, nature and, where possible, palaeoecological organisation of these primitive ecosystems. Proof of biogenicity requires a combinatorial approach creating a data network relating palaeoenvironment, morphology and biogeochemistry. In this chapter, split into four manuscripts, an endeavour is made to comprehensively characterise some of the biomes of Palaeoarchaean life from the BGB.

With the exception of the Mesoarchaean Moodies Group, robust, widely accepted biosignatures in the BGB are restricted to the silicified volcanogenic horizons represented by banded and massive cherts. Palaeoarchaean banded carbonaceous chert horizons sometimes contain microbial mats and/or stromatolites, which are generally considered promising evidence for life. These microbial mat communities were anaerobic and likely exhibited some degree of extremotolerance, whether to one or more of elevated salinity, UV radiation, elevated seawater temperatures, or the presence of highly concentrated metal and metalloid elements if growing in the vicinity or downstream of the widespread volcano-hydrothermal activity that characterised the Archaean hydrosphere. Such organo-sedimentary structures are ascribed high importance in the ExoMars 2020 rover search for Martian biosignatures. Herein is presented a multi-modal, multi-scalar appraisal of biogenic organo-sedimentary structures from the BGB (together with one informative example from the Pilbara). These studies consider bulk and *in situ* stratigraphy and micro-stratigraphy in two and three dimensions, the characteristics of the aqueous chemistry of the palaeodepositional environment, characterisation of the carbonaceous material that constitutes these biosignatures, and comparison between these fossils and potential modern analogues.

The first manuscript presents a review of the various proposed traces for life in the BGB, accompanied with a brief critical review of the evidence for the biogenicity of each. This review finds that there is much convincing evidence for a diverse Palaeoarchaean biosphere which, when combined with available knowledge from the East Pilbara, suggests that early life had already evolved to occupy multiple niches, both photosynthetic and chemosynthetic, by 3.3-3.5 Ga. The review also notes that biosignatures are most common in the vicinity of actively silica-mineralising systems, i.e., the volcano-hydrothermal palaeoenvironments that are reflected in banded and massive carbonaceous chert horizons. Since the preservation of microbial biomass is otherwise highly variable throughout the Precambrian fossil record, it is perhaps most appropriate to direct the search for biosignatures on Mars toward volcano-sedimentary outcrops that exhibit some indication of this significantly enhanced preservation potential. The material described in this manuscript should be considered the maximum potential stage of evolution (i.e., prokaryotic) for a similar biosphere that may have existed in the comparable, contemporaneous habitable niches on Mars.

The second manuscript presents in more detail the case for the biogenicity of the oldest traces of life in the BGB, microbial mats of the 3.472 Ga Middle Marker horizon. Using a micropalaeontological approach of combined petrography – optical microscopy, SEM-EDS and Raman spectroscopy (augmented by X-ray CT in the fourth manuscript of this chapter) – a case is built for the biogenicity of these features founded on multiple bio-indicative characteristics related to their occurrence, morphology and biogeochemistry. Broad comparability between this horizon and other contemporaneous fossiliferous cherts in terms of apparent microbial consortia, volcano-hydrothermal setting and preservation in silica-rich fluids implies that the Middle Marker horizon represents the oldest example of a regionally important Palaeoarchaean microbial biome.

In light of this, the third manuscript presents a combination of bulk ICP-MS and targeted *in situ* laser ablation ICP-MS to conduct a quantitative major, trace and rare earth element plus yttrium (REE+Y) study of four fossiliferous cherts spanning almost the entirety of the 150 Ma Palaeoarchaean fossil record of the BGB. This study is key to contextualising microbial biosignatures, and finds notable similarities between the four studied horizons and concludes that while the regional environment of the Palaeoarchaean was a hydrothermally influenced ocean, the horizons specifically colonised by anoxygenic photosynthetic microbial life represent intersectional disequilibria between marine, riverine and hydrothermal aqueous inputs. Using the characteristics of normalised REE+Y plots, this manuscript proposes that shallow-water epicontinental basins were regionally significant loci for microbial mat consortia across the Palaeoarchaean Earth. This gives a previously unrecognised importance to continental terrigenous inputs as far back as the Palaeoarchaean and suggests that partially restricted basins with marine and terrestrial inputs were important microbial biomes on the early Earth. Moreover, the similarity between the characteristics of the four studied horizons supports the idea that widespread photosynthetic biomes developed and flourished rapidly in the Palaeoarchaean. In essence, this manuscript states that although microbial life had emerged within multiple niches by 3.3-3.5 Ga (as described in the first manuscript), well-developed microbial mat consortia may be detected within recurrent palaeoenvironments that may have formed a regionally significant habitable realm (a "Gaian biosphere"). Such findings could be applied in the search for life on Mars, where regionally important, although perhaps not interconnected, bodies of water – approximately temporally equivalent to those of the Palaeoarchaean but perhaps of a more ephemeral nature – may have hosted biomes and ecotones of life in the Noachian.

The third manuscript suggests that fossilised microbial biomes can be characterised within the framework of their palaeoenvironment as in the case of modern biomes. This explicitly states that the elemental budget of the palaeoenvironment is the governance of the biome within, and may control, at all scales, the reactions between members of the ecosystems forming the biome. Since individual microfossils are rarely preserved in even rapidly mineralising Archaean cherts (and it is thus usually impossible to define biocoenoses on a case-by-case basis), we assess in the final manuscript whether organismal characteristics, in three dimensions, and at the scale of individual laminations, may shed light on the *in vivo* processes of the ecosystem. The fourth manuscript conducts a geobiological-palaeobiological study to determine whether fossilised microbialites (stromatolites and microbial mats) can preserve morphologies indicative of interactions with the geochemistry of their palaeoenvironment. This study conducts a comprehensive geobiological and biogeochemical characterisation of natural

and experimentally grown microbial mats that developed in saline solutions or various chemistries using correlated optical microscopy, SEM, μPIXE, Raman spectroscopy and X-ray μCT. This manuscript proposes the use of morphogenetic biosignatures where possible in lieu of morphological biosignatures, since morphogenetic biosignatures identifiable by correlative microscopy approaches reflect unambiguously biological processes in organo-sedimentary structures, thus overcoming the ambiguity of the biological interpretation of morphology. Morphogenetic biosignatures may potentially be used to identify biocoenoses within fossiliferous horizons in deep time.

These four manuscripts demonstrate the variety of proposed biosignatures in the Palaeoarchaean and highlight the wide range of techniques required in the demonstration of the palaeoenvironment, morphology and biogeochemistry of the earliest traces of life. Although photosynthetic biosignatures, usually in the form of microbial mats and stromatolites, present the most robust biosignatures in terms of deducing biogenicity and ecophysiology, their comprehensive analysis is nonetheless a challenging endeavour requiring a correlative microscopy approach that will not be entirely possible *in situ* on Mars. Mars rover instrumentation has the potential to conduct fundamental characterisation of the petrography, petrology, and potentially chemistry of these fossils, i.e., to determine their context and macrostructural morphology, and to parameterise their biogeochemistry, and will govern the selection of appropriate specimens for Mars Sample Return.

Manuscript 1 – Traces of early life from the Barberton greenstone belt, South Africa

Abstract

There is much convincing evidence for early life in the Barberton greenstone belt (3.47-3.22 Ga), portraying a diverse Palaeoarchaean biosphere that occupied both marine and terrestrial habitats. This stands testament to an already widespread distribution and diversity of life on the early Earth. We here present an up-to-date review of fifty years of accumulated evidence for life in the Barberton greenstone belt and outline and evaluate the reasoning for biogenicity in each case. Fossils of microbial life are present throughout the stratigraphy, from the oldest chert unit (the Middle Marker horizon) to the uppermost siliciclastic sediments (the Moodies Group). Although putative phototrophs could develop in nutrient poor, oligotrophic areas away from hydrothermal vents, interpreted chemotrophs appear to have been strongly controlled by proximity to hydrothermally derived nutrients. The Palaeoarchaean was a time of surprising biological diversity, and this record is best accessed by investigating the biomes preserved in chertified horizons.

1. Introduction

The Palaeoarchaean (3.55-3.22 Ga) Barberton greenstone belt (BGB) of southern Africa preserves a volcano-sedimentary sequence consisting of folded volcanic and sedimentary rocks that have been divided into three major stratigraphic units: the 3.55-3.26 Ga Onverwacht Group, the 3.26-3.23 Ga Fig Tree Group, and the 3.23-3.22 Ga Moodies Group (Fig. 1: Viljoen and Viljoen, 1969; Kröner et al., 1991, 1996; Byerly et al., 1996, 2018; Lowe and Byerly, 1999, 2007). Lowe and Knauth (1977), Lanier and Lowe (1982), and Hofmann et al. (2013) describe the full range of silicified sedimentary rocks in the BGB. Silicified volcaniclastic and pyroclastic units are the most significant, usually having the appearance of black-white-grey-green layered cherts. Rarer dacitic volcanic detritus has also been described in some sedimentary units (Lowe, 1999), as have other felsic inputs (Lanier and Lowe, 1982), although these represent a minor component in the dominantly mafic-ultramafic stratigraphy of the Onverwacht Group. Grey-black stratiform cherts are a minor component of the stratigraphy but, as outlined herein, are significant in the search for biosignatures. These units reflect silicified mixtures of clastic, volcanic, and carbonate material. Preserved sedimentary features and geochemical signatures indicate aspects of their local palaeoenvironments (Lowe and Knauth, 1977; Lanier and Lowe, 1982; Paris, 1985; Paris et al., 1985; Hofmann, 2011; Hofmann et al., 2013; Westall et al., 2015a). Stratiform sedimentary cherts are commonly cut, and intruded, by penecontemporaneous vein cherts that, together with evidence for underlying zones of silicification, have been used to infer a widespread, diffuse hydrothermal environment (Hofmann and Bolhar, 2007; Hofmann and Harris, 2008; Westall et al., 2015a, 2018), typical also of the contemporaneous Pilbara Craton (e.g. Nijman et al., 1999; Van Kranendonk, 2006).

Indeed, the BGB is one of only two well-preserved Archaean sequences on Earth, the other being the greenstone belts of the Pilbara Supergroup in the contemporaneous East Pilbara Terrane of the Pilbara Craton, Western Australia (Hickman and Van Kranendonk, 2012; Van Kranendonk et al., 2018). Unique to these two terranes are their low metamorphic grade, from prehnite-pumpellyite (100-250˚C) to lower greenschist facies (250-300˚C) (Tice et al., 2004;

van Zuilen et al., 2007). Regional metamorphism in the BGB has been dated at 3.3-2.9 Ga (Dziggel et al., 2002; Byerly et al., 2018).

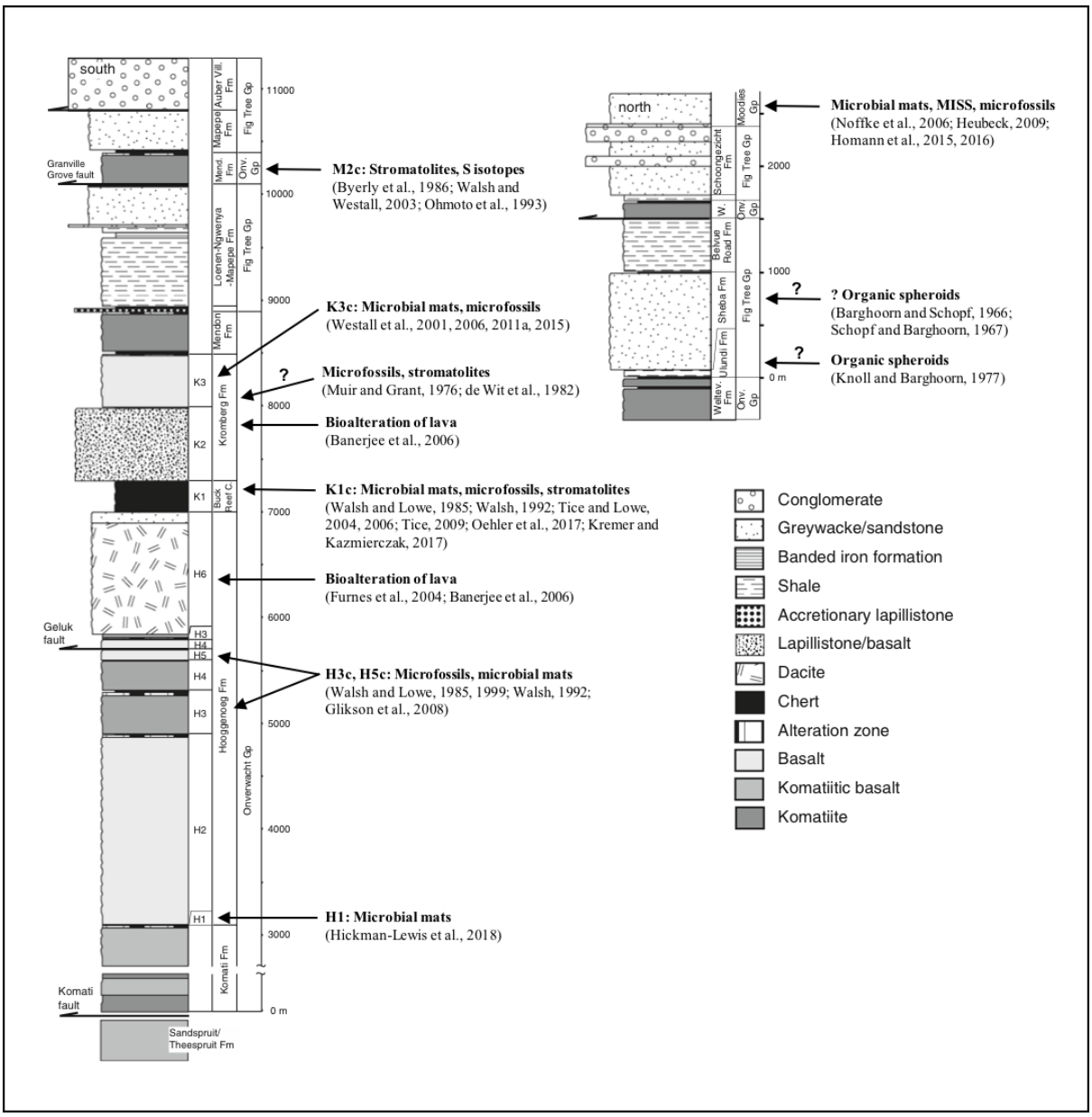

Fig 1. Generalised stratigraphy of the Barberton greenstone belt. Traces of life have been proposed from throughout this sequence, from the base of the Hooggenoeg Formation to the uppermost reaches of the Moodies Group. Adapted from Hofmann (2011).

2. Traces of the ancient biosphere

In addition to its being a window on early Earth processes, the BGB is also recognised for its preservation of a rich diversity of life. Morphological, geochemical, and mineralogical biosignatures are commonly put forward as tell-tale signs of the ancient biosphere. The most compelling evidence for ancient life in the BGB rests on the morphological biosignatures preserved in stratiform cherts with textural evidence for deposition in shallow-water environments (e.g., Walsh, 1992; Tice and Lowe, 2004, 2006; Westall and Southam, 2006;

Westall et al., 2011a, 2015a; Hickman-Lewis et al., 2018). Traces of early life in the BGB have also been described from the shallow subsurface of sedimentary environments (Westall et al., 2015a; Homann et al., 2016), from the surfaces of volcanic clasts (Westall et al., 2006, 2015), as endolithic trace fossils in pillow basalts (Furnes et al., 2004; 2007; Banerjee et al., 2006), as microbial mats on the surfaces of shallow water and beach sediments (Walsh, 1992; Walsh and Lowe, 1999; Tice and Lowe, 2004, 2006; Tice, 2009; Westall et al., 2006, 2011, 2015; Hickman-Lewis et al., 2018), in peritidal-terrestrial settings (Noffke et al., 2006; Heubeck, 2009; Homann et al., 2015), and, possibly, in the water column (Walsh, 1992; Javaux et al., 2010; Oehler et al., 2017). These diverse traces of life have been reported from throughout the BGB stratigraphy, being particular rich in the 3.416-3.334 Ga Kromberg Formation and in the 3.22 Ga Moodies Group (Fig. 1).

Although identification of compartmentalised organic material had been described in the BGB around fifty years ago (e.g., Pflug, 1966; Engel et al., 1968; Nagy and Nagy, 1969), previous reviews summarising the many reported Archaean microfossils (Schopf and Walter, 1983; Schopf, 1992; Altermann, 2001) agree that all but two instances of these early reported cellular remains should be treated as non-fossils, the exceptions being those of Muir and Grant (1976) and Knoll and Barghoorn (1977).

2.1. The 3.472-3.416 Ga Hooggenoeg Formation, Onverwacht Group

The Hooggenoeg Formation consists of komatiite and basalt with interbedded thin, silicified sedimentary horizons, and has been interpreted as an episodic volcanic environment characterised by pulses of volcanism punctuated by quiescent periods of sedimentation (Lowe and Byerly, 1999, 2007). Chertified horizons are often stratiform, whereas massive vein cherts occur both as bedding-parallel units and nonconformable veins, which intrude and distend volcanic beds (Hofmann and Bolhar, 2007).

2.1.1. Middle Marker (H1)

The 3.472 Ga Middle Marker horizon contains finely laminated, carbonaceous, crinkly, non-isopachous horizons interpreted as microbial mats with flat-lying and micro-tufted morphologies (Hickman-Lewis et al., 2018) (Figs. 2-3). These structures meet most of the morphological criteria for biogenicity: (1) they are fine, kerogenous laminations exhibiting anastomosis; (2) they are wavy-crinkly on large and small spatial scales and are laterally discontinuous at the micron scale, but broadly continuous at the centimetre scale; (3) their gross structure approximates that of modern microbial mats, i.e., layers of organic-rich material with a film- or filament-like appearance alternating with layers of detrital material or entrained particles; (4) the presence of folded, torn, crumpled, and rolled fragments demonstrably indigenous to the laminations strongly imply an initial cohesive quality; (5) their non-isopachous laminae thicken toward crests, suggesting growth out of the laminar bottom-flow waters toward more dynamic, nutrient-rich waters above or a phototactic microbial component; (6) they mantle macroscale sedimentary features; and (7) their growth is templated by the underlying grain topography and entrained particles are oriented, suggesting an effort to biostabilise the sedimentary surface during colonisation (Hickman-Lewis et al., 2018).

These seven lines of evidence demonstrate that these structures were surface-colonising, bio-stabilising biofilms. Their micro-tufted and crinkled relief resembles that of anoxygenic photosynthesising microbial communities and is dimensionally comparable with

similar micro-tufted biofabrics from the contemporaneous Dresser Formation (Noffke et al., 2013). Some mats have a plastically deformed morphology, giving a macro-tufted appearance, evidencing their *in vivo* plasticity (Fig. 3). The degraded remains of microbial laminae, including fragments of contorted biofilms, are common (Figs. 2-3). Three-dimensional studies using μCT have shown that some entrained particles are surrounded by string-like aggregates of carbonaceous material that resemble filaments (Hickman-Lewis et al., 2019).

These microbial mats occur in shallow-water, bedded volcaniclastic sandstones and siltstones and, more rarely, in coarse volcaniclastic sandstones. The anticorrelation of mat horizons with volcaniclastic influx indicates that they cyclically flourished on newly deposited volcanogenic sediments, but perished with changing hydrodynamic conditions, when a new depositional cycle began. The volcaniclastic substrate provided bio-essential and bio-functional elements for their development during a non-depositional regime, but the mat community perished during heavy influxes of coarse, tuffaceous material. Their recurrent recolonisation of the substrate implies in-sediment motility. Lenticular microstructures, similar to those interpreted as microfossils by Walsh (1992), Sugitani et al. (2010, 2015), and Oehler et al. (2017), are present in some mat laminae but do not possess the biologically indicative morphologies of the Pilbara or Kromberg Formation examples. Massive black carbonaceous cherts in the Middle Marker horizon, much as for many other Onverwacht Group (and Pilbara) cherts, contain abundant organic material with plausibly biogenic precursors, but no microfossils.

2.1.2. Hooggenoeg Formation cherts H3c and H5c

Microbial traces in the Hooggenoeg Formation were first described by Walsh and Lowe (1985) and Walsh (1992), who reported laminations of fine carbonaceous material with solid and hollow filamentous objects in the H5c and H3c cherts (Fig. 5). Simple, hollow, unbranched filaments, 0.2-2.5 mm in diameter, have regular, micrometre-scale constrictions, emanate from carbonaceous particles, and are associated with stratiform laminations interpreted as phototrophic mats. These filaments were interpreted as bona fide microfossils.

In an extensive petrographic study of the Hooggenoeg and Kromberg formations, Walsh and Lowe (1999) identified three types of chert; black and white banded, black laminated, and massive black chert. Of these, the black and white banded cherts contain fine, microbial mat-like, carbonaceous laminations interbedded with layers of simple and composite carbonaceous grains (Fig. 5A-B). Walsh and Lowe (1999) noted that the mat-like layers are overlain by volcaniclastic deposits, implying that growth was restricted or halted by these events (see Middle Marker microbial mats in Section 2.1.1). Massive black and black laminated cherts from the Hooggenoeg Formation do not feature mat-like laminations but do contain aggregated carbonaceous matter forming clotted textures, speculatively interpreted as of biogenic origin (Lowe and Knauth, 1977; Walsh and Lowe, 1999). The morphological observations of biosignatures in these Hooggenoeg cherts are supported by exceptionally negative in situ C-isotopic fractionations ($\delta^{13}C$ = –40.8‰; Walsh and Lowe, 1999) that are compatible with primitive, perhaps methane-based, microbial metabolisms.

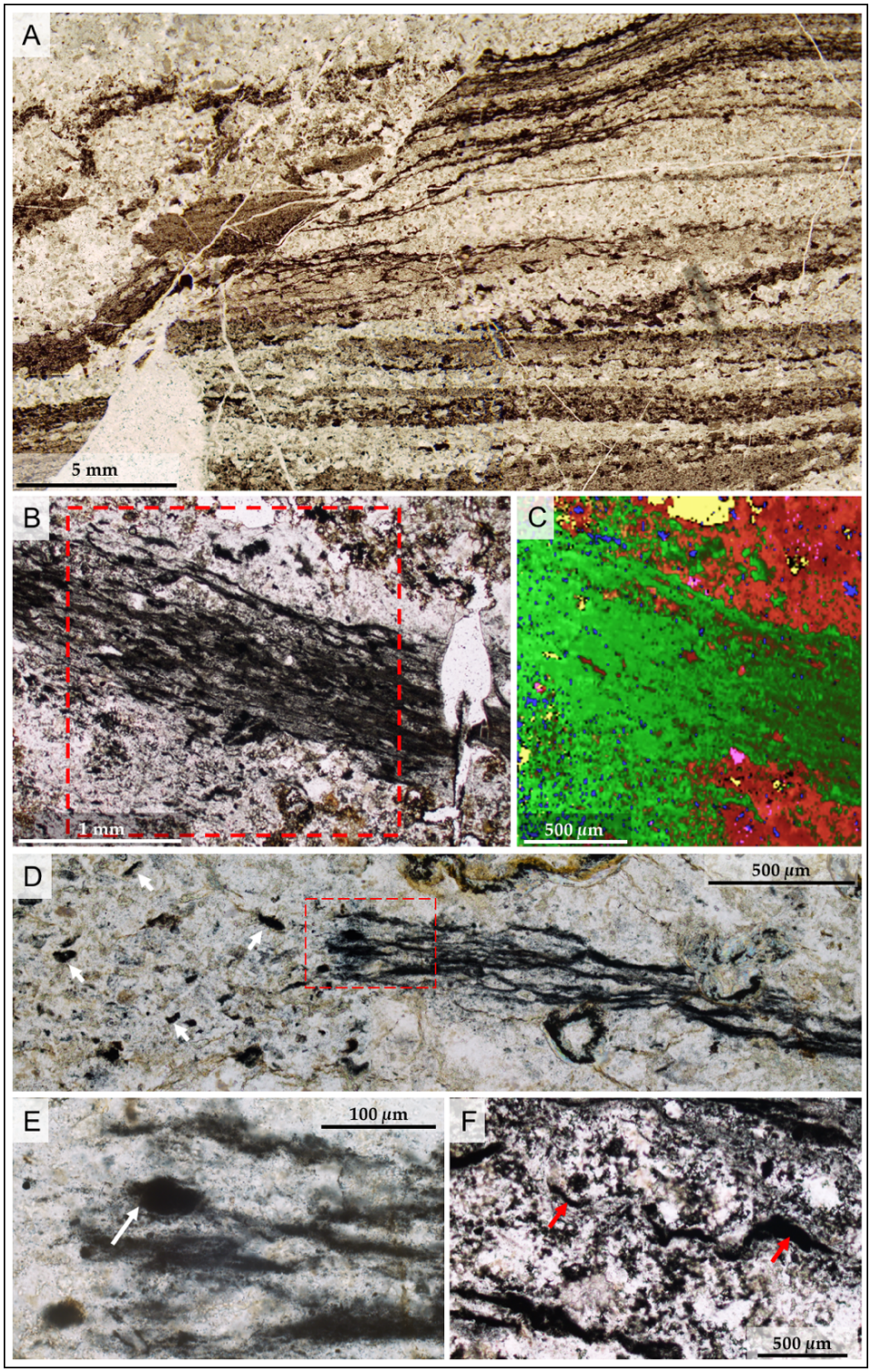

Fig. 2. Crinkly, microtufted, biofilm-like laminations from the Middle Marker (H1 chert) interpreted as microbial mats. **A**) Crinkled, micro-tufted mats that mantle sedimentary fabrics. **B**) Thick, crinkly microbial mat with a gross structure of carbonaceous laminations separated by siliceous lenses. **C**) Raman map of the indicated area in B, in which carbon = green, quartz = red-orange, anatase = blue, siderite = fuchsia, araldite (resin) = yellow. **D-E**) Frayed mat; E shows indicated area in D. Arrows indicate lenticular objects similar to proposed microfossils in Figure 6 but demonstrably part of the mat, of variable mineralogical composition, and thus likely biomorphs. **F**) Carbonaceous flakes and wisps, which may represent eroded fragments of crinkly microbial mats. All images from Hickman-Lewis et al. (2018).

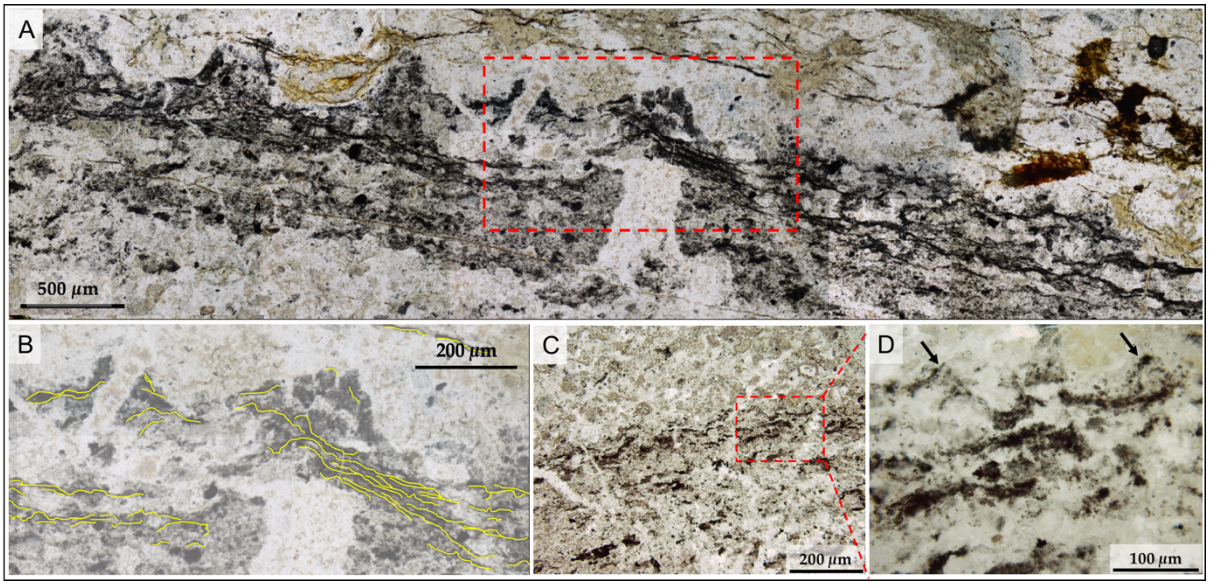

Fig. 3. Laminations with plastically deformed, pseudo-tufted morphologies, interpreted as microbial mats, from the Middle Marker horizon (H1 chert). **A**) Microbial mats with a gross structure of lower filament-like laminations intercalated with rounded particles and upper dominantly granular zones. **B**) Interpretative diagram of filaments within the tuft indicated in A. Very few filaments continue into the tuft but those that do signify primary growth and in vivo plasticity. **C-D**) Degraded mat; **D**) two poorly preserved relict tufts (arrowed). Poor preservation is likely due to taphonomy within a coarse volcaniclastic sandstone siltstone. All images from Hickman-Lewis et al. (2018).

Glikson et al. (2008) described granular, spheroidal, cell-like objects from cherts H5c and H3c, which show patterns akin to cell division, compartmentalisation, and cell wall degradation (Fig. 5D-F). These putative fossils are compared with modern fossil *Methanocaldococcus jannaschii*, although their morphology is so simple and preservation so poor that it is challenging to prove biogenicity on these grounds, let alone determine species.

2.1.3. Upper Hooggenoeg hyaloclastites and basalts

Numerous recent studies have focused on the traces of primitive life in basalts from both terrestrial and marine environments (e.g., Thorseth et al., 1995; Furnes et al., 1999, 2001; McLoughlin et al., 2010; Kelly et al., 2014). Just hours after eruption, microbial colonisation of basaltic rinds can begin (Thorseth et al., 1995; Furnes and Staudigel, 1999; Furnes et al., 1999, 2001). In submarine pillow lavas, these biosignatures take the form of two alteration textures: a granular coalescence of submicron-sized spherical particles or a network of irregular tubular structures; the latter is often attributed to biological processes (Furnes et al., 2001, 2007). Both textures are abundant in the upper hundreds of meters of modern oceanic crust, and the discovery of a suite of textures comparable to tubular microstructures in the upper Hooggenoeg and lower Kromberg formations (Furnes et al., 2004; Banerjee et al., 2006) has prompted considerable debate regarding their utility as biosignatures.

Microtubular structures in 3.472 to 3.456 Ga Hooggenoeg hyaloclastites and pillow lavas (Fig. 4A: Armstrong et al., 1990) are better preserved than those found in the Kromberg pillow lavas (Fig. 4B). Broadly, these structures are tubules 1-9 mm wide and up to 200 mm long and are dominantly titanite-mineralised with accessory chlorite and quartz (Fig. 4C-D). Developing in the vicinity of fractures, they exhibit irregular, asymmetric growth patterns, and

peculiar instances of bifurcation or sharp changes in direction when encountering another tubule. These mineralised structures resemble modern microbial alteration textures, although they are generally appreciably larger (Banerjee et al., 2006). Elemental enrichments in C, N, and P were reported by Furnes et al. (2004) and Banerjee et al. (2006); C was generally found to be enriched in samples containing a high abundance of microtubules (Fig. 4E-F; Furnes et al., 2004). Additionally, a slight separation between the mean $\delta^{13}C$ of glassy rims and inter-pillow hyaloclastites (more negative) versus their crystalline interiors (less negative/more positive) of pillows signifies some divergent processes, and the range of $\delta^{13}C$ values was deemed too large to fit a Rayleigh fractionation curve for decarbonation reactions (Banerjee et al., 2006). The authors ascribe these anomalies to microbial activity, though neither individual microfossils nor metabolisms have been unambiguously linked to these structures (Banerjee et al., 2006; Furnes et al., 2007).

Furnes et al. (2004, 2007) propose a formational model by which water, flowing incessantly through the cavities of volcanic rock, both provides nutrients to colonies of chasmolithic microorganisms and removes waste products contributing to alteration of the rock. Eventually, the fractures and cavities become completely sealed by titanite, although in more recent examples phyllosilicates, such as the zeolite phillipsite, are more common alteration minerals (Cavalazzi et al., 2011). The hypothesis of Furnes et al. (2004, 2007) requires that titanite is an early alteration product, forming at temperatures clement to life. If, indeed, these features are microbial, they would represent traces of endolithic organisms, possibly actively boring euendoliths fuelled by Fe^{2+} and Mn^{2+} ions that are replete in the alteration interface of dissolving volcanic glass.

A recent geological-geochemical-geochronological series of studies has brought the biogenicity of the Hooggenoeg tubular structures into question (McLoughlin et al., 2012; Grosch and McLoughlin, 2014, 2015; Grosch et al., 2016). Initial concerns were raised by McLoughlin et al. (2012), who were unable to relocate the carbon-rich tube linings (Fig. 4E-F) described by Furnes et al. (2004) and Banerjee et al. (2006). Grosch and McLoughlin (2014) further argued that the microtubules are of too wide a range in both diameter and length to be compatible with a biogenic population, having a size distribution an order of magnitude larger than expected. Moreover, the age of the infilling titanite, when measured using U-Pb systematics, yields values of 2.819 ± 0.20 Ga to 2.913 ± 0.31 Ga, some 650 Ma younger than the host rock (Grosch et al., 2016). Consequently, these authors consider the structures to have failed the pivotal tests of antiquity and syngenicity. Instead, they suggest the tubular structures formed through growth of porphyroblasts genetically crystallising as a product of retrograde thermal-contact metamorphism at temperatures around 240-360˚C (McLoughlin and Grosch, 2014; Grosch and McLoughlin, 2014, 2015; Grosch et al., 2016). μX-ray absorption near-edge spectroscopy (μXANES) shows that, at the Fe-K edge in chlorite, titanite is located in low-temperature chlorite bands and microdomains, compatible with retrograde metamorphic formation (Grosch et al., 2016). Such an interpretation supports an observed morphological continuum of titanite-mineralised structures created through a process such as grain boundary migration.

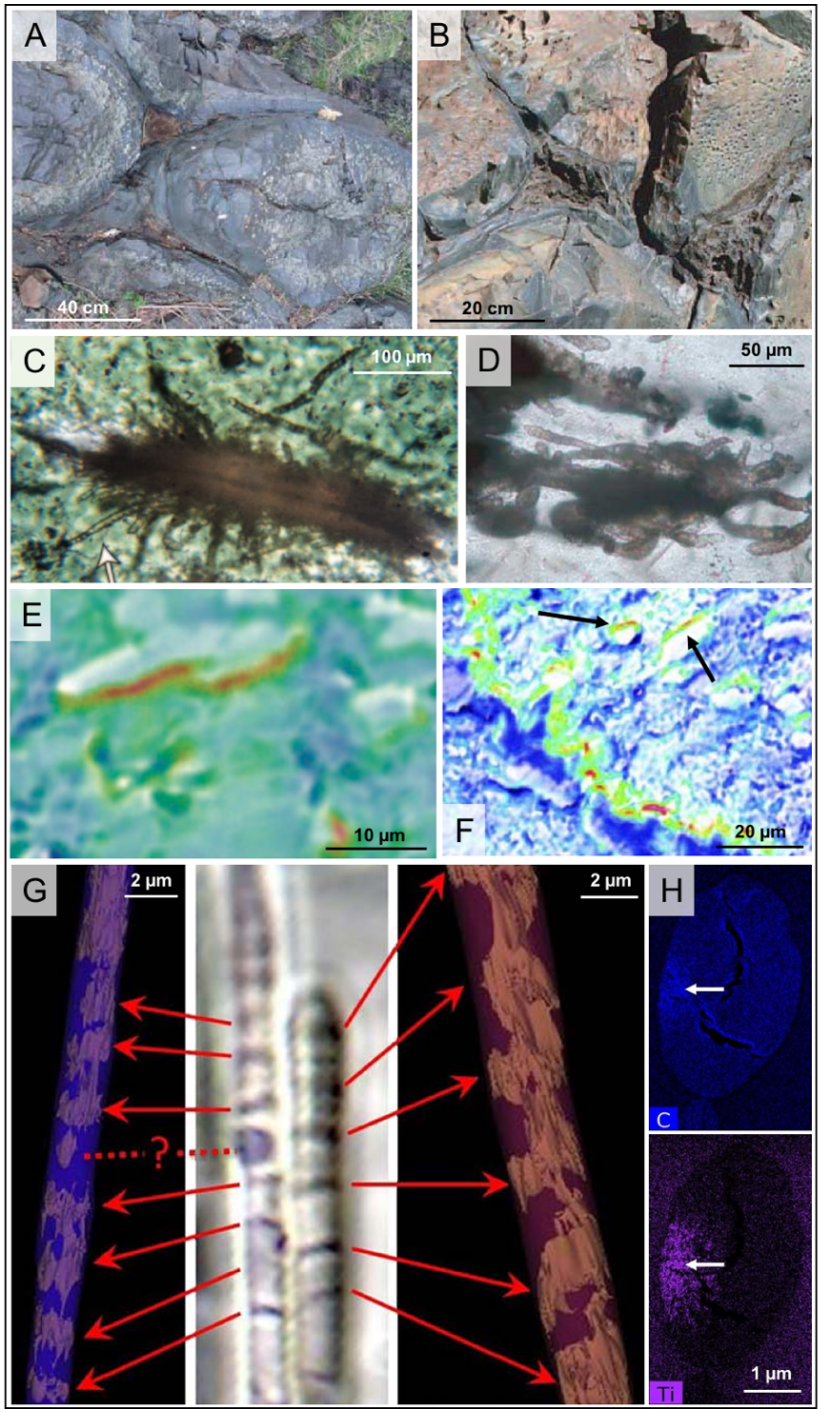

Fig. 4. Microtubules from the Hooggenoeg and Kromberg formations compared with recent examples from the Argo Abyssal Plain. **A**) Outcrop photograph of well-preserved pillow basalts and hyaloclastites in which the Hooggenoeg microtubules are found. **B**) Outcrop photograph of vesicular pillow lavas in which are found the Kromberg tubules. **C-D**) Putative bacterial microtubule morphologies from interpillow hyaloclastite in the Hooggenoeg Formation. See septate appearance in D; **E**) Carbon map for the arrowed tubule in C showing concentration of carbon within. **F**) Carbon concentrations at the margin of titanite-mineralised structures and within tubules (arrowed). **G**) Recent tubules from the Argo Abyssal Plain, showing correlation of void space with features previously interpreted as septa. **H**) Co-occurrence of organic C (top) and Ti (bottom) within an Argo Abyssal Plain microtubule, possibly implying C as a locus for titanite mineralisation. Images A-B, D, and F from Banerjee et al. (2006), courtesy of Neil Banerjee; C and E from Furnes et al. (2004), courtesy of Harald Furnes; G-H from Wacey et al. (2017), courtesy of David Wacey.

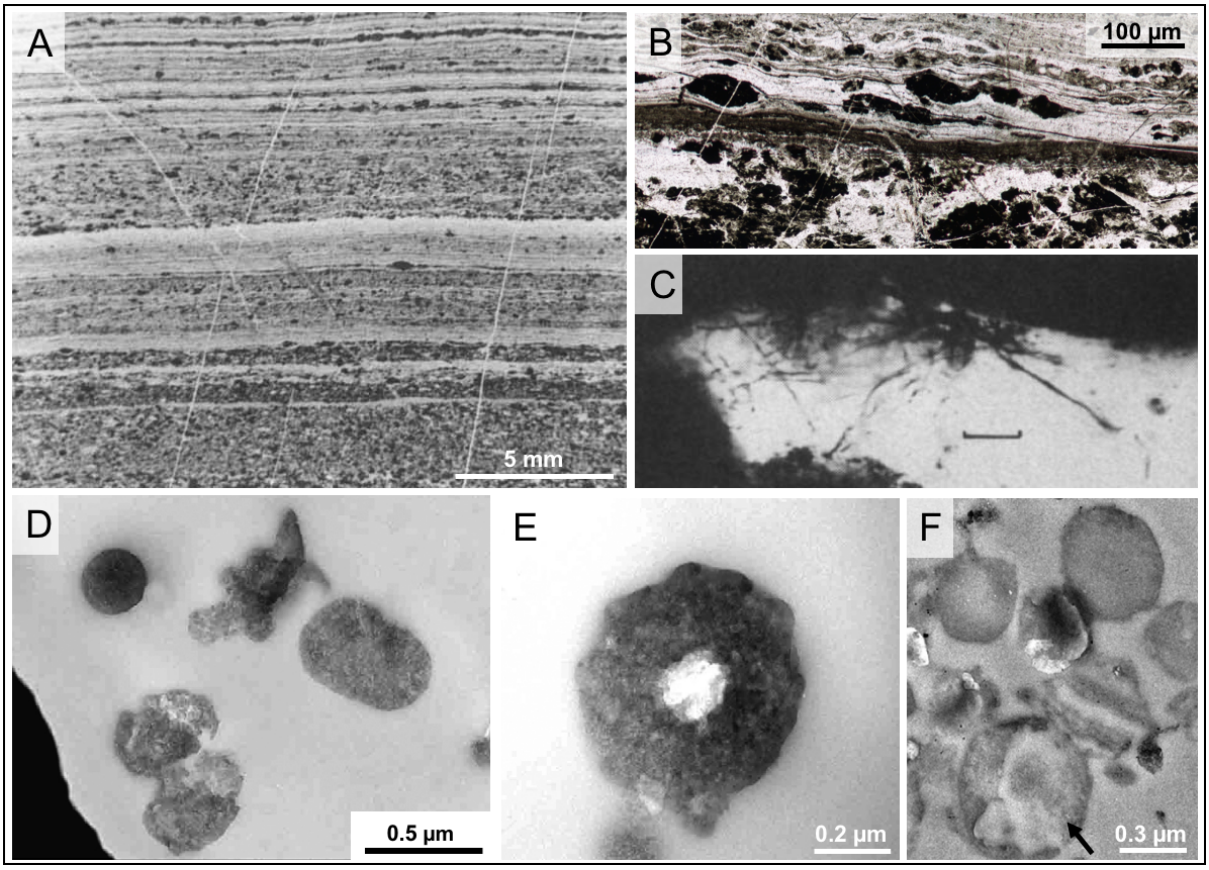

Fig. 5. Interpreted microbial fabrics and microfossils from the Hooggenoeg Formation (cherts H5c and H3c). **A**) Photomicrograph of laminated carbonaceous material interpreted as phototrophic microbial mats. Note the cyclicity of mats, separated by near-pure chert layers. **B**) Optical photomicrograph of composite carbonaceous particles trapped between laminations. The plastic deformation of laminations around the particles is testament to their in vivo cohesiveness and plasticity. **C**) Photomicrograph of hollow filaments with regular constructions, emanating from a large carbonaceous particle. These filaments represent one of the earliest putative biosignatures to have been tested against strict biogenicity criteria. **D**) Transmission electron microscopy (TEM) image of spherical objects interpreted as possible cells undergoing early stages of division. **E**) TEM image of granular, cell-like body showing porosity and a central cavity, comparable with modern fossilised *Methanocaldococcus jannaschii*. **F**) TEM image of spherical objects interpreted as cells. Arrow indicates a missing fragment of hypothesised cell wall. Scale bar dimension in C not given in original publication; estimated at 5 mm. A from Walsh (1992), C from Walsh and Lowe (1985), courtesy of Maud M. Walsh; D-F from Glikson et al. (2008).

Staudigel et al. (2015) have suggested that thermal metamorphic reheating may have reset the U-Pb signatures of microbially precipitated titanite, resulting in artificially younger ages. Wacey et al. (2017), studying young (145 Ma) fossil microtubules of the Argo Abyssal Plain, have interpreted septa-like features within the tubules as arising from the cracking of clay mineral infill (Fig. 4G) and have demonstrated that much of the reported carbon in such tubules arises from carbonate minerals. Where organic carbon is present, it is associated with elevated Ti (Fig. 4H), which might explain the propensity for titanite mineralisation in ancient examples. Wacey et al. (2017) caution that the organic carbon present could as easily stem from biology as it could from simple introduction by seawater. Hence, the debate on the biogenicity of these microtubules is yet to reach a universally accepted conclusion.

2.2. The 3.416-3.334 Ga Kromberg Formation, Onverwacht Group

The Kromberg Formation contains the richest diversity of putative traces of life in the BGB (Figs. 6-12 and 13A-C), including a wide variety of microfossils, stromatolites, microbial mats, and masses of organic carbon with biological origins. The Buck Reef Chert and Josefsdal Chert of this formation contain particularly diverse evidence of a fossilised biosphere.

2.2.1. Buck Reef Chert (K1)

The 3.416 Ga Buck Reef Chert (unit K1 of Lowe and Byerly, 1999) has been described as an Archaean shallow-water to deep-water environment (Tice and Lowe, 2004, 2006). It was deposited as part of the regressive-transgressive Buck Ridge volcano-sedimentary complex (Nijman and de Vries, 2009; de Vries et al., 2010). The stratigraphy consists of a basal evaporite facies, over which lies a middle platform facies, capped by a deeper basin facies (Tice and Lowe, 2004; Greco et al., 2018). Sedimentary structures, including ripple marks and plastic deformation corresponding to tidal or storm activity, together with geochemical evidence of terrigenous clastic sedimentation (Al, Zr and Cr ratios), suggest that the unit was deposited on an open marine shelf, above deep storm wave base (Tice and Lowe, 2004; de Vries et al., 2010).

Putative microfossils were first described from the Buck Reef Chert by Walsh and Lowe (1985) and Walsh (1992), the latter providing the first systematic description of microfossil morphologies in the BGB. Walsh (1992) described spheroidal, ellipsoidal, lenticular, and filamentous putative microfossils, although they are rare features in the numerous studied thin sections. As in the Hooggenoeg Formation, elongated, hollow, filamentous objects with regular constrictions were described as microfossils (Fig. 6A-C). Additionally, small spheroidal, ellipsoidal, and lenticular carbonaceous microstructures were described as probable microfossils. Spheroids and ellipsoids are 10-84 mm in diameter and have granular walls composed of carbonaceous material and pyrite equivalent to that of filamentous microfossils. They occur in aggregates, suggestive of a community composition (Fig. 6D-F). However, their simple form and the absence of high-resolution microscopic study (cf. Wacey et al., 2016a) leaves open the possibility of an abiogenic origin.

Diaphanous, fusiform, lenticular structures (previously termed spindle structures) with hollow centres (Walsh, 1992) are a common putative microfossil morphology in both the BGB and Pilbara Craton (e.g., Sugitani et al., 2010, 2015). Oehler et al. (2017) reviewed lenticular objects from the Pilbara and BGB and proposed that they are microfossils with a planktonic stage in their life cycle. Taphonomic variation within lenticular microfossil-like objects is very large. They display up to two central cavities and have the possibility of equatorial appendages and a wide array of shapes, sizes, and habits, ranging from isolated to colonial (Fig. 6G-J).
Spheroidal objects in unit K1c2 (Fig. 6K-L: Kremer and Kazmierczak, 2017) are described as comparable with variably degraded fossil pleurocapsalean cyanobacteria. Although occurring in “groups” and occasionally containing central objects interpreted as organelle-like features, their simple appearance and tendency to form angular vertices (i.e., not rounded, as might be expected for biology) may hinder the biological interpretation.

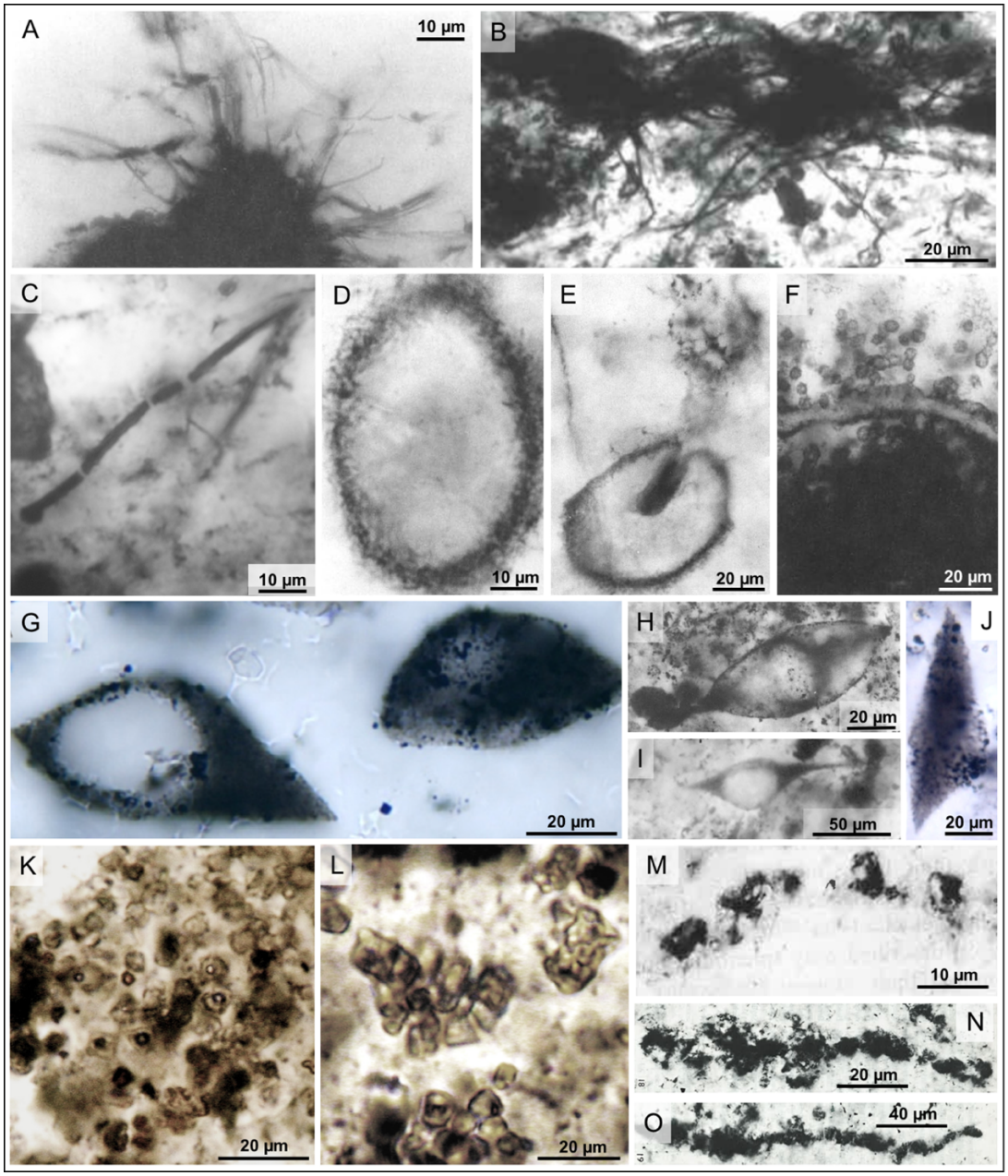

Fig. 6. Putative microfossils from the Kromberg cherts. **A-C**) Preserved filamentous structures interpreted as microfossils. **A**) Hollow, threadlike filaments, constricting at regular intervals, radiating from a carbonaceous particle. **B**) Tangled mass of hollow, cylindrical filaments composed of fine carbonaceous material and pyrite microcrystals. **C**) Single filament with regular constrictions. **D-F**) Ellipsoidal and spheroidal objects interpreted as probable microfossils. **D**) Simple ellipsoidal carbonaceous object. **E**) Ellipsoidal object with aperture; material emanating from the object has been interpreted as its excreted products. **F**) Agglomeration of thin-walled spheroidal objects, occurring as isolated features and interconnected chains, interpreted as probable microfossils. **G-J**) Lenticular objects interpreted as microfossils. These have variable taphonomy within individual populations and morphologies, which may or may not include interior voids and equatorial appendages. **K**) Coccoidal objects, many with internal structure, which bear superficial morphological similarity to younger coccoidal cells. **L**) Degraded coccoidal objects deemed of similar colonial habit to modern pleurocapsalean cyanobacteria. **M**) Isolated carbonaceous spheroids interpreted as probable bacterial fossils. **N-O**) Chains of carbonaceous spheroids forming filament-like structures, interpreted as probable bacterial fossils. A, D-F, and H Ffom Walsh (1992), courtesy of Maud M. Walsh; B from Walsh and Westall (2003); G and J from Oehler et al. (2017), courtesy of Dorothy Z. Oehler; K-L from Kremer and Kazmierczak (2017), courtesy of Barbara Kremer; M-O from Muir and Grant (1976). C and I are original images courtesy of Maud M. Walsh.

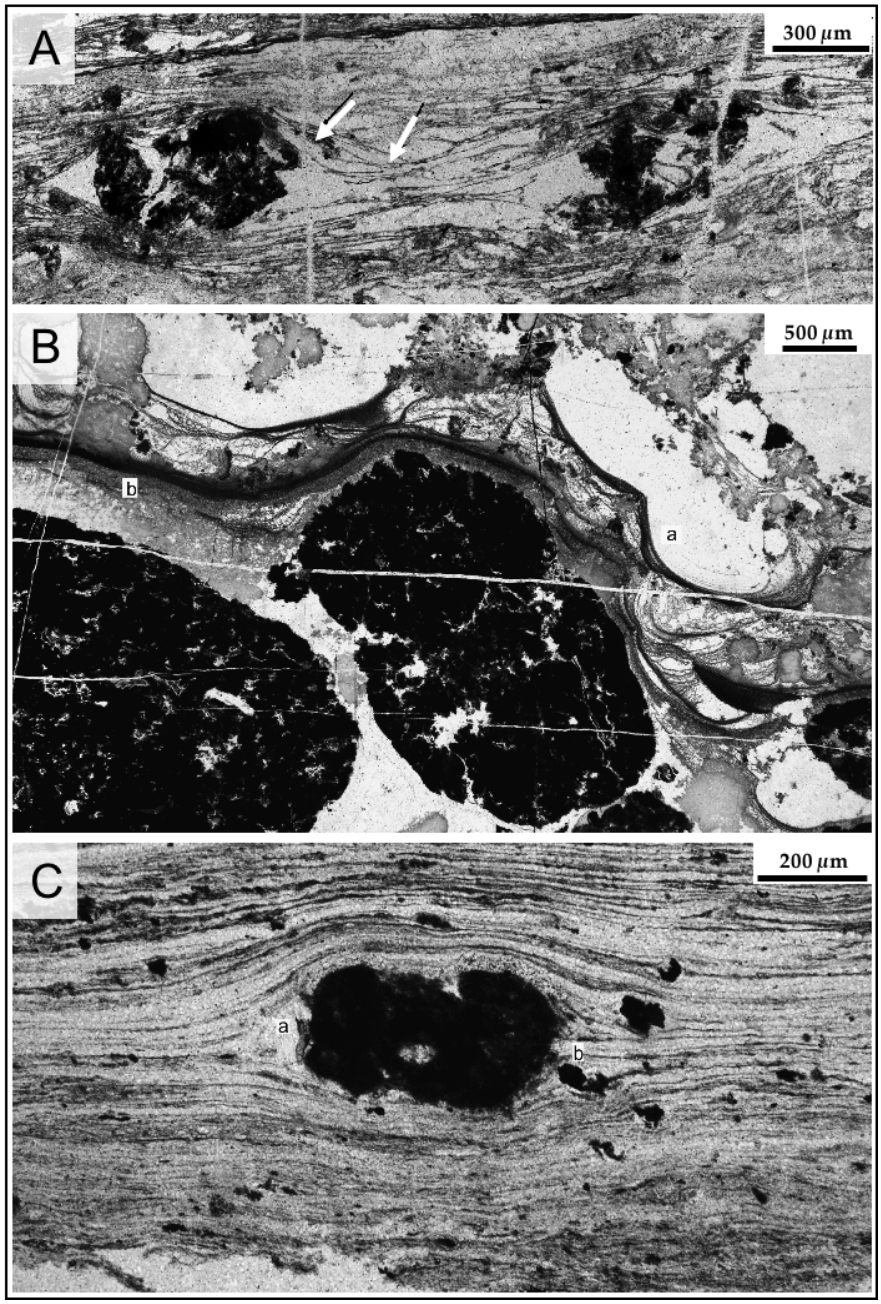

Fig. 7. Microbial mat morphologies from the 3.42 Ga Buck Reef Chert, following the tripartite classification of Tice (2009). **A**) Alpha-type mat, consisting of thin, filament-like, anastomosing, lensing laminations (arrowed) surrounding eyelet-like structures that often contain carbonaceous particles. **B**) Beta-type mat, consisting of a dense, black upper layer (a) grading into a more disperse, meshwork-like mat below (b). The mat is punctuated by many open lenses in which are found silica grains, and drapes large carbonaceous particles. **C**) Gamma-type mat, comprising fine laminations and entraining small detrital carbonaceous particles. Laminations either drape or terminate against particles. Images from Tice (2009), courtesy of Michael M. Tice.

Tice and Lowe (2004, 2006), Tice et al. (2004), Tice (2009) and Greco et al. (2018) described anastomosing carbonaceous laminations identified as phototrophic microbial mats and their erosional fragments in layered green-black-grey cherts from the lower platform facies of this unit (Figs. 7-8). Tice (2009) set out a three-morphotype classification for these microbial mats: (1) alpha-laminations, which are fine carbonaceous laminations loosely draping underlying clasts to form eyelet structures (Fig. 7A); (2) beta-laminations, which are a series

of dense meshworks of carbonaceous filaments that drape and cling to detrital grains and incorporate concave chalcedony lenses (Fig. 7B); and (3) gamma-laminations, which occur in thick, evenly spaced stacks and tightly drape detrital grains (Fig. 7C). Alpha- and beta-type mats grew in shallower waters than gamma-type mats, under shear stresses that indicate an erosional regime (comparable to both the Middle Marker microbial mats and Moodies Group microbially induced sedimentary structures) and in high-turbidity waters (Tice et al., 2011). These laminations are perhaps most accurately compared with carbonate ramp microbialites. Filamentous structures with dimensions of 1-1.5 mm by 100 mm locally constitute the laminae (Fig. 7A, arrows).

Further evidence for the biogenic origin of these laminations is found in remarkably well-preserved roll-up structures (Fig. 8), several millimetres in size, which are clear evidence for the erosion and current reworking of an initially plastically deformable microbial mat; i.e., a filamentous mat bound by extracellular polymeric substance (EPS). Similar microscopic structures indicating cohesion have been identified in other units by Westall et al. (2015) and Hickman-Lewis et al. (2016). $\delta^{13}C$ values from –35 to –20‰ in the Buck Reef Chert, while within the range of abiotic hydrocarbon formation (see Lindsay et al., 2005), are compatible with biological activity (Walsh and Lowe, 1999). Furthermore, the composition of carbonaceous matter in a hydrothermal-serpentinising volcanic section of the Buck Reef Chert, with the characteristics ($\delta^{13}C$ and N/C ratio) of indigenous metamorphosed biological material, reveals that abiological serpentinisation reactions are an unlikely source for the distinct hydrocarbons of the mats (cf. van Zuilen et al., 2007). Rare carbonaceous matter in the deep basin lithofacies is attributed to the influx of detrital grains from shallow environments.

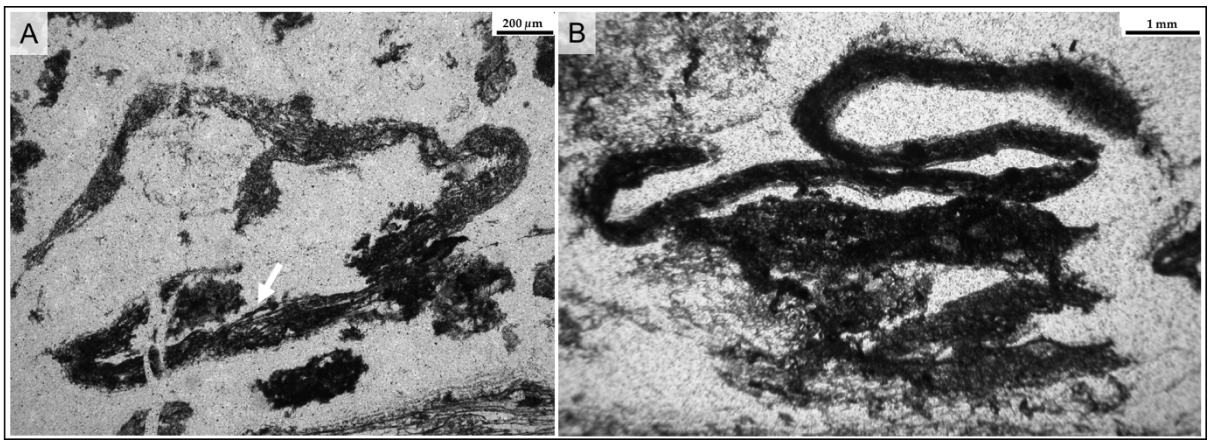

Fig. 8. Roll-up structures from the 3.42 Ga Buck Reef Chert interpreted as the erosional products of microbial mats. **A**) Rolled up fragment of an alpha-type mat, with small open lens (arrowed), comparable with the microstructure in Figure 7A. **B**) Rolled up fragment of a beta-type mat comparable with the uppermost dark laminations of the draping mat in Fig 7B. Structures such as these denote *in vivo* cohesiveness and propensity for plastic deformation. Images from Tice and Lowe (2004) and Tice (2009), courtesy of Michael M. Tice.

2.2.2. Josefsdal Chert (K3c)

The Josefsdal Chert is considered to be the lateral equivalent of the 3.33 Ga Footbridge Chert (Lowe, 1999; Lowe et al., 2012), located in a fault-bounded horizon of volcano-sedimentary rocks. Black-white-green layered Josefsdal cherts contain numerous sedimentary structures indicative of a shallow-water environment, including ripple and flaser bedding

diagnostic of tidal environments, and graded bedding and cross-stratification signifying oscillating current direction (Westall et al., 2006, 2015). Repetitive, fining-upward sequences reflect periodic influxes of sediment, followed by quiescent episodes. Evaporitic mineralogies and associated desiccation cracks imply episodic partial subaerial exposure (Westall et al., 2006, 2011). More recent studies (Westall et al., 2015) subdivided the stratigraphy into four distinct facies: (A) hummocky, cross-stratified, well-sorted sandstone, representing upper shoreface tidal or tempest deposits (Dumas and Arnott, 2006); (B) Fe-rich, parallel laminated rhythmites indicative of a tidal shoreface setting; (C) black-and-white layered chert with clotted carbonaceous textures; and (D) green-grey bedded sandstone deposited during alternating quiescent and dynamic hydrological regimes. These represent a regressive-transgressive sequence of deposition terminated by renewed volcanism.

The evidence for contemporaneous hydrothermal activity is plentiful in facies A-C. Near-monocrystalline chert veins intrude the sediments both conformably and discordantly. Thin, stratiform hydrothermal veins percolated through the sediments, creating soft sediment deformation features and tearing apart carbonaceous microbial biofilms, thus indicating contemporaneous infiltration and early silicification. Positive Eu anomalies and tracer elements, such as Fe, Cu, Ni, Zn, As and Ba, which were scavenged by the phyllosilicate-altered volcanic detritus, provide evidence for the presence of pervasive hydrothermal fluids (Westall et al., 2015, 2018). Two types of biosignatures have been proposed in the Josefsdal Chert: (1) bedding plane parallel carbonaceous layers interpreted as the remains of phototrophic biofilms (Figs. 9-11) and (2) clotted carbonaceous aggregates interpreted as degraded chemotrophic biomass (Fig. 12).

Carbonaceous laminations. Packets of thin (≤ 10 mm) wavy carbonaceous laminae coat and stabilise underlying bedding plane surfaces (Fig. 9A-B; cf. Noffke et al., 2006, 2013), often incorporating silt to sand-sized detrital volcanic clasts or quartz grains (Westall et al., 2006, 2011, 2015). Morphological preservation of the laminae is variable, depending on sediment grade and rapidity of silicification. In coarse-grained facies, laminae are less well preserved, often appearing simply as faintly laminated carbonaceous coverings atop detrital layers. Preservation is best in the hydrothermally influenced facies (such as C; cf. Westall et al., 2015), where silicification was extremely rapid (Fig. 9A).

One 10 mm-thick laminated microbial horizon is preserved in three dimensions with such a high degree of morphological fidelity that it has been possible to investigate its physical and biogeochemical features down to the nanometre, molecular, and elemental scales (Figs. 9C-F, 10-11: Westall et al., 2006, 2011). The upper, originally microbially active, layer consists of very thin (<1 mm), turgid microbial filaments encased in a thick coating of remineralised extracellular polymeric substances (EPS, Figs. 9E-F, 10B). Portions of the filamentous biofilm were overturned, rolled up, or even torn out under the influence of flowing water (Fig. 9D; cf. roll-up structures in the Buck Reef Chert, Tice and Lowe, 2004; Tice et al., 2011), whereas the uppermost layers are intercalated with several layers of micron-thick evaporite minerals comprising aragonite, gypsum, carbonate, and a halide (probably halite; cf. Vai and Ricci Lucchi, 1977), indicating partial subaerial exposure (Fig. 11; Westall et al., 2006, 2011a).

Although the top layer of the biofilm is beautifully preserved, the underlying portion, consisting of degraded kerogen, has a reticulate structure intermixed with carbonate (aragonite) nanocrystals with traces of sulphate (Fig. 11E-G). The presence of elevated sulphur values within the kerogenous matter (up to 1% S), as well as the S-containing molecule thiophene

(Fig. 11H), together with the incipient calcification of the biofilm, suggests microbial degradation of the lower portion of the film, possibly by organotrophic sulphate-reducing bacteria (SRB). Together, the morphology of the microbial features and indications of direct interaction with their sedimentary environment (trapping, sediment stabilisation, deformation due to current flow, etc.), coupled with geochemical evidence of negative carbon isotope fractionation of –22.7 to –26.8‰, an elemental signature of C, N, and S in the biofilm, and indication of SRB degradation, confirm that the biofilm structure meets many criteria for syngenicity and biogenicity (e.g., Brasier et al., 2002, 2004, 2006; Westall et al., 2006, 2011; Wacey, 2009; Noffke, 2010).

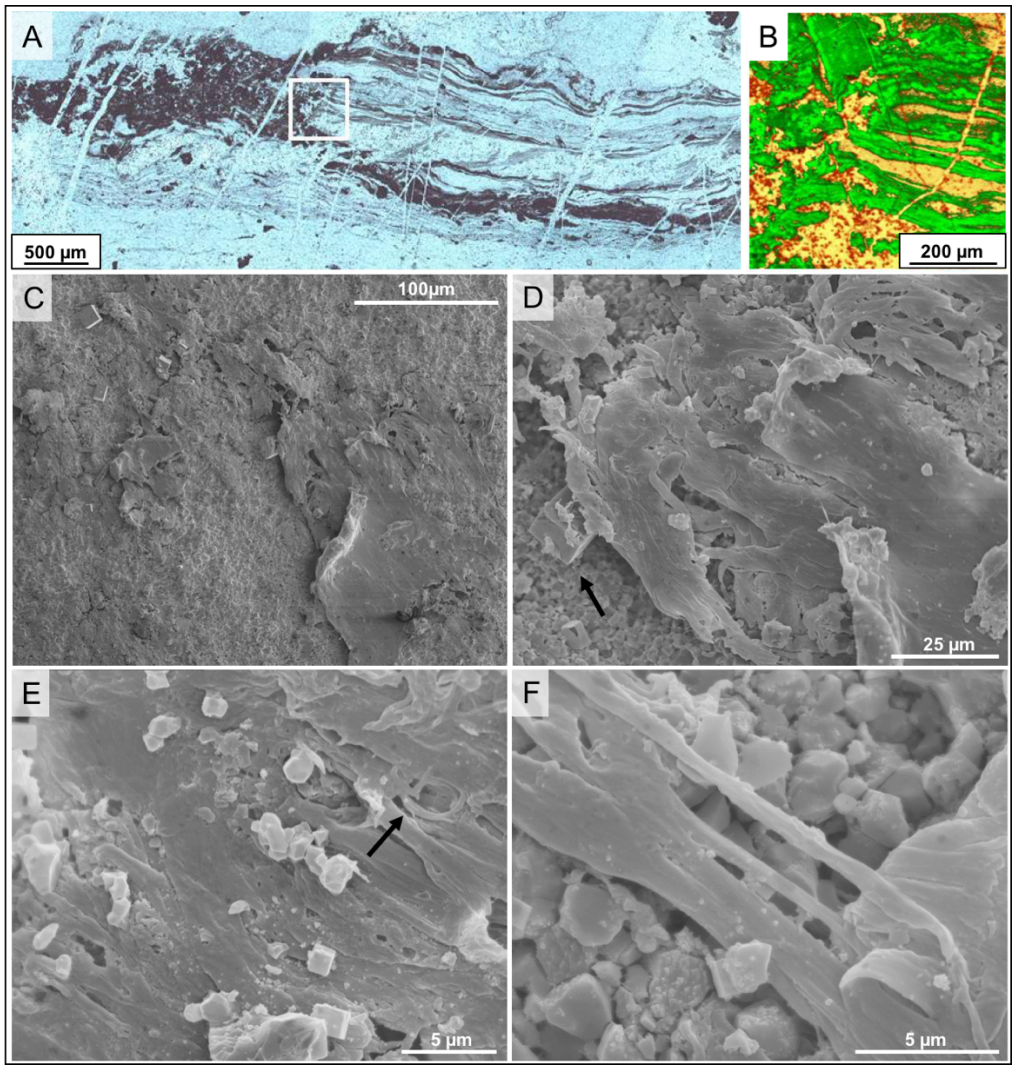

Fig. 9. Phototrophic biosignatures of the 3.33 Ga Josefsdal Chert. **A**) Photomicrograph of an undulating, multi-laminated phototrophic mat. White box indicates the region of B. Note the non-isopachous laminae. **B**) Raman spectroscopic map within the mat, where carbon = green and the silica matrix = yellow orange. **C-F**) SEM micrographs showing the exceptional preservation of the microbial biofilm and indications of subaerial exposure. **C**) Plan view of one section of the mat, showing overturned fragments, filamentous textures, and entrained evaporite minerals. **D**) Close-up of the rolled over section of the mat; note the syngenetic halide crystal covered by the mat (arrowed). **E**) View of mat filaments, showing a rounded region in which a particle was formerly embedded (arrowed). **F**) Close-up view of individual filaments of the mat, which demonstrably entrain particles (lower centre) and roll over (lower right). Images A-B from Westall et al. (2015).

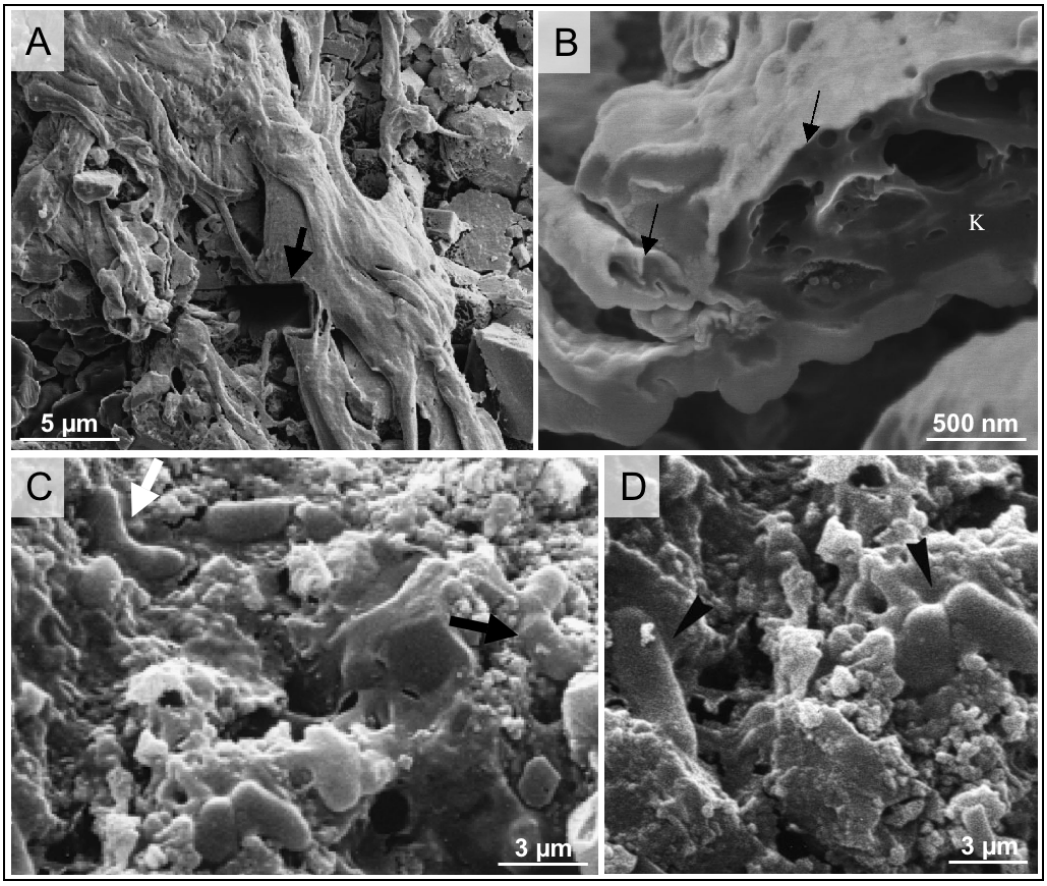

Fig. 10. High-resolution imagery depicting the Josefsdal Chert biofilm and its putative microbial inhabitants. **A**) Portion of the biofilm, bound by string-like, glutinous EPS. Arrow indicates location of FIB cut shown in B (FIB wafer not shown). **B**) Cross section through microbial biofilm, showing kerogenous material (K) and the fine upper kerogen layer (arrows). **C-D**) Sausage-shaped objects (arrowed) from the bedding plane of the biofilm, interpreted as potential vibrioid bacteria. A-C from Westall et al. (2006), D from Westall et al. (2001).

On the same bedding plane and adjacent to the biofilm is found a group of turgid, curved rod-shaped bacteriomorph structures, up to 3 mm in length and about 1 mm in diameter, enveloped in a film-like substance (Fig. 10C-D). The morphology of these features is very similar to that of vibrioid bacteria, while the filmy coating is suggestive of EPS. These observations and the close association of the bacteria-like group with the phototrophic biofilm suggest a common biogenic origin, although their simple morphology and irregular occurrence mean that no further interpretations can be attempted without more detailed investigation (see Altermann, 2001).

The fact that the phototrophic biofilm survived in partially exposed evaporitic conditions implies a level of halotolerancy (Kamekura, 1998). Similar styles of preservation during the silicification of EPS, microbial films, and microfossils occur in modern hot spring-type deposits (Konhauser et al., 2003; Papineau et al., 2005). Although the UV environment of the early Earth was harsh by comparison with present-day standards (Cockell and Raven, 2004; Cnossen et al., 2007), the occurrence of life occupying an emergent terrestrial niche in both Barberton (in the Josefsdal Chert and Moodies Group) and in the Pilbara (Dresser Formation: Van Kranendonk, 2006; Djokic et al., 2017) implies the existence of mechanisms to minimise cell damage due to radiation.

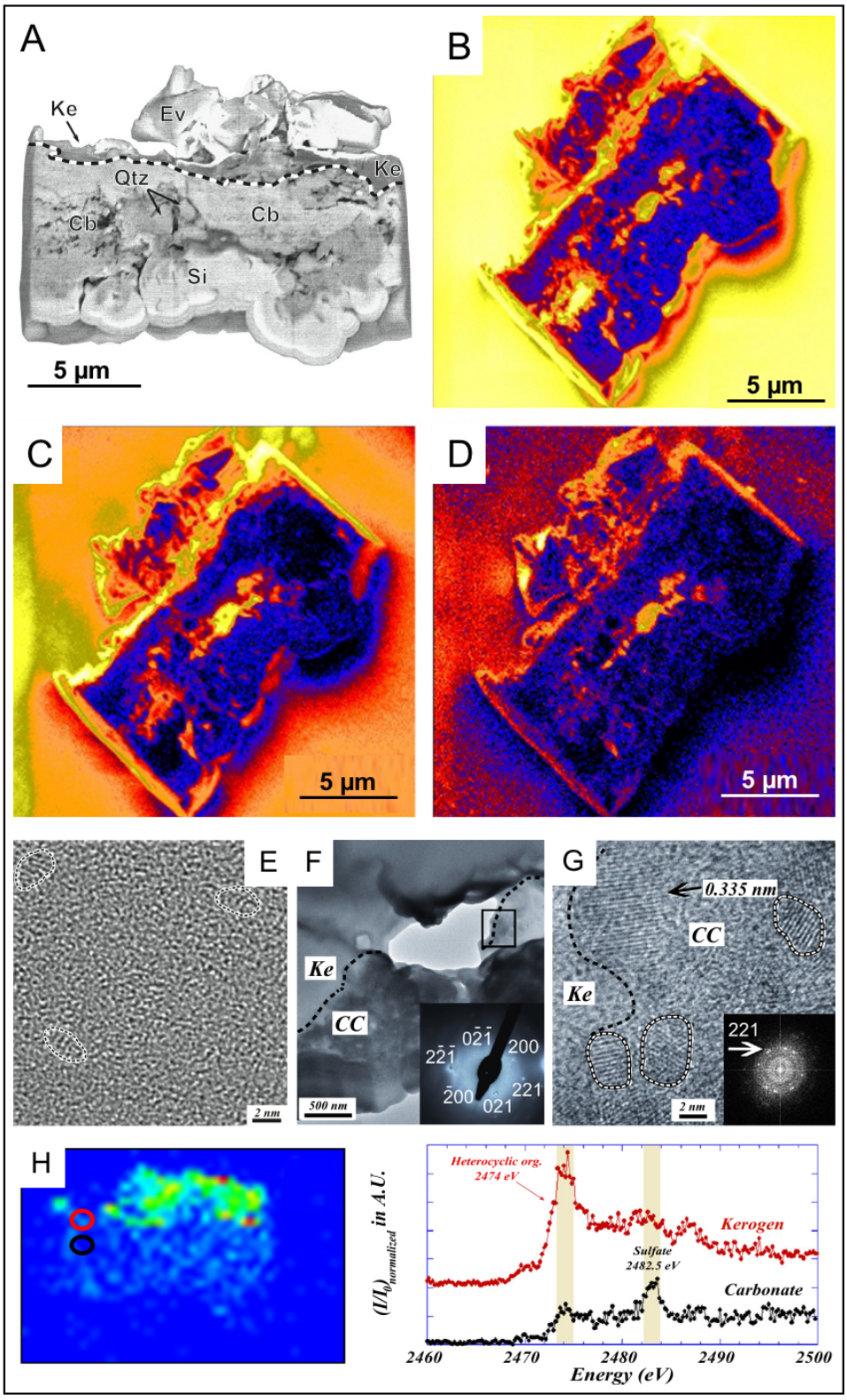

Fig. 11. High-resolution microscopy and geochemistry of the Josefsdal Chert microbial biofilm using FIB-milled sections. **A**) Backscatter SEM image of a FIB-cut cross-section through the biofilm. Ev = evaporite embedded in top of biofilm, Ke = thin kerogen layer, Cb = calcified biofilm constituting the main body of the section, Qtz = floating grains of quartz within the biofilm, Si = silica. **B-D**) NanoSIMS elemental mapping, using the section in A, of C (as ^{12}C), N (as $^{12}C/^{12}C^{14}N$), and S (as ^{32}S). These maps show clear spatial correlation between C, N, and S within kerogenous material. **E**) High-resolution TEM within the kerogenous region, showing locally accumulated polyaromatic structures that indicate maturity of the kerogen. **F-G**) Nanostructure of the calcified

biofilm: **F**) shows the contact zone between kerogen (Ke) and calcification (CC); inset diffractogram shows the distribution of the crystal planes of aragonite;(G shows HRTEM image of the calcified region, demonstrating that multiple carbonate nanocrystals of aragonite (inset Fast Fourier Transform) occur within the calcified region. **H**) μXANES mapping of sulphur within the slice shown in A; green indicates pseudomorphed syngenetic evaporites embedded in the biofilm. μXANES spot spectral analyses indicates the presence of inorganic sulphur and the heterocyclic molecule thiophene. All images from Westall et al. (2011a).

Clotted carbonaceous textures. Clotted carbonaceous material that is prevalent in the hydrothermal facies of the Josefsdal Chert (Fig. 12), particularly in Facies A and C (cf. Westall et al., 2015a), imparts a matt black colour to the chert (Fig. 12A). Clotted textures can be divided into two types: (1) "free-floating," carbonaceous accumulations with either a cloud-like, irregular morphology with "scalloped" edges, or "spiky" morphologies (Fig. 12C) and (2) thick, irregular, non-isopachous carbonaceous coatings on volcanic particles (Fig. 12D-F). Both are intercalated with biofilms. The "spiky" carbonaceous clots, up to several hundreds of microns in size, occur in a largely clast-free, siliceous matrix deposited parallel to bedding planes (Fig. 12B). Faint laminations of fine-grained carbonaceous matter within the silica deposit and the association of the clots with bedding-parallel phototrophic biofilms indicate that this is a chemical sediment, plausibly originating as a silica gel (cf. Ledevin et al., 2014; Ledevin, 2018). These siliceous laminae are lateral, bedding plane-parallel, extensions of vertical hydrothermal veins, indicating a hydrothermal origin of the siliceous fluids from which the gel precipitated. The carbonaceous matter appears to have formed around the volcanic fragments, its irregular three-dimensional morphology suggesting in situ growth. Overall, an irregular morphology, carbonaceous composition, in situ mode of growth, formation within a nutrient-rich hydrothermal precipitate, and association with phototrophic biofilms testify to the probable biogenicity of these clots ("carbon clumps," cf. Walsh, 1992).

2.2.3. Lower Kromberg basalts

As highlighted in Section 2.1, microtubular structures akin to modern microbial alteration textures in pillow basalts and hyaloclastites have been discovered from in vesicular pillow lavas in the lower Kromberg Formation, but these are less well-preserved than those of the Hooggenoeg Formation. A similar debate concerning the biogenicity of the tubules has surrounded the Kromberg examples (Furnes et al., 2004, 2007; Banerjee et al., 2006; McLoughlin et al., 2012; Grosch and McLoughlin, 2014, 2015).

2.2.4. Other Kromberg cherts

Muir and Grant (1976) described spheroidal objects interpreted as isolated and paired unicells within stromatolitic fabrics and segmented filaments from unspecified cherts of the Kromberg Formation (Fig. 6M-O). Whether the fabrics are truly stromatolitic is unclear from the images provided. Unicell-like spheroids are usually 1.6-5 mm, with similar size frequency distributions between samples, although there are also larger objects (up to 12 mm) with thicker, porous walls. In a number of cases, these spheroids are paired and, when in this association, sizes are reduced relative to isolated spheroids, perhaps indicative of cell division processes. Spheroids also occur as chains forming filamentous structures (Fig. 6N-O), Further assertions of cells showing a "multicellular tissue" fabric, however, resemble displaced carbon after silicification and metamorphism (cf. Brasier et al., 2006).

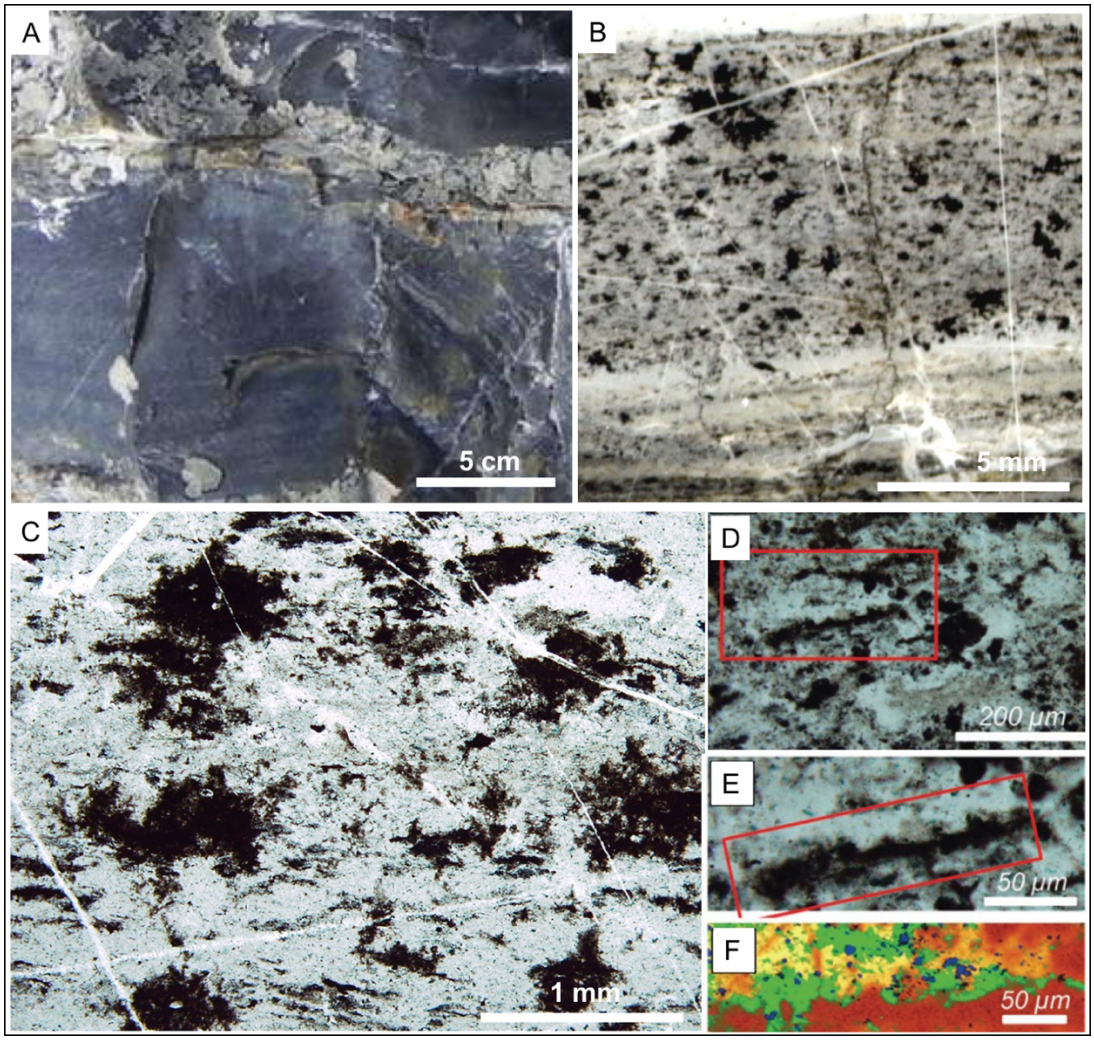

Fig. 12. Putative chemotrophic biosignatures of the 3.33 Ga Josefsdal Chert. **A**) Outcrop photograph of black chert in which putative chemotrophic biosignatures are found. Coeval hydrothermal activity is evidenced as vertical and stratiform silica veins, which extensively permeate the sediments. **B**) Thin section view showing a horizon rich in carbonaceous clot-like structures that co-occur with carbonaceous wisps from eroded microbial mats. **C**) Irregularly shaped carbonaceous clots, which grew in situ and were preserved three dimensionally, in hydrothermal silica. These objects ("carbon clumps" or clots) were interpreted as degraded chemotrophic biomass. **D-E**) Organic carbon coating of a pseudomorphed volcanic clast (within red box). Note that the coating is discontinuous, non-isopachous, and intimately associated with phyllosilicate alteration on the surface of the particle, thus leading to its interpretation as a degraded surficial lithotrophic biomass. Red box indicates the region of F. **F**) Raman spectroscopy map of the area indicated in C, where green = carbon, orange-yellow = silica, and blue = anatase (a proxy for the presence of phyllosilicate alteration of the volcanic particle). Note the irregular distribution of carbon and the association of carbon with anatase. Images D-F from Westall et al. (2015a).

Muir and Grant (1976) also described small and large filaments, which are perhaps better understood as straight or sinuous chains of cell-like objects up to around 100 mm in length. These objects were interpreted as cells, discarded sheaths, and the degraded products of several distinct, size-delineated species of cyanobacteria (Muir and Grant, 1976). As with many other early propositions of microfossils, simple or enigmatic morphology leaves open the possibility of an abiogenic genesis.

Additionally, stromatolitic fabrics were reported in coarse-laminated carbonates of the Kromberg chert by de Wit et al. (1982). These structures have domical cross sections and

laminae that vary in thickness and gradient, being particularly non-isopachous in the regions of crests (Fig. 13A-C). Although these stromatolite-like structures are thickly laminated relative to most reported examples, they are of similar morphology, distribution, and dimensions to *bona fide* stromatolites from the Belingwe greenstone belt. Primary mineralogy has been replaced largely with silica (Fig. 13C), while some calcite has recrystallised into euhedral rhombs. In plan view, the stromatolites are elongate and do not conform to either the geometry or orientation of demonstrably deformational structures in the immediate vicinity. de Wit et al. (1982) suggested that proximal hydrothermal activity (evidenced by vent structures) supported the proliferation of stromatolite communities, and that, within this shallow environment, a constant fresh supply of chemical nutrients would have been effective in sustaining a primitive biome.

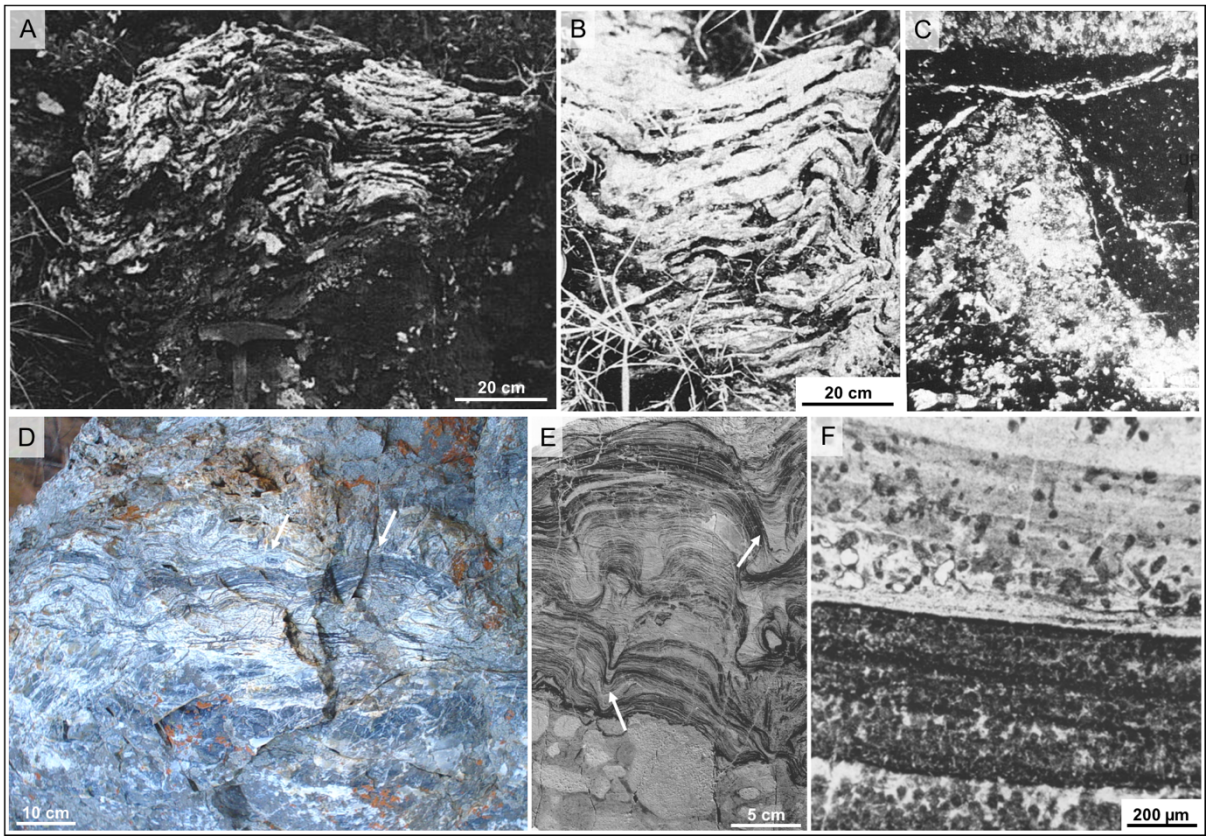

Fig. 13. Interpreted stromatolites from the Kromberg and Mendon formations. **A-C**) Laminated, conical structures from the Kromberg Formation, interpreted as stromatolites. **A**) Field photograph of coarsely laminated, stromatolitic carbonate rocks. **B**) Dome-trough fabric. **C**) In thin section, stromatolitic laminations are clearly non-isopachous and vary considerably over short distances, particularly around crests. No scale given in original publication. **D-F**) Laminated, domal pseudocolumnar structures from the Mendon Formation, interpreted as stromatolites. **D**) Field photograph of low-relief, domal stromatolites; domes arrowed. **E**) Polished slab of domal pseudocolumnar-laminated stromatolites; pseudocolumnar fabric arrowed. **F**) Laminae of stromatolite, showing multiple variations: primary laminae (50-100 mm) are carbonaceous, secondary laminae (up to 500 mm) are tourmaline rich. A-C from de Wit et al. (1982); D courtesy of Axel Hofmann. E-F from Byerly and Palmer (1991).

2.3. The 3.334-3.258 Ga Mendon Formation, Onverwacht Group

Byerly et al. (1986) described stromatolite-like features from three locations in what is now identified as the 3.298 Ga M2c horizon of the Mendon Formation of the Onverwacht Group

(Decker et al., 2015; Lowe and Byerly, 2015). The structures consist of fine, crinkly, dark laminations (possibly carbonaceous) forming typically low-amplitude domes, 1-3 cm wide, and 0.5-3 cm high (Fig. 13D), with some instances of pseudocolumnar-like structures (Fig. 13E). At higher magnification, the laminations are heterogeneous, consisting of thin, carbonaceous laminae and thicker, tourmaline-rich laminae (Fig. 13F). The domes are asymmetrical and plan views show that they are elongated. These domical shapes are linked to each other by bridging laminae, which also exhibit subparallel crinkly layering.

Byerly et al. (1986, 1996) and Byerly and Palmer (1991) noted that these stromatolites occur within cherts that overlie silicified komatiite flows. The spatial distribution of domes linked by tabular laminae suggest that the stromatolites formed in a relatively quiescent environment (Byerly et al., 1986). The fact that the structures appear to be formed on basement highs suggests that, aside from a shallow-water environment, they required a hard substrate and/or little clastic input into the environment. Common stromatolite flake breccias indicate some dynamic breakup, or erosion, of the stromatolites. Interestingly, tourmaline was found to be a common component of the stromatolitic layers, an observation interpreted as a tracer for boron-enriched hydrothermal fluids stemming from remobilisation of boron-rich evaporites (Byerly and Palmer, 1991). Alternatively, Lowe and Byerly (2015) interpreted the tourmaline mineralisation to have been caused by heating and partial evaporation of remobilising seawater caused by the impact that deposited spherule layer S8.

Furthermore, pyrites in shale and chert from the Mendon Formation have been used to evoke a vestige of SRB. Ohmoto et al. (1993) argued that $\delta^{34}S$ values of up to 12‰ are more supportive of an origin involving bacterial sulfate reduction than one of purely magmatic-hydrothermal origin, however, Wacey (2009) caution that further multiple sulfur isotope studies and comparison with Pilbara cherts of a similar age will be necessary to fully elucidate these findings.

2.4. The 3.26-3.23 Ga Fig Tree Group

The Fig Tree Group includes deeper water turbiditic greywacke and shale with sediments having a considerable felsic volcanic component in the uppermost horizons in the north (Lowe and Byerly, 1999), and a shallower water association of greywackes grading into shales and sandstones, and capped by volcanics, in the south (Lowe and Nocita, 1999). The very few reports of biologically promising features in this sequence are morphologically simple (Fig. 14) and many have not been sustained under modern biogenicity criteria.

2.4.1. 3.260 Ga Swartkoppie and 3.245 Sheba formations

The Swartkoppie Formation is the transitional unit between the Onverwacht and Fig Tree groups and is interbedded conformably with the basal sediments of the Fig Tree Group. The environment of deposition is shallow-water nearshore, as indicated by cross-stratification, oolitic textures, and flat-pebble conglomerates. Carbonaceous microspheroids within this unit were interpreted as isolated and paired unicells, exhibiting multiple phases of the cell cycle (Fig. 14A-B: Knoll and Barghoorn, 1977; Schopf, 2006). Interpreted as prokaryotic algae, they are small (1-4 mm), with a size frequency distribution similar to modern and ancient prokaryotic communities (Fig. 14G), and are morphologically varied, being flattened, wrinkled, or folded through sedimentary compaction in a fashion similar to comparable fossils in Proterozoic rocks. Their size frequency distribution and occurrence in isolated and paired

associations draw a strong comparison with the spheroids described as unicells by Muir and Grant (1976). In rare instances, organic contents are preserved within cells, ergo these structures cannot be the product of carbonaceous matter condensation around, and adherence to, mineral grains, as is the proposed case for the "Apex chert" pseudofossils (Brasier et al., 2015; Wacey et al., 2016b). The case for the biogenicity of these microspheroids is therefore compelling.

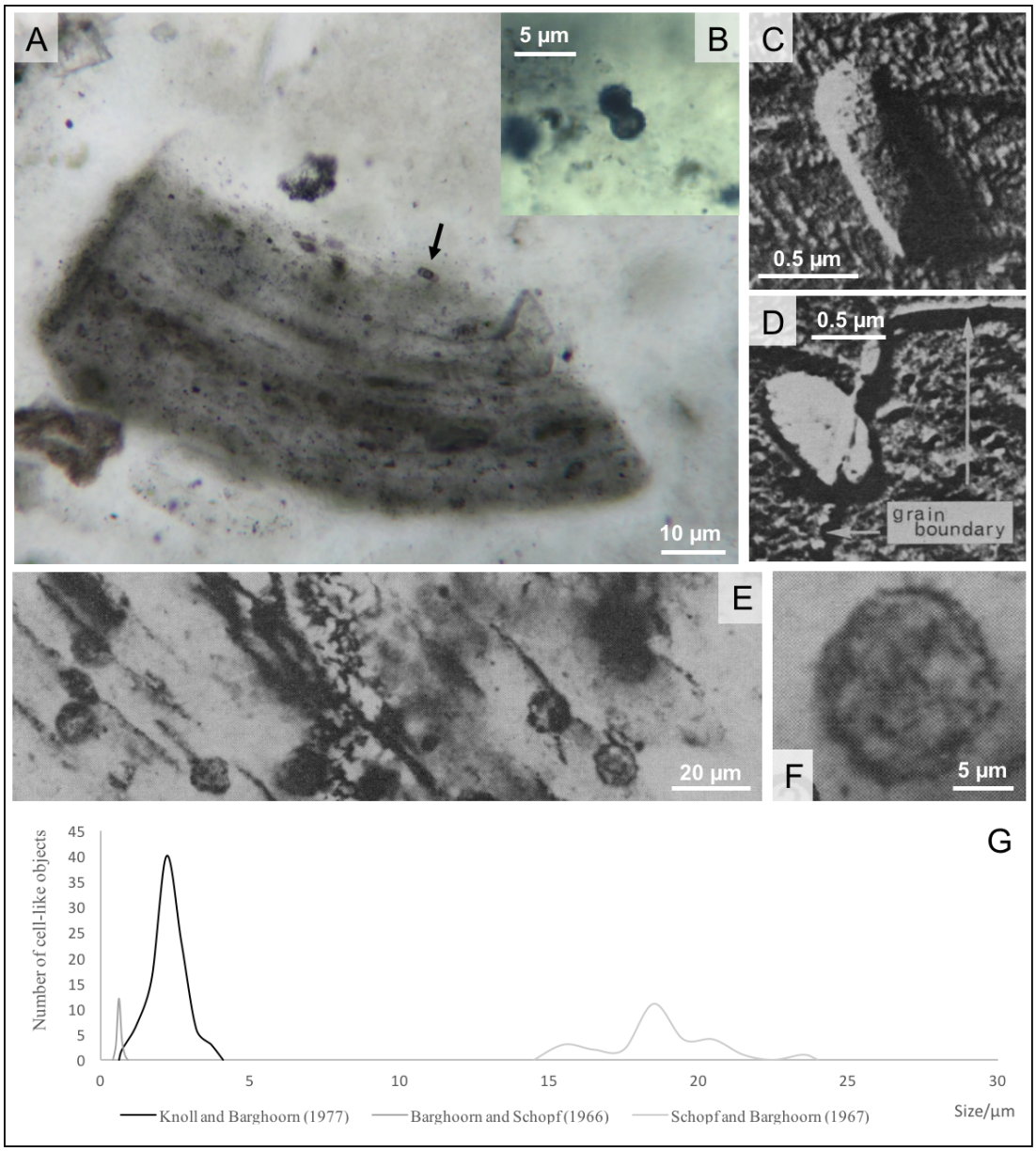

Fig. 14. Microspheroidal and rod-like organic remains from the 3.260 Swartkoppie and Sheba formations, interpreted as unicellular microfossils. **A**) Photomicrograph showing an example of an organic-rich clast in which are found micron-scale spheroids (arrowed). **B**) Organic remains interpreted as paired unicells undergoing cell division. **C-D**) Interpreted rod-like unicellular relics from the Sheba Formation. C shows a cell-like object *in situ* and D a cell-like object traversing a grain boundary. **E-F**) Spheroidal objects compared with alga, though perhaps better interpreted as the end objects of ambient inclusion trails. **G**) Size frequency distribution of these three populations of organic material. A-B courtesy of Andrew H. Knoll; C-D from Barghoorn and Schopf (1966); E-F from Schopf and Barghoorn (1967).

In the Sheba Formation, unicell-like objects were described by Barghoorn and Schopf (1966) and Schopf and Barghoorn (1967). Aside from a biology-like morphology (Fig. 14C-F) and size frequency distribution (Fig. 14G) and a tendency to transgress mineral grain margins (Fig. 14D), these have no remarkable indications of biogenicity. Indeed, any colonial aspect they may have is unclear, and their frequent occurrence as "globules" at the end of lineations (Fig. 14E) perhaps more closely aligns them with ambient inclusion trails of abiological origin or micro-tectonic features. Against the biogenicity criteria of Schopf and Walter (1983) and Schopf (1992), these are the best considered non-fossils.

2.5. The 3.22 Ga Moodies Group

The 3.22 Ga Moodies Group is predominantly a sequence of fine- to coarse-grained quartz and feldspar-bearing sandstones, with subordinate intercalated conglomerates, siltstones, and thin volcaniclastic, tuffaceous layers (Figs. 15, 16A; Eriksson, 1978; Heubeck and Lowe, 1994a, 1994b, 1999). These sediments portray Earth's oldest well-preserved, siliciclastic, tidal-deltaic, alluvial palaeoenvironment (Heubeck and Lowe, 1994a,b), and its constituent biota are therefore Earth's oldest well-developed peritidal-terrestrial microbial communities. A diverse microbial consortium has been described from the lower Moodies Group and within the Clutha Formation and surrounding stratigraphy.

2.5.1. Microbial Mats

Microbial mats and structural traces of microbial activity fitting the definition of microbially induced sedimentary structures (MISS, cf. Noffke et al., 2001; Noffke, 2009, 2010) were first identified in the lower Moodies Group by Noffke et al. (2006). These structures have since been traced over more than 15 km of outcrop. Carbonaceous wrinkle structures parallel to sedimentary bedding, associated with overlying, now-desiccated sandy surfaces and carbon-rich roll-up structures document a microbial mat community in which the microbial edifice was responsible for the stabilisation of the substrate (Fig. 15E-F; Noffke et al., 2006). Further microbial horizons in the lower Moodies Group (specifically layers MdQ1, Mdch, and MdQ2; nomenclature of Heubeck and Lowe, 1994b) with anastomosing, tufted, and bulbous morphologies were described by Heubeck (2009) and Homann et al. (2015). A number of macroscopic features, such as microbial sand-chip conglomerates (Fig. 15D) and microbially induced syneresis cracks (Fig. 15E; see also McMahon et al., 2016), and microscopic features such as quartz grains "floating" in carbonaceous substrate (Fig. 15F) and EPS-bound networks (Fig. 15G) and laminated mat chips (Fig. 15H) irrefutably argue for the presence of mat-building organisms.

These macroscopic and microscopic features meet a number of the morphological criteria for epibenthic, anoxygenic photosynthesising communities at the sediment-water interface. Wrinkle structures and subsequent syneresis cracks in the same sequence signify cohesive, ductile deformation of microbial mats and the surfaces that they bind after subaerial desiccation (Noffke et al., 2006), whereas roll-up laminae of carbonaceous mat material are indicative of an initial plasticity (see Walsh and Westall, 2003; Tice and Lowe, 2004; Hickman-Lewis et al., 2016a). A further indicator of biological mediation comes in the form of entrained, oriented grains (Fig. 15F) between the filaments of the mat (Heubeck, 2009; Gamper et al., 2012; Homann et al., 2015), a feature identified also in MISS fabrics in younger Barberton rocks (Noffke et al., 2006), as well as more ancient examples from the Josefsdal Chert (Westall

et al., 2006, 2011a), the Dresser Formation (Noffke et al., 2013), the Middle Marker horizon (Hickman-Lewis et al., 2018, 2019), and the Apex chert (Hickman-Lewis et al., 2016a,b).

Palaeoenvironment, or at least hydraulic conditions, clearly control the diversity and morphology of microbial mats (Fig. 16). The highest abundances of microbial mats are identified in quartzitic sandstones of the upper intertidal to supratidal facies, wherein examples of flat and wrinkled mats occur alongside mats that onlap and entrain large clasts, and higher relief tufted laminations are associated with gas- or fluid-escape structures (Homann et al., 2015). Mat fabrics are also noted in tidal coast facies (Fig. 15B-D; Homann et al., 2015), where they are occasionally interrupted by loose pebbles and cobble stringers. These microbial mats are associated with local environmental cycles, always occurring at the tops of sedimentary sequences (Noffke et al., 2006).

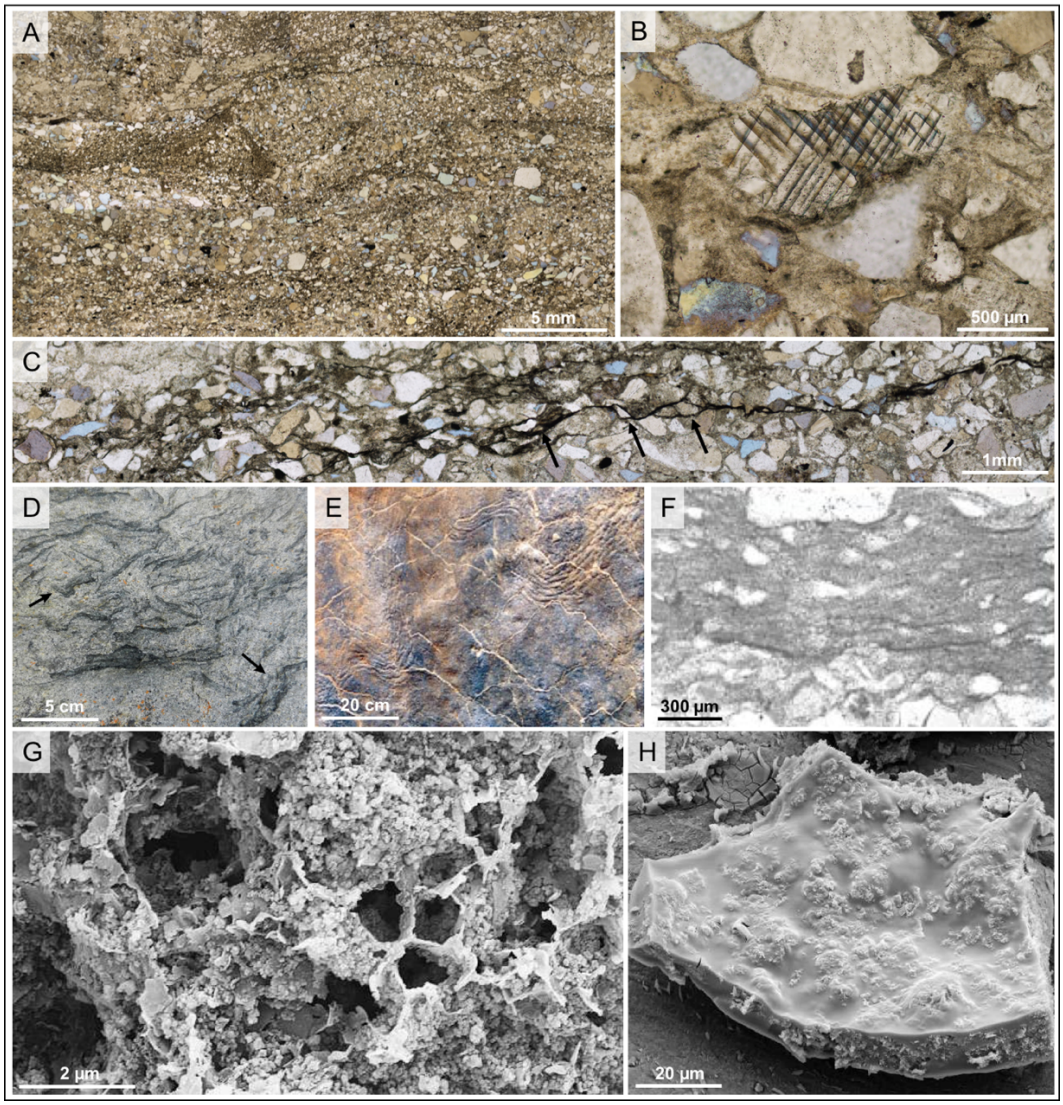

Fig. 15. Microbial fabrics from the Moodies Group. **A**) Anastomosing mat fabric within coarse-grained siliciclastic sediment. **B**) Mineralogical character of the siliciclastic sediment. **C**) Single layer of microbial mat, characterised by the entraining and orienting of grains (arrowed). **D**) Field photograph of a microbial sand-chip conglomerate; arrows indicate the curved shape of some mat chips. **E**) Microbial wrinkle structures and subsequent syneresis cracks at the bedding surface. **F**) Microbially induced sedimentary structure fabric, in which quartz grains appear to "float" within a matrix of carbonaceous material, originally mat laminae. **G**) SEM

micrograph of microbial laminations from the Moodies Group; voids are interpreted as of biological origin (rounded) or as the former location of siliciclastic grains (angular). **H**) Microbial mat chip with bulbous surface and preserved internal lamination. D from Homann et al. (2015), courtesy of Martin Homann; E-F from Noffke et al. (2006), courtesy of Nora Noffke; G-H from Gamper et al. (2012).

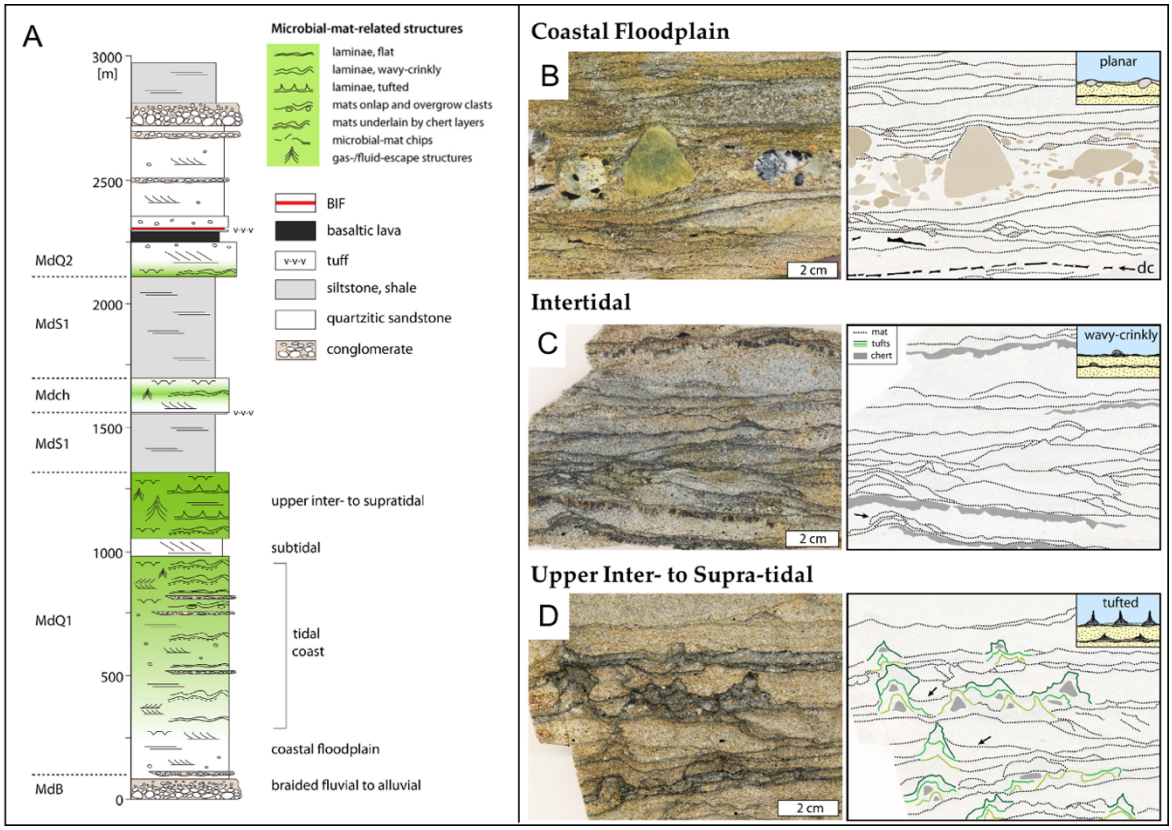

Fig. 16. Palaeoenvironmental correlations with microbial mat morphotype in the 3.22 Ga Moodies Group. **A**) Generalised stratigraphic column of the Moodies Group, showing the relative abundance of microbial mats by morphology: a clear correlation exists in which mats are restricted to shallow-water, tidal-zone palaeoenvironments, with differing hydrodynamic regimes favouring certain morphologies. Darker green indicates higher abundances of mat fabrics. **B-D**) Polished slabs and interpretative sketches of three mat morphotypes corresponding to three different palaeoenvironments in the Moodies Group. Note the increase in complexity with hydraulic energy. Adapted from Homann et al. (2015) with the permission of Martin Homann.

2.5.2. Coelobionts

Traces of coelobiontic (cavity-dwelling) microbial activity in cavities beneath Moodies Group microbial mats were described by Homann et al. (2016) (Fig. 17). Morphological evidence of their biogenicity includes downward-growing protrusions and pendant columns of laminated, kerogenous composition (Fig. 17B-D), syngenetically accompanied by threadlike, filamentous microstructures (Fig. 17E), which have been proposed as bona fide microfossils on the basis of their regularity of subdivision, intimate association with kerogenous cavity fabrics, and differential preservation of the interior and outermost layer (i.e., the cell wall; Homann et al., 2016).

2.5.3. Acritarchs

Large, organic-walled, cohesive, spherical organic structures within Clutha Formation microbial mat horizons (after Heubeck and Lowe, 1994b) have been interpreted as isolated

acritarchs (Javaux et al., 2010), i.e., objects of presumed biology with uncertain affinity. Having sizes ranging from 50 up to 300 mm, their morphology consists of cell lumen-like features contained within taphonomically wrinkled spheroids (Fig. 18). If biological, organisms of this size are uncommon within even advanced Archaea, thus Javaux et al. (2010) suggest that they may be stem clades of cyanobacteria or even eukaryotes, although their true biological affinity remains unconfirmed.

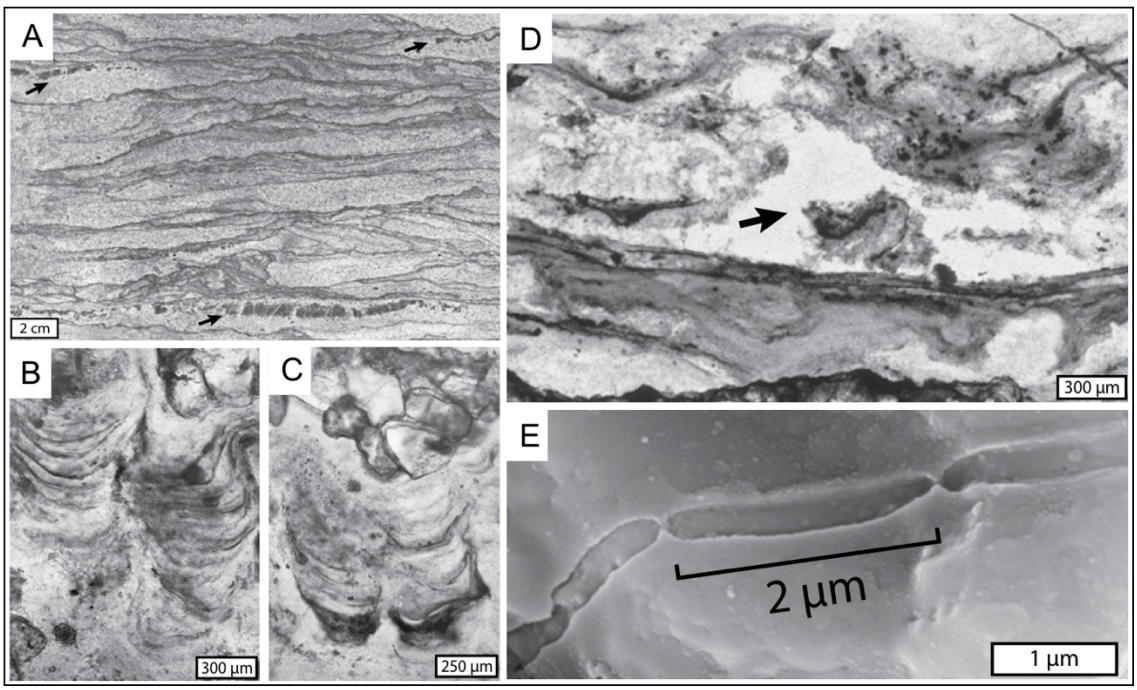

Fig. 17. Coelobiontic cavity-dwelling organisms from the 3.22 Ga Moodies Group. **A**) Macroscale setting of the coelobiontic biosignatures. Cavities (arrowed) occur beneath microbial mats comparable with those in Fig. 16. **B-C**) Examples of downward-growing, undulose microstromatoloids composed of kerogenous laminae. Note the attachment to the cavity ceiling in B. **D**) Single lamina detached from underlying laminations and plastically deformed (arrowed). Note microstromatoloids to the upper left of the photomicrograph. **E**) Chain of regularly segmented, tubular structures permineralised by chert, interpreted as bacteria indigenous to the cavities. Images from Homann et al. (2016), courtesy of Martin Homann.

3. Discussion

3.1. Distribution of traces of ancient life in the Barberton greenstone belt

Multiple microscopic and macroscopic features from the BGB have been considered convincing traces of early life. Putative biosignatures are both morphological and geochemical and include microfossils, microbial mats, stromatolites, microbially induced sedimentary structures, tubular alteration textures in basaltic rocks, isotope fractionation, and biomineralisation. At present, all putative biosignatures come from bedded cherts, basalts, or quartz-rich sandstones and occur throughout the stratigraphy of the BGB, except the oldest Komati Formation and underlying units. The Kromberg Formation and Moodies Group contain an especially rich, well-preserved, record of early life (Fig. 1). Biosignatures are also common in the Hooggenoeg and Mendon formations. However, there is a relative paucity of biosignatures in the Fig Tree Group. The oldest traces of life described herein, from the Middle

Marker horizon of the ca. 3.47-3.41 Ga Hooggenoeg Formation (Hickman-Lewis et al., 2018, 2019), constitute some of the earliest convincing evidence for life on Earth.

Microfossils of multitudinous forms have been proposed in the Onverwacht Formation, Fig Tree Group, and Moodies Group. The simple morphology of many of these objects mean that it is difficult to (1) pass the necessary complexity criteria for biogenicity (e.g., Schopf and Walter, 1983; Buick, 1991; Schopf, 1992, 1993; Wacey, 2009; Westall and Cavalazzi, 2011) and (2) overcome the large number of alternative abiotic formational mechanisms for such morphologies. Simple spherical, ellipsoidal, or rod-shaped microfossil-like objects (Muir and Grant, 1976; Knoll and Barghoorn, 1977; Walsh, 1992; Westall et al., 2001; Glikson et al., 2008; Kremer and Kazmierczak, 2017) often have appearances that could be interpreted mineralogically (Altermann, 2001; Wacey, 2009) or simply as the condensation of carbon around crystalline nuclei. Lenticular objects, interpreted as microfossils, have a poorly understood function within ancient microfossil assemblages. High-resolution correlative microscopy (outlined in Wacey et al., 2016b) would greatly assist in the assessment of their biogenicity and ecology.

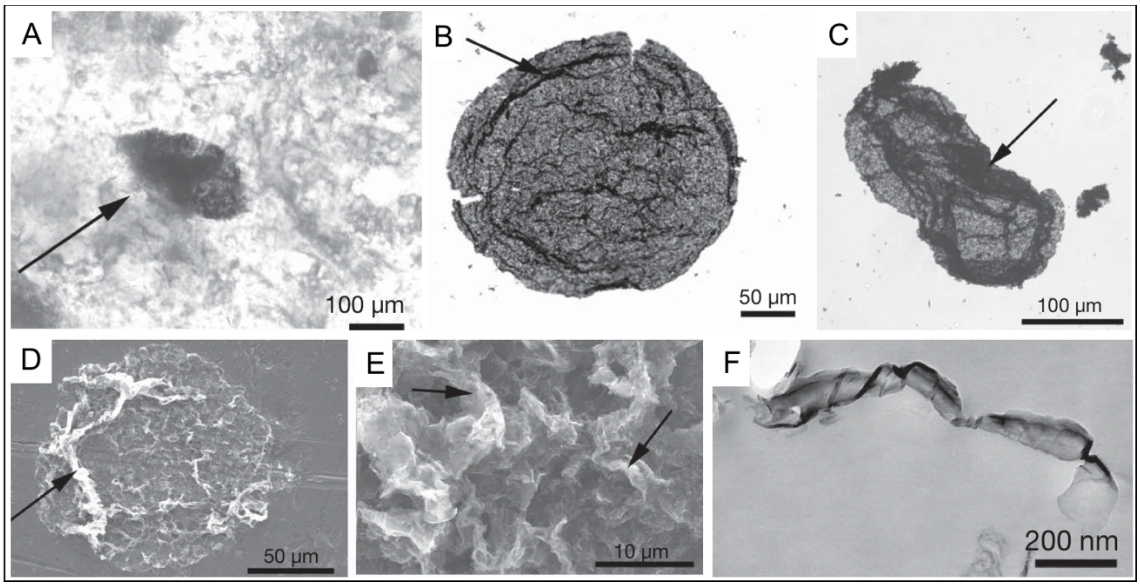

Fig. 18. Irregular, spherical carbonaceous structures from the 3.22 Ga Moodies Group, interpreted as acritarchs (putative biological objects of uncertain affinity). **A**) Light microscopy image of a crumpled putative acritarch (arrowed) in thin section, subparallel to bedding. **B-C**) Equivalent microstructures extracted from rock by acid maceration, featuring concentric folding (arrow in B) and collapse (arrow in C). **D-E**) Backscattered SEM images at low and high magnifications showing the highly folded, wrinkled surface texture of the carbonaceous material. **F**) TEM image of an ultrathin section of wall fabric, showing tearing and wrinkling, i.e., soft structural deformation, of the interpreted acritarch. Images from Javaux et al. (2010).

While three-dimensional, high-relief stromatolites are common across much of the stratigraphy in the time-equivalent Pilbara Craton, stromatolites in the BGB are solely described from the Kromberg and Mendon formations (de Wit et al., 1982; Byerly et al., 1986; Byerly and Palmer, 1991; Lowe and Byerly, 2015). Some phototrophic microbial mats could also be interpreted as tabular stromatoloids (see Noffke and Awramik, 2013). The diversity of stromatolite morphologies exhibited by the Kromberg and Mendon forms is also notably reduced when compared with examples from the Strelley Pool (Allwood et al., 2006) and

Dresser formations (e.g., Van Kranendonk, 2011). Flat-lying microbial laminations, however, are replete in the BGB. Laminated, filament-, or biofilm-like textures constitute some of the most ubiquitous probable traces of ancient life and are a reasonably frequent biosignature in the black-white-grey-green laminated cherts discussed herein (Westall et al., 2001, 2006, 2011a, 2015a,b; Walsh and Westall, 2003; Tice and Lowe, 2004, 2006; Noffke et al., 2006, 2013; Tice, 2009; Homann et al., 2015; Hickman-Lewis et al., 2018). Where laminations show an intimate relationship with the intercalated sediments, for instance, indications of cohesiveness, grain trapping and baffling and an occurrence at regular, predictable stratigraphic intervals, the biogenicity of these laminations should be assumed, even in the absence of architect microfossils. Figure 19 aims to elucidate this point by demonstrating in-sediment relationships of filament-like microbial mats and MISS of various age and with varying degrees of preservation from throughout the Archaean. A similar pattern of grain orientation, lamina-grain relationships, and gross structure is evident, which yields information on the in vivo character of the microbial ecosystem.

3.2. Microbial biomes of the Barberton greenstone belt

The varied environments in which the putative traces of life are described implies that they reflect a wide range of microbial biomes. Metabolisms ranging from phototrophy (Walsh and Lowe, 1985; Walsh, 1992; Walsh and Westall, 2003; Tice and Lowe, 2004; Tice et al., 2004; Westall et al., 2006, 2011a; Homann et al., 2015; Kremer and Kazmierczak, 2017; Hickman-Lewis et al., 2018) through chemoautotrophy (Westall et al., 2015a,b) to chemolithotrophy (Furnes et al., 2004, 2007; Banerjee et al., 2006; Westall et al., 2015a,b; Homann et al., 2016) have been suggested, although there is no definitive proof for any of these modes of life. Stromatolites and microbial mats are perhaps the most conspicuous evidence of microbial communities. Carbonaceous laminations, though of seemingly simple morphology and rarely containing preserved microfossils or palimpsest microstructures, have frequently been interpreted as microbial mats, usually by virtue of a large number of morphological characteristics indicative of their biogenicity and vestiges of interactions with the surrounding sediments. Due to their common occurrence in shallow-water, laminated, black-and-white cherts, a phototrophic affinity has been inferred (Walsh and Lowe, 1985, 1999; Westall et al., 2006, 2011a; Homann et al., 2015; Hickman-Lewis et al., 2018). A relatively high level of tolerance to UV radiation is probable because some of this microbial life inhabited very shallow water or subaerial (terrestrial) environments, and morphological adaptations to changing palaeoenvironmental conditions are evident.

More enigmatic chemotrophic biosignatures have also been proposed in the BGB, invariably within hydrothermally and volcanically influenced lithologies. Westall et al. (2015a,b) interpreted carbon encrustations on volcanic grains as degraded chemotrophic biomass based on their irregular morphology (abiotic deposition by precipitation of carbon of hydrothermal origin around the volcanic clasts should produce a non-isopachous crust; Pope et al., 2000), their similarity in occurrence and appearance to known colonies of microbes coating volcanic particles (Westall et al., 2011b), and their association with biofilms in what is demonstrably a nutrient-rich hydrothermal environment (see Margulis et al., 1983; Juniper et al., 1995; Walsh and Lowe, 1985; Walsh, 1992). The hydrothermal fluids present could have provided the chemolithotrophic microbes with nutrients and small organic molecules, as well as H_2 from microbial alteration of volcanic clasts where present (cf. Parkes et al., 2011).

The importance of hydrothermal activity for nurturing primitive bacterial life remains contested. Although certain formations are unambiguously replete with evidence for hydrothermal veins (de Wit et al., 1982; Hofmann, 2011; Westall et al., 2015a), and despite the presence of silicification gradients stemming from veining zones beneath every BGB chert unit (Hofmann and Bolhar, 2007; Hofmann and Harris, 2008; Hofmann, 2011), the relevance of hydrothermal activity to other formations is disputed, most notably, the Buck Reef Chert. The importance of hydrothermal activity lies in that it favours the flourishing of chemotrophic biomass, and certainly a correlation is seen between chemotrophic biomass and proximity to hydrothermal systems (Westall et al., 2015a; consider also Van Kranendonk, 2007).

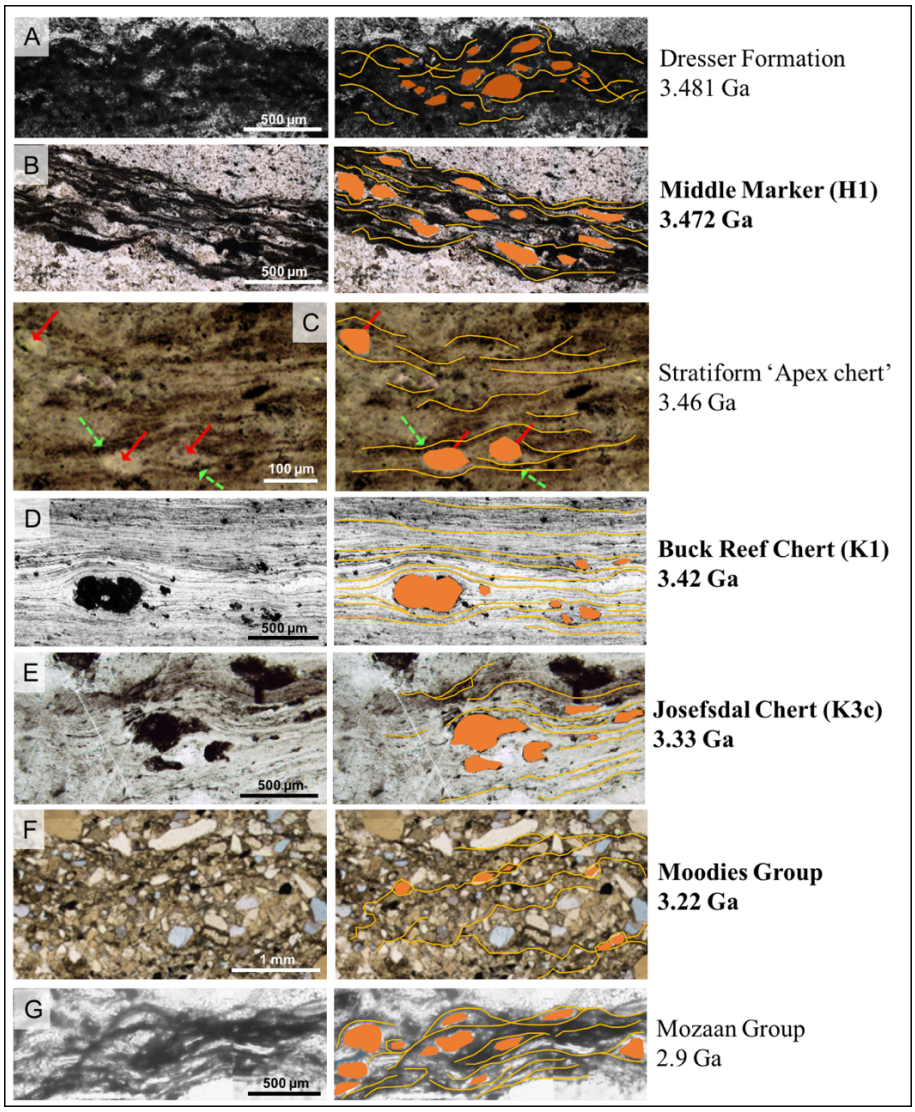

Fig. 19. Atlas of filamentous and filament-like microbial mats and microbially induced sedimentary structures from the Barberton greenstone belt (bold), with similar Pilbara and Mozaan examples provided for comparison. Each photomicrograph is accompanied by an interpretative sketch of the filament-like structures (yellow) and grains (orange) entrained and baffled between the filaments. **A**) Tangled, filament-like MISS from the 3.481 Ga Dresser Formation. **B**) Microbial mat from the 3.472 Ga Middle Marker horizon. **C**) Faint, filament-like MISS from the 3.46 Ga stratiform "Apex chert." **D**) Microbial mats from the 3.42 Buck Reef Chert. **E**) MISS fabrics from the 3.33 Ga Josefsdal Chert. **F**) Microbial mats from the 3.22 Ga Moodies Group. **G**) Mesoarchaean MISS from the 2.9 Ga Mozaan Group. A from Noffke et al. (2013); C from Hickman-Lewis et al. (2016a); D from Tice and Lowe (2006); G from Noffke et al. (2003). Images A and G courtesy of Nora Noffke.

3.3. Hydrothermally influenced habitats from the Palaeoarchaean

From both palaeobiological and taphonomic viewpoints, the obvious advantage of hydrothermal systems is that their silica-saturated effluent has the ability to preserve delicate biosignatures with relatively high fidelity. Hydrothermal effusions are invariably associated with chert deposits (Hofmann, 2005; Hofmann and Bolhar, 2007; Hofmann and Harris, 2008), the lithology from which most ancient biosignatures are described (Wacey, 2009; Westall, 2016). Field and geochemical evidence clearly supports that hydrothermal, silica-rich fluids intruded rock and sediment (de Vries, 2004; van den Boorn et al., 2007, 2010; Hofmann and Bolhar, 2007; Nijman and De Vries, 2009; Westall et al., 2015a) and it is known from experimental studies (Orange et al., 2009) and direct observation of Palaeoarchaean biosignatures that encapsulation and preservation must have occurred within days to weeks (Westall et al., 2006, 2011a,b, 2015a,b; Hickman-Lewis et al., 2016b). After diagenesis, the fractureless (conchoidal) crystallography of silica imparts an enhanced resilience to weathering and erosion, permitting these biosignatures to survive through deep time.

During the lifetime of the hydrothermal vent, the proximal region receives a multiplicity of nutrients in the form of organic molecules produced abiotically during serpentinisation processes, remobilised carbon from buried biogenic and meteoritic facies, the bioessential transition metal ions required as catalysts in multiple enzymatic and metabolic processes, and reactive mineral surfaces from which free energy can be liberated and utilised. Life flourished in disequilibria and these regions, being zones of contact between hot (up to 250˚C), often alkaline, hydrothermal effluent and cooler (>70˚C), more acidic, Archaean seawater, would have provided gradients in temperature, pH, redox environments (eH), and aqueous chemistry (Westall et al., 2015a, 2018), even far downstream of the vent (Nisbet and Sleep, 2001). Therefore, given the prevalence of hydrothermal activity, while there may be a bias toward preservation in hydrothermal systems, it is not surprising that the most diverse Archaean biological communities known are found in such localities.

Petrographic (e.g., Westall et al., 2015a), geochemical (e.g., Orberger et al., 2006), and tomographic (Hickman-Lewis et al., 2016b) studies leave little doubt that the effects of silicification were profound throughout the Archaean and into the Proterozoic; indeed, silicification both preserves and obfuscates original sedimentary textures and biosignatures (Orberger et al., 2006; van Zuilen et al., 2012; Hickman-Lewis et al., 2016b; Westall, 2016; Ledevin, 2018). Although the slight coarsening, typically into spherulites, of microcrystalline silica can (but does not always) disaggregate and distend the form of biosignatures (Brasier et al., 2006; van Zuilen et al., 2012), the preservational powers of entombment by silica are unmatched in their fidelity of morphological preservation and the length over which such preservation is maintained. Thus, cherts yield some of our finest insights into the Precambrian cellular record (Westall et al., 2001, 2006; Schopf, 2006; Hickman-Lewis et al., 2016b; Westall, 2016; van Zuilen, 2018).

4. Conclusions

There is much convincing evidence for early life in the Barberton greenstone belt (3.47-3.22 Ga), portraying a diverse Palaeoarchaean biosphere that occupied both marine and terrestrial habitats. This stands testament to the already widespread distribution and diversity of life on the early Earth (Altermann and Kazmierczak, 2003; Westall and Southam, 2006; Van

Kranendonk, 2011; Westall, 2016). The particularly exceptional preservation of biosignatures in microcrystalline cherts of the Buck Reef Chert and Josefsdal Chert and in silicified quartz-rich sandstones of the Moodies Group provides a precious window into the anaerobic Palaeoarchaean biosphere. In the Josefsdal Chert and Moodies Group, a multitude of observed habitats have been colonised, from subsurface volcanic sediments to the surfaces of shallow-water beach and terrestrial sediments, and possibly within hydrothermal effluent itself. Although phototrophs could also develop in nutrient poor, oligotrophic areas away from hydrothermal vents, chemotrophs appear to have been strongly controlled by proximity to hydrothermally derived nutrients. The Palaeoarchaean was a time of surprising biological diversity, and this record is best accessed by investigating the biomes preserved in chertified horizons.

Manuscript 2 – Most ancient evidence for life in the Barberton greenstone belt: microbial mats and biofabrics of the ~3.47 Ga Middle Marker horizon

Abstract

The Middle Marker – horizon H1 of the Hooggenoeg Formation – is the oldest sedimentary horizon in the Barberton greenstone belt and one of the oldest sedimentary horizons on Earth. Herein, we describe a range of carbonaceous microstructures in this unit which bear resemblance to phototrophic microbial biofilms, biosedimentary structures, and interpreted microfossils in contemporaneous greenstone belts from the Early Archaean. Post-depositional iron-rich fluid cycling through these sediments has resulted in the precipitation of pseudo-laminated structures, which also bear resemblance, at the micron-scale, to certain microbial mat-like structures, although are certainly abiogenic. Poor preservation of multiple putative microbial horizons due to coarse volcaniclastic sedimentation and synsedimentary fragmentation by hydrothermal fluid also makes a conclusive assessment of biogenicity challenging. Nonetheless, several laminated morphologies within volcaniclastic sandstones and siltstones and coarse-grained volcaniclastic sandstones are recognisable as syngenetic photosynthetic microbial biofilms and microbially induced sedimentary structures; therefore, the Middle Marker preserves the oldest evidence for life in the Barberton greenstone belt. Among these biosignatures are fine, crinkly, micro-tufted, laminated microbial mats, pseudo-tufted laminations and wisp-like carbonaceous fragments interpreted as either partially formed biofilms or their erosional products. In the same sediments, lenticular objects, which have previously been interpreted as bona fide microfossils, are rare but recurrent finds whose biogenicity we question. The Middle Marker preserves an ancient record of epibenthic microbial communities flourishing, struggling and perishing in parallel with a waning volcanic cycle, an environment upon which they depended and through which they endured. Direct comparisons can be made between environment-level characters of the Middle Marker and other Early Archaean cherts, suggesting that shallow-water, platformal, volcanogenic-hydrothermal biocoenoses were major microbial habitats throughout the Archaean.

1. Introduction

The Barberton greenstone belt, within the Kaapvaal Craton (Fig. 1), is one of several ancient sequences that provides a window into sedimentary depositional environments of the early Earth. Together with the Pilbara, it is one of only two well-preserved palaeontological enclaves from which remnants of ancient bacterial life have been convincingly described (Wacey, 2009; Westall, 2016; Hickman-Lewis et al., 2018). Its stratigraphy has been examined in detail by Lowe and Byerly (1999, 2007) and Hofmann (2011). Claims of varying validity for ancient life have included microbial fossils and organic remains (Barghoorn and Schopf, 1966; Pflug, 1966; Engel et al. 1968; Nagy and Nagy, 1969; Muir and Grant, 1976; Knoll and Barghoorn, 1977; Walsh and Lowe, 1985; Walsh, 1992; Westall and Gernecke, 1998; Westall et al., 2001, 2006, 2015; Javaux et al., 2010; Homann et al., 2016; Oehler et al., 2017; Kremer and Kazmierczak, 2017), microbial edifices such as stromatolites (Buick et al., 1981; Byerly et al., 1986; Walsh and Westall, 2003), microbial mats or microbially induced sedimentary structures (Walsh, 1992; Walsh and Lowe, 1999; Tice and Lowe, 2004, 2006; Tice et al., 2004;

Westall et al., 2006, 2011, 2015; Noffke et al., 2006a,b; Tice, 2009; Heubeck, 2009; Gamper et al., 2012; Homann et al., 2015), and lava-hosted microtubules (Furnes et al., 2004, 2007; Banerjee et al., 2006). As with most examples of putative ancient life, the substantial weight of the burden of proof (Westall and Cavalazzi, 2011; Brasier et al., 2011), together with the lack of a 'smoking gun' due to the predicament of long-term preservation (Tice and Lowe, 2006) means that most of these claims have faced criticism (see Wacey, 2009, for a recapitulation of many such claims and refutations).

1.1. Geological setting

The Middle Marker horizon is the sedimentary unit defining the base of the Hooggenoeg Formation in the Onverwacht Group (Fig. 2; Viljoen and Viljoen, 1969). It is thus the oldest identified sedimentary horizon in the Barberton greenstone belt. Detrital zircon dating yields an age, terminus post quem, of 3.472 ± 0.005 Ga (Armstrong et al., 1990), which may be taken as accurate, and not an overestimation, since much of the underlying crust of the Kaapvaal craton appears to be little older (Drabon et al., 2017). Additionally, felsic material in the Middle Marker is a likely source rock for common zircons (Hofmann et al., 2013). The Middle Marker is a 3–6 m thick layer consisting of mostly silicified current-deposited volcaniclastic material, and black chert which possibly results from the silicification of a non-volcanic protolith (Lanier and Lowe, 1982). In a previous sedimentological study of this horizon, Lanier and Lowe (1982) deduced a depositional environment involving a cone-flanking, prograding sedimentary platform, in which volcaniclastic sediments were deposited from a waning subaerial volcanic system, in a basin isolated from continental terranes. Although energetic, basin-wide tidal activity was minor, local current- and wave-driven subaqueous deposition has been noted, and a subtidal environment is implied for those parts of the sequence. A significant felsic component suggests that this chert represents a waning cycle of volcanism between two pulses of mafic magmatic activity (Viljoen and Viljoen, 1969; Lanier and Lowe, 1982), although Lowe (1999a,b) notes that Al_2O_3, Zr, TiO_2 and Cr ratios (i.e. the immobile elements) unambiguously document the simultaneous input of komatiitic ashes. Hofmann et al. (2013) further note that while elevated Gd_N/Yb_N and La_N/Sm_N indicate felsic contributions, komatiitic ashes are a common constituent in the unit.

1.2. Sedimentology of the Middle Marker horizon

Having undergone no greater than lowest greenschist metamorphism (Hurley et al., 1972; Lanier and Lowe, 1982; Bourbin et al., 2013; Delarue et al., 2016), primary sedimentary textures and geochemical signatures from the Middle Marker are relatively well-preserved. Since it is the oldest sedimentary horizon in the Barberton greenstone belt and one of the oldest sedimentary horizons on Earth, it provides a particularly pertinent insight into ancient volcaniclastic settings. Lanier and Lowe (1982) demarcated the chert into three stratigraphic divisions – lower, middle, and upper (Fig. 3) – which are here summarised.

The lower unit consists of thinly laminated grey-black chert deposited atop a pillowed, mafic volcanic substrate, and features interstratified, cross-laminated, fine- to medium-grained volcaniclastics. The abundance and grain size of these volcaniclasts increase upward in the lower unit. Light and dark couplets define thin horizontal and lenticular laminations. Other sedimentary structures, such as ripples, flaser bedding and high-angle microscale cross-bedding, are taken as indicative of entirely submarine, low-energy deposition in shallow-water,

alternating between traction and suspension sedimentation (Reineck, 1967; Paris et al., 1985; Lanier and Lowe, 1982). Soft sediment deformation, such as lenticular load structures, are also common. Flaser bedding, together with accretionary lapilli, suggest an increasing influence of volcanism upward in the strata. Our study also notes geochemical and textural evidence for diffuse hydrothermal-like infiltration through laminated volcaniclastic sandstones and siltstones which, where most intense, disrupts original sedimentary features (cf. Paris et al., 1985; Hofmann, 2011).

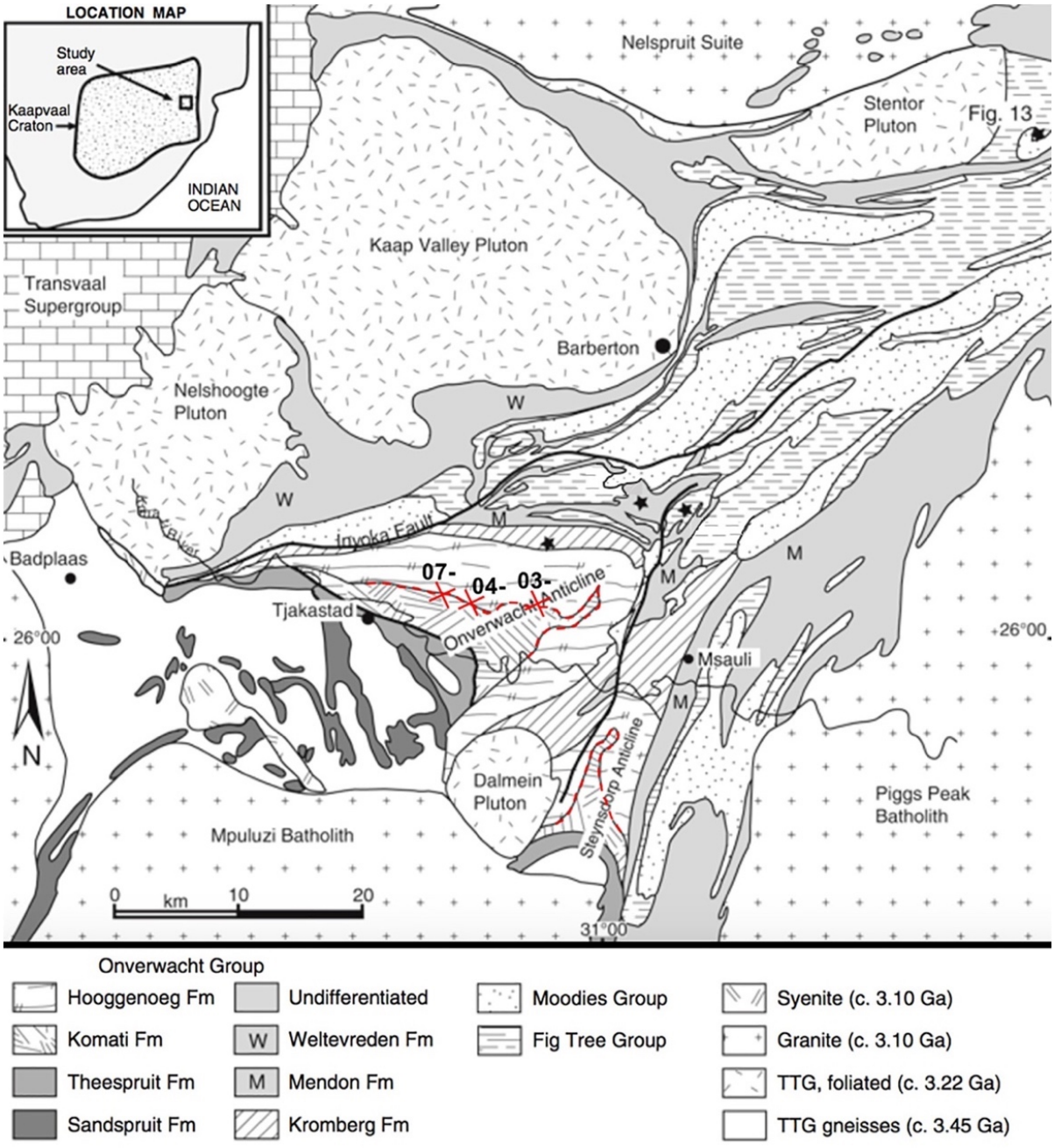

Fig. 1. Geological map of the Barberton Greenstone Belt; inset shows location within the Kaapvaal craton. The Middle Marker (dashed red lines) outcrops through the Onverwacht and Steynsdorp anticlines at the contact zone of the Komati and Hooggenoeg formations. Study areas are marked with red crosses. Modified from Hofmann (2005).

The middle section is dominantly even-bedded, coarser-grained volcaniclastic material weathered green to buff in colour, which contains many accretionary lapilli (Lowe and Knauth, 1978; Lowe and Byerly, 2007). The protolith contains crystal, vitreous and lithic components from volcanic sources (Lanier and Lowe, 1982). Sedimentary structures include trough bedding and tabular cross-stratification of volcaniclastic sandstone, separated by minor chert layers. Trough scours contain fine-grained sediments with interpreted wave-ripple cross-lamination (Lanier and Lowe, 1982; Lowe and Byerly, 1999). Ripped-up clasts of grey-black chert from the underlying layers are common in the overlying layers of volcaniclastic detritus. The middle section therefore depicts the shoaling of water concomitant with an increase of coarse sediment supply and high-energy currents.

Finally, the upper unit is composed mostly of fine-grained grey-black chert with local thin beds of volcaniclastics and conglomeratic rocks. This chert is massive and poorly stratified, although small-scale sedimentary structures, such as fine laminations and cross-stratification, together with relict fine clastic textures, suggest that the protolith was detrital (Lanier and Lowe, 1982). The upper unit therefore represents a fine-grained airfall deposit, the conclusion of waning volcanism, into a low-energy, subaqueous basin. The co-occurrence of pyrite and gypsum, the latter pseudomorphed, denotes deposition in anoxic conditions (Siesser and Rogers, 1976, Lanier and Lowe, 1982) at warm temperatures of up to 52–58°C, concurrent with calculated contemporaneous ocean temperatures from alternative proxies (Knauth, 2005; Tartèse et al., 2017). Chert conglomerate is found in the upper reaches of the Middle Marker, which mixes grey chert and volcaniclastic detritus in what is interpreted as a combination of cracking and current reworking of the sediment (Lanier and Lowe, 1982). Desiccation cracks at the top of the grey chert suggest some subaerial exposure, and thus the sequence is broadly aligned with an intertidal-supratidal flat environment.

In what follows, we describe and evaluate the biogenicity of previously unrecognised putative microbial mat fabrics, microbially induced sedimentary structures and microfossil-like objects within the Middle Marker horizon. Some of these features may represent the most ancient evidence for microbial life in the Barberton region, and the second oldest convincing evidence for life on Earth.

2. Materials and Methods

2.1. Materials

All samples studied come from outcrops of the horizon on the western limb of the Onverwacht anticline, which is the least metamorphosed section of Middle Marker outcrop (Fig. 1). By contrast, the Middle Marker of the Steynsdorp anticline has undergone a greater degree of thermal metamorphism, and is characterised by a coarsened quartz matrix, while that of the eastern limb of the Onverwacht anticline is highly metamorphosed, with most original textural features destroyed (Lanier and Lowe, 1982).

Samples were collected during field campaigns in 2003, 2004 and 2007 (Table 1). All sample collection localities can be readily relocated by means of their co-ordinates in Global Positioning Systems (G.P.S.). Samples are stored at the CNRS Centre de Biophysique Moléculaire (CBM), Orléans.

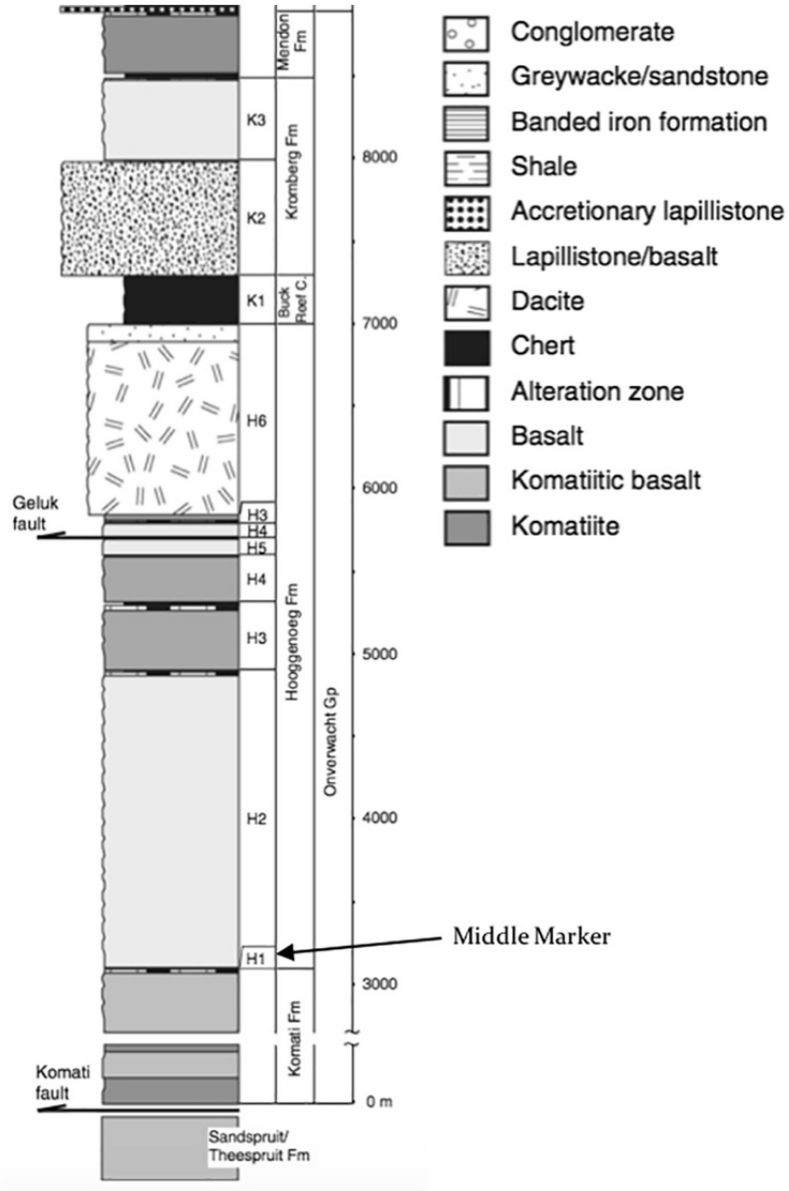

Fig. 2. Stratigraphic column depicting the Onverwacht Group from the western limb of the Onverwacht anticline, indicating the position of the Middle Marker. Adapted from Hofmann (2011).

2.2. Optical Petrography

Optical petrography was performed at the Universià di Bologna using a Zeiss Axioplan microscope, and at the CBM (CNRS, Orléans) using an Olympus BX51 microscope.

2.3. SEM

SEM was conducted at the Universià di Bologna using a Phillips 515 electron microscope equipped with high-performance EDX at 8-15kV. Point analyses were gathered for 100 s (approximately 5,000 counts), using accelerating tension of 5-8kV such that the 'overwhelming' of point analyses by ubiquitous silicification is minimised, i.e. the volume of analysis (a pear-shape beneath the sample surface) is small. Maps were run for 200 frames, approximating 20-25 $x10^6$ counts. This long acquisition time is necessary for the samples studied: cherts of this age are typically up 94-99% silica (e.g. Hofmann and Harris, 2008;

Hofmann, 2011; Westall et al., 2015), and thus gathering a statistically significant complement of counts for other elements is time-consuming.

2.4. Confocal laser Raman spectroscopy

Confocal laser Raman spectroscopy was conducted at the CBM (CNRS Orléans), using a WITec Alpha500 RA system and a green laser at 532 nm wavelength with a laser power set at 5 mW so as to avoid the thermal alteration of carbonaceous matter. Data was refined using WITec Project software and colour-coded Raman mineralogical maps produced as described in Foucher et al. (2017). Raman band intensity ratios were calculated from these analyses (Table 2).

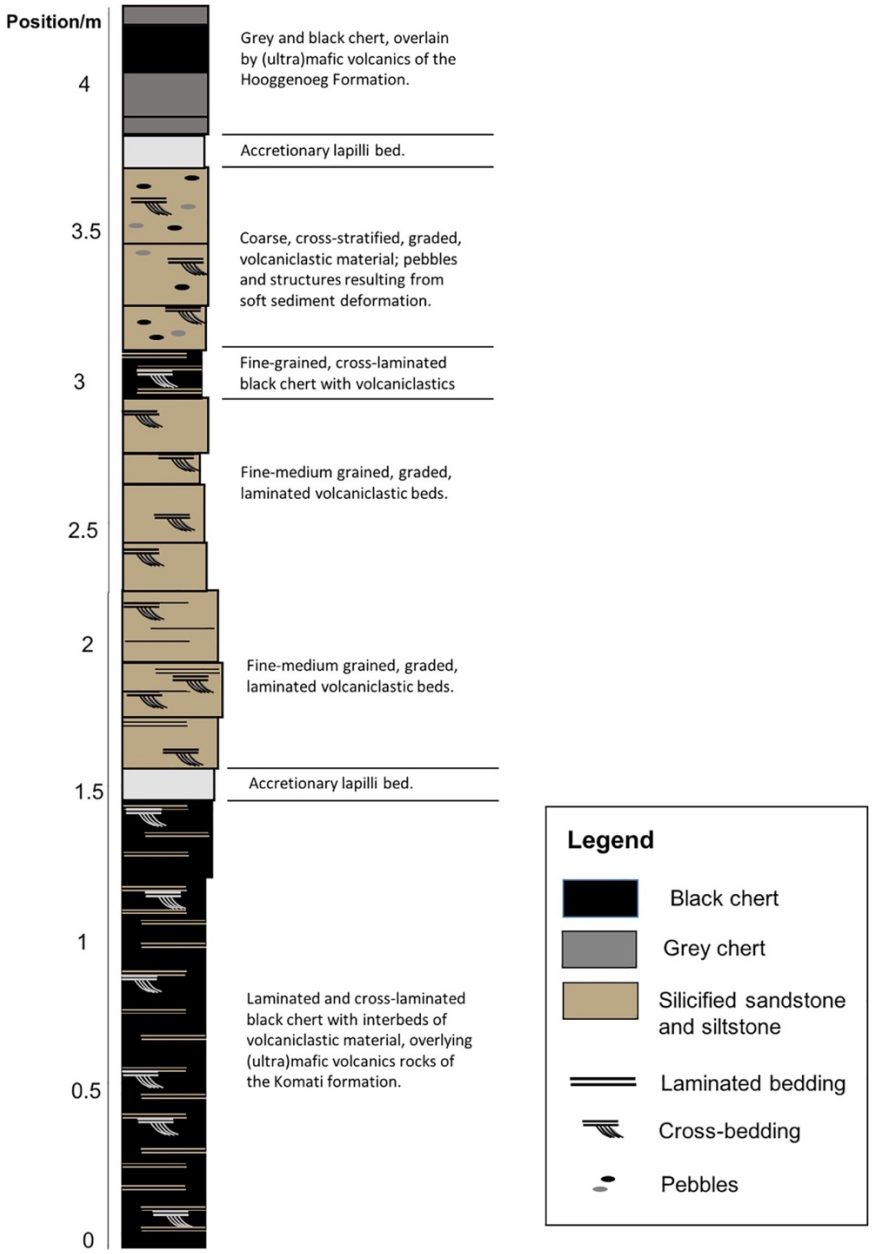

Fig. 3. Generalised stratigraphic column of the Middle Marker from the western limb of the Onverwacht anticline. Adapted from, and annotated after, Lanier and Lowe (1982) and personal field observations (2018).

3. Results I – Lithofacies

3.1. Lithofacies

Petrographic analyses separate the studied samples into three distinct lithofacies: (i) coarse felsic volcaniclastic sandstone, having angular grains up to 3 mm in size, including accretionary lapilli, with weak, macro-scale cross-bedding (Fig. 4A–C); (ii) massive black chert rich in organic carbon, hereafter termed clotted carbonaceous chert (after Lowe and Knauth, 1977), composed of angular or sub-rounded particles of organic carbon up to 2 mm diameter either suspended in a silica matrix or in grain-supported textures, with silica-replaced rounded particles (Fig. 4D,E); and (iii) laminated, green-grey, volcaniclastic sandstone–siltstone, having millimetre-scale alterations between volcaniclastic-rich layers and grey-black chertified layers rich in organic-carbon (Fig. 4F–H). Massive black clotted carbonaceous cherts appear homogeneous in hand specimen, coarse volcaniclastic sandstones are yellow–brown and faintly stratified, while laminated sandstones and siltstones are green-grey in colour and stratified by dark planar and crinkly laminations.

3.1.1. Facies 1: Coarse volcaniclastic sandstone

The volcaniclastic fraction (> 70%) is composed of poorly sorted volcanic glass, randomly distributed mafic and felsic minerals, and lithic fragments (Fig. 4A,B). Some samples are dominantly accretionary lapilli (Fig. 4C). Their mineralogy is dominantly altered feldspars and amphiboles (likely hornblende), angular shards of volcanic glass, minerals with yellow pleochroism, that are possibly sericitised feldspar (cf. Hurley et al., 1972), together with pyrite and very minor proportions of oxides. SEM-EDS reveals a relict Fe-Mg richness in certain zones, which corroborates mafic input (Lowe, 1999a,b; Hofmann et al., 2013), however, these minerals show that widespread alteration to sericite, chlorite and Fe-Al-bearing minerals (Hurley et al., 1972) has occurred (Figs. 5–7). Cr indicates Cr-spinel (chromite), a mineral which is usually resistant to silicification (Cr in Fig. 6B). Raman spectroscopy identified dispersed anatase and rutile within an overwhelmingly silica matrix. This matrix is characterised by a yellow-orange, web-like alteration texture (Fig. 4B). Fine-grained silica has pervasively replaced many components and obfuscates the original mineralogy, such that mineralogical identifications are often necessarily made on crystal habit alone. Basaltic rocks, particularly volcanic glass, alter extremely rapidly to produce a thin phyllosilicate alteration layer; this has been extensively experimentally demonstrated (Oelkers and Gíslaison, 2001; Gíslason and Oelkers, 2003; Wolff-Boenisch et al., 2006; Westall et al., 2018) and is apparent from the Al-rich composition of the groundmass. In Early Archaean sediments, the edges of volcanic glass shards are often outlined by anatase, whereas muscovite and stilpnomelane (see spectra in Fig. 7) can result from potassium metasomatism. The high feldspar content of the volcaniclastics suggests a significant input from felsic pyroclastic material, whereas their poor sorting and angular grain morphology suggests a proximal eruption, after which negligible transportation and reworking of the sediment has occurred. Perceptible imbrication in some layers suggests local, albeit weak, currents (Fig. 4A).

A pervasive web-like alteration texture fills pore space and coats grains (Fig. 4B). It bifurcates and anastomoses irregularly, but follows exactly the grain margins. In void spaces between grains, the laminations are ‘connected’ by a web-like fabric.

3.1.2. Facies 2: Clotted carbonaceous chert

Clotted carbonaceous chert (cf. Lowe and Knauth, 1977; Hickman-Lewis et al., 2016) is a chert rich in organic, kerogen-like carbonaceous material. Such massive, silicified rocks consist of carbonaceous 'clots', which may be either well-rounded or irregular (see Fig. 4D,E), within a silica matrix (cf. Facies C of the Josefsdal Chert, Westall et al., 2015). In hand sample and thin section, these cherts appear matt black, with infrequent layering (Fig. 4D). The spatial interrelationship between silica and carbon gives the chert its characteristic millimetre-scale 'clotted' texture.

Clotted carbonaceous cherts include ~50% medium-coarse sand-grade, carbonaceous particles (Figs. 4D,E and 8): this comprises 70% angular composite particles, > 25% angular simple particles and < 5% flakes and wisps (cf. Walsh and Lowe, 1999; Hickman-Lewis et al., 2016). Aside from carbonaceous matter, this lithofacies contains ~ 45% microcrystalline silica (Figs. 4D,E and 8B) and 5% dispersed volcanogenic material, indicated by the proxy mineral anatase (Fig. 8B). Composite carbonaceous particles are constructed of up to hundreds of sub-angular simple carbonaceous particles (cf. Greco et al., 2018). Wisps of carbon, though bearing superficial semblance to biogenic roll-up structures (Walsh and Westall, 2003; Tice and Lowe, 2004), clearly follow the boundaries of sub-angular grains.

3.1.3. Facies 3: Laminated, green-grey volcaniclastic sandstone-siltstone

Laminated sandstone-siltstones are the most texturally diverse of the three lithofacies. They consist of volcaniclastic and volcanic components equivalent to coarse volcaniclastic sandstones, with grains sizes of 0.1–2 mm, and are laminated on the millimetre- to centimetre-scale (Fig. 4F–H). The matrix contains detrital mafic and felsic minerals, including altered pyroxene (diopside-augite), plagioclase, amphiboles, silicified volcaniclastics altered to phyllosilicate mineralogies, and prismatic minerals which EDS point analyses identify as chlorite and Fe-Al phyllosilicates (Fig. 7; Hurley et al., 1972). The green-grey colour of this lithofacies is imparted by extensive chlorite alteration. Raman analyses of the lithofacies identify dispersed siderite and anatase particles, often associated with organic matter. Layers of volcanogenic sediments are invariably topped by multi-laminar organic carbon-rich laminations (Fig. 4F). By contrast to the other lithofacies, evidence for current-induced sedimentation is relatively common: cross-stratification, well-sorted layers, surficial sediment deformation features and imbricated clasts are present, all of which necessitate at least local, weak current activity (see also Lanier and Lowe, 1982).

Laminated fabrics rich in organic carbon are frequent features of the micro-stratigraphy, occurring every 1–10 mm, and are morphologically diverse (Figs. 4 and 7). Most are crinkly and continuous over the scale of tens of centimetres in samples (Fig. 4F) although others are flat-lying and undulatory (Fig. 4H). They are conformable with the sedimentary sequence and therefore primary fabrics. In contrast to the coarse volcaniclastic sandstones and clotted carbonaceous cherts, organic carbon is a volumetrically significant component of this lithofacies: it occurs predictably, recurrently and identically at the centimetre-scale.

Table 1. Sampling localites and sample characteristics.

Table 1
Sample details.

Sample	Location	Classification	Description and specific characteristics
03SA01	S 25°58′47″ E 30°53′91,7″	Coarse-grained volcaniclastic sandstone	Coarse, angular volcaniclasts within silica matrix. Rare carbonaceous laminations. Relatively high feldspathic content. Well-bedded, some graded bedding. Widespread alteration of particles, forming Fe-rich coatings.
03SA02	S 25°58′47″ E 30°53′91,7″	Coarse-grained volcaniclastic sandstone with subordinate interbeds of laminated black chert	
03SA03	S 25°58′47″ E 30°53′91,7″	Coarse-grained volcaniclastic sandstone	Coarse, angular volcaniclastics and a large volume of accretionary lapilli interbedded with thin carbonaceous laminations. Well-bedded, some graded bedding. Widespread alteration of particles, forming Fe-rich coatings.
04SA12A	S 25°58.434′ E 30°55.592′	Laminated sedimentary black chert	
04SA12B	S 25°58.434′ E 30°55.592′	Coarse laminated sedimentary black chert	Frequent carbonaceous laminations in graded bedding sequences. Coarser grain size results in poorer preservation of carbonaceous fabrics.
04SA12C	S 25°58.434′ E 30°55.592′	Massive black chert; contact with overlying coarse volcaniclastic sandstone	
04SA14	S 25°58.426′ E 30°55.357′	Laminated volcaniclastic sandstone and siltstone	
04SA16	S 25°58.438′ E 30°55.616′	Coarse laminated sedimentary black chert	
07SA21A	S 25°58′12,8″ E 30°53′04,0″	Laminated volcaniclastic sandstone and siltstone	Fine-medium silicified volcaniclastic sandstone with regular carbonaceous laminations. Angular clasts with a general trend of upward coarsening leading to repeated couplets of volcaniclastics and carbonaceous laminations.
07SA21B	S 25°58′12,8″ E 30°53′04,0″	Laminated volcaniclastic sandstone and siltstone	
07SA22	S 25°58′12,8″ E 30°53′04,0″	Massive, clotted black chert	Angular carbonaceous clots in a matrix-supported rock.
07SA23A	S 25°58′12,8″ E 30°53′04,0″	Coarse volcanic detritus with regions of volcaniclastic sandstone	Very coarse volcanic particles substantially altered to sericite, illite, chlorite and other phyllosilicates, surrounded by a silica matrix.
07SA23B	S 25°58′12,8″ E 30°53′04,0″	Laminated volcaniclastic sandstone and siltstone	Medium-coarse volcanic material and volcaniclasts interbedded with regular carbonaceous laminations. Some reverse graded bedding; carbonaceous laminations usually overlain by very coarse, substantially altered volcanic material.
07SA24	S 25°58′12,8″ E 30°53′04,0″	Massive, clotted black chert	Carbonaceous clots form a grain-supported texture together with rounded silica-replaced grains. Frequent cross-cutting microquartz veins.
07SA25	S 25°58′12,8″ E 30°53′04,0″	Massive, clotted black chert	Well-rounded carbonaceous particles form a grain-supported texture together with rounded silica-replaced grains. Frequent cross-cutting microquartz veins.

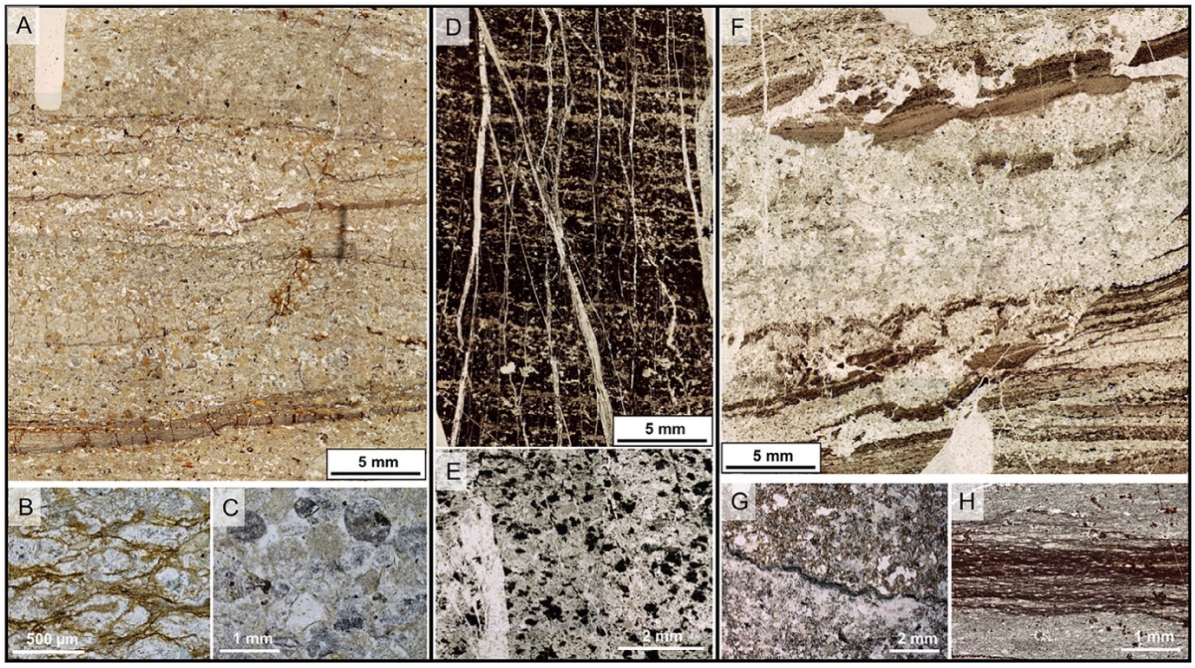

Fig. 4. Atlas of the three major lithofacies in the Middle Marker. **A–C**) Thin section mosaic of coarse-grained volcaniclastic sandstones, cross-bedded on the macro-scale. **A**) Thin section scan of volcaniclastic sandstone 03SA03. **B**) Photomicrograph of 03SA01, showing the yellow-brown, web-like fabric which pervades all void spaces. **C**) Accretionary lapilli. **D-E**) Massive, black, clotted carbonaceous chert. **D**) Thin section mosaic of 07SA25, clotted carbonaceous chert with sub-rounded clots and flakes, interspersed with rounded quartz grains and microcrystalline matrix. The section is cross-cut and interbedded with vertical and stratiform microquartz and coarse quartz veins. **E**) Photomicrograph of 07SA22, showing irregular, spiky, carbonaceous clots intermixed with siliceous particles. **F–H**) Laminated volcaniclastic sandstones and siltstones. **F**) Thin section mosaic of laminated crinkly carbonaceous fabrics interbedded with graded volcaniclastic deposits, bearing the hallmarks of deposition in a shallow marine environment. **G**) Crinkly-wavy, thick, carbonaceous lamination overlain by volcaniclastic detritus. **H**) Low-relief, crinkly lamination, incorporating oriented quartz grains, in volcaniclastic siltstone.

3.1.4. Geochemical indications of palaeoenvironment

Major and trace element data gathered from 'bulk' hand sample analysis can shed light on the palaeoenvironmental and chemical oceanographic conditions of deposition (see Grassineau et al., 2002; Gourcerol et al., 2015, 2016). Representative samples of each of the three lithofacies heretofore identified (coarse volcaniclastic sandstone, 03SA01; clotted carbonaceous chert, 07SA22; and laminated volcaniclastic sandstone and siltstone; 07SA21, 07SA23, 04SA14) were analysed by ICP-OES and ICP-MS. Most samples show a bulk composition consistent with a mostly altered mafic and minor felsic precursor (high Al, Fe, Mg, K content) whereas one sample, 07SA23, shows a remarkably high Ca content (Fig. 5A). This is consistent with an observed 9 wt% calcite content in this sample (X-ray diffraction, results not shown).

Rare earth element plus yttrium (REE + Y) analyses normalised to Mud from Queensland (MuQ, cf. Kamber et al., 2005) of the same samples show – with the notable exception of sample 04SA14 – a generally increasing trend from light rare earth elements (LREEs) to heavy rare earth elements (HREEs). Two of the samples of laminated volcaniclastic sandstone and siltstone (07SA21, 07SA23) and the sample of coarse volcaniclastic sandstone (03SA01) show pronounced positive Eu anomalies, one of which also shows a weakly positive

Y anomaly (Fig. 5B). 04SA14 shows almost the inverse of this trend, and much higher concentrations of REE+Y. By contrast, the sample of clotted carbonaceous chert shows a largely flat REE + Y trend.

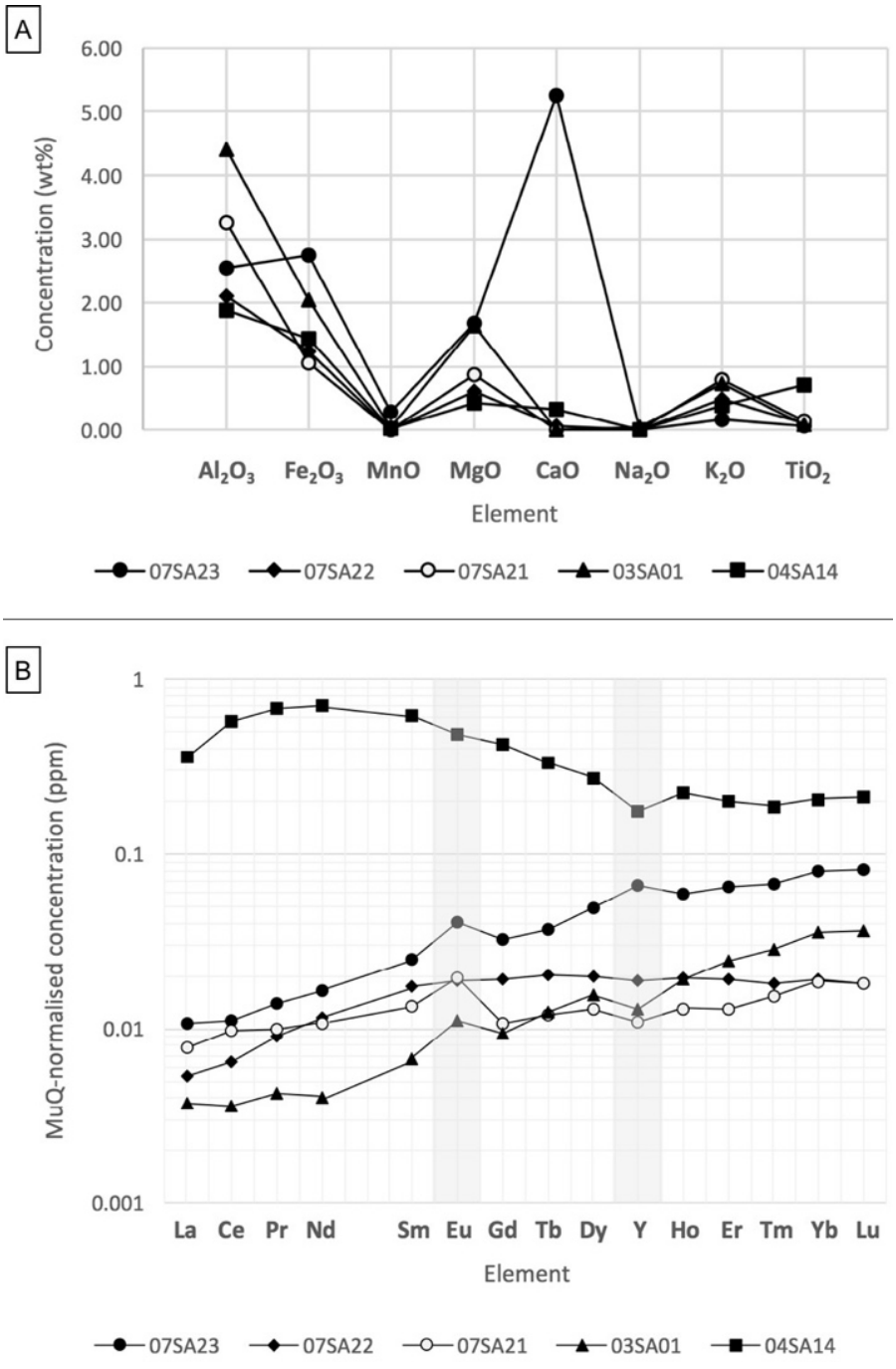

Fig. 5. Bulk geochemical characterisation of several of the samples used in the study, using representative samples of the three lithofacies (see Fig. 4, Table 1). **A**) Major element concentrations. **B**) REE + Y plots normalised to Mud from Queensland (MuQ; Kamber et al., 2005). The generally incremental positive trend indicates a dominant seawater component, whereas the weakly positive Eu anomaly indicates a minor component from hydrothermal fluid. The trend of 04SA14 is very much the inverse of the other samples, and shows remarkably heightened REE + Y concentrations; this effect has been attributed to post-diagenetic alteration, and therefore this sample is likely uninformative of the depositional setting of the unit.

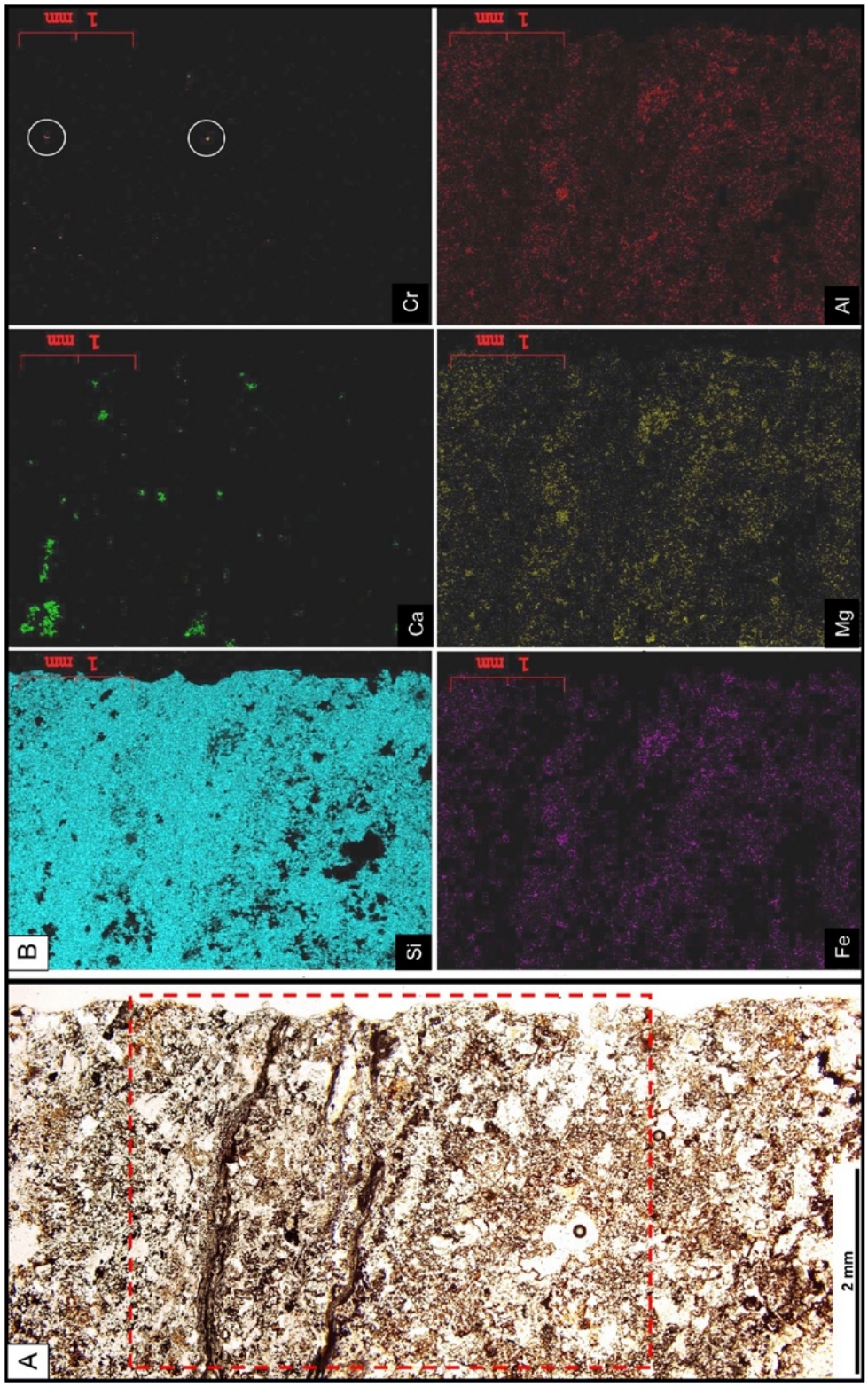

Fig. 6. SEM-EDX analyses of volcaniclastic material. **A**) Buff-brown-green coarse volcaniclastic sandstone with carbonaceous laminations. Red box indicates the region of the element maps. **B**) Element maps for silicon, calcium, chromium, iron, magnesium and aluminium show a broad mixture of mafic (Fe-Mg) and felsic (Ca-Al) mineralogy. Co-occurrence of Fe-Mg-Al signifies the alteration of volcanic glass and crystals to chlorite and/or smectite. In D) chromite spinel grains (unsilicified) are circled. Note the anticorrelation of silica with carbonaceous material.

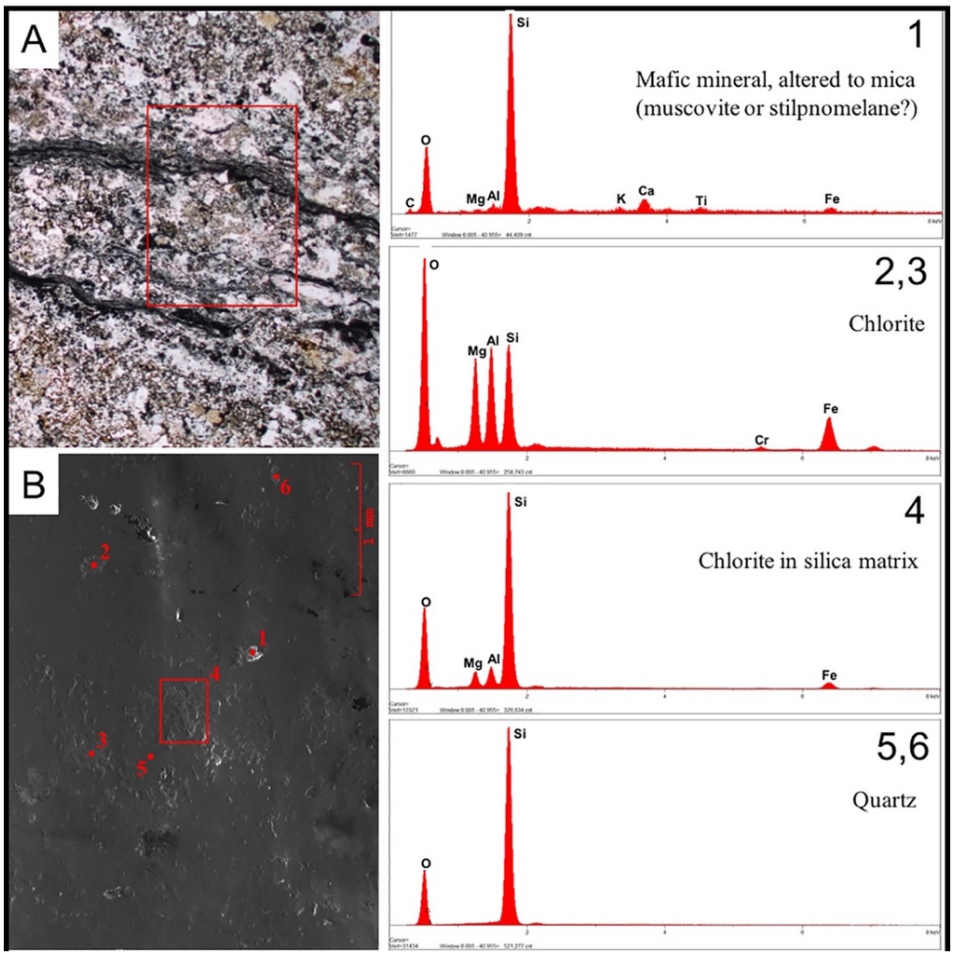

Fig. 7. SEM-EDX point analyses of volcaniclastic material. **A**) Typical coarse volcaniclastic sandstone from the same region as Fig. 5. Red box indicates region of B. **B**) Points and regions analysed by SEM-EDX. Results are numbered. Broadly, the matrix is a silica-chlorite mix.

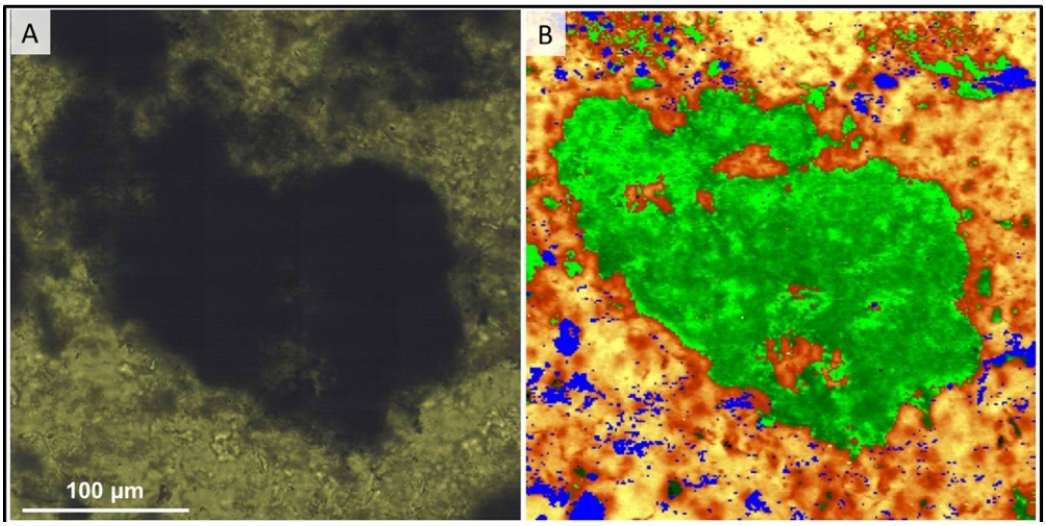

Fig. 8. Raman spectroscopic mapping of an individual clot in massive clotted carbonaceous chert. **A**) Photomicrograph of clot and matrix in plane-polarised light. **B**) Raman spectroscopy mapping in which carbonaceous material = green, quartz = yellow-orange, anatase = blue.

4. Results II – Laminated fabrics and carbonaceous microstructures

4.1. Fine, crinkly, micro-tufted laminations

Fine, crinkly, often micro-tufted laminations (Figs. 9A–C, 10–12), occurring in packets of thickness from 200μm to 2.5mm, are the most common carbonaceous laminated feature in the Middle Marker. They have a gross structure composed of fine, non-isopachous sets of laminae which drape and bind detrital quartz and volcanogenic grains, and are intercalated with silica lenses and layers (Figs. 10 and 11B–E). Single laminae exhibit bifurcation and anastomosis. The entrained, oriented grains have identical chemistry to the groundmass, i.e. Fe-Mg-Al-K mafic and felsic particles (Fig. 12E,F). Lamina packets generally mantle sedimentary layers (Fig. 10A,B) and frequently drape grains which are oriented parallel to their laminae (Figs. 10 and 11C–E). Surficial relief is low, generally below 100μm, and, where present, occurs as microscopic tufts (Figs. 9A and 10A,B). Tufts manifest themselves at regular intervals (every several tens of microns laterally), and with greater regularity when on inclined stratification. At low magnification, crinkly laminations appear continuous over tens of centimetres, however, they are in fact constructed of many shorter film-like objects of 50–300 μm in length (Fig. 11C–E). They exhibit ductile response to micro-faults, intrusions and loading (Fig. 11).

The compression of crinkly, laminated layers is laterally heterogeneous. Where compressed, little of the original voluminous fabric is preserved; instead, these features are preserved as faintly laminated carbonaceous layers within which quartz grains ‘float’ without grain-to-grain contact (Fig. 10D,E). In the matrices immediately above each laminated horizon are multiple wisp-like and lenticular objects which are possibly eroded and reworked fragments of the lamination itself (see Section 4.4). Additionally, some crinkly laminae appear to have been splintered in a brittle fashion, or frayed (see Section 4.4). In the latter case, eroded fragments, again including wisps and flakes, are common in the immediate vicinity.

Every crinkly laminated layer is abruptly overlain by a deposit of coarse, angular, poorly sorted volcanic and volcaniclastic detritus, often glassy or tephra-dominated, which appears to have been deposited rapidly, therein immediately changing the regime to deposition (Figs. 10 and 11). Ergo, crinkly laminations develop during erosional regimes, and their formation is halted during depositional regimes.

4.2. Pseudo-tufted laminations

Tufted laminations are particularly thick (up to 2.5 mm) carbonaceous layers (Figs. 13 and 14). They comprise a mixture of wiry, crinkly, filament-like laminations (identical to those described in Section 4.1.) admixed with microgranular material, and the scale of relief exhibited by individual tufts is an order of magnitude greater than those of crinkly laminations. The microstratigraphy of each tufted layer is tripartite: lower regions with a chaotic mixture of elongate carbonaceous flakes (cf. Schieber et al., 2007; Noffke, 2010; Harazim et al., 2013; Hickman-Lewis et al., 2016) and varied simple particles including clots of carbon; middle regions of crinkly, filament-like laminae entraining medium-sized sand-grade particles and exhibiting anastomosis; and an upper region of tufts (Figs. 13A–D and 14). Microgranular material is concentrated in the upper regions of the tufts and intermingled with laminations at the base of the layers. Tufts have a relief of up to 0.8 mm, a basal width of up to 1.2 mm, and occur at regular intervals along the lamination. The filament-like laminations that constitute

the base often inflect upward into the tufts (see interpretative diagrams in Fig. 13C,D), though some rare tufts fail to preserve any laminations within their upper reaches (Fig. 14A). Some less well-preserved carbonaceous laminations resemble degraded examples of tufted laminations. (Fig. 14E,F) The troughs connecting tufts are often associated with dense grains settled out of deposition, demonstrating that tufts were the result of plastic deformation, thus we term these structures 'pseudo-tufted' laminations.

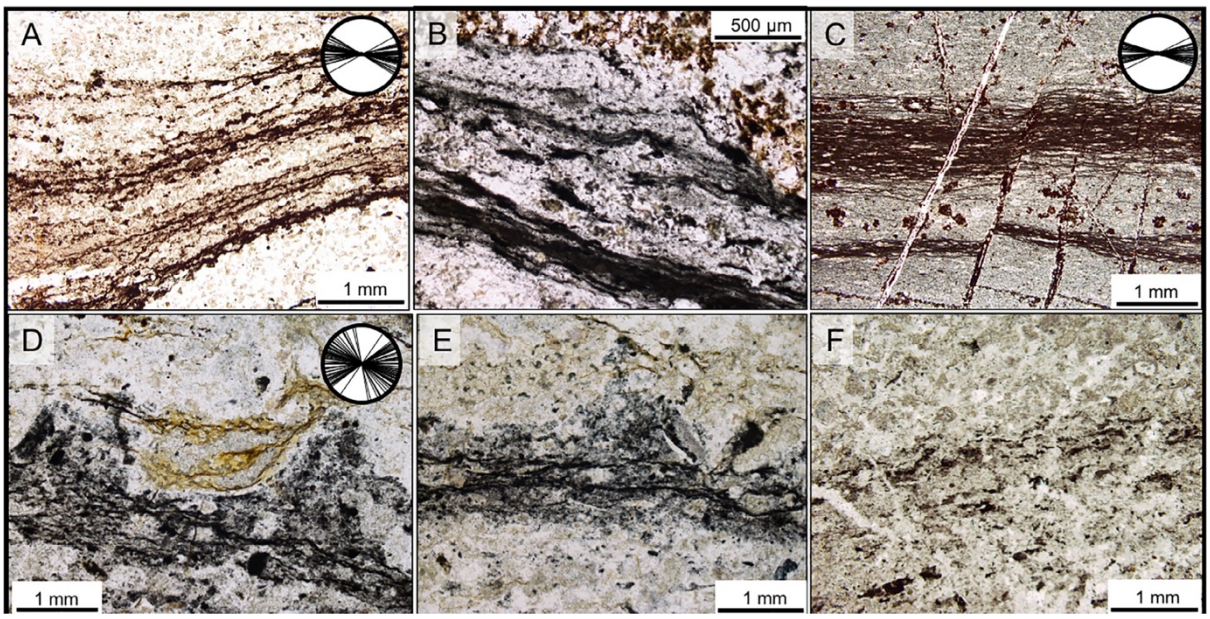

Fig. 9. Laminated textures from the Middle Marker horizon which are interpreted as of microbial genesis. Where applicable, a rose diagram of lamination orientations is provided; a dumb-bell shape is compatible with biological morphospace (after Noffke et al., 2013). **A-B**) Crinkly, filament-like laminations, which have a gross structure of carbonaceous laminations intercalated with siliceous and volcaniclastic layers, and which mantle sedimentary textures of the host rock. **C**) Low-relief, crinkly-wavy lamination, displaced by micro-faults. Note entrained quartz grains. **D-E**) Pseudo-tufted carbonaceous laminations; rose diagram in D applies to both. **F**) Degraded carbonaceous material in a laminated volcaniclastic sandstone, interpreted as being originally a pseudo-tufted lamination.

4.3. Wisps, flakes and roll-up structures

Carbonaceous wisps (cf. Walsh and Lowe, 1999) and flakes (cf. Noffke, 2010; Schieber et al., 2012; Hickman-Lewis et al., 2016), are commonplace throughout the sediments (Figs. 11 and 15), although rare to absent in massive clotted carbonaceous cherts. Having compositions and dimensions equivalent to the fine, crinkly, film-like laminations, and exhibiting the same signatures of originally plastic, cohesive behaviour (i.e. forming roll-up structures), these microstructures are likely fragments of the crinkly laminations. Erosional processes acting at the surfaces of laminations are evidenced by the presence of tear-up structures (Figs. 9B, 10E and 15A,B). A tear-up structure probably represents the precursor to a wisp or flake, whereas a roll-up structure, such as seen in the matrix, represents the current-reworked end-product of the eroded fragment of microbial mat.

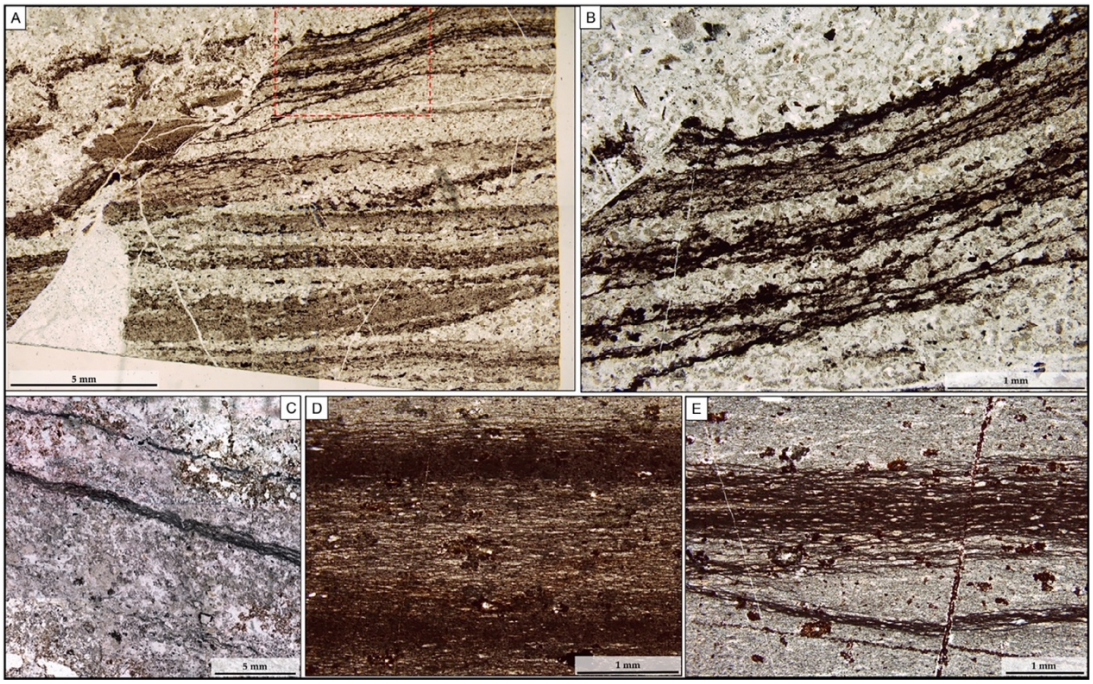

Fig. 10. Morphologies of crinkly, filament-like laminations interpreted as microbial mats. **A**) Low-magnification view of multi-laminar microbial mats preserved over parallel and inclined stratification. Note the plastic deformation of carbonaceous laminations at the micro-fault (upper centre). **B**) Higher-magnification image of the region outlined by the red box in A. Laminations appear crinkly by virtue of their micro-tufted topography. Note the gross structure of carbonaceous laminae intercalated with lenses of silicified volcanic particles, and the thickening of carbonaceous laminae toward crests. **C**) Low magnification photomicrograph of crinkly-wavy laminations in a coarse laminated volcaniclastic sandstone, occurring at the top of a graded sequence. **D-E**) Low-relief, crinkly laminations which entrain oriented quartz grains. D has witnessed a greater degree of compression that E. **E**) exhibits plastic deformation.

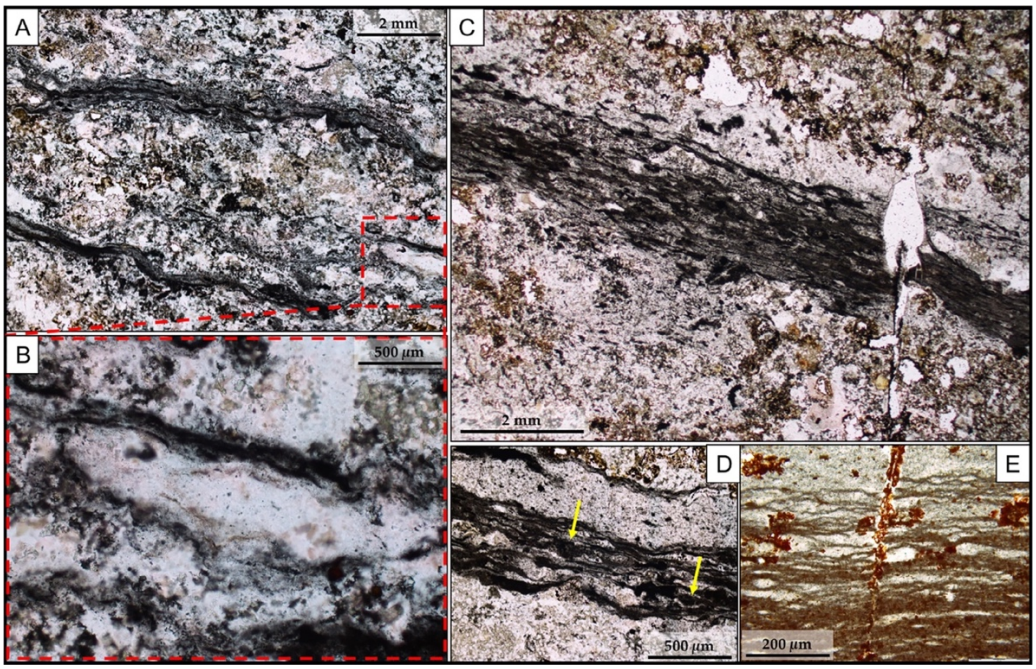

Fig. 11. Characteristic features and details of crinkly, filament-like microbial laminations interpreted as microbial mats. **A**) Multi-laminar microbial mat which surrounds a mass of pyroclastic, volcaniclastic material. Structure in

B is indicated by red box. **B**) Individual laminae surround a silica lense. **C**) Crinkly-wavy laminations in a coarse laminated volcaniclastic sandstone, overlain by coarse pyroclastic material which inhibits microbial growth. Note the mantling of the rhombic grain below (lower centre). **D**) Crinkly laminations within which are lenticular objects (arrowed). See Fig. 16 for further examples and Section 4.4. for detailed explanation. **E**) Trapped, baffled, oriented quartz particles within an interpreted microbial mat.

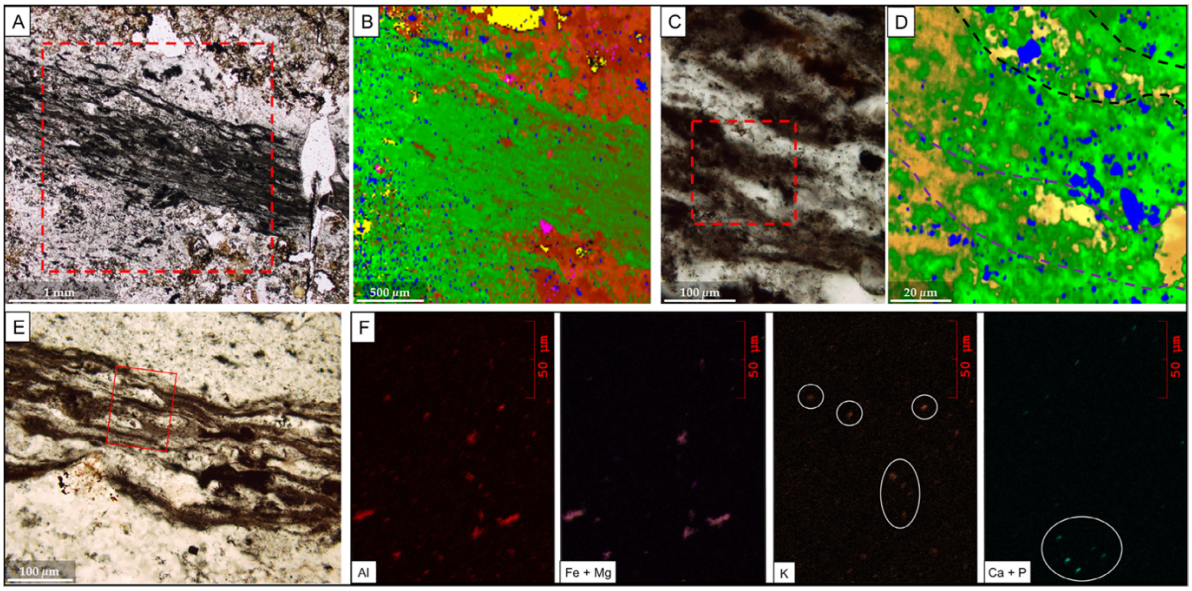

Fig. 12. Raman and SEM-EDX mineralogical and elemental mapping of carbonaceous crinkly, filament-like laminations in laminated volcaniclastic sandstones-siltstones, interpreted as microbial mats. **A**) Photomicrograph of thick lamination; red box indicates area of Raman mineralogical map in B. **B**) Raman spectroscopic map, in which carbonaceous material = green, quartz = orange, anatase = blue, siderite = pink, araldite (resin) in voids = yellow. Note the concentration of carbonaceous material both within the microbial mat and within the clotted fabric directly below. A gross structure of carbonaceous material separated by volumetrically inferior siliceous lenses oriented parallel to the laminae is clear. **C**) High-magnification image of the crinkly, filament-like lamination. Red box indicates area of Raman mineralogical map in D. **D**) Raman spectroscopic map in which carbonaceous material = green, quartz = yellow-orange and anatase = blue. Dotted lines indicate the gross structure, and separate lamina regions (dominated by carbon) and lense regions (dominated by quartz). **E**) Crinkly-wavy lamination. Red box indicates the region mapped by SEM-EDX in **F**). **F**) SEM maps of Al, Fe + Mg, K and Ca + P, demonstrating that, in addition to quartz, oriented particles of both mafic and felsic volcanogenic material have been trapped within the mat. The map of K likely indicates unsilicified feldspathic grains, and Ca + P indicates apatite grains.

4.4. Lenticular objects

Within several horizons of laminated volcaniclastic sandstones and shales, lenticular structures, formerly termed spindle-like structures (cf. Walsh, 1992; Sugitani et al., 2009, 2015; Oehler et al., 2017), are either intercalated with, or are contiguous within, carbonaceous laminae (Fig. 15). These structures have a size of 30–300 µm, and are morphologically consistent with other lenticular structures throughout the matrices of the same samples, often having tapering margins and central voids (Fig. 15). Fig. 15A shows a set of frayed laminae; in the immediately adjacent region, which is mostly volcaniclastic detritus, there are at least four such lenticular objects. That the lenticular structures within the laminae have an elongate, oriented distribution parallel to the laminae (Figs. 11D and 15B,C) suggests their syngenicity with the laminae.

In the matrix, lenticular structures occur randomly but frequently, and are likely derived from the erosion of different fine, crinkly, film-like laminations. They have various compositions, spanning carbonaceous through tuffaceous to vitreous (Fig. 15E–H), and exhibit a wide range of sizes and morphologies dependent upon the presence of equatorial extensions, of which there may be up to two.

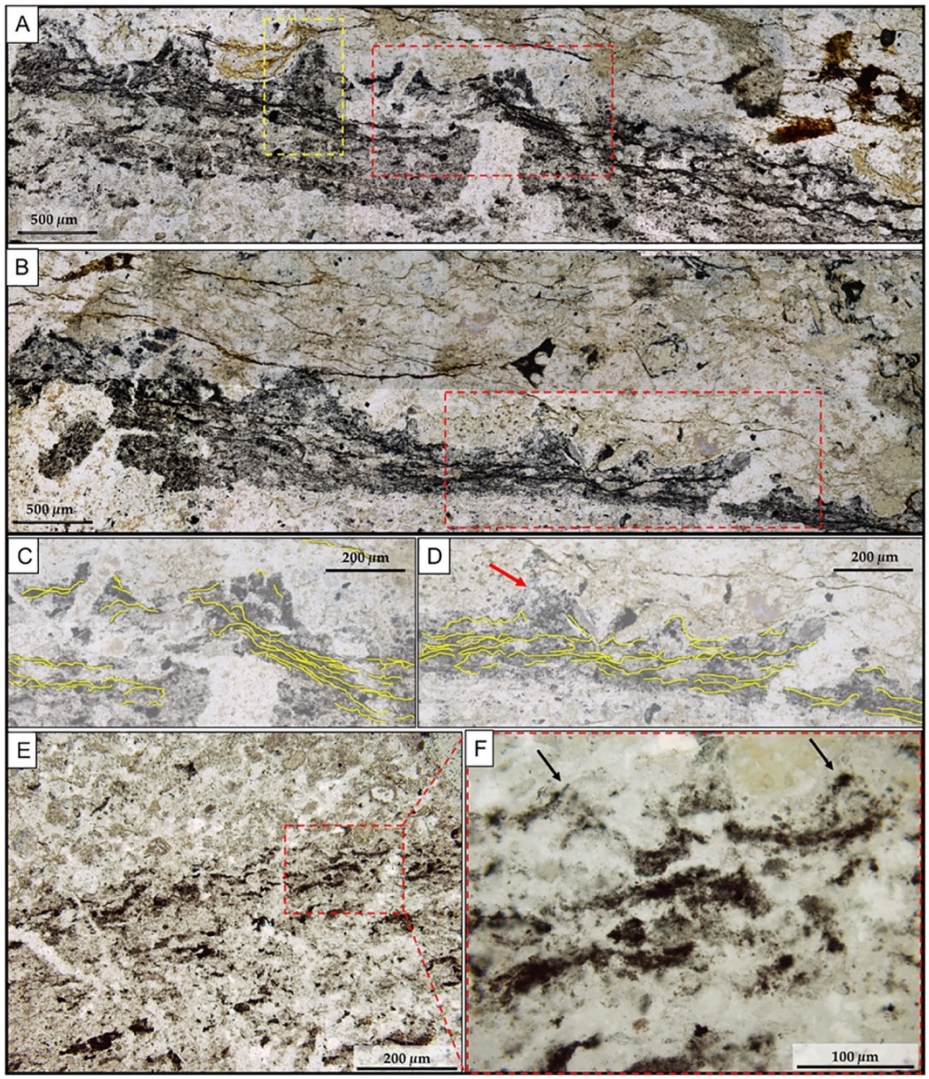

Fig. 13. A-B) Tufted layers in laminated volcaniclastic sandstones and siltstones, interpreted as pseudo-tufted microbial mats. These are dark grey, carbonaceous edifices with clear peaks and troughs which represent a secondary morphology (see main text for explanation). Crinkly, biofilm-like laminations are common in the lower part of the layers, and occasionally reach the crests. Red box in A indicates the region shown in C; red box in B indicates the region shown in D; yellow box indicates the region of the Raman spectroscopic mapping in Fig. 13. **C-D**) Interpretation of the occurrence of individual crinkly biofilm-like laminae within mats. Note that across both tufts, there is small amount of preservation of biofilm within the crest region, suggesting that tufts are coeval with the laminae below. In the tuft, granular fabrics dominate, which may have formed due to Ostwald ripening of silica spherules (red arrow). **E-F**) Carbonaceous layers with a weakly preserved tuft-like morphology, interpreted as degraded pseudo-tufted microbial mats. Red box in E indicates region of F. Arrows in F indicate probable ex-tufts. There is little to no preservation of interpreted microbial biofilms therein.

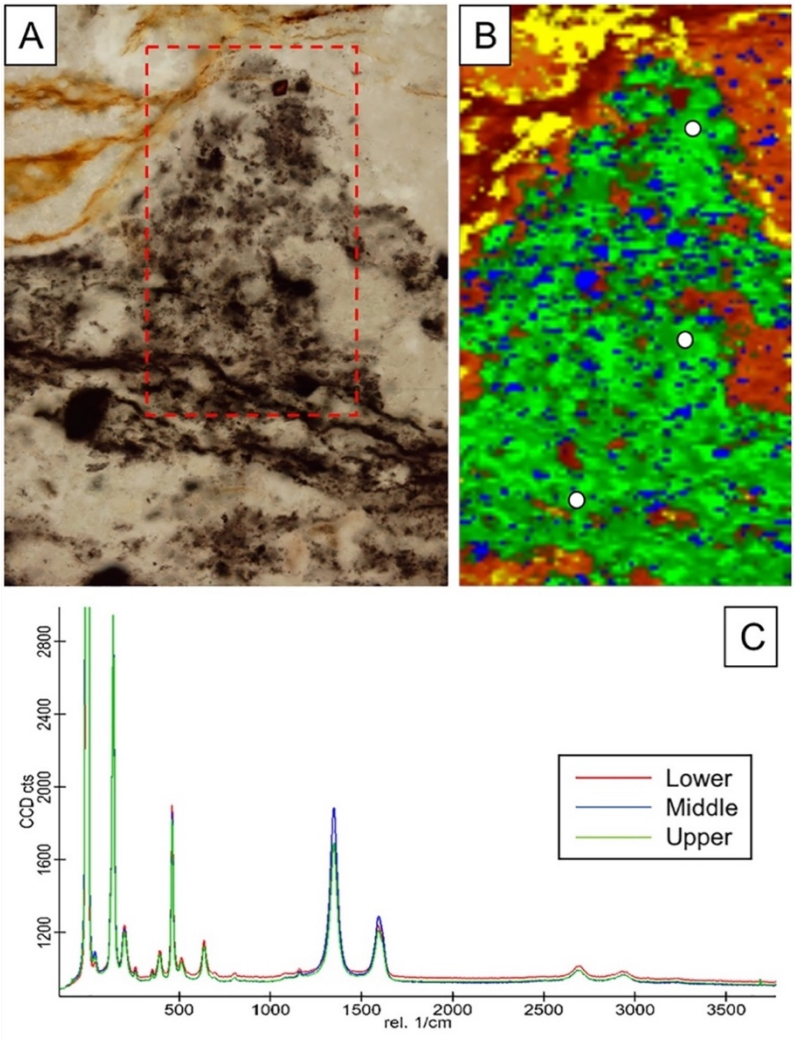

Fig. 14. Raman spectroscopic mapping and point analyses within the tuft indicated in Fig. 12A. **A**) Photomicrograph in plane-polarised light of single tuft, with laminated base and granular crest. Red box indicates region of B. **B**) Raman spectroscopic map, in which carbonaceous matter = green, silica = orange, anatase = blue, and araldite (resin) = yellow. The three white circles indicate the point spectra displayed in C. **C**) Point spectra of carbonaceous material in the lower mat-like region, and middle-upper granular regions. Indistinguishable spectra suggest syngenetic carbonaceous material.

5. Discussion I: Sedimentary and palaeoenvironmental setting

The Middle Marker sediments document the accumulation of volcaniclastic and marine material in a sedimentary regime between two long periods of dominantly mafic volcanic activity, the Komati and Hooggenoeg formations (Anhaeusser, 1973, 1978; Lowe and Byerly, 2007). The Middle Marker horizon thus reflects the waning stage of the final volcanic episode in the Komati Formation (Lanier and Lowe, 1982). As reported in previous studies (Lanier and Lowe, 1982; Lowe, 1999a,b; Hofmann et al., 2013), volcaniclastic material is the dominant constituent. SEM-EDS and ICP-OES analyses document the co-occurrence of mafic (Fe-Mg) and felsic (Al-K-Si) mineral compositions, evidencing their simultaneous input (Figs. 5–7 and 12). We have not observed the large volumes of carbonates described by previous workers (Hurley et al., 1972; Condie, 1981; Tankard et al., 1982), solely rare siderite (Fig. 12B) and rare rhombic crystals which are possibly silicified carbonates (not shown). X-ray diffraction

(XRD) analyses of some of these samples show minor calcite (up to 9 wt%; results not shown), which seems curious in light of the 'acidic' portrayal of the Archaean world. We suggest that, although the majority of the hydrosphere would have been acidic by virtue of the high pCO2 Archaean atmosphere, the precipitation of calcite could have been permitted in the immediate vicinity of the resurgence of hydrothermal-seawater fluids, where their reaction with mafic oceanic crust necessarily produces alkaline microcosms (Kempe and Degens, 1985). Indeed, in the absence of knowing the degree of stratification of the basin in which the Middle Marker sediments were deposited, we cannot comment on the relative abundances of carbonate described in previous studies, since the propensity for its precipitation cannot be estimated.

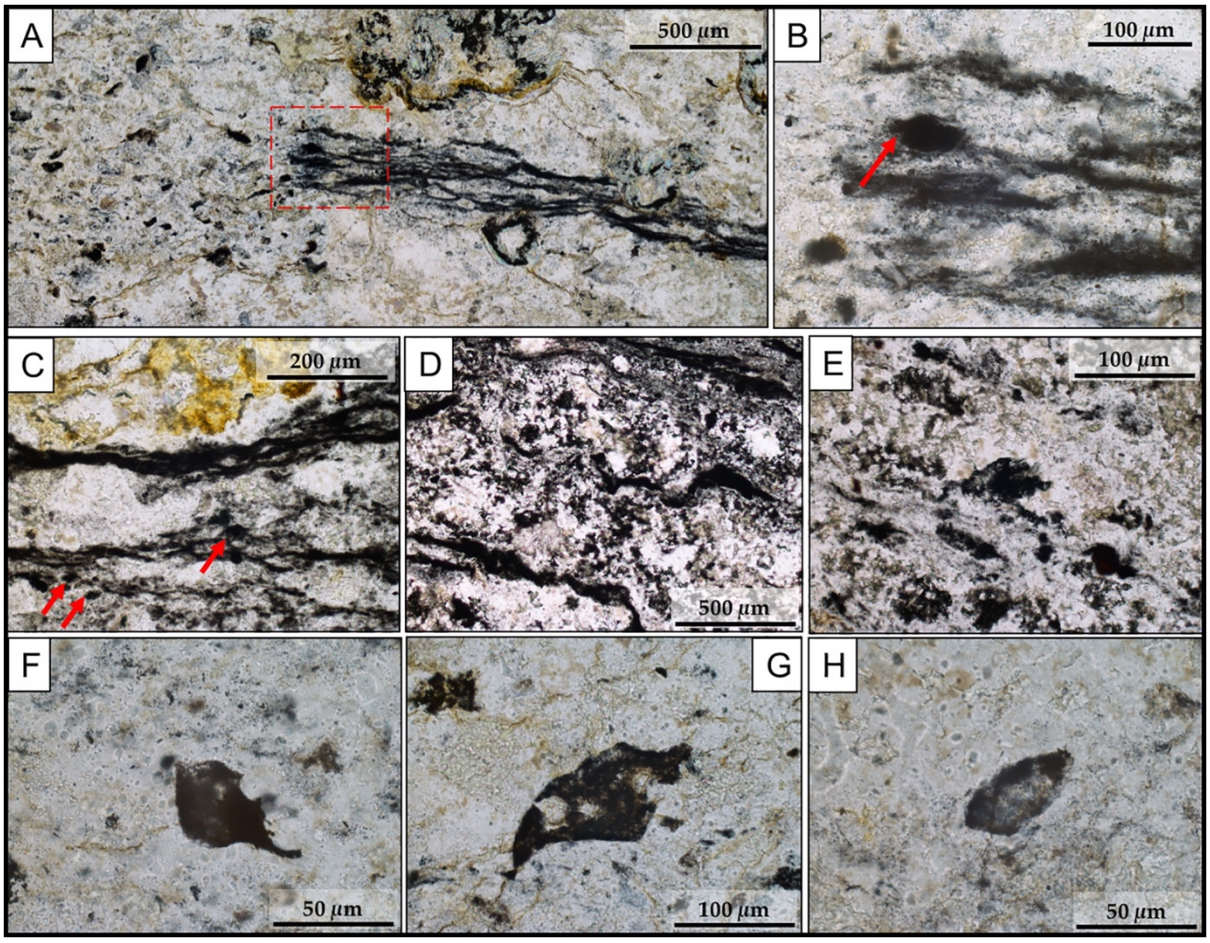

Fig. 15. Associations of wisps, flakes and lenticular objects with crinkly, filament-like microbial mats. **A**) Frayed mat in a laminated volcaniclastic siltstone, with randomly distributed carbonaceous detritus, including flakes and lenticular objects, in the adjacent matrix. Red box indicates region of B. **B**) High-magnification view of the region outlined in A, showing a lenticular object (arrowed), which is clearly contiguous with the primary lamination of the mat fabric. **C**) Lenticular objects occurring as part of the primary lamination of another crinkly, filament-like microbial mat. **D**) Non-isopachous, elongate wisps or flakes in the matrix between two microbial mats. The base of one such mat is visible to the upper right. **E-H**) Lenticular objects of differing composition, found randomly oriented in the matrix of mat-rich, volcaniclastic siltstones. E and F are carbonaceous, G is an altered volcanic particle, H is anatase.

The sedimentary structures identified evidence shallow water deposition (broadly shallowing upward through the sequence as the volcanic cone progrades), and we concur with previous estimates of up to tens of metres of water depth (Lanier and Lowe, 1982; Lowe and

Byerly, 2007). Lowe and Byerly (2007) describe the Middle Marker chert as having regional extent across the Onverwacht anticline, and therefore suggested its deposition on a flat, open, tide- or wave-influenced volcanic shelf. The observations herein of grain sizes varying from silt to coarse-grade sand, usually in graded sequences (Fig. 4), support this view. Although sedimentary structures testify to local wave influence, there are equally periods of quiescence. Previous reports suggested that carbonaceous material is minor and mostly occurs as either thin layers of relatively pure organic carbon-rich chert and/or simple particles mixed in komatiitic ash (Hurley et al., 1972; Lowe and Byerly, 2007), however, this study, using Raman spectroscopy and SEM-EDS, has unambiguously demonstrated that there are in fact a multitude of carbonaceous structures, usually occurring as laminations between cycles of volcanogenic deposits in shallow-water, laminated volcaniclastic sandstones and siltstones.

The carbonaceous material shows a thermal maturity consistent with the history of the rock (Fig. 16). All spectra of carbonaceous material show pronounced D and G bands centred around 1350 cm^{-1} and 1600 cm^{-1}, respectively, and a low-intensity second-order signal. This implies that the carbon has low 2D structural organisation, little to no 3D structural ordering (Lespade et al., 1982), and is thus not graphitised (Marshall et al., 2007). A shoulder on the D1 band between 1130 cm^{-1} and 1260 cm^{-1} is present in all types of analysed carbonaceous matter, further indicative of a low crystallinity (Sadezky et al., 2005), which has been reported from similar stratiform cherts (Sforna et al., 2014; Hickman-Lewis et al., 2016).

The intensity ratio of the D and G bands (I_{D1}/I_G) and the structural disorder ratio $I_{D1}/(I_{D1} + I_G)$ correlate with the degree of structural disorder, and this can assist in environmental interpretations of the different facies of carbonaceous material in the Middle Marker. In laminated carbonaceous sandstones and siltstones (Fig. 16A,C), the elevated I_{D1}/I_G ratio (1.11–1.46) and higher structural disorder ratio (52.5–59.3%) relative to massive clotted carbonaceous cherts (Fig. 16B; for which the same values are 1.05 and 51.3%, see Table 2) indicate a greater degree of structural disorder in the laminated facies. In contrast, the higher degree of structural order in the clotted carbonaceous chert together with the narrower D1 band suggest that it has undergone more severe thermal maturation (Marshall et al., 2007; van Zuilen et al., 2007). For Archaean samples, this thermal maturation is most parsimoniously linked to either metamorphism or localised hydrothermal alteration (Marshall et al., 2007; Sforna et al., 2014). Given the close proximity from which samples were collected, and the stratigraphic range over which they occur (the horizon is < 6 m thick) differential lateral or vertical metamorphism is an unlikely cause of the eventual differences in structural order, and thus the true reason must be both early diagenetic and local. By contrast, the laminated sandstones and siltstones contain stratiform silica veins, which are more consistent with a diffuse, distal hydrothermal scenario (after Hofmann and Bolhar, 2007; cf. Paris et al., 1985).

Dann and Grove (2007) note that the volcanic rocks beneath the Middle Marker are altered by seafloor hydrothermal processes, and this is unsurprising since every chert unit in the Barberton greenstone belt is underlain by such a diffuse, gradational hydrothermal sequence (Hofmann and Bolhar, 2007; Hofmann and Harris, 2008; Hofmann, 2011), as are silicified rocks in contemporaneous greenstone belts, e.g. the Nondweni (Hofmann and Wilson, 2007), and throughout the Warrawoona cherts of the Pilbara (Brasier et al., 2005, 2006). REE + Y data (MuQ-normalised) for the samples studied herein exhibit trends which can broadly be described as gradually increasing from LREEs to HREEs with positive Eu anomalies and occasional weakly positive Y anomalies (Fig. 5). This is indicative of the mixing of seawater

with hydrothermal effluent (Bau and Dulski, 1996; Grassineau et al., 2002; Gourcerol et al., 2015, 2016). The sole REE + Y pattern with an inverse trend at high concentrations (04SA14; Fig. 5B), can be attributed to post-diagenetic alteration (Gourcerol et al., 2015), and is therefore uninformative of the palaeoenvironment of its deposition. Extensive veins of percolating pure silica, which disrupt primary sedimentary structure and cause soft-sediment deformation (Figs. 4D,F, 10A,B, 12E and 13A,B) further testify to the presence of some amount of contemporaneous hydrothermal fluid circulation during deposition of the Middle Marker, despite no recognition of these features by Lanier and Lowe (1982). An elevated silica content at the seafloor-sediment interface, and thus early silicification, explains both the volumetric preservation of carbonaceous laminations (e.g. Fig. 12A,E) and the low degree of compaction throughout.

Considering the doubtless high concentration of silica in Precambrian oceans (Siever, 1992; Maliva et al., 2005; Knauth, 2005) and the necessity for high heat flux out of the interior of the ancient Earth (de Wit and Hart, 1993; Sleep et al., 2001; Ernst et al., 2016), the evidently early, syndepositional silicification of the Middle Marker rocks is probably most parsimoniously met by diffuse hydrothermal venting (Hofmann and Bolhar, 2007; Hofmann, 2011; Westall et al., 2018) into Si-rich seas. Our interpretation of the depositional environment of the Middle Marker is consequently a product of previous observations, i.e. shallow, wave-active waters in the photic zone on a regionally extensive volcanically and hydrothermally active shelf.

Table 2
Raman spectral parameters.

Structure	I_{D1}/I_G	$I_{D1}/(I_{D1} + I_G)$
Fine, crinkly, biofilm-like lamination	1.11	52.6
Pseudo-tufted lamination	1.28–1.46	57.8–59.3
Clotted carbonaceous material	1.05	51.3

Table 2. Raman spectral parameters from spectra shown in Figure 16.

6. Discussion II: Microbial palaeontology and assessments of biogenicity

6.1. Putative microbial features

A number of the carbonaceous features herein described can be considered microbially influenced (Fig. 9). The microstructures described in Section 4 are comparable to microbial mats, their erosional products, and their traces in the sedimentary record (microbially induced sedimentary structures such as biostabilisation), as well as to proposed microfossils. These carbonaceous features can be broadly classified into four morphotypes:

i) fine, crinkly, biofilm-like laminations;
ii) ii) pseudo-tufted laminations;
iii) wisps, flakes, and roll-up structures;
iv) iv) lenticular objects.

It is possible that some of these objects, namely wisps, flakes, and roll-ups, are the erosional products of microbial mats (see Section 4.4.). Additionally, where no cellular organic matter is preserved, a combination of i) morphospace, ii) indications of in vivo cohesiveness resulting from sediments being bound by glutinous EPS (Decho, 1990; Sutherland, 2001; Neu et al., 2003; Gerdes et al., 2000), and iii) lamina-grain interactions (see Section 4.3) can shed light on biogenicity. Such traces are termed microbially induced sedimentary structures (MISS, cf. Noffke et al., 2001). Laterally differential taphonomy of microbial fabrics in the Middle Marker occasionally results in no carbonaceous material being preserved (Figs. 4A and 15D).

The volumetric significance of putative microbial fabrics is relatively minor: they occur as thin, regular, horizons of <200μm to ~2500μm thickness dependent upon morphotype. Multiple morphotypes of laminations can occur within a single sample, though fine, crinkly, film-like laminations (Figs. 10–12) are the most common. One axiomatic trend is that putative microbial horizons are anticorrelated with the deposition of volcaniclastic material, occurring always at the apogee of graded sequences, during the erosional regime. This is entirely consistent with the occurrence of mat fabrics described by Noffke (2003, 2010) and Tice (2009). From the sedimentological model advanced by Lanier and Lowe (1982), this suggests that they developed mostly during pauses between magmatic pulses during the waning volcanic cycle. Indeed, our sedimentological interpretation corroborates that of Lanier and Lowe (1982), with the addition of diffuse hydrothermal activity to account for (i) near-pure silica layers; (ii) percolating veins of silica which occurred syndepositionally and disrupted sedimentary fabric; and (iii) exceptional volume preservation of putative microbial fabrics. The presence of hydrothermal activity is unsurprising, presumably originating from the ubiquitous volcanic systems which characterised the Early Archaean surface environment (Sleep et al., 2001; Brasier et al., 2005, 2006, 2013; Van Kranendonk, 2006, 2007; Westall et al., 2011, 2015; Arndt and Nisbet, 2012; Westall, 2016).

The abiotic null hypothesis (cf. Brasier et al., 2004) to be overcome in the case of all putative microbial features is “that laminated features reflect sedimentary horizons, pressure solution fronts, or diagenetic mineralisation, and that taphonomic differences are purely the product of differential primary sedimentation”.

6.2. Assessment of biogenicity

Thorough assessments of biogenicity are requisite in the proof of all ancient biosignatures (Buick, 1990; Brasier et al., 2005; Wacey, 2009; Westall and Cavalazzi, 2011) and an assertion of biology is worthless without proof of (i) occurrence in an environment clement to life; (ii) syngenicity of the object of interest with the primary rock fabric; and (iii) objectivistic, non-reductive assessments of biogenicity against a wide range of criteria. This culminates in an argument for biogenicity which, since the Archaean geological record preserves an imperfect fossil record, obeys classical rationalism in its reason and deduction.

6.2.1. Geological plausibility (palaeoenvironment)

The Middle Marker sediments represent a shallow marine environment associated with volcanic activity (Lanier and Lowe, 1982) in the vicinity of minor hydrothermal outflow, a situation entirely compatible with the environmental settings of Palaeoarchaean marine microbial consortia from throughout the Kaapvaal and Pilbara cratons (e.g. Walter et al., 1980; Schopf and Walter, 1983; Buick, 1984; Walsh, 1992; Westall et al., 2001, 2006, 2011, 2015;

Noffke et al., 2003, 2006a,b, 2013; Sugitani et al., 2007, 2010; Hickman-Lewis et al., 2016; Oehler et al., 2017). Modern microbial mat communities readily occur in similar tidal-intertidal settings (Gerdes and Krumbein, 1987; Gerdes, 2007; Noffke, 2003, 2010). The Middle Marker would thus have been a promising niche for the flourishing of phototrophic and, presumably, symbiotic chemotrophic communities on a large spatial scale, being a moderately thermophilic, photic zone setting. It seems to have been within the stream of metal fluxes from volcanic (Fig. 5A) and hydrothermal sources (Fig. 5B) and in an environment where currents would create a nutrient flux. This is consistent with Early Archaean microbial biomes (Nisbet and Fowler, 1996; Nisbet, 2000; Nisbet and Sleep, 2001; Grosch and Hazen, 2015).

Prokaryotic microbial communities appear to have endured on the Earth for at least 3.5 Ga (Altermann and Kazmierczak, 2003; Schopf, 2006; Wacey, 2009; Westall and Cavalazzi, 2011; Hickman-Lewis et al., 2018), and thus these ecologies are entirely compatible with both the age and environment of the formation. Since the Middle Marker appears not to have undergone early catagenesis or metamorphism (Delarue et al., 2016), high-fidelity primary preservation is expected and recognised.

6.2.2. Textural syngenicity

All interpreted microbial mat horizons are conformable with bedding or cross-stratification in the Middle Marker sediments and are constant across individual thin sections and hand samples (Figs. 9–13 and 15). Putative microbial fabrics always occur at the top of graded volcaniclastic layers, i.e., they exhibit preferential growth at specific surfaces. Such similarity indicates a pattern of episodic growth of putative microbial laminations governed by clastic and marine inputs to their environments. Putative microbial fabrics in the Middle Marker are endemic to laminated volcaniclastic sandstones and siltstones, although a restricted range of fabrics are detected in coarse-grained volcaniclastic sandstones. Differential preservation potential may influence this distribution.

Most laminations drape and enwrap adjacent grains: this trapping-baffling behaviour is often described in chemotrophic and phototrophic microbial sediments and necessarily occurs during formation (Oschmann, 2000; Noffke, 2010; Noffke et al., 2003, 2006b, 2013; Homann et al., 2015). The syngenicity of putative microbial features with their host rocks is thus incontestable.

All proposed microbial morphologies have undergone similar degrees of lower greenschist metamorphism, and have broadly similar thermal maturities, as indicated by Raman spectra in Fig. 16 (Dziggel et al., 2002, 2006; van Zuilen et al., 2007). Raman spectral analyses from points within the microstratigraphy of a pseudo-tufted lamination show no trend, and thus indicate no differences in maturity throughout: this, and other, microbial fabrics are thus texturally syngenetic and exhibit responsive growth to their sedimentary environment. The eventual shared granular taphonomy of all carbonaceous microbial-like features in the Middle Marker argues strongly against a sedimentological origin, for which a continuum of eventual ‘taphonomies’ would be expected. Thus, the likelihood of these morphologically diverse laminations having an identical sedimentary precursor is highly improbable. This refutes the null hypothesis asserted in Section 6.1, and further supports the biological interpretation.

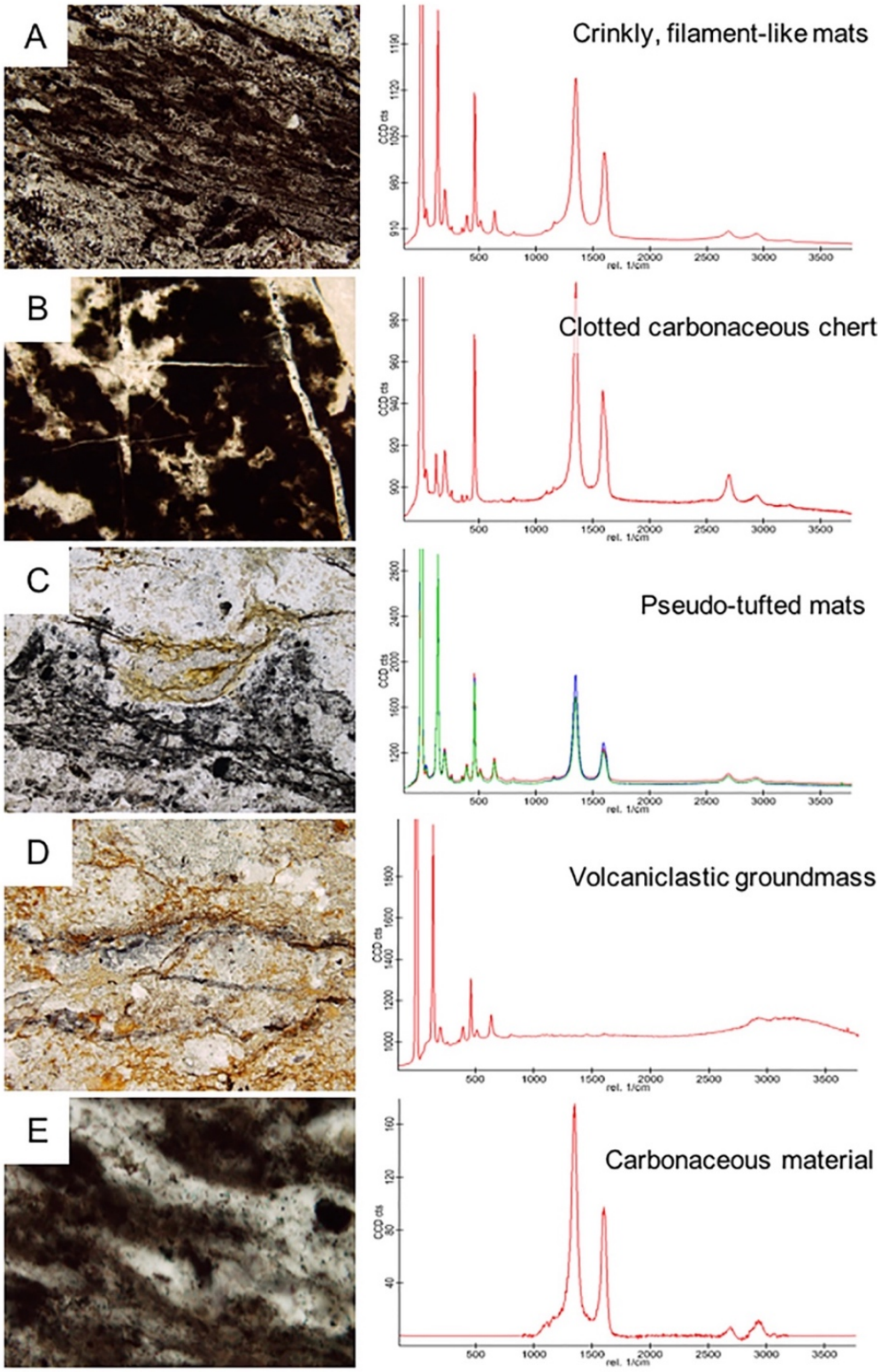

Fig. 16. Comparison of Raman spectra between different occurrences of carbonaceous matter in the Middle Marker. **A**) Spectrum from laminae in crinkly, filament-like microbial mats. **B**) Spectrum from clots in massive, clotted carbonaceous cherts. **C**) Spectrum from laminae and microclasts in tufted microbial mats. **D**) Spectrum from volcaniclastic groundmass for comparison; note the dominance of the anatase signal. **E**) Extracted signal from carbonaceous material from crinkly, filament-like laminations, which constitute the most promising biosignature in the Middle Marker. See Table 2 for spectral analyses.

6.2.3. Biogenicity

In the following sections, we assess the biogenicity of the five morphotypes of microbial-like features through comparison of shared traits with similar structures, and through testing against a range of biogenicity criteria.

i) Fine, crinkly, laminations

Fine, crinkly laminations are superficially similar to thin fossil microbial biofilms. Their stratigraphic context, occurring always at sedimentary inflection points in shallow-water marine deposits between volcanic eruptions, is consistent with the occurrence of proposed biofabrics in cherts of the Mozaan Group (Noffke et al., 2003), Hooggenoeg Formation (Walsh and Lowe, 1985, 1999; Walsh, 1992; Walsh and Westall, 2003; Tice and Lowe, 2004; Tice, 2009), Josefsdal Chert (Westall et al., 2006, 2015), stratiform Apex chert (Hickman-Lewis et al., 2016, 2017) and Dresser Formation (Noffke et al., 2013). There is a particularly close morphological resemblance between these laminations and those of the contemporaneous Dresser Formation and younger Mozaan Group, both of which have been classified as microbial mats or microbially induced sedimentary structures.

Individual laminae are non-isopachous and exhibit anastomosis incompatible with a sedimentary or diagenetic precursor. In most cases, plastic deformation cannot be attributed to compaction or particle settling, and thus the varying thickness of the layers is primary (Figs. 10–12). This primary, non-isopachous character has been erected as a biogenicity criterion for microbial mats growing in the presence of sunlight (Buick, 1984; Pope and Grotzinger, 2000; Pope et al., 2000).

These putative microbial biofilms meet most of the morphological criteria for biogenicity:(i) they are fine, kerogenous laminations which alternate with pure silica layers and lenses, each lamination being 5–30 μm thick and slightly wavy, with a crinkled relief of no more than 0.5–1 cm (Walsh, 1992; Walsh and Westall, 2003; Gerdes, 2007; Noffke et al., 2013); (ii) they are wavy or crinkly on both large and small spatial scales (compare Figs. 10B and 11C), and are laterally discontinuous at the micron-scale, but broadly continuous at the centimetre-scale (Walsh and Lowe, 1999; Walsh and Westall, 2003; Greco et al., 2018); (iii) their gross structure approximates that of modern microbial mats, i.e. they alternate layers of organic-rich material with a film- or filament-like construction (cf. Hickman-Lewis et al., 2017) with layers of detrital material or entrained particles (Figs. 10B, 11 and 12C,D; Noffke et al., 2001; Noffke, 2009, 2010); (iv) the presence of folded, torn, crumpled and rolled fragments demonstrably indigenous to the laminations strongly implies an initial cohesive plasticity (after Simonson et al., 1993; Sumner, 1997; Walsh and Westall, 2003; Tice and Lowe, 2004); (v) their non-isopachous laminae thicken toward crests (Figs. 10A,B and 11; Pope and Grotzinger, 2000; Pope et al., 2000), suggesting growth out of the laminar bottom flow waters toward more dynamic, nutrient-rich waters above (Gerdes, 2007); (vi) they mantle macro-scale features such as bedding planes, cross-stratification (Fig. 10A,B) and sediment lenses (Homann et al., 2015); and (vii) their growth is templated by the underlying grain topography and entrained particles are oriented (Fig. 11), suggesting an effort to bio-stabilise the sedimentary surface during colonisation (Gerdes et al., 1991; Noffke, 2003; Noffke et al., 2003, 2013; Heubeck, 2009; Gerdes, 2007). These seven lines of evidence convincingly demonstrate that these structures were surface-colonising, biostabilising biofilms. Their micro-tufted and crinkled relief resembles that of anoxygenic, photosynthesising microbial

communities (Tice and Lowe, 2006; Heubeck, 2009). Intimate intergrowth with bound substrate grains suggests originally glutinous, mucilaginous material i.e. extracellular polymeric substances (EPS; Noffke, 2003; Westall et al., 2006). The original filamentous texture may have been 'hazed' by diagenetic processes ("Archaeanisation"; after Knoll et al., 1988; Noffke et al., 2006b), accounting for the lack of individual architect microfossil aggregations preserved within the mats.

The micro-tufted relief is of near-identical dimensions to tufted-crinkle microbial laminations in the contemporaneous Dresser Formation (Noffke et al., 2013), which are interpreted as indicators of growth in the subtidal zone (Gerdes and Krumbein, 1987; Noffke et al., 2001). Their multi-laminar morphology signifies continuous and successful growth during the transient habitable niche between volcanic inputs; indeed, in modern microbial mats a microbial biofilm may begin to colonise a surface in only tens of minutes (Paterson et al., 1998, 2003; Busscher and Mei, 2000). Laterally discontinuous crinkly biofilm 'fragments' may suggest growth in a stressed environment, in which the struggle to grow was balanced against resilience to volcaniclastic input. Based on assertions of such morphologies being indicative of phototrophic metabolisms (e.g. Bosak et al., 2009; Flannery and Walter, 2011), the crinkly, finely laminated biofilms of the Middle Marker are interpreted as the remains of areally extensive, probably anoxygenic, photosynthetic communities flourishing in water depths of not more than 5–10 m (after Noffke et al., 2006a; Homann et al., 2015).

ii) Pseudo-tufted laminations

Pseudo-tufted laminations bear considerable resemblance to modern and ancient microstromatoloid-like structures (Gerdes, 2007; Homann et al., 2015), the fossil examples of which are often interpreted to indicate photosynthesis (Bosak et al., 2009, 2013; Flannery and Walter, 2011; Gamper et al., 2012). Interpretive diagrams illustrating the trajectories of laminae within tufted horizons show that some, but not all, laminations appear to continue upward into the crests (Fig. 13C,D). However, many troughs between tufts are associated with the settling of dense particles from the water column, thus soft sediment deformation is a likely cause of this topography, in contrast to the unambiguously primary micro-tufted topography of fine, crinkly microbial mats.

The fine, crinkly laminations bear morphological similarity to both the fine, crinkly laminae described above and alpha-type laminations from the 3.42 Ga Buck Reef Chert, interpreted as microbial mats by Tice and Lowe (2006) and Tice (2009). Although the Middle Marker laminations are less well-preserved, several salient similarities are noted: (i) they anastomose and bifurcate around carbonaceous particles and can form lamina stacks (Fig. 13A–D and 14A); (ii) they have near-constant, slightly variable lamina thickness; (iii) they crumple and fold (Fig. 13C,D), indicating cohesive strength at the sediment surface (Neu et al., 2003) during deposition and diagenesis; and (iv) they occur in a microfacies which is rich in simple carbonaceous grains, mat-like laminations and silicified grains, but poor in terrigenous detrital matter (cf. microfacies III of Tice and Lowe, 2006). These four lines of evidence strongly support a biogenic interpretation. The sub-millimetric relief of laminae, together with a crinkly, wavy laminar morphology, are evocative of photosynthetic microbial mats (Gerdes, 2007; Heubeck, 2009; Bosak et al., 2009), thus these likely represent epibenthic, probably anoxygenic, photosynthetic communities.

Speculatively, it is possible that a stratified microbial community is present in the lower and middle-upper regions: the microbial mats directly overlie clotted carbonaceous textures, which have been interpreted as biomass clumps (Walsh and Lowe, 1999) and as degraded chemotrophic colonies (Westall et al., 2015). A similar interstratified relationship between mats and clots exists in Hooggenoeg cherts (Walsh, 1992; K. Hickman-Lewis, unpublished data) and in the Josefsdal Chert (Westall et al., 2015). Autotrophic-heterotrophic symbiosis results long-term stability of the overall system (Decho and Kawaguchi, 2003), and such community structure maximises the ecological efficiency of biomass (Reitner, 2010), indeed, microbial stratification occurs naturally as a result of micrometre-scale gradients in microbial mats (Revsbech, 1989).

iii) Wisps and roll-up structures

Isolated wisps are elongate, tapered carbonaceous objects which float in the silica matrix. Interpretations of their origins include (i) compressed products of lobate carbonaceous particles (Walsh and Lowe, 1999), (ii) eroded and redeposited fragments of shale-grade, clay-rich sediment (Schieber et al., 2012); (iii) ripped-up fragments of microbial mat (Schieber, 1986, 1998; Schieber et al., 2007, Noffke, 2010) or natural biofilm detachment (Busscher and Mei, 2000; Neu et al., 2003), and (iv) ambiguous objects of equally probable biological or sedimentary origin in the absence of identification of the parent structure (Hickman-Lewis et al., 2016).

It is difficult to trace the protolith of wisp- or flake-like structures in Archaean rocks, thus biological inferences are made on dimensional comparisons with known microbial mats. Where dimensions are roughly equivalent, and where morphology suggests initial plasticity (Schieber, 1986, 1998), a biological origin may be reasonably supposed. This is true for the wisps and flakes described in the Middle Marker cherts. Their compositional and dimensional similarity to fine, crinkly microbial mats, and their occurrence in the vicinity of fractured mats, suggest that wisps and flakes represent the eroded fragments of microbial mats. Preserved tear-up structures at the surfaces of crinkly mats evidence their erosion in situ.

iv) Spindles and lentils

In the first systematic description of Archaean microfossils, Walsh (1992) designated spindle-like carbonaceous microstructures in Hooggenoeg and Kromberg cherts to be probable fossils since they passed six of the seven criteria for biogenicity set down by Buick (1990). Since that study, the range of described spindle-like and lenticular objects has proliferated, and their interpretation as microfossils is now presumed (Sugitani et al., 2007, 2009, 2010, 2015; Grey and Sugitani, 2009; Oehler et al., 2009, 2017; House et al., 2013). Walsh (1992) deemed that the central cavity in most spindles precluded their identification as carbon-coated gypsum crystals, and independent mineralogical identifications confirm that they are often carbonaceous and can contain organic contents interpreted as degraded cellular remains (Sugitani et al., 2010, 2015). Their size distributions (Walsh, 1992; Sugitani et al., 2009) usually support a biological, rather than mineralogical, identity.

Lenticular objects in the Middle Marker are found within fine, crinkly microbial mats (Fig. 15). The objects we identify bear considerable morphological similarity to those of past studies, though are of great compositional variation, from vitreous, glassy material (phyllosilicates; Fig. 15D) to carbon (Fig. 15E,F). Additionally, their occurrence as seemingly

entrained particles in interpreted microbial mats (Fig. 15B,C), and their dispersion into the microcrystalline matrix with other eroded mat fragments mean that it is impossible to distinguish them from other detrital entrained objects. There is no indication of their being part of the mat-building community, nor do they exhibit the community-like behaviour shown by other lenticular microfossil-like objects (e.g. Sugitani et al., 2015).

Walsh (1992) noted that by comparison to recent microfossils, poor preservation had rendered the morphology of spindle- or lentil-like microfossils too simple to draw parallels. The lenticular objects described herein pose a similar challenge. Although a large amount of data exists to support the biogenicity of other occurrences of lenticular microfossil-like objects, our own findings, together with observations by others (D. Wacey, personal communication), support that some of these objects are simply grains of detrital entrained volcanogenic material within microbial mats. Therefore, we find no evidence for a biological interpretation of lenticular objects in the Middle Marker horizon.

6.2.4. Cautions and considerations in the biological interpretation

Size range. Although carbonaceous laminations in Early Archaean cherts are frequently interpreted biologically, several shortcomings persist in this assertion, apart from the degradation of their organic material through diagenesis and taphonomy.

Archaean phototrophic biofilms are much less thick than the modern examples with which they are equated, comprising sets of laminae which are usually less than tens of microns in thickness, and having total thicknesses of less than several hundred microns (Golubic, 1976; Monty, 1976; Margulis et al., 1983). This issue can be circumnavigated via two explanations. Walsh (1992) and Walsh and Lowe (1999) suggest that compaction during diagenesis may cause this thinning. Westall et al. (2006, 2015) have implied that it could be the result of anaerobic biomass having low growth rates; indeed, it is known that anoxygenic microbes produce biomass at a rate much slower than oxygenic organisms (McCollum and Amend, 2005; Parkes et al., 2014). Comparing these possibilities, a fundamental mechanical dichotomy exists in the compaction hypothesis: since both carbonaceous particles and flattened wisps occur at the same millimetric stratigraphic level, yet the former are sometimes judged to produce the latter (Walsh and Lowe, 1999), it is irreconcilable that both can exist in concert. This is evident even in photomicrographs from Walsh and Lowe (1999). Considering the metabolic hypothesis, the disparities in both biofilm size and thickness of biofilm packets are minimised if one considers chemosynthetic microbial mats composed of either modern (Bailey et al., 2009) or fossil (Cavalazzi, 2007; Cavalazzi et al., 2007; Homann et al., 2016) filamentous microbiota. Thus, the second hypothesis is most plausible. Consequently, this study finds no untenable smallness in the size exhibited by putative microbial mats that could preclude a biological interpretation.

Metabolism. Since chemotrophic microbes can only be definitively delineated from phototrophic microbes by gene sequencing analyses of the architect community (Williams and Reimers, 1982), and since the preservation of interpreted microbial mats in the Middle Marker is of insufficient fidelity to identify individual fossils, it is impossible to estimate the relative roles played by chemosynthetic and photosynthetic metabolisms. However, it is known that the Archaean Earth was largely anoxic, and thus widespread mats such as these should not be expected to have performed oxygenic metabolism, a standpoint supported by phylogenetics (Batustuzzi et al., 2004). Walsh (1992) highlights that, through geological time, phototrophs

have tended to dominate the shallow-water niche. Specific topographic morphologies, such as tufts, also have a strong affinity to phototrophic microbes (Bosak et al., 2009). For these reasons, it is supposed that the microbial fabrics described herein were built by anoxygenic phototrophs.

Alternative, abiotic formation of wisps and flakes. As explained above, for wisps and flakes, the erosion of fine-grained, clay-rich, carbonaceous sediment has been experimentally demonstrated, using flume equipment, to produce flake-rich sediment of entirely abiotic genesis (Schieber et al., 2012). Thus, despite inferring the erosion of microbial mats in the formation of wisps and flakes, it is impossible, at this time, to prove this without knowing the exact provenance of the organic material. Nonetheless, the explanation in Section 6.2.3. provides support for the biogenicity of wisps and flakes.

The conundrum of lenticular objects. In Middle Marker metasediments, lenticular objects occur as entrained particles within the laminae of interpreted microbial mats, and as isolated, seemingly eroded objects from these mats (Fig. 15). Their wide range in size, their highly variable composition and mineralogy, and their striking resemblance to natural variations in laminar thickness within the mats argue for variable, abiotic mechanisms of formation.

7. Discussion III: The Middle Marker horizon and its microbial inhabitants as the oldest example of a globally important, Early Archaean biocoenosis

Presented herein is a document of the oldest fully developed microbial ecosystem inhabiting a particular marine environment that appears to have been common in the Early Archaean of the Barberton greenstone belt, and seemingly also in the Pilbara. The evolution of the Middle Marker horizon is synthesised in Fig. 17. Together with evidence from other Early Archaean habitats, major trends in microbial ecology and ecosystem-environment dynamics can be drawn.

The Middle Marker volcaniclastic platform deposits record cycles of volcanic activity and variable associated hydrothermal fluid influence – as determined by major and trace element geochemistry (Fig. 5) – and this system hosted photosynthetic and presumably chemosynthetic microorganisms. These shallow water deposits record offshore to shelfal-supratidal depositional conditions on the regional to local scale wherein, on the microbial scale, phototrophs colonised all available bedding plane surfaces. Textural evidence for hydrothermal input is documented not only by the pervasive silicification of the sediments but also by soft sediment deformation features produced by forceful infiltration parallel to the soft, cohesive biofilm layers, generating elongate, pod-like structures (e.g. Fig. 11). Because of rapid silicification, there is little to no compaction of the delicate microbial biofilms. Thus, the varying thicknesses of the phototrophic biofilms testify to varying sedimentation rates: where sedimentation rates are low or zero, the thickness of the biofilm packets is higher, reaching up to several millimetres (e.g. Fig. 10D,E). Higher sedimentation rates during depositional regimes, on the other hand, overwhelm the biofilms and the packets of individual laminae are on the order of only tens of microns in thickness.

One of the striking features of the Middle Marker sedimentary environment and its microbial communities is the similarity with other volcaniclastic platform deposits in the Early Archaean. The 3.33Ga Josefsdal Chert (equivalent to unit K1c of the Kromberg Formation;

Lowe and Byerly, 1999), is a similarly widespread platform deposit, albeit at times much thicker than the Middle Marker owing to growth fault control of the depositional basin (Westall et al., 2015). Sedimentologically, it also documents a shallowing upward cycle culminating in supratidal deposits with variable current and wave influence. However, while the large felsic component of the Middle Marker indicates the waning phase of a volcanic cycle, the overwhelmingly basaltic compositions of the volcanic clasts of the Josefsdal Chert document an earlier phase of volcanism. Microbial mats and other biofabrics are similarly common in the Middle Marker and Josefsdal Chert. Further to this, Tice and Lowe (2004, 2006) and Greco et al. (2018) described phototrophic biofilms from platform deposits recording a similar palaeoenvironmental setting in the 3.42 Ga Buck Reef Chert. Westall et al. (2006, 2011) investigating felsic/basaltic shallow water deposits in the 3.45 Ga Kitty's Gap Chert of the Pilbara also documented phototrophic biofilm remnants, and delicate chemolithotrophic colonies at the surfaces of volcanic clasts. Finally, Hickman-Lewis et al. (2016) described probable microbial fabrics in shallow-water, micro-clastic cherts in the vicinity of hydrothermal activity in the 3.46 Ga stratiform 'Apex chert' at Chinaman Creek.

There is a striking similarity in the facies-biocoenosis associations of these units, outlined in Table 3. Facies 1 of the Middle Marker and Facies A of the Josefsdal Chert are both characterised by coarser volcanogenic sandstones deposited in upper offshore to shoreface environments, and can be compared to Microfacies I of the Buck Reef Chert and the voluminous silicified volcaniclastics in the stratiform 'Apex chert'. Facies 2 of the Middle Marker, black, carbonaceous, clotted cherts are the equivalent of Facies C in the Josefsdal Chert, both facies being influenced by heat probably of hydrothermal and diagenetic origin; this is evident both from their REE + Y patterns and Raman ID/IG intensity ratios. A comparison here can be made to clotted carbonaceous cherts in the stratiform 'Apex chert'. Facies 3 in the Middle Marker comprises finely layered green-grey cherts representing mostly ashfall with minor current reworking. This facies is comparable to Facies D of the Josefsdal Chert and to microbial horizons in Hooggenoeg formation chert H5c (Walsh, 1992), the main difference being that the black carbonaceous layers in the latter are much thinner than in the former, a difference probably related to sedimentation rate.

In terms of microbial biosignatures, probable photosynthetic and chemosynthetic biofilms occur throughout these cherts. Photosynthetic organisms required access to sunlight, which was amply provided by their shallow water setting, their carbon sourced from dissolved CO_2 in seawater. Mixed colonies of phototrophs and chemotrophs presumably occurred close to hydrothermal vents, supported by correlative evidence between multiple chert units (Table 3). Despite the compositional differences between the felsic-mafic Middle Marker horizon, 'Apex chert' and Buck Reef Chert and the mostly mafic Josefsdal Chert, comparable biosignatures suggest that similar microbial consortia inhabited different chert types. Photosynthetic biofilms, however, are most widespread in the Middle Marker and Buck Reef Chert. Whereas relatively low sedimentation rates in Facies 3 of the Middle Marker favoured the development of mm- to cm-scale phototrophic biofilms, the higher sedimentation rates of Facies D in the Josefsdal Chert (cf. Westall et al., 2015, see Table 3) resulted in poorly developed biofilms. This indicates that the distribution and success of microbial biomes is governed by both geochemical and mechanical-hydrodynamic parameters.

Preservation of the microbial biosignatures was due to early silicification. Very high concentrations of silica in pore waters contributed to rapid silicification and preservation of the

inorganic and the organic components of the sediments (see Westall et al., 2018). In the coarser grained facies, higher sedimentation rates entail more poorly developed, and poorly preserved, phototrophic biofilms. Approximately 150 Ma separates the oldest (Middle Marker) and youngest (Josefsdal Chert) of the chertified sediments compared here, yet the sedimentological features, facies, environmental conditions and microbial inhabitants throughout all are equivalent.

The biosignatures of the Middle Marker document that microbial life was already thriving in shallow water, platformal volcaniclastic sediments by 3.472 Ga. Salient similarities with comparable shallow-water sediments and their microbial inhabitants in contemporaneous and younger horizons spanning the Early Archaean world paint a picture of an early Earth teeming with microbial life.

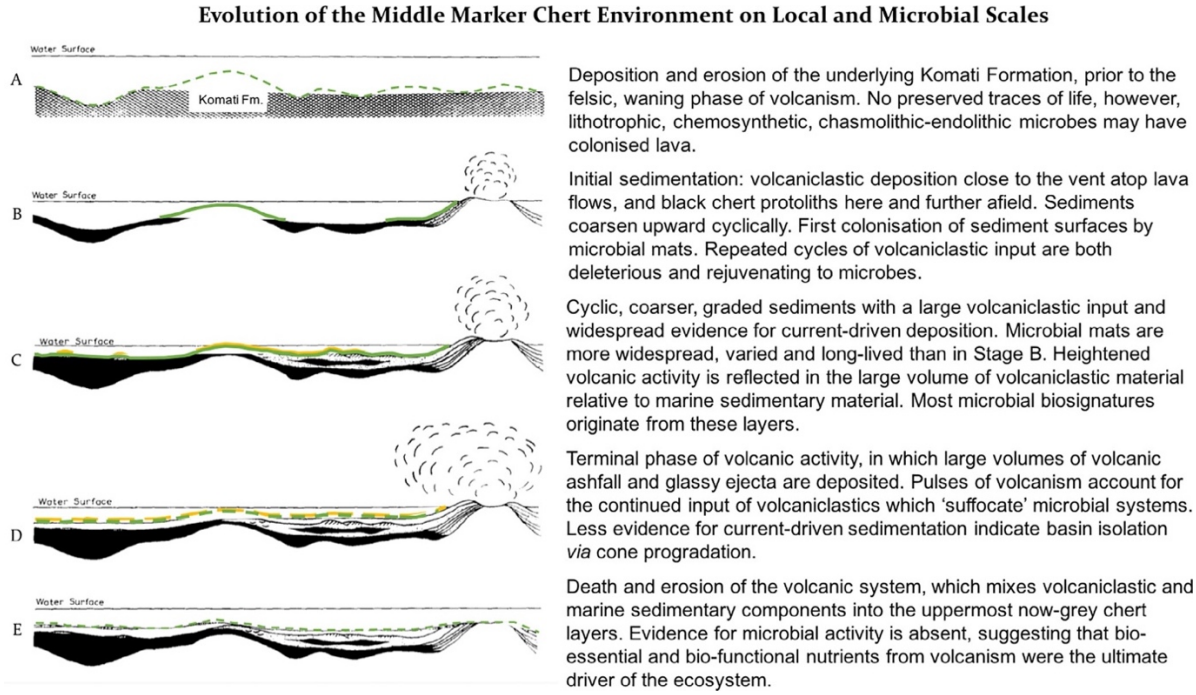

Fig. 17. Co-evolution of the environment of the Middle Marker chert and its microbial inhabitants. Though not preserved, there were possibly chemosynthetic ecosystems flourishing in the seafloor komatiites (the cryptoendolithic biosphere) prior to, and following, volcaniclastic sedimentation in the basin. Life has an apparent dependency on the nutrients provided by volcanism.

8. Conclusions

The ~3.47 Ga Middle Marker horizon is the oldest chert unit in the Barberton greenstone belt. It is a sequence of layered mafic and felsic volcaniclastic deposits with a proximal volcanic source. Sedimentary structures within indicate water depths of up to tens of metres, while soft-sediment deformation is in response to synsedimentary intrusion by percolating, penetrative stratiform silica veins. Thus, the Middle Marker is interpreted to have deposited on a shallow-water volcanic-hydrothermal shelf. A number of laminated structures in the Middle Marker sediments bear remarkable resemblance to microbial mat textures from contemporaneous and younger sediments from similar palaeoenvironments, and the thorough assessment of biogenicity conducted herein strongly supports the biological interpretation of

kerogenous mat-like laminations. Biogenic origins are evident for crinkly, filament-like laminations and pseudo-tufted laminations. Isolated carbonaceous wisps and flake-like particles are probable biosignatures, interpreted as the eroded remnants of crinkly, filament-like laminations on the basis of spatial occurrence and equivalent dimensions. All of these structures exhibit micron-scale morphological characters typical of microbial mats and evidence in-sediment cohesiveness which corroborates in vivo plasticity.

Table 3
Comparison of Palaeoarchaean shallow-water biocoenoses.

Location	Middle Marker horizon (3.472 Ga)	Josefsdal Chert (3.33 Ga)
Depositional Environment	Shallow-water platform, shallowing up sequence; variable current influence	Shallow-water platform, shallowing up sequence; variable current/wind influence
Main lithology	Mafic, felsic + some komatiitic	Basaltic + some felsic
Facies	1: Coarse volcaniclastic sandstone	Facies A: coarse basaltic sandstone
	2: Massive black clotted carbonaceous chert	Facies C: black clotted carbonaceous chert
	3: Laminated green-grey siltstones and sandstones, alternating with carbonaceous microbial biofilms	Facies D: Finely laminated green-grey siltstones and sandstones alternating with carbonaceous layers Facies B: Great thicknesses of phototrophic biofilms
Hydrothermal activity	Locally present, minor component in laminated chert	Ubiquitous; locally predominant
Phototrophic biofilms	Widespread in Facies 3, rare in Facies 1, absent in Facies 2	Occur in all sedimentary facies
Chemotrophic microfossils	If present, limited to those localities interpreted as close to hydrothermal effusions	Limited to localities close to hydrothermal vents

Location	Buck Reef Chert (3.42 Ga)	Stratiform 'Apex chert' (3.46 Ga)
Depositional Environment	Deepening up sequence with major shallow platformal section	Shallow-water platform with variable current influence
Main lithology	Mafic and felsic	Mafic (basaltic) and felsic
Facies	Microfacies I: high clastic component, volcaniclastic and carbonaceous sediment	~ Silicified volcaniclastics
	Microfacies II: simple and complex carbonaceous grains with little clastic component	Clotted carbonaceous chert
	Microfacies III: complex and simple carbonaceous grains with microbial mats	Microclastic chert and banded black-grey-white chert with rare carbonaceous lamination
	Microfacies III, platformal facies with great thicknesses of microbial biofilms	? Laminated metalliferous cherts
Hydrothermal activity	Controversial; probably present in some facies	Ubiquitous; multiple traceable black chert veins – terminating within laminated chert – along strike
Phototrophic biofilms	Widespread in Microfacies III	Probable eroded clasts of microbial-like structures in microclastic cherts
Chemotrophic microfossils		If present, filament-like horizons interpreted as microbial in microclastic cherts

Table 3. Comparison of Palaeoarchaean biomes/biocoenoses from chert horizons of the Barberton and Pilbara.

Randomly distributed lenticular objects, directly comparable to similar features interpreted as bona fide microfossils in Early Archaean sediments, are a further enigmatic microstructure. In the Middle Marker horizon, the distribution of these objects, both within primary and secondary chert fabrics, within and outside of microbial mats, and encompassing a wide range of sizes, mineralogies and taphonomies, does not support their biological interpretation. Though a wealth of data in support of the biological origins of such structures

has been reported (structures whose veracity we do not here challenge), the lenticular objects in this study appear to be either ordinary detrital particles within the microbial mats, or mineralogical features unrelated to any specific sedimentary fabric, and thus of abiotic origin.

The Middle Marker horizon preserves a record of early prokaryotic diversity on Earth. A consortium of photosynthetic and probably associated chemosynthetic microbes flourished in these shallow waters, their success seemingly tied to volcaniclastic input from volcanic pulses: each flux provides the necessary bio-essential elements for catalysing primitive metabolisms, as evidenced by the rapid colonisation of the tops of volcano-sedimentary layers. By contrast, volcanogenic input spells destruction for the microbial ecosystem when deposited in larger volume atop a successful mat-building community. Thus, volcanogenic material provides both the geochemical impetus to foster microbial growth and the physical-mechanical-hydrodynamic constraints that destroy microbial ecosystems. The shallow-water, volcaniclastic biocoenosis of Archaean life was therefore one characterised by microbial struggle: the ecosystem flourished in times of erosion (or non-deposition), and perished in times of deposition. This biocoenosis appears to have been common and widespread on the Archaean Earth, and facies-biocoenosis similarities across such units are evident. The biofabrics of the Middle Marker are the most ancient evidence for life in the Barberton greenstone belt, and the second oldest convincing evidence for life on Earth.

Manuscript 3 – Reconstructing Archaean microbial biomes using trace and rare earth element systematics

Abstract

Palaeoarchaean cherts preserve some of the most ancient traces of life, but such palaeobiological testament is rarely assimilated into fossil-calibrated ecosystem or biome models. Trace and rare earth element plus yttrium (REE+Y) compositions reliably decode the palaeodepositional settings of these cherts, and thus constrain the environments within which early microbial life flourished. Herein, we present a systematic study comparing bulk inductively coupled plasma mass spectrometry (ICP-MS) of four cherts from the Barberton greenstone belt, South Africa (the 3.472 Ga Middle Maker horizon, 3.45 Ga Hooggenoeg H5c chert, 3.334 Ga Footbridge Chert and ~3.33 Ga Josefsdal Chert), with *in situ* laser ablation (LA) ICP-MS transects through multiple microbial laminations therein. *In situ* analyses can be interpreted in the framework of bulk analyses, correlating microbial biomes to their regional and local geochemical environments. Bulk ICP-MS analyses typically exhibit fractionated REE+Y patterns typical of anoxic hydrogenous sedimentation when normalised to Mud from Queensland (MUQ), supporting previous assertions that the Palaeoarchaean habitable realm was a hydrothermally influenced ocean. Suppressed La, Eu and Y anomalies, together with largely supra-chondritic Y/Ho ratios, however, indicate some degree of restriction from the open ocean and the influence of non-marine waters. *In situ* LA ICP-MS transects through microbial mat horizons are characterised by flat, LREE-enriched MUQ-normalised REE+Y patterns indicating strong non-marine influences from terrigenous, riverine fluids, although recurrent resurgences of marine REE+Y chemistry (increased Y/Ho ratios, La and Y anomalies) occur within the microbial laminations themselves. These findings show that widespread microbial life developed in semi-restricted basins with strong terrigenous, continental influences from mixed mafic and felsic erosion sources (estimated by trace element compositions and Cr/V versus Y/Ni trace element plots). Periodic seawater recharge into these basins generated disequilibrium conditions under which microbial life flourished. This systematic approach highlights both the development of emergent, volcanic, continental landmasses in the Palaeoarchaean, and their influence as loci for early microbial biomes, more than 100 Ma before the earliest evidence for large-scale terrestrial ecosystems. Throughout the Palaeoarchaean, semi-restricted, epicontinental basins represent an important, hitherto unrecognised, microbial habitat for some of the earliest photosynthetic life and may have been a precursor and contemporary to terrestrial microbial ecosystems, such as the lacustrine and riverine biomes identified in Mesoarchaean and Neoarchaean sequences. Understanding the distribution of Archaean life in terms of biomes should form a keystone of the strategy for Precambrian palaeoecology. The relative importance of biomes through time could, if accounting for the preservation potentials of individual palaeoenvironments, illuminate microbial evolutionary trajectories through the lens of environmental reconstruction.

1. Introduction

Quantitative and semi-quantitative geochemical tools capable of elucidating microbial- and regional-scale palaeoenvironments on the early Earth are of paramount importance in

understanding the distribution and settings of early life and the co-evolution of Earth and Life. An imprint of the palaeodepositional environments of Archaean metasediments (cherts) can be preserved within their rare earth element plus yttrium (REE+Y) compositions (Bau and Dulski, 1996; Kamber and Webb, 2001; Bolhar et al., 2004; Kamber et al., 2004; Bolhar and Van Kranendonk, 2007; Sugahara et al., 2010; Allwood et al., 2010; Gourcerol et al., 2015, 2016). Most ancient biosignatures are relatively well-preserved within cherts by virtue of the early and rapid 'time capsule' preservation afforded by silicification, where post-diagenetic alteration is very minor compared to other rocks, such as carbonates, evaporites or volcaniclastics (Westall et al., 2011, 2015; Hickman-Lewis et al., 2017). Indeed, silicification occurs sufficiently early and rapidly that microfossils, microbial mats and other organo-sedimentary fabrics can be preserved in volume during life processes (e.g. Knoll and Barghoorn, 1977; Walsh, 1992; Tice and Lowe, 2006a; Westall et al., 2011, 2015; Hickman-Lewis et al., 2017, 2018a; Greco et al., 2018). This suggests that the timescale of silicification may be less than weeks to months, supported by experimental silicification of prokaryotes indicating that the process begins within 24 hours (Orange et al., 2009). The systematic variation of REE+Y with depositional facies in Precambrian sediments can be reliably archived within such very short depositional timescales, fluctuating predictably between microband and layer deposition (Bau and Dulski, 1996; Tice and Lowe, 2006b; Allwood et al., 2010; Sugahara et al., 2010; Gourcerol et al., 2015, 2016) and thus has the potential to preserve geochemistry on timescales relevant to microbial horizons. The MUQ-normalised REE+Y composition of aqueous reservoirs has been relatively constant since the Archaean, typically including positive La, Gd and Y anomalies and the enrichment of heavy REE (HREE) over light REE (LREE) (Bolhar et al., 2004, 2015; Shields and Webb, 2004). Archaean marine precipitates do not exhibit negative Ce anomalies due to the prevailing anoxic conditions in the early oceans being reducing with respect to the Ce^{4+}/Ce^{3+} couple (Kamber et al., 2004; Bolhar et al., 2015), but show pronounced Eu anomalies attributed to enhanced hydrothermal contributions on global and local scales (Danielson et al., 1992; Hofmann and Harris, 2008). Characteristic REE+Y patterns can therefore be inferred to represent similar geochemical processes throughout deep geological time and decode the nature of palaeo-waters (Shields and Webb, 2004).

The delineation of characteristics defining multiple microbial horizons throughout the ancient geological record would ameliorate our understanding of the evolution of biogeochemical landscapes and ecosystems in deep time. The task facing this work is thus defining and applying an approach for the reconstruction of microbial biomes on the Palaeoarchaean Earth using REE+Y chemistry to distinguish characteristics of the palaeoenvironments inhabited by early life (Fig. 1A) on bulk and fine scales.

1.1. Building a biome model of the Palaeoarchaean: review and perspectives

The Barberton greenstone belt, South Africa, and the East Pilbara terrane, Western Australia, are the oldest well-preserved sedimentary successions within which are recognised the earliest convincing traces of life within discernible palaeoenvironments (e.g. Wacey, 2009; Brasier et al., 2011; Hickman-Lewis et al., 2018b). Many well-preserved biosignatures from these successions manifest themselves as organo-sedimentary structures, including stromatolites, biolaminites and microbial mats. Although it is challenging to infer a microbial ecosystem based solely on palaeontological evidence, correlations between morphologies of fossil and modern microbial mats and their occurrence in rocks reflecting shallow-water

depositional conditions suggest that anoxygenic photosynthetic microbial communities were already flourishing by 3.4-3.5 Ga (Walsh and Lowe, 1999; Nisbet and Fowler, 1999; Tice and Lowe, 2006a; Allwood et al., 2009; Westall et al., 2011; Noffke et al., 2013; Westall et al., 2011, 2015; Schopf et al., 2017; Hickman-Lewis et al., 2016, 2018a,b; Greco et al., 2018). In addition, evidence for chemosynthetic biomass is present in some horizons characterised by higher heat flux, i.e. hydrothermal and mineralising systems (Rasmussen, 2000; Westall et al., 2015). These distributions are consistent with isotope records and modelled early biogeochemical cycles (e.g., Nisbet, 1995; Nisbet and Fowler, 1999; Grassineau et al., 2003; Lenton and Daines, 2016).

Numerous environmental niches were colonised by around 3.5 Ga (Brasier et al., 2011; Knoll et al., 2016) and presumably formed a co-operative, globally significant biosphere (Nisbet, 1995). Anoxygenic submarine platforms were seemingly widely colonised (see references above), however, there is similarly evidence for life in periodically or continually exposed terrestrial environments (Westall et al., 2011; Djokic et al., 2017; Homann et al., 2018) and possibly within the water column (Walsh, 1992; Oehler et al., 2017; Sugitani, 2018). Ichnofossils from the Archaean remain contentious despite resembling modern bacterial alteration textures, and there is therefore less constraint on the early subsurface biosphere (Furnes et al., 2004, 2007). Our foci herein are the widespread, presumably phototrophic microbial mats which, having large areal distribution and occurring at the geosphere-hydrosphere-atmosphere interface, were likely the major drivers of biogeochemistry at the surface of the early Earth (Nisbet and Fowler, 1999; Lenton and Daines, 2016). These microbial mats are organo-sedimentary horizons (Figs. 2) representing the presumably photosynthetic portion of biomes in their palaeo-sedimentary context.

To set a framework for the reconstruction of the anoxygenic photosynthetic Archaean biome, we have selected microbially influenced horizons from four cherts spanning approximately 150 Ma of the Palaeoarchaean of the Barberton greenstone belt: the 3.472 Ga Middle Marker horizon, the ~3.47-3.45 Ga Hooggenoeg cherts H5c and H3c, the 3.334 Ga Footbridge Chert and the ~3.33 Ga Josefsdal Chert (Figs. 2-3). Cherts are sedimentary horizons with high silica content reflecting a silica-saturated environment (Kamber and Webb, 2001; Ledevin et al., 2014), the silica saturation resulting from water-rock dissolution interactions and hydrothermal venting or circulation (Danielson et al., 1992; Hofmann and Harris, 2008; Westall et al., 2015) and/or from the precipitation of silica directly from silica-supersaturated seawater (Tice and Lowe, 2006a,b; Ledevin et al., 2014). Ledevin, 2018 provides a comprehensive analysis of this debate. Cherts occur immediately above zones of progressively increasing silicification of the underlying volcanic and volcaniclastic sequences (Hofmann and Bolhar, 2007; Hofmann and Harris, 2008; Hofmann, 2011). These silicification zones are interpreted as resulting from diffuse, low-temperature hydrothermal circulation of seawater in an oceanic plateau-like setting (Bolhar et al., 2004; Hofmann and Harris, 2008). Hydrothermal convection cells beneath chert horizons were initiated by high regional heat flow and the cooling and dissolution of volcanic rock, and imply that the overlying seawater-sediment interface was a thermophilic environment (Hofmann and Bolhar, 2007). Previous trace and rare earth element-based research into the palaeoenvironments represented by such fossiliferous cherts in the Barberton region has painted a largely homogeneous view of the seawater-sediment interface during the Palaeoarchaean-Mesoarchaean as marine-dominated. The absence of a negative Ce anomaly denotes anoxic conditions (*cf*. Bau and Dulski, 1996;

Kamber and Webb, 2001), whereas some LREE enrichment and unsilicified phases illustrate variable detrital sources of mafic, dacitic and felsic compositions contributing to the clastic component in cherts (Lowe, 1999; Hofmann et al., 2013; Ledevin et al., 2014). The relative contributions of these sources have not yet been determined, but their significance relative to hydrogenous precipitation is generally assumed to be minor (Kamber, 2015; Cawood et al., 2018) and thus deposition is envisaged in environments dominated by the influence of the open ocean (e.g., Hofmann and Wilson, 2007; Hofmann and Harris, 2008; Westall et al., 2015; Hickman-Lewis et al., 2018). Similar work on contemporaneous fossiliferous horizons from the East Pilbara terrane, including the 3.481 Ga Dresser Formation and the 3.43 Ga Strelley Pool Formation, shows a less complex scenario, with well-fractionated REE+Y patterns indicating that these horizons formed under typical open ocean Archaean hydrogenous sedimentation (Van Kranendonk et al., 2003; Allwood et al., 2010). In bulk, the petrography, geochemistry and fossil evidence in Palaeoarchaean chert horizons across both terranes implies that they formed by comparable processes (Hofmann and Bolhar, 2008; Hofmann et al., 2013) and may have hosted similar, globally important microbial communities (Nisbet, 1995; Hickman-Lewis et al., 2018a). Although these bulk-determined conditions are assumed to be relevant to the environment of early life, the petrological context of the geochemistry with respect to fossiliferous horizons has been little investigated.

It is not until the Mesoarchaean and Neoarchaean that widespread evidence for significant continental (terrigenous) inputs are seen in the REE+Y patterns of fossiliferous cherts and carbonates. Grassineau et al. (2002) found that limestones in the 2.7 Ga Belingwe greenstone belt (Zimbabwe) had LREE-rich REE+Y patterns that evidenced deposition in the presence of locally sourced coastal material. Kamber et al. (2004) measured stromatolitic carbonates from the 2.7 Ga Mushandike Limestone (Zimbabwe) with a negative REE+Y slope in spite of positive La and Gd anomalies and a superchondritic Y/Ho ratio, shown to result from deposition in a restricted epicontinental sea with strong influence from local LREE-enriched continents. Contemporaneous stromatolitic carbonates from the Fortescue Group (Pilbara) were found to exhibit flat REE+Y patterns, lack La and Gd anomalies, and have supra-chondritic Y/Ho ratios, leading Bolhar and Van Kranendonk (2007) to interpret the palaeodepositional setting as a lagoonal-lacustrine environment dominated by freshwater influx. Sugahara et al. (2010) and Bolhar et al. (2015) studied older (3.0-2.9 Ga) horizons from the Pongola Supergroup (South Africa-Eswatini) and Mount Goldsworthy greenstone belt (Western Australia), finding variable influence from continental sources. Sugahara et al. (2010) noted MREE-enriched normalised REE+Y patterns, chondritic to supra-chondritic Y/Ho values and La anomalies in black cherts associated with evaporites that they interpreted to have formed in water masses significantly influenced by continental run-off, and with negligible hydrothermal influence. Chemical and clastic sedimentary rocks of the Pongola Supergroup exhibit LREE and MREE enrichment and show suppressed La, Gd, Y and Eu anomalies that suggest deposition in a restricted basin with fluctuating, but generally restricted, exchange with the open ocean (Bolhar et al., 2015). Other stromatolitic carbonates and iron formations of the Mesoarchaean-Neoarchaean show REE+Y patterns typical of marine deposition (e.g., Bau and Dulski, 1996; Kamber and Webb, 2001). Stüeken et al. (2015, 2017) performed detailed studies deducing the metabolic networks of Neoarchaean lacustrine systems, showing that these were also substantial ecosystems atop the later Archaean continents. Most recently, Homann et al. (2015, 2018) have conducted a substantial study of the earliest exclusively terrestrial ecosystem

in the 3.22 Ga Moodies Group, the uppermost stratigraphy of the Barberton greenstone belt. The fact that both continentally influenced and marine-dominated aqueous geochemistries and microbial consortia are found in Mid-Late Archaean sediments indicates that microbial biomes had, by this time, expanded into numerous tectonic settings. Whether this is the case for Early Archaean biomes, such as those hypothesised by Nisbet (1995, 2000), remains an unanswered question.

Each of the chosen cherts in this study represents a shallow-water, sedimentary habitable environment with well-described microbial communities, which we herein reconstruct at three scales of increasing specificity using bulk and laser ablation (LA) inductively coupled plasma mass spectrometry (ICP-MS) (Fig. 1):

- 'regional', combining sedimentological observations with bulk ICP-MS data (spanning a scale of macroscopic observation from stratigraphy to hand sample);
- 'local', combining bulk ICP-MS data and *in situ* LA ICP-MS data from the stratigraphy immediately surrounding microbial horizons (from hand sample to thin section); and
- 'biome', by conducting *in situ* LA ICP-MS transect analyses through microbial layers (spanning a scale from thin section to only several millimetres within the section, directly related to microbial activity). This highest resolution of analysis resolves aqueous chemistry on the short timescales during which sedimentary horizons were colonised by microbial life (Fig. 1) and is a direct measure of the prevailing palaeoenvironmental characteristics of the biome.

1.2. REE+Y geochemistry as an indicator of palaeoenvironment: interpretation and consideration

The trace and REE+Y compositions of cherts are determined by their contents within quartz (e.g., Kamber et al., 2004) and their association with Fe-Mn oxyhydroxide particles and other detrital phases that have undergone variable silicification (e.g., Ledevin et al., 2014; Gourcerol et al., 2015; Bolhar et al., 2015). Pervasive silicification associated with the presence of chert horizons may dilute the REE+Y signature, but characteristic patterns remain when normalised (Hofmann and Bolhar, 2007; Hofmann and Harris, 2008). As explained above, early and rapid silicification means that the REE+Y compositions of microbial horizons in ancient cherts reflect the ambient environment within which these ecosystems developed, flourished and were preserved, and are specific to the millimetric horizon studied, i.e., they represent a short-term palaeoenvironmental snapshot of direct relevance to the microbial inhabitants. Terrigenous clastic material may dominate REE+Y signals, and is often considered a '*contamination*', however, we do not advocate this terminology since the terrigenous fraction is a natural, syn-depositional fraction of these sediments. Silica, either nucleating by sorption onto detrital particles in the water column (Ledevin et al., 2014) or precipitating out of cooling, rock-buffered fluid resulting from the breakdown of olivine, pyroxene, feldspar and volcanic glass in the sub-seafloor silicification zones beneath chert (Lowe, 1999; Hofmann and Harris, 2008), forms a rapidly crystallising ooze at the seafloor that entraps detrital particles and autochthonous carbonaceous material alike. The three-dimensional preservation of microbial mats (i.e., in volume) demonstrates that early silicification occurred within the timescales of mat growth. Both the geochemical characteristics and the elemental composition of microbial biomes are a function of all fluid and mineral inputs, co-occurring at the seafloor (Lowe, 1999),

which was the locus of microbial mat growth. Bio-available trace elements and REEs govern the metabolic landscape of the biome in question, and all mineral phases present contribute to this elemental budget. Further to this, post-depositional processes including diagenesis, hydrothermal reactivation and multiple metamorphic events have been comprehensively demonstrated to have negligible effects on REE+Y composition (e.g. Bau and Dulski, 1996; Bolhar et al., 2005; Gourcerol et al., 2016). This is evidenced by the fact that specific REE+Y patterns coinciding with expected palaeodepositional conditions, e.g., deposition in a shallow-water oxic or anoxic environment, endure through even upper greenschist facies metamorphism (Bau and Dulski, 1996). The REE+Y compositions of cherts may thus reflect the combinatorial influences of:

1) precipitation from Archaean marine water (Bau and Dulski, 1996; Van Kranendonk et al., 2003; Bolhar et al., 2004; Kamber and Webb, 2004);
2) hydrothermal fluids emanating from vent systems (Danielson et al., 1992; Bolhar et al., 2005; Allwood et al., 2010; Gourcerol et al., 2015);
3) additional non-marine influences, for instance lagoonal-lacustrine, riverine and local pore waters, some of which are enriched in the REE due to their siliciclastic fraction (Hoyle et al., 1984; Elderfield et al., 1990; Kamber et al., 2004; Bolhar and Van Kranendonk, 2007);
4) chemical inheritance after replacement of the protolith (Hanor and Duchac, 1990; Hofmann et al., 2013); and
5) complexation by organic molecules, such as carboxylate and phosphate groups in cell walls and extracellular polymeric substances (Takahashi et al., 2005; Censi et al., 2013; Freslon et al., 2014).

In geological samples, normalisation to remove natural variations in REE+Y and allow comparison with upper crustal reservoirs is performed for Archaean rocks using Mud from Queensland (MUQ; *cf*. Kamber et al., 2005), which represents a bimodal felsic and mafic input, i.e. the expected terrigenous input from greenstone belts into Archaean oceans. When MUQ-normalised, most Precambrian marine sedimentary deposits can be abstractly characterised by a REE+Y pattern of seawater with hydrothermal and other influences (Bau and Dulski, 1996; Allwood et al., 2010; Gourcerol et al., 2015), exhibiting:

i. enrichment in heavy rare earth elements (HREE) relative to light rare earth elements (LREE), and therefore low $(Pr/Yb)_{MUQ}$;
ii. super-chondritic Y/Ho ratios ($Y/Ho \geq 27$);
iii. well-developed negative Ce anomalies only if oxidation of Ce^{3+} to Ce^{4+} occurs in the water column;
iv. variably positive Eu anomalies ($Eu^*/Eu_{MUQ} > 1.2$) reflecting hydrothermal contributions; herein, Eu anomalies will not be considered as signifying hydrothermal activity unless they exceed 1.2, since such values can also arise from enrichment within feldspars in tonalite-tronjhemite-granodiorite suites (Kerrich et al., 2013);
v. positive Y, La, Gd and Lu anomalies linked to marine input;
vi. flattened patterns *via* enrichment in LREEs (Hoyle et al., 1984; Elderfield et al., 1990; Bolhar and Van Kranendonk, 2007) resulting from terrigenous, riverine influences,

which are rapidly altered to typical seawater patterns during estuarine interaction with marine waters (Hoyle et al., 1984; Lawrence and Kamber, 2006); and

vii. MREE and especially HREE enrichment (Sm, Tm, Yb and Lu) resulting from inner sphere complexes during adsorption onto microbial cellular material (Takahashi et al., 2005; Censi et al., 2013; Freslon et al., 2014).

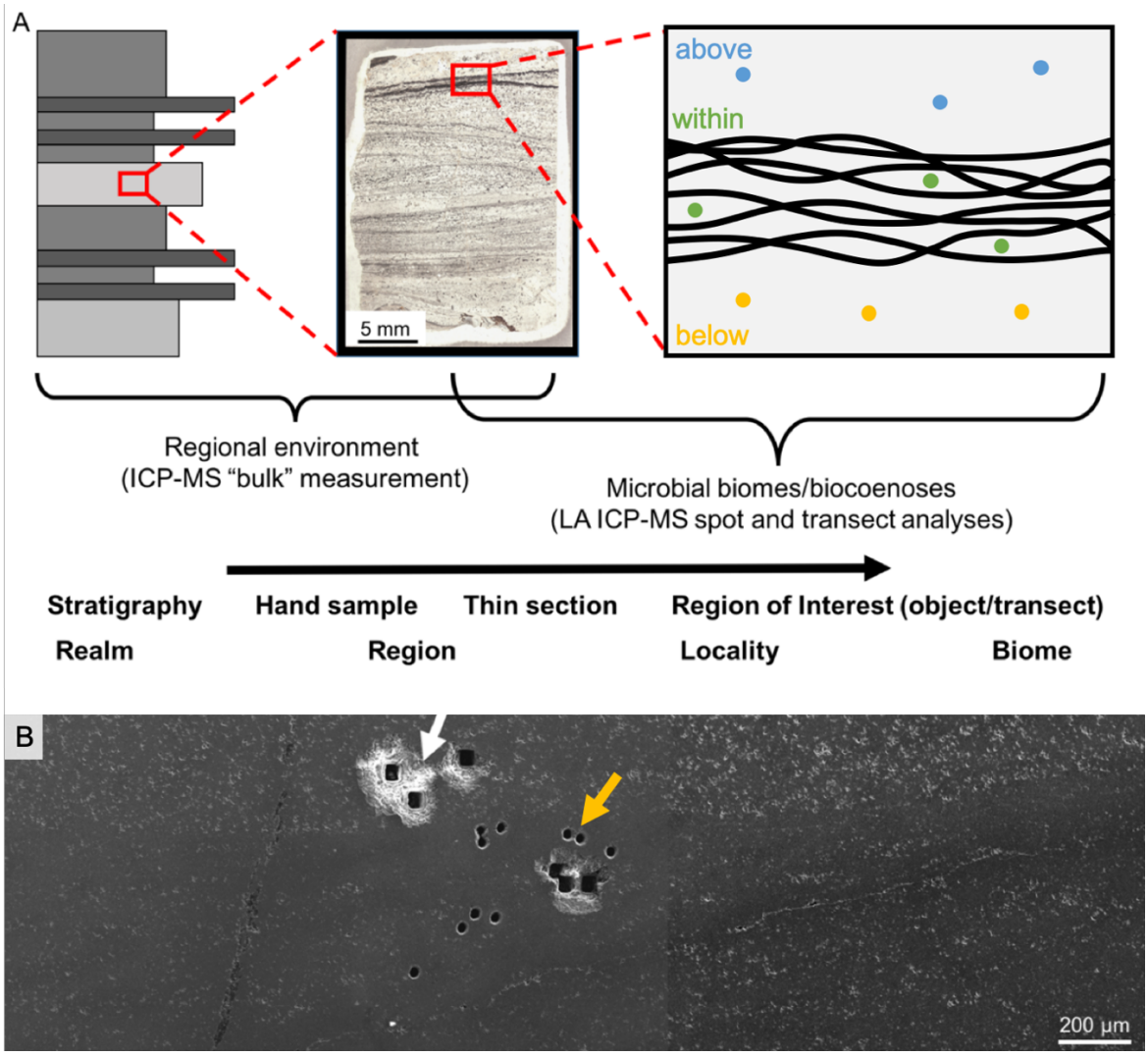

Fig. 1. Analytical approach and rationale linking bulk ICP-MS and *in situ* LA ICP-MS measurements to their palaeoenvironmental significance. Bulk ICP-MS analyses of hand samples, with respect to the stratigraphic and outcrop context, are informative for regional-scale environments. These findings can be linked to thin section petrography. *In situ* LA ICP-MS spot (coloured points) and transect (e.g. a sequence of points) analyses within thin sections link the local environment and biome-scale geochemistry that accompanies the flourishing of microbial ecosystems. Transects were taken across mat-bearing horizons, incorporating the cherts above and below the mats as shown by the yellow, green and blue points. These analyses are reciprocatively linked to thin section petrography and can thus be placed within local and regional palaeoenvironmental contexts together with hand sample and stratigraphic analyses. **B**) SEM micrograph showing transect of LA ICP-MS point analyses through a microbial mat. Spot analyses are 65 µm (white arrow) or 40 µm (yellow arrow) depending upon the size of the analysed region of interest.

The concentration of REE+Y in sediments is a function of the geology of the source region and qualitatively similar sources can exhibit very different REE+Y concentrations with similar

anomaly characteristics. The riverine REE+Y chemistries reported in Elderfield et al. (1990) and Freslon et al. (2014), for example, show markedly different REE+Y concentrations, however, the trend of the normalised pattern and its anomaly characteristics are comparable. This is because, unlike concentration, anomalies (e.g., in La, Ce, Eu, Gd, Y and Lu) reflect complexation phenomena unique to the chemistry of the hydrosphere (whether marine or non-marine). When normalised to their source rocks, marine deposits generally exhibit a non-smooth abundance pattern with relatively low $(Pr/Yb)_{MUQ}$ (Bau and Dulski, 1996; Bau, 1999). Although there are similarities in the REE+Y patterns of Archaean and modern sediments (Bau and Dulski, 1996; Shields and Webb, 2004; Thurston et al., 2012) the influence of hydrothermal fluids was greater in the Archaean oceans (Danielson et al., 1992; Klinkhammer et al., 1994; Wheat et al., 2002), accounting for the positive Eu anomaly in almost all previously reported hydrogenous REE+Y patterns from Archaean sediments. Anoxic Archaean conditions further negate the redox effects culminating in negative Ce anomalies (De Carlo and Green, 2002; Kamber et al., 2004; Allwood et al., 2010; Tostevin et al., 2016), although the magnitude of Ce/Ce^*_{MUQ} can be altered even by small-scale changes in pH and redox (De Carlo and Green, 2002; Gourcerol et al., 2016), for example in restricted settings (Gourcerol et al., 2016). The creation of artefact Ce anomalies is, however, unlikely in Archaean hydrogenous deposits due to the low levels of free O_2 present in the atmosphere (Bolhar and Van Kranendonk, 2007). Consequently, while an obvious negative Ce anomaly indicates marine precipitation in environments in which dissolved O_2 was present in sufficient abundance to promote oxidation of Ce^{3+}, the absence of a Ce anomaly can be considered equivocal (Tostevin et al., 2016).

Non-marine influences (e.g. hydrothermal and riverine water) may have significant impacts on the REE+Y pattern because they are highly enriched in lanthanide series elements relative to marine compositions (Elderfield et al., 1990; Klinkhammer et al., 1994; Alibo and Nozaki, 1999; Tostevin et al., 2016). This would mathematically result in the suppression of anomalies due to near-uniformly increased LREE, MREE and HREE concentration. Freslon et al. (2014) have suggested, however, that the REE+Y pattern of organic-rich sediments could be primarily controlled by biogeochemical processes relating to sedimentary organic matter and not by the composition of the sediment source. Considering the REE+Y patterns for organic matter presented by Takahashi et al. (2005) and Freslon et al. (2014), organic-rich samples with strong MREE (Sm-Tb) and HREE (Tm-Lu) enrichment may signify this effect.

Finally, although positive Gd anomalies are often identified as a feature of the REE+Y pattern of seawater (e.g. Bau and Dulski, 1996, Kamber et al., 2004; Lawrence and Kamber, 2006), the high sensitivity of Gd to oxyhydroxide interactions and the relative concentrations of its neighbour elements (Eu and Tb) means that it may also exhibit a negative anomaly in seawater (Alibo and Nozaki, 1999; Kamber et al., 2004; Gourcerol et al., 2015, 2016). We have elected not to consider Gd in our discussion due to the low concentrations of Gd, Eu and Tb in the analytes studied.

2. Materials and Methods

Samples were collected during multiple fieldwork campaigns to the Barberton greenstone belt between 1999 and 2014, and all may be readily relocated by their co-ordinates in Global Positioning Systems (G.P.S.). Samples are stored in the CNRS Orléans Lithothèque.

2.1. Geological setting and petrography of microbial mats

Optical photomicrographs were acquired using an Olympus BX-51 equipped with a CCD camera (CNRS CBM, Orléans). Stratigraphic and petrographic descriptions of the context of the microbial horizons studied herein are as follows.

2.1.1. Middle Marker H1 (~3.472 Ga)

The Middle Marker horizon is a thin chert unit (Fig. 3A), at the base of the Hooggenoeg Formation, charting the deposition of a shallow, wave- and current-influenced prograding volcanic cone within a semi-restricted basin (Lanier and Lowe, 1982; Paris et al., 1985; Hickman-Lewis et al., 2018a). Sediments include coarse volcaniclastic sandstones, laminated volcaniclastic sandstones and siltstones and massive, clotted carbonaceous chert, with localised carbonate sedimentation, within which has been noted copious evidence for shallow water deposition, including ripple marks and ashfall deposits (Fig. 3C, E; Hickman-Lewis et al., 2018a). Previous bulk characterisation of major and trace element geochemistry suggests inputs from mafic and felsic volcaniclastic inputs (Hofmann et al., 2013; Hickman-Lewis et al., 2018a). Five representative samples were studied in bulk: three black-white-grey banded cherts (04SA14, 07SA21 and 07SA23) and two massive cherts with a significant volcaniclastic component (03SA01 and 07SA22).

The Middle Marker horizon preserves an assemblage of morphologically diverse microbial mats, preserved in laminated volcaniclastic sandstones and siltstones that deposited in the photic zone, hence their interpretation as anoxygenic photosynthesisers (Hickman-Lewis et al., 2018a). Multi-laminar, crinkly-wavy, micro-tufted, carbonaceous laminations are common features mantling the primary sedimentary structures. The mats studied herein constitute a representative multi-laminar, micro-tufted carbonaceous horizon (ca. 1 cm thick; sample 07SA23) from laminated volcaniclastic sandstones (Fig. 2A). Two samples of massive carbonaceous black chert from the non-mat-based stratigraphy (samples 07SA22 and 07SA25), were also studied in order to understand local-scale geochemical conditions (Figs. 2B).

2.1.2. Hooggenoeg chert H5c (3.47-3.45 Ga)

The Hooggenoeg Chert H5 member is a unit of ultramafic and mafic rocks, overlain by silicified volcaniclastic sedimentary rocks and laminated, black-grey carbonaceous chert with botryoidal stratiform veins (H5c; Fig. 2G) (Lowe and Byerly, 1999; Hofmann, 2011). Chert veins crosscutting silicified volcanic rocks immediately below the chert horizons throughout the Hooggenoeg Formation are interpreted as the result of shallow hydrothermal convection of seawater (Hofmann and Bolhar, 2007; Hofmann, 2011). Early silicification in the laminated chert is indicated by a planar contact with the overlying conglomerate (Hofmann and Bolhar, 2007). Four samples of black and white laminated (01SA56 and 07S28) and massive (01SA09 and 03SA16) were studied in bulk.

Biosignatures from Hooggenoeg chert H5c, including filamentous microfossils and carbonaceous laminations, were among the first to be systematically described from the Barberton greenstone belt (Walsh, 1992; Walsh and Lowe, 1999). The morphological similarity of the described laminations to modern and fossil microbial mats, together with common trapped and bound particles within, is convincing evidence for their biogenicity. Roll-up and anastomosing structures provide evidence of *in vivo* plasticity. The microbial mats studied herein (from sample 03SA15) have flat-laminated morphologies (Fig. 2C), similar to

those described in Walsh (1992) and Walsh and Lowe (1999). A further sample of adjacent massive carbonaceous chert (sample 03SA04; Figs. 2D) was analysed to understand local-scale geochemical environments.

2.1.3. Footbridge Chert K3c (3.334 Ga)

The Footbridge Chert is a sequence of laminated and massive cherts (Fig. 3H), which shows evidence for deposition in alternately shallow-water (Westall et al., 2001) and deep-water (i.e., below storm wave base; Lowe and Byerly, 1999) conditions. Much of the K3c chert is underlain by silicified pillow basalt, and cross-cutting and stratiform botryoidal veins continue through the laminated chert (Hofmann and Bolhar, 2007). Two laminated shallow-water cherts (12SA49 and 12SA50) and one sample of silicified volcaniclastic green-grey chert (96SA02) were studied in bulk.

Thin, carbonaceous laminations can be identified in the shallow-water horizons of some banded cherts, although these structures have never before been described. Their similarity to known microbial mats from the Archaean makes their biogenic interpretation plausible and unsurprising. Within the studied samples of black and white laminated chert (03SA09), carbonaceous laminations drape over and anastomose around large, rounded carbonaceous grains and over layers comprising detrital deposits of volcaniclastic particles (Fig. 2E). These laminations form 'eyelet' structures around enclosed particles (*cf*. alpha-type laminations from the Buck Reef Chert; Tice and Lowe, 2006a,b), and roll-up and rip-up structures are often noted at the surfaces of laminations. Above one of the studied mat horizons, a particularly well-preserved, frayed, torn-up mat chip can be linked to the eroded surface morphology of the corresponding horizon (Fig. 2E). A very high degree of volumetric preservation is recorded within each microbial horizon, suggesting almost immediate seafloor silicification. A sample of massive chert from immediately below these microbial horizons (03SA09') was also studied for local-scale comparison (Figs. 2F).

2.1.4. Josefsdal Chert ~K3c (c. 3.33 Ga)

The Josefsdal Chert is an 8-30 m thick sequence of volcaniclastic sandstones, chert with variable hydrothermal influence and biogenic sediments (Fig. 2B, D, F), deposited in a shallow basin atop basaltic pillow lavas (Westall et al., 2015). The sequence includes localised chemical cherts that appear to have precipitated as a silica-rich ooze (*cf*. Ledevin et al., 2014). The basin appears to have been protected, indicated by a general lack of large-scale sedimentary bedforms indicative of open sea conditions and the parallel-laminated structure of most microbial mat horizons. Within the Josefsdal Chert, thin microbial biofilms, both flat-laminated and undulating, occur in both banded sedimentary and chemical cherts, and bear morphological similarity to those described in the Hooggenoeg Formation, trapping and binding grains and mantling large carbonaceous particles (Westall et al., 2011, 2015). Putative microfossils occur in the same horizons (Westall et al., 2001, 2015). Previous high-resolution geochemical analyses of one such biofilm implies that it consisted of a consortium of phototrophic organisms and sulphate-reducing bacteria (Westall et al., 2011).

The samples studied herein include finely laminated chemical chert strata (Figs. 2H, 3D) associated with hydrothermal vent systems and shallow-water sedimentary strata (Figs. 2B), of which the latter are laminated, organic carbon-bearing sediments from upper shoreface settings, including both detrital and microbial carbonaceous laminations (Fig. 2F; Westall et

al., 2015). Bulk analyses were conducted in a number of black-grey-white banded cherts and massive cherts (see Table 2), and 'biome'-scale transect analyses were conducted across microbial horizons in banded cherts (12SA18 and 12SA36) and a massive chert (99SA07).

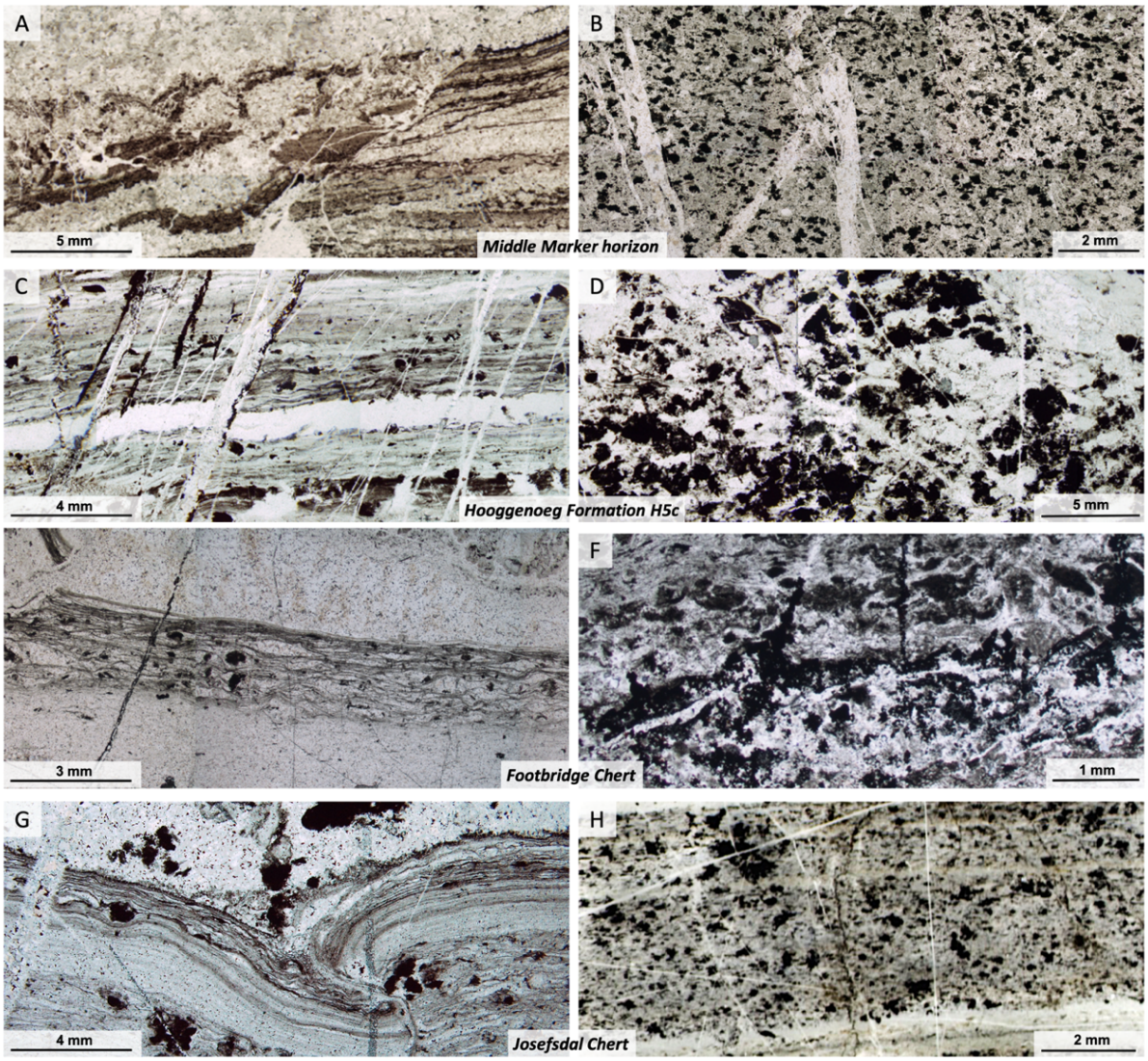

Figure 2. Petrographic detail of some samples studied herein, demonstrating the equivalence of the types of sediments used, despite their provenance from four horizons spanning 150 Ma. Further photomicrographs are presented in the Supplementary Material. **A**) Silicified sediments from the Middle Marker horizon characterised by a thick set of micro-tufted microbial mats (sample 07SA23). The mats are preserved poorly, and distended, at the left-hand side of the image. **B**) Massive, structureless black chert from the Middle Marker horizon, comprising matrix-supported irregular carbonaceous particles (sample 07SA22). **C**) Laminated black and white chert from Hooggenoeg Chert H5c, showing well-preserved biofilm-like laminations intercalated with near-pure silica layers. **D**) Massive, clotted carbonaceous chert from Hooggenoeg Chert H5c (sample 03SA04). **E**) Exquisitely preserved microbial mat from the Footbridge Chert, overlain by granular carbonaceous sediment layers (03SA09). **F**) Weakly laminated, massive chert from the Footbridge Chert (sample 03SA09'). **G**) Deformed, finely laminated microbial biofilms from the Josefsdal Chert (sample 12SA18). **H**) Weakly laminated clotted carbonaceous chert from the Josefsdal Chert (sample 99SA07).

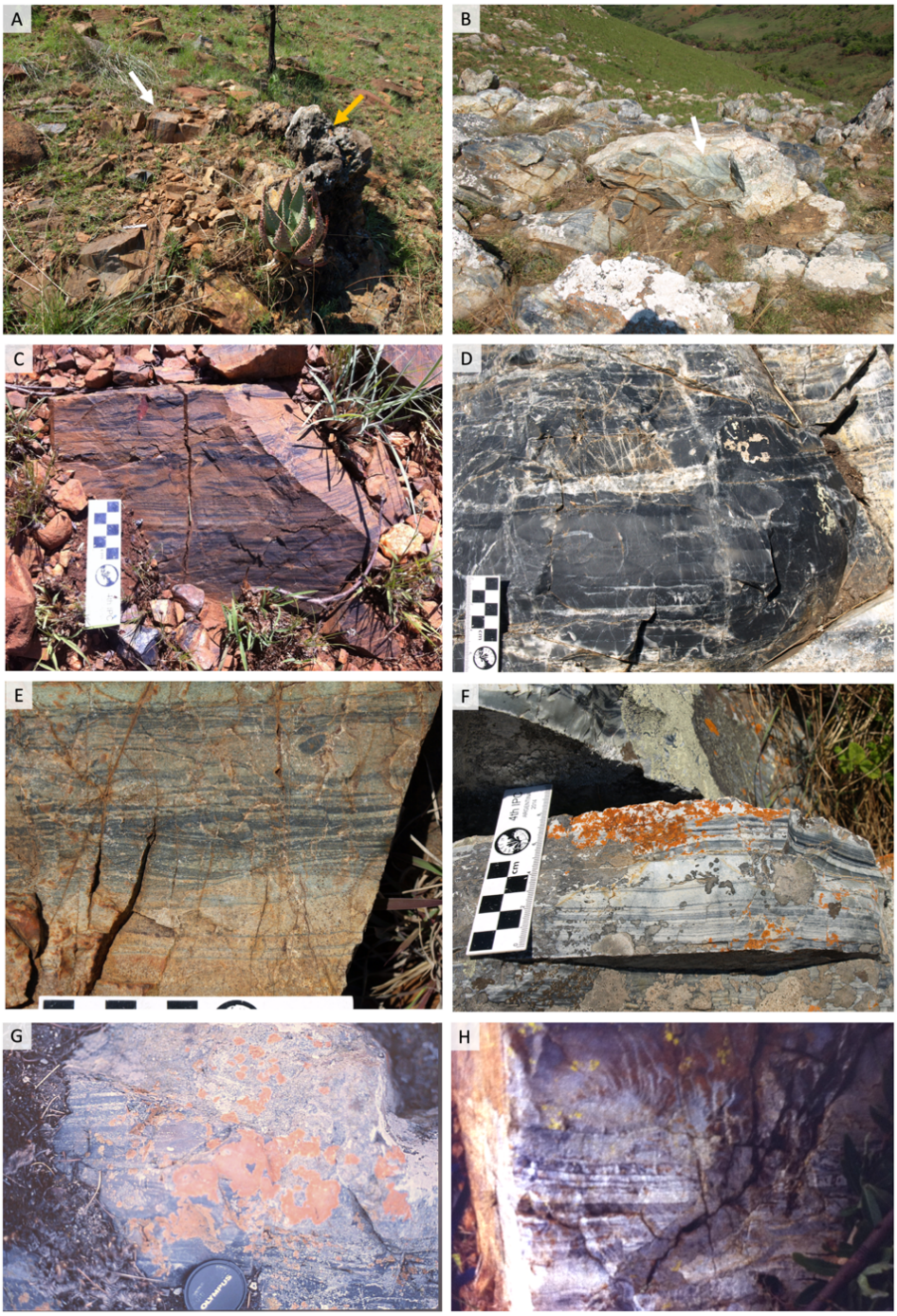

Figure 3. Field photographs showing sampling localities and outcrop characteristics. **A**) Field photograph of the Middle Marker horizon (north of Tjakastad, Mpumalanga province, South Africa) showing laminated cherts (white arrow) overlying basalt (gold arrow). **B**) Field photograph of the Josefsdal Chert (between Ekulindeni, Mpumalanga province, South Africa, and Bulembu, Hhohho region, Eswatini), showing laminated green-grey cherts (white arrow). **C**) Outcrop photograph of ripple-laminated, fine-grained silicified siltstone from the Middle Marker horizon, containing carbonaceous microbial laminations (sample 07SA23). **D**) Outcrop photograph of black, massive, faintly-laminated carbonaceous chemical chert from the Josefsdal Chert (sample 99SA07). **E**) Detail of laminated chert from the Middle Marker horizon. **F**) Detail of grey-green laminated chert from the Josefsdal Chert. **G**) Outcrop photograph of black and white laminated chert from Hooggenoeg Formation Chert H5c (sample 03SA15). Lens cap for scale. **H**) Outcrop photograph of black and white laminated chert from the Footbridge Chert (samples 03SA09 and 03SA09'). Hammer shaft for scale.

2.2. Geochemistry of fossiliferous horizons

2.2.1. Bulk ICP-OES and ICP-MS

Inductively coupled plasma optical emission spectrometry (ICP-OES) and mass spectrometry (ICP-MS) analyses were undertaken at the Centre de Recherches Pétrographiques et Géochimiques (CRPG), Nancy, France, using Thermo Fisher ICap 6500 and Agilent 7700X instruments. Analysed powders were sub-sampled from chips of the original hand samples demonstrably free from obvious alteration or secondary veining in order to focus on both characteristic biosignature-free matrices ('regional' scale) and microbial horizons and their immediate environs ('local' scale), thereby enabling direct comparison with LA ICP-MS measurements ('biome' scale) (Fig. 1). Results of bulk ICP-OES major element analyses are shown in Figure 9. Results of bulk ICP-MS analyses are shown as extended trace element diagrams in Figure 10, as REE+Y curves in Figure 11, and as mixing line diagrams (see Section 2.3.) in Figure 12.

2.2.2. In situ laser ablation ICP-MS

For laser ablation (LA) ICP-MS, thin sections of between 60 µm and 100 µm thickness were produced from complementary samples in which regions of interest (ROIs) in chert were identified using high-magnification optical microscopy. ROIs were selected to be clean and free from impurities including minerals which might impart additional trace element contamination of the primary signature (after Gourcerol et al., 2015). Indeed, only a small volume of contaminant material is required to suppress true REE+Y characteristics (Allwood et al., 2010; Gourcerol et al., 2015); thus, to assure the validity of our conclusions regarding the co-evolution of life with its environment ('local' scale), the REE+Y composition measured stems only from the interaction of aqueous fluid reservoirs and genuine primary inputs, such as contemporaneous terrigenous material. Due to the rapidity of silicification outlined above, these phases can be considered important in defining the elemental budget and geochemical environment of their horizon.

Within each sample hosting laminated microbial biosignatures, multiple transects of point analyses were taken through the microbial horizon with the objective of capturing the fine-scale palaeoenvironmental characteristics in the short timescales preceding, during and following microbial colonisation ('biome' scale). In order to specifically address the palaeodepositional setting of microbial mats, we analysed exclusively chert domains within mat layers, and not the organic matter itself. As noted in Section 1.2, high rates of MREE and HREE scavenging occur in microbial and sedimentary organic matter and can dominate the REE+Y pattern (Takahashi et al., 2005; Censi et al., 2013; Freslon et al., 2014). By avoiding carbonaceous material, we therefore ensure that analyses within microbial layers indicate exclusively the large-scale fluid sources from which trace and rare earth elements originate. Transects were bounded by analyses in overlying and underlying microcrystalline chert (Fig. 1B).

Data were acquired using a XSeries II ICP-MS (Thermo Fischer Scientific) coupled to a 213 nm Nd:YAG laser ablation system (New Wave Research) housed at Centro Interdipartimentale Grandi Strumenti (CIGS), Università di Modena e Reggio Emilia, Italy. Helium was used as the carrier gas to transport ablated material from the LA sample chamber to the mass spectrometer torch. Standard Reference Materials NIST 610, NIST 612 and NIST

614 (National Institute of Standards and Technology) were used to perform external calibration and mass spectrometer tuning, and were measured during each analysis with equivalent spot size, frequency, duration and laser intensity to the sample analyses (Table 1). Instrumental performance was optimised daily using NIST 612 as reference material in order to obtain maximum signal intensity. The mass spectrometer parameters were tuned for the maximum signals of the isotopes ^{139}La, ^{232}Th and ^{238}U while ablating a line on NIST 612 with the following parameters: line width = 100 μm, repetition rate = 10 Hz, laser output = 100%.

To obtain high-quality analytical data, several laser parameters, such as the ablated area, beam intensity, frequency and ablation duration were systematically varied in order to evaluate the effects of these instrumental settings on signal quality. Several preliminary tests were performed on a representative sample (07SA23), in order to determine the ideal parameters used during the experiments. During preliminary tests, it was also demonstrated that pre-ablation was necessary to remove possible contaminants from the sample surface before data acquisition. The signal acquired during each analysis involved three steps: pre-ablation, blank acquisition and ablation. The signal acquired during pre-ablation was not used for the calculation, as this first step was only used to remove possible contaminants from the sample surface. After pre-ablation, the laser was turned off and the blank signal was acquired. Since the blank signal was acquired when the laser was not firing on the sample, it is representative of the background. This step was immediately followed by turning on the laser and ablating the sample, generating a time-dependent signal. The signal corresponding to the blank was used to correct for the background: once appropriate time-resolved sections were chosen for the blank and the sample, the average background signal intensity was subtracted from the average signal intensities of the sample. A summary of the LA parameters used during the experimental sessions are presented in Table 1.

Parameters	*Values*
Pre–ablation:	
Spot size (μm)	40/65 (depending on the size of the region of interest)
Frequency (Hz)	10
Duration (s)	5
Laser intensity (%)	25
Ablation:	
Spot size (μm)	40/65 (depending on the size of the region of interest)
Frequency (Hz)	20
Duration (s)	30
Laser intensity (%)	100
Total acquisition time (s)	150
Laser warm up (s)	25
Wash out (s)	30
He flow rate (mL/min)	600
Mass spectrometer dwell time per analyte (ms)	30

Table 1. Parameters used during laser ablation ICP-MS experiments.

The concentrations of the analytes of interest were obtained by comparison with an external calibration curve, which was calculated by performing analyses of NIST 610, 612 and 614 during each analytical session. Quantitative data were obtained for the signals of the following isotopes: ^{7}Li, ^{9}Be, ^{23}Na, ^{26}Mg, ^{27}Al, ^{28}Si, ^{31}P, ^{39}K, ^{44}Ca, ^{45}Sc, ^{47}Ti, ^{51}V, ^{52}Cr, ^{55}Mn,

^{56}Fe, ^{59}Co, ^{60}Ni, ^{63}Cu, ^{66}Zn, ^{69}Ga, ^{75}As, ^{85}Rb, ^{88}Sr, ^{89}Y, ^{90}Zr, ^{93}Nb, ^{95}Mo, ^{107}Ag, ^{109}Ag, ^{111}Cd, ^{115}In, ^{118}Sn, ^{123}Sb, ^{133}Cs, ^{137}Ba, ^{139}La, ^{140}Ce, ^{141}Pr, ^{146}Nd, ^{147}Sm, ^{153}Eu, ^{157}Gd, ^{159}Tb, ^{163}Dy, ^{165}Ho, ^{166}Er, ^{169}Tm, ^{172}Yb, ^{175}Lu, ^{178}Hf, ^{181}Ta, ^{182}W, ^{197}Au, ^{205}Tl, ^{208}Pb, ^{232}Th, ^{238}U. Generally, at least three spots were acquired in each region of interest (see Supplementary Tables) in order to assure an appropriate statistic. The results of *in situ* laser ablation ICP-MS analyses are shown as REE+Y curves in Figure 13, on mixing lines in Figure 14, and in terms of the changing chemistry through transect analyses in Figure 15.

Elemental anomalies relative to combinations of neighbouring and near-neighbouring elements in ICP-MS and LA ICP-MS plots were calculated according to the methods presented in Lawrence and Kamber (2006) and Lawrence et al. (2006), and are as follows:

$$La/La^*_{MUQ} = La_{MUQ}/(Pr^*_{MUQ}(Pr_{MUQ}/Nd_{MUQ})^2)$$

$$Ce/Ce^*_{MUQ} = Ce_{MUQ}/(Pr^*_{MUQ}(Pr_{MUQ}/Nd_{MUQ})$$

$$Pr/Pr^*_{MUQ} = Pr_{MUQ}/(0.5Ce_{MUQ} + 0.5Nd_{MUQ})$$

$$Eu/Eu^*_{MUQ} = Eu_{MUQ}/(Sm^2_{MUQ} \times Tb_{MUQ})^{1/3}$$

$$Gd/Gd^*_{MUQ} = Gd_{MUQ}/(Tb^2_{MUQ} \times Sm_{MUQ})^{1/3}$$

$$Y/Y^*_{MUQ} = Y_{MUQ}/(0.5Er_{MUQ} \times 0.5Ho_{MUQ})$$

2.3. Mixing line diagrams

The respective influences of high-temperature (>250°C) hydrothermal fluids and detrital inputs were assessed using calculated binary mixing lines (Figs. 12, 14). End-members reflecting seawater, hydrothermal fluid and detrital terrigenous influence were selected, respectively, as follows after Gourcerol et al. (2016):

- modern seawater from the North Pacific (Alibo and Nozaki, 1999);
- chert from a banded iron formation of the Abitibi greenstone belt, Canada, (Thurston et al., 2012) characterised by a strong Eu anomaly (Eu/Eu^*_{MUQ} = 30.01); and
- Mud from Queensland (MUQ), which illustrates a bimodal terrigenous input (Kamber et al., 2004).

Gourcerol et al. (2016) determined that a brecciated chert sample from Thurston et al. (2012) with a large Eu anomaly (Eu^*/Eu_{MUQ} = 30.01) provides an accurate model for Archaean hydrothermal effluent, since pre-Proterozoic hydrothermal venting regions were characterised by fluid mixing with an inverse pH gradient (alkali to acid) when compared to modern hydrothermal systems (Shibuya et al., 2010). Consequently, the Eu/Sm and Sm/Yb ratios, which are respectively a quantitative measurement of the strength of the Eu anomaly and a measure of the flatness of the REE+Y pattern, may be used to quantify the influence of high-temperature (>250°C) hydrothermal fluids, which are characterised by a flat REE+Y pattern devoid of all except the Eu anomaly. Most Archaean samples plot either on or above the mixing line calculated from the seawater and hydrothermal end-members since the Sm/Yb ratio is particularly sensitive to high-pressure residual metamorphic phases, which may influence the

primary geochemical signature of the chert if plotting particularly far from the mixing line. Points far from the mixing line are not pristine and will not be considered in our discussion.

$(Pr/Nd)_{MUQ}$ versus Y/Ho ratios, which are respectively measurements of the flatness of the REE+Y pattern and the chondritic values of the fluid, were used to qualitatively assess detrital terrigenous input during chert deposition, since terrigenous input is characterised by a flat REE+Y pattern and a chondritic Y/Ho ratio. A conservative mixing line was calculated using seawater samples selected from the North Pacific (Alibo and Nozaki, 1999) and the MUQ composite (Kamber et al., 2004) as end-members. Note that the percentage values in this diagram should be considered to represent the relative influence of the end members rather than a quantitative measure between the two. Further details on the application of these assessments and the rationale for the construction of mixing lines is presented in Gourcerol et al. (2016). Together, these two mixing plots indicate, using independent elemental ratios, the importance of marine *versus* hydrothermal and marine *versus* terrigenous (or non-marine) inputs. In the case of a significant non-marine input, one must consider the strength of the Eu anomaly in distinguishing whether the input is riverine or hydrothermal.

3. Results

3.1. Evaluation of contamination and metamorphism

Since even small quantities of clastic- or mineral-related input can affect the REE+Y signal of hydrogenous chert, we have followed the approach of Bolhar and Van Kranendonk (2007), Sugahara et al. (2010) and Bolhar et al. (2015) to test that clastic or terrigenous components can be considered an *input*, and not *contamination*, to the palaeoenvironment. For each formation, we tested multiple parameters (La, Eu, Ce and Y anomalies and Y/Ho ratios) against total REE+Y, Ti content, and against one another, as a proxy for contamination of the signal by clastic input or other hydrospheric influences, demonstrating that there are no systematic relationships between any two such parameters (Fig. 4-6), ergo '*contamination'* by clastic material does not affect the REE+Y signals reported (*cf.* Sugahara et al., 2010; Bolhar et al., 2015). Since similar values are obtained for various parameters (e.g. anomalies) irrespective of the Ti content, fluid chemistry rather than clastic contamination is the dominant control on REE+Y composition (Bolhar et al., 2015) (see also Figs. 7-8).

Post-Archaean trace element mobilisation by either system reactivation or metamorphism is not relevant to the final REE+Y signature (Bau, 1999) since the formations studied underwent a maximum of lower greenschist facies metamorphism (< 350˚C, 2-3 kbar) and, in many cases, zeolite facies metamorphism (< 300˚C, < 2-3 kbar) (see listing in Wacey, 2009), which is insufficient to significantly alter REE+Y signals and their interpretation (Bau and Dulski, 1996). In addition to the identifiable trends resulting from complexation in the hydrosphere, effects from terrigenous or continental inputs are also primary, their signals entombed by early, rapid silicification, and are an important consideration in interpretation.

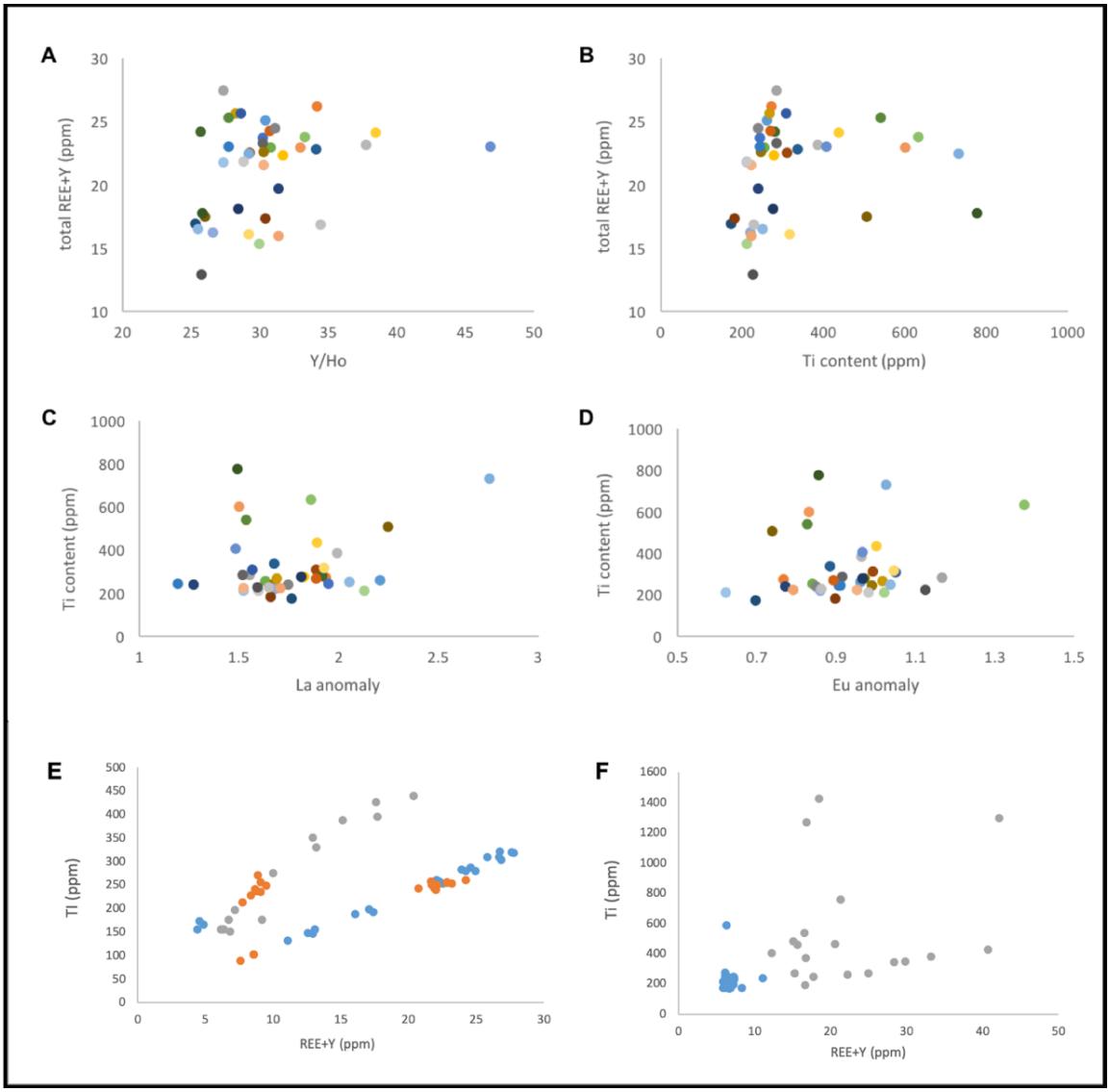

Fig. 4. Plots of total REE+Y concentrations against Y/Ho, and total REE+Y, La anomaly and Eu anomaly against Ti content for samples of the Middle Marker horizon (A-D), Footbridge Chert (E) and Josefsdal Chert (F). Points are individually coloured consistently within the figure in order to allow comparison. The lack of correlation between any of these parameters, with the exception of the Footbridge Chert, signifies that the abundances of REE+Y and any complexation phenomena reflected in calculated anomalies are not artefacts resulting from the input of contaminative terrigenous input (after Sugahara et al., 2010; Bolhar et al., 2015). In the case of the Footbridge Chert, subsequent analyses of La versus Ce anomalies (La/La^*_{MUQ} versus Ce/Ce^*_{MUQ}), La versus Eu anomalies (La/La^*_{MUQ} versus Eu/Eu^*_{MUQ}), and Ce anomaly (Ce/Ce^*_{MUQ}) versus Y/Ho ratio, demonstrate that despite the correlation shown in this figure, the anomaly characteristics are unaffected by contaminative phases.

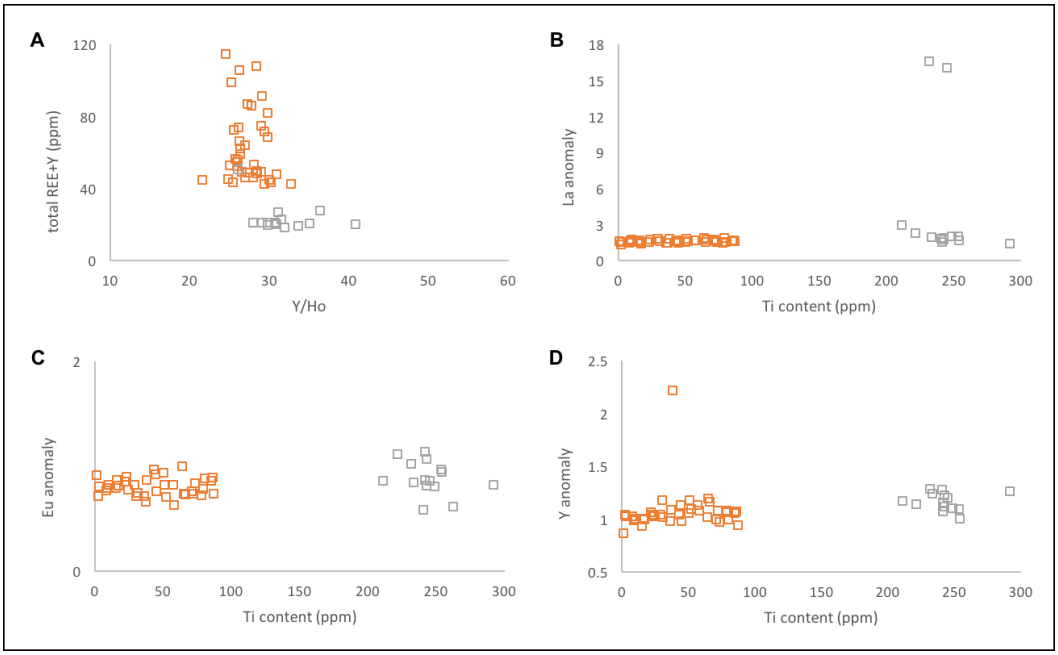

Fig. 5. Plots of Y/Ho versus total REE+Y and La, Eu and Y anomalies against Ti content for the Hooggenoeg Formation samples. Orange symbols represent sample 03SA15 and grey symbols sample 03SA04. The lack of correlation between any of the parameters either within or between samples indicates that the REE+Y patterns are not artefacts created by terrigenous input (after Sugahara et al., 2010; Bolhar et al., 2015). For example, although the Ti content is much higher in sample 03SA04, it exhibits similar values for all anomalies, indicating that the same chemical oceanographic phenomena are active within the samples, and thus that terrigenous input, for which Ti content is a proxy, is an important, but separate feature of these samples. Ti content is indicative of the proximity of the location of deposition to the terrigenous source.

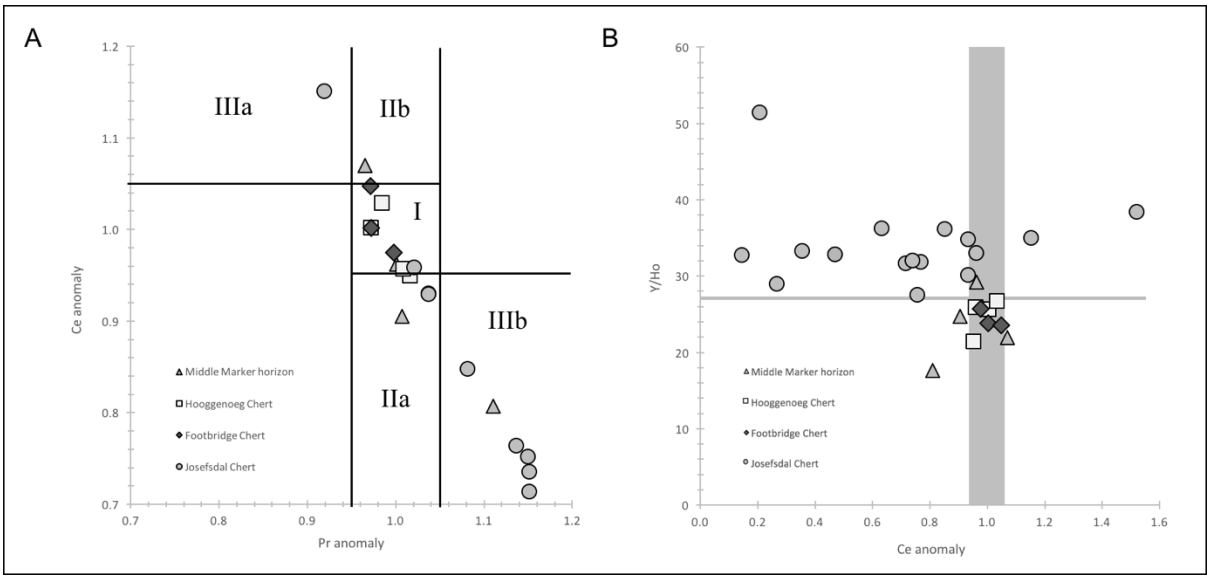

Fig. 6. Further REE+Y characteristics of the bulk samples analysed. **A**) Evaluation of 'true' Ce anomaly following the method of Bau and Dulski (1996), in which Pr anomaly is plotted against Ce anomaly. Zone I = no La or Ce anomaly; zone IIa = negative La anomaly, no Ce anomaly; zone IIb = positive La anomaly, no Ce anomaly; zone IIIa = positive La and Ce anomalies; zone IIIb = negative La and Ce anomalies. **B**) Ce anomaly versus Y/Ho ratio. Vertical grey line denotes the significance boundaries for the Ce anomaly as in A. Horizontal grey line indicates the Y/Ho ratio of 27, i.e. super-chondritic values of Y/Ho.

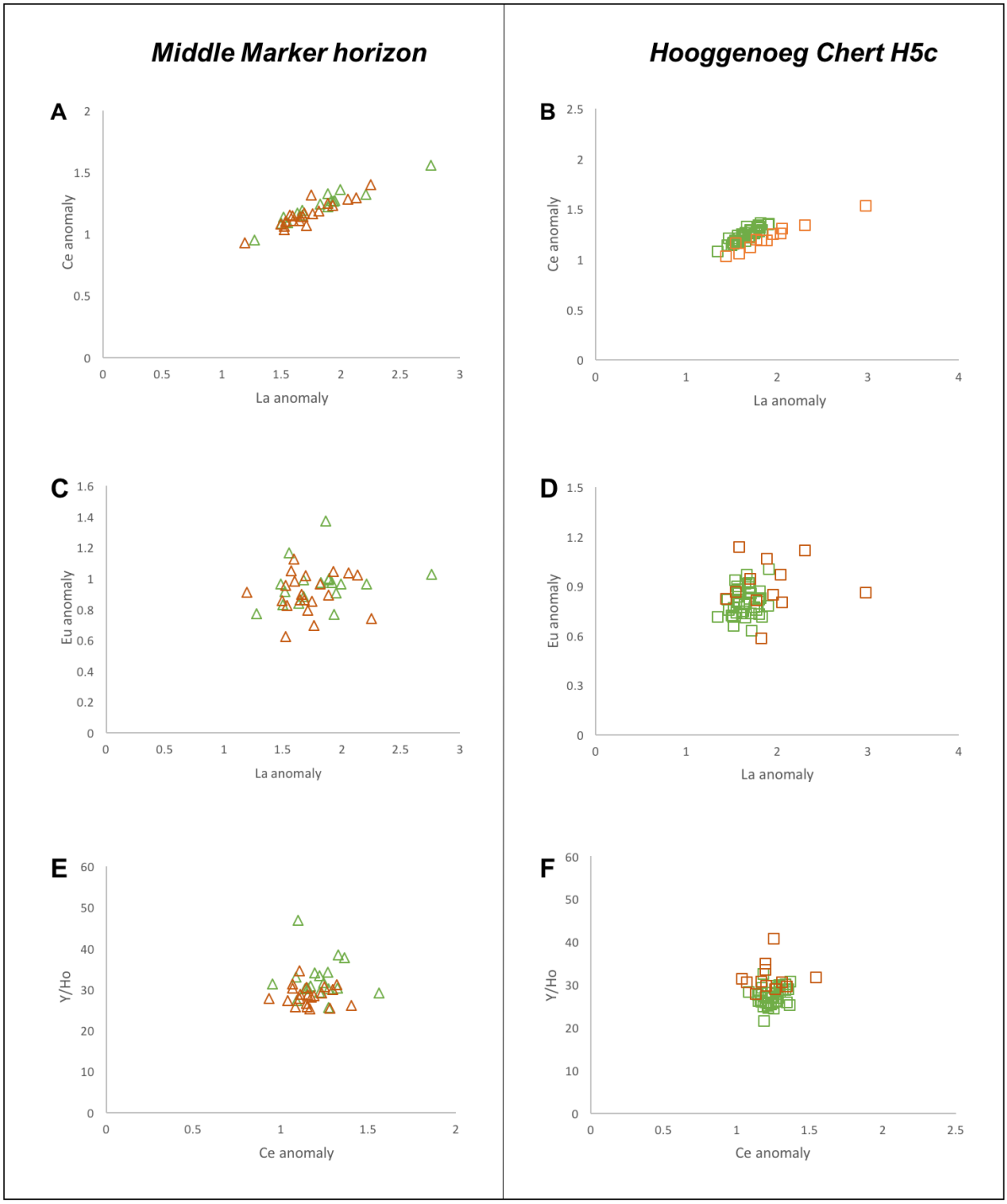

Fig. 7. Graphs of La versus Ce anomalies (La/La*$_{MUQ}$ versus Ce/Ce*$_{MUQ}$), La versus Eu anomalies (La/La*$_{MUQ}$ versus Eu/Eu*$_{MUQ}$), and Ce anomaly (Ce/Ce*$_{MUQ}$) versus Y/Ho ratio for Middle Marker horizon and Hooggenoeg Chert samples. Results used are from *in situ* LA ICP-MS analyses. Green symbols indicate microbial horizons; orange symbols indicate layers bearing no microbial fossils.

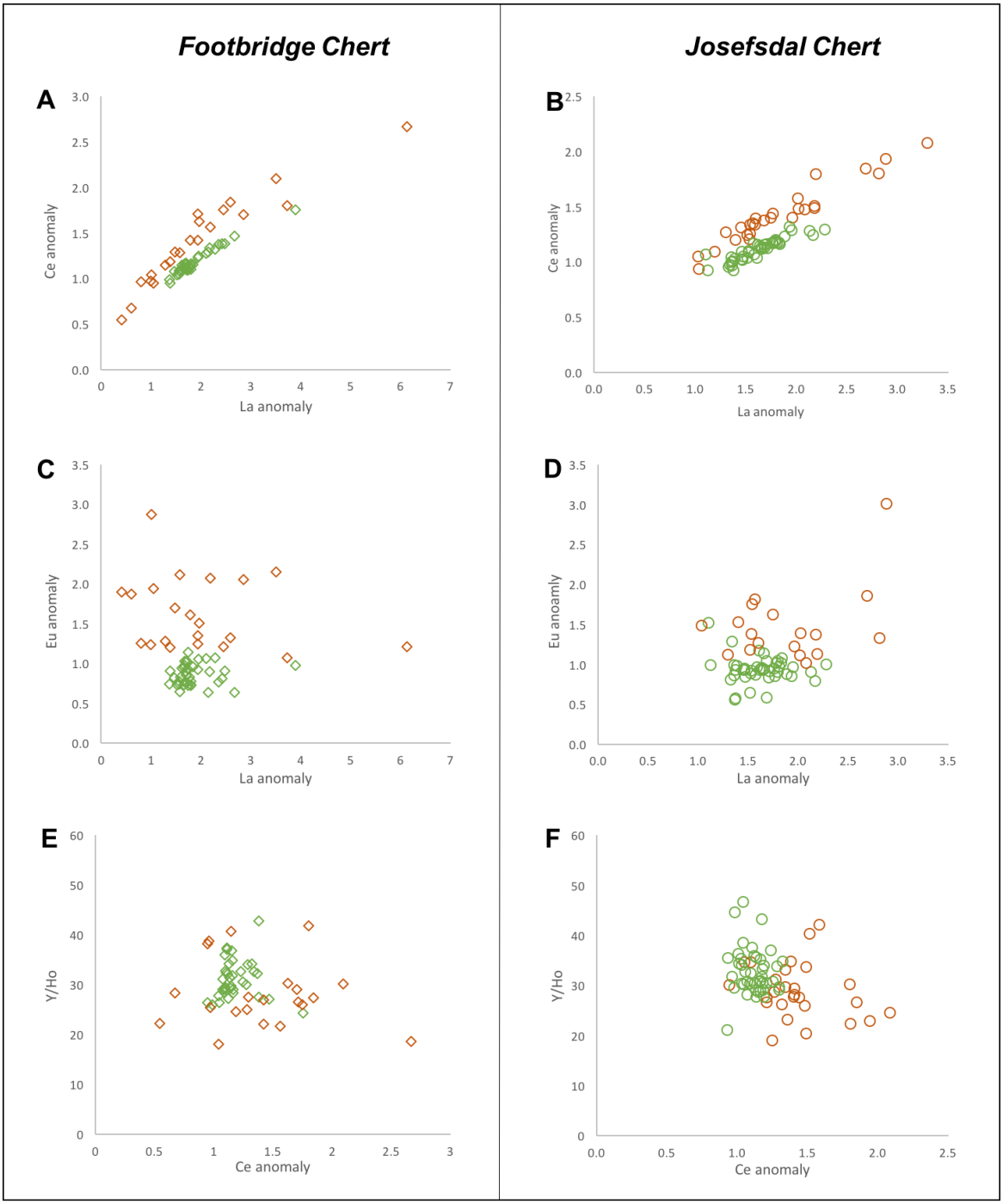

Fig. 8. Graphs of La versus Ce anomalies (La/La*$_{MUQ}$ versus Ce/Ce*$_{MUQ}$), La versus Eu anomalies (La/La*$_{MUQ}$ versus Eu/Eu*$_{MUQ}$), and Ce anomaly (Ce/Ce*$_{MUQ}$) versus Y/Ho ratio for Footbridge Chert and Josefsdal Chert samples. Results used are from *in situ* LA ICP-MS analyses. Green symbols indicate microbial horizons; orange symbols indicate layers bearing no microbial fossils.

3.2. Bulk ICP-OES and ICP-MS

Bulk ICP-OES shows that Middle Marker horizon cherts vary between 80.9% and 94.8% SiO_2 and contain relatively high Al_2O_3, Fe_2O_3, MgO and K_2O content; furthermore, one sample has high (5.26 wt%) CaO content (Fig. 9A), which is corroborated by XRD measurements estimating ≤ 9 wt% calcite (results not shown). Bulk ICP-MS of this sample (07SA23) demonstrates that trace elements are present in low concentrations relative to the

other studied cherts (Fig. 10). Cr and Mn are present at high concentrations, whereas Cd, Ta, Pb, Th and U are present in exceptionally low quantities (Fig. 10A, E).

In bulk sample (ICP-MS results), MUQ-normalised REE+Y characteristics show an enrichment of HREEs over LREEs: La anomalies are negative to negligible (La/La^*_{MUQ} = 0.74-1.09), Ce anomalies are weakly negative (Ce/Ce^*_{MUQ} = 0.81-1.07), Eu anomalies are weakly positive (Eu/Eu^*_{MUQ} = 0.98-1.46), and Y anomalies are generally negative (Y/Y^*_{MUQ} = 0.58-1.07) (Figs. 11A and 12, Table 2). Pr-Ce anomaly systematics indicate that the Ce/Ce^*_{MUQ} is often a 'true' anomaly (Fig. 6; *cf*. Bau and Dulski, 1996). Y/Ho values are sub-chondritic to super-chondritic, ranging between 17.7 and 29.3 (Table 2, Fig. 12).

Four samples of Hooggenoeg chert were studied by bulk ICP-OES and ICP-MS, which show two divergent chemical trends. 07SA28 and 01SA56 have relatively high concentrations of most major elements, whereas 01SA09 and 03SA16 contain considerably lower concentrations (Fig. 9B). SiO_2 ranges between 85.4% and 95.4%, however, 07SA28 is notably poor in SiO_2 (47.8%), having instead particularly high Al_2O_3, MgO and K_2O, reflecting volcanogenic input and/or limited silicification. 01SA56 is also rich in Al_2O_3, Fe_2O_3, MgO and TiO_2. ICP-MS bulk analyses show no clear trends in trace element composition between samples. The average composition of the Hooggenoeg Formation samples shows that they have significantly higher concentrations of many transition metals relative to the other cherts, including Fe, Co, Ni, Cu and Zn, and are also rich in Sc, Ti, As, Sr, Y and Ba (Fig. 10B, E).

In bulk sample (ICP-MS results), MUQ-normalised REE+Y characteristics show either typical seawater patterns of HREE > LREE (07SA28 and 03SA16), similar to Middle Marker cherts, or flatter patterns with MREE enrichment (01SA56 and 01SA09) (Fig. 6B). Eu anomalies are positive (1.23-2.19) (Figs. 11B, 12, Table 2). Other anomalies include weakly positive La/La^*_{MUQ} (0.89-1.22) and negligible Ce/Ce^*_{MUQ} (0.95-1.03, i.e. no 'true' anomaly; Fig. 12), and slightly negative Y/Y^*_{MUQ} (0.91-0.99). Y/Ho ratios are sub-chondritic (21.5-26.9; Table 2, Fig. 12).

Three representative bulk samples were chosen from the Footbridge Chert: samples 12SA49 and 12SA50 – two silicified shallow-water volcaniclastic sediments – contain higher Al_2O_3 and Fe_2O_3 than most other samples, but lower SiO_2 content (77.4-80.4%) (Fig. 9). 96SA02 – a silicified volcanic rock representative of the regional environment (*cf*. Lowe and Byerly, 1999) – comprises 96.0% SiO_2 and has high concentrations of Ni, Cu, As, Sn and W (Fig. 10C).

In bulk sample (ICP-MS results), MUQ-normalised REE+Y characteristics are quite different to most other samples (Fig. 11C). In samples 12SA49 and 12SA50, LREEs are strongly enriched relative to HREEs, and the absolute concentrations of REE+Y are very high. In the third sample, 96SA02, strong enrichment is present in MREEs. La/La^*_{MUQ}, Ce/Ce^*_{MUQ} and Y/Y^*_{MUQ} are negligible (respectively, 0.93-1.09, 0.98-1.00 and 0.93-1.02), however, Eu/Eu^*_{MUQ} is positive but not significant (1.13) in 96SA02 and 1.53-1.95 in the shallow-water laminated sediments (Fig. 12A-B, Table 2). The three samples are characterised by sub-chondritic Y/Ho values, which range from 23.6 to 25.8 (Table 2; Fig. 12).

The selected samples of Josefsdal Chert include intermixed volcanogenic and chemical sedimentary rocks, interpreted as hydrothermally influenced deposits, near-pure chert of proposed chemical precipitate origin, and shallow-water, laminated, organic carbon-bearing silicified volcanogenic sediments, in which microbial biofilms are preserved. All Josefsdal Chert samples have high SiO_2 contents between 85.5% and 99.9%. Other major and trace

elements are generally present at relatively low quantities in comparison to the other units studied herein, with the exception of Pb and Sb (Figs. 9D, 10D-E) No clear between-sample trends in trace elements exist.

Bulk REE+Y compositions (ICP-MS results) are characteristic of the mixing of marine and hydrothermal waters, but are enriched in LREE relative to other cherts (Fig. 11D): La/La^*_{MUQ} ranges from weakly negative to strongly positive (0.68-2.90), Ce/Ce^*_{MUQ} spans a range from very negative to weakly positive (0.14-1.15), Eu/Eu^*_{MUQ} is always positive (1.01-2.02), and Y/Y^*_{MUQ} is weakly to strongly positive (1.13-2.02) (Fig. 12, Table 2). Y/Ho ratios are weakly to strongly super-chondritic (29.1-51.5) in all samples (Fig. 12).

Mixing line diagrams show that these bulk samples generally indicate some contribution from hydrothermal activity: Eu/Sm versus Sm/Yb plots show that Middle Marker horizon samples indicate only 0.5-2% hydrothermal contribution, those of the Hooggenoeg H5 chert show 2-6% contribution, samples from the Footbridge Chert 3.5-5%, and those of the Josefsdal Chert 0.5-5% (though most Josefsdal Chert samples fall between 2-5%) (Fig. 12C). Y/Ho versus $(Pr/Nd)_{MUQ}$ diagrams, though qualitative, and for comparative use only, suggest that the influence of seawater was greater in the Josefsdal Chert and Middle Marker horizon than in the Hooggennoeg H5 chert and the Footbridge Chert samples (Fig. 12D). La and Eu anomalies fall within the regions of values delimited by previous analyses of fossiliferous sedimentary cherts (e.g. Sugahara et al., 2010), although La anomalies in our samples are generally somewhat lower.

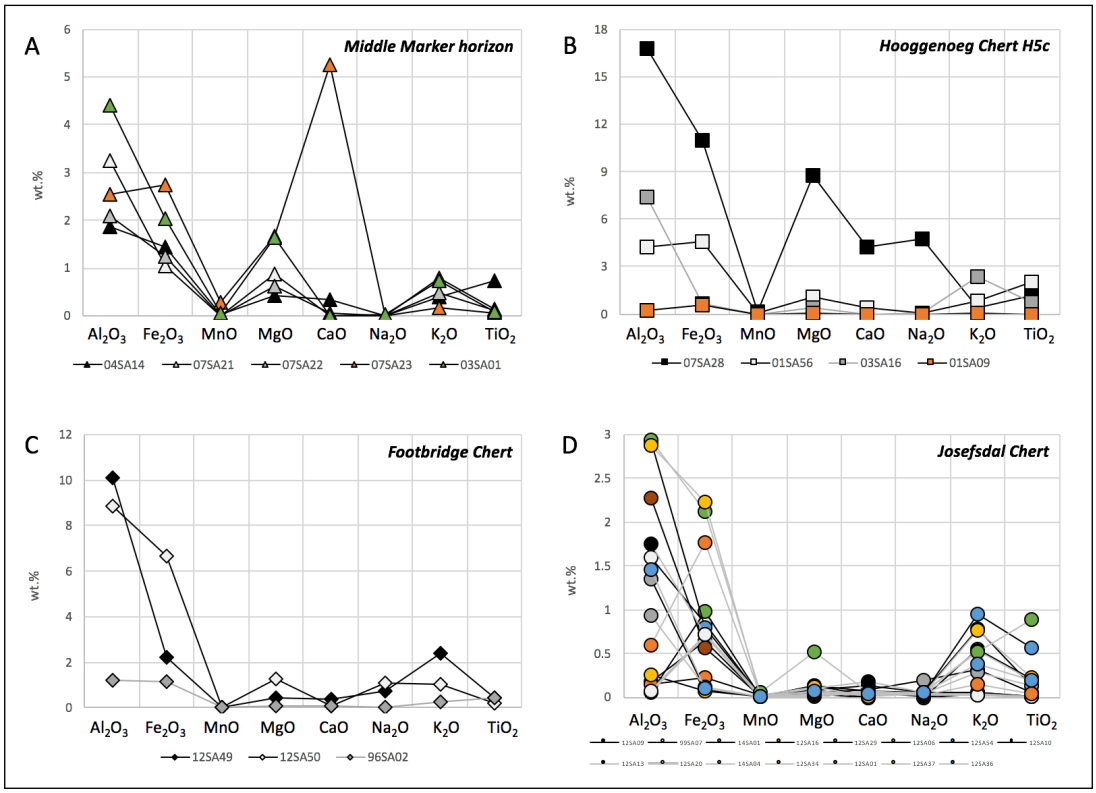

Fig. 9. ICP-OES analyses of major element concentrations in bulk samples. **A**) Middle Marker horizon. **B**) Hooggenoeg Chert H5c. **C**) Footbridge Chert. **D**) Josefsdal Chert. This colour coding is specific to bulk samples and used only for this figure and Fig. 10.

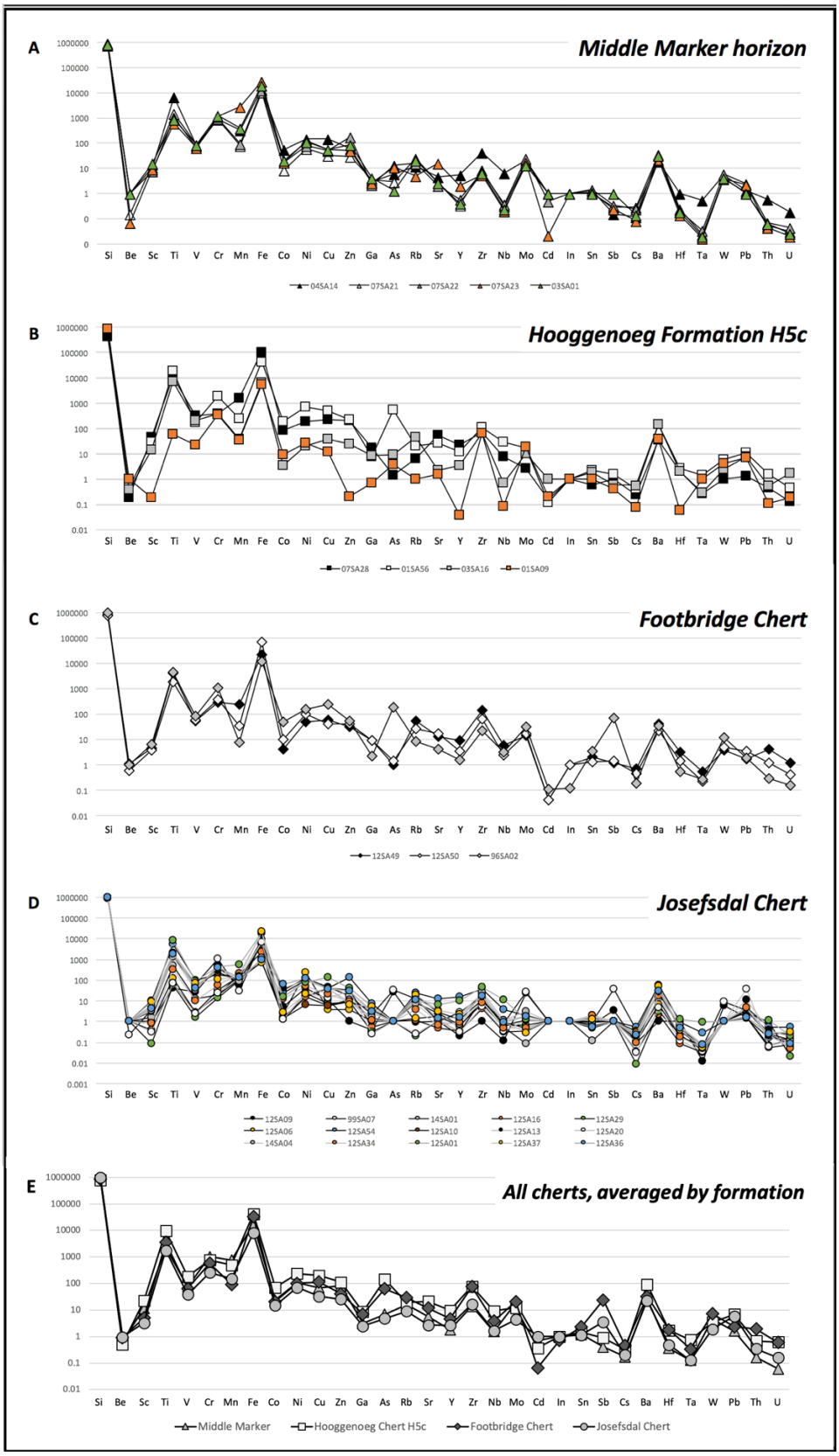

Fig. 10. Extended ICP-MS major and trace element compositions of samples. **A**) Middle Marker horizon. **B**) Hooggenoeg Chert H5c. **C**) Footbridge Chert. **D**) Josefsdal Chert. **E**) Averaged compositions from the four studied formations illustrating their similar chemical trends.

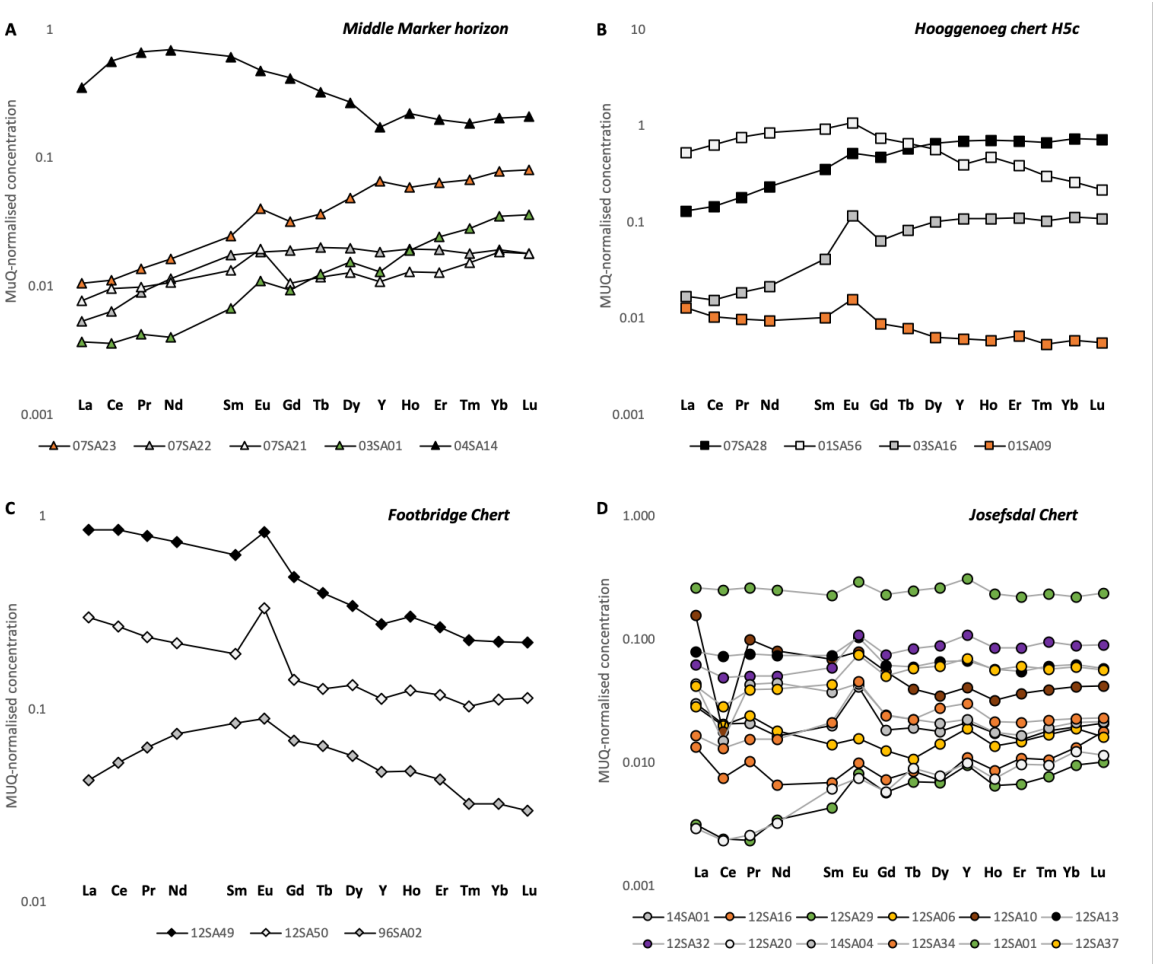

Fig. 11. MUQ-normalised bulk ICP-MS measurements of REE+Y in the four studied formations. **A**) Middle Marker horizon samples, exhibiting the typical pattern of Archaean hydrogenous sedimentation, with the exception of sample 04SA14, whose geochemistry may have been altered by post-diagenetic effects. **B**) Hooggenoeg Formation chert H5c samples: two samples (07SA28 and 03SA16) exhibit typical patterns of Archaean seawater, whereas another two (01SA56 and 01SA09) show inverse patterns in which LREE are enriched relative to HREE. **C**) Footbridge Chert samples: two samples, 12SA49 and 12SA50, show LREE enrichment over HREE with characteristics of Archaean seawater. Sample 96SA02 exhibits MREE enrichment superimposed on a similar trend. **D**) Josefsdal Chert samples, generally exhibiting the typical patterns of Archaean hydrogenous sedimentation with elevated LREE concentration.

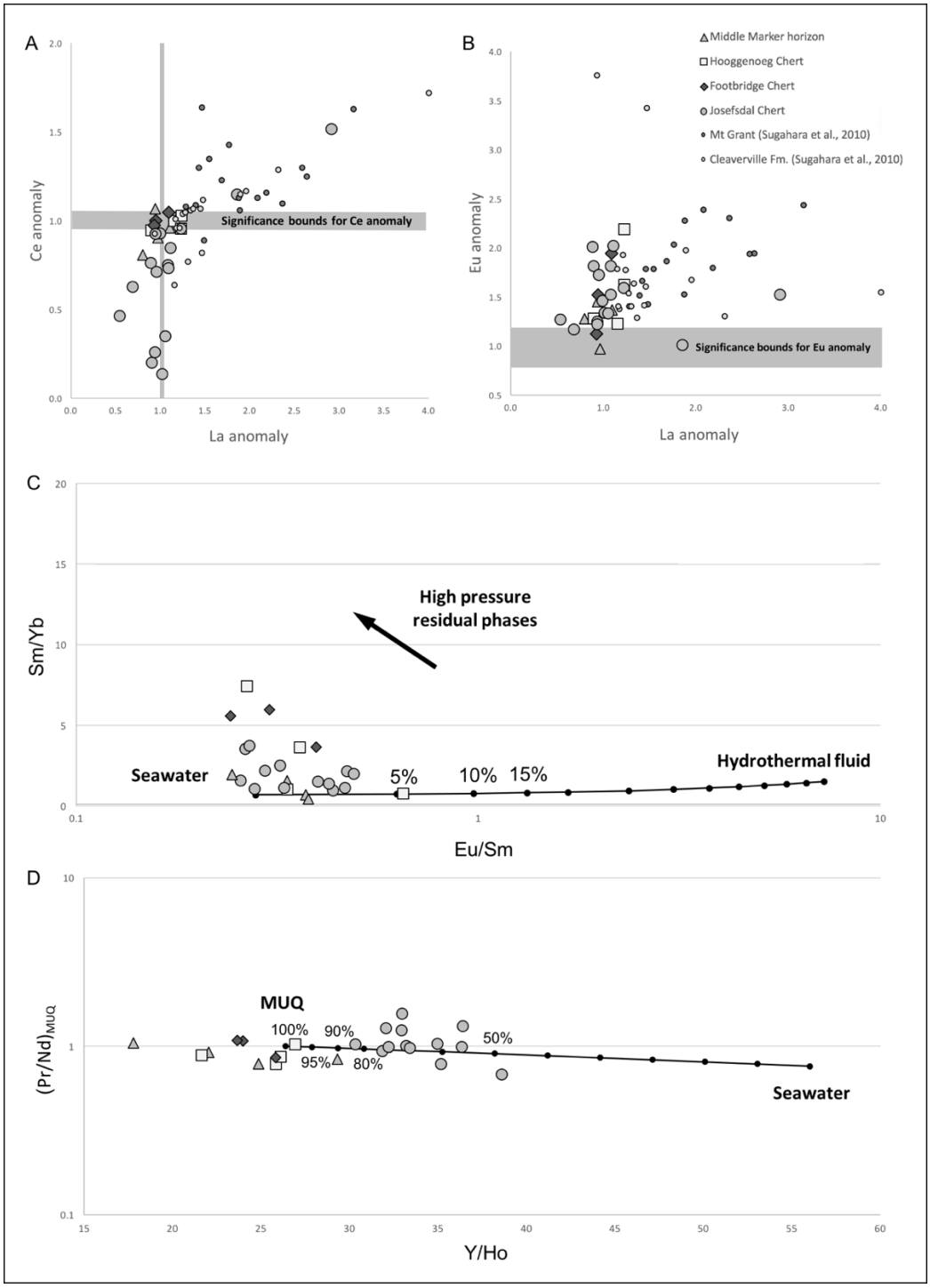

Fig 12. Results of bulk ICP-MS analyses compared, where relevant, to those of other fossiliferous, carbonaceous cherts (from Sugahara et al., 2010). **A**) La anomaly versus Ce anomaly. Vertical grey line denotes La/La^*_{MUQ} = 1, i.e. no significant La anomaly. Horizontal grey zone denotes the significance bounds of the Ce anomaly, i.e. Ce/Ce^*_{MUQ} between 0.95 and 1.05 are deemed not significant (after Bau and Dulski, 1996). **B**) La/La^*_{MUQ} versus Eu/Eu^*_{MUQ}, the former diagnostic of marine hydrogenous depositions, the latter denoting the contribution of hydrothermal fluids. Horizontal grey line denotes the significance bounds of the Eu anomaly, i.e. Eu/Eu^*_{MUQ} is only significant if greater than 1.2 (Kerrich et al., 2013). **C**) Eu/Sm versus Sm/Yb mixing line plot showing the quantitative contribution of hydrothermal fluid to each of the bulk samples analysed. **D**) Y/Ho versus $(Pr/Nd)_{MUQ}$ conservative mixing line plot qualitatively assessing the terrigenous (non-marine) influence on each of the bulk samples analysed. C-D are plotted after methods described in Gourcerol et al. (2016), outline in the main text.

3.3. *In situ* LA ICP-MS analyses

In Figures 13-14, coloured curves and symbols refer to microbial horizons, whereas black curves and symbols refer to non-microbial horizons. These results are superimposed upon both bulk ICP-MS analyses and one another in the diagrams such that comparison between the fossiliferous and non-fossiliferous horizons may be easily made.

In situ LA-ICP-MS analyses were conducted in three samples from the Middle Marker: two massive carbonaceous cherts (07SA22 and 07SA25) and one laminated, microbial mat-rich silicified volcaniclastic sandstone (07SA23) (Fig. 2A-B). A transect of point analyses was taken through a thick microbial mat set within 07SA23, and point analyses were acquired at multiple ROIs within massive cherts, which lack clear stratigraphy.

In 07SA23 (Fig. 13A, 15A, Table 3), La/La^*_{MUQ} and Ce/Ce^*_{MUQ} show a slightly increased average within the mats. Eu anomalies are weakly negative and similar throughout the transect: below (0.77-1.17), within (0.83-1.37) and above (0.84-0.97) the mats. Finally, Y anomalies, weakly positive throughout, are again higher within the mat-rich layer. Y/Ho values are consistently chondritic to super-chondritic, ranging between 25.7 and 34.2 below the mats, 29.2-46.8 within, and 30.2-31.7 above, ergo, elevated within the mat-rich laminations (Figs. 6, 15, Table 3). For samples 07SA22 and 07SA25 (Fig. 13B, Table 3), La, Y, and Ce anomalies are positive (La/La^*_{MUQ} = 1.19 and 2.25, Y/Y^*_{MUQ} = 1.04 and 1.23 and Ce/Ce^*_{MUQ} = 1.07 and 1.40), whereas Eu anomalies are generally slightly negative to negligible (0.70 and 1.12). Y/Ho ratios are chondritic to super-chondritic, lower than in the silicified laminated chert, ranging from 25.3-34.5 (Figs. 7, 15A, Table 3).

Eu/Sm versus Sm/Yb mixing line plots show that most points are close to the seawater end-member. Sample 07SA23, a laminated sandstone-siltstone with well-developed microbial fabrics, indicates up to 1-2% hydrothermal contribution (Fig. 14A, coloured triangles). Massive carbonaceous chert, by contrast, indicates negligible hydrothermal contribution (Fig. 14A, black triangles). Terrigenous contribution is high in all samples: 30-95% in laminated chert (Fig. 14B, coloured triangles) and 70-100% in massive carbonaceous chert (Fig. 14B, black triangles).

Two further samples of Hooggenoeg Chert H5c were studied by *in situ* LA ICP-MS (Fig. 13C-D, Table 3): 03SA15, which includes thick (~1 cm) sequences of silicified microbial mats, and 03SA04, silicified, shallow-water, carbon-rich sediments. Transects were taken throughout the mat sequences, whereas for 03SA04, analyses were performed at several ROIs throughout the sample (Fig. 2C-D).

For 03SA15 (Fig. 13C, 15B, Table 3), La/La^*_{MUQ} and Ce/Ce^*_{MUQ} are positive and broadly consistent throughout the transects, although La anomalies show a slight increase in the mat-rich layer. Eu/Eu^*_{MUQ} is weakly negative and broadly consistent throughout. Finally, Y/Y^*_{MUQ} markedly increases in the mat-rich layer. Y/Ho ratios are slightly elevated in the mat-bearing layer (Figs. 7, 15B, Table 3). In 03SA04 (Fig. 13D), La/La^*_{MUQ} = 1.43-2.98 (with three anomalous values of 16.01, 16.57 and 55.83), Ce/Ce^*_{MUQ} is 1.03-3.48 (with an anomalous value of 5.35), Eu/Eu^*_{MUQ} anomalies are variable and Y/Y^*_{MUQ} anomalies are weakly positive. Y/Ho ranges from 25.9 to 40.8 with all but one measurement yielding super-chondritic values (Fig. 6). In 03SA15, negligible hydrothermal contribution is suggested (Fig. 14C, coloured squares) but 78-100% terrigenous component (Fig. 14D, coloured squares), whereas for 03SA04, there is up to 2% contribution from hydrothermal fluids (Fig. 14C, black squares) and a terrigenous component of 50-90% (Fig. 14D, black squares).

In situ LA ICP-MS was performed on two further samples of shallow-water sediments from the Footbridge Chert. 03SA09 is a laminated black and white chert with copious microbial mat laminations, two of which were selected and analysed by transects (Figs. 2E). 03SA09' is a massive chert sourced from directly below 03SA09; the chert is nonetheless carbon-bearing, characterised by massive fabrics of clotted and disseminated carbonaceous material (Fig. 2F), and analyses were taken from ROIs throughout this sample. MUQ-normalised REE+Y patterns for the mat-bearing sample 03SA09 are very flat, indicating considerable terrigenous influence (Figs. 13E-F), whereas those of massive chert 03SA09' bear hallmarks of typical marine patterns (Fig. 13G).

For 03SA09 (Fig. 13E-F, 15C-D, Table 3), La/La^*_{MUQ} anomalies increase within one of the two studied mat-bearing horizons, but increase in chert above the second. Ce/Ce^*_{MUQ} also increases within one mat-bearing horizon. Eu/Eu^*_{MUQ} values are negative and consistent throughout the transects. Finally, Y/Y^*_{MUQ} anomalies also increase within one mat-bearing layer and Y/Ho ratios show a slight increase within the mat-bearing layers (Fig. 15C-D). Eu/Sm versus Sm/Yb diagrams estimate a negligible to 1% hydrothermal component (Fig. 14E), since almost all points plot to the left of the seawater end of the mixing curve. The estimated terrigenous component is between 45% and 100% (Fig. 14F). In 03SA09' (Fig. 13G), remarkably different characteristics in REE+Y patterns emerge. La/La^*_{MUQ} ranges from negative to strongly positive (0.41-6.13), Ce/Ce^*_{MUQ} is negative to positive (0.55-2.67), Eu/Eu^*_{MUQ} is weakly to strongly positive (1.21-2.87), and Y/Y^*_{MUQ} is weakly positive (0.83-1.47). Y/Ho values range from 18.1 to 41.8 (Fig. 8). In contrast to the mat-bearing sample, the quantitative estimate of hydrothermal input suggests a contribution of up to 8% (Fig. 14E), but the terrigenous contribution is similar, between 50-100% (Fig. 14F).

In situ LA ICP-MS was conducted on three further samples of Josefsdal Chert. 12SA18 and 12SA36 are two shallow-water sediments with well-developed microbial mat horizons, which were analysed, as for other mat-bearing samples, by transects bounded by chert layers (Fig. 2G). The third sample, 99SA07, is a clotted carbonaceous chert comprising irregularly shaped carbonaceous clots within a silica matrix. Analyses were conducted at multiple ROIs throughout the sample (Fig. 2H).

Within 12SA18 (Fig. 13H, 15E, Table 2), La/La^*_{MUQ}, Ce/Ce^*_{MUQ} and Eu/Eu^*_{MUQ} increase upward through the transect. Y anomalies are constant through the transect. Y/Ho ratios show a slight increase within the mat-bearing layer. Within 12SA36 (Fig. 13I, Table 3), La anomalies are 1.12-1.39 below, 1.34-1.92 within and 1.10-2.13 above the mat. Ce anomalies are 0.92-1.03 below, 0.93-1.32 within and 1.07-1.28 above the mat. Eu anomalies are 0.56-0.99 below, 0.58-1.29 within and 0.84-1.52 above the mat. Y anomalies are 0.96-1.19 below, 0.95-1.57 within and 1.08-1.29 above the mat. Evidently, average La/La^*_{MUQ} and Y/Y^*_{MUQ} increase within mat-bearing layers (Fig. 15E). Y/Ho ratios also increases to superchondritic values within the mat-bearing layer (Table 3, Figs. 8, 15E). In 99SA07, Eu anomalies are considerably elevated (Eu/Eu^*_{MUQ} = 1.12-3.01; Fig. 13J) Eu/Sm versus Sm/Yb plots for the mat-rich sediments (12SA18 and 12SA36) suggest up to 1% hydrothermal contribution (Fig. 14G), and Y/Ho versus Pr/Nd_{MUQ} diagrams indicate ~40-90% terrigenous contribution (Fig. 14H). 99SA07, by contrast, indicates up to 5% hydrothermal contribution (Fig. 14G) and 31-100% terrigenous influence (Fig. 14H).

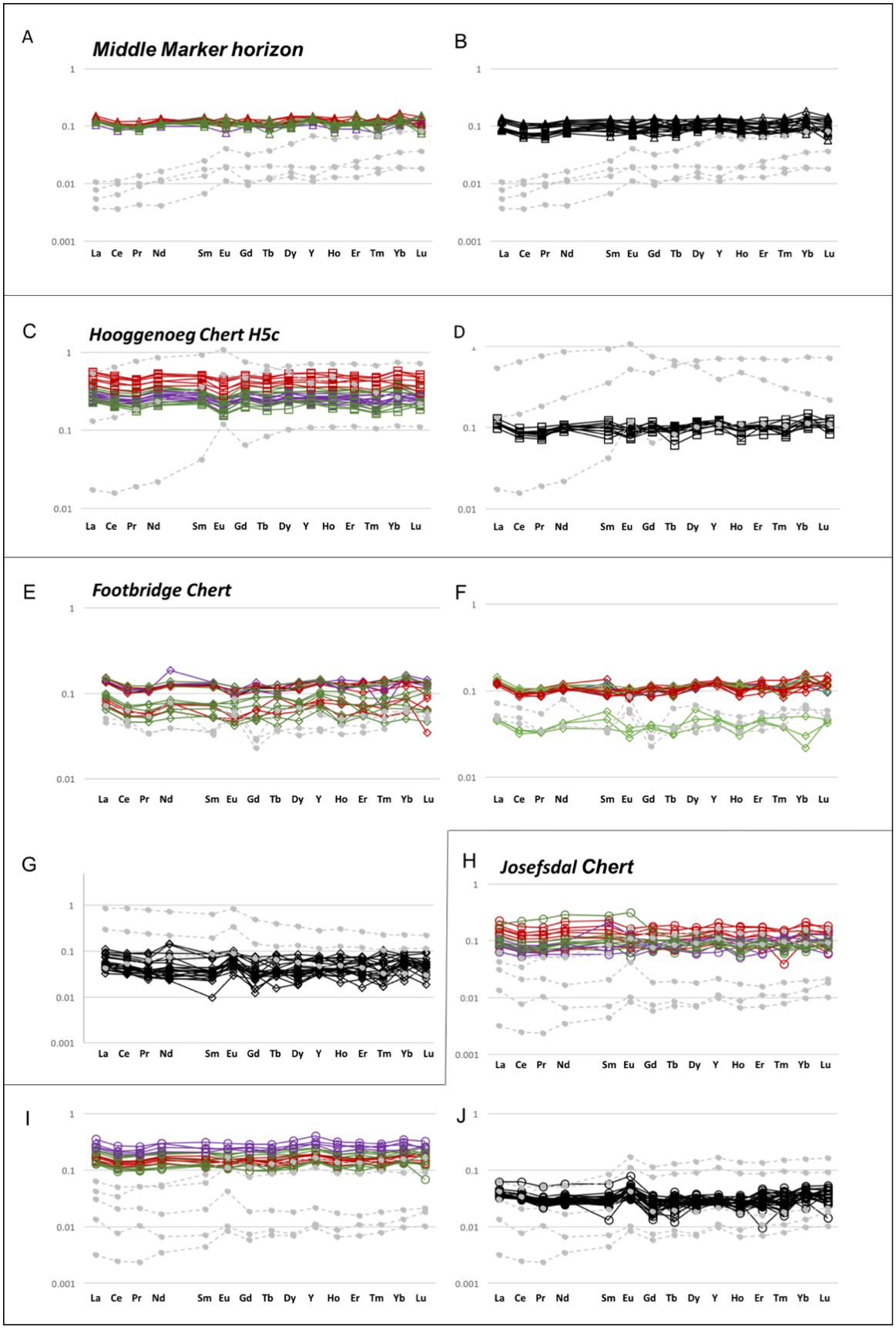

Fig. 13. *In situ* LA ICP-MS results (solid lines) compared with bulk ICP-MS (dashed grey lines, as shown in Fig. 11) showing the REE+Y composition of the studied cherts. Bulk ICP-MS results should be taken to represent prevailing local to regional palaeoenvironmental conditions, whereas *in situ* LA ICP-MS results indicate

palaeoenvironmental conditions specific to the short timescales during which microbial colonisation occurred (biome-scale palaeoenvironments from transect analyses). **A-B**) Middle Marker horizon; **C-D**) Hooggenoeg Formation chert H5c; **E-G**) Footbridge Chert; **H-J**) Josefsdal Chert. All microbial horizons show elevated REE+Y content, and particularly higher concentrations in LREEs. La and Y anomalies, together with mostly super-chondritic Y/Ho ratios, denote the influence of seawater throughout the deposition of all units. Transects taken through microbial horizons in all cherts (i.e., A, C, E-F, H-I) show a flatter pattern often with negative Eu anomalies, suggesting elevated terrigenous influence and reduced hydrothermal influence. E-F show LA ICP-MS results from G as dotted grey lines to emphasise the pronounced Eu anomaly, which is absent in microbial horizons. G uses bulk results from the Footbridge Chert as dotted grey lines. Coloured lines represent series of analyses in microbial horizons: red lines indicate analyses taken immediately below, green lines analyses within, and purple lines analyses immediately above microbial horizons. Black lines represent non-microbial horizons.

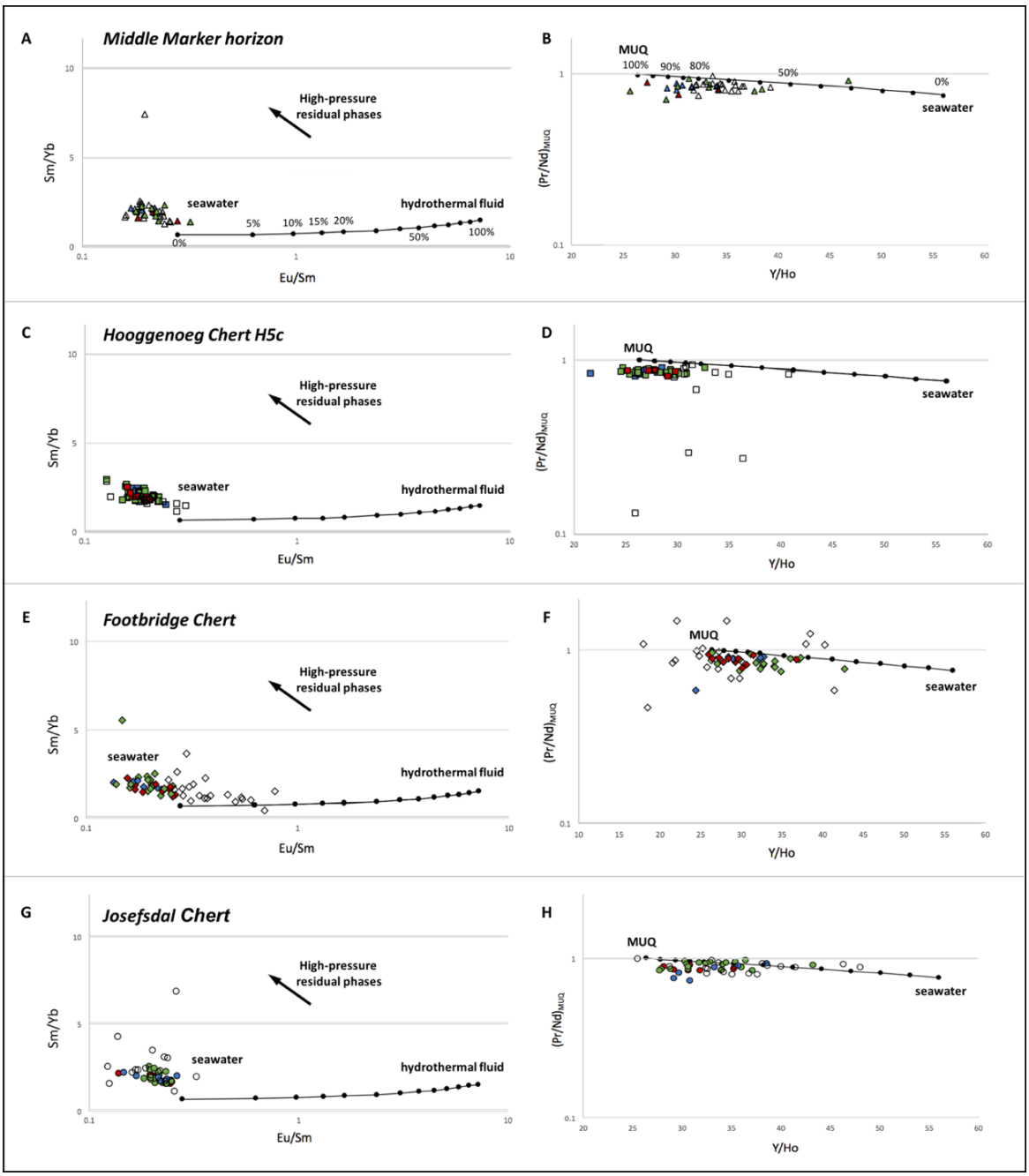

Fig. 14. *In situ* LA ICP-MS data plotted against mixing lines of hydrothermal fluid to seawater and seawater to MUQ-type terrigenous input, identical to those shown for bulk samples in Figure 9. **A-B**) Middle Marker horizon;

C-D) Hooggenoeg Chert H5c; **E-F**) Footbridge Chert; **G-H**) Josefsdal Chert. **A, C, E, G**) Eu/Sm versus Sm/Yb diagrams quantitatively assess hydrothermal input. Points lying far above this mixing line (as with points of Sm/Yb > 5 in A and G) have incorporated high-pressure residual metamorphic phases, which overprint the original geochemical signatures. Coloured circles represent series of analyses taken in microbial transects, unfilled circles represent analyses taken in non-microbial horizons. Most microbial horizons record minor hydrothermal influence (up to 2%), whereas non-microbial horizons show elevated hydrothermal influence (up to 8%). In all cases, analyses taken in non-microbial horizons plot further to the right on the Eu/Sm versus Sm/Yb mixing line due to higher contributions from hydrothermal fluids. **B, D, F, H**) Y/Ho versus Pr/Sm_{MUQ} plotted on a qualitative, conservative mixing line between seawater and an idealised terrigenous input. Samples lying on or below this mixing line reflect the combined influenced of marine, terrigenous and hydrothermal fluid inputs, and samples which do not reach 100% terrigenous influence may be considered "relatively less influenced" by terrigenous inputs (Gourcerol et al., 2016). Most samples are clustered around 60-100% MUQ, which is compelling evidence for deposition in palaeoenvironments strongly influenced by terrigneous inputs. Red symbols indicate analyses taken below, green symbols analyses within, and blue symbols analyses above microbial horizons. Unfilled symbols are analyses conducted in non-microbial horizons.

3.4. 'Biome'-scale analyses: a summary of transect results from i*n situ* LA ICP-MS

In order to assess micro-scale changes in REE+Y composition during microbial colonisation – and therefore the geochemical environment of Palaeoarchaean biomes – transects were taken through carbonaceous laminations representing microbial mats (Fig. 15; Table 3), which were rapidly fossilised during the timescale of their life cycle. These results should enable us to trace variability in REE+Y composition on timescales relevant to the growth of microbial communities. These transect results indicate: i) the specific fluid chemistries of the immediate environment encouraging the development of microbial ecosystems; and ii) whether rhythmic alternation between the microbial horizons and the surrounding cherts unveils cyclic palaeoenvironmental phenomena accompanying microbial horizons. As shown in Figure 15, the results are similar across several millimetres within the four cherts studied:

- Y/Ho ratios increase from generally chondritic (~15-30) below the mat-bearing horizons to superchondritic values within (~25-50), before decreasing to chondritic values above the microbial mats;
- La and Y anomalies are generally more positive within mat-bearing horizons;
- Ce anomalies usually increase within the mat bearing horizons, and may decrease above the horizons;
- Eu anomalies are generally consistently negative throughout microbial horizons, in contrast to the bulk analyses; unlike the other anomalies, they do not change within microbial laminations.

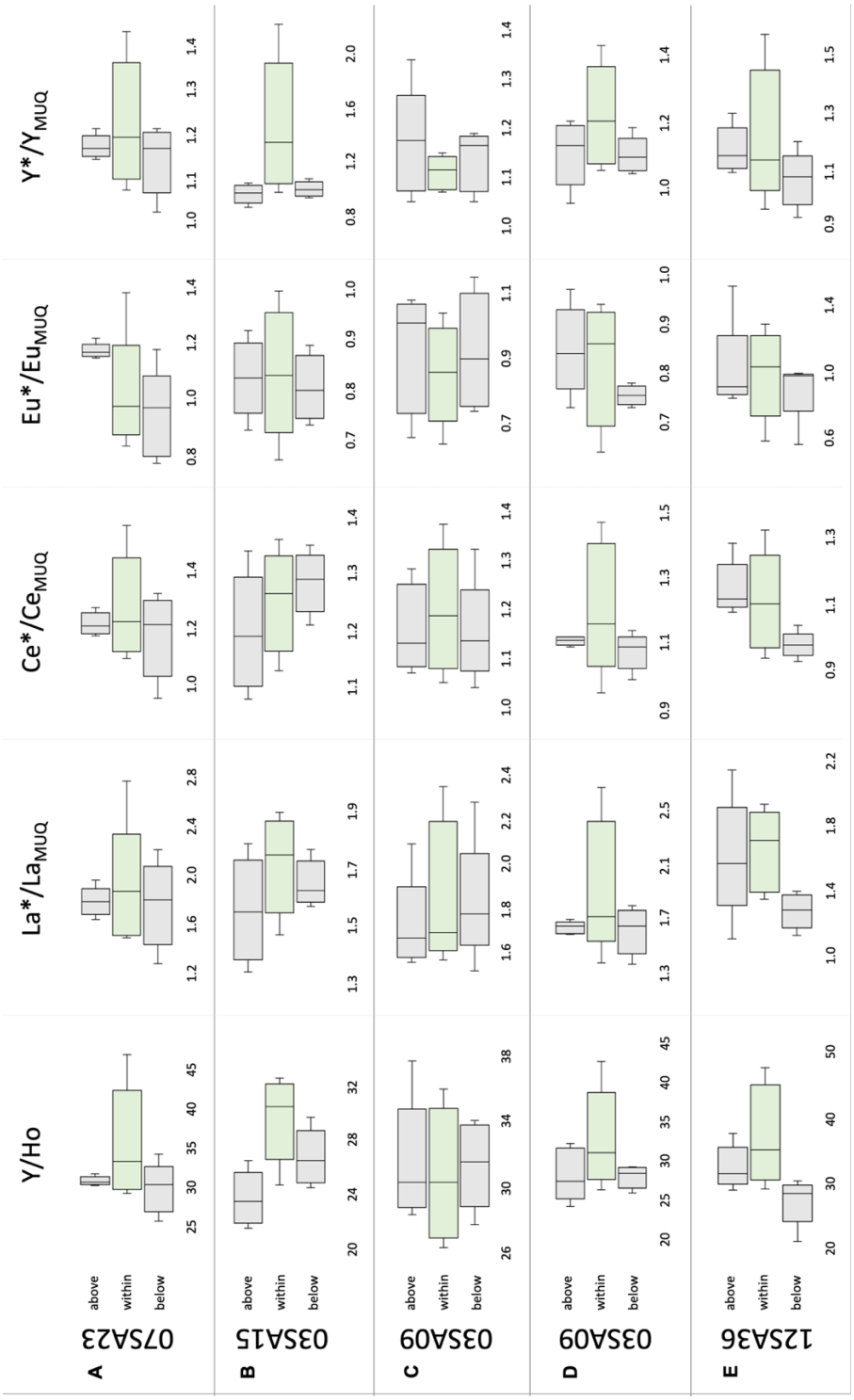

Fig. 15. Representative *in situ* LA ICP-MS transect analyses of microbial horizons from the studied samples: **A-B**) Hooggenoeg Formation, **C-D**) Kromberg Formation. For each sample, LA ICP-MS point analyses were conducted below, within and above the microbial horizons, indicated by the red circled areas. At the left of each image, green bars denote the petrographic basis on which areas of analysis were defined as 'within' the microbial mats. For each of the transects, the changes in Y/Ho ratio and La, Ce, Eu and Y anomalies (La/La*$_{MUQ}$, Ce/Ce*$_{MUQ}$, Eu/Eu*$_{MUQ}$ and Y/Y*$_{MUQ}$) are shown as minima (leftmost point), maxima (rightmost point) and averages (line) below, within and above the microbial mat-bearing horizons. Y/Ho ratio, La and Y anomalies generally increase within microbial horizons, whereas Ce anomalies sometimes increase, and Eu anomalies show no significant change.

4. Discussion

4.1. Palaeoarchaean regional habitats

The biosphere is defined as the habitable realm, and contains a diversity of biomes, which in turn contain a certain number of ecosystems. In this section, we will parameterise the palaeoenvironmental conditions in which the biomes preserved in the four studied cherts developed. REE+Y patterns of all bulk chert samples (ICP-MS results) indicate a complex redox scenario: the regional environment of widespread, shallow-water, Palaeoarchaean microbial mats was characterised by hydrogenous sedimentary deposition with clear influence from non-marine sources, e.g. hydrothermal fluids, and terrigenous input (Figs. 11-12). In the Palaeoarchaean, terrigenous input would have been mostly derived from volcanogenic landmasses (Fig. 16). This resembles, to some extent, the modern scenario wherein most primary biological productivity is spatially correlated with continental runoff (Jeandel and Oelkers, 2015) containing 10-1,000 times the REE+Y concentration of typical seawater (Elderfield et al., 1990; Alibo and Nozaki, 1999).

With the exception of the Footbridge Chert, the MUQ-normalised patterns of bulk samples show HREE enrichment relative to LREE (Fig. 11), reflecting the differential dissolution of REE+Y into marine water as a function of ionic radii, surface and solution complexation stabilities, and oxidation onto oxyhydroxide particle surfaces (Bau, 1999; Allwood et al., 2010). The Footbridge Chert samples show negative slopes in MUQ-normalised REE+Y plots. Kamber et al. (2004) previously reported LREEs > HREEs in stromatolitic carbonate from the 2.8 Ga Mushandike Limestone of Zimbabwe, inferring the erosion of very local sources (i.e., a strong continental input) and precipitation in a basin completely restricted from the open ocean. The MREE enrichment seen in 96SA02 along with increased V, Cr, Ni, Cu, As, Sn and W content (and therefore low Y/Ni and higher Cr/V; Fig. 16), suggests increased volcanogenic influence, likely from a dominantly komatiitic precursor (Hanor and Duchac, 1990; Nisbet and Fowler, 1999; Lowe and Byerly, 1999). We interpret these horizons of the Footbridge Chert as deposited in a comparable highly restricted basin setting, subjected to subaerial volcanogenic input from komatiitic volcanism and with very limited, if any, exchange with the open ocean.

In all other samples, despite their consistent enrichment in HREE relative to LREE, La/La^*_{MUQ}, Ce/Ce^*_{MUQ} and Y/Y^*_{MUQ}, which generally indicate hydrogenous sedimentation, are often suppressed or negligible in bulk measurements. This is consistent with deposition in semi-restricted conditions (Bau, 1999; Bolhar et al., 2015; Gourcerol et al., 2016), where continental inputs with high REE+Y concentrations dilute the strength of anomalies. Notwithstanding, HREE enrichment (low $(Pr/Yb)_{MUQ}$), together with frequently positive La/La^*_{MUQ} and Y/Y^*_{MUQ}, indicate marine influence. Our measured bulk REE+Y geochemistry indicates that numerous fossiliferous cherts from throughout 150 Ma of the Palaeoarchaean of South Africa show evidence for deposition in restricted basins with variable marine influence resulting from periodic connection with the open ocean.

Eu/Eu^*_{MUQ} in bulk ICP-MS measurements from the four studied horizons is almost always positive (Figs. 11, 12B; Table 2). Customarily, positive Eu anomalies are ascribed to the influx of hydrothermal fluids, which are otherwise devoid of LREE or HREE enrichment and/or other hydrogenous anomalies (Danielson et al., 1992; Bau and Dulski, 1996; Allwood et al., 2010; Gourcerol et al., 2015). The high REE+Y content of hydrothermal fluids relative

to seawater (Klinkhammer et al., 1994; Wheat et al., 2002; Tostevin et al., 2016) implies that hydrothermal (and riverine) fluid inputs would, as with basin restriction, mathematically reduce hydrogenous anomalies, accounting for reduced La/La^*_{MUQ}, Ce/Ce^*_{MUQ} and Y/Y^*_{MUQ} in Archaean seawater relative to modern seawater, in which hydrothermal contributions are comparatively minor. The positive Eu/Eu^*_{MUQ} in bulk analyses (greater than 1.2 *cf*. Kerrich et al., 2013) therefore testify to the regional significance of hydrothermal influence in Archaean habitable environments, which is likely a result of the increased Eu content in Archaean seawater on a global scale (Danielson, 1992; Sugahara et al., 2010; Allwood et al., 2010). Differences in Eu/Eu^*_{MUQ} between the Middle Marker sediments (up to 1.46) and those of the Hooggenoeg, Footbridge and Josefsdal cherts (up to 2.19, 1.95 and 2.02, respectively) may indicate either the relative influence of hydrothermal fluid or its temperature, i.e., a lesser quantity and/or lower temperature hydrothermal fluids may have influenced the Middle Marker horizon, and greater quantity and/or higher-temperature fluids the other studied units.

Chondritic Y/Ho values together with positive Eu/Eu^*_{MUQ} and low La/La^*_{MUQ} and Y/Y^*_{MUQ} in the Middle Marker horizon, Hooggenoeg Chert H5c and Footbridge Chert (Figs. 6, 12) denote that precipitation on the regional scale was strongly influenced by non-marine inputs; due to the positive Eu/Eu^*_{MUQ}, this is seemingly most parsimoniously explained as fluids of hydrothermal origin (*cf*. Bolhar et al., 2005). Nonetheless, the relative flatness of some patterns (i.e. high LREE concentrations) suggests significant terrigenous input (Hoyle et al., 1984; Elderfield et al., 1990; Bolhar and Van Kranendonk, 2007). As indicated above, although the Josefsdal Chert shows superchondritic Y/Ho ratios, i.e., marine input, the consistently high concentrations of LREE are nonetheless testament to strong terrigenous input. Of the four studied cherts, we suggest that the fossiliferous lithofacies of the Josefsdal Chert were relatively most influenced by interaction with the open ocean. Previous trace and REE palaeoenvironmental reconstructions from Archaean cherts have found little evidence for such strong terrigenous influence before the Mesoarchaean (3.0-2.9 Ga), the most ancient examples of similar environmental setting being those from the Pongola Supergroup (Bolhar et al., 2015) and Mount Goldsworthy greenstone belt (Sugahara et al., 2010). Our findings are thus inconsistent with the prevailing view of exposed Archaean landmasses as very minor volcanic islands (see references in Section 1.1.), and suggest that volumetrically significant, exposed (proto-)continents were already developing during the Palaeoarchaean. The initiation of continent building may have commenced during the Palaeoarchaean (e.g. Cawood et al., 2018), and these less fractionated REE+Y patterns appear to be a testament and support for such early development of subaerial landmasses.

In terms of geomorphology, the regional-scale environments of deposition of these four cherts were therefore semi-restricted water bodies with variable marine influence at the margins of emergent volcanic landmasses, a schematic of which is presented in Figure 17. These epicontinental basins evidence inputs from seawater (plus hydrothermal fluids), shown by their REE+Y patterns (Fig. 11) and their position on Eu/Sm versus Sm/Yb mixing lines (Fig. 12C). Further strong influences from continental, volcanogenic, terrigenous material are evident both from high trace and REE contents (Figs. 10-11) and their position on $(Pr/Nd)_{MUQ}$ versus Y/Ho mixing lines (Fig. 12D). Previous field and petrographic evidence, showing copious sedimentary evidence for shallow-water deposition in shoreface and tidal shelf settings has indicated a coastal environmental setting for these cherts (Lanier and Lowe, 1982; Lowe and Byerly, 1999; Hofmann, 2011; Westall et al., 2015; Hickman-Lewis et al., 2018a). Despite

this, the true importance of continental inputs has been hitherto unrecognised. Although REE+Y enriched hydrothermal inputs certainly influenced marine realms on the early Earth (Danielson et al., 1992; Nisbet and Sleep, 2001; Hofmann and Bolhar, 2007; Hofmann, 2011), our findings of suppressed La, Eu and Y anomalies, together with the flat, LREE-enriched normalised REE+Y patterns characterising all studied microbial horizons is consistent only with REE+Y inheritance from continental outflow into basins with variably restricted communication with the open ocean. The chemistry of the source rocks may be estimated for these metasediments by separating the trace elements enriched in ultramafic, felsic and intermediate calc-alkaline, and mixed volcanic sources (Fig. 16). Plotting Y/Ni against Cr/V determined by bulk ICP-MS shows that all bulk samples plot clearly within the ultramafic field (Fig. 16) and thus the majority composition of the continental landmass in each case was mafic-komatiitic.

In restricted environments, pH may be estimated from Ce/Ce^*_{MUQ}: when pH > 5, REE+Y patterns exhibit negative Ce/Ce^*_{MUQ}, whereas at pH < 5, a positive Ce/Ce^*_{MUQ} is generated (for complete rationale, see Bau, 1999; Gourcerol et al., 2016). Although most samples show no 'true' Ce/Ce^*_{MUQ} (falling within Zone I of the Pr-Ce anomaly diagram of Bau and Dulski, 1996; Fig. 6), several samples of the Josefsdal Chert and Middle Marker horizon exhibit anomalies. Negative Ce/Ce^*_{MUQ} values in the Middle Marker horizon suggest that the unit deposited in an environment with pH ≥ 5. In the Josefsdal Chert, both alkaline and strongly acidic pH values are indicated, i.e. the ambient pH fluctuated, perhaps due to the presence of alteration-prone volcanic glass in mildly acidic shallow waters. Hofmann and Bolhar (2007) and Hofmann and Harris (2008) demonstrated that hydrothermal cycling commonly occurs through volcanic sequences beneath sedimentary horizons. The interaction of these fluids with overlying acidic Palaeoarchaean seawater could have contributed to these fluctuating redox states (Shibuya et al., 2010). Ce anomalies are insignificant in both the Hooggenoeg Chert H5c and the Footbridge Chert, suggesting either that the pH is indeterminable from the studied samples, or that the pH was around 5, which is consistent with some estimates of Archaean ocean pH (e.g. Pinti, 2005).

4.2. Characterisation of biomes preserved in Barberton cherts

Complementary analyses at centimetric to sub-millimetric scales allow the reconstruction of regional- and biome-scale geochemical landscapes (Fig. 1). Through a combination of i) bulk ICP-MS analyses, quantifying the 'regional' or 'local'-scale redox landscape (Figs. 9-12, 16), and ii) *in situ* LA ICP-MS analyses quantifying the fluid chemistry of individual microbial horizons (Figs. 13-16), one can distinguish differences between the prevailing conditions in the microbial palaeoenvironment (the biome, this section) and the wider redox landscape (the habitat; Section 4.1.). We demonstrated above that the regional environments of all four studied fossiliferous cherts were epicontinental basins with variable restriction from the open ocean, bearing some similarity to previous findings in Mesoarchaean and Neoarchaean cherts, where continental inputs are generally more significant (e.g. Grassineau et al., 2002; Kamber et al., 2004; Bolhar and Van Kranendonk, 2007; Suguhara et al., 2010; Bolhar et al., 2015). In this section, we discuss exclusively the characteristics of Palaeoarchaean microbial biomes within these basins, as determined using transect LA ICP-MS analyses through fossiliferous horizons (according to the schematic in Fig. 1).

In all studied suites of fossiliferous samples, notably flatter REE+Y patterns in microbial horizons compared with the background signal (Fig. 13) indicate that Palaeoarchaean photosynthetic biomass flourished where significant inputs from exposed continental landmasses influenced the habitat (higher concentrations of LREE relative to hydrogenous deposition; Hoyle et al., 1984; Elderfield et al., 1990; Bolhar and Van Kranendonk, 2007). Both the REE+Y patterns of LA ICP-MS data and plots of this data against Eu/Sm versus Sm/Yb and Y/Ho versus Pr/Nd_{MUQ} mixing lines suggest that all habitats and most biomes were influenced by seawater, terrigenous inputs and hydrothermal fluids (Figs. 13-14). The higher absolute concentration of REE+Y and the almost complete suppression of visual anomalies in REE+Y patterns (Fig. 13) is consistent with riverine aqueous chemistries dominating these inputs. Y/Ho versus Pr/Nd_{MUQ} diagrams show significant terrigenous contributions in the four studied units (Fig. 14) compared to, for example, Precambrian banded iron formations (Gourcerol et al., 2016) or microbial carbonates (Van Kranendonk et al., 2003; Allwood et al., 2010). Y/Ho ratios vary from sub-chondritic to superchondritic in the four cherts, suggesting lesser seawater influence than in both the open oceans and the silicification zones underlying most banded cherts (Hofmann and Bolhar, 2007; Hofmann and Harris, 2008). Eu/Sm versus Sm/Yb mixing line calculations quantitatively estimate that, while microbial biomes themselves show low (negligible to 2%) hydrothermal contribution, the local environment (habitat; Section 4.1.) was comparably more influenced (up to 8%). Therefore, widespread, presumably photosynthetic, microbial mats flourished during periods of decreased hydrothermal input, correlating with decreased volcanism and increased local erosion of terrigenous material. This mirrors the biogeochemical control exerted by continental outflow on modern-day primary productivity (Jeandel and Oelkers, 2015). All four studied horizons are essentially volcanogenic (Lanier and Lowe, 1982; Walsh, 1992; Lowe, 1999; Lowe and Byerly et al., 1999; Westall et al., 2015) and, thus, an ever-evolving interplay between sedimentation, ocean chemistry and microbiology suggests that widespread epibenthic Palaeoarchaean biomes occupied a delicate and complex aqueous biogeochemical niche driven by fluid inputs (Fig. 14), chemical inheritance from the substrate (Fig. 16) and physical constraints resulting from volcanogenic sedimentation (Fig. 17).

The influx of detrital substrate seems to have been mineralogically diverse during periods of microbial colonisation, with increased mixed and felsic contributions relative to the ultramafic bulk signature (Fig. 16). Whereas non-microbial horizons and all bulk samples plot within the ultramafic region of the Y/Ni versus Cr/V plot, microbial horizons plot dominantly within the mixed sources region. Such correlation between the flourishing of microbial life and the evolved or fractionated nature of the substrate suggests a link between lithological diversity and the enhanced productivity of primary biomass. This underlines the importance of small emerged landmasses – of greater lithological and mineralogical diversity than oceanic crust due to subaerial weathering – as loci of well-developed microbial communities. We propose that this is a consequence of both the wide range of bio-utile elements provided by mixed igneous source rocks, and the disequilibrium conditions present in basins characterised by a confluence of mixed fluid inputs.

Although the LA ICP-MS patterns appear flat, they retain, particularly within microbial horizons, the superchondritic Y/Ho ratios and weak anomaly characteristics of seawater, which are marginally strengthened in layers of biomass (Fig. 16). Although oxyhydroxides, which are enriched within microbial layers, have enhanced sensitivity to Ho over Y, the chondritic/sub-

chondritic Y/Ho ratios expected in microbial mats (Censi et al., 2013) are not observed in our mat transect analyses. As highlighted in the methods (Section 2.2.2.), we analysed only chert within fossiliferous horizons, and not the organic material itself, since, according to Freslon et al. (2014), biogeochemical reactions, and not the geochemistry of the source fluid reservoir, may dominate the REE+Y signature of organic material-rich rocks. Despite this, the fossiliferous nature of these sediments necessitates that we consider REE+Y binding by organic material as a control of REE+Y compositions observed by LA ICP-MS. Distinct signals are associated with REE binding by organic material: Takahashi et al. (2005) found that MREE and especially HREE were preferentially scavenged by organic material in both living and fossil microbial mat material, such that Tm, Yb and Lu are significantly enriched relative to other elements, with a complementary distinct convex trend resulting from MREE enrichment. Censi et al. (2013) and Freslon et al. (2014) conducted similar studies and found that the MREE enrichment was common in organic material from many settings. Since our LA ICP-MS analyses were conducted in chert intercalations within and around microbial mats, and since we do not observe any of the MREE and HREE enrichments viewed invariably in the studies cited above, our analyses are demonstrably free from the influence of scavenging by organic matter. Consequently, both the bulk ICP-MS and *in situ* LA ICP-MS measurements reflect exclusively the aqueous chemistry of the depositional fluids present at the time of microbial mat growth.

The small-scale variations observed through the transects are thus primary compositional fluctuations and show that periodic seawater recharge of the basin drove the microbial colonisation of nutrient-rich, mineralogically diverse substrates. The fluctuating magnitude of anomalies together with the microstratigraphic delimitation of microbial mats underscores the semi-restricted nature of the basins (Fig. 17). The recurrence of trends in increasing Y/Ho, La^*/La_{MUQ} and Y^*/Y_{MUQ} through microbial mat transects in the four studied units (Fig. 15; Table 3) is consistent with microbial ecosystems developing in response to local environmental disequilibrium between the reservoirs feeding the basin: hydrothermally influenced marine influx and terrigenous outflow.

The negative Eu/Eu^*_{MUQ} in transect analyses may partly result from inner sphere MREE binding onto carboxylate and phosphate sites in microbial cellular and extracellular material (Censi et al., 2013) of autochthonous and allochthonous origins, for example relict biogenic detritus, rip-up and roll-up mat fragments, EPS and other macromolecular carbon. This is, however, inconsistent with the lack of evidence for any other interaction between organic materials and REE. Gao and Wedepohl (1995) suggested that the negative Eu/Eu^*_{MUQ} in some Archaean rocks is explained by the denudation of granitic material in the source region. We prefer this explanation, especially in light of previous estimations of zircons originating in hydrous, SiO_2-saturated, meta- and peraluminous melts approximating modern-day arc-type andesites and Himalayan-type leucogranites (Harrison, 2009) or diverse suites of I-type and S-type granites (Burnham and Berry, 2017). If such granites interacted with the terrestrial hydrosphere during alkaline aqueous chemistry fluctuations, they could conceivable contribute to the REE+Y signal in the resulting chemical precipitate. The question of negative Eu^*/Eu_{MUQ} remains open to discussion.

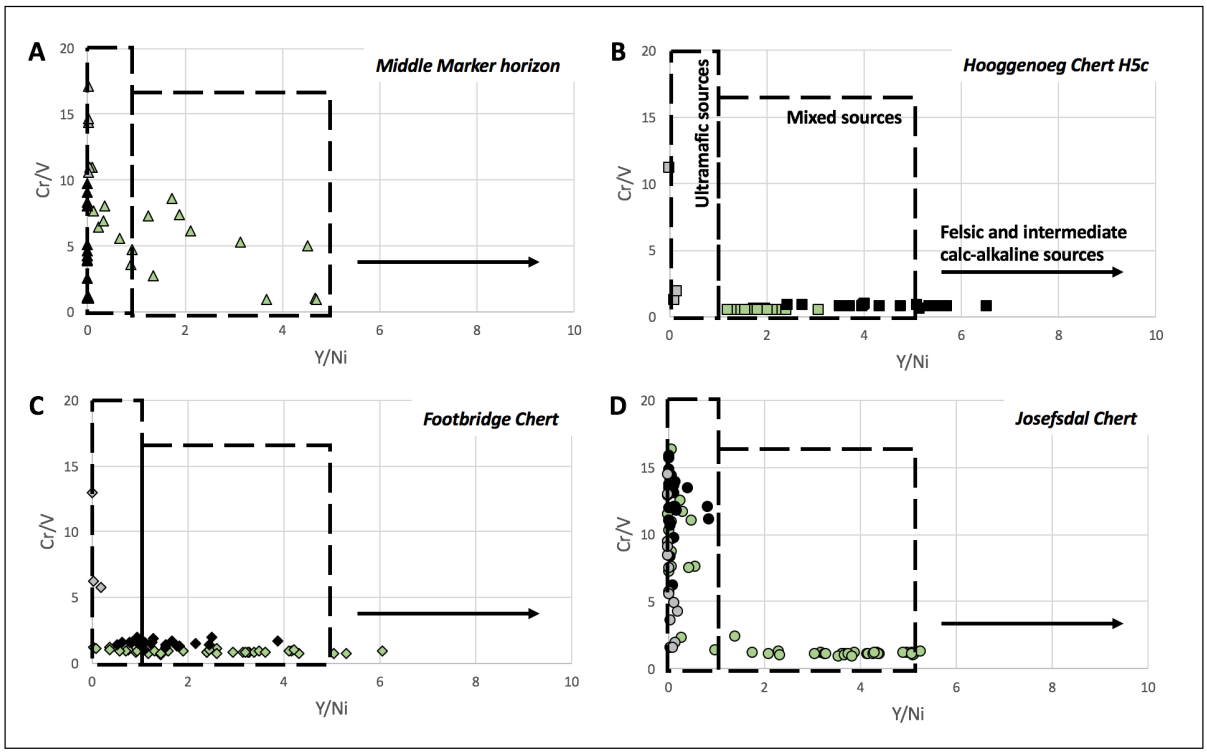

Fig. 16. Bulk ICP-MS and *in situ* LA ICP-MS results of Cr/V versus Y/Ni that qualify the relative importance of ultramafic (komatiitic-basaltic), felsic and calc-alkaline, and mixed source substrates (zones indicated in B). In all cases, bulk analyses (grey symbols) plot within the ultramafic field. With the exception of the Hooggenoeg Formation samples, *in situ* LA ICP-MS results of the non-microbial chert horizons (black symbols) also suggest ultramafic precursors whereas LA ICP-MS analyses acquired within microbial horizons (green symbols) – including those for the Hooggenoeg chert – plot within the mixed sources field. This indicates that microbial colonisation correlates with periods of increased mineralogical diversity associated with mixed volcanogenic substrates.

To summarise this section, our findings prove that exposed landmasses (early continents) in the Palaeoarchaean provided loci around which well-developed microbial biomes flourished (Fig. 17). These biomes were characterised by a complex interplay of marine and riverine chemistries. Since REE+Y patterns rapidly fractionate in estuarine settings (e.g., Elderfield et al., 1990; Bau, 1999), the endurance of the riverine pattern observed in our results necessitates a significant degree of basin restriction before interaction with marine waters. Marine resurgences fuelled disequilibrium settings and correlate with the specific snapshots in deep time during which microbial life flourished in the basin.

This signature is recurrently found in four horizons spanning 150 Ma, which corresponds to almost the entire Palaeoarchaean fossil record of South Africa, and it is thus probable that such small emergent landmasses were relatively common at this time. Evidence for the subaerial exposure of landmasses (Westall et al., 2011; Sugahara et al., 2010; Djokic et al., 2017; Homann et al., 2018) and the development of major crustal bodies of importance to the process of continent-building (Hickman, 2012; Kamber, 2015; Van Kranendonk et al., 2015; Dhuime et al., 2015; Cawood et al., 2018) are increasingly reported from Early Archaean sequences. Our findings substantiate that partially restricted epicontinental basins – likely resulting from these new crustal developments, and the rigidity of the continental-type lithosphere formed – provided the ideal regional habitat within which globally important

biomes of early life developed and persisted over long geological timescales. Denoting the fine-scale characteristics of this hitherto unrecognised Palaeoarchaean biome was possible only through coupling bulk and *in situ* trace and REE systematics.

4.3. Biome reconstruction in the Palaeoarchaean

A number of recent studies have appraised fossiliferous Archaean sediments at the level of ecosystems or biocoenoses (Schopf et al., 2017; Hickman-Lewis et al., 2018a; Stüeken and Buick, 2018; Homann et al., 2018) and provide the basis for quantitative Archaean biome reconstruction. Focussing on early anaerobic ecosystems – specifically microbial mats that likely reflect anoxygenic photosynthetic communities – we have herein reconstructed an epicontinental basin biome represented by four units from the Barberton greenstone belt. These horizons span almost 150 Ma, which suggests that such biomes were probably widespread and persistent during any hiatus in volcanic activity. This fossil-calibrated geobiological approach has unveiled significant, shallow-water, epicontinental basin biomes associated with exposed Archaean landmasses and periodic fluxes of marine waters. Phototrophic microbial mats are key relics of the ecosystems preserved in the ancient fossil record, and their ubiquitous presence in shallow-water habitats – at the interface of the atmosphere, hydrosphere and geosphere – argues for their importance in Archaean biogeochemical cycling (Nisbet and Fowler, 1999; Lenton and Daines, 2016).

The REE+Y patterns reported within these microbial horizons are unique for the Palaeoarchaean (Fig. 13). Although most previous REE+Y studies of carbonaceous cherts have suggested overwhelmingly marine palaeodepositional environments for fossil-bearing cherts (e.g. Kamber and Webb, 2001; Van Kranendonk et al., 2003; Hofmann and Bolhar, 2007; Hofmann and Harris, 2008; Allwood et al., 2010), we suggest that this might be the result of an issue of analytical scale, evident in that the bulk ICP-MS analyses herein produced similar results. Bulk analyses are not applicable at microbially relevant resolutions. Such terrigenous, landmass-dependent, epicontinental sea-type biomes as described herein had, until recently, been found only in rocks up to 3.0 Ga (Grassineau et al., 2002; Kamber et al., 2004; Bolhar and Van Kranendonk, 2007; Sugahara et al., 2010; Stüeken et al., 2017), in all cases explained as basin settings strongly influenced by continental waters. Terrestrial palaeoenvironments in the Moodies Group (Homann et al., 2018) and the Dresser Formation (Djokic et al., 2017) suggest that exposed landmasses may also have produced a minor Archaean biome adjacent to the presumably more widespread epicontinental marine biome described herein. Only in the case of the Mesoarchaean Moodies Group has the regional significance of the biome been demonstrated.

Our use of *in situ* LA ICP-MS transects through individual microbial mats (Fig. 15) has reconstructed the changing character of Archaean microbial biomes at the highest micro-stratigraphic resolution thus far. The resulting MUQ-normalised patterns tell a very different story to the bulk analysis of cherts: they are flat, rich in LREE, and of higher REE+Y content than any known seawater (Fig. 13). This, together with chondritic to supra-chondritic Y/Ho ratios, implies significant non-marine influence. Due to the high REE+Y concentration and lack of a positive Eu anomaly, these results strongly resemble riverine fluid chemistries (Hoyle et al., 1984; Elderfield et al., 1990; Bolhar and Van Kranendonk, 2007). This indicates that although the regional palaeoenvironment of each of the four studied cherts was similar to that of the regional Archaean condition (marine waters influenced by hydrothermal fluids), the

microbial biome itself flourished in times of enhanced continental influence. This likely corresponds to quiescent, semi-isolated basins, which were not necessarily strongly influenced by local hydrothermal activity (Fig. 17). Limited sedimentary structures indicative of current activity in samples and stratigraphy associated with microbial mats sustains this reconstruction (e.g. Lowe and Knauth, 1977; Lanier and Lowe, 1982; Paris et al., 1985; Walsh, 1992; Westall et al., 2015). The epicontinental basin microbial biome may have repeatedly proliferated by virtue of the diverse mineralogy provided by mafic-felsic (continental) inputs (Fig. 16) together with periodic basin recharge by seawater (elevated Y/Ho and positive La/La^*_{MUQ} and Y/Y^*_{MUQ}) providing biologically conducive disequilibrium conditions in biogeochemistry.

It is likely not a coincidence that similar relationships between regional- and biome-scale environments have emerged from the four studied cherts. Rather, we suggest that the geomorphology of the Palaeoarchaean Earth favoured wide realms of shallow epicontinental basins (*cf*. Nijman et al., 2017) teeming with microbial life over the course of many millions of years, perhaps governed by local and regional volcanic cycles (Fig. 17) (*cf*. Fig. 2 of Braiser et al., 2006). Groups of exposed landmasses were the loci of regionally important microbial mat-based ecosystems. This supports that individual microbial biomes were globally significant in the Palaeoarchaean (*cf*. Nisbet, 1995; Hickman-Lewis et al., 2018). Increased lithospheric heat flux during the Archaean would necessarily have formed topographically varied surface geomorphology as a function of the geometry of crustal heat escape (de Wit and Hart, 1982), perhaps by heat-pipe mechanisms. Topographically variable Archaean crust atop long-lived, geostatically stable igneous bases (Kamber, 2015; Van Kranendonk et al., 2015) would have provided sustained geomorphological realms characterised by shallow-water, epicontinental environments able to host microbial life. Consistent results within and between formations within this tectonic framework thus indicate that epicontinental basin biomes were a major part of the Archaean biosphere, and perhaps globally impactful in Archaean biogeochemical regulation.

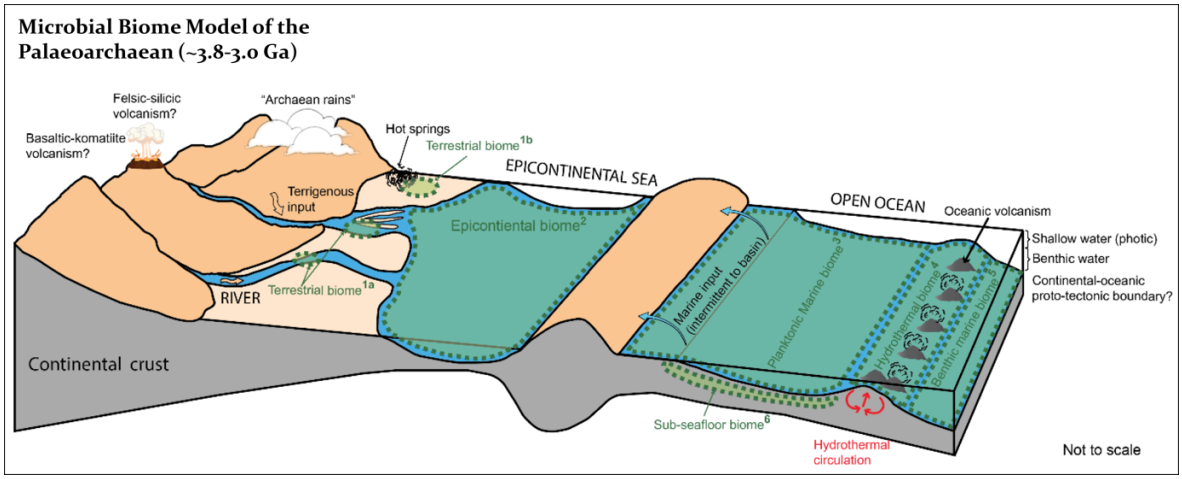

Fig. 17. A model for microbial biomes and their host environments throughout the Palaeoarchaean considering this study and a large volume of previous research. The epicontinental basin biome, outlined in this contribution, can be found at the centre of the diagram, perched atop the small landmass, and is periodically restricted from the open ocean. The benthic marine biome colonises available seafloor in the presence of proximal and distal hydrothermal systems. Subjacent to the benthic marine biome is the sub-seafloor biome. Submarine and subaerial hydrothermal systems host thermophilic, chemosynthetic microbial life. Terrestrial fluvial and fluvio-deltaic siliciclastic systems were colonised by around 3.2 Ga, perhaps signalling an evolutionary trajectory in prokaryotes

toward terrestrial forms or reflecting the rise of ecological niches associated with modern-style continents. Finally, the planktonic marine biome is presumed. The epicontinental basin biome occurs uniquely at the interface of marine, terrestrial and atmospheric realms, and might therefore constitute an important driver or factor in biogeochemical cycles on the early Earth. The balance of these biomes was presumably driven by a combination of volcanic, marine, hydrothermal and riverine activity, and therefore influenced by the advent of modern-style plate tectonics. Superscripts corresponding to each biome indicate corresponding Archaean units: 1a) Fortescue Group (Bolhar and Van Kranendonk, 2007), Moodies Group (Homann et al., 2018); 1b) Dresser Formation (Djokic et al., 2017); 2) Mushandike Limestone (Kamber et al., 2004); Middle Marker horizon, Hooggenoeg Chert H5c, Footbridge Chert, Josefsdal Chert (this study); 3) Mount Goldsworthy-Mount Grant cherts (Suguhara et al., 2010; Sugitani, 2018), Kromberg Formation horizons (Walsh, 1992; Oehler et al., 2017); 4) Kangaroo Caves (Rasmussen, 2000); 5) Buck Reef Chert (Walsh, 1992; Tice and Lowe, 2006a,b; Greco et al., 2018), stratiform 'Apex chert' (Hickman-Lewis et al., 2016); 6) Sub-seafloor biome (Furnes et al., 2004, 2007).

Nisbet (1995, 2000), Nisbet and Fowler (1999) and Nisbet and Sleep (2001) presented the first palaeoecological hypotheses for the diverse biomes of Archaean life. As justly noted therein, at the time, much of our understanding of the distribution of life on the early Earth was *predicted* or *surmised* (Nisbet, 2000), but an increasing awareness of the range of biosignatures dating from the earliest geological record means that this no longer true. The distribution of early life was raised again a decade later by Brasier et al. (2011), who noted that a lack of appreciation of the diversity of early life may also result from a reductionist prejudice to focus only on a restricted range of environments. Environmental evolution through the early stages of Earth history follows an anaerobic to aerobic evolutionary trajectory (Knoll et al., 2016), which is independently evident in the composition of metal-bearing oxidoreductases (Moore et al., 2017). This trajectory is presumably linked to the progressive opening of ecological niches as the surface of the Earth diversified mineralogically. The Palaeoarchaean marine realm was doubtless characterised by a rich diversity of microbial life, both in shallow-water coastal environments and possibly within the water column (Nisbet, 2000; Nisbet and Sleep, 2001). Chemosynthetic biomes in the deposits around hydrothermal vent systems and in the subseafloor are a further ecosystem which has yet to be fully appraised in the Archaean (Rasmussen, 2000; Westall et al., 2015; McMahon and Ivarsson, 2019). Emergent and terrestrial niches inhabited by radiotolerant, halotolerant microbial life (Westall et al., 2011; Djokic et al., 2017; Homann et al., 2018) were seemingly a more minor biome, occurring sporadically throughout the ancient rock record, although this could be a function of palaeoenvironmental preservation potential.

We here add a well-defined epicontinental basin biome to this suite (Fig. 17). Epicontinental basins are habitable by virtue of the complex interactions of hydrogenous and terrigenous inputs within. The relative importance of biomes in fossiliferous units through time could, if accounting for the preservation potentials of individual palaeoenvironments, aid our understanding of microbial evolutionary trajectories through the lens of environmental reconstruction. We are therefore at a point of expansion in historical geobiology: multiple scales of geological and geochemical assessment may unveil, as demonstrated herein, similarities between fossiliferous units in deep time, and may allow the construction of a biome-based biogeographical model of the Archaean Eon which should yield biome-level evolutionary trajectories co-evolving with the geosphere. Such large-scale appraisals relevant to the co-evolution of Earth and Life, rather than traditional approaches of estimating the Archaean biogeochemical landscape on a microfossil-by-microfossil basis, provide a multi-

resolution correlative palaeoecological lens through which the diversity of biogeochemistry on the Archaean Earth may be understood.

5. Conclusions

We herein make two conclusions regarding our current understanding of the biomes and biogeochemical landscapes of the early Earth:

I) At high analytical resolutions, differences between the geochemical environment of early life (the biome) and that of the wider region (the habitat) are evident. Studies reporting exclusively shallow water marine depositional conditions for microbial mat-bearing cherts may have mistakenly made this conclusion as a result of conducting only bulk analyses in which fine-scale, fluctuating REE+Y signals in microbial horizons are overwhelmed by signals reflecting the regional depositional environment. Herein, we have studied four microbial horizons spanning around 150 Ma and have shown that complex fluid chemistries correlate with the presence of microbial mat ecosystems. This is consistent with principles of modern biological oceanography: 50-75% of primary productivity occurs in disequilibrium interfaces close to riverine outputs into the open ocean (Jeandel and Oelkers, 2015). Future geobiological studies must focus on multi-scalar geochemistry in order to identify the defining characteristics of the palaeo-biome.

II) Epicontinental basins, into which riverine waters (perhaps fluxes of rainfall; *cf*. Arndt and Nisbet, 2012) transported significant input, were globally important biomes of the Palaeoarchaean. These biomes, existing at the hydrosphere-geosphere-atmosphere interface, were an anoxygenic "*Matworld*" scenario (*cf*. Lenton and Daines, 2016) and are a testament to the importance of microbial ecosystems in the regulation of biogeochemistry throughout deep time. Prior to globally distributed large continents, systems of Archaean basins (Nijman et al., 2017), many of which were likely semi-restricted, fostered networks of anoxygenic consortia across portions of the early Earth. Biome diversity increased during the Mesoarchaean-Neoarchaean, and again with the Great Oxygenation Event. Metabolic trajectories within such critical transitional periods may be observed through the reconstruction of such biomes. This may be of particular interest in the Archaean for the period between 3.2 and 2.7 Ga, during which much of the continental crust developed and available niches diversified.

Table 2 – REE+Y and anomaly characteristics from bulk ICP-MS.

A) Middle Marker	**03SA01**	**07SA21**	**07SA22**	**07SA23**
La/La*	0.7492	0.9337	0.9620	1.0949
Ce/Ce*	0.8081	1.0701	0.9057	0.9628
Y/Y*	0.5795	0.8460	0.9601	1.0735
Eu/Eu*	1.2978	1.4574	0.9758	1.3706
Y/Ho	17.747	22.006	24.821	29.287
Pr/Pr*	1.1104	0.9654	1.0073	1.0006
$(Pr/Yb)_{MUQ}$	0.1210	0.5321	0.4712	0.1747
Hydrothermal contribution	2%	2%	0.5%	2%
Detrital influence	100%	100%	100%	90%
B) Hooggenoeg Fm. H5c	**01SA09**	**01SA56**	**03SA16**	**07SA28**
La/La*	1.2244	0.8903	1.2210	1.1466
Ce/Ce*	1.0304	1.0304	0.9584	1.0033
Y/Y*	0.9754	0.9119	0.9909	0.9927
Eu/Eu*	1.6284	1.2886	2.1949	1.2325
Y/Ho	26.877	21.581	26.040	25.798
Pr/Pr*	0.9841	0.9841	1.0077	0.9713
$(Pr/Yb)_{MUQ}$	1.6608	2.8868	0.1657	0.2495
Hydrothermal contribution	4%	5%	6%	2%
Detrital influence	98%	100%	100%	100%

C) Footbridge Chert	***96SA02***	***12SA49***	***12SA50***
La/La*	0.9255	0.9390	1.0866
Ce/Ce*	0.9756	1.0022	1.0483
Y/Y*	1.0403	0.9757	0.9288
Eu/Eu*	1.1287	1.5265	1.9542
Y/Ho	25.785	23.942	23.628
Pr/Pr*	0.9979	0.9722	0.9713
$(Pr/Yb)_{MUQ}$	1.9598	3.5197	2.1157
Hydrothermal contribution	3.5%	5%	5%
Detrital influence	100%	100%	100%

D) Josefsdal Chert	***14SA01***	***12SA16***	***12SA29***	***12SA06***	***12SA22***	***12SA10***
La/La*	0.8810	0.5321	2.9026	0.6778	0.9460	1.0116
Ce/Ce*	0.7655	0.4676	1.5181	0.6307	0.7148	0.1417
Y/Y*	1.3007	1.1259	1.4478	1.3288	1.1827	1.2303
Eu/Eu*	2.0143	1.2753	1.5298	1.1746	1.7304	1.3436
Y/Ho	32.024	32.953	38.5685	36.385	31.828	32.901
Pr/Pr*	1.1357	1.4591	0.7996	1.2568	1.1512	2.0442
$(Pr/Yb)_{MUQ}$	1.0732	0.7758	0.2439	1.2665	0.3238	2.4186
Hydrothermal contribution	5%	2%	3%	0.5%	3.5%	2.5%
Detrital influence	80%	78%	58%	67%	72%	78%

	12SA13	***12SA32***	***12SA20***	***14SA04***	***12SA34***	***12SA01***	***12SA37***
La/La*	0.9875	1.2185	1.8489	1.0466	1.1045	0.9322	1.0786
Ce/Ce*	0.9310	0.9598	1.1521	0.3528	0.8493	0.9303	0.7369

Y/Y*	1.1879	1.1907	1.2771	1.1653	1.4026	1.3688	1.1904
Eu/Eu*	1.4671	1.5981	1.0142	1.3418	2.0245	1.2306	1.5316
Y/Ho	30.308	33.188	35.146	33.397	36.330	34.946	32.185
Pr/Pr*	1.0364	1.0206	0.9187	01.465	1.0807	1.0807	1.1505
$(Pr/Yb)_{MUQ}$	1.2312	0.5675	0.2092	2.0426	0.6817	1.1885	0.6547
Hydrothermal contribution	2.5%	3%	0.5%	2.5%	5%	2%	3%
Detrital influence	82%	77%	70%	76%	67%	71%	80%

Table 3 – REE+Y and anomaly characteristics from *in situ* LA ICP-MS.

A) Middle Marker horizon	***07SA23 (microbial mat)***			***07SA22 and 07SA25 (clotted/clastic cherts)***
	below	***within***	***above***	
La/La*	1.27-2.20	1.48-2.76	1.63-1.95	1.19-2.25
Ce/Ce*	0.95-1.32	1.09-1.56	1.17-1.27	1.07-1.40
Y/Y*	1.02-1.21	1.07-1.43	1.14-1.21	1.04-1.23
Eu/Eu*	0.77-1.17	0.83-1.37	0.84-0.97	0.70-1.12
Y/Ho	25.7-34.2	29.2-46.8	30.2-31.7	25.3-34.5
$(Pr/Yb)_{MUQ}$	0.77			0.86
Hydrothermal contribution	Up to 2%			Negligible
Detrital influence	30-95%			70-100%
B) Hooggenoeg Fm. H5c	***03SA15 (microbial mat)***			***03SA04 (clastic chert)***
	below	***within***	***above***	
La/La*	1.57-1.77	1.47-1.90	1.34-1.79	1.43-2.98
Ce/Ce*	1.21-1.35	1.13-1.36	1.08-1.34	1.03-3.48
Y/Y*	0.94-1.08	0.98-2.22	0.87-1.05	1.01-1.28
Eu/Eu*	0.73-0.89	0.66-1.00	0.72-0.92	0.59-1.14
Y/Ho	24.5-29.7	24.7-32.6	21.5-26.5	25.9-40.8
$(Pr/Yb)_{MUQ}$	0.86			0.76
Hydrothermal contribution	Negligible			Up to 2%
Detrital influence	80-100%			50-90%

C) Footbridge Chert	***03SA09 (lower mat)***			***03SA09 (upper mat)***			***03SA09' (clastic chert)***
	below	***within***	***above***	***below***	***within***	***above***	
La/La*	1.37-1.80	1.38-2.67	1.59-3.89	1.52-2.29	1.57-2.36	1.56-2.10	0.41-6.13
Ce/Ce*	0.99-1.14	1.08-1.47	1.09-1.75	1.04-1.28	1.05-1.37	1.07-1.28	0.55-2.67
Y/Y*	1.04-1.18	1.05-1.43	0.95-1.20	1.05-1.19	1.07-1.15	1.05-1.34	0.83-1.47

Eu/Eu*	0.73-0.78	0.64-1.02	0.73-0.97	0.73-1.14	0.63-1.03	0.65-1.07	1.21-2.87
Y/Ho	26.0-29.3	26.4-42.7	24.4-32.3	27.8-34.1	26.4-36.0	28.4-37.7	18.1-41.8
$(Pr/Yb)_{MUQ}$	0.80			0.80			0.80
Hydrothermal contribution	Negligible to 1%						Up to 8%
Detrital influence	45-100%						50-100%
D) Josefsdal Chert	***12SA18 (microbial mat)***			***12SA36 (microbial mat)***			***99SA07 (clotted chert)***
	below	***within***	***above***	***below***	***within***	***above***	
La/La*	1.45-1.83	1.35-1.88	1.51-2.28	1.12-1.39	1.34-1.92	1.10-2.13	1.03-3.28
Ce/Ce*	1.03-1.18	0.96-1.24	1.03-1.30	0.92-1.03	0.93-1.32	1.07-1.28	0.94-2.08
Y/Y*	1.03-1.25	1.03-1.36	1.09-1.35	0.92-1.19	0.95-1.57	1.08-1.29	0.74-1.32
Eu/Eu*	0.92-1.02	0.59-1.05	0.65-1.14	0.56-0.99	0.58-1.29	0.84-1.52	1.12-3.01
Y/Ho	27.9-34.1	27.8-43.2	29.2-38.5	21.2-30.4	29.2-46.7	29.0-37.6	19.1-42.2
$(Pr/Yb)_{MUQ}$	0.81			0.93			0.76
Hydrothermal contribution	Negligible to 1%						Up to 5%
Detrital influence	40-90%						31-100%

Manuscript 4 – Mechanistic morphogenesis of organo-sedimentary structures growing under geochemically stressed conditions: keystone to proving the biogenicity of some Archaean stromatolites?

Abstract

Morphologically diverse organo-sedimentary structures (including microbial mats and stromatolites) provide a palaeobiological record through more than three billion years of Earth history. Since understanding much of the Archaean fossil record is contingent upon proving the biogenicity of such structures, mechanistic interpretations of well-preserved fossil microbialites can reinforce our understanding of their biogeochemistry and distinguish unambiguous biological characteristics in these structures, which represent some of the earliest records of life. Mechanistic morphogenetic understanding relies upon the analysis of geomicrobiological experiments. Herein, we report morphological-biogeochemical comparisons between micromorphologies observed in growth experiments using photosynthetic mats built by the cyanobacterium *Coleofasciculus chthonoplastes* (formerly *Microcoleus*) and green anoxygenic phototrophic *Chloroflexus* spp. (i.e., *Coleofasciculus*-*Chloroflexus* mats) and Precambrian organo-sedimentary structures, demonstrating parallels between them. In elevated ambient concentrations of Cu (toxic to *Coleofasciculus*), *Coleofasciculus*-*Chloroflexus* mats respond by forming centimetre-scale pinnacle-like structures (supra-lamina complexities) at their surfaces. μPIXE mapping shows that Cu and other metals become concentrated within surficial sheath-EPS-*Chloroflexus*-rich layers, producing density-differential micromorphologies with distinct fabric orientations that are detectable using X-ray computed micro-tomography (X-ray μCT). Similar micromorphologies are also detectable in stromatolites from the 3.481 Ga Dresser Formation (Pilbara, Western Australia). The cause-response link between the presence of toxic elements (geochemical stress) and the development of multi-layered topographical complexities in organo-sedimentary structures may thus be considered an indicator of biogenicity, being an indisputably biological and predictable morphogenetic response reflecting, in this case, the differential responses of *Coleofasciculus* and *Chloroflexus* to Cu. Growth models for microbialite morphogenesis rely upon linking morphology to intrinsic (biological) and extrinsic (environmental) influences. Since the pinnacles of *Coleofasciculus*-*Chloroflexus* mats have an unambiguously biological origin linked to extrinsic geochemistry, we suggest that similar micromorphologies observed in ancient organo-sedimentary structures are biologically indicative. An identical *Coleofasciculus*-*Chloroflexus* community subjected to salinity stress also produced pinnacles but did not produce identifiable micromorphologies in three dimensions since salinity seems not to negatively impact either organism, and therefore cannot be used as a morphogenetic tool for the interpretation of density-homogeneous micro-tufted mats, for example those of the 3.472 Ga Middle Marker horizon. Thus, although correlative microscopy is the keystone to confirming the biogenicity of certain Precambrian stromatolites, it remains crucial to separately interrogate each putative trace of ancient life, ideally using three-dimensional analyses, to determine, where possible, palaeoenvironmental influences on eventual morphologies. Widespread volcanism and hydrothermal effusion into the early oceans likely concentrated toxic elements in early biomes. Morphological diversity in fossil microbialites could, therefore, reflect either (or both of) differential exposure to ambient fluids

enriched in toxic elements and/or changing ecosystem structure and tolerance to elements through evolutionary time, for example after incorporation into enzymes. Proof of biogenicity through deducing morphogenesis (i.e., a process preserved in the fossil record) overcomes many of the shortcomings inherent to the proof of biogenicity by descriptions of morphology alone.

1. Introduction

Organo-sedimentary structures (OSS) of microbial origin include microbial mats (complex, laminated, sediment-binding ecosystems), biofilms (the individual, surface-attached, laminar components of microbial mats), stromatolites (biosedimentary structures accreting from a locus and driven by concomitant mat growth and mineral precipitation) and microbially induced sedimentary structures (MISS; sedimentary textures recording the prior presence of microbial mats or biofilms). Together, these present an archive of biology and palaeobiological processes through more than three quarters of Earth's history (e.g., Walter et al., 1980; Walsh, 1992; Hofmann et al., 1999; Noffke, 2010; Bosak et al., 2013; Westall et al., 2015; Hickman-Lewis et al., 2016, 2018). Such structures are usually constructed by phototrophic microorganisms that require ready access to sunlight and, therefore, formed in shallow water environments. In the geological record, OSS are usually preserved as biolaminites, organic-rich laminations within sediments (Gerdes et al. 1991; Gerdes and Klenke, 2007), or as stromatolites, laminated, usually carbonate- or silica-preserved structures charting the co-occurrence of biomass growth and mineral precipitation (Hofmann et al., 1999; Awramik and Grey, 2005; Bosak et al., 2013). Most importantly, OSS reflect biological communities presumed to have played a significant role in biogeochemical cycling through time, particularly during early Earth history (Nisbet and Fowler, 1999; Lowe and Tice, 2007; Bosak et al. 2013; Knoll et al., 2016). This may be by virtue of their occurrence in shallow-water environments at the interface of the hydrosphere, geosphere and atmosphere. Although phototrophic microbes may have been the primary producers and mat-forming organisms, OSS comprise an assemblage of microcolonies varying in both lateral and vertical distribution (Decho, 2000; Gautret et al. 2006), and may contribute measurably to multiple biogeochemical cycles. In modern and ancient settings alike, OSS encompass wide morphological variation (Doemel and Brock, 1977; Tice and Lowe, 2006; Gerdes and Klenke, 2007; Noffke, 2010; Hickman-Lewis et al., 2018), the reasons for which remain incompletely appraised. Herein, we suggest that the origins of diverse OSS morphologies may be explained by defining the morphogenetic factors driving their shapes, i.e., the growth processes preserved in their morphologies. This approach may overcome the ambiguity in assessing the origins of OSS using only morphology, which has historically led to uncertainty in the distinction of processes related to biology from those exclusively reflecting environmental factors.

1.1. Morphogenesis of organo-sedimentary structures

Pulsed and cyclical *in vivo* changes of form are typical growth phenomena in biotic systems at both the organismal and community scale. The diversity of morphology in microbial OSS should be explicable through identifying the drivers of change, and a number of holistic mathematical models linking microbial mat and stromatolite morphogenesis to biophysical, physiological and palaeoenvironmental parameters have sought to describe these processes (Hofmann, 1973; Verrecchia, 1996; Grotzinger and Rothman, 1996; Grotzinger and Knoll,

1999; Batchelor et al., 2000, 2003, 2004; Dupraz et al., 2006; Bosak et al., 2007, 2010; Petroff et al., 2010, 2013; Tice et al., 2011; Cuerno et al., 2012). Such studies have highlighted that the necessary framework for understanding the morphogenesis of OSS should incorporate basic features of microbial growth (intrinsic factors) and its responses to environmental variables (extrinsic factors) (Grotzinger and Knoll, 1999; Reid et al., 2003; Batchelor et al., 2003; Awramik and Grey, 2005; Dupraz et al., 2006; Tice et al., 2011; Sim et al., 2012; Bosak et al., 2013). Intrinsic factors include growth rates, structural accretion by sediment trapping and binding (biostabilisation), mineral precipitation, community or trophic structure through time, quorum sensing and organismal collaboration and competition, elemental cycling and exopolymer composition and adhesiveness. Extrinsic factors include nutrient availability, seawater chemistry, hydrodynamic stresses and shear, together with sedimentation rates and burial.

What factors act to determine the eventual morphospace of OSS and what are the interrelationships between physicochemical drivers? To what extent do hydrodynamic, biophysical or geochemical forcings govern OSS? Can mechanistic morphogenetics distinguish between biotic and abiotic origins for controversial OSS from the Archaean fossil record? Endeavours to model or experimentally grow OSS have as their objective the identification of a set of factors that uniquely reflect biological activity. These factors are non-linear and non-determinative, and form a *network* of interdependent forcings, the resulting structures being microbially derived laminations of alternating composition. Geomicrobiological appraisals of modern microbial mats (Burne and Moore, 1987; Reid et al., 2003), growth experiments (Bosak et al., 2007, 2010; Sim et al., 2012) and image analysis (Batchelor et al., 2000, 2003, 2004) provide both the 'raw material' for quantitative morphogenetic and morphometric analyses and a qualitative framework within which fossil OSS may be interpreted. Biogeochemical processes observed in natural or experimental environments have been incorporated into mathematical growth models, aiding in the definition of parameters relevant to any framework for microbialite morphogenesis. It is conceivable that recognisable, unambiguously biological, and predictable morphogenetic indicators may emerge from the fossil record. We use the terminology determined by these observation-based models to discuss our comparative morphogenesis approach (defined in the following text).

Growth models of OSS fall broadly into three categories. The first involves variants on the Kardar-Parisi-Zhang (KPZ) equation (Kardar et al., 1986), a three-dimensional Eden growth model, which may be qualitatively stated as the definition of each term:

change of height with time = upward growth velocity + interfacial growth in the normal direction + erosional and sedimentational smoothing + uncorrelated random noise

The noise term reflects stochastic environmental fluctuations. Batchelor et al. (2000, 2003, 2004) criticised this equation as failing to adequately consider bulk biological behavior (e.g. phototaxis) modified the equation into the deterministic KPZ, which may be qualitatively stated as:

change of height with time = surface relaxation + interfacial growth in the normal direction + upward growth velocity

The deterministic KPZ proposed by Batchelor et al. (2000) includes no randomness, and is thus dependent upon the parameters of the primary baseline. It has been suggested to be

unsuitable for recreating biogenic overhanging forms (Dupraz et al., 2006; Cuerno et al., 2012), but certain interlinked intrinsic and extrinsic factors can be extracted. Batchelor et al. (2004) found that models with *upward growth* < *interfacial growth* produced broader, domical structures, whereas *interfacial growth* < *upward growth* produced angular conical structures. The thickening of laminations at the crest region evidences phototactic behaviour, thus validating photosynthesis as a major primary metabolic pathway in many OSS.

The second basis for models is diffusion-controlled growth (diffusion-limited aggregation (DLA) and diffusion-reaction). DLA involves Brownian particle motion able to form aggregative, fractal-like clusters reflecting microstromatolites depending upon the availability of environmental particles. Diffusion control of growth reflects the principal 'extrinsic' effect on stromatolite morphogenesis: material or molecular flux encouraging growth (e.g., Reid et al., 2003; Petroff et al., 2010, 2013). The growth vector is a function of diffusion rate through the mat volume, which is determined by mat thickness, curvature, the ratio of mat thickness to curvature, and surface normal growth (Petroff et al., 2013). The rate of mineral precipitation scales with diffusive flux, and since regions of greater curvature allow chemical flux through a larger surface area, they will grow more rapidly (Petroff et al., 2013). This diffusion-reaction model thus reproduces conical stromatolite morphologies with lamination specificities, i.e. thickened crest regions.

The third modelling approach applies various life rules related to the evolution of cellular automata (CA), broadly defined as cell system interactions on the local scale (microscale) that govern the global (macroscale) biological system. Dupraz et al. (2006) combined the DLA model (extrinsic effects) with simple aspects of CA (intrinsic effects), yielding a DLA-CA model to explain branching Proterozoic forms. By varying substrate morphology and including community cell-relation phenomena, such as inter-cell dynamics, links between biology and the environment may be quantified.

The reader will at this point recognise that, while differing in their approaches, models of OSS growth answer common questions and are resoundingly useful in defining the natural processes that dominate OSS development. We consider that biological influence is generally neglected relative to environmental influence and, where biogenicity is controversial, as in some Archaean OSS, this may result in overly cautious interpretation even when structures are virtually indistinguishable from younger biological forms (Awramik and Grey, 2005; Bosak et al., 2013). Further complexity is added by the fact that, over the course of several months, microbial mats develop distinctive three-dimensional micromorphologies provided no sedimentary influx suffocates the system (Gerdes and Klenke, 2007). Such a complex climax consortium evidences the temporal evolution of a biotic system and is not exclusively upward as modelled, but incorporates biological complexities including competition and collaboration. For example, microbial mats are tiered by autotrophic and heterotrophic metabolisms during the formative and consuming stages (Gerdes et al., 1991), producing lamina-scale phenotypes. At the lamination scale, much information may be extracted from the fossil record of OSS to explain the interaction of microbial mats with their environments in deep time. Consequently, strong criteria for the biogenicity of ancient OSS may be found at the scale of individual laminae.

In this study, we aim to evaluate the biological origin of Precambrian OSS based on 3D correlative microscopy of comparable microstructures formed by modern microbial communities containing dense populations of filamentous organisms that may reflect non-oxygenic phototrophic (non-cyanobacterial) communities from the Palaeoarchaean. We describe microstructures associated with modern living microbial communities growing under environmental stresses: environments enriched in toxic elements and with elevated salinity. This permits us to demonstrate that correlative geomicrobiological, morphological and geochemical analysis of samples in three dimensions has the potential to establish the biogenicity of Precambrian structures within a morphogenetic framework inspired by the interrelation of processes defined by observation and modelling. Such an approach contributes to a unified morphogenetic theory for OSS incorporating intrinsic ecophysiology and extrinsic palaeoenvironmental factors.

2. Materials and Methods

2.1. Geomicrobiology and geochemistry (Modern samples)

Photosynthetic microbial mats built by the cyanobacterium *Coleofasciculus chthonoplastes* (formerly known as *Microcoleus chthonoplastes*, see Siegesmund et al., 2008; hereafter referred to as *Coleofasciculus*) and the green anoxygenic phototrophs *Chloroflexus* spp. (i.e., *Coleofasciculus*-*Chloroflexus* mats) were collected in April 2011 (sample 805; Fig. 1C-E) and February 2012 (sample 1011; Fig. 1F-G) from the hypersaline lake *La Salada de Chiprana*, NE Spain (N 41˚14'21.8" W 0˚11'10.9") at water depths of 25-50 cm (Fig. 1A-B). Sample 805 was flat-laminated, whereas sample 1011 showed natural pinnacle formation due to high salinity (120 g/L^{-1}) resulting from the particularly dry year 2011. Sample 805, which showed a smooth surface without pinnacles, was collected during favourable ambient conditions and transported alive to the laboratory for culturing experiments. Sample 1011 was directly fixed in glutaraldehyde and conserved for comparison as a representation of a highly stressed community. Sample 805, which showed a smooth surface without pinnacles, was collected during more favourable ambient conditions and transported alive to the laboratory for culturing experiments.

Subsamples of field sample 805 were cultured for six months in aquaria enriched in Fe and Mn at different concentrations at ambient temperatures under a diel cycle of 12-hour light under a Philips-HPI T Plus 400 W lamp and 12-hour darkness. Photosynthetically active radiation (PAR) intensity (light intensity when photosynthesis occurs, measured as the amount of energy in light wavelengths between 400 and 700 nm) was 167 $\mu mol.m^2.sec^{-1}$ (LiCor 250A photometer equipped with a LI-190SA Quantum Sensor). Synthetic seawater solutions (Ocean Instant) were enriched with $10mg.l^{-1}$ Fe, $10\mu g.l^{-1}$ Cu and $10\mu g.l^{-1}$ Mn (sample 805-Fe) and $5mg.l^{-1}$ Cu, $10\mu g.l^{-1}$ Fe and $10\mu g.l^{-1}$ Mn (sample 805-Cu), using commercially available chemicals ($CuSO_4.5H_2O$, $N_2O_9Fe.{}_9H_2O$ and $[CH_3COO]_2Mn.4H_2O$). In all cases, these solutions produced a mildly alkaline pH (7.2-8.0).

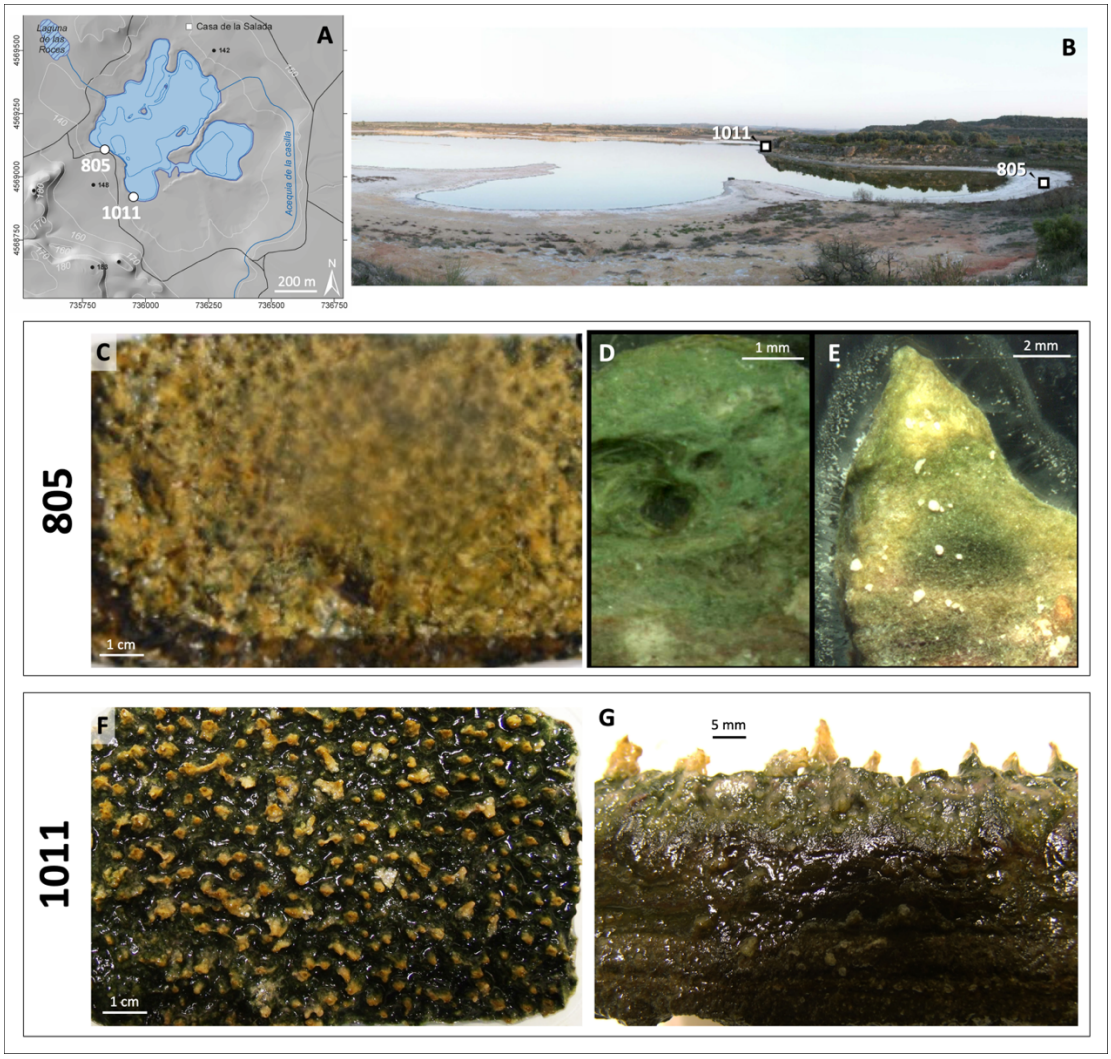

Fig. 1. Modern microbialite samples and collection locality. **A**) Map showing extent of *La Salada Chiprana* during the collection periods. Sample locations indicated. **B**) Field photograph of *La Salada Chiprana*. **C**) Original field sample of microbial mat 805 before culturing. **D**) Section through field sample 805 before culturing. **E**) Representative large pinnacle-like structure (supra-lamina complexity) that developed in the Cu-enriched medium (sample 805-Cu); similar structures were studied by SEM (Figs. 2G-L, 3), PIXE (Fig. 4) and X-ray µCT (Fig. 5). F-G) Sample 1011. **F**) Original field sample of microbial mat 1011, exhibiting natural tuft-like convexities as a result of elevated salinity in *La Salada Chiprana*. **G**) Cross-section view through sample 1011, showing stratification of the microbial community and millimetre-scale tufts. A fragment of this sample was studied by X-ray µCT (Fig. 6).

The biomass and photosynthetic activity of both the *Coleofasciculus* and *Chloroflexus* microbial communities were measured using FIRe (Fluorescence Induction and Relaxation) fluorometry (Satlantic Inc.) fitted with a Satlantic fibre optic probe attachment. The oxygenic photosynthetic response of cyanobacteria (*Coleofasciculus*) was traced at 680 nm (Photosystem II fluorescence; Gorbunov and Falkowski, 2004) while the photochemistry of anoxygenic photosynthetic bacteria (purple sulfur and green non-sulfur bacteria, Chloroflexaceae) was characterised by monitoring the fluorescence signal at 880 nm (fluorescence of the Bacteriochlorophyll-*a*-containing type II reaction centres in Chloroflexaceae) (Fetisova et al., 1988). Measurements (n=7 for each treatment) were

performed after 4 weeks' incubation and at the end of the experiment (after 24 weeks' incubation) with the emitting blue diode placed at 0.7 ± 0.1 cm above microbial mat surface.

Liquid-N_2 cryofixed and lyophilised samples taken from mat growth experiments (samples 805, 805-Fe and 805-Cu) and naturally grown (sample 1011) were observed using a Hitachi TM3000 SEM (ISTO-Orléans) (Figs. 2-3). The same cut sections of these microbial mats (sample 805) were mounted on carbon adhesive discs for *in situ* particle-induced X-ray emission (PIXE) elemental analysis using the microbeam line of the AIFIRA facility at CNRS-CENBG (CNRS Bordeaux-Gradignan; Sorieul et al., 2014). For comparative purposes, we detail the findings from the mats grown in solutions enriched in Fe and Cu (Fig. 4). µPIXE analyses were performed using a 3 MeV proton beam for 60-90 minutes. The experimental setup comprised two PIXE detectors and one RBS detector; both PIXE detectors were equipped with a 500 µm 'Funny Filter' with a 2 mm diameter hole size. Samples 805-Cu and 1011 were then mounted for X-ray micro-scale computed tomography (µCT) analysis to observe their 3D interior structures (Figs. 5-6).

2.2. Microbial palaeontology (Precambrian samples)

A second, comparative, sample set, consisting of two Precambrian OSS sourced from the East Pilbara terrane of Western Australia (domical-conical stromatolites from the 3.481 Ga Dresser Formation, sample 00AU23, hereafter DF1) and the Barberton greenstone belt of South Africa (micro-tufted microbial mats from the 3.472 Ga Middle Marker horizon, sample 07SA23, hereafter MM1), both of which exhibit, at different scales, complex surface topographies (Figs. 7-8), was used as a comparative dataset. The OSS of both the Dresser Formation and Middle Marker horizon have been deemed biological in origin (Walter et al., 1980; Buick et al., 1981; Hickman-Lewis et al., 2018).

Correlated three-dimensional reconstructions and geochemical studies of the Modern samples were used as a framework within which to interpret these Precambrian OSS. Since SEM imaging and EDS elemental analyses of these Precambrian samples yields little complementary information to aid comparison with the modern dataset due to chemical dilution resulting from extreme and early silicification, we report the morphology and mineralogy of Precambrian OSS using optical microscopy and Raman spectroscopy. Optical microscopy used an Olympus BX-51 (CNRS-Orléans).

2.3. Raman spectroscopy (Precambrian samples)

Raman spectroscopy was conducted with a WITec Alpha500 RA system using a frequency-doubled Nd:YAG green laser (wavelength 532 nm) at CNRS-CBM (CNRS Orléans). The system used a motorised table to move the sample continuously below a laser beam focussed onto the sample *via* a microscope objective. Spectra form a dataset, spatially referenced over the scanned area, that was processed to obtain compositional maps. Compounds were then represented either by different colours or as concentration maps according to intensity. A detailed explanation of Raman mapping can be found in Foucher et al. (2017). Scanning parameters are reported in the caption of Figure 9.

2.4. Micro-scale X-ray computed tomography (Modern and Precambrian samples)

Flexible possibilities in sample preparation mean that X-ray µCT was applied to both Modern (Figs. 5-6) and Precambrian samples (Figs. 10-12), and therefore forms the direct link

for morphometric comparisons between the two. Sample 805-Cu was prepared as a lyophilised fragment of a ~7 mm pinnacle from the upper surface of a microbial mat (Fig. 5A). Sample 1011 was prepared as a cut fragment of glutaraldehyde-fixed mat including a ~6 mm tuft (Fig. 6A-B). A cylinder of 8 mm diameter was cut through a macroscopically visible domical structure from the Dresser Formation (sample DF1) and a cylinder of 2 mm was cored through a microbial mat sequence from the Middle Marker horizon (sample MM1). X-ray CT scanning was conducted at CNRS-ISTO (CNRS Orléans) using a 180NF Phoenix Nanotom, operating with an accelerating voltage of 180 kV, a filament current of 170 nA, and an operating voltage of 120 V (see figure captions for acquisition parameters). Attenuation of the X-ray beam passing through the sample is dependent on sample characteristics (Ketcham and Carlson, 2001; Baker et al., 2012; Sutton et al., 2014). The choice of scanning parameters reflects the variations in size and X-ray density of the sample. The voltage and current of the X-ray source were controlled in order to keep the former as low as possible to achieve maximum composition-based contrast whilst allowing sufficient penetration to scan the entirety of the sample volume. The interested reader can find a comprehensive overview of tomographic analysis in Sutton et al. (2014). The distance of the sample from the X-ray source controls the number of X-rays passing through the sample and thus the resolution, i.e., a sample mounted closer to the X-ray source will scan at a higher resolution. During the acquisition, the turntable rotates and each view is taken at an interval of 360° divided by the total number of projections with an image size of 2304*2304 pixels. For our samples, the total number of projections ranged between 1200 and 2000 and the resolution from 1.19 µm to 6.89 µm per pixel. Sectional images of the samples were reconstructed by determining the attenuation coefficients for each line of pixels using Beer's law and generating a stack of slices corresponding to successive 2D sections of the sample. Corrections were applied in order to reduce the effects of beam hardening, ring artefacts and misalignment. The 3D volumes of each phase were extracted from the stack of sectional images using the segmentation tool of VG-Studio Max software (Volume Graphics).

3. Results

3.1. Modern Samples

3.1.1. Macrophotography, optical light microscopy, SEM and FIRe photochemistry

Coleofasciculus and *Chloroflexus* were present throughout the microbial stratigraphy of field sample 805 (before culturing), although *Coleofasciculus* dominated the surface layer while *Chloroflexus* was more common at depth (Fig. 2M-O). Light microscopy and SEM observations of the micromorphological characteristics of the cultured subsamples of 805 after a 24-week incubation period are shown in Figure 2, for both the incubation in Fe-enriched saline water (sample 805-Fe; Fig. 2A-F) and Cu-enriched saline water (sample 805-Cu; Fig. 2G-L). Under Fe enrichment (sample 805-Fe), the macroscopic morphology and community structure of the mat did not change with respect to the field sample 805. In contrast, for samples incubated in Cu-enriched aquaria (sample 805-Cu), large pinnacle-like structures formed within several days (Fig. 1E, 3A-C), i.e., the microbial stratigraphy changed during Cu incubation, and that the morphology and community structure of 805-Cu mats were different to the field sample 805 and cultured sample 805-Fe. In the 805-Fe subsample, as in field sample 805, the upper green layer was dominated by oxygen-producing *Coleofasciculus* trichomes

(Fig. 2C, F) and rare sheaths (Fig. 2D), whereas the lower darker layers were rich in the green anoxygenic phototrophs *Chloroflexus* (Fig. 2F). In contrast, the mat between the pinnacles of 805-Cu showed an inverted community structure, where the cyanobacterial *Coleofasciculus* layer was at depth (Fig. 2L), overlain by a surficial layer of densely packed *Coleofasciculus* sheaths with EPS and *Chloroflexus* filaments (Fig. 2I-K). This inverted community structure was also observed in pinnacles: the inner *Coleofasciculus*-rich biomass is overlain by a thin layer of *Chloroflexus* and EPS (Fig. 3A-C).

SEM images of the tufts from sample 1011, which had the same initial biological community as 805, do not show segregation; *Coleofasciculus* and *Chloroflexus* are well-mixed throughout the tuft (Fig. 3G-J), although the uppermost biomass is evidently under stress due the presence of gypsum (Fig 3E). Gypsum and celestine (Fig. 3F) are interspersed with biomass throughout the tuft, with a significant concentration of sub-mm scale grains at the top of the pinnacle. Throughout the tuft, filaments show incipient gypsum mineralisation (Fig. 3J). The lack of community segregation in sample 1011 (Fig. 3D-J) denotes that neither member was adversely affected by salt stress.

Fluorescence Induction Relaxation (FIRe, Ocean Instruments) measurements showed that the biomass and photosynthetic activity of *Coleofasciculus* (traced at 680 nm) did not change in the presence of Fe, but biomass strongly decreased in the presence of Cu. Both the biomass and photosynthetic response of *Chloroflexus* (traced at 880 nm) increased in the presence of Fe and Cu, particularly in the case of Cu. Hence, we conclude that *Coleofasciculus* is intolerant to Cu, whereas *Chloroflexus* shows tolerance to elevated Cu concentrations. This is consistent with SEM images (Figure 2G-L), which demonstrate that the surficial layer of biomass in the presence of elevated Cu consisted of a dense mixture of sheaths, EPS and *Chloroflexus* filaments, i.e., reduced *Coleofasciculus* biomass and productivity.

3.1.2. PIXE

The results of two μPIXE mapping experiments are presented here for comparative purposes, highlighting the elemental distributions in biological material in samples 805-Fe (Fig. 4A-B) and 805-Cu (Fig. 4C-E). In both cases, cellular material (both *Coleofasciculus* and *Chloroflexus*) is broadly associated with enrichments of K, Na, Mg, S and P. In sample 805-Fe concentration, Fe is dispersed throughout biological material such that it appears negligibly concentrated and does not visibly correlate with other elements, only within minor oxide particles attached to microbial filaments (Fig. 4B). PIXE element maps from 805-Cu present a different scenario. In the studied mat fragment, Cu, Mn and Fe are concentrated in the upper layers at the base of the pinnacle (the top of the mat; Fig. 4E) which, according to SEM imagery, corresponds largely to the exuded exopolymers and the empty sheaths of *Coleofasciculus* (Fig. 2H-K), i.e. a region of lower *Coleofasciculus* biomass and increased *Chloroflexus* biomass. There is a negative correlation between the association K-Na-Ca-Mg-S-P in biomass beneath the upper polymer-rich layer and the association Cu-Mn-Fe in the polymer-rich layer (Fig. 4E). In contrast to 805-Fe, Fe and Mn are located almost exclusively in the upper tens of micrometres and are not dispersed throughout the volume of the mat.

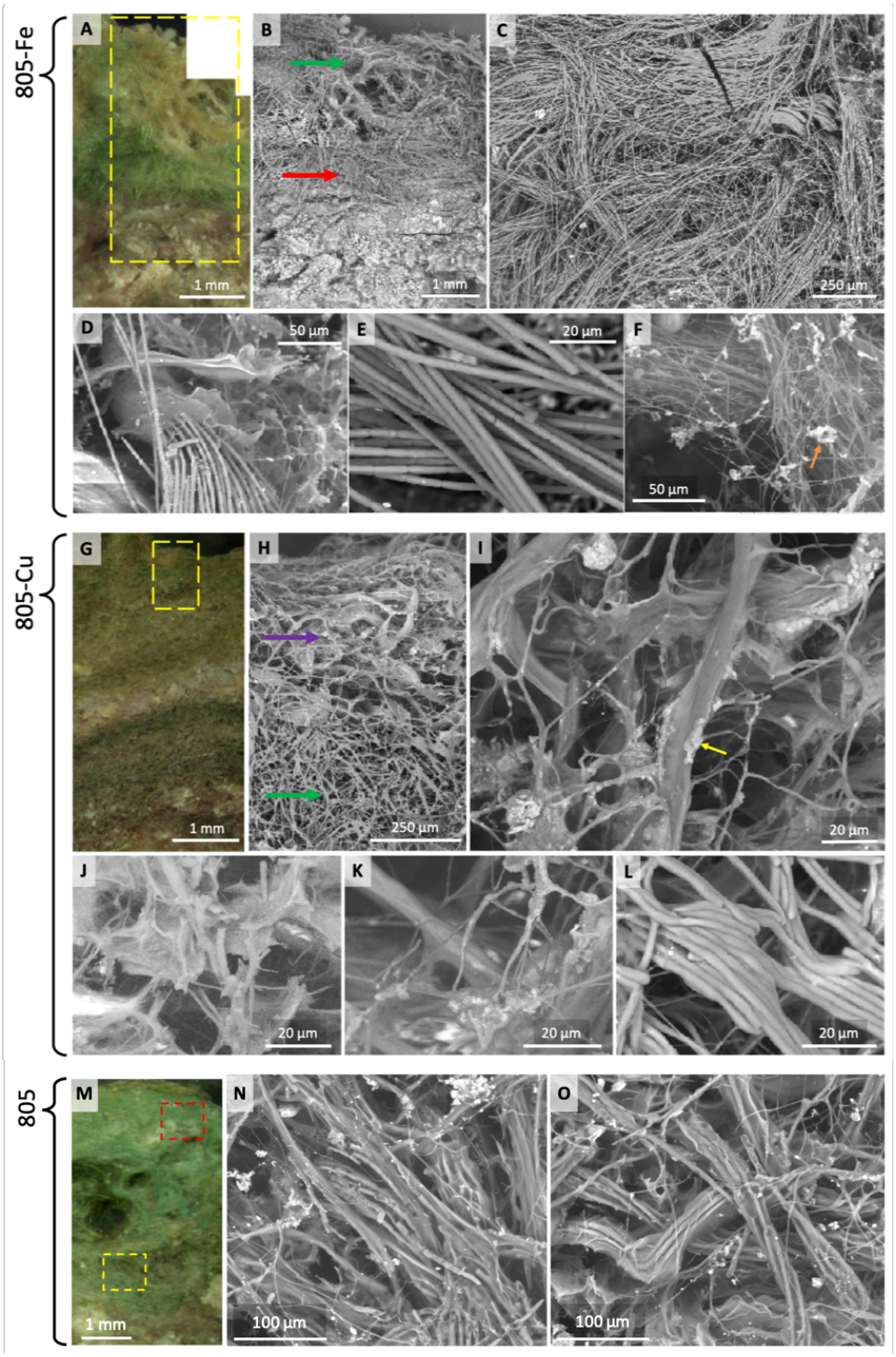

Fig. 2. Micromorphological characteristics of microbial mat sample 805 after a 24-week incubation period in (A-F) Fe-enriched saline water (sample 805-Fe) and (G-L) Cu-enriched saline water (sample 805-Cu). The original field sample 805 is included for comparison (M-O). **A-B**) Photograph and SEM micrograph of a vertical cut through mat 805-Fe showing stratification of the community. The upper green layers represent the major photosynthetically active, *Coleofasciculus*-rich layer (green arrow), whereas the lower darker layers represent those rich in the green anoxygenic phototroph *Chloroflexus* (red arrow). Yellow box indicates region imaged in B. **C-E**) Main green photosynthetically active layer of *Coleofasciculus* trichomes, large portions of which are outside the sheaths, and with very low densities of EPS. **C, E**) Restricted portions with trichomes, sheaths and EPS fibrillar networks. **F**) *Chloroflexus*-rich layer at the base of the upper green layer, with iron oxide (orange

arrow) precipitation on filaments. **G**) Vertical cut through mat 805-Cu, showing community stratification, with the green Chloroflexaceae bacteria overlying the cyanobacterial layer dominated by *Coleofasciculus*. Yellow box indicates region imaged in H. **H**) SEM micrograph showing the interface between the surficial sheath-rich layer (purple arrow) with EPS and Chloroflexus filaments and the underlying green, *Coleofasciculus*-rich layer (green arrow). **I-K**) Characteristics of the surface layer, composed mostly of sheaths accumulating Cu deposits (example arrowed) and web-like *Chloroflexus* filaments. **L**) *Coleofasciculus*-rich layer beneath the surface layer. Note that the community structure in the Cu-enriched growth experiment is broadly the inverse of that in the Fe-rich growth experiment, with the primary producer (*Coleofasciculus*) being the surficial organism in Fe-rich conditions, but occurring beneath an upper mixed layer of bacteria and bacterial products in Cu-rich growth media. **M-O**) Original field sample 805 before culturing in metal-rich aquaria. M) Photograph of a vertical cut through sample 805, showing the uppermost 5 mm. **N-O**) Representative photographs of the sample from the zones indicated by the red (N) and yellow (O) boxes. Filaments of *Coleofasciculus* and *Chloroflexus* are well-mixed throughout the uppermost millimetres but note that *Chloroflexus* is considerably more abundant in the lower region (O).

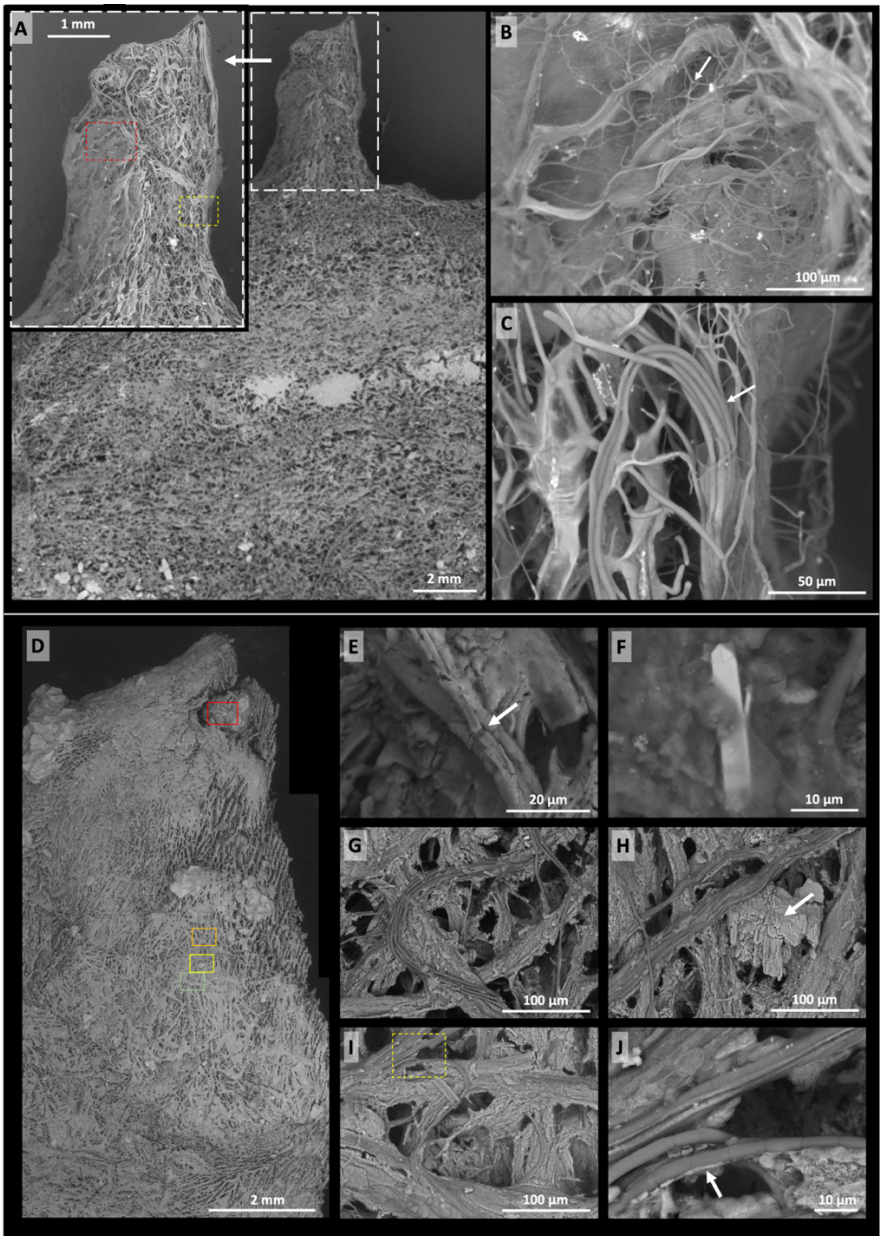

Fig. 3. Micromorphological characteristics of supra-lamina complexities in sample 805-Cu (A-C) and sample 1011 (D-J). **A**) SEM micrograph of lyophilised microbial mats from sample 805-Cu showing a cross-section through a representative pinnacle-like convexity. Inset shows high-magnification view. Red box indicates region

of B; yellow box indicates region of C. **B**) Fine network of *Chloroflexus* filaments (arrowed) at the surface of the pinnacle. **C**) Thicker clumps of *Coleofasciculus* filaments (arrowed) in the interior of the pinnacle. **D**) SEM micrograph showing a cross-section through a tuft from sample 1011. **E**) Broken, distended *Coleofasciculus* filaments (arrow) atop a gypsum grain (from region of red box). **F**) Prismatic celestine crystal associated with microbial filaments. **G-H**) Well-mixed network of *Coleofasciculus* and *Chloroflexus* filaments with gypsum crystals (example arrowed) that characterises the biomass of the tuft (from regions of orange and yellow boxes). **I-J**) Cyanobacterial trichomes (from region of green box) showing incipient mineralisation by gypsum (arrow in J). Yellow box in I shows region of J.

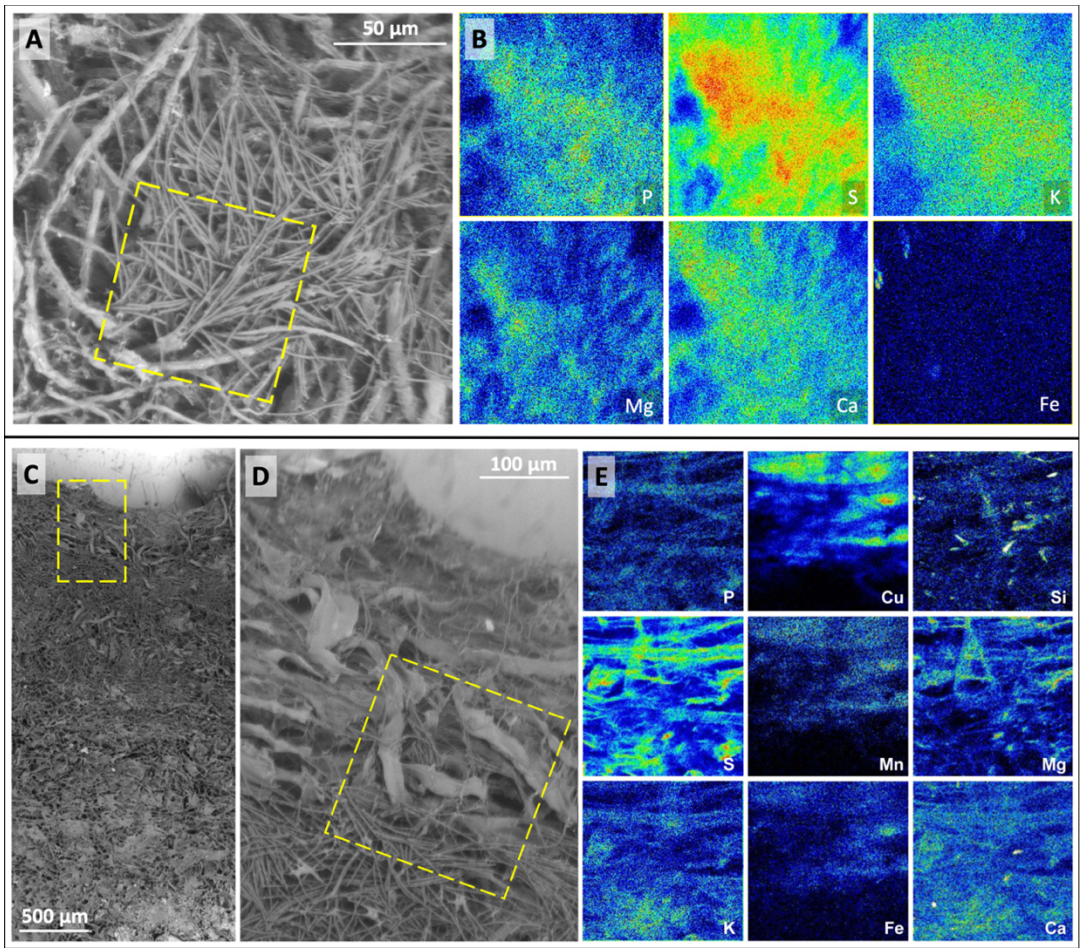

Fig. 4. PIXE microbeam elemental mapping of major and trace elements associated with bacterial biomass in samples 805-Fe (A-B) and 805-Cu (C-E). **A**) SEM micrograph showing tangled filaments in mats cultured under Fe enrichment (805-Fe). Yellow box indicates region of analysis. **B**) Elemental maps of P, S, K, Mg, Ca and Fe, showing that bio-essential P, S, K, Mg and Ca are associated with all biomass. Fe, although highly enriched in the culturing medium, is not preferentially concentrated into specific biomass, but distributed throughout. **C**) SEM micrograph showing stratified microbial mats cultured under Cu enrichment (805-Cu). Yellow box indicates location of D. **D**) High-magnification view of the contact zone between the overlying sheath-EPS-*Chloroflexus* layer and the underlying *Coleofasciculus*-dominated layer. Yellow box indicates region of analysis. **E**) Elemental maps of P, S, K, Cu, Mn, Fe, Si, Mg and Ca. Here, the three metallic elements, Cu, Mn and Fe, are concentrated in the upper sheath-EPS-*Chloroflexus* layer, but are absent in the underlying *Coleofasciculus*-rich layer.

3.1.3. X-ray µCT

Fragments from samples 805-Cu and 1011 – the two samples exhibiting surface relief in the form of pinnacles or tufts – were analysed using X-ray µCT with the objective of detecting 3D morphological features not observable by optical microscopy or SEM. Sample

805-Cu was studied by μCT at a pixel size of 6.87 μm. Carefully separating the higher and lower density pixels corresponding to the microbial material delineated sequences of alternately dense and less dense laminations composed of filamentous material (Fig. 5B-C). Achieving this density delineation relies on iterative separation of higher and lower values in the histogram peak corresponding to biological material in VG-Studio Max software. This distribution directly echoes combined SEM and μPIXE observations, which distinguished *Coleofasciculus*-rich underlying laminations (Fig. 2L) overlain by laminations comprising discarded sheaths, EPS and *Chloroflexus* (Fig. 2H-K) with differential enrichment in heavy metals (Cu, Fe, Mn) after growth experiments (Fig. 4E). In μCT renderings, *Coleofasciculus* (dominant in terms of biomass) is rendered in green (less dense; Fig. 5) and *Chloroflexus*-rich layers incorporating heavy metals are rendered in red (denser; Fig. 5). Consistent with μPIXE scans, all cellular material incorporates a range of lower atomic number elements (K-Na-Ca-Mg-S-P), but there is a strong enrichment of heavier Cu, Mn and Fe in the upper layers. The large pinnacle itself is also dominantly composed of *Coleofasciculus*-rich biomass (Fig. 5B), further corroborating SEM observations (Fig. 3) and suggesting that *Coleofasciculus* is the architect of large, pinnacle-like surface convexities. μCT scans reveal that the pinnacle-covering revetment shows different filament orientations (mostly horizontal; Fig. 5D) and a density consistent with *Chloroflexus*-rich biomass. This revetment is thin and discontinuous, becoming increasingly patchy toward the top of the pinnacle (Fig 5B), suggesting that its formation is a consequence of pinnacle growth, i.e., *Coleofasciculus* forms the pinnacle while the *Chloroflexus*-rich layer either follows pinnacle growth or is disrupted by it, confirming the 3D distribution of biomass observed in Figure 3A-C. The two communities form a supra-lamina convexity (the pinnacle) that preserves two fabrics rendered with high fidelity using μCT (Fig. 5D):

- An interior fabric with domains of both horizontally laminated and randomly oriented filaments of homogeneous size, wherein the degree of randomness in orientation increases with height;
- An exterior revetment of mostly vertically oriented filaments with a bimodal size distribution (some very fine, some thick).

A representative tuft from sample 1011 was also analysed using μCT at an almost identical pixel size of 6.88 μm. In contrast to sample 805, the biomass was homogeneous (not stratified) and exhibited neither alternating lamination densities, nor a dense revetment surrounding the tuft-like convexity (Fig. 6C). This is consistent with SEM images of a well-mixed community throughout (Fig. 3D-J). Denser particles occur both within the tuft and at its peak (Figs. 3D, 6D), but are gypsum and celestine (XRD and EDS analyses, not shown), which had precipitated as a result of evaporative processes. Contrary to the tufts of sample 805-Cu, the pinnacles in sample 1011 did not produce textural divisions that are visible in μCT, nor intimate micromorphological relationships between biomass (Fig. 6C-E). Crucially, this comparison demonstrates that differing geochemical stresses do not necessarily produce convergent micromorphological expressions. It is thus reasonable only to use *detectable* micromorphologies as a morphogenetic tool to explain the origins of fossil OSS under the assumption that remnants of these micromorphologies may be preserved in the fossil record. This comparison is made in Section 3.2.

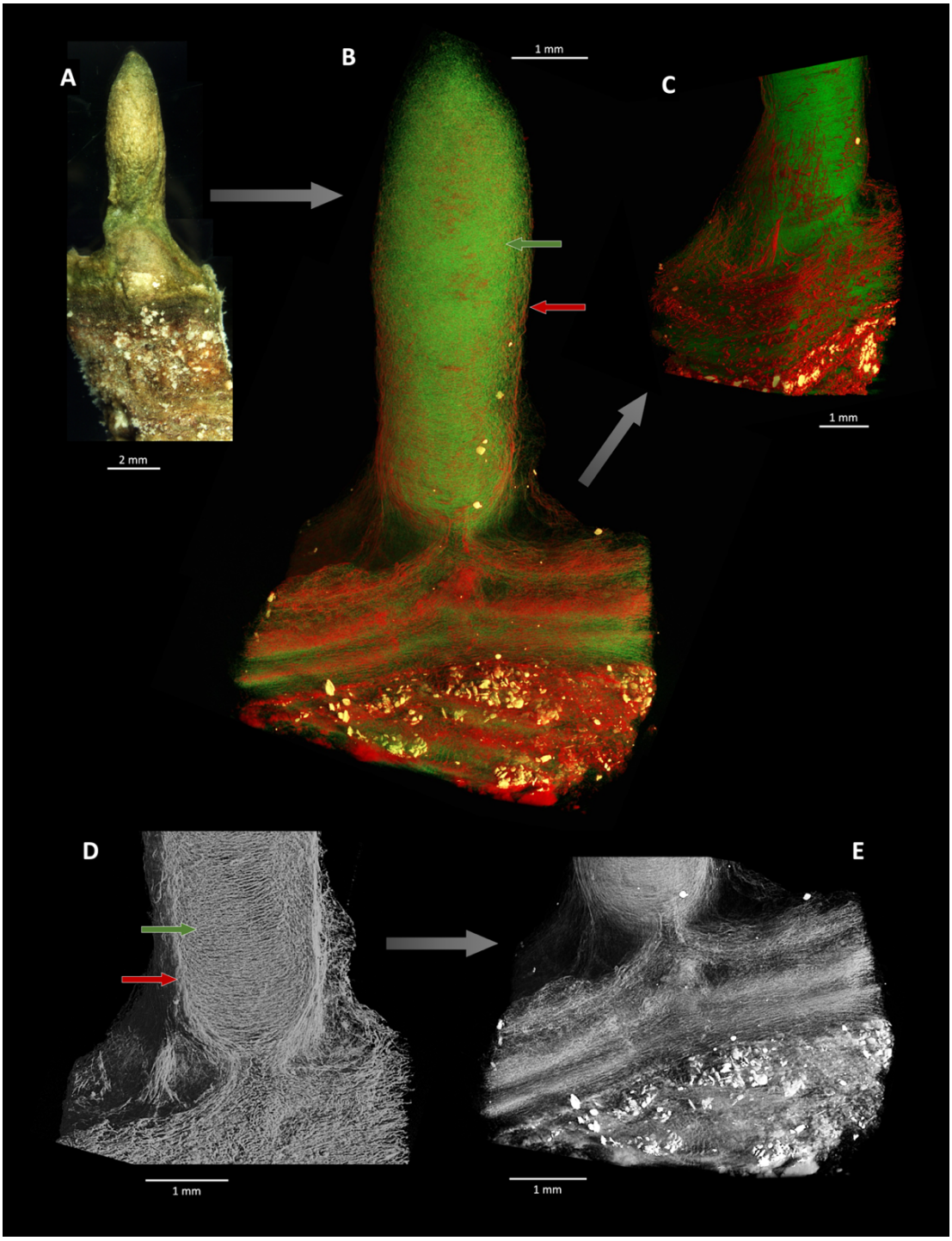

Fig. 5. Micro-scale X-ray computed tomography of a lyophilised pinnacle-like structure from sample 805-Cu. **A**) Photograph of analysed pinnacle. **B**) Three-dimensional rendering of the same structure, separating three phases: green = filamentous *Coleofaciculus* biomass; red = heavier, metal-enriched biomass corresponding to sheath-EPS-*Chloroflexus*-rich layers; gold = denser mineral phases. Note that the metal-enriched layer rendered in red (red arrow) forms a partial revetment around the less dense pinnacle biomass (green arrow). **C**) Close up view of pinnacle base. **D**) Cross-section view through pinnacle showing vertical orientation of filaments in the revetment (red arrow) and horizontal lamination of the inner biomass (green arrow). **E**) Cross-section view through basal microbial mat material showing filamentous variation and dense particles. Conditions of acquisition: voltage = 120 kV; current = 150 mA; frame acquisition time = 750 ms; number of views = 1,200; pixel size = 6.87 µm. Grey arrows indicate correspondence between images.

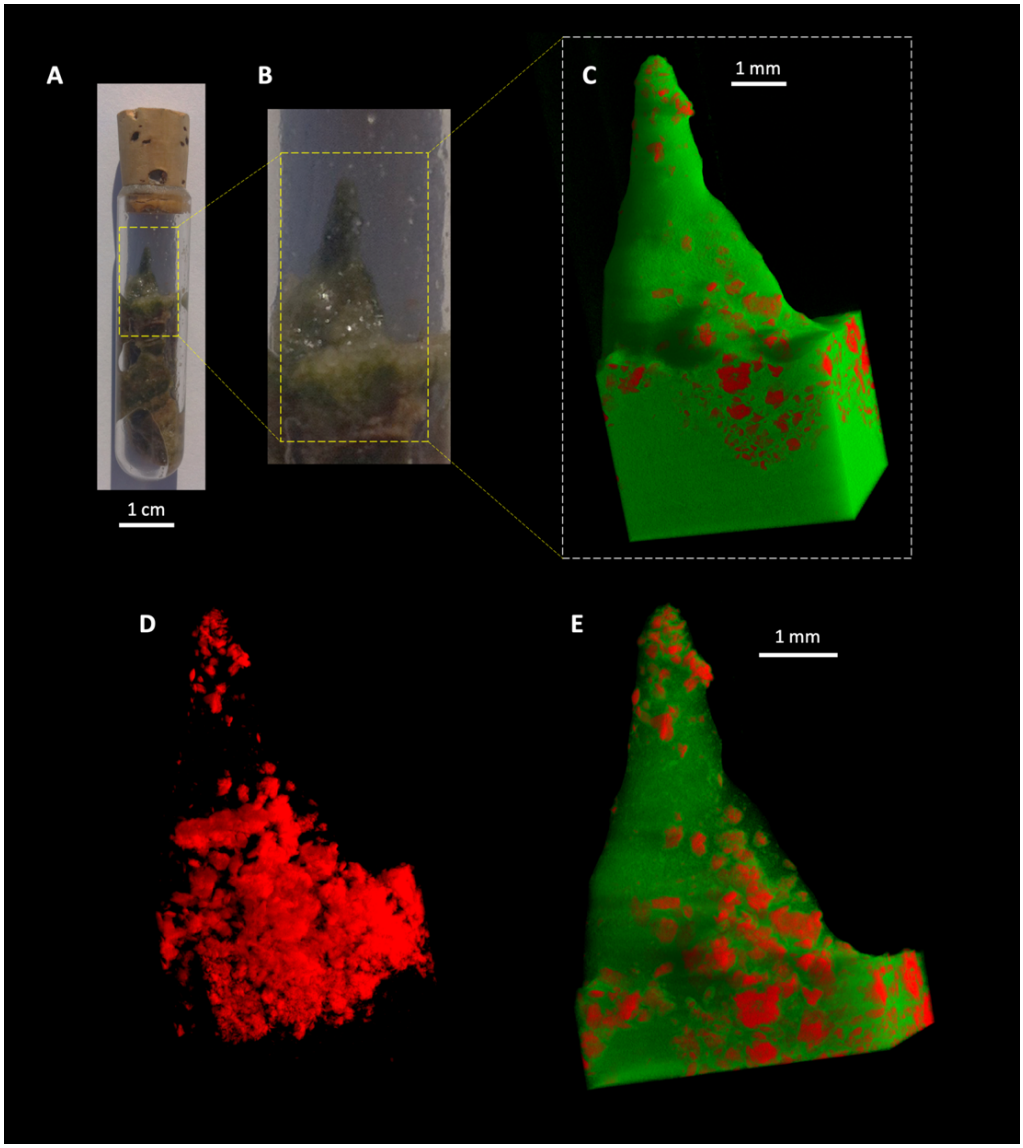

Fig. 6. Micro-scale X-ray computed tomography of a glutaraldehyde-fixed tufted microbial mat from sample 1011, grown naturally under high salinity. **A-B**) Photographs of sample 1011 contained in a sealed glass tube during analysis to prevent its obliteration due to water content. **C**) Three-dimensional rendering of the scanned volume, distinguishing two phases: green = homogeneous biomass; red = gypsum. No fine-scale density contrasts between bacterial biomass exist, i.e., biomass resolves within similar densities (equivalent to green in Figure 7). **D**) Distribution of gypsum and celestine within the tuft, i.e., at the base and at the top of the tuft. **E**) Relationship of biomass and gypsum and celestine within the tuft, where biomass is rendered semi-transparent. Note that there are no identifiable textural relationships between biomass and salts that indicate fabric formation due to salt stress. Conditions of acquisition: voltage = 120 kV; current = 150 µA; frame acquisition time = 750 ms; number of views = 1,700; pixel size = 6.88 µm.

3.2. Precambrian Samples

3.2.1. Petrographic characterisation

Domical-conical stromatolites from the Dresser Formation (sample DF1) exhibit convexities on the scale of millimetres to centimetres (Fig. 7). Sampled stromatolites have a laminar-domical macrostructure, and supra-laminar micromorphologies (in this case, supra-

domical complexities with conical forms). In other words, the laminations forming centimetre-scale domical structures (the macrostructure; Fig. 7E-F) also form irregular conical complexities that rise out of individual domes. Thin section observations show that laminae are non-isopachous, i.e., of inconsistent thickness throughout three dimensions, and are punctuated by fenestrae (Fig. 7A-D). Raman spectroscopy shows that the stromatolites comprise silica (SiO_2), baryte ($BaSO_4$) and haematite (Fe_2O_3) (Fig. 9A-F), three minerals that may be easily separated in μCT due to their density differences (2.65, 4.48 and 5.24 gcm^{-1}, respectively). Together with fenestrae, which are either voids or poorly silica-infilled spaces, the relationships between all phases may be easily reconstructed in three dimensions. The Dresser stromatolites thus make ideal candidates in which μCT may resolve lamination-scale features indicative of the biological processes. The ease with which one can analyse individual laminations in 3D enables direct comparison with the μCT scans of samples 805-Cu and 1011, which have superficially similar topography. Furthermore, modern and Precambrian samples are often of similar dimensions and, if formed by similar microbial consortia (phototrophs including cyanobacteria and/or anoxygenic photosynthesisers), may enable ecophysiological morphogenetic comparison.

Micro-tufted microbial mats from the Middle Marker horizon (sample MM1; Fig. 8) present a complementary case. These laminations occur in fine-grained silicified sediments, and feature tufts around 100 μm in size (Hickman-Lewis et al., 2018), similar to microbial structures from the Dresser Formation (Noffke et al., 2013). Raman spectroscopy identifies three major phases (the silica matrix, laminated carbonaceous material and anatase) and two minor phases (muscovite and rutile), the latter occurring as isolated grains (Fig. 9G-L). The petrological context of these microbial mats presents a challenge for μCT, since the atomic masses of C and Si – the dominant phases in the structure and matrix – are very similar. Raman spectroscopy indicates that TiO_2 (anatase) co-occurs with laminated carbonaceous material (Fig. 9K), which may ease the visibility of laminations in μCT renderings.

3.2.2. X-ray μCT

Sample DF1 has a domical-conical macrostructure (Fig. 10A-B) and is composed of three variably dense phases that can be readily extracted in volumes of stromatolite DF1 (Fig. 10C), corresponding to silica, baryte and haematite (red, yellow and white in Fig. 10). The sample also includes a large volume percentage of fenestral void space (blue in Fig. 10B, arrowed in Fig. 11). Three cone-like microstructures (supra-domical complexities) were identified within the scanned volume and analysed using μCT (Figs. 10D-F, 11). These conical micromorphologies preserve two fabrics:

- A poorly preserved, less dense (red-yellow, i.e. mostly silica) interior fabrics with a mostly randomly oriented structure. The central region has weak remnant lamination (indicated by dashed white lines in Figs. 10D, 11A).
- An exterior fabric of thick laminations overlying the interior fabric, producing a revetment of slightly higher density (yellow-red, i.e. mostly haematite; arrowed in Fig. 10D).

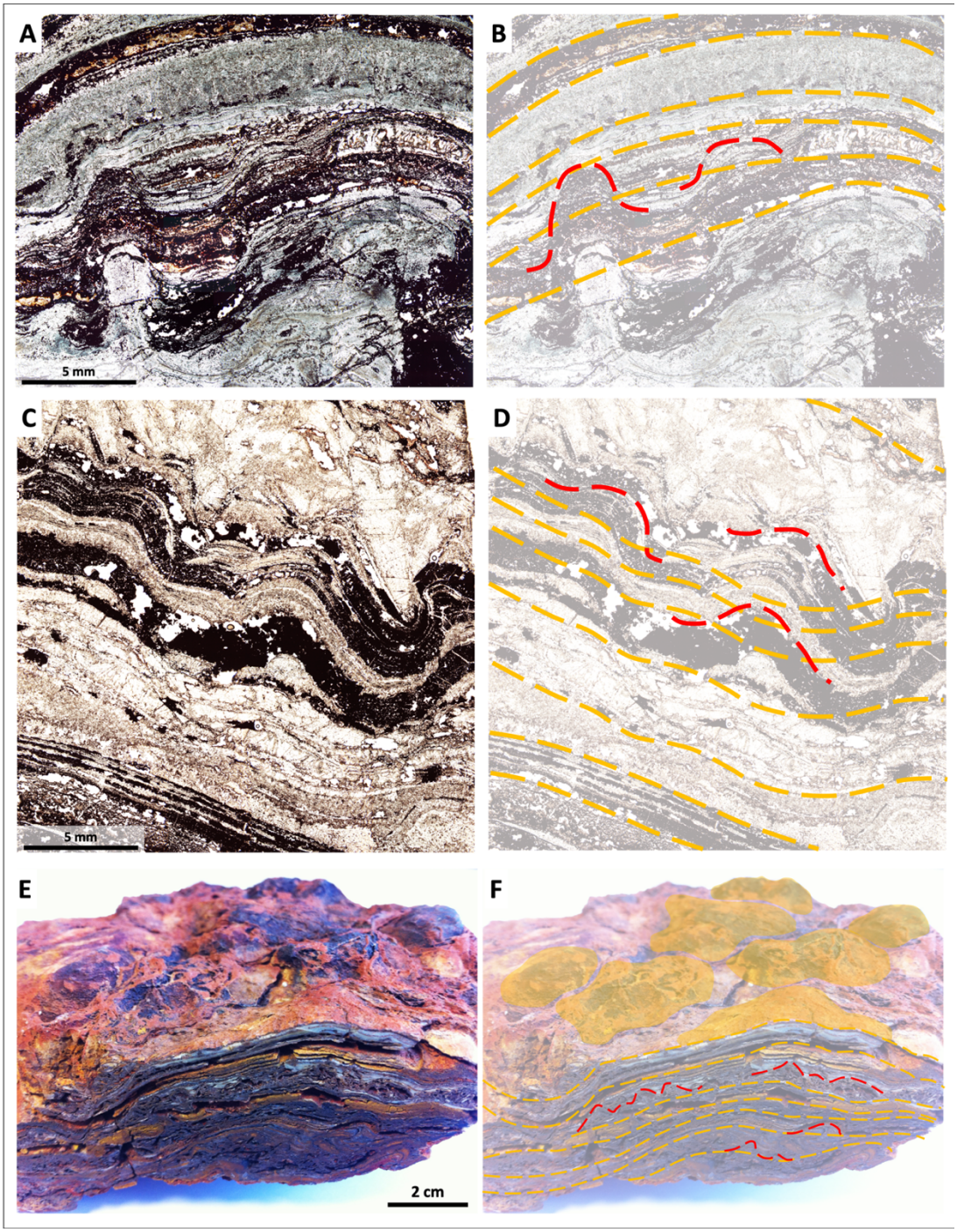

Fig. 7. Petrography of 3.481 Ga Dresser Formation organo-sedimentary structures (stromatolites, sample DF1). Images at the left are unaltered, images at the right show interpreted horizons corresponding to a macrostructure with domical macrostructure (gold dashed lines) and the supra-lamina conical complexities arising from certain laminations (red dashed lines). Note the difference in scale of the topography of the macrostructure (centimetre-scale, not wholly observed within the photomicrographs) and supra-lamina complexities (millimetre-scale). **A-B**) Photomicrograph of domical stromatolite from which samples were taken for Raman analysis (Fig. 9) and X-ray µCT scanning (Figs. 10-11). **C-D**) Undulating domical stromatolites from a second sample. **E-F**) Photograph of representative hand sample with domed upper surface.

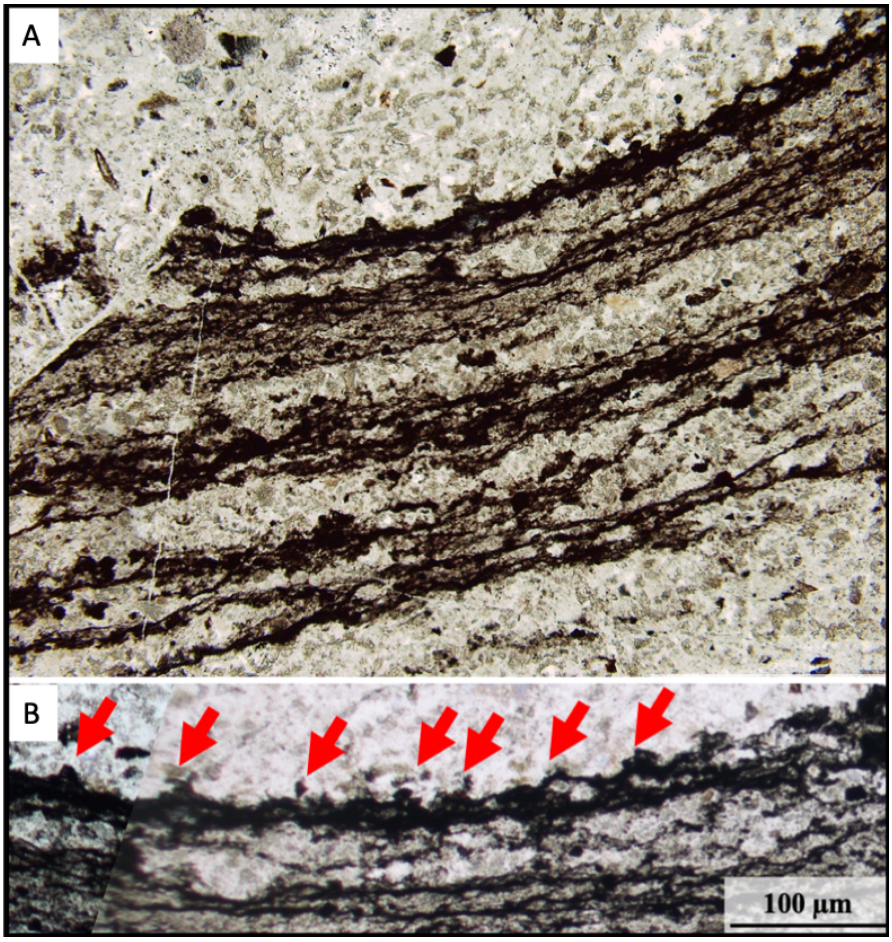

Fig. 8. Micro-tufted, multi-laminar microbial mat from the 3.472 Ga Middle Marker horizon (sample MM1), from which samples were taken for Raman analysis (Fig. 9) and X-ray µCT scanning (Fig. 12). **A**) Wide view (field of view = 2 mm). **B**) Close-up view of micro-tufted laminations, each tuft indicated by an arrow.

Sample MM1 presents a different case. The association of carbonaceous material with anatase allows the clear distinction of the microbial mat in three dimensions. Three phases can be distinguished in our X-ray µCT scans:

- the silica matrix (grey in Fig. 12), which is present throughout the entire sample volume;
- carbonaceous material (green in Fig. 12), enriched in microbial laminations;
- denser phases (red in Fig. 12) corresponding to anatase associated with the microbial laminations and altered volcanic particles and unsilicified particles both entrained within the laminations and scattered throughout the matrix. Dense particles are sometimes surrounded by filament-like carbonaceous material (arrowed in Fig. 12).

X-ray µCT of sub-volumes from the analysed cylinder illuminates the non-isopachous character of the laminations (Fig. 12B, G), demonstrates the ubiquitous silicification of the sample (Fig. 12F, L), and illuminates the microstratigraphy within individual lamina sets (e.g. Fig. 12H). It is not, however, possible to distinguish interior and exterior fabrics within these smaller-scale convexities. The microbial laminations comprise carbonaceous material and microcrystalline silica, the latter being the preservational agent and the overwhelmingly dominant matrix component.

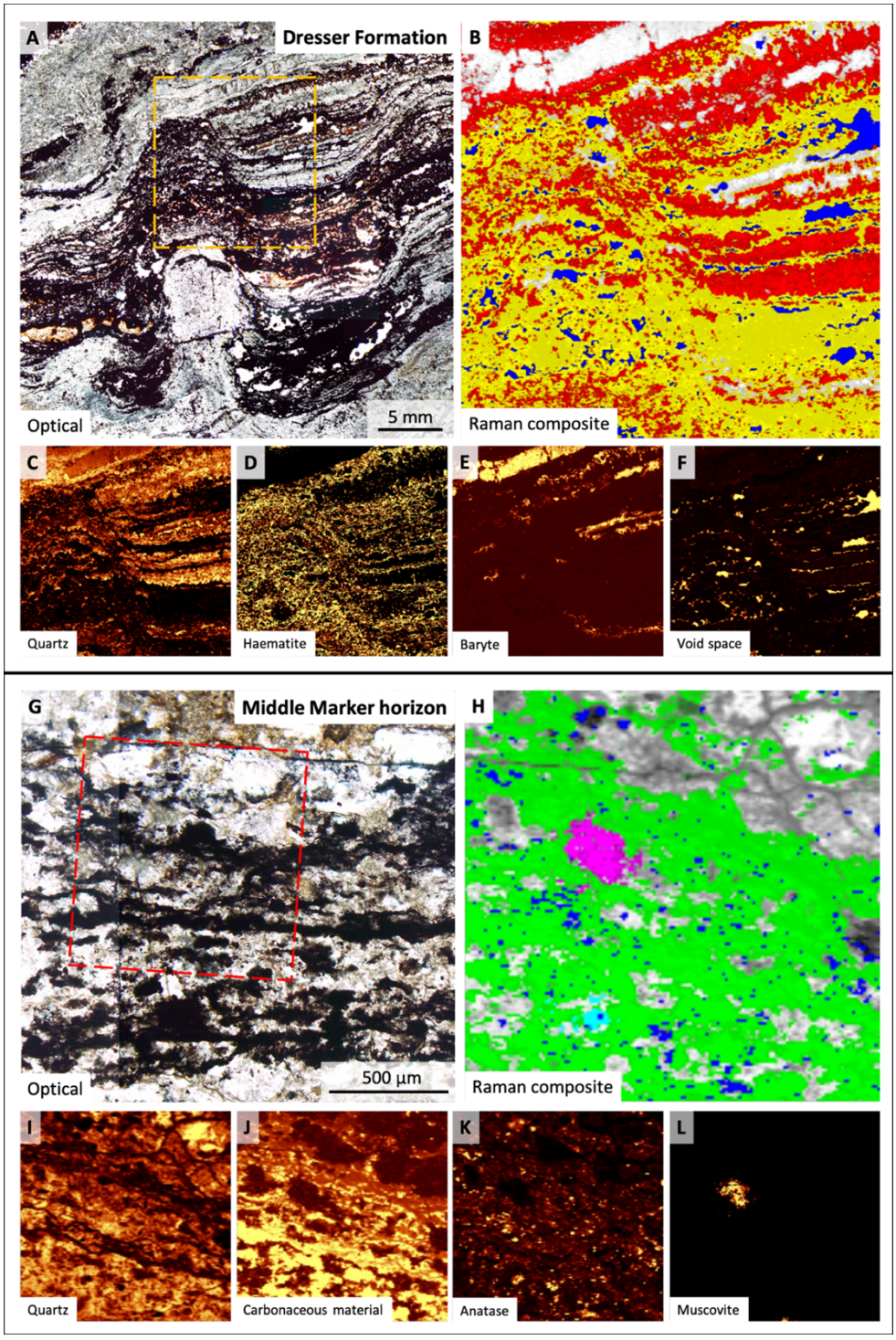

Fig. 9. Raman spectroscopy mineralogical mapping of the two studied Precambrian samples. **A-F**) Dresser Formation stromatolites (sample DF1). **A**) Photomicrograph of the supra-lamina conical complexity analysed. Box indicates region of analysis. **B**) Composite Raman map: yellow = haematite; red = quartz; white = baryte; blue = void space (araldite resin). **C-F**) Raman heat maps for quartz, haematite, baryte and void space. Scan parameters: objective Nikon E Plan 20x, 5x5 mm², 400x400 pixels (spectra), laser power 8 mW. **G-L**) Middle Marker microbial mats (sample MM1). **G**) Photomicrograph showing several microbial laminations in a coarse, sand-grade, silicified sediment. Red box indicates region of analysis. **H**) Composite Raman map: grey = quartz; green = carbonaceous material; dark blue = anatase; fuchsia = muscovite; light blue = rutile. **I-L**) Raman heat maps for quartz, carbonaceous material, anatase and muscovite. Note correlation of carbonaceous material with anatase. Scan parameters: objective Nikon E Plan 20x, 1.2x1.2 mm², 150x150 pixels (spectra), laser power 5 mW.

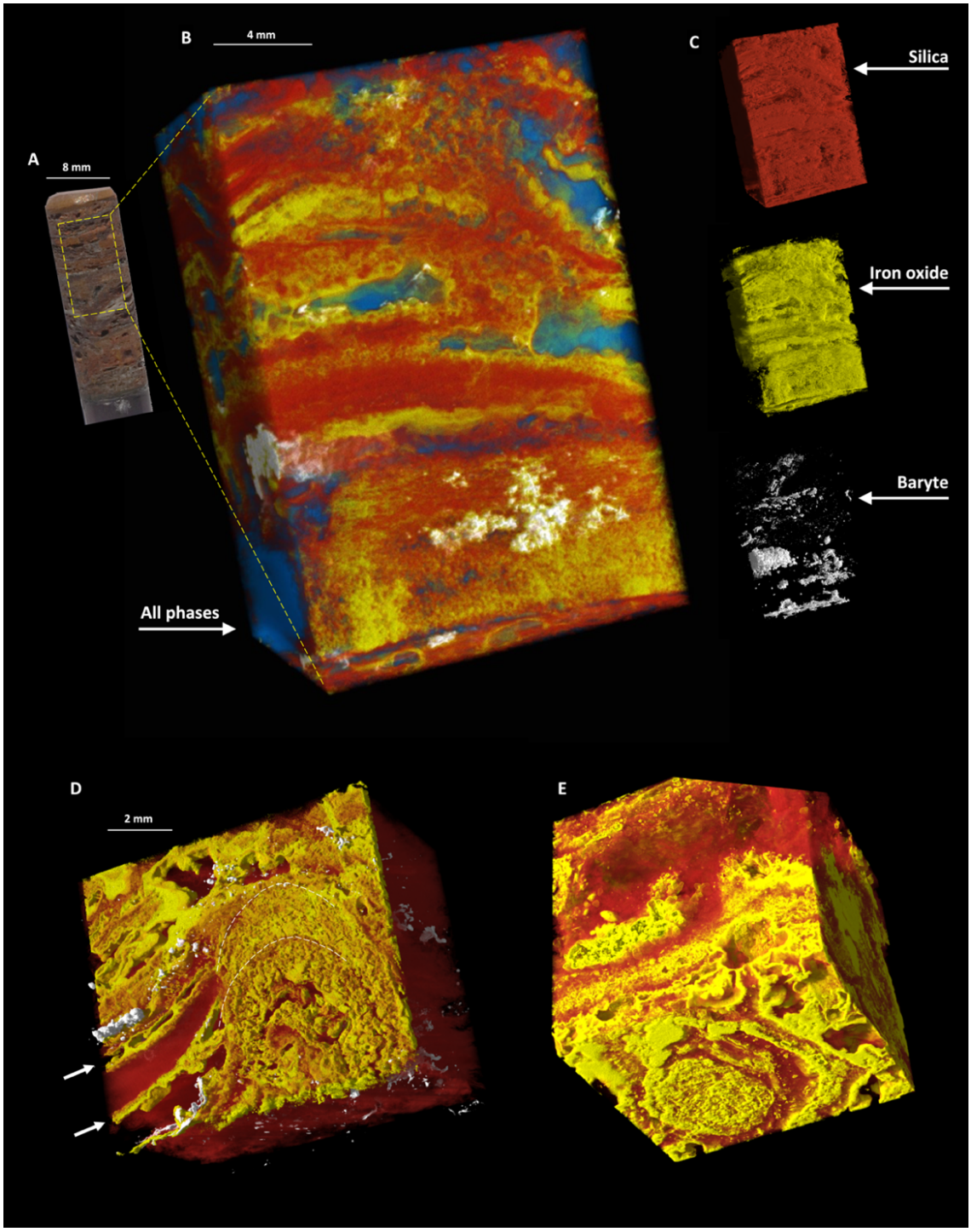

Fig. 10. X-ray µCT of a domical stromatolite from the Dresser Formation (sample DF1). **A**) Photograph of the cylinder analysed. **B**) Three-dimensional rendering: yellow = silica; red = iron oxide (haematite); white = baryte; blue = void space. **C**) Distributions of the three mineral phases from the volume shown in B. **D-E**) Tomographic reconstructions of two conical structures (supra-domical complexities) superposed on the limbs of the domical stromatolite. Morphological comparison can be made with the pinnacular microbial mat grown in a Cu-enriched medium (sample 805-Cu; Fig. 5). White dashed lines indicate weak remnant laminations forming the silicified body of the dome. White arrows indicate haematite laminations forming poorly preserved revetment-like fabrics around the cone, analogous to those of the sheath-EPS-Chloroflexus layers surrounding the pinnacles of sample 805-Cu (Fig. 5C-D). **E**) Basal view of dome (circular cross-section visible). Conditions of acquisition: voltage = 120 kV; current = 150 µA; frame acquisition time = 750 ms; views = 2,000; pixel size = 3.86 µm.

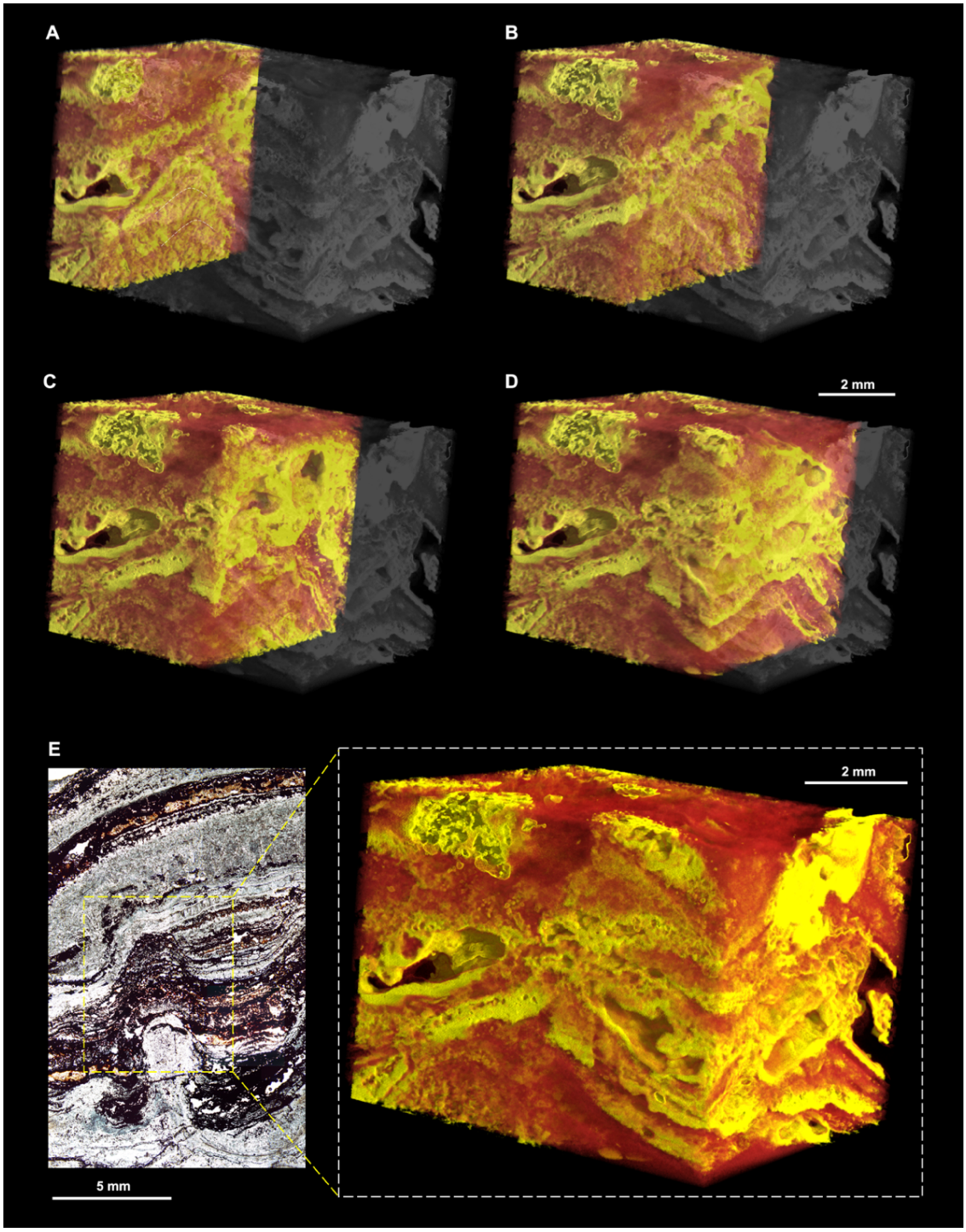

Fig. 11. Tomographic reconstruction of a cone from the Dresser Formation stromatolite (sample DF1), using a cylinder cut from the sample corresponding to photomicrograph E. **A-D**) Sequential reconstructions through the volume of the cone showing fabrics of interest: weakly laminated central region (dashed white lines in A) surrounded by a strongly laminated layer resembling the revetment layer in Fig. 5C, and a fenestral cavity (void space). These scans clearly elucidate the three-dimensional lamina-specific characteristics of the stromatolite and the relationships of microfabrics that can be equated to those of modern microbialites. Ghost volume of the entire sample is shown on each scan to allow interpretation of microstructures within the macrostructure. **E**) Whole volume scan of the cone shown in A-D, directly compared with a photomicrograph of the conical-domical structure to which it corresponds. Conditions of acquisition: voltage = 120 kV; current = 150 µA; frame acquisition time = 750 ms; views = 2,000; pixel size = 3.86 µm.

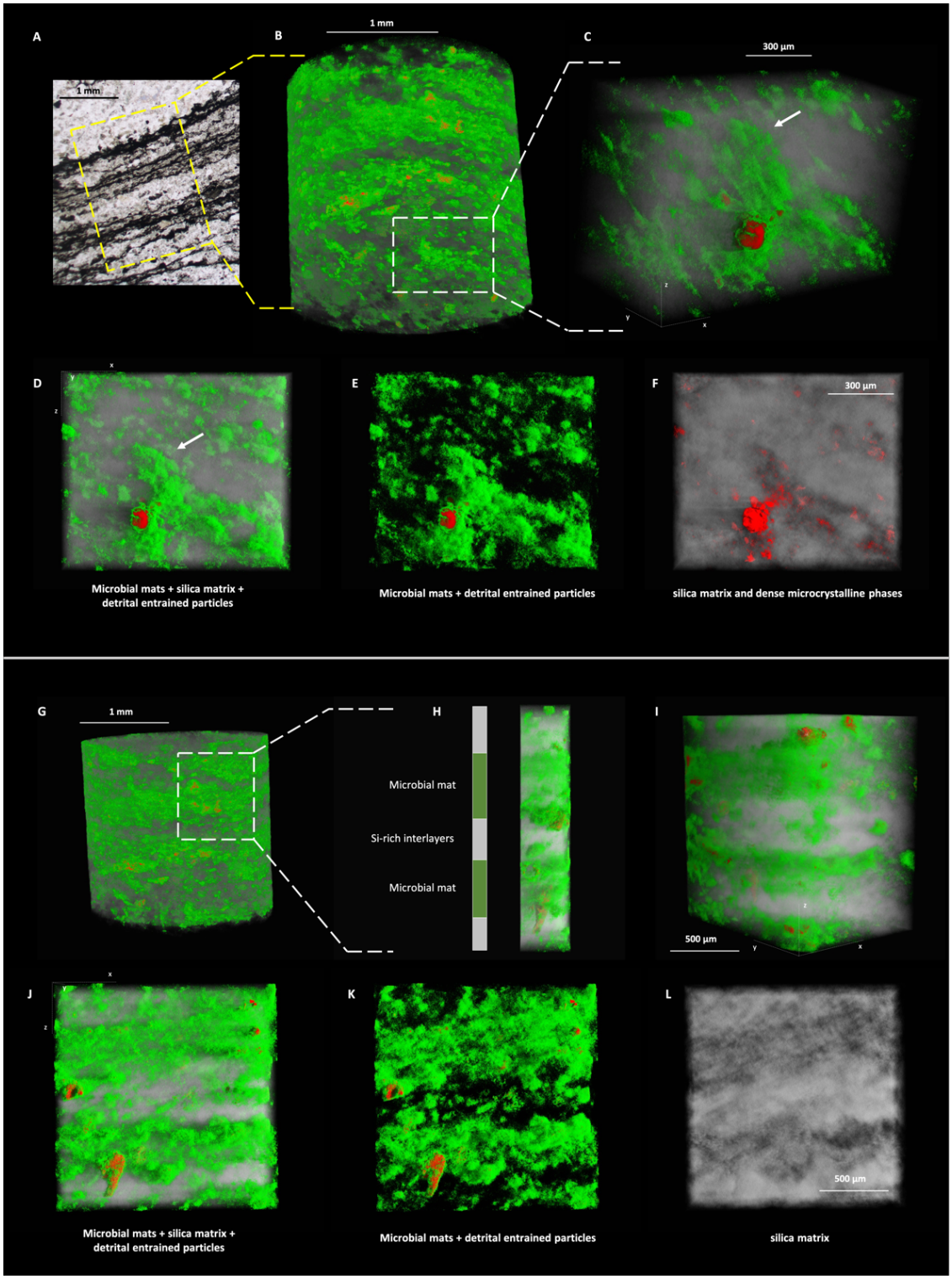

Fig. 12. X-ray µCT scans of carbonaceous laminations in a biolaminated sediment from the Middle Marker horizon (sample MM1). **A-B**) Photomicrograph and X-ray µCT scan of micro-tufted microbial mats. Yellow box in A indicates lamina stack equivalent to that shown in B. White box in µCT scan indicates sub-volume shown in C-F. **C**) Perspective view of sub-volume containing a ~400 µm tuft preserved in three dimensions (arrowed). Green = carbonaceous lamination; grey = silica matrix; red = denser phases. **D-F**) Anterior views through the tuft (arrow in C equivalent to arrow in D). Note the association of denser material, resulting largely from anatase accumulation (see Fig 9K), with laminations (E-F). Note also the large red particle, which appears to be an equant grain bound by microbial filaments. **G**) Sub-volume from the same cylinder comprising flat-laminated microbial mats (white box). **H**) End view of the second sub-volume, distinguishing microbial mat laminations (green) and

silica-rich interlayers (grey). Colour-coded column indicates layering. **I)** Perspective view of the sub-volume showing the non-isopachous nature of the laminae. Red objects indicate denser phases entrained within the laminations. **J-L**) Anterior views of the sub-volume showing the alternation of layers rich in carbonaceous matter and rich in silica. Phases are coloured consistently by density throughout this figure. Conditions of acquisition: voltage = 110 kV; current = 100 μA; frame acquisition time = 1,000 ms; views = 1,800; pixel size = 1.19 μm.

4. Discussion

4.1. Comparative morphogenesis in modern and ancient microbialites

The following provides a summary of the results obtained together with potential implications:

i) Microbial mat communities grown in the presence of enriched concentrations of toxic Cu (sample 805-Cu) formed large surface convexities, termed pinnacles, atop their macrostructure (Figs. 1, 3). Pinnacles did not develop in the presence of other metal enrichments (Fe, Ni, Mn and Sr were tested; Fe results shown (sample 805-Fe) in Fig. 4A). We thus infer a causal relationship between elevated Cu concentrations and the development of surface convexities. Phototaxis can be excluded as the driver of pinnacle growth, as the light intensity at the surface of the mats was homogeneous.

ii) SEM imaging (Figs. 2-3) and μPIXE elemental mapping (Fig. 4) demonstrate that the community forming both the mat and pinnacles (*Coleofasciculus*-*Chloroflexus*) appears to stratify into two distinct layers in the presence of Cu (Fig. 5D). The first is an inner *Coleofasciculus*-rich layer which exhibits some laminated micromorphology, and the second is a thin sheath-EPS-*Chloroflexus* layer (Fig. 2-3) forming a sparse revetment on and between the pinnacles (Fig. 5). This spatial segregation (the inverse of that in the 805 field sample) occurs as a function of organismal tolerance to Cu, i.e. *Chloroflexus* is Cu-tolerant, whereas *Coleofasciculus* is intolerant to Cu and retreats to the interior, producing EPS and discarding sheaths in the outer layer (Fig. 2H-I).

iii) Since heavy metal enrichments (Cu, Fe, Mn) give rise to density contrasts, X-ray μCT can corroborate this morphogenetic process, detecting the slight density differences between the denser sheath-EPS-*Chloroflexus* layer and the less dense *Coleofasciculus* layer (Fig. 5), consistent with the binding of heavy elements in the former. Although only Cu is toxic, its sequestration co-locates with Mn and Fe, suggesting that the exuded EPS is non-specific in its capacity for metal binding (see Decho, 2000; Gupta and Diwan, 2017). (Fig. 4E). Fe and Mn are not toxic to either of these organisms, but their downward diffusion is nonetheless limited by the ecophysiology of the microbial consortium. μCT shows that *Coleofasciculus* is the architect of the pinnacles, which grow out of the *Coleofasciculus* layer beneath (Fig. 5B, E), consistent with its enhanced response to Cu toxicity. Pinnacle formation is thus a mitigation of toxicity stress. X-ray μCT also discerns the textures of density-distinct layers: horizontally and randomly oriented filaments in the inner region and vertically oriented filaments in the revetment (Fig. 5).

iv) Although microbial mats from the same sampling locality and with the same initial community composition can develop superficially similar pinnacle or tuft-like

morphologies in the presence of different geochemical stressors (i.e., toxic elements for samples 805-Cu and increased salinity for sample 1011), not all forcings create micromorphological features that can be tomographically distinguished by tomography and used as interpretative tools for fossil morphogenesis. X-ray μCT cannot resolve density contrasts where no such contrasts exist, as in sample 1011 (Fig. 6C) which, despite having experienced salinity stress, has not segregated its community (Fig. 3D-J). Ergo, reactions to geochemical stresses may or may not bestow upon the geological record a detectable 3D morphology from which the causal stressor in a fossil example could be determined. Unlike many conical OSS, the supra-lamina complexities studied herein are not exclusively biophysical responses but result from interactions with the environment over small temporal and spatial scales (Batchelor et al., 2004; Petroff et al., 2013).

v) X-ray μCT scans of two Precambrian OSS – samples DF1 and MM1 – show that these ancient microbialites exhibit 3D characteristics that echo those in samples 805 and 1011. The comparison is particularly close, despite some recrystallisation, in the case of the Dresser Formation domical-conical stromatolite (DF1) and sample 805-Cu. Both feature two-layer microstructures consisting of a poorly laminated central region (the cone/pinnacle) surrounded by a revetment. The Middle Marker mats (MM1), contrastingly, can be compared qualitatively to sample 1011, but it is difficult to make conclusive statements concerning their morphogenesis, since the modern process analogue sample 1011 did not exhibit induced micromorphologies resulting directly from salinity stress.

vi) Both modern and Precambrian OSS exhibit multi-scale topographic complexities, e.g. pinnacles and cones atop flat-lying, undulating or domical macrostructure. Morphologies in modern samples studied by μCT (pinnacles, cones and tufts) are supra-lamina complexities resulting from geochemical stresses over short timescales. These millimetric features, superimposed upon the macrostructure, may reflect either what Petroff et al. (2013) called "growth in a randomly fluctuating environment" or intrinsically stochastic processes resulting from biofilm-scale complexities, for example, biofilm roughness, surface fractal dimension, biofilm compactness and interior transport potential (Picioreanu et al., 1998). Similar structures in ancient OSS may be interpreted as having an equivalent morphogenesis.

It is thus possible to make a comparison between the modern and ancient OSS studied in terms of pulsed growth in response to a changing environment. In the following, we focus on biophysical and ecophysiological processes, parameters and models that might further substantiate this idea, and assess the potential of interpreting Precambrian OSS using modern microbialites as process analogues. This will aim to answer i) to what extent are palaeoenvironmental characteristics reflected in micromorphological signatures, and how might these signatures be observed using three-dimensional correlative microscopy? and ii) can detectable features at the scale of individual laminations confirm the morphogenesis (and therefore biogenicity) of ancient OSS in the absence of microfossil preservation?

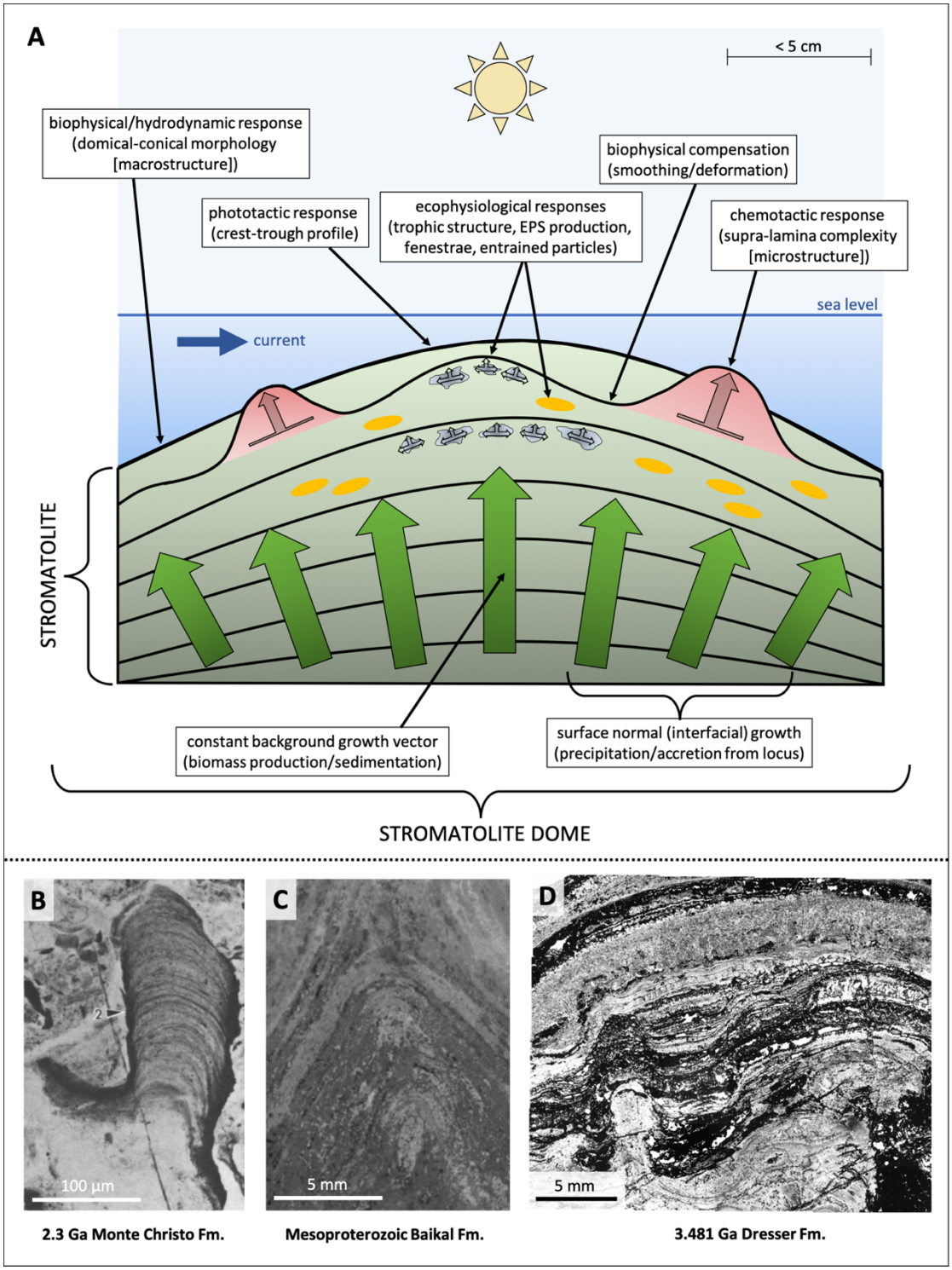

Fig. 13. Synthesis of our approach to the mechanistic morphogenesis of organo-sedimentary structures growing under geochemically stressed conditions, with relevant examples from the geological record. The growth vectors considered are those evoked in the mathematical models described in Section 1.2., such that this schematic might be used as a means of predicting stromatolite morphology, or retrospectively resolving misfits in observed morphology with model predictions. **A**) Schematic growth model highlighting ecophysiological, biophysical and hydrodynamic processes involved in stromatolite growth together with resulting macroscopic and microscopic morphologies. **B-D**) Three examples of topographic complexities in stromatolites from the geological record (Lanier, 1986; Bosak et al., 2013, this study). The morphology of B is dominated by phototactic processes and surface normal growth, producing recognisable overhangs. C is controlled by surface normal and phototactic

processes, with considerable ecophysiological contributions (non-isopachous laminae, fenestrae) providing distinctive evidence for biology. D, as described herein, is a more complex morphology characterised by phototactic, surface normal, and ecophysiological processes, upon which is superimposed evidence for chemotactic forcing on short timescales. Mesoscopic study of stromatolite morphology (e.g. Petroff et al. 2010, 2013) and outcrop study of centimetre- and metre-scale stromatolite reefs (e.g. Allwood et al., 2009) could underpin the significance of microscopic, lamina-scale characteristics (this study).

4.2. Three-dimensional morphogenetic signatures

Microbialite growth is governed by a wide range of parameters relating to community composition (intrinsic) and the external environment (extrinsic), each of which leaves deducible traces in the structure (Fig. 13). Comparing modern and ancient OSS to identify microstructural similarities meets the challenge of stromatolite 'bioconfusion' raised by Awramik and Grey (2005): that we should be able to make estimations of biogenicity in controversial ancient stromatolites based on uniformitarian comparisons against modern stromatolites, however, we will fail to do so for as long we lack a unified morphogenetic framework. Mathematical modelling of stromatolite growth based upon observations of natural samples, as outlined in Section 1.2, has been crucial in parameterising morphogenetic processes. The definitions of the terms of each equation provide a means of predicting the eventual morphologies of OSS, and mismatches between expected and measured morphologies identify inconsistencies requiring explanation (Cuerno et al., 1986), which may be biological.

In vivo, the biogenetic processes in microbial biofilms are governed by the production of autoinducer molecules that interact with biofilms and control their interactions with the environment as a function of local cell-population densities (Dupraz et al., 2006; Karatan and Watnick, 2009; Tice et al., 2011; Decho et al., 2012). Autoinductive signaling is strongly linked to the concentration of quorum-sensing bacterial cells, and controls phenotype expression, for example, the formation of biofilms after the adhesion of members of the community onto one another through the production of a matrix of extracellular polymeric substance (EPS) (Busscher and van der Mei, 2012). Although many functions of EPS are speculative (Tice et al., 2011), it certainly functions as a structural entity (Decho, 1990) and as one part of the external environmental compartment of the metallome (*sensu* Williams, 2001; Fraústo da Silva and Williams, 2001), which is to say that it supports the biofilm and hosts both sequestered metals and extracellular metalloenzymes within the biofilm microenvironment (Geesey and Jang, 1989; Schultz-Lam et al., 1993; Loaëc et al., 1998; Decho, 2000; Busscher and van der Mei, 2012). Carboxyl residues of peptidoglycan and teichuronic and teichonic acids within the cell wall, proteinic outer-membrane lipopolysaccharide polymers (and capsules where present), such as carboxylate (alduronate and pyruvate), hydroxyl (tridentate), sulfates and amine groups are active sites of metal sequestration (Geesey and Jang, 1989), and may account for the aggregation of microbe-metal signatures (Margulis et al., 1983; Juniper et al., 1995; Cameron et al., 2012). This immobilised metallic signature, the cell-associated metallome, may also leave an imprint in the fossil record since it is difficult to resolubilise metal out of specific organic sinks, such as bacterial cellular products, which tend to outcompete other chemicals in natural systems in terms of metal retention (Schultz-Lam et al., 1993). Although metallic elements serve essential functions to most bacterial metabolic pathways (Zerkle et al., 2005; Robbins et al., 2016; Moore et al., 2017), many, including Fe, Ti, Zn, Cu and As, are toxic to certain microbial strains and communities. When toxic metals are enriched in the local environment, induced production of EPS and modification of the local environment has often

been observed as a mechanism to sequester these elements (Sánchez-Román et al., 2014; Armendariz et al., 2015; Nocelli et al., 2016). This may be particularly necessary at the interface between microbial mats and the overlying water column since the basal millimetres of the medium are characterised by laminar, poorly mixed flow (cf. Tice et al., 2011) in which toxic elements may become concentrated. This situation resembles the aquaria studied herein, where Cu- and Fe-enriched waters remained in contact with the growing mat, and a response to toxicity was observed: the volume of EPS at the surface of sample 805-Cu (Fig. 2G-L) is far greater than that at the surface of sample 805-Fe (Fig. 2A-F). This environmentally driven phenotypic modification to sample 805-Cu accompanies ecosystem restructuring and results in non-specific metal-binding by EPS, demonstrated by correlated SEM imaging, PIXE elemental mapping and μCT three-dimensional reconstruction. EPS, abandoned cyanobacterial sheaths, and Cu-tolerant *Chloroflexus* are spatially correlated with enrichments in heavy elements (Fe, Mn, Cu) in the upper region of the mat, making possible their distinction in 3D scans. Neither SEM imaging nor X-ray μCT of sample 1011 show density- or orientation-distinct microfabrics but rather a well-mixed community throughout the tufts. This is most likely because salt stress does not adversely affect either of the members of the community, but is possibly due to perturbation of the surficial layer by osmotic pressure. The phenotypes exhibited by samples 805-Cu and 1011 are therefore distinct and morphogenetically explicable as functions of biological interaction with the environment.

Since chemical diffusion through the mat is greatest at regions of high curvature (Petroff et al., 2010, 2013), increased EPS production in surficially complex structures in the presence of stress should contribute to increase their surficial complexity. EPS production is thus a morphogenetic and morphological parameter that is driven by both intrinsic biological and extrinsic environmental factors. We tentatively suggest that this process is a candidate for quantifying the random noise parameter of the KPZ equation, and that the produced morphology is a definitively biological microstructure: EPS- and sheath-rich layers, i.e., with extracellular contributions from both *Coleofasciculus* and *Chloroflexus*, surrounding biomass-dominated layers. Attempts to model the fit of microbialite growth in environments stressed by variable concentrations of biotoxic elements would be a promising means by which to confirm geochemical stress as a driver of morphological complexity. Future modelling efforts taking into account differential microbial responses to an applied stress field may enable the small scales at which models are no longer applicable due to increased contributions from 'noise' to be quantified. Since EPS has a high potential for fossilisation (Orange et al., 2012), a surficial complexity of small scale (pinnacle/cone/tuft) may be exceptionally preserved in the fossil record as a biologically indicative, macroscopically visible structure, as shown herein (Figs. 7, 8, 13). The pinnacles observed in 805-Cu are identifiable, discordant features at the scale of an individual lamination with spatial orientations perpendicular to the main body of the mat (Fig. 5C). The main body of samples 805-Fe and 805-Cu is a gently undulating, flat-laminated structure with mostly horizontal fabric and textural elements, however, this flatness may simply be a representation of the hydrodynamic stillness of the mat growth experiments relative to natural conditions; a repeating domical structure is more likely in hydrodynamically active environments (Petroff et al., 2010; Bosak et al., 2013). Fabric elements within pinnacles trend in multiple orientations: the *Coleofasciculus* interior is horizontally laminated, whereas the exterior EPS-sheath-*Chloroflexus* revetment is essentially vertically laminated (Fig. 5C). This micromorphological parallel between the pinnacles of sample 805-Cu and the supra-

domical structures of sample DF1 allows us to advocate the biogenicity of the latter controversial Archaean structures in light of modern examples. In contrast to previous estimates of their biogenicity, which have relied on characteristics of the macrostructure (Walter et al., 1980; Buick et al., 1981) and microfossil-like objects of unclear affinity (Ueno et al., 2001), we have provided herein a mechanistic interpretation of the micromorphology of these Dresser Formation stromatolites with reference to a well-characterised process analogue (sample 805-Cu). Our reasoning is logically consistent with that when ancient OSS are essentially identical to younger OSS, similar processes and forcings were likely involved in their formation (Awramik and Grey, 2005). We advance the suggestion of Cuerno et al. (2012), providing a mechanistic demonstration of a biogenic origin for structures that are not readily explicable through the terms defined by mathematical morphogenesis at small scales. A brief literature survey shows that such 'unpredictable' complexity is common in contemporaneous and younger stromatolites of biological origin (e.g., Walter et al., 1980; Lanier, 1986; Ueno et al., 2001; Kazmierczak and Kempe, 2006; Allwood et al., 2007; Harwood and Sumner, 2012), but is not present in stromatolite-like structures of more likely abiological origin (de Wit et al., 1982; Lindsay et al., 2005; McLoughlin et al., 2008), where the eventual morphologies can be predicted in terms of either KPZ or diffusion-limited dynamics alone. Given the valid application of KPZ, DLA and DLA-CA models to OSS of varying morphology, it is highly likely that the specific model required for morphogenetic studies of Precambrian OSS must be determined on a case-by-case basis, considering the petrological context given by correlative biogeochemical analyses.

Microbialite macrostructure is a function of particle accretion, hydrodynamics and competition irrespective of internal complexity (Hofmann, 1973; Petroff et al., 2010, 2013). This is corroborated by the 3D analyses shown herein but bulk morphology (the macrostructure) does not seem able to unambiguously prove biological origin. We propose that supra-lamina morphological complexities comprising the microstructure, in contrast to the macrostructure, may be demonstrated as being exclusively biogenic within the framework shown in Figure 13. Strategies of resilience to environmental stress, e.g., metal immobilisation, may have given rise to the multi-layer heterogeneous micromorphologies discernible by X-ray μCT. This provides an interpretation of DF1 stromatolites based upon the *morphogenesis* of the modern 805-Cu. Sample MM1, although exhibiting some parallels with sample 1011, for example, a homogeneous laminated structure entraining dense, suspended particles and tuft-like surface morphologies, does not preserve morphogenetically diagnostic textures. Since no unambiguously biogenic textural heterogeneities are identifiable in three-dimensional correlative microscopy, no mechanistic interpretation can be made regarding sample MM1 despite its qualitatively similar morphology to sample 1011. Tufted and reticulate mats such as these have been ascribed passive origins unrelated to stressed environments, for example the gliding motility of certain bacteria that causes reticulate structures to build after the collision, alignment and clumping of cells (Shepard and Sumner, 2010), or generalised behavioural processes in mat-building organisms with specific morphologies, such as sheathed filamentous microbes (Flannery and Walter, 2011). Regrettably, the approach developed herein does not allow us to make conclusive judgement as to whether such processes played a part in the morphogenesis of the studied tufted and micro-tufted microbialites.

Supra-laminar surface complexities are short-term growth phenomena likely preserved only in rapidly mineralised OSS, such as the silicified examples shown herein. In the Precambrian examples studied, the agent of preservation is silica, which was highly concentrated in the Archaean oceans as a consequence of the alteration of bedrock lithology, a lack of biological sinks and Si-rich hydrothermal effusions. Where such exquisite preservation is achieved, the three-dimensional correlative microscopy approach applied herein may assist in the determination of the correct morphogenetic model for understanding the origins of putatively biogenic OSS and distinguishing indications of their interaction with the palaeoenvironment. Microstructures with predictable biogenic origins should be considered strong morphological biogenicity criteria. In conclusion, 3D microstructures exceptionally preserved in ancient OSS may record short-term snapshots of the interactions between palaeobiology and palaeoenvironment. Such a bio-indicator circumvents the issues inherent in proving biology based only on *morphology*, since such structures uniquely prove biology based on *morphogenesis*. Morphogenetic bio-indicators should be considered a keystone to demonstrating the biogenicity of fossil OSS at the scale of individual laminations.

4.3. Morphogenesis reflecting evolutionary strategies through time

Have tolerances to elements changed over geological time in different microbial phyla? Differences in the magnitude of response to stressors and the temporal change in OSS morphologies throughout geological time (e.g. conical-domical Archaean forms versus dendritic Proterozoic forms) remain questions to be solved, but are potentially linked to evolutionary processes. Grotzinger and Knoll (1999), for instance, noted that whereas Archaean stromatolites appear to accrete mostly by lamina precipitation and preservation, Palaeoproterozoic and younger forms develop mostly *via* carbonate precipitation. In these two Era-defined groups of OSS, the magnitudes of certain terms in morphogenetic equations would be very different, implying a differing balance between intrinsic and extrinsic factors. The vast record of OSS with varied morphologies but similar structural elements (laminations, biominerals, bound particles, carbonate precipitation; Fig. 13) is evidence that they develop through a class of common morphogenetic processes producing a diverse suite of structures.

The timescale of growth of a biofilm is estimated at days to weeks (Gerdes and Klenke, 2007) and most fossil biolaminites and individual stromatolitic lamina therefore represent weeks to months of growth. Precambrian OSS can be classified either as stage 2 or stage 3 developing and climax consortia (Gerdes et al., 1991; Gerdes and Klenke, 2007; Noffke, 2010), and therefore once hosted trophic stratification, although this biological diversity is seemingly not preserved in the fossil record. The laminations inherent to all classes of OSS represent brief moments in geological time. The relationships between organisms with varying tolerance to certain geochemical stressors could form a part of the morphogenetic processes responsible for short-term changes of shape and form in Precambrian fossil OSS. While hydrodynamic factors define the macromorphology of OSS, short-term environmental stressors form demonstrably biosynthetic micromorphological peculiarities (e.g., pinnacles in sample 805-Cu) that do not follow the trends of structural elements in the macrostructure. Although one can only speculate on the differences in community composition between microbial mats and stromatolites in deep time, we note that since Archaean habitats would have contained higher concentrations of many metal and metalloid elements due to widespread volcanic activity and hydrothermal fluxes (Williams and Fraústo da Silva, 2003; Hofmann et al., 2011; Westall et al., 2018) the

morphological response to such enrichments at the scale of individual laminae should be more pronounced if communities exhibited similar responses then and now. Growth experiments show that mat-building consortia are capable of producing centimetric morphological responses to stress, but the consortia involved in the experiments presented herein (and indeed all other experiments with similar goals) are not necessarily direct analogues of Archaean communities, e.g. they include cyanobacteria, for which there is no compelling evidence before 2.7 Ga (Buick, 2008). Furthermore, metallic elements that are nowadays recognised as toxic often form an integral part of the metabolic machinery of anaerobic prokaryotes (Zerkle et al., 2005; Sforna et al., 2014), which were common mat-builders in the Archaean (Nisbet and Fowler, 1999; Knoll et al., 2016). The changing role of metals through geological time and their gradual incorporation or exclusion from the enzymes governing primary benthic productivity may have influenced microbial mat architecture over hundreds of millions of years. Morphological differences in OSS through time therefore represent, at the lamina-scale, either or both of i) differential exposure to ambient fluids enriched in toxic elements at the time of growth and ii) changing tolerances to toxic elements through geological time, as the loci of primary productivity shifted from anaerobic to aerobic photosynthesisers.

5. Conclusions

The modern and Precambrian examples analysed herein teach two several lessons for the interpretation of OSS morphogenesis in two and three dimensions. Where modern process analogues producing micromorphologies under certain experimental stresses yield 3D textural distinctions matching the micromorphologies of Precambrian structures, we propose that the former may be used as an interpretative framework for the latter. This provides a *morphogenesis*-based proof of biogenicity for ancient OSS, and overcomes the issues inherent in the proof of biogenicity based only on morphology, since morphologies may be the result of either biological or abiological processes. Where modern process analogues do not produce distinct micromorphologies, even in macromorphologies that grow under explicit ecophysiological stress, they may not be used as interpretative frameworks for Precambrian examples. Mechanistic palaeobiological interpretations based on morphogenesis are potentially powerful tools for determining the biogenicity of fossil OSS, but must be used with caution. Using this rationale, we have demonstrated that stromatolites from the Dresser Formation may be deemed biological based on 3D morphologies tied to morphogenesis, however, microbial mats from the Middle Marker horizon require further evidence than just morphology to determine their intrinsic ecophysiological growth processes. Morphologies of OSS that cannot be predicted by mathematical modelling (e.g., overhangs, supra-lamina complexities, localised fenestral cavities) should be considered indicative of microbial processes. Supra-lamination complexities as described herein are lamina-scale features that develop on short timescales in response to local geochemical stress and are a product of unpredictable growth. They may prove stromatolite biogenesis in the absence of microfossil preservation. Since microfossils are very rarely preserved in Archaean stromatolites, the burden of proof for stromatolite biogenicity usually falls upon characteristics of their laminations.

Although morphological similarity between two laminated structures is not sufficient evidence to draw a direct *palaeobiological* parallel between them, it is consistent with the

structures having similar *morphogenesis*. The study of OSS in deep time must be conducted at multiple scales in two and three dimensions within the morphology of the structure (Fig. 13), and the interpretation of such structures is greatly assisted by microbial growth experimentation and modelling considerations. When unexpected morphologies can be explained using observed growth phenomena (morphogenesis) in modern process analogue microbialites, the case for the biogenicity of ancient OSS is significantly strengthened and processes generating their morphologies may be inferred. Archaean microbialites rarely yield diagnostic evidence of the organisms responsible for their formation, but understanding the processes involved in their co-evolution with the palaeoenvironment may yet illuminate some aspects of their biogenesis. The wide range of OSS morphologies observed throughout the geological record may be the result of geochemical stresses and changing elemental tolerances through time (i.e., the 'environmental dipsticks' of Grotzinger and Knoll, 1999), although this requires a more complete understanding of the differences between the architect communities of Archaean, Proterozoic and Phanerozoic microbialites.

Chapter III – Biosignatures in the absence of obvious cellular preservation: nano-structural characterisation of putative biomass and palaeo-metallomic trace element biosignatures

This chapter includes the work contained in the following manuscripts:

Hickman-Lewis, K., Cavalazzi, B., Sorieul, S., Gautret, P., Foucher, F., Whitehouse, M.J., Jeon, H., Cockell, C.S., Georgelin, T., Westall, F. Palaeo-metallomic biosignatures and the influence of early ocean chemistry on cell biochemistry. In preparation for *Science Advances* or *Nature Communications*.

Hickman-Lewis, K., Negrea, R., Zhao, X., Ghica, C., Maraloiu, V.-A., Franchi, I.A., Miccinilli, E., Westall, F., Cavalazzi, B. Nanoscale characterisation of the organic material constituting clots in Palaeoarchaean cherts. In preparation for *Science Advances* or *Nature Communications*.

Introduction

Chapter II conducted a multi-technique, multi-scalar assessment of the palaeobiological record of photosynthetic organisms preserved in several Palaeoarchaean cherts. Although anoxygenic photosynthesisers were probably responsible for most primary productivity on the early Earth, and likely drove and modulated multiple biogeochemical cycles by virtue of their presence at the intersection of the geosphere, hydrosphere and atmosphere, they do not account for the totality of the metabolic network of their biomes. The Archaean fossil record is sporadic and reflects only a small percentage of the expected biological communities therein. In light of the fact that much generic carbonaceous material (CM) in the ancient rock record, dating back even to the Eoarchaean, has been ascribed a possible biological origin (Rosing, 1999; Walsh and Lowe, 1999; Tice and Lowe, 2006; van Zuilen et al., 2007), this third chapter seeks to conduct high-resolution appraisals of enigmatic CM of potential biogenic, and furthermore potential chemosynthetic, origin in the chertified horizons studied in Chapter II, and evaluate the precursor of this CM.

Moreover, when considering the possibility of life on Mars, it is necessary to take into consideration that the balance of primary productivity between photosynthesis and chemosynthesis may not be the same as that of Earth. The incident solar energy at the surface of Mars during the Noachian under the "Faint Young Sun" would have been far lower than that incident upon the Earth at the same time. Most Noachian sequences on Mars also appear to have been heavily influenced by volcanism during the early, geodynamically active period of the planet (Westall et al., 2015). Organisms driven by endogenous planetary processes may therefore have played a key role, but these typically extremophilic chemosynthetic microbes have a subtle fossil record when compared to photosynthetic consortia.

In this chapter, a multi-scalar appraisal of enigmatic CM forming clotted carbonaceous structures is reported, again considering the three tenets of the burden of proof of biogenicity: palaeoenvironment, morphology and (bio)geochemistry. Since clotted carbonaceous structures preserve neither cellular nor community construction morphologies, the importance of geochemical data becomes necessarily greater. The two manuscripts presented in this chapter seek to evaluate whether the microstructure, nanostructure, bonding state, isotopic fractionation and trace element composition of clotted CM are more logically explained in terms of biosynthetic or abiological processes. Either conclusion would be highly informative of the genesis of organic carbon in early Earth environments and, if biological, could provide signals of biogenesis to be used as a biosignature in the search for life on Mars.

The first manuscript characterises clotted CM using TEM, STEM-EDS, HRTEM coupled to EELS, and NanoSIMS. It is found that CM forms two distinct types of clots: Type 1 clots, that are large, irregular, stellate objects occurring in chemical sediments, and Type 2 clots, that are smaller, sub-spherical objects occurring in shallow-water microbialite sediments. HRTEM and EELS show that both types of clot are formed of amorphous carbon that has undergone some variable graphitisation into turbostratic and graphitic swirling and ribbon-like carbon nanostructures. This carbon is mostly concentrated as interstitial aggregations between microquartz grains but occurs also as sub-micron scale globules containing anhedral nanosulphide crystals. The bonding state and nanostructure of this carbon suggest derivation from heterogeneous, largely non-graphitising precursors, now permeated by silica, and is consistent with a biogenic origin. NanoSIMS shows that clots exhibit co-occurring bio-

essential C, N and S, and $\delta^{13}C$ fractionations mostly between –8.6 and –28.0‰, indicative of multiple biological pathways, with some very low $\delta^{13}C$ values between –77.3 and –126.0‰, which correspond only to methanotrophy, biogenic methane and the anaerobic oxidation of methane (AOM) and cannot be explained by any known abiotic processes. Based on previous work (Moreau and Sharp, 2004; De Gregorio and Sharp, 2006; Bontognali et al., 2012; Lepot et al., 2013), this clotted carbon is thus considered to be kerogenous and have a biological precursor. We hypothesise that the extremely low carbon isotope values correlated with nanosulphide grains are consistent with at least a partial contribution from AOM, together with at least one other metabolism that cannot be determined from these approaches alone.

Having demonstrated the biogenetic origin of this CM, the second manuscript presented in this chapter seeks to determine whether the metabolic affinity of the precursor CM can be determined. Although the few highly negative $\delta^{13}C$ values of –77.3 to –126.0‰ are compatible only with methane-related metabolisms, the majority of the $\delta^{13}C$ values are less negative and can be explained by several metabolic pathways (anaerobic photosynthesis, nitrogen fixation, sulphate reduction, methanogenesis). To decode metabolic origin, we define and develop the concept of the *palaeo-metallome*, a trace element biosignature that includes the inorganic elemental complement of the cell and its associated extracellular polymers, accompanying the proteome and genome that have zero preservational potential in deep time. The definition of the *palaeo-metallome* is consistent with the approach of metallomics, stating that cells concentration elements according to their biosynthetic requirements (Williams, 2001), and this signature is likely to be preserved since cellular material readily outcompetes other organic reservoirs in metal retention both *in vivo* and through mineralisation and diagenesis (Schultze-Lam et al., 1993). We use μPIXE ion beam analysis to spatially quantify trace metals and metalloids in clotted CM and find that bio-functional Fe, V, Ni, As, Cu and Co are significantly concentrated within. The relative concentrations of these elements, and particularly the high concentrations of V, Ni and Co, are consistent with lithotrophic and organotrophic microbiota cycling methane or nitrogen. More broadly, these are the elements associated with the metallocofactors of oxidoreductase enzymes in thermophilic prokaryotes, hence further consistency with the expected nature of much primitive life. The findings using μPIXE support the conclusions of the first manuscript. More broadly, the enrichment in these elements provides the first empirical support for one of the hypotheses on the origin and evolution of metabolism: that the dependency of biology on now-trace elements – for example, V, Ni, As, Co – is a relict consequence of their richness in the habitats of early life.

Overall, this chapter endeavours to apply challenging and novel techniques to the study of enigmatic carbonaceous material. The approaches within present the highest resolution study possible of such material and have the potential to be highly informative of 'hidden' biomass in the early fossil record, i.e., CM that stems from biology but does not preserve obvious cellular morphologies. The ultimate objectives of these approaches are to detect biogenicity and metabolic affinity in the absence of obvious cellular preservation and to determine patterns in correlated structural and geochemical characteristics that are able to unveil more of the totality of biology present in early Earth biomes. For example, the co-occurrence of certain trace elements associated with CM could be considered a biosignature reflecting the nature of the precursor biomass.

Although the techniques used herein are not applicable to rover exploration of Mars (although the PIXL instrument aboard Mars 2020 can gather datasets that resemble a low-

resolution version of the μPIXE results reported herein), they may form a crucial stage of the analysis of carbon-bearing material brought back to Earth as part of a Mars Sample Return mission. These techniques are either non-destructive (μPIXE), or require only a very small amount of material, not exceeding several tens of square microns (STEM-EDS, HRTEM, NanoSIMS, SIMS). Since returned Martian samples will be extremely limited, maximising their scientific potential will be of paramount importance. The correlative biogeochemical approach proposed in this chapter can be spatially targeted on small quantities of carbon-bearing material and potentially yield much information regarding its origins.

Manuscript 1 – Nanoscale characterisation of clots in Palaeoarchaean clotted carbonaceous cherts

Abstract

Carbonaceous clots are one of the principal modes of organic matter accumulation in Archaean cherts, yet their origins remain unclear. Previous studies have focussed either on coarse-scale petrographic descriptions or isotopic data alone to suggest a biological origin for these features. We herein combine multiple micro- and nano-scale approaches in an attempt to deduce the origins of clots. We subdivide clots into two types, both of which are common across multiple Archaean cherts: Type 1 clots are large, stellate, scalloped objects that occur in fine-grained chemical sediments; Type 2 clots are smaller, sub-rounded features associated with microbial mat laminations, associated with nanopyrite crystals. FIB-milled sections were extracted from both clot morphotypes. TEM observations show that carbon mostly occurs as an interstitial phase between microquartz crystals, however, in Type 2 clots, carbon also occurs as globules of 100–600 nm diameter. High-resolution TEM micrographs show substantial nanostructural heterogeneity in the carbon, which contains mostly amorphous carbon with domains of highly but irregularly stacked, curled, swirling, and ribbon-like structures, and some elongate planar structures. Morphology and variable interlayer distances indicate that this corresponds to a mixture of amorphous, turbostratic and graphitised carbon, with rare graphite fragments. This is confirmed by electron energy loss spectroscopy (EELS) at the C K-edge, where spectra vary between two endmembers, an amorphous bonding state and a graphitised bonding state. The latter is characterised by well-developed C K-edge spectral features including distinct π* and σ* anti-bond transitions. NanoSIMS analyses of the same structures yield $\delta^{13}C$ fractionations between –8.6 and –28.0‰ and show the clear co-occurrence of the bio-essential elements C, N and S throughout clotted carbonaceous material. S occurs both in the aforementioned pyrite nanocrystals and is more broadly distributed throughout the carbonaceous material as organo-sulphur. Taken together, TEM, HRTEM, EELS and NanoSIMS data suggest that these carbonaceous clots have an origin as biomass, being composed of lightly graphitised, poorly ordered, predominantly amorphous carbon, having a narrow range of isotopic fractionation consistent with biology, and exhibiting co-occurring C, N and S. Clot-like structures such as these could go some way to explaining the 'missing' fossil record of the Archaean, and support that biomes of the early Earth were sustained by diverse and highly productive epibenthic and endobenthic ecosystems.

1. Introduction

1.1. The problem with Archaean carbon

The Early Archaean rock record incorporates a significant component of carbonaceous material (CM), mostly within banded and massive cherts (e.g., Walsh and Lowe, 1999; Tice and Lowe, 2006; Hofmann, 2011; van Zuilen, 2018). This accumulated CM likely originated from either or both of processes of abiotic generation and the biological productivity of early ecosystems (e.g. Sleep et al., 2011). The specific origins of much of the ubiquitous CM in Archaean meta-sediments remain subject to debate. The sporadic fossil record of the Early Archaean is, however, inconsistent with the large primary productivity estimated for that time

by Canfield et al. (2006) (2.8 x10^{14} mol/year), implying that much of the ubiquitous CM in the geological record, despite not having preserved original cellular morphology, is of biogenic origin. Rosing (1999) was the first to analytically demonstrate that aggregations of CM with no obvious fossil morphology could reflect precursor biomass, and this was further supported by Tice and Lowe (2006), van Zuilen et al. (2007) and Ohtomo et al. (2014), who showed that generic CM in Archaean cherts are both syngenetic with the host rock and has $\delta^{13}C$ values consistent with biological fractionation. Taphonomic and post-diagenetic processes typically result in the loss of original cellular morphology and the alteration of bio-essential elements (e.g., CHNOPS) and biosynthetic molecular chemistry. Nonetheless, an imprint of the biological character of the original material can be retained when early entombment by silicification preserves carbonaceous fossil material.

Particularly enigmatic amongst Archaean carbonaceous microstructures are clots, although these represent perhaps the most significant mode of primary organic carbon accumulation in Archaean cherts. Clots have been recurrently interpreted as potentially biogenic features, supported by both their petrological context and $\delta^{13}C$ values consistent with biological fractionation (Walsh and Lowe, 1999; Tice and Lowe, 2006; van Zuilen et al., 2007; Lepot et al., 2013; Westall et al., 2015). Determining the origin of carbonaceous clots could aid our understanding of the synthesis of organic matter, whether biotic or abiotic, in palaeodepositional environments of the early Earth. If this CM has a biogenic precursor, it may be possible to determine the nature of this precursor through the characteristics and heterogeneities of both CM and associated inorganic phases observed at high-resolution, considering the effects of maturation (*cf*. Buseck et al., 1988).

We here conduct *in situ*, nano-scale characterisation of carbonaceous clots (Figs. 1-2) using a combination of TEM and HRTEM imaging, coupled with STEM-EDX, EELS and NanoSIMS to analyse the chemistry of carbon and associated inorganic phases, in order to proffer new insight as to the origins of these structures. Studied clots were sourced from clot-rich, black-grey-white banded, carbonaceous horizons in three Archaean cherts, the 3.472 Ga Middle Marker horizon, the 3.45 Ga Hooggenoeg H5c chert, and the 3.33 Ga Josefsdal Chert, all of the Barberton greenstone belt, South Africa.

1.2. Archaean clotted carbonaceous cherts

The first report of clotted textures in Archaean sediments (Lowe and Knauth, 1977) described irregular, granular textures in the resulting rocks, which were termed clotted carbonaceous cherts. Clotted carbonaceous cherts have since been found to be common constituents of numerous Archaean successions and, despite the lack of obvious cellular preservation therein, are conventionally interpreted as fossiliferous or biogenic features of their host sediments (Walsh and Lowe, 1999; Tice and Lowe, 2006; Bontognali et al., 2012; Westall et al., 2015; Duda et al., 2018; Igisu et al., 2018). Isotopic and trace and rare earth element studies of clotted carbonaceous chert horizons indicate the importance of marine, riverine (terrigenous) and hydrothermal contributions to the palaeoenvironment, and suggest that it was thermophilic (Ledevin et al., 2014; Westall et al., 2015; Hickman-Lewis et al., in review). The presence of pyrite, lack of oxygen-sensitive mineral phases, and lack of a well-developed Ce anomaly indicate that the depositional conditions were reducing and anoxic (Hickman-Lewis et al., in review).

Most petrographic appraisals of clots in carbonaceous chert suggest that they originated from fragments of presumably phototrophic microbial mats due to the common co-occurrence of clots (also termed composite carbonaceous grains) and mat-like laminations (Walsh, 1992; Walsh and Lowe, 1999; Tice and Lowe, 2006). Certain studies have also supposed that laminated wisps of carbon may have originated from the compaction of clots (e.g., Walsh and Lowe, 1999), although this latter hypothesis is not sustained by petrographic evidence showing clots and laminated carbon in the same sedimentary layers without differential compaction. Other studies noting an increased concentration of clot-like textures in hydrothermally influenced environments have either proposed that these features may be abiogenic volcanogenic fragments or have insufficient petrographic context to indicate their origins (fluffy grains; Brasier et al., 2006, 2011; Hickman-Lewis et al., 2016), or have suggested that their context indicates that they may reflect the degraded remnants of chemosynthetic biomass (Westall et al., 2015).

Elemental, isotopic and molecular geochemistry of similar clotted microstructures from contemporaneous cherts has painted a complementary picture. Lepot et al. (2013) and Morag et al. (2016) conducted carbon isotope studies, noting $\delta^{13}C$ values consistent with biology (around –29 to –40‰ and –25 to –38‰, in respectively the Strelley Pool Chert and Dresser Formation). These studies were, however, unable to exclude abiotic processes of CM genesis. A more comprehensive appraisal of clot-like CM from the Strelley Pool Chert showed that it contains organic sulphur with a $\delta^{34}S$ range of 20‰ centred upon –11.5‰ and a $\Delta^{33}S$ range of –0.2 to +2.1‰, which suggests mixed inputs from microbial sulphate reduction and microbial sulphur disproportionation (Bontognali et al., 2012). In hydrothermal vein cherts from the Dresser Formation, Raman spectroscopy and Fourier Transform IR spectroscopy (Igisu et al., 2018) and catalytic hydropyrolysis fractions (Duda et al., 2018) from clot-like objects has also been compellingly used to argue for a biological precursor. Igisu et al. (2018) noted similarities between the intensity ratios of the asymmetric aliphatic CH_3 and CH_2 bands (the $R_{3/2}$ ratio) in Archaean clots and degraded lipids from extant prokaryotic bacteria. Duda et al. (2018) showed that the hydropyrolysed *n*-alkane content of kerogen-like material constituting clots had a restricted distribution (mostly below *n*-C_{18}, and almost entirely below *n*-C_{22}), which matches the signal from the hydropyrolysed products of modern bacteria. Notwithstanding, in both of these studies, the carbonaceous material measured is explicitly stated to be representative of only a small fraction of the organic material present in the samples and may have been subjected to pre-depositional oxidation. Furthermore, the hydropyrolysis products were compared to extant cyanobacteria, which are not representative of expected microbial consortia at 3.5 Ga (the earliest evidence for cyanobacterial-like behaviour in microbial sediments is not observed until 2.7-2.5 Ga; Bosak et al., 2007, 2009; Shepard and Sumner, 2010; Flannery and Walter, 2011). Taken together, however, these geobiochemical studies support that there is evidence for a biogenic origin of clotted microstructures. Despite these investigations, however, the origin of clots remains far from being unambiguously resolved.

2. Materials and Methods

Samples of clotted carbonaceous cherts were collected from the 3.33 Ga Josefsdal Chert, the 3.45 Ga Hooggenoeg H5c chert and the 3.472 Ga Middle Marker horizon. These three horizons indicate shallow-water deposition in thermophilic volcanic settings, with

combined influences from marine, riverine, and hydrothermal inputs, as indicated by stratigraphic and sedimentological data, Si and O isotopic compositions and trace and rare earth element contents (Lowe and Knauth, 1977; Ledevin et al., 2014; Westall et al., 2015; Hickman-Lewis et al., in review). Rare earth element plus yttrium (REE+Y) compositions, when normalised to Mud from Queensland (MuQ), for example, exhibit weakly to strongly fractionated patterns with variably positive La, Y, Gd and Eu anomalies and chondritic to superchondritic Y/Ho ratios (Chapter II, Manuscript 3). Before detailed TEM techniques were applied, regions of interest within clots were identified and characterised using optical microscopy and SEM-EDS.

2.1. Optical Microscopy

Optical microscopy in transmitted and reflected light was conducted at the Centre de Biophysique Moléculaire (CBM) CNRS-Orléans, France, using an Olympus BX-51 to acquire photomicrographs. Observations were conducted on uncovered standard (30 μm thick) polished petrographic thin sections.

2.2. Scanning Electron Microscopy and Energy Dispersive X-ray Spectroscopy

Thin sections were Au-coated and examined using a PHILPS 515 SEM operating at 15 kV and fitted with an EDAX DX-4 detector at the Dipartimento di Scienze Biologiche, Geologiche e Ambientali (BiGeA), University of Bologna, Bologna, Italy. Regions of interest were mapped at multiple magnifications until fields of view relevant to the scales of focussed electron beam-cut sections (i.e., less than 10 μm) could be easily identified.

2.3. Focussed Ion Beam DB system (FIB-SEM DB)

Multiple TEM specimens (50 to 100 nm thick; average dimension: 4 x 7 μm^2) were prepared from clots (see Fig. 3A-C) in the studied thin sections using a DB FEI Strata equipped with a field emission gun (FEG) electron source and a Ga+ ion beam, at the Istituto Nazionale di Ricerca Metrologica (INRiM), Torino, Italy. The energy and current of both beams were optimised, i.e., milling operating were conducted at low Ga-ion currents, to reduce specimen damage during TEM specimen preparation. The final ion-polishing steps were operating at 2 kV and 10 pA. DB FIB-SEM was also used to image (backscattered electrons) the FIB-milled sections for preliminary observations of features for potential study by TEM techniques. The FIB-milled specimens were attached to a Cu-TEM grid (FEI; Fig. 3D) mounted on a flip-stage in the FIB, using an *in situ* nanomanipulator (Omniprobe). Specimens were further thinned by ion milling during TEM observation where necessary. The final thickness of the specimen was estimated in the FIB using secondary electrons induced by the incident electron beam.

2.4. Transmission Electron Microscopy (TEM, STEM, HRTEM, EELS)

All TEM investigations were undertaken at the National Institute of Materials Physics, Magurele, Romania. TEM analyses were performed on FIB specimens to document the textural nature of the Type 1 and Type 2 carbonaceous clots in Archaean sediments. Observations were conducted using a JEM ARM 200F High-Resolution Electron Microscope operating at 200 kV equipped with a JEOL JED-2300T EDS unit and a Gatan Quantum SE unit for EELS analyses.

2.5. NanoSIMS

NanoSIMS analyses were conducted at the School of Physical Sciences, Open University, Milton Keynes, United Kingdom, using a Cameca NanoSIMS 50L. The instrumental setup measured ^{12}C, ^{13}C, $^{12}C^{14}N$, ^{15}N, ^{16}O and ^{32}S. Measurements were conducted on Au-coated thin sections in regions adjacent to the extracted FIB-milled ultrathin sections, and on the ultrathin sections themselves.

3. Results

3.1. Optical-petrographic characterisation

Clots are constructed of multiple CM-rich domains (Fig. 3A) in a silica-rich matrix (*sensu* Walsh, 1992) and are widely variable in size. Larger clots comprise many tens of CM-rich domains, whereas the smallest may include only three-four domains. At higher magnification, clots can be seen to comprise a network of discontinuous CM separated by microcrystals of silica (e.g., Fig. 2C). Two morphotypes of clots were identified consistently across samples and are demonstrably primary fabric elements. Type 1 clots are 200-2,000 µm in diameter (average diameter = 700 µm), irregular and stellate in their three-dimensional morphology, and are dispersed throughout the matrix (samples 99SA07, 03SA15 and 07SA22) (Fig. 1). Associated with Type 1 clots, SEM-EDX identified aluminous phyllosilicates (muscovite and chlorite), Cr-spinel, Fe- and Fe-Ni-Cu sulphides, anatase, apatite and K- and K-Al-feldspar, and stilpnomelane (results not shown). Type 1 clots occur in near-pure siliceous sediments (ICP-MS results = 85-99% SiO_2), but also occur in volcaniclastic units (massive and weakly laminated cherts, 80-85% SiO_2) (cf. Westall et al., 2015). Type 2 clots are sub-spheroidal features, between 50 and 1000 µm in diameter (average longitudinal and equatorial diameters = 200 µm and 100 µm, respectively), either draped or enwrapped by thin CM mat laminations (samples 12SA16 and 01SA14) (Fig. 2). SEM-EDX identified pyrite, chlorite, muscovite, feldspar, anatase and rutile associated with these clots. Clots between microbial mat laminations occur in lense-like eyelet structures (*sensu* Tice and Lowe, 2006). Type 2 clots occur only in shallow-water, laminated, microbialite sediments (black and white banded cherts). These morphotypes are recurrent throughout samples from the studied horizons.

3.2. Transmission electron microscopy

TEM, HRTEM and STEM-EDX were used to identify and study the µm-, nm- and atomic-scale structure, relationships and elemental compositions of phases within clots, using FIB-milled ultrathin sections from both types of clots. EELS at the carbon K-edge was used for designating the energy band structure and bonding state of CM.

3.2.1. TEM and STEM-EDX

STEM HAADF micrographs of TEM foils extracted from both Type 1 and Type 2 clots show that they comprise dominantly 1-4 µm micro-quartz crystals and CM (Figs. 4-5). Additional inorganic phases analysed by EDX confirm the presence of Al-Mg-Cr-Fe-Ti silicates (Fig. 4E-F) and Ca-Mg-Fe silicates, corresponding to aluminous silicates and feldspars. Further rare detrital phases include zircon and apatite. Clots are therefore best described as carbon-mineral clusters or aggregations that have been perfused with silica-rich

fluid, which crystallised as micro-quartz and led to their silicification. CM mostly occurs in the interstitial regions, as fragments of several tens to hundreds of nanometres interleaved between micro-quartz crystals, concentrated at grain boundaries and triple junctions (Fig. 4B-D). This interstitial CM thus forms a broadly continuous network in three dimensions through the clot. In Type 2 clots, CM also occurs as spheroidal globules (< 400 nm), mostly situated around the margins of, but also rarely within, micro-quartz crystals (Fig. 5A-C). Each of these globules is associated with a single anhedral crystal at its periphery (Fig. 5D), which appears white in HAADF STEM images. STEM-EDS analyses of this mineral phase demonstrate that its composition is Ni-rich sulphide, i.e., pyrite-pentlandite (Fig. 5D-F). In all studied ultrathin sections, CM accumulated in only interstitial and globular morphologies.

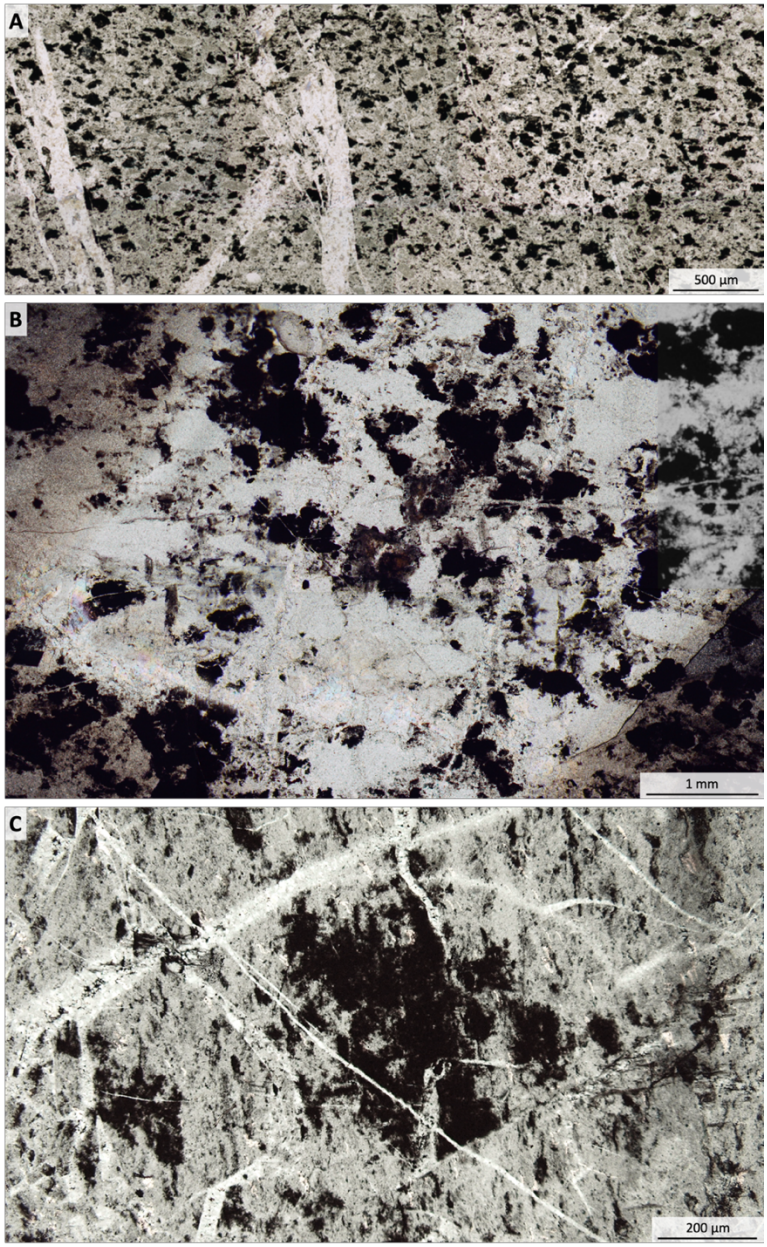

Fig. 1. Type 1 clots. **A**) Small, irregular disseminated clots in highly silicified volcaniclastic sediment (sample 07SA22). **B**) Large, irregular, scalloped clots distributed throughout silica-rich chemical sediment (sample 03SA15). **C**) Irregular, stellate, scalloped clot in silica-rich chemical sediment (sample 99SA07).

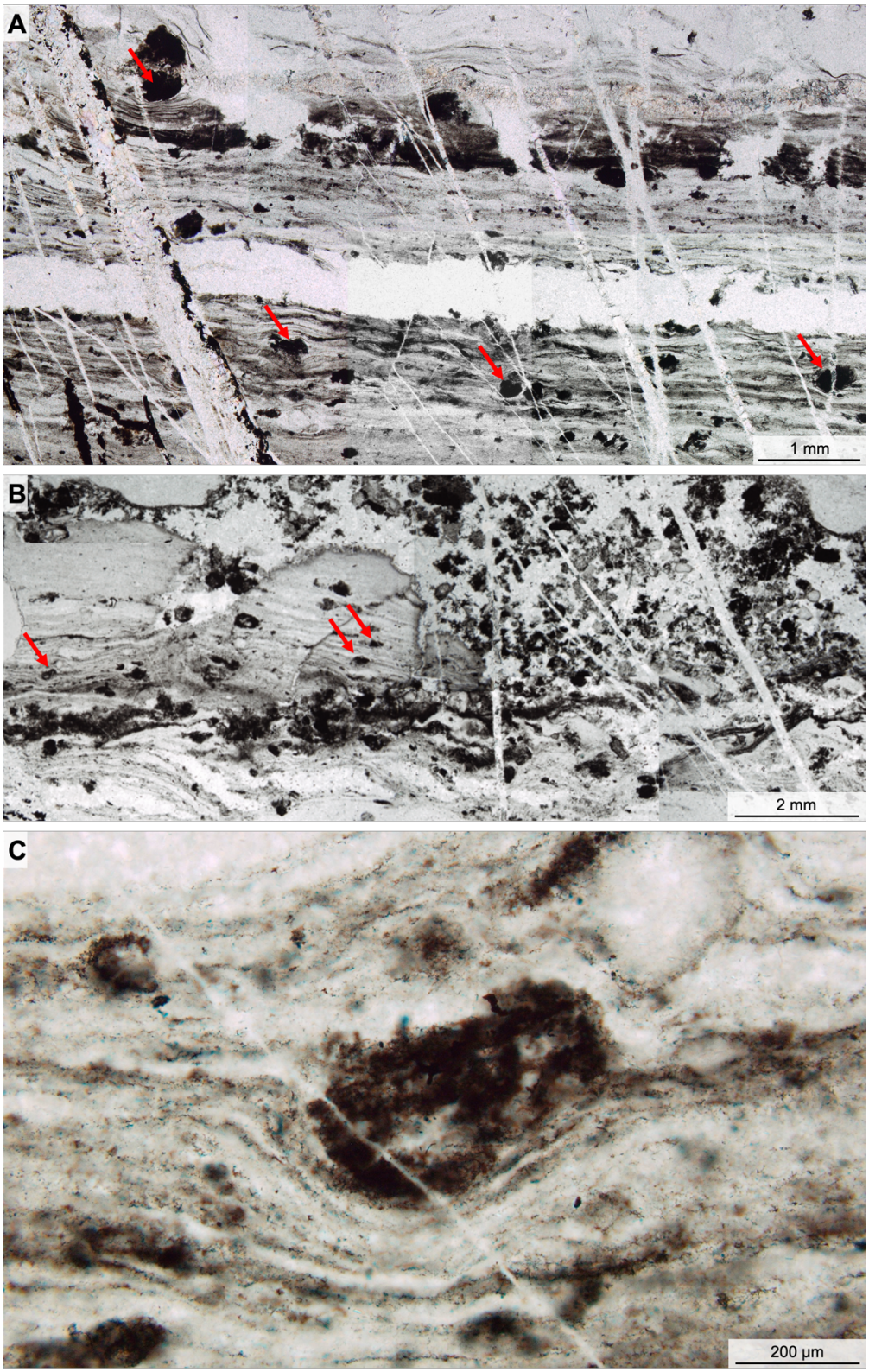

Fig. 2. Type 2 clots (examples arrowed). **A**) Sub-rounded clots entrained within laminar, undulating microbial mat laminations. **B**) Sub-rounded clots in highly silicified microbially laminated sediment. **C**) Small, sub-rounded clot enwrapped by microbial biofilms.

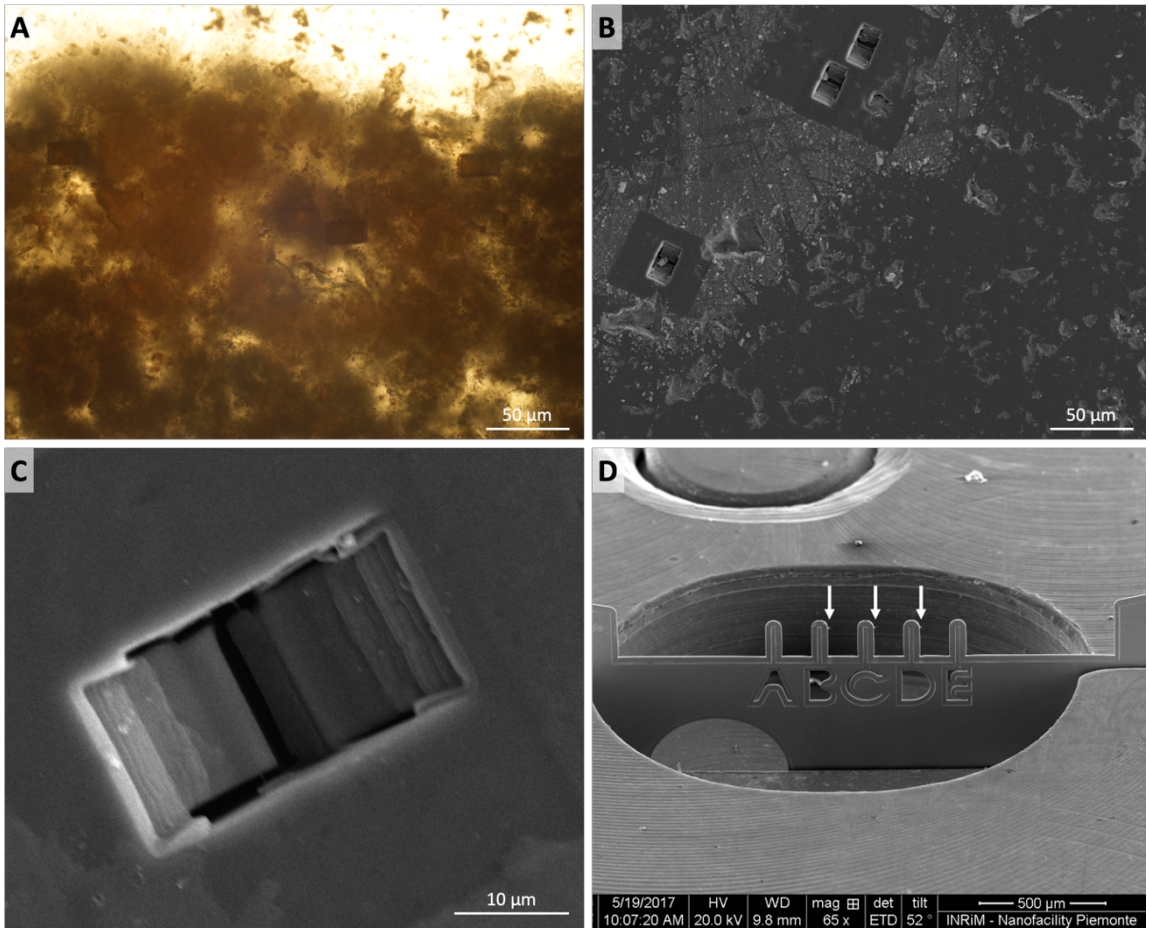

Fig. 3. Sampling and mounting of FIB-milled ultrathin sections. **A**) High-magnification optical photomicrograph within a Type 2 clot. Note the multi-domain structure with several tens of C-rich zones (terminology of Walsh, 1992). Four FIB-milled ultrathin sections were excavated from this clot; see dark rectangular regions. **B**) SEM micrograph showing three regions from which FIB sections were excavated. **C**) High-magnification SEM micrograph of FIB section excavation. **D**) TEM sample holder with three FIB sections (arrowed) mounted for analysis.

3.2.2. HRTEM and EELS

Selected representative examples of both morphologies of CM were studied at higher magnification. Across all samples, HRTEM micrographs show that sub-micrometric fragments of CM in both the interstitial and globular morphologies have considerable nanostructural diversity (Figs. 6-7). CM comprises predominantly amorphous carbon, curled/swirling, ribbon-like nanostructures, and rare linear and tangled nanostructures. Amorphous carbon includes polyaromatic domains corresponding to polycyclic aromatic hydrocarbons (e.g., Fig. 6A-B, 7A-B; De Gregorio and Sharp, 2006). Curled and swirling CM nanostructures with curved, folded and, rarely, circular/sub-circular shapes and distinct, highly stacked fringes are common throughout CM fragments. Some of these nanostructures comprise ordered, highly stacked graphene sheets, although others feature mostly highly sub-parallel lattice fringes. The less well-ordered carbon has a lattice spacing around 0.35 to 0.385 nm and occurs in curled/swirling and curved nanostructures (Fig. 6B-D, 7F-G). This material, with short and undulating fringes, represents poorly aligned stacks of graphene, termed turbostratic carbon (*sensu* Langenhorst

and Solozhenko, 2002). Longer (up to several tens of nanometres), well-developed, more highly stacked fringes in ribbon-like nanostructures with interplanar spacings between 0.35-0.36 nm are also moderately common features in the CM (Fig. 6D-E). These structures are consistent with polyaromatic domains of moderately graphitised carbon (Welz et al., 2006). The rarest nanostructures are linear, consisting of well-developed, highly stacked fringes with an interplanar spacing of 0.334-0.34 nm, i.e., graphite (Figs. 6F, 7C). Graphite occurs only at or close to the margins of interstitial CM, whereas no graphite was observed in the globular CM in Type 2 clots. The CM constituting all clots is therefore highly diverse, dominated by amorphous and poorly ordered carbon that has undergone the initial stages of graphitisation. SAED patterns extracted from regions observed using HRTEM exhibit diffuse rings corroborating the mostly amorphous, poorly crystalline nature of the CM (Fig. 7H-I). This is also consistent with Raman spectra of this, and other contemporaneous, carbonaceous material, which exhibits a broad D band (disordered carbon) around 1,350 cm^{-1} and a lesser G-band (graphitic carbon) around 1,580 cm^{-1}, i.e., moderately disordered CM.

EELS carbon K-edge analyses acquired from CM show a range of spectra that can broadly be separated into two groups based on the fine structure between 285 and 325 eV (Fig. 8). The first group of spectra show a well-developed π^* transition peak at 285 eV, separate from the σ^* transition beginning at 291.7 eV. After the σ_1^* peak at 291.7 eV, there is distinct fine structure throughout the σ_2^* region, including features at 293 and 298 eV and a broad high-intensity feature between 315 and 325 eV. These spectra indicate poorly ordered graphite (Fig. 8D-E), i.e., a state between amorphous carbon and graphite (see Berhault et al., 2001, their Fig. 7; Langenhorst and Solozhenko, 2002; their Fig. 6). The second group of spectra are characterised by a present, but often less distinct, π^* transition and lack the σ_1^* and σ_2^* peaks. There is little fine structure after 291 eV and no fine structure after 325 eV in the second group of spectra. These spectra represent amorphous carbon (Fig. 8F) with very limited graphitisation (cf. Langenhorst and Solozhenko, 2002; their Fig. 6; Hamon et al., 2004; their Fig. 5). Amorphous and partially graphitised carbon thus co-occur within interleaved fragments and globules of carbonaceous material, i.e., the bonding state of the carbon includes both 3 co-ordinated sp^2 and 4 co-ordinated sp^3 fractions. The varying characteristics of the fine structure in EELS spectra are consistent with nanostructurally heterogeneous CM as observed in HRTEM micrographs.

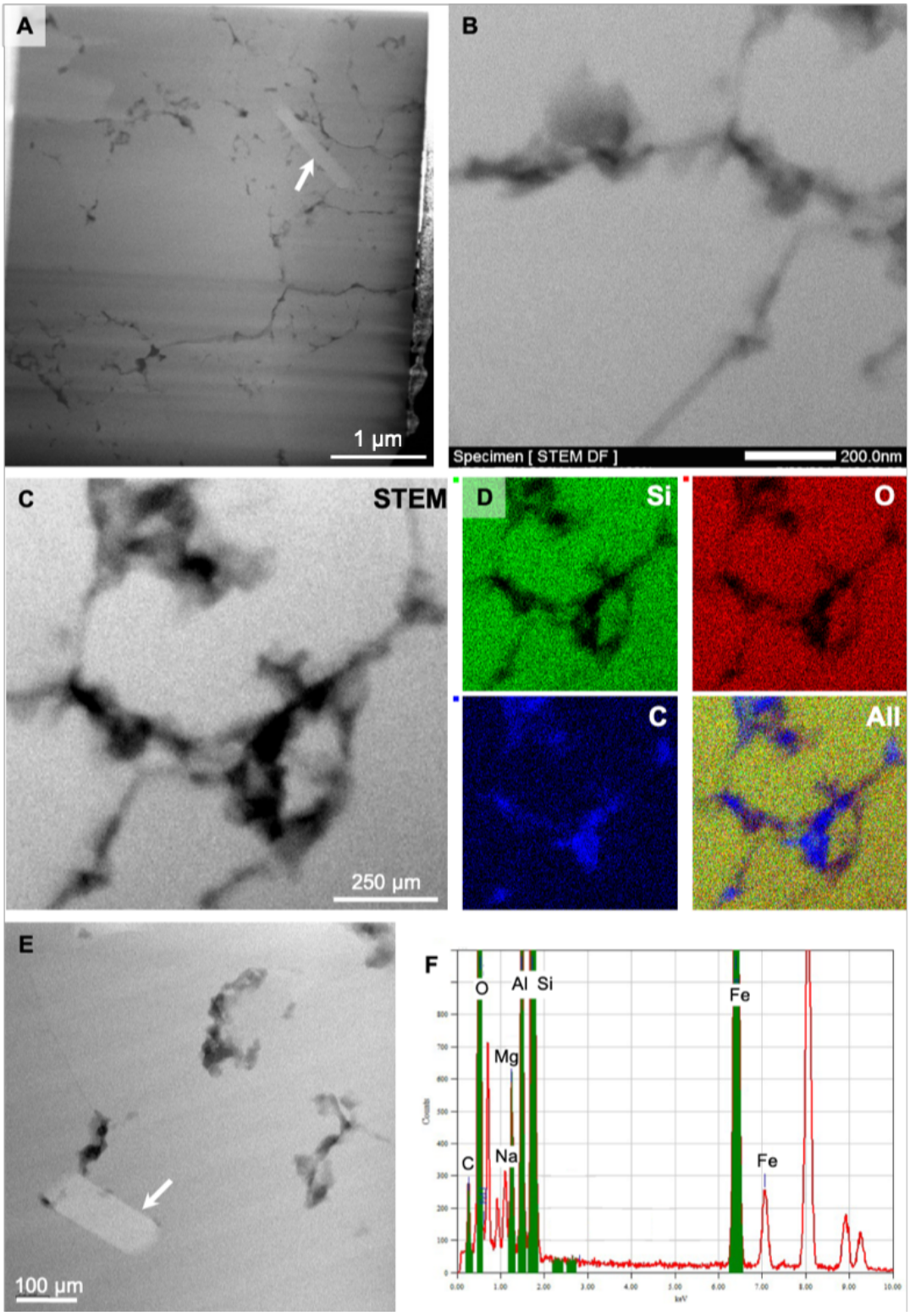

Fig. 4. Microscale petrographic characterisation of Type 1 clots (sample 99SA07). **A**) Representative HAADF TEM micrograph showing interstitial carbonaceous material (black), quartz matrix (dark grey), and tabular minerals (light grey). **B**) Higher-magnification view of interstitial carbonaceous matter. **C**) Scanning TEM image of interstitial carbonaceous material between quartz microcrystals. **D**) EDX maps of Si, O and C for the region of C. Lower right image is a composite of all maps. **E**) TEM micrograph showing tabular minerals (arrowed) associated with carbonaceous material. **F**) Point EDX spectra for the mineral arrowed in E. The composition is Fe-Al-Mg-(Na) silicate, i.e., an iron-rich aluminosilicate.

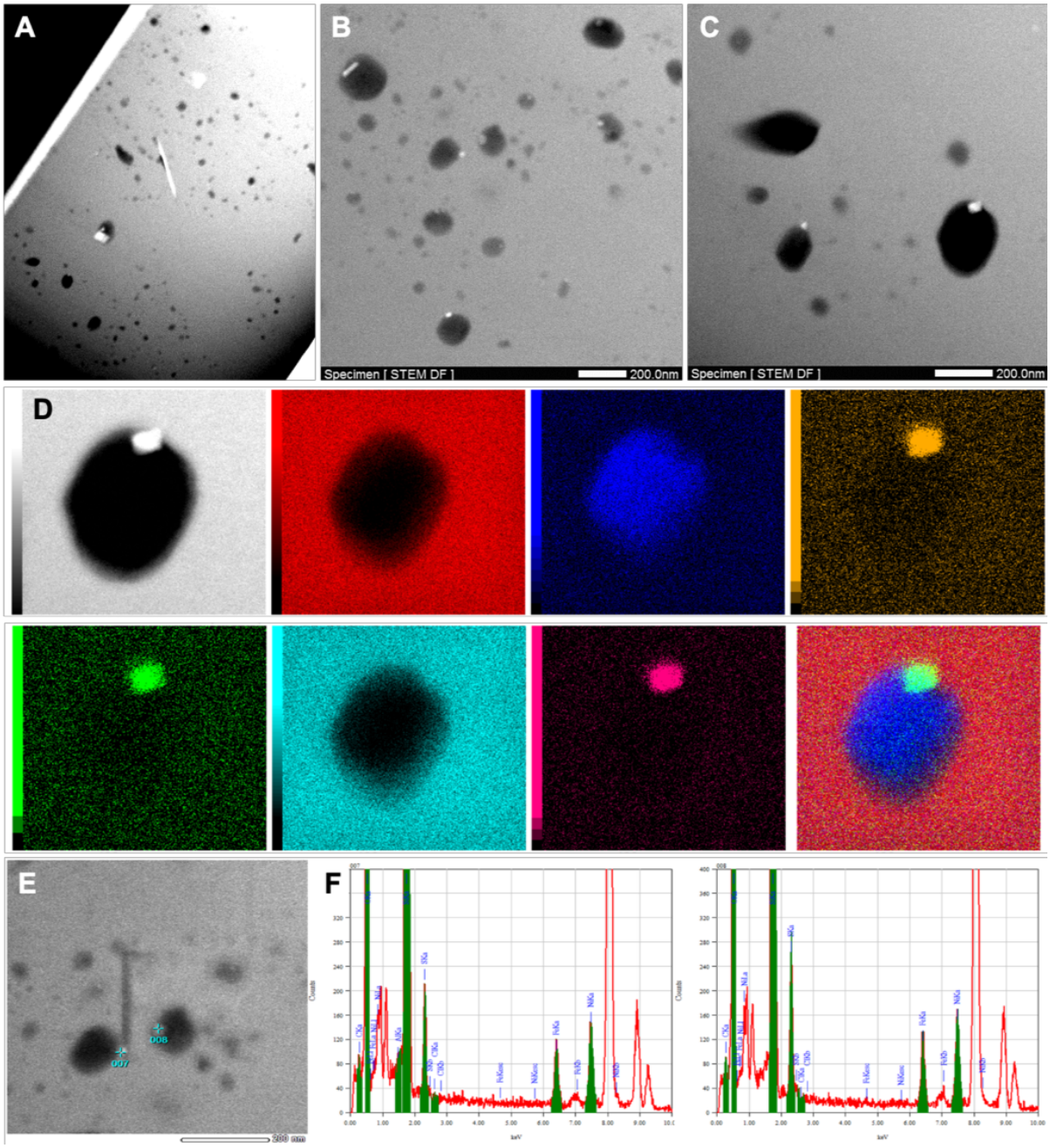

Fig. 5. Microscale petrographic characterisation of Type 2 clots (sample 12SA16). **A**) TEM micrograph where carbonaceous material mostly occurs as globules. **B-C**) Higher magnification views of sub-spheroidal globules, which are invariably associated with a single dense inorganic phase at their outer margin. **D**) STEM-EDX maps of a globule, indicating that the mineral is (Fe,Ni)S, i.e., the pyrite-pentlandite series. **E-F**) Point EDX analyses of two sulphide minerals.

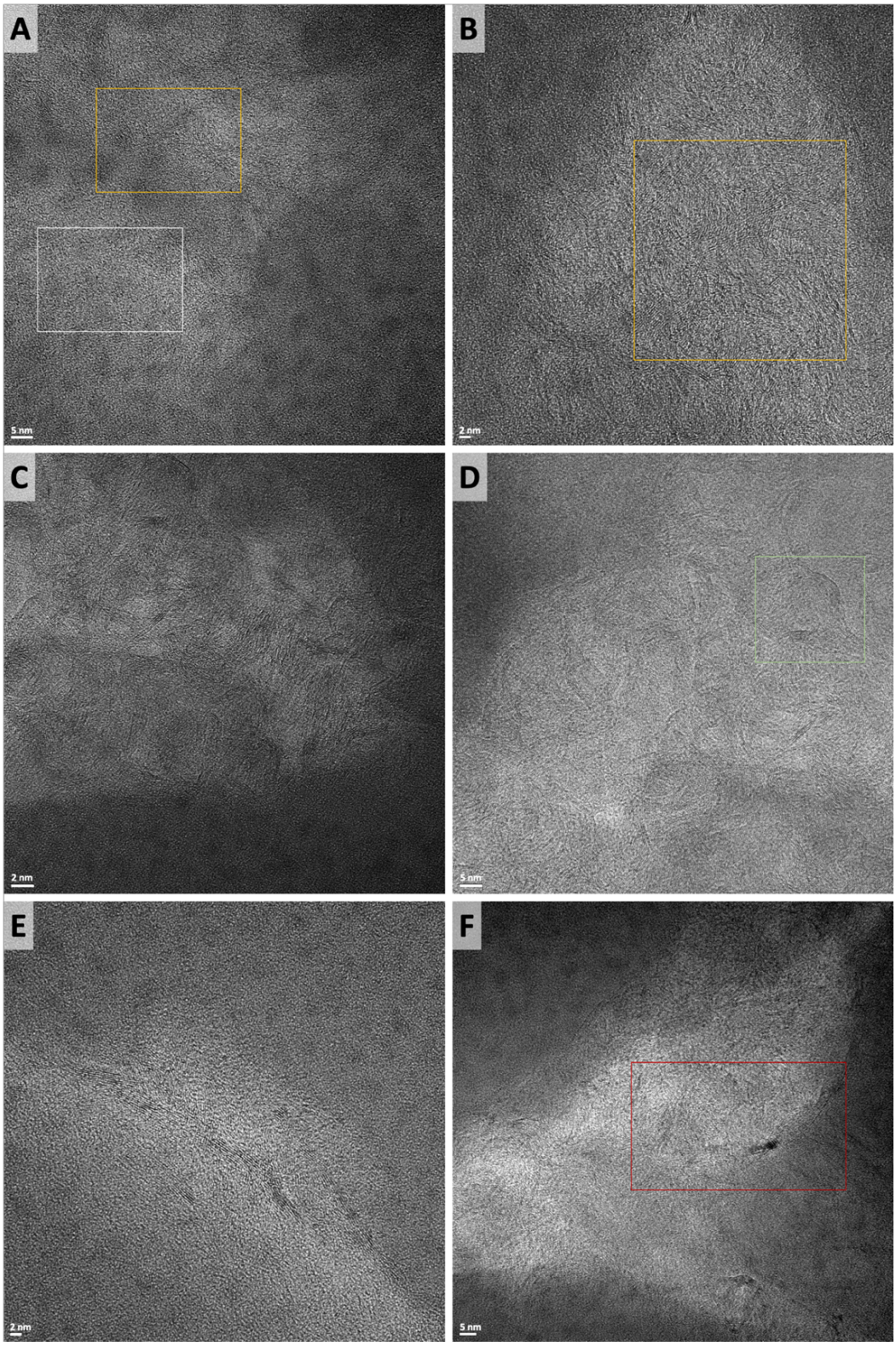

Fig. 6. Nanostructures of carbonaceous material identified in HRTEM micrographs in a sequence of increasing graphitisation (inspired by Buseck et al., 1988). Note the heterogeneity of structures in each micrograph. **A**) Mostly amorphous carbon (white box) associated with some poorly ordered, stacked fringes (orange box) corresponding to turbostratic carbon. Amorphous carbon corresponds to regions of polyaromatic hydrocarbons (after De Gregorio and Sharp, 2006). **B**) Poorly ordered turbostratic carbon with some swirled and curling nanostructures with increased stacking of graphene sheets (orange box) indicating increased ordering. **C**) Region of well-developed curled and swirling carbon nanostructures interspersed with amorphous carbon. **D**) Highly

stacked graphene sheets forming ribbon-like nanostructures and rare circular structures, interspersed with amorphous and turbostratic carbon. **E**) Highly stacked graphene fringes with regular interlayer spacing forming elongated, ribbon-like nanostructures, indicating a further increased degree of graphitisation (Welz et al., 2006). **F**) Heterogeneous carbon nanostructures including rare, highly ordered graphite flakes. Graphite flakes are typically located at the margins of interstitial carbonaceous material, and may result from pressure applied by adjacent phases (Welz et al., 2006). Curled/swirling and ribbon-like nanostructures are also present.

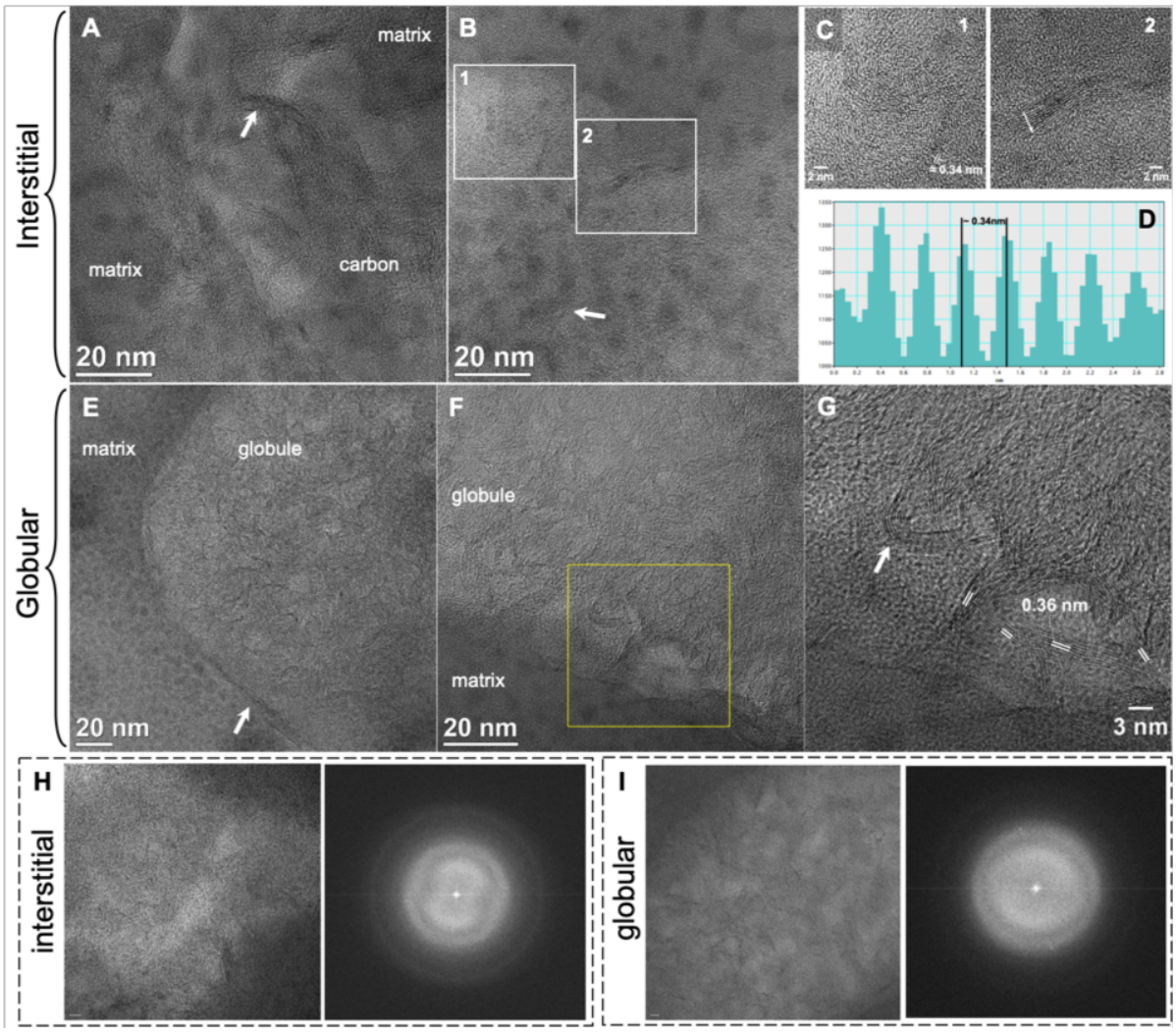

Fig. 7. Comparison between HRTEM characterisation of interstitial and globular carbon. **A-C**) Representative nanostructure of interstitial carbon. **A**) Zone of ribbon-like graphitised carbon forming Moiré-type features (arrowed), surrounded by amorphous carbon. **B**) Zone of mostly amorphous and turbostratic carbon (arrowed) with several linear graphite fragments (boxes 1 and 2). **C-D**) Intensity profiles over the fringe structures shown in boxes 1 and 2, which indicate a d-distance interlayer spacing of 0.34 nm, consistent with graphite (example given in D uses transect 2). E-G) Nanostructural characterisation of globular carbon. **E**) Contact zone between curled nanostructures in the carbonaceous globule (right) and the homogeneous silica matrix (left). Arrow indicates linear ribbon-like graphitised carbon fragments aggregating at the contact zone likely due to pressure from confining silica. **F**) Higher-magnification view of curled ribbons of graphitised carbon intermixed with amorphous and turbostratic carbon. Yellow box shows region of G. **G**) High-resolution micrograph showing graphitised (example arrowed) with interplanar d-distances of 0.36 nm, consistent with turbostratic (poorly graphitised) carbon. **H-I**) SAED FFT of interstitial and globular carbon, both of which show diffuse rings consistent with mixed amorphous and graphitic carbon.

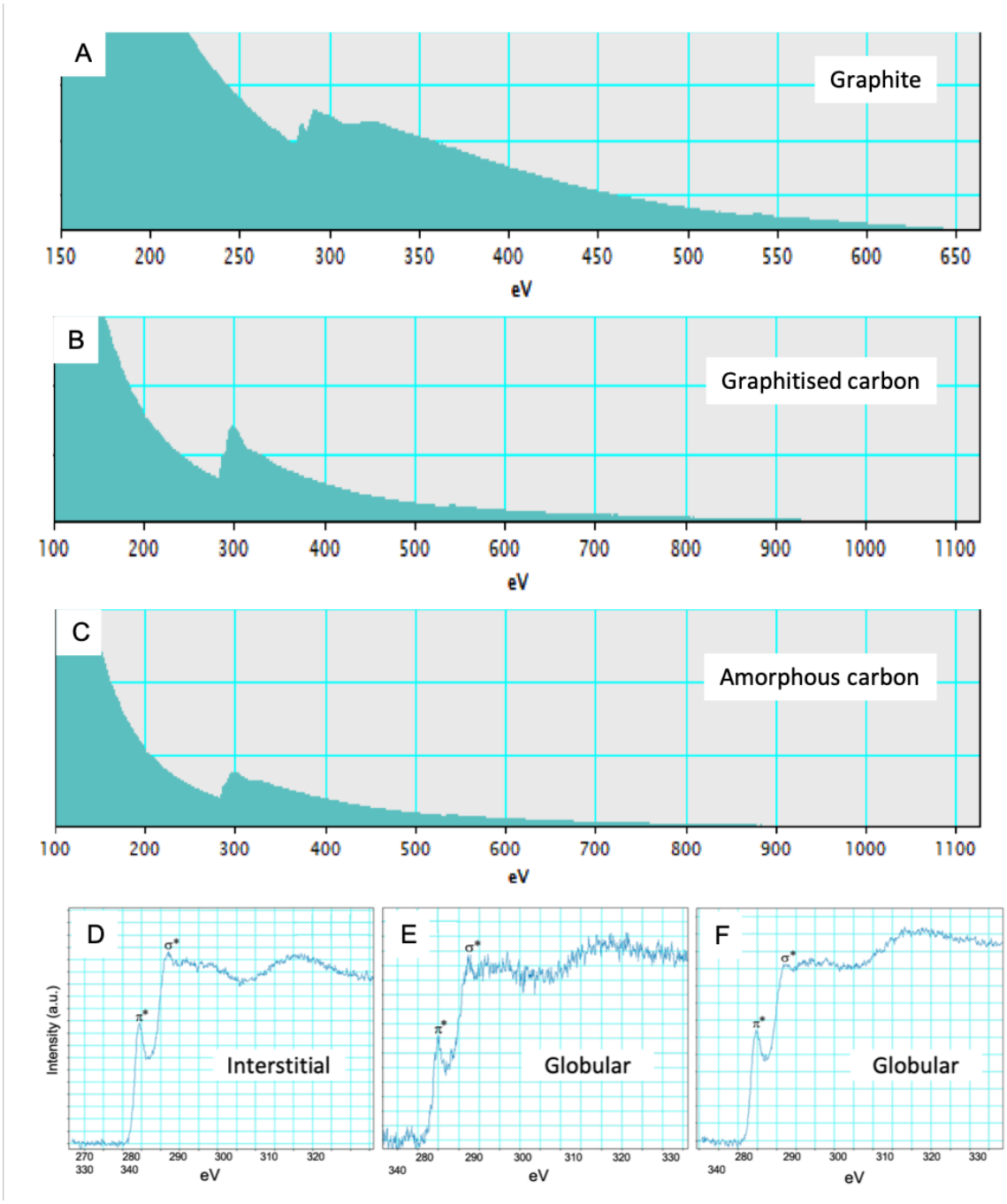

Fig. 8. EELS spectra from carbonaceous clots. **A**) EELS spectra of highly graphitised carbon with well-defined π* and σ* transitions at 285 eV and 291.7 eV, respectively, and a flattened C K-edge structure between 300 and 325 eV. **B**) EELS spectra of less well-graphitised carbon with incipient σ* transition, which is considered to be the first indicator of graphitisation (after De Gregorio and Sharp, 2006), but no separate π* transition. **C**) EELS spectra from amorphous carbon showing a more rounded shape and a slight hump in place of the π* transition at 285 eV. **D**) Representative EELS spectra of interstitial carbon showing well-defined π* and σ* transitions and C K-edge fine structure between 295 and 325 eV, indicating a dominance of sp^2 bonding, consistent with graphitised carbon. **E-F**) Representative EELS spectra of globular carbon showing well-defined π* transitions and a clear σ* transition peak only in E. In F, there is neither a well-developed σ* peak nor fine C K-edge structure between 295 and 325 eV. E is thus consistent with more graphitised carbon, whereas F shows the characteristics of mostly amorphous carbon.

3.3. NanoSIMS

NanoSIMS was conducted on both Type 1 and Type 2 clots. Mapped regions of 5-10 μm^2 showed clearly that C, N and S were strongly correlated within regions identified as CM, and that these three elements were anti-correlated with O (proxy for SiO_2) (Fig. 9). C counts were sufficiently high to enable the determination of C isotopes (see Fig. 10), however, due to issues of low counting, N isotopes values were not obtained. Values for $\delta^{13}C$ in Type 1 clots from the Middle Marker horizon were –14.1 to –25.9‰, which correlate with values from Type 1 clots in the Hooggenoeg Formation H5c chert, of –19.7 to –28.0‰. Type 1 clots from the Josefsdal Chert showed less negative values of –8.6 to –14.0‰. Type 2 clots were not observed in the Middle Marker horizon, however, those from the Hooggenoeg Formation H5c chert and the Josefsdal Chert showed broadly similar negative isotopic fractionation, of –16.6 to –26.1‰ and –7.7 to –21.0, respectively. In thin section, NanoSIMS-determined C isotope fractionations were slightly more negative in Type 2 clots than in Type 1 clots (Fig. 10). $\delta^{13}C$ values in the FIB sections measured, coming from globule-rich samples of Hooggenoeg and Josefsdal clots, were significantly more negative, at –115.8 to –126.0‰ and –77.3 to –78.5‰, respectively.

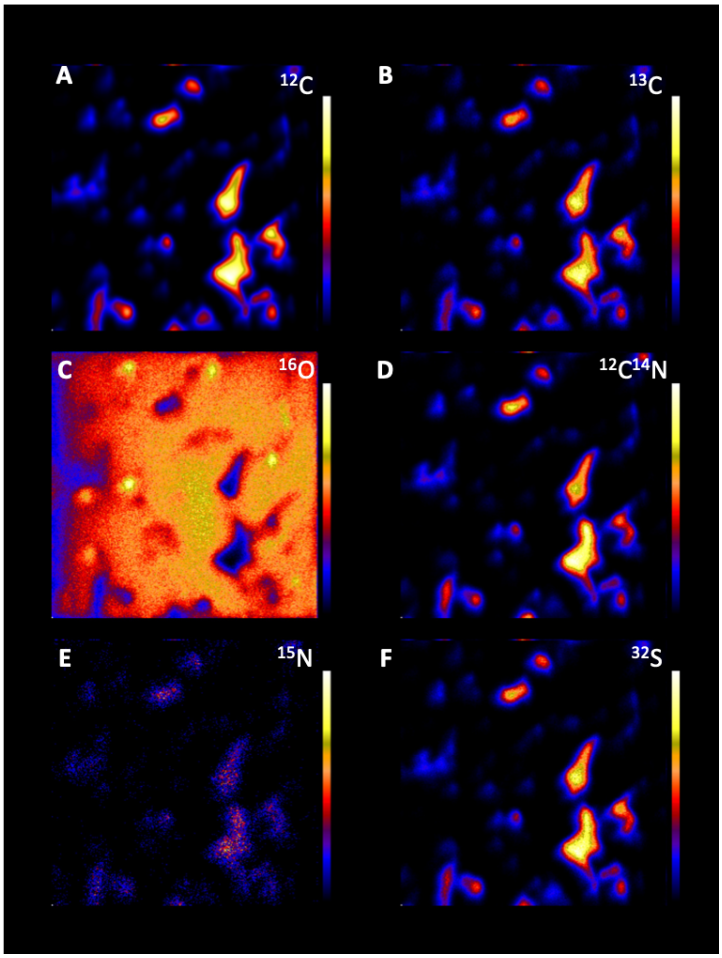

Fig. 9. Representative NanoSIMS ion maps from a Type 1 clot (sample 07SA22). CM shows the co-occurrence of the bio-essential elements C, N and S. The association C-N-S is anti-correlated with O, which can be taken as a proxy for the silica (SiO_2) matrix. Note the ^{12}C enrichment (concentrations in A relative to B), the low concentrations of N (D-E) and the presence of CM-associated organo-sulphur (F).

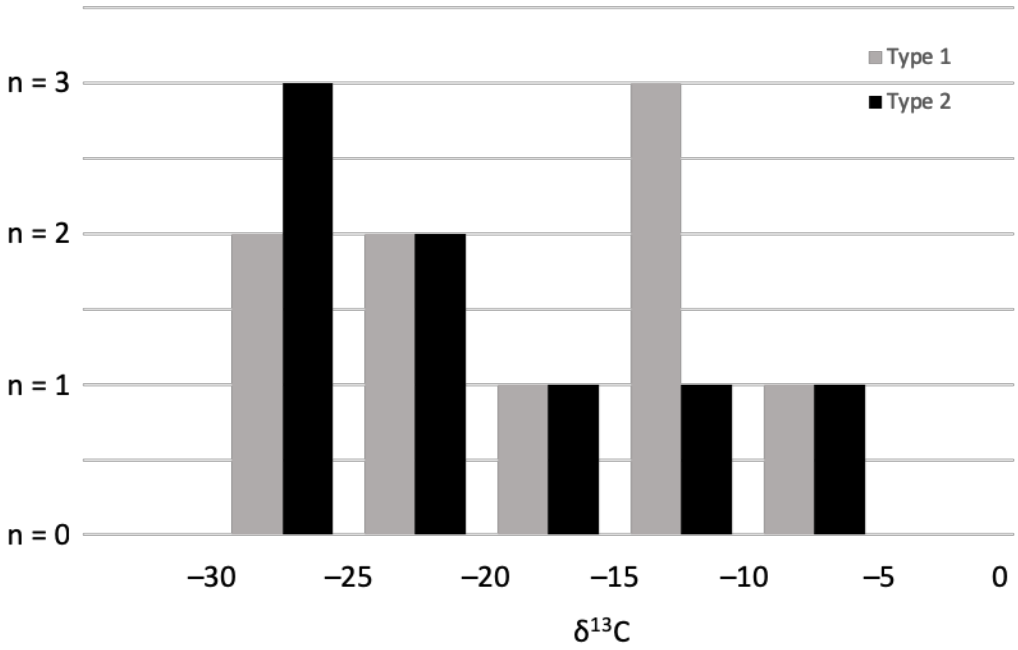

Fig. 10. Carbon isotope ratios ($\delta^{13}C$) calculated for Type 1 and 2 clots using NanoSIMS on thin sections. Extremely negative NanoSIMS results from FIB-milled ultrathin sections are not plotted. Note that the limited range of negative values ($\delta^{13}C$ = –8.6 to –28.0‰) and that $\delta^{13}C$ values in Type 2 clots are generally more negative than $\delta^{13}C$ values in Type 1 clots.

4. Discussion

4.1. Parameterising two morphotypes of clots

Clotted carbonaceous cherts have been identified in Palaeoarchaean meta-sediments from sequences in both the Barberton and Pilbara (Lowe and Knauth, 1977; Walsh and Lowe, 1999; Lowe and Byerly, 2007; Allwood et al., 2010; Bontognali et al., 2012; Lepot et al., 2013; Westall et al., 2015; Hickman-Lewis et al., 2016, 2018; Morag et al., 2016; Duda et al., 2018; Igisu et al., 2018). Similar clotted textures have also been noted in younger and recent sediments (Margulis et al., 1983; Qu et al., 2018) and in seafloor exhalative products (Juniper et al., 1995; Crowell et al., 2008). Overall, these studies have been generally descriptive in their assessment of clots, and suffer from a lack of multimodal, high-resolution documentation of clotted textures. Consequently, no precise definition of structures termed ‘clots’ has been given, and their identification is inconsistent. We have herein classified clots as multi-domain carbonaceous agglomerations that can be categorised into two morphotypes.

Type 1 clots are irregular, and impart a mottled, inkspot-like fabric to the host rock (as in samples 99SA07, 03SA15 and 07SA22) (Fig. 1). Their stellate, scalloped cross-sections and continuity in three dimensions, when taken together with their lack of parallelism with the faint laminations of the host rock, suggest that they developed *in situ* in a semi-lithified, gel-like sediment, in which they were preserved in volume. Type 1 clots do not show a grain-supported fabric in their host cherts, as would be the case for pelagic marine snow or detrital carbonaceous material deposits. This discounts an origin either as redeposited and sequestered mixed biogenic and abiogenic CM (cf. Duda et al., 2018) or as detrital biogenic material (Igisu et al., 2018). Type 1 clots carry a strong resemblance to the biotic texture termed “*Metallogenium”*

(Zavarzin et al., 1981; Margulis et al., 1983), which has been used as an interpretative framework for stellate microfossils in younger Precambrian successions (Margulis et al., 1983).

Type 2 clots occur oriented parallel to photosynthetic microbial mat laminations in microbialite sediments (as in samples 01SA14 and 12SA16) (Fig. 2). They are identical to 'composite carbonaceous grains' described in contemporaneous shallow-water cherts (Walsh and Lowe, 1999; Tice and Lowe, 2006). Intimate, impinging relationships with the surrounding laminations show that clots and laminations developed syndepositionally (Fig. 2C) and that clots were rapidly enwrapped or covered by mats (Fig. 2A-B). Both Type 1 and Type 2 clots are lithofacies-specific. The former occur only in near-pure, hydrothermally influenced, chert and the latter within river- and hydrothermal vent-influenced shoreface volcaniclastic sediments. The first of these is not a common lithofacies, providing compelling evidence for clots being an environmentally constrained phenomenon. Our literature survey indicates that all previously reported clots can be characterised into these two morphotypes, and that Type 1 clots are surprisingly common throughout both cherts and carbonates in the Archaean. Some structures described as clots in the Dresser Formation (Morag et al., 2016; their Fig. 4b) do not meet any existing definition for clots and should be discounted as simple grain boundary mullions akin to those described in the Apex chert (Brasier et al., 2005; their Fig. 14d).

4.2. Micrometric and nanometric characterisation of CM in clots

Clots are CM-mineral aggregations that have been extensively perfused by silica during preservation. Raman spectra of the CM show broad D-bands that predominate over less-intense G-bands, indicating that they are composed of mostly disordered material similar to kerogenous CM in contemporaneous cherts (van Zuilen et al., 2007). CM changes structure and composition with time as a function of the precursor material and the stages of maturation undergone (Oberlin et al., 1974, 1980; Buseck et al., 1988; Strullu-Derrien et al., 2019). This continuum of evolution remains relatively poorly constrained, since it is not clear whether the evolution of synthetic amorphous carbon should necessarily match that of natural carbon, even when both have amorphous precursors. This is because amorphous carbon itself does not have a fixed composition, even if biomass, as an example, may be approximated to CH_3COOH, and since the original molecular composition of organic carbon can determine its preservation potential and resilience to diagenetic and post-diagenetic alteration (Zonneveld et al., 2010; Strullu-Derrien et al., 2019). Sulphurisation, for example, can enhance the preservation potential of organic carbon (Lemelle et al., 2008; Eigenbrode et al., 2018). The intricate, complex organisation of carbonaceous material at the nanoscale observed in all samples studied herein is nonetheless consistent with diverse precursors including non-graphitising carbon such as porous amorphous carbon (Buseck and Huang, 1985; Buseck et al., 1988; Welz et al., 2006; Ohtomo et al., 2014).

TEM shows that most carbonaceous material is present as interstitial phases along grain boundaries of quartz (Fig. 4), identical to the distended distribution of carbonaceous material in the cell walls of silicified Proterozoic microfossils (e.g. De Gregorio and Sharp, 2003; Moreau and Sharp, 2004; Kempe et al., 2005; Wacey et al., 2011, 2012, 2013; Lepot et al., 2013) and consistent with an origin as kerogen displaced by silicification (De Gregorio and Sharp, 2006). Crucially, since microfossil-like morphologies are not retained visually at such fine scales, this spatial distribution demonstrates that, at sub-micron scales, the CM constituting even unambiguous fossil biomass does not conform to 'fossil-like' morphologies. In essence,

this states that, although many authors have considered biogenic interpretations to require some biology-like morphology (Buick, 1990; Schopf, 2006), this viewpoint is irrelevant when considering that the nanoscale distribution of CM may or may not form cell-like structures. De Gregorio and Sharp (2006) suggested that disseminated CM not related to microbe-like structures is an adequate proxy for determining the characteristics of biogenic CM in the same fabric generations, which is to say that the distribution of CM fragments is an unimportant criterion for biogenicity at the nanoscale. The distribution of CM observed herein, is not, in this respect, indistinguishable from CM of uncertain, potentially abiotic genesis (De Gregorio and Sharp, 2006; Le Guillou et al., 2012; Wacey et al. 2016). Fischer Tropsch-type synthesis could theoretically also produce kerogen-like material with possibly indistinguishable nanostructure, although no research exists to suggest this. Globular carbon is a second, less common mode of CM occurrence, and is specific to Type 2 clots; globules are almost always associated with a single nanosulphide crystal (Fig. 5). Higher-resolution work (HRTEM, EELS, NanoSIMS) was thus required to comprehensively assess the origin of these clots.

HRTEM micrographs of both interstitial and globular carbon show a wide variety of carbon nanostructures (Fig. 6-7): disordered amorphous, poorly ordered turbostratic carbon (graphene sheet interlayer distance = 0.35-0.385 nm), partially ordered ribbon-like, curled and bent carbon (0.35-0.36 nm), and rare well-ordered linear graphitic structures (0.334-0.34 nm) (Fig. 5A-G). These structures are set within a matrix of amorphous carbon, in which localised PAH-like domains are observed. SAED patterns depict diffuse rings diagnostic of amorphous carbon with weak graphitisation (after Buseck and Huang, 1985; De Gregorio and Sharp, 2006; De Gregorio et al., 2011) (Fig. 7H-I). The absence of planar graphite within globules suggests either that these structures have undergone more limited graphitisation than interstitial carbon, or that these structures are composed of non-graphitising precursor CM (Oberlin and Oberlin, 1983). Since both interstitial and globular CM are primary fabric elements and since there is no significant difference between the thermal maturity suggested by Raman spectra of Type 1 and Type 2 clots, we suggest that a differential precursor composition between graphitising and non-graphitising CM is more likely, although pressure from adjacent phases (i.e., silica; see Fig. 7E-F) could also play a role in the increased ordering of both interstitial and globular CM at margins (Welz et al., 2006).

Curled, distorted graphene sheets, diffusively stacked within carbonaceous aggregations and forming Moiré-type interference phenomena (Fig. 7A), are common microstructures resulting from pyrolysed, pressurised organic material (Buseck and Huang, 1985; Buseck et al., 1988; Beyssac et al., 2002). Biogenic organic material containing a wide range of functional groups is a plausible source of multifarious carbonaceous nano-fragments with repeated parallel orientations, particularly because many biogenic organic compounds are resistant to graphitisation (Buseck and Huang, 1985; Ohtomo et al., 2014). Although heterogeneous structure in graphitised material may have been caused by synsedimentary fluid flows – in these cherts, probably of hydrothermal origin (Hofmann, 2011; Westall et al., 2015) – or by mineral templating (van Zuilen et al., 2012), the structures studied do not show any petrographic indication of secondary recrystallisation. Micron-scale globules have also been interpreted as the pyrolysed products of biomolecules including lipids when combined with biologically indicative $\delta^{13}C$ ratios (De Gregorio and Sharp, 2006; Lepot et al., 2013). These globules bear no resemblance to pyrobitumen, which forms macro-scale, irregular "aggregations" of CM with radioactive mineral inclusions (cf. Buick et al., 1998; Rasmussen

and Buick, 2000). This potential origin should be discounted in spite of the presence of intra-basinal hydrocarbon generation in the proximal Witwatersrand Basin (Spangenberg and Frimmel, 2001). Despite extensive, high-magnification SEM observation of the matrix, globules with pyrite crystals are observed only in Type 2 clots, and should therefore be considered an integral fabric element and not linked to secondary fluid remobilisation.

The survival of diverse nanostructures in these clots is testament to the rapid preservation of the CM, since curled and ribbon-like CM tends to break down during early to late diagenetic alteration (Ohtomo et al., 2014). The absence of large composite and small flake-like structures, straight, 'tube-like' structures, or hexagonal structures implies that this CM has undergone minimal secondary recrystallisation after deposition. As in Ohtomo et al. (2014), we find no evidence that the studied samples underwent intense heating or evaporation-condensation cycles, or were subjected to any natural electric discharge that might generate artificial nanocarbon structures.

EELS spectra at the carbon K-edge exhibit characteristics indicating the bonding state and co-ordination number of the CM. These measurements are very sensitive to differences in bonding state between disordered CM. In graphitised CM, sp^2 bonding (i.e., non-diamond bonding) results from the hybridisation of 2s orbitals, where a π bond is formed perpendicular to the σ bond (Hamon et al., 2004). The unoccupied π^* and σ^* anti-bond transitions are then identifiable in EELS spectra and allow their interpretation. Spectra obtained herein show a range of carbonaceous bonding structures between two end members corresponding to amorphous carbon and graphitic carbon (Fig. 8). Variations in the electron energy loss near-edge fine structure (ELNES) of the carbon K-edge between 285 and 325 eV (i.e., the region of the π^* and σ^* anti-bond transitions) can be explained through the variable graphitisation of carbonaceous matter. The σ^* peak is considered a sensitive indicator of graphitisation, its sharp onset peak at 292 eV being the first feature to develop as graphitisation commences (Miner, 1988; De Gregorio and Sharp, 2006). The sharpening of this peak makes more prominent the distinction between the π^* and σ^* anti-bond transition states, which in purely amorphous carbon forms small humps on an otherwise featureless carbon K-edge region. EELS spectra with well-developed carbon K-edge energy loss near-edge fine structure and HRTEM observations of graphite fringes co-occur, signalling rare fragments of highly graphitised carbon related to pressure from surrounding carbon and silica (Welz et al., 2006) (Fig. 8D-E). De Gregorio and Sharp (2006) and De Gregorio et al. (2011) suggested that, in kerogenous carbon, the π^* peak can be attributed to sp^2-bonded carbon in polyaromatic domains of kerogen which, at the time of development of the σ^* peak, i.e., the onset of graphitisation, begin to be organised into increasingly parallel sheets. De Gregorio and Sharp (2006) also suggested that since biogenic organic material is of an amorphous nature, structurally amorphous kerogen-like material in cherts can be consistent with a biogenic origin. Meteoritic carbon, however, is also largely amorphous (Le Guillou et al., 2012). Although biological organic material is structural amorphous, early diagenetic and later metamorphic processes that have acted on Archaean rocks mean that most biological material shows some degree of graphitisation (Buseck et al., 1988; Miner, 1988; De Gregorio and Sharp, 2006).

We find that the combination of HRTEM and EELS data reported above are consistent with, but do not unambiguously demonstrate, biological precursor CM in terms of distribution, structural heterogeneity, and carbon bonding state (C-C and C-O). Clots consist of dominantly

poorly ordered (i.e., slightly graphitised) amorphous carbon with regions of turbostratic and ribbon-like, highly stacked fringes, and rare graphitic nanostructures. This CM is therefore likely kerogen.

4.3. Nanometric characterisation of the C-N-S geochemistry of clots

NanoSIMS ion mapping demonstrated the co-occurrence of C with N and, pivotally, S, within kerogen. The association C-N-S in NanoSIMS mapping has previously been demonstrated in structures of biogenic origin, both microfossils and biofabrics (Wacey, 2010; Wacey et al., 2011; Westall et al., 2011; Hickman-Lewis et al., 2016). C, N and S are strongly correlated throughout CM (Fig. 9), although S is also strongly enriched in sub-micron pyrite crystals (Fig. 5D). The association of anhedral, sub-micron pyrite crystals with kerogen is a known bio-indicator related to intracellular mineralisation (Wacey et al., 2011), whereas S more generally distributed throughout CM, termed organo-sulphur, can also arise biologically carry an isotopic signal indicating biological fractionation by microbial sulphate reduction and sulphur disproportionation (Bontognali et al., 2012). Pyrite precipitation can also be an induced by-product of the anaerobic oxidation of methane (AOM; Lin et al., 2011; Zhang et al., 2014). In our samples, NanoSIMS ion mapping shows that organo-sulphur occurs throughout both Type 1 and Type 2 clots. Pyrite crystals, as already observed in TEM images, occur only in Type 2 clots. These two morphotypes may thus derive from different organic precursors.

δ^{13}C fractionations determined by NanoSIMS on thin sections from both Type 1 (–8.6 to –28.0‰) and Type 2 (–16.6 to –26.1‰) clots are all consistent with biological fractionation (Fig. 10). These values are within the ranges common for multiple lineages that had developed by the Palaeoarchaean: anaerobic photosynthesisers, methanogens and sulphate-reducing bacteria (Schidlowski, 1984, 1988; Londry and Des Marais, 2003; Vieth and Wilkes, 2009), but also within the wide δ^{13}C range of abiogenic CM (McCollum and Seewald, 2006; Proskurowski, 2009). The restricted range of values, however, is inconsistent with processes of abiotic hydrocarbon generation (see discussion in Lepot et al., 2013; Morag et al., 2016) and is too high for methanotrophic organisms. The presence of organo-sulphur throughout all clots suggests that some contribution was derived from MSR and/or sulphur disproportionating bacteria (Bontognali et al., 2012). δ^{13}C fractionations from globular carbon in FIB-milled sections from Type 2 clots, however, yields values consistent with methanotrophy. Values of –77.3 to –78.5‰ in the Hooggenoeg Formation H5c chert fall within the range of biogenic methane and AOM (cf. Vieth and Wilkes, 2009; Segarra et al., 2015), whereas the extremely negative values of –115.8 to –126.0‰ in the Josefsdal Chert Type 2 are comparable only to values in methanotrophic bacteria (Vieth and Wilkes, 2009). These lowest values are inconsistent with abiotic hydrocarbon generation. Type 2 clots may therefore stem from biomass including a contribution from methane-cycling microbes. The presence of pyrite nanocrystals hints at a contribution from organisms performing AOM, however, further data (δ^{34}S and Δ^{33}S) are required to confirm this. Nitrogen isotope data were not obtained due to a low number of counts despite the long experimental times, and thus we make no statement on the possibility of N-cycling biomass precursors. All NanoSIMS δ^{13}C data, however, support a biological origin for the CM constituting clots.

Taken together, the correlative microscopy approach of TEM, STEM-EDS, HRTEM-EELS and NanoSIMS used herein reflects the highest-resolution study of Archaean CM performed to date. The results of each technique fit most closely with a biogenic interpretation

of the studied clots; indeed, an implausible series of genetic and metamorphic processes would be required to explain the consistency in nanostructural and compositions characteristics observed in these samples, spanning 150 Ma of Palaeoarchaean time. We conclude that clots reflect diverse precursor biomass and are therefore kerogenous biosignatures.

4.4. Clots and the Archaean carbon conundrum

The origins of much of the ubiquitous CM in Palaeoarchaean meta-sediments has been subject to debate. Microbial fossils have been in identified in each of the studied cherts (Walsh, 1992; Walsh and Lowe, 1999; Westall et al., 2001, 2011, 2015; Hickman-Lewis et al., 2018) and thus these cherts represent habitable environments. Their palaeoenvironments included inputs from volcanic activity and marine, riverine and hydrothermal fluids that aided in sustaining early biomes (Hickman-Lewis et al., in review; Chapter II, Manuscript 3). Coupled sub-micron analyses of carbonaceous clots in clotted carbonaceous cherts from the Palaeoarchaean have shown that these enigmatic structures, a common constituent of fossiliferous banded black-grey-white cherts containing some of the earliest traces of life, have both nanostructural and geochemical characteristics suggesting that they are derived from biomass. TEM-HRTEM-EELS deduced that clots comprise kerogen with a wide variety of carbon nanostructures, suggesting a diverse range of amorphous precursor compounds (De Gregorio and Sharp, 2006). Negative carbon isotope ratios determined by NanoSIMS could indicate one or more potential metabolic origins. The presence of organo-sulphur and nano-sulphide crystals indicate that at least one of the contributions came from MRS and/or sulphur disproportionation. Extremely negative carbon isotope fractionation may be associated with methane-cycling; if so, the pyrite crystals could be associated with AOM.

In spite of the fact that clots do not exhibit obvious cellular preservation in either optical microscopy or TEM observations, their biogenic interpretation would be consistent with modelled Archaean biogeochemistry in that it would help to explain the 'missing' fossil record of the early Earth. Canfield et al. (2006) estimated that the productivity of the early biosphere may have only been 10% of modern-day productivity, but this is nonetheless far greater than accounted for by the Archaean fossil record. Recognising nano-scale bio-indicative patterns in rapidly silicified kerogen from habitable biomes allows the gaps in the Archaean fossil record to be filled in using direct fossil evidence without the requirement for obvious cellular preservation. The clotted structures described herein are a potential example of such kerogen.

5. Conclusions

Using correlative optical microscopy, analytical TEM, HRTEM-EELS, and NanoSIMS, we have shown that carbonaceous material with a petrological context as clots has many characteristics indicative of a biological precursor. Clots may be subdivided into Type 1 and Type 2 clots based on petrographic observations. The carbonaceous material constituting them occurs as an interstitial phase and, in Type 2 clots, globular phases associated with nanosulphides. The nanostructure of the carbon is dominated by amorphous carbon, with poorly ordered turbostratic carbon and rarer graphitised carbon swirls and ribbons, suggesting that it originated from diverse precursors with limited graphitising potential. NanoSIMS demonstrated both the co-occurrence of C, N and S in carbonaceous material, and measured carbon isotope ratios are consistently negative. When taken together, these data are most

plausibly explained by a biological precursor. Exceptionally negative carbon isotope ratios indicate a contribution from methane-producing organisms. If clotted material is considered biological, the productivity of Archaean biomes would have been far greater than the fossil record indicates. The nanoscale techniques used herein provide a means of proposing biological origin in the absence of obvious cellular preservation.

Manuscript 2 – Palaeo-metallomic biosignatures in 3.33 Ga cherts, and the influence of early ocean chemistry on cell biochemistry

Abstract

Modern biological dependency on trace elements is thought to be a consequence of their function in biochemical processes and availability for biological incorporation in the habitats of early life. Furthermore, the development of biological systems seems to have been constrained by Earth's evolving physical and chemical conditions. Although most studies of early life rely on morphological signatures, a more complete understanding of the co-evolution of life and early habitats may be given by linking biomass to multiple lines of geochemical evidence. In this study, we use particle-induced X-ray emission (PIXE) to provide spatially quantitative analyses of metal and metalloid elements with metabolic function within kerogenous organic material within 3.33 Ga cherts of the Barberton greenstone belt. We demonstrate that a number of bio-essential elements – particularly transition metals – are recurrently enriched to similar magnitudes within carbonaceous material from hydrothermally influenced sediments. Transmission electron microscopy demonstrates that these signals cannot be due to metal accumulation in nanomineral phases, and are thus indigenous to the organic material (kerogen). The trace element enrichments in this kerogen are comparable to the elemental composition of anaerobic, thermophilic bacteria, i.e., their "metallome", evidencing the bio-accumulation of Fe, V, Ni, As, Cu and Co. Coupled with a negative carbon isotope fractionation signature consistent with biological fractionation (between –8.6 and –28.0‰, and averaging –15.5‰ to –21.0‰,), this carbonaceous material therefore likely has a biological origin. Enriched V, Ni and Co suggests that the biomass possibly originated from lithotrophic and organotrophic microbiota cycling methane or nitrogen. The approach reported herein provides an entirely novel, non-destructive method of estimating biogenicity and perhaps microbial affinity in the absence of obvious cellular preservation. Biogeochemical evidence presented herein extends the palaeo-metallomic record to more than 3 Ga, implying that metallome evolution could be tracked through deep time as a means of deducing metabolic networks in fossiliferous horizons. Using this approach on controversial fossil material from the Archaean has the potential to sustain or reject its biogenicity. Most importantly, these findings are the first empirical support for that cellular dependence upon trace elements is a function of the environment in which primitive life evolved.

"*The system of cell chemistry…cannot be divorced from the environment any more than it can be separated from a code. All the basic chemicals and energy come from the environment and this remains true to this day*"

R.J.P. Williams and J.J.R Fraústo da Silva (*Journal of Theoretical Biology*, 2003)

1. Introduction

1.1. Patterns that are indicative of process and defined by their environments

Carbonaceous material (CM) occurs as a wide range of morphologies in Palaeoarchaean (~3.6-3.2 Ga) rocks, such as laminations (including microbial mats), microfossils, discrete grains, wisps and flakes, diffuse clouds, and clots (Walsh and Lowe,

1999; Lepot et al., 2013; Westall et al., 2015; Hickman-Lewis et al., 2016). The origin of CM in rocks of this age, having been submitted to low-grade metamorphism, is often enigmatic by virtue of the fact that it is difficult to distinguish between CM originating from biogenic precursors and CM originating from abiotic processes (van Zuilen et al., 2007; Brasier et al., 2011). This is further compounded by that both geneses would have played a role in early habitable environments, for example, hydrothermally influenced shallow seas. Similarities in the occurrence, morphology and chemistry of CM from similar and diverse settings should support common origins: generally, abiotic processes are more likely to form an unexceptional continuum in geological-geochemical metrics, whereas more striking patterns and restricted ranges in characteristics are expected in CM with shared biological origins, in spite of subsequent alteration (van Zuilen et al., 2007; Marshall et al., 2007; Lepot et al., 2013; Greco et al., 2018).

Quantitative approaches capable of characterising the geochemical signatures of geobiological interactions in deep time are therefore of great value in ameliorating our understanding of the early biosphere and its co-evolution with the geosphere. Such patterns have previously been discerned in CM from the Barberton greenstone belt (BGB), South Africa, indicating that most CM bears the hallmarks of metamorphosed biological material in terms of carbon isotope ratios, N/C values, spectral characteristics from Raman spectroscopy, and the correlation of bio-essential CHNOPS elements (van Zuilen et al., 2007; Westall et al., 2011; Greco et al., 2018). Patterns in the molecular compositions of similarly ancient CM from the Pilbara craton of Western Australia yield a restricted range in several characteristic parameters, also indicative of biology (Marshall et al., 2007; Wacey, 2010). In the case of unambiguously biogenic CM, repeated similarities in spectral or molecular characteristics might provide an indication of the different metabolic affinities of the precursor material (e.g. Greco et al., 2018; Duda et al., 2018). In the past, this has also been estimated by well-constrained grouping of carbon isotope fractionation according to biosynthetic pathways (Grassineau et al., 2005; Lepot et al., 2013), though the ambiguity inherent in the interpretation of carbon isotope fractionation necessitates further complementary data, for example Raman spectroscopic characterisation of the disorder of CM (van Zuilen et al., 2007).

Such tests of biogenicity are immeasurably valuable to Precambrian palaeobiology but do not incontrovertibly indicate the specific biological pathways responsible for the generation of this biomass. Indeed, although trends and patterns in carbon isotopic ratios related to microfossils and organo-sedimentary structures can be interpreted as effects of a specific organism or consortium (Grassineau et al., 2005; Schopf et al., 2017), the carbon isotopic ratios reported for Archaean "biomass", ranging mostly between –10 and –40‰, are consistent with multiple biological pathways, for example, anoxygenic photosynthesis, sulphate-reduction, photoferrotrophy, methanogenesis (Schidlowski, 1984; 1988; Vieth and Wilkes, 2009), and furthermore with the products of Fischer-Tropsch-type processes (e.g., McCollum and Seewald, 2006), the latter of which are highly relevant in the environments of early life. Further information regarding the biosynthetic pathways and metabolic affinities reflected in fossil material may potentially be obtained through decoding its palaeo-metallomic signature. Metals are crucial to numerous enzymatic and metabolic processes (e.g., Fraústo da Silva and Williams, 2001; Williams and Fraústo da Silva, 2003; Moore et al., 2017), and are thus present in oxidoreductases and other enzymes, and as proteinic structural elements essential to metabolism. This elemental complement is often termed the "metallome". Decoding such

patterns of metal enrichment in fossil biomass, though historically difficult due to limits of instrumental resolution and limited understanding of the rapidity of silicification processes, may be possible using quantified ion-beam analyses of rapidly silicified CM. Such CM is replete in the chert horizons of the BGB.

1.2. A hypothesis toward estimating the palaeo-metallome of Precambrian biomass

The metallome is the vital component of biosynthetic chemistry comprising the entirety of the metals and metalloids present within a biological system, i.e., the inorganic component of the proteome and genome (Williams, 2001; Fraústo da Silva and Williams, 2001; Williams and Fraústo da Silva, 2003). This biological system, in palaeobiological terms, is best appraised as the totality of elemental concentrations within cellular, or cellularly derived, fossils. The relative proportions of elements may then be linked to their potential presence in proteins, metabolites and other biomolecules, according to the definition of metallomics (Lobinski et al., 2010). A palaeo-metallomic biosignature in the rock record should therefore chart, systematically, the functional interactions between the cell and its external environmental compartment (the source of the elements constituting the metallome), i.e. the result of bioaccumulated material flow between environment and organism, consistent with the definition of the metallome (Williams and Fraústo da Silva, 2003). The palaeo-metallome should retain the elemental complement of its environment with augmentation according to biological requirements.

Fraústo da Silva and Williams (2001) and Williams and Fraústo da Silva (2003) proposed that modern biological dependencies upon trace metals – as intracellular catalysts and structural elements – could have been the inevitable consequence of the richness of these elements in the environments of early life. They termed this “an economic utilisation of resources”. The spirit of this idea is evidentially sustained by the Palaeoarchaean geological record, which presents copious outcrop and geochemical evidence for widespread nutrient-rich hydrothermal fluids influencing the environments colonised by early life (Hofmann and Bolhar, 2007; Westall et al., 2011, 2015, 2018). The organisms inhabiting these globally significant environments are estimated to have been thermophilic and, if immediately linked to hydrothermal effusions, chemosynthetic (Gaucher et al., 2010; Arndt and Nisbet, 2012; Westall et al., 2015; Schopf et al., 2017). Regrettably, the chemosynthetic biosphere leaves enigmatic vestiges of its existence in the rock record, and determining the biogenicity of such fossils is beset with contention due to the simple morphologies of individual and community occurrences of organisms and their subsequent alteration by early-late diagenesis and metamorphism if not immediately preserved by silicification. The Palaeoarchaean fossil record nonetheless presents an ideal window on the chemosynthetic biosphere: it dates from a time when life on Earth was driven dominantly by internal heat, in which thermophilic life could have occurred across widespread, shallow-water ecosystems (Arndt and Nisbet, 2012). From ancient biosignatures, chemotrophic and phototrophic metabolisms have been predicted perhaps as early as 3.8 Ga (Schidlowski et al., 1984, 1988; Canfield et al., 2006; Gaucher et al., 2010; Arndt and Nisbet, 2012; Westall et al., 2015).

Deducing metallomic biosignatures from CM in Precambrian rocks (this study) will pose very different challenges to the determination of the metallome in Recent or Phanerozoic samples (Liermann et al., 2007; Cameron et al., 2012; Edwards et al., 2014). While it should be possible to analyse enigmatic carbonaceous matter of plausible biotic origin (e.g., Fig. 1)

and calculate its elemental composition, linking elemental concentrations to functions within the genome or proteome is impossible due to the lack of preservation of either the genome or proteome in ancient fossils. It is therefore more prudent to consider a highly conservative approach akin to that of previous fossil metallome studies involving the quantification of the spatial distribution of trace metals within structures of biological origin followed by an attempt to link these metal enrichments to metal-enabled biosynthetic pathways (Wogelius et al., 2011; Edwards et al., 2014).

1.3. Putative carbonaceous fossils as a test of the palaeo-metallome hypothesis

The 3.33 Ga Josefsdal Chert (JC; equivalent to Kromberg Formation unit K3c, BGB) (Fig. 2) contains exceptionally well-preserved microbial vestiges in the forms of microfossils and biofilms (e.g., Westall et al., 2011, 2015). The exceptional preservation of carbonaceous biosignatures stands testament to the rapidity of silicification process responsible for their fossilisation. Where fossil microbial material is preserved in three dimensions, silicification was necessarily rapid and early, and commenced during the life cycle of the organism. The "time capsule" preservation afforded by silicification, i.e. rapid encapsulation, lithification, and close to zero post-diagenetic alteration and defence against leaching, assures that geochemical signatures are preserved (for example REE+Y signals signifying the palaeodepositional conditions; Fig. 3) and Raman spectral characteristics diagnosing that the thermal maturity of the CM is commensurate with that of the host rock (Fig. 4). Post-diagenetic mobilisation of metals out of biological organic matter is also not significant due to the high retention of these elements by biopolymers relative to other sedimentary organic matter (Schultze-Lam et al., 1993; Orange et al., 2011; Marshall et al., 2017). Indeed, trace element geochemistry representative of even microband-scale fluctuations in ambient biogeochemistry can be preserved within chertified sedimentary horizons (Bau and Dulski, 1996; Allwood et al., 2010; Schopf et al., 2017).

Two CM textures of biological promise, yet lacking obvious cellular preservation, have been described in the JC:

i) irregular clots of 100-2,000 μm diameter, 'free-floating' within laminated black chert (Figs. 1, 4A-B); and
ii) ii) irregular 'coatings' on altered volcanic particles (Figs. 1, 4C-D).

In both cases, non-isopachous, irregular morphologies argue strongly against their being an abiotic or reworked condensation fabric as seen in other contemporaneous CM (Wacey et al., 2016; Duda et al., 2018). In the case clots, these 'free-floating' morphologies, co-occurring with intact and degraded microbial mats, were interpreted as putative degraded chemosynthetic biomass growing in situ within a gel-like sediment by Westall et al. (2015), within which micrometric volcanic particles, easily identifiable in optical and SEM imaging, also occur (Figs. 5-7). This is further supported by the presence of micron-scale, anhedral pyrite crystals within the carbonaceous material (Figs. 5-7), since such morphologies and occurrences of pyrite are consistent with microbial metabolism (e.g., Lerouge et al., 2011). Micro-pyrites are potential products of the degradation of biogenic organic material after sulphur-reducing bacteria, examples of which are noted elsewhere in the Archaean geological record (Wacey et al., 2011; Schopf et al., 2017). Coating-like fabrics on volcanic particles were interpreted as putative lithotrophic coverings of specific lithic fragments (cf. Westall et al., 2011, 2015).

Clotted carbonaceous material such as this was first ascribed a potential biological origin when its multi-domain, aggregate-like nature was noted (see Walsh, 1992) and compared to microbe-mineral clots in modern marine environments (Margulis et al., 1983; Juniper et al., 1995). In both of the morphologies presented in this study, the degree of preservation at the cellular level is such that no vestige of original morphology remains (Fig. 1). Nonetheless, both the modes of occurrence and geological context of this CM, together with carbon isotopic fractionations from CM of the same lithofacies (see Westall et al., 2006, 2011), are consistent with the CM originating from photoautotrophic or chemoautotrophic biomass. Furthermore, this material should not be interpreted as detrital biogenic or abiogenic matter, as pyrobitumen or volcanogenic pseudofossil-like material, nor as redistributed and sequestered CM.

These features are best interpreted as CM microstructures having grown *in situ* in hydrothermally influenced sediments and are plausibly biogenic. These enigmatic carbonaceous objects therefore provide an ideal test subject for the challenge facing this work: to evaluate, with non-destructive, non-invasive methods, the potential biogenicity and metabolic affinity of Precambrian CM in the absence of obvious cellular structure, in terms of its *palaeo-metallomic biosignature*. In terms of linking the potential palaeo-metallome to metabolism, the chosen techniques must be spatially quantitative across the range of elements relevant to biosynthesis.

2. Materials and Methods

2.1. Materials and petrographic characterisation

Samples were collected during field campaigns to the Barberton greenstone belt between 1999 and 2014, during which time a detailed appraisal of the stratigraphy and sedimentology was conducted. The geology, stratigraphy and lithological associations of the Josefsdal Chert are detailed in Westall et al. (2015) and will not be repeated here. For optical microscopy, an Olympus BX51 microscope (CNRS-CBM, Orléans) was used. Unless stated otherwise, all optical images shown are in plane polarised light. Raman spectroscopy used a WITec Alpha500 RA (CNRS-CBM, Orléans) equipped with a green laser at 532 nm wavelength and a laser power of 5 mW to avoid thermal alteration of the sample. SEM analyses used Hitachi T3000 (ITSO, Orléans) and JEOL (Dipartimento BiGeA, Università of Bologna) instruments (Figs. 5-9). Elemental maps were run for 150-200 frames in order to accrue sufficient counts, and point analyses of minerals for 100-300 s. Regions of interests were chosen so as to avoid identifiable alteration textures, pressure solution fronts and secondary veining (Fig. 10).

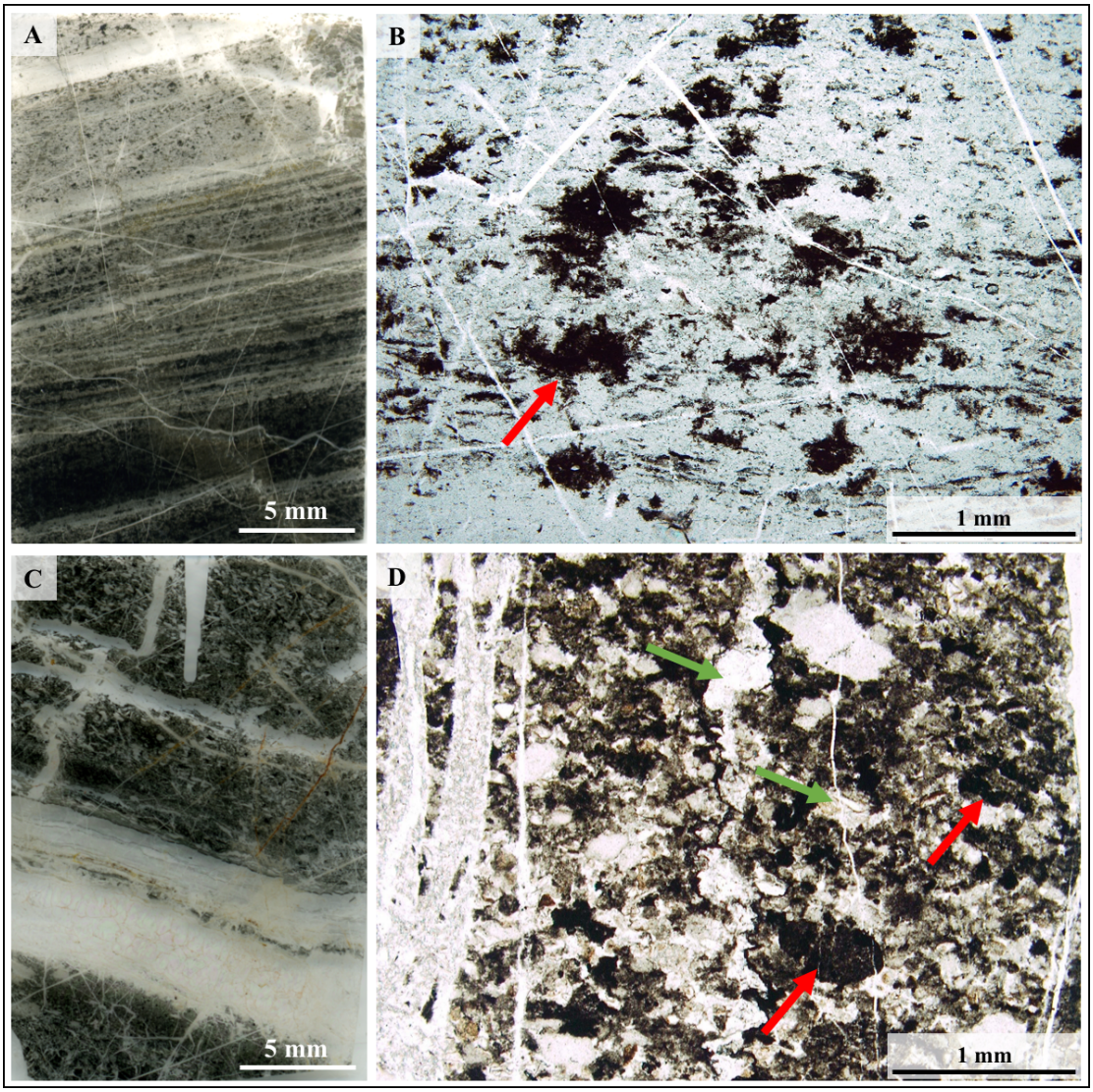

Fig. 1. Representative photomicrographs of studied cherts and fundamental petrographic characteristics of features of interest. **A**) Faintly laminated clotted carbon-bearing black chert. **B**) Small, irregular, scalloped carbonaceous clots (example arrowed) which are preserved in hydrothermally derived silica, and whose three-dimensional preservation suggests growth *in situ*. Carbonaceous material is associated with silt-grade fragments of altered volcanic grains, aluminosilicates and anhedral pyrite. **C**) Coarse, laminated black and white chert with near-pure chalcedonic silica-rich layers. **D**) Optical photomicrograph showing carbon-coated altered volcanic grains (example red arrowed, dark regions) and other lithic particles (example green arrowed, lighter regions).

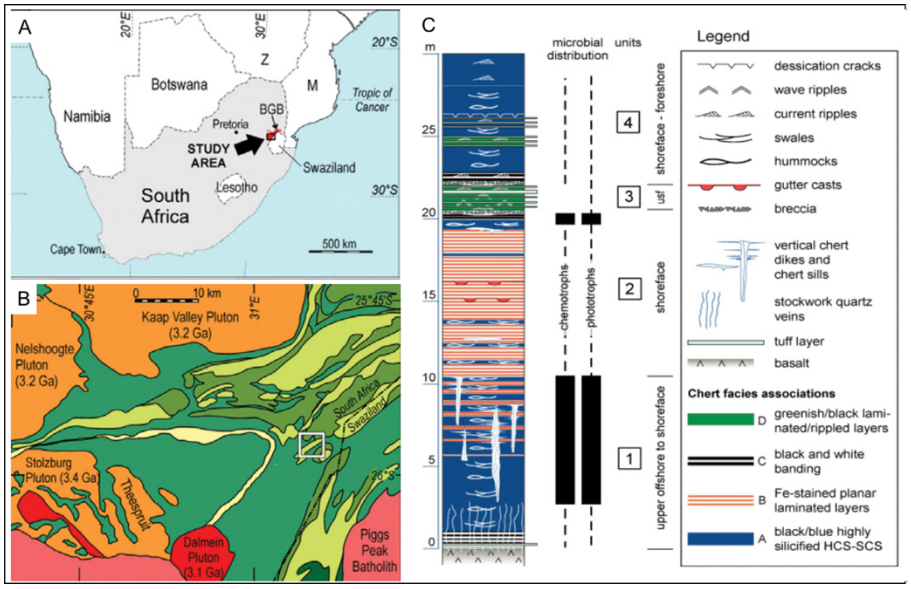

Fig. 2. Location, geological setting and stratigraphy of the Josefsdal Chert (equivalent to K3c; Lowe and Byerly, 1999). **A**) Location of the Barberton greenstone belt within South Africa and Swaziland. **B**) Location of the study area (white box) within the Barberton greenstone belt. **C**) Stratigraphic column of the Josefsdal Chert; the studied samples come from Facies C, hydrothermally influenced banded black and white cherts from units 3 and 4. Adapted from Westall et al. (2015).

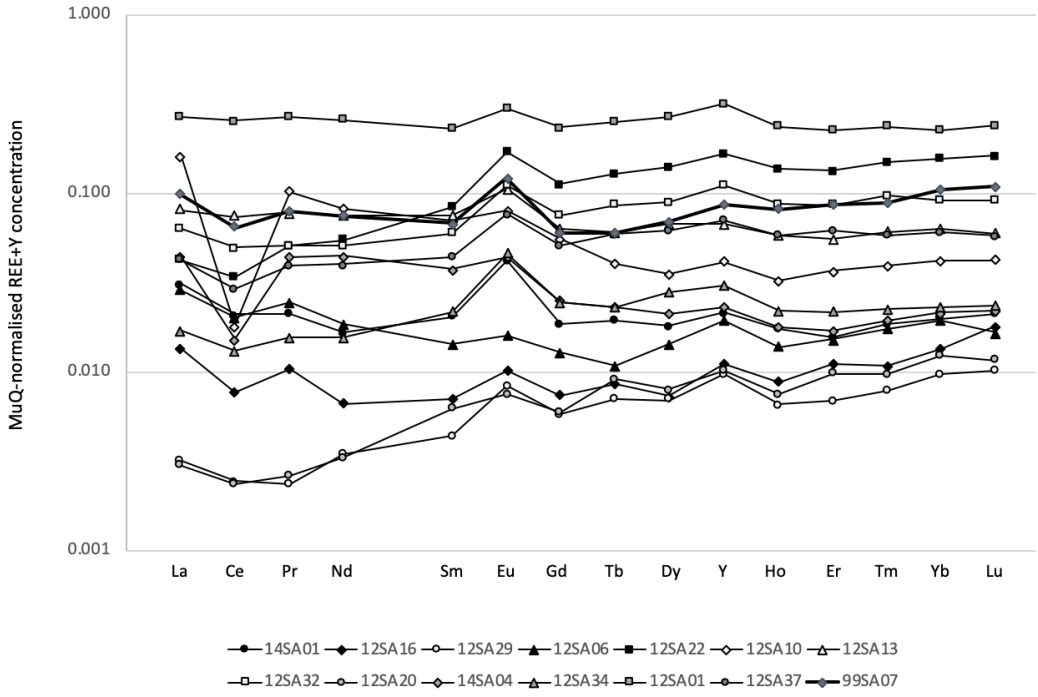

Fig. 3. Rare earth element plus yttrium (REE+Y) compositions of the studied samples and numerous other samples from horizons of the Josefsdal Chert, normalised to Mud from Queensland (MuQ), a trace and rare earth element dataset that approximates bimodal sediment input to the Archaean oceans (Kamber et al., 2005). The shallowly positive gradient, heavy REE enrichment, weakly positive La anomalies and Y anomalies, together with weakly to strongly positive Eu anomalies and the absence of a negative Ce anomaly, demonstrate that the depositional palaeoenvironment was an anoxic marine basin setting with hydrothermal influence.

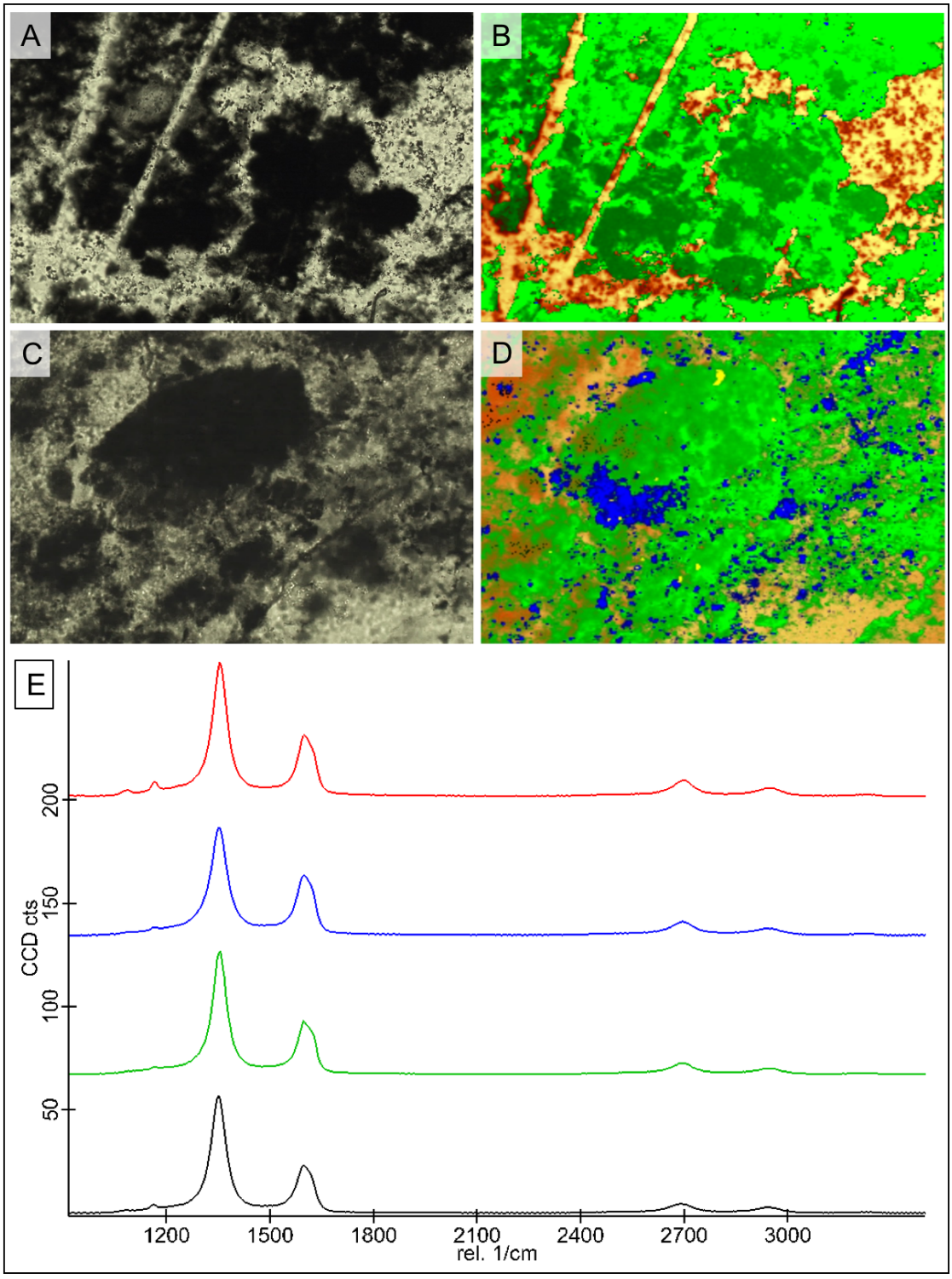

Fig. 4. Optical microscopy and Raman spectroscopy mapping of the structures of interest. A-B) Irregular clot in clotted carbonaceous chert. C-D) Volcanic particle coated in carbonaceous material in a volcaniclastic sediment. Green = carbon; yellow-orange = silica and blue = anatase. E) Averaged Raman spectra of carbonaceous matter within the structures of interest for four samples (99SA07, 12SA09, 12SA16 and 14SA01).

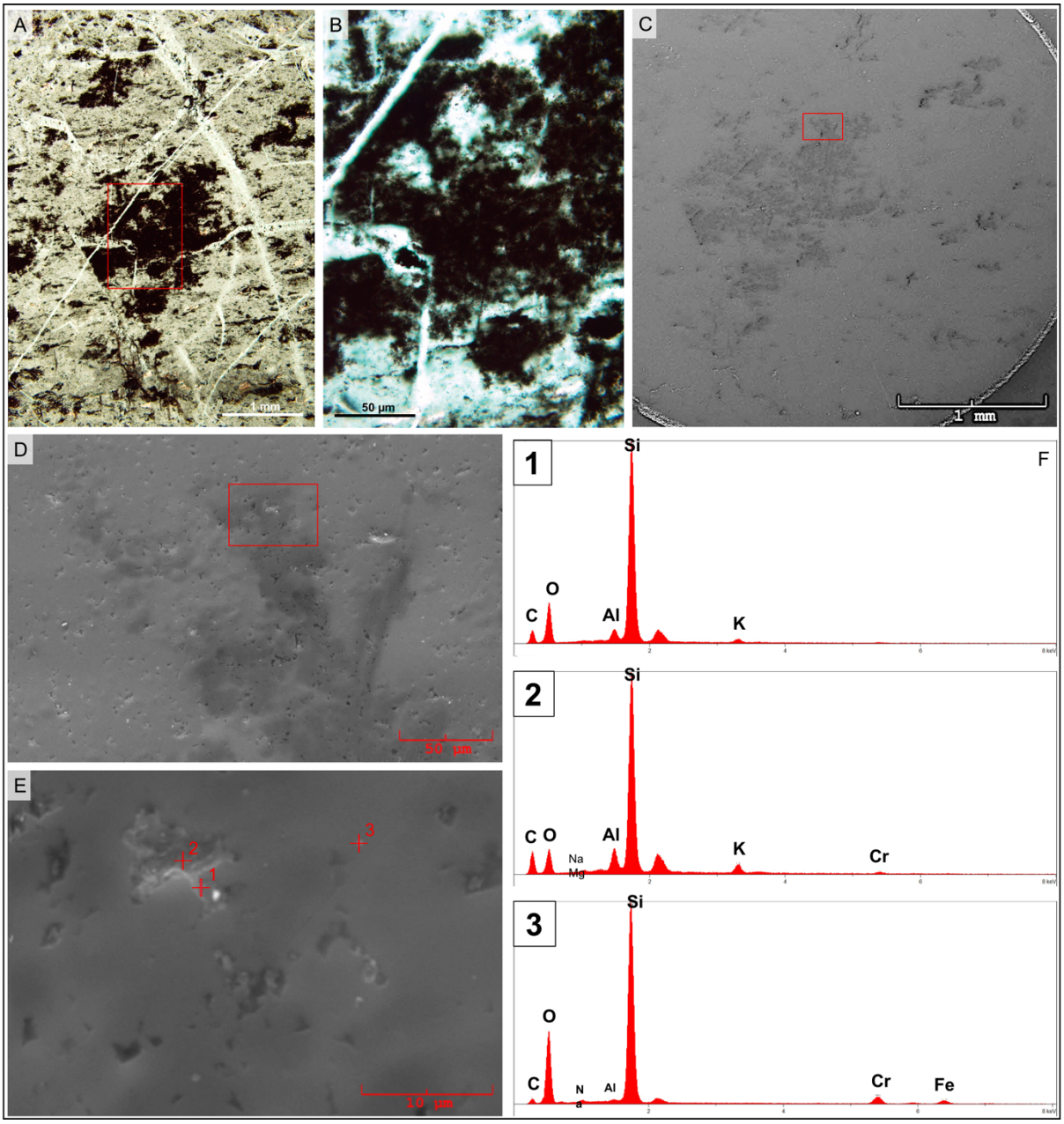

Fig. 5. SEM-EDS of irregular clots in clotted carbonaceous chert (sample 99SA07, region 1). **A**) Transmitted light photomicrograph of irregular clot in thin section; boxed area detailed in B. **B**) Detail of irregular clot. **C**) Electron image of the same clot; red box indicates region of D. Carbonaceous matter is dark grey, silica is light grey. **D**) Electron image of limb of clot; red box indicates region of E. **E**) Regions of EDS point analyses (numbered crosses). **F**) EDS point analyses on Au-coated sample accounting for point enrichments in Al, Na, Mg, K, Cr and Fe. Spectra 1 and 2 are aluminous phyllosilicates, whereas spectrum 3 is likely a sub-micron chromite spinel.

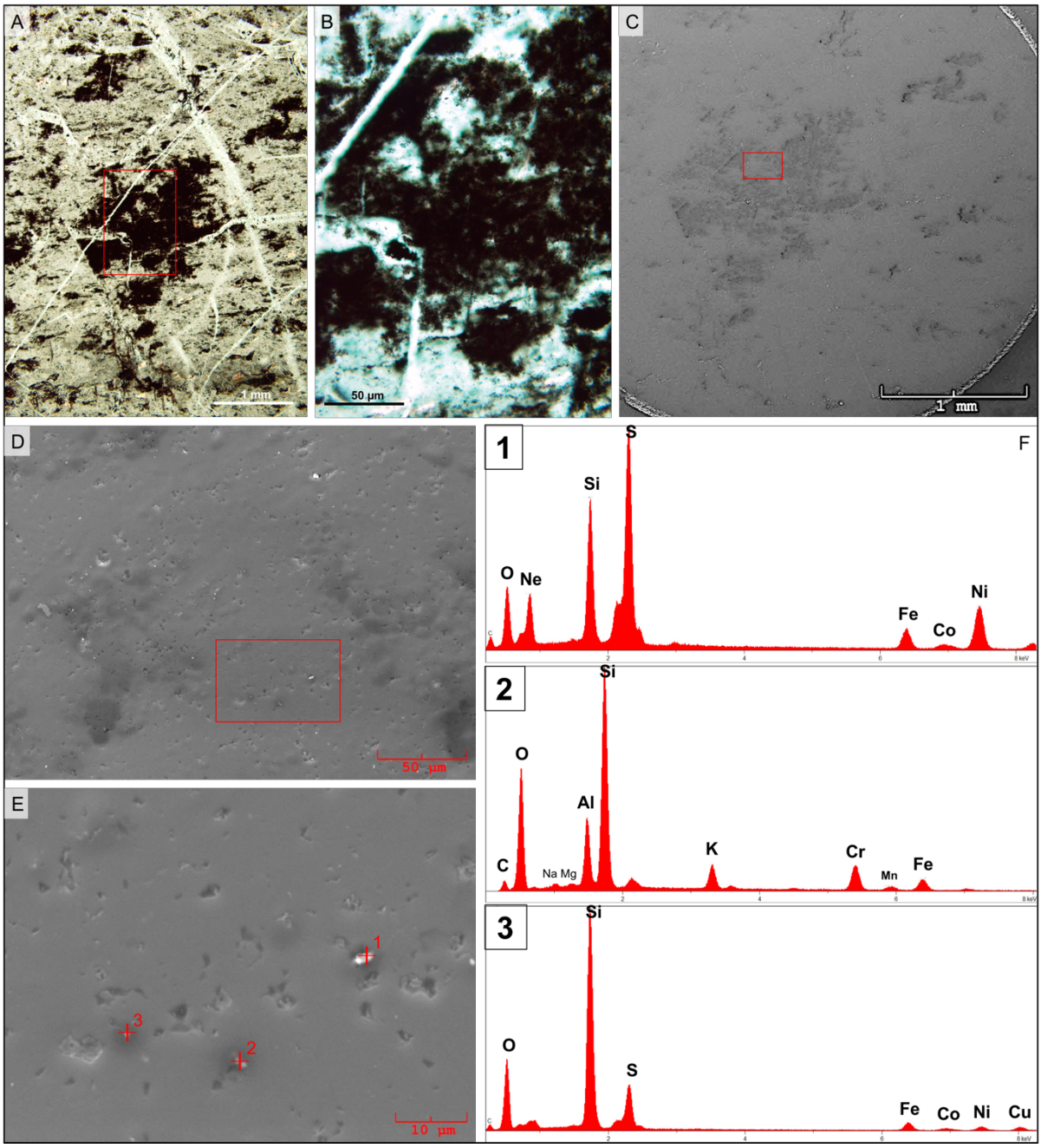

Fig. 6. SEM-EDS of irregular clots in clotted carbonaceous chert (sample 99SA07, region 2). **A**) Transmitted light photomicrograph of irregular clot in thin section; boxed area detailed in B. **B**) Detail of irregular clot. **C**) Electron image of the clot in A; red box indicates region of D. Carbonaceous matter is dark grey, silica is light grey. **D**) Electron image of interior of clot; red box indicates region of E. **E**) Regions of EDS point analyses. **F**) EDS point analyses on Au-coated sample accounting for point enrichments in Al, Na, Mg, S, K, Cr, Mn, Co, Fe and Ni. Spectra 1 and 3 are Fe-Ni sulphides (pyrite-pentlandite), whereas spectrum 2 is an aluminous phyllosilicate.

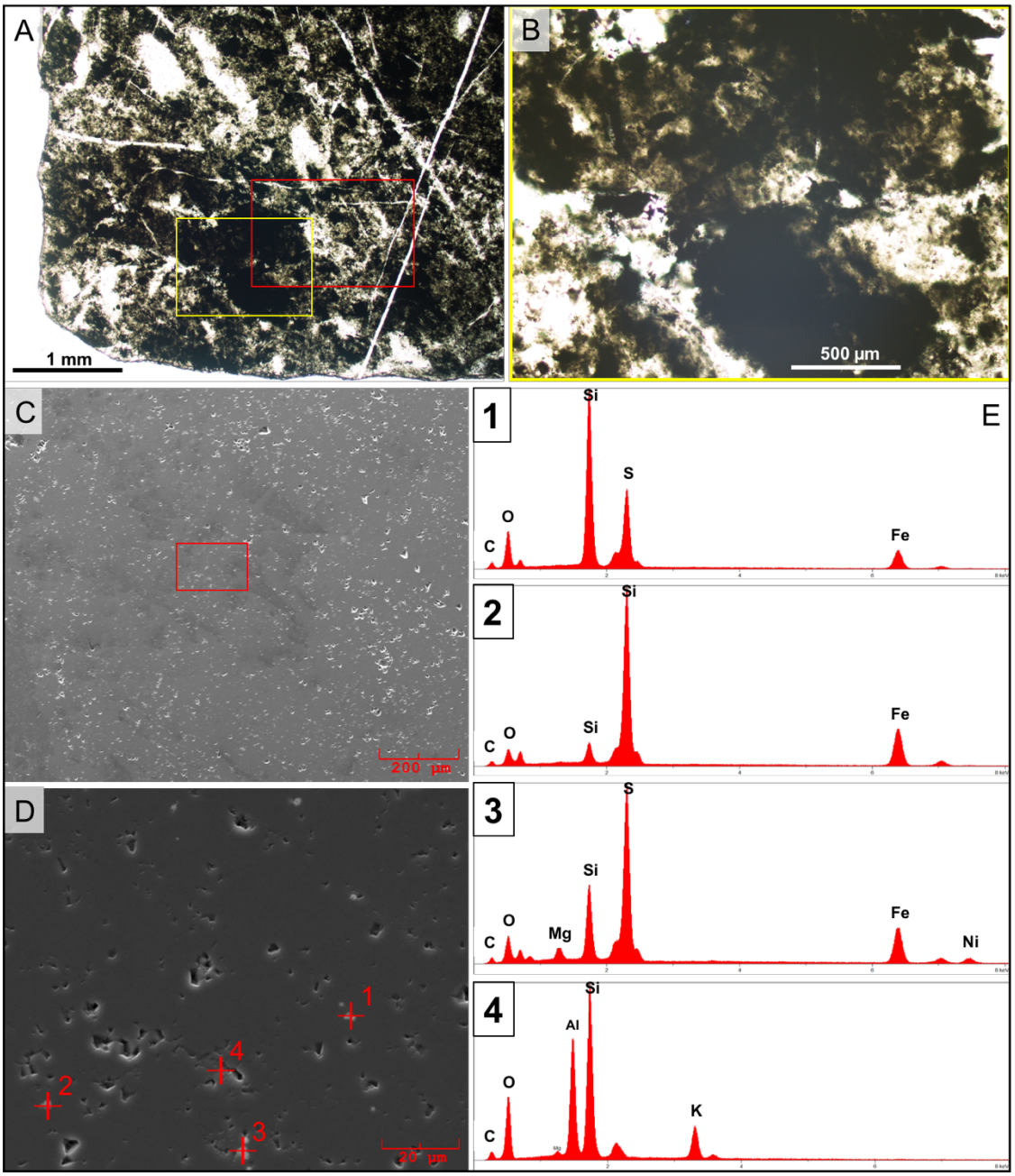

Fig. 7. SEM-EDS of irregular clots in clotted carbonaceous chert (sample 12SA09). **A**) Transmitted light photomicrograph of irregular clot in volcanogenic groundmass in thin section. Yellow box indicates region of B; red box indicates region of C. **B**) Detail of irregular clot. **C**) Electron image of the clot in A; red box indicates region of D. Carbonaceous matter is dark grey, silica is light grey. **D**) Region of EDS point analyses. **E**) EDS point analyses on Au-coated sample accounting for point enrichments in Al, Na, Mg, S, K, Cr, Mn, Co, Fe and Ni. Sepctra 1 and 3 are Fe-Ni sulphides (pyrite-pentlandite), whereas spectrum 2 is an aluminous phyllosilicate.

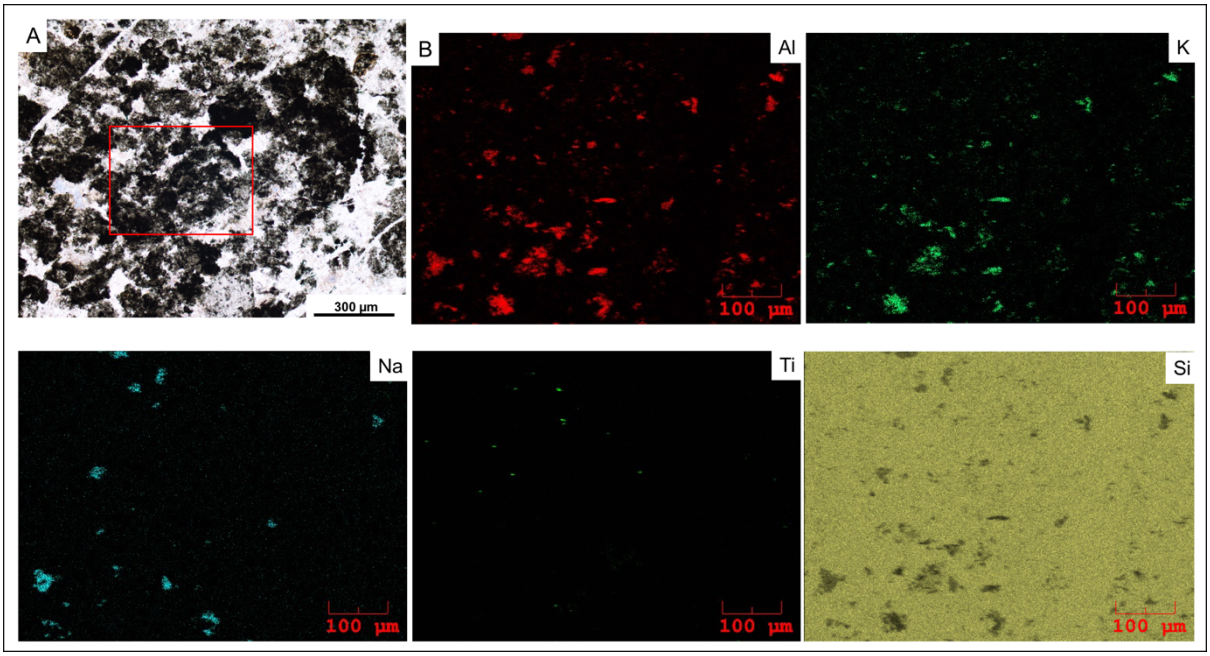

Fig. 8. SEM-EDX mapping of carbon-coated volcanic grains (sample 14SA01). **A**) Transmitted light photomicrograph of carbon-coated volcanogenic grains. Red box indicates the region of the EDX maps. **B**) EDX maps of Al, K, Na, Ti and Si. Correlated Al-K-Na-(Mg)-(Fe) indicates particles of mafic and felsic genesis, likely feldspars, pyroxenes and minor olivine, the latter represented by slight enrichments in Mg. Na-Al-K enrichments in tabular particles are probably relict feldspars. Ti is enriched in ilmenite and rutile. Ti corresponds to rutile crystals. SiO_2 is overwhelmingly the major constituent of the rock.

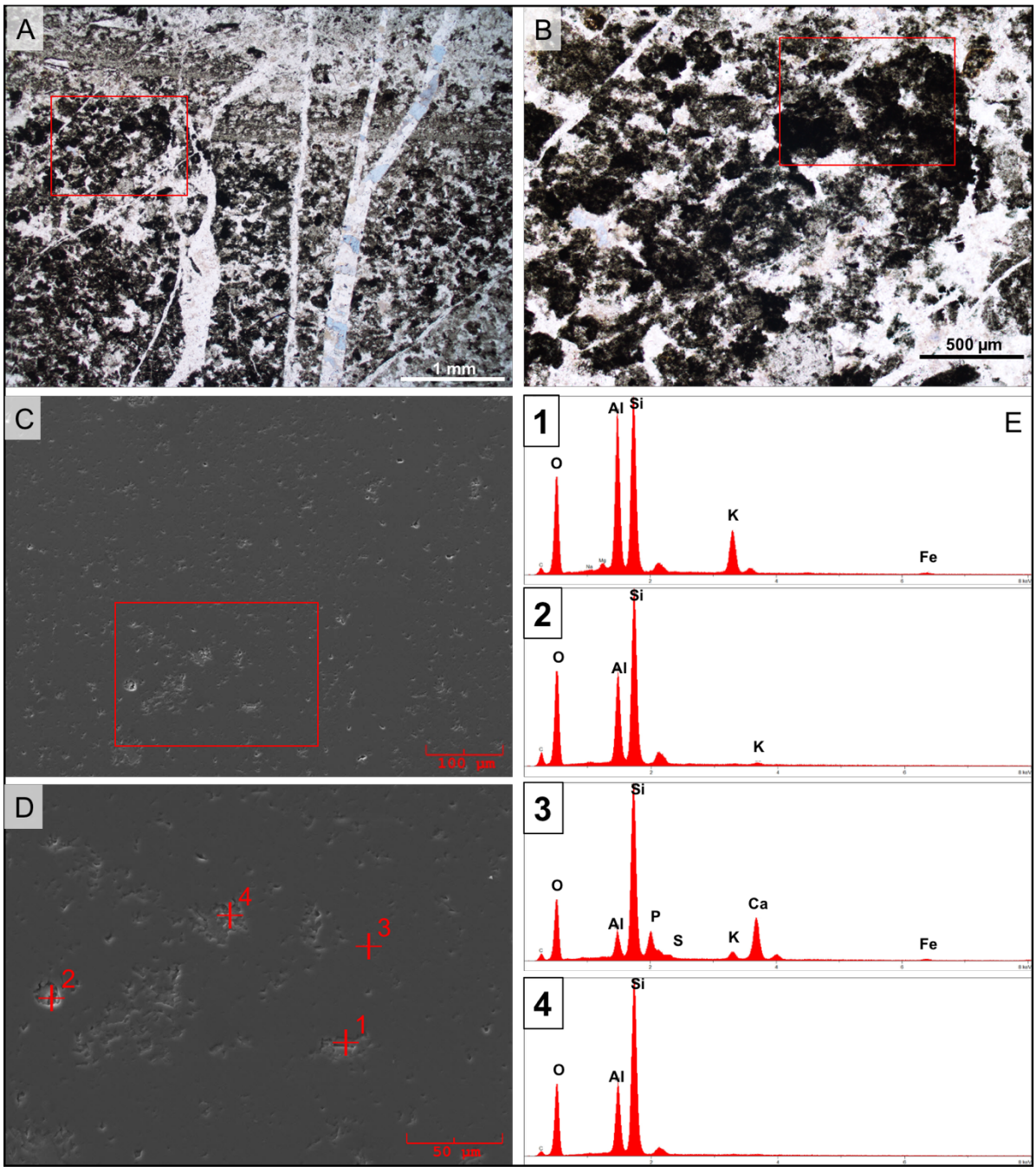

Fig. 9. SEM-EDS of carbon-coated volcanic particles (sample 14SA01). **A**) Petrographic image of carbon-coated volcanogenic particles. Red box indicates region of B. **B**) Detail of carbon-coated volcanic particles. Red box indicates region of C. **C**) Electron image of the particle in B; red box indicates region of D. **D**) Region of EDS point analyses. **E**) EDS point analyses accounting for point enrichments in Al, Na, Mg, P, K, Ca and Fe. 1 is an altered alkali feldspar, 2 and 4 are aluminous phyllosilicates, 3 is apatite with pyrite and K-feldspar (both unseen) seemingly within the region of analysis.

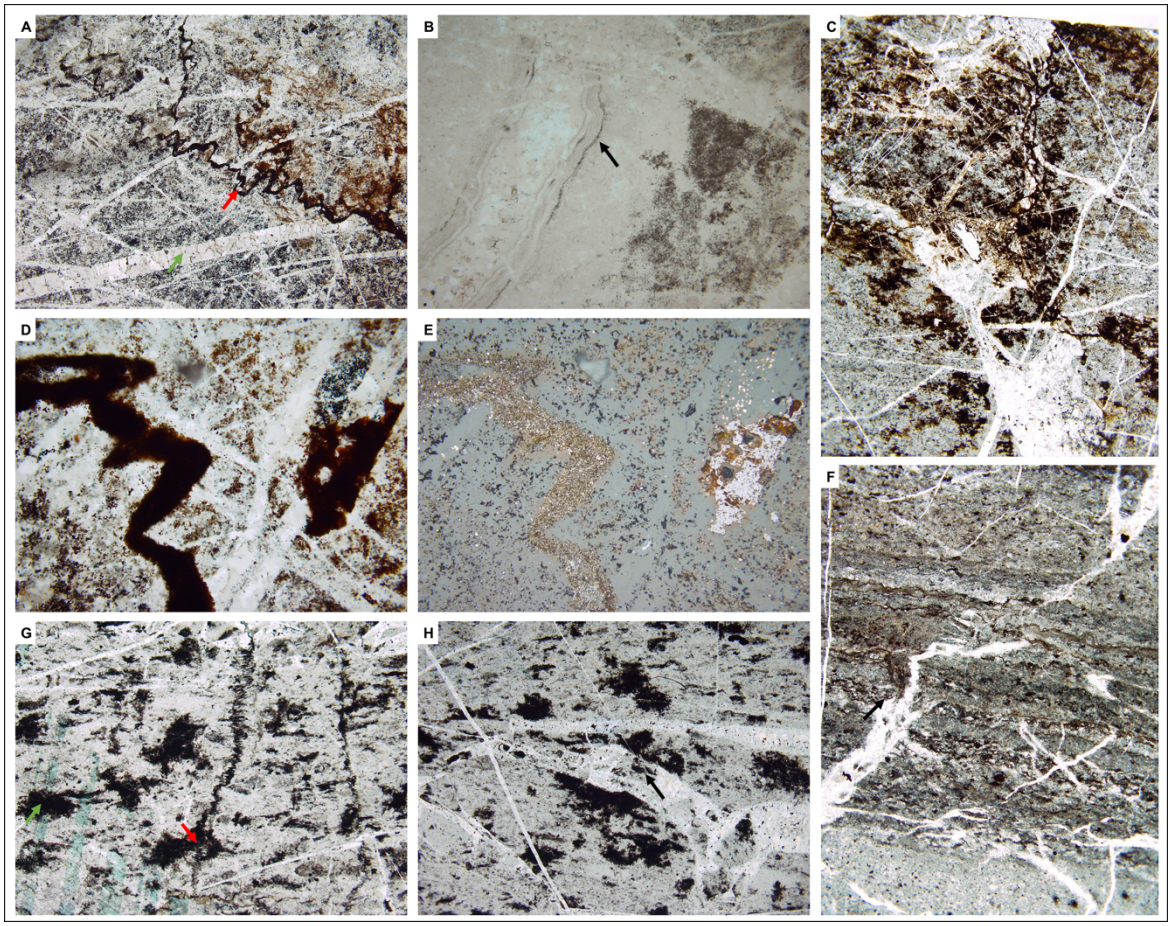

Fig. 10. Optical petrographic images indicating features or fabrics of demonstrably secondary origin, and which were avoided in the selection of regions of analysis in order to assure that the recorded geochemical signature is primary. **A**) Stylolite (red arrow) resulting from pressure solution fronts, and large secondary megaquartz vein (green arrow). **B**) Botryoidal chert fabrics developing within penecontemporaneous veins and leading to the secondary displacement of carbonaceous material (arrowed). **C**) Metal-bearing fluid alteration textures and chaotic secondary vein fabrics which may leach elements into their immediate vicinity. (dark and stained regions). **D-E**) Stylolites rich in metal oxides of probable syn- or post-diagenetic origin and large secondary oxide particle of no relevance to the primary sedimentary fabric. **F**) Primary laminated chert altered and distended by secondary quartz veins. Note the disruption of primary carbonaceous laminations (arrowed). **G**) Irregular clots in direct contact with stylolites (cut across), considered unreliable for analysis (red arrow). Clots further from the stylolite are considered appropriate targets for analysis (green arrow). **H**) Carbonaceous material entrained within post-depositional megaquartz vein (arrowed), the primary character of which cannot be assured; therefore, these are considered unsuitable for analysis.

2.2. Methods

2.2.1. Micro-scale particle induced X-ray emission (μ-PIXE)

In brief, micro-scale particle induced X-ray emission (μ-PIXE) analysis permits mapping of the distribution and concentration of trace elements that are below the detection limits of energy-dispersive spectroscopy (EDS). PIXE is a non-invasive ion beam technique able to study transition metals, large-ion lithophile elements (LILE) and high field strength elements (HFSE) (Halden et al., 1995; Sorieul et al., 2014). Measured X-ray yields can be converted into concentrations of the element according to detector-specific sensitivity (Campbell et al., 1995). Sixteen elements (P, S, K, Ca, Ti, V, Cr, Mn, Fe, Co, Ni, Cu, Zn, As,

Zr, Mo) were selected for their known roles in biogeochemistry, many of which are integral to the prokaryotic metallome. C (detected as CM using Raman spectroscopy; Fig. 4), P, S, Fe and K are bio-essential whereas Cr, Cu and, to some extent, Fe and Zn in high concentration, are low-toxicity elements, albeit with functional roles in the metallome (Zerkle et al., 2005). A number of the selected elements also have functions as enzymatic co-factors and have been identified as readily bioavailable in the early oceans and therefore define the metalloproteomic possibilities of prokaryotic evolution (Williams and Fraústo da Silva, 2003; Saito et al., 2003; Zerkle et al., 2005; Moore et al., 2017).

μ-PIXE combined with Rutherford Backscattering Spectrometry (RBS) was performed using the microbeam beamline of the AIFIRA facility (CENBG, Gradignan), which is described in detail in Sorieul et al. (2014). Our experimental setup used the 3 MeV proton microbeam (1 μm) with a current of 200 pA, and a high energy range of 40 keV to mitigate the issue of overlap amongst the K and L X-ray lines (Halden et al., 1995). Three Si-detectors (one RBS and two PIXE) collected data: the RBS detector was used for charge monitoring, since lithological samples are insulators, whereas the two PIXE detectors were used for elemental quantification and mapping. The first PIXE detector was equipped with an Al-"Funny Filter" (thickness 100 μm, hole size 2 mm) and a Kapton filter (thickness 50 μm). Kapton is used to filter out elements at lower atomic weights and is therefore key to determining the true concentrations of heavier trace elements, particularly for those of higher atomic mass than Ti. Increasing the hole size increases count rate, but has no effect on the rate of detection of individual elements. The second PIXE detector was equipped with an Al-"Funny Filter" (thickness 100 μm, hole size 1 mm) and was used for complete characterisation of the sample. No filter was applied to the RBS detector. The studied samples are 85.1-99.6% silica, therefore required long experimental times (8 to 12 hours) in order to accrue quantifiable counts for trace elements. All analyses were conducted with a dead time of less than 10% in order to avoid pile-up and spectra distortion. Dependent upon the size of the region of interest, scans were either set as 50 μm, 100 μm or 200 μm squares. PIXE is a non-destructive, non-invasive, *in situ* method for measuring trace element data in cherts when compared with previously used methods, such as HF total digestion. Multiple examples of each CM morphology were measured to produce a statistically significant dataset, depending upon their abundance in the studied samples. The matrix i.e., the palaeodepositional fluid, serves as the ideal benchmark against which elemental concentrations of specific microstructures can be normalised and compared. Multiple analyses of the matrix adjacent to microstructures of interest were conducted in each sample, providing the average matrix values for elemental concentration. X-ray counts can be converted into concentrations following the rationale and methods described in Halden et al. (1995) and Campbell et al. (1995), which detail the utility and capability of PIXE in determining, with a micrometric resolution, spatially resolved concentrations of the elements of interest.

The quantification of PIXE data involves a sequential workflow using three programs: SupaVisio, SIMNRA and Gupix (Campbell et al., 1995; Maxwell et al., 1995; Mayer, 1999). SupaVisio permits the selection of regions of interest, the spectra of which are extracted from the spectrum of the entire region of analysis. Each extracted RBS spectrum was treated with SIMNRA for charge determination (Mayer, 1999). The charges determined were used for the quantification of sixteen elements of interest (P, S, K, Ca, Ti, V, Cr, Mn, Fe, Co, Ni, Cu, Zn, As, Zr, Mo) with Gupix (Maxwell et al., 1995). The algorithm used by Gupix (see Maxwell et

al., 1995) calculates a limit of detection for the alpha- and beta-ray (K) of each element (quantification of L and M rays is also possible, though was not of relevance to the elements considered in this study and the energy range analysed), from which the user assesses the presence or absence of the element. Where close to the limit of detection (within 10% considering analytical error), we took a conservative approach and deemed the element absent. Therefore, all stated concentrations are low estimates.

In all quantifications, we consider a 'mineral effect' (Fig. 11), since much elemental incorporation of trace and rare earth elements can occur into the lattices of the microminerals associated with CM microstructures. This was deemed sensible based upon the element maps generated in SupaVisio, since while many trace elements are broadly enriched within carbonaceous matter, they are occasionally especially enriched within small regions, which correspond to minerals (Fig. 11C-E). Discounting any quantified analysis in which the value determined is more than five times the average of all other analyses of that type removes the 'mineral effect' for that element. The application of the 'mineral effect' may prevent the quantification of concentration within an element at depth where it is not directly identifiable by petrographic observation but nonetheless skews the results to higher averages. The presence of pyrite and volcanogenic mineral phases was confirmed by optical microscopy and TEM imaging. Pre-analysis screening of the regions of analysis was conducted in order to minimise the quantification of contaminative phases unrelated to carbonaceous material. Although other researchers have considered that the accumulation of trace and rare earth elements in micromineral phases may be able to be linked to bio-accumulation), we strongly advise against such an approach, for which no mechanistic understanding of process exists. Herein, we present a conservative approach that directly links trace element concentrations to organic material without the need for unconstrained transitional processes relaying element enrichments between biology and mineralogy.

In PIXE datasets, there is no direct correlation between the appearance of concentration in the maps, which is a function of the number of counts at any specific point, and the concentration of that element, which is a function of the detector-specific quantification of that element according to the algorithm of Gupix (see Halden et al., 1995; Campbell et al., 1995; Maxwell et al., 1995). Although the detection of some elements is below the theoretical detection limit of PIXE (~100 ppm for most elements), the ability to map their occurrence in discrete energy channels is consistent with their occurrence as shown in the individual element maps, but at concentrations well below the theoretical limit of detection for PIXE (< 100 ppm) (Halden et al., 1995; Campbell et al., 1995). The limit of detection (LOD) is defined as the concentration of an element that would give rise to an X-ray peak having an intensity equal to the three-sigma fluctuation of the background underlying the peak. In Gupix software, the LOD is defined as 3 times the square root of the background over 1 full-width half-maximum centred on the principal peak centroid. This corresponds to the LOD definition used for fluorescence spectrometry. The value of the LOD can vary with the concentration of the detected element, the preparation of the sample and more generally with the conditions of analysis. In order to achieve both the best conditions of analysis and the lowest background, we used the soft borosilicate glass NIST1411 standard as a reference material. We also mounted and fixed the samples to avoid any parasitic radiation due to beam interactions with the chert matrix. PIXE standardisation is based on the accurate determination of an instrumental constant independent of the X-ray energy. In practice, several uncertainties arise, mainly from either inaccurate

characterisation by the detector or uncertainties in X-ray transmission. Gupix software takes into consideration all of these deviations from the ideal measurement through the determination of a parameter termed the "H-factor". To enable this parameterisation, two standards were used: soft borosilicate glass NIST1411 and stainless steel AISI 15-7PH. The combination of these two standards covers the energy range in which all potential trace elements could be detected (1 to 20 keV). NIST1411 was also selected in order to evaluate the matrix effect and finely tune the beam conditions and detection setup for these analyses.

To summarise Section 2.2.1., we developed a protocol using µ-PIXE to make a conservative estimation of the trace element concentrations within CM from pervasively silicified Archaean cherts. By excluding concentrations due to enrichment within mineral particles, we do not run the risk of significantly overinterpreted bio-accumulation and directly quantify the elements indigenous to the CM. The rapid silicification of these cherts and lack of remobilisation possible from biological organic matter sinks (see Schultze-Lam et al., 1993), means that this method is well-adapted to quantifying the palaeo-metallome.

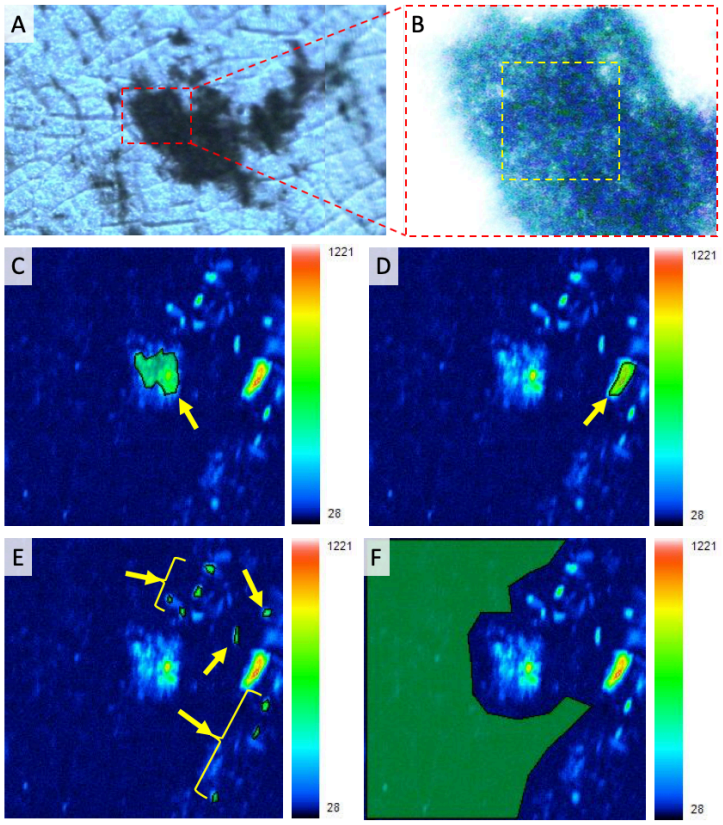

Fig. 11. Application of the 'mineral effect', identification of micron-scale mineral phases and analysis of the selected area from which the elemental complement of carbonaceous material was calculated using PIXE software. **A-B**) PIXE instrument optical views of a section of the studied clot. Region of analysis shown by yellow box = 200 µm square). **C-E**) Yellow arrows indicating the presence of mineral particles that were discounted in the analysis of carbonaceous material, since they may skew the results of metal enrichment to higher values. **F**) Example area of carbonaceous material characterised by PIXE, which is demonstrably free of mineral particles. Consequently, all metal enrichment reported in this region will be indigenous to carbonaceous material. The reported results show only the analyses from carefully selected and strictly characterised areas such as these.

2.2.2. Carbon isotope ratio mass spectrometry

In situ carbon isotope ratios and corresponding $\delta^{13}C_{PDB}$ values were calculated from measurements using a CAMECA IMS1280 large-geometry SIMS instrument at the Swedish Museum of Natural History operating in scanning ion imaging mode. Samples were gold-coated immediately prior to analysis. Following a 60 s pre-sputter with 20 kV incident energy, a ca. 1 nA Cs beam was rastered over a 25 x 25 μm area to remove the gold coating, and the beam was reduced to a critically focussed < 1 μm analytical spot, with a beam current of ca. 100 pA, which was rastered over an area of 20 x 20 μm during data acquisition. A low-energy electron flooding gun was utilised to prevent charge build up on insulating target areas. Sputtered secondary ions were steered back onto the ion optic axis using the dynamic transfer optical system, a secondary raster that is synchronised with the primary raster to permit the acquisition of data from a scanned area at high mass resolution. The secondary ion species $^{12}C^-$ and $^{13}C^-$ were separated at a mass resolution of 4000 (M/ΔM), in order to resolve ^{13}C from $^{12}C^1H$ and detected sequentially in the axial ion-counting electron multiplier (EM_{ax}) with counting times of 1 s and 5 s respectively over 100 cycles. The resulting ion images were processed using CAMECA Winimage2 software to identify regions of interest (ROIs) of high C concentration, from which the $^{13}C/^{12}C$ ratios were calculated, with the 44 ns EM_{ax} deadtime correction applied at the pixel level. Analyses of an in-house reference material, Cpyr2, a pyrolysed graphite disc with a $\delta^{13}C_{PDB}$ value of -35.4 ‰ (G.D. Layne, Memorial University of Newfoundland, personal communication) were performed using exactly the same primary beam and raster conditions in order to retain identical sputtering conditions and, hence, mass bias relative to the target graphitised carbonaceous material. Nonetheless, the much higher secondary count rates from a 100% graphite target precluded use of the EM and instead data were acquired simultaneously in two low noise Faraday Cups (FCs), ^{13}C in the axial FC2 and ^{12}C in L'2 FC operating at mass resolutions of 4000 and 2530, respectively. The instrumental mass bias determined from the Cpyr2 analyses was then applied to the ratios obtained from the target ROIs to yield their $\delta^{13}C_{PDB}$.

3. Results and Discussion

3.1. Palaeoenvironmental calibration

The elemental complement of the environment is of critical importance to the interpretation of the metallome of its inhabitants, since the environmental 'container' provides the elemental budget for the metabolic landscape within (Williams and Fraústo da Silva, 2003). The mode of occurrence of elemental enrichments in carbonaceous material are then key to distinguishing its origin within the environment. The palaeoenvironment must be demonstrated to be habitable and, in the event of interpreting the metal enrichment as a palaeo-metallomic signature, the predicted organisms and metabolisms should be consistent with the estimated environment.

Bulk and *in situ* geochemical data for the Josefsdal Chert indicate that the environment of deposition was a volcano-hydrothermal basin setting (Westall et al., 2001, 2006, 2015; Hofmann et al., 2013; Hubert, 2015; this study). Rare earth element plus yttrium (REE+Y) plots normalised to Mud from Queensland (MuQ) are the appropriate method by which to analyse the relative contributions of chemically distinct fluid reservoirs to Archaean sediments (Kamber et al., 2005; Gourcerol et al., 2015). Positive La and Y anomalies (Eqs. 1-2) and the

enrichment of heavy REE over light REE in bulk ICP-MS analyses testify to the presence of marine inputs (Fig. 1). Weakly to strongly positive Eu anomalies (up to 2.02; Eq. 3) are attributed to hydrothermal inputs. Although some Eu enrichment can be attributed to sequestration of MREE by feldspars, anomalies higher than 1.20 are incompatible with this alternative explanation (Kerrich et al., 2013).

Eq.1 $La/La^*_{MUQ} = La_{MUQ}/(Pr^*_{MUQ}(Pr_{MUQ}/Nd_{MUQ})^2)$

Eq. 2 $Eu/Eu^*_{MUQ} = Eu_{MUQ}/(Sm^2_{MUQ} * Tb_{MUQ})^{1/3}$

Eq. 3 $Y/Y^*_{MUQ} = Y_{MUQ}/(0.5Er_{MUQ} * 0.5Ho_{MUQ})$

In all studied samples, the major environmental parameters are therefore hydrogenous, of marine and hydrothermal origins (Fig. 3). The shallow gradient is indicative of elevated light REE input, which is most plausibly interpreted as the result of terrigenous contributions, i.e., the depositional environment was restricted and strongly influenced by proximal exposed landmasses (Kamber et al., 2004; Sugahara et al., 2010; Bolhar et al., 2015; Hickman-Lewis et al., in review). Differential values for the anomalies of interest indicate the fluctuating importance of these various fluid reservoirs during the deposition of the Josefsdal Chert (Hickman-Lewis et al., in review). The presence of volcano-hydrothermal inputs in the depositional palaeoenvironment indicate that it would have been a thermophilic habitable setting (Westall et al., 2015). The high concentrations of LREE and trace elements denote elevated influences from volcanic and terrigenous inputs. For the Early Archaean, it is likely that most exposed landmasses were of volcanogenic origin (Lowe and Byerly, 1999; Kamber, 2015; Cawood et al., 2018). The lack of a negative Ce anomaly indicates anoxic palaeodepositional fluids (Gourcerol et al., 2015; Bolhar et al., 2015). High concentrations of Fe- and Mn-oxyhydroxides in semi-restricted settings such as this were able to concentrate REE+Y elements and make these elements bio-available (Jeandel and Oelkers, 2015). The environment of the Josefsdal Chert was therefore metal-rich (and more broadly had a rich elemental budget), thermophilic, anoxic, and replete with chemical disequilibria as a result of the confluence of fluids of different origins. The studied samples thus reflect a habitable environment that was perhaps typical of basin settings for life on the early Earth (see Discussions of Hickman-Lewis et al., 2018, in review).

3.2. Trace element distribution and concentration within carbonaceous material

For the two CM morphologies of biological promise studied herein – irregular clots and carbonaceous coatings on volcanic particles (Fig. 1) – the following reports their elemental enrichments or depletions relative to the ambient environment (taken to be the chert matrix; Figs. 12-13, Tables 1-2), i.e. the enrichment factor is calculated as in the following examples: i) 100% represents (ambient fluid conditions)/(concentration within the matrix) = 1; ii) 50% represents (ambient fluid conditions)/(concentration within the matrix) = 0.5. For comparison, we provide corresponding data for the matrix and other CM (flakes; Fig. 14; Table 1). We have taken into account a 'mineral effect' to discount elemental enrichments solely due to the presence of mineral particles within CM (Fig. 11), such that the analysis of only CM itself is used. This involved the exclusion of any highly concentrated, spot-specific (i.e., not diffusely distributed) enrichments of any element. As shown in Figures 5-9, the studied clots contained micron-scale mineral phases. The size and frequency of occurrence of micron-scale mineral

phases directly corresponds to the frequency with which mineral phases are observed in SEM images. Furthermore, the remaining CM shows a weaker enrichment in metals relative to the matrix with a pattern of occurrence that directly matches that shown in high-resolution optical and electron microscopy. Although elements within complexes were likely the means by which ions were made bio-available (Konhauser, 2007), it is impossible to unambiguously petrogenetically link minerals to the CM within which they are located (Fig. 5-9). TEM measurements further show that clots do not contain nanoscopic minerals (Fig. 15). Nanoscopic minerals are therefore not the source of metal enrichment.

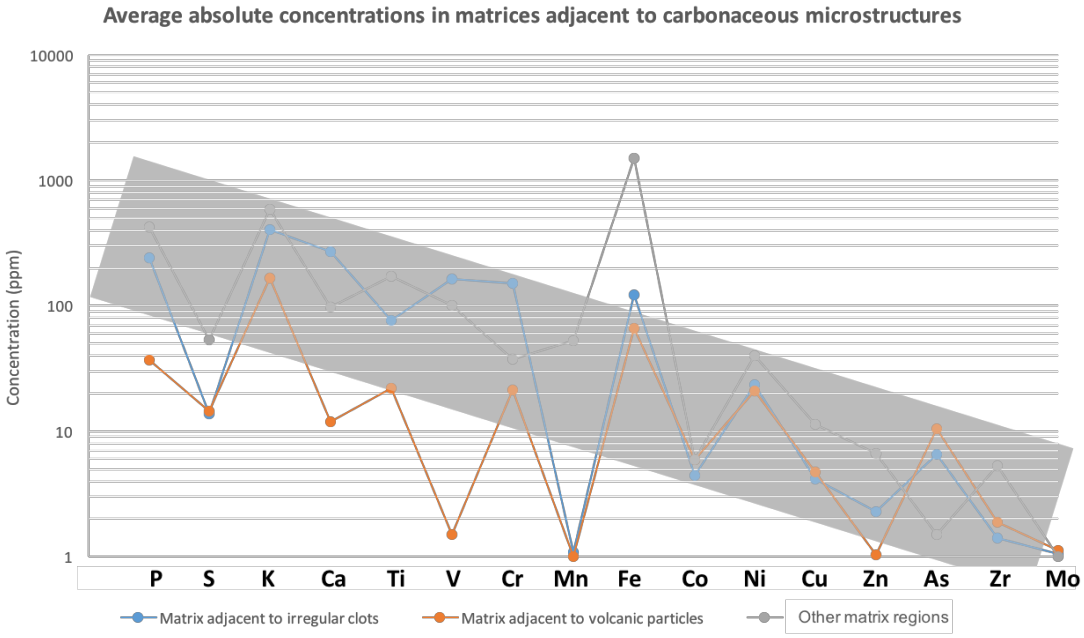

Fig. 12. Average concentrations of the sixteen studied elements within the matrices adjacent to the carbonaceous microstructures of interest. Concentrations are broadly equivalent, with the exception of greatly enriched Fe in sample 12SA34 (matrix adjacent to flakes), which can be accounted for by the presence of randomly distributed siderite, and the low V and Ca in matrices adjacent to coated grains. The grey trend-line is comparable to that of the ICP-MS data (Fig. 22A) and all trends bear similarity to the flakes trend-line (Fig. 22D), indicating no directional concentration by the flakes.

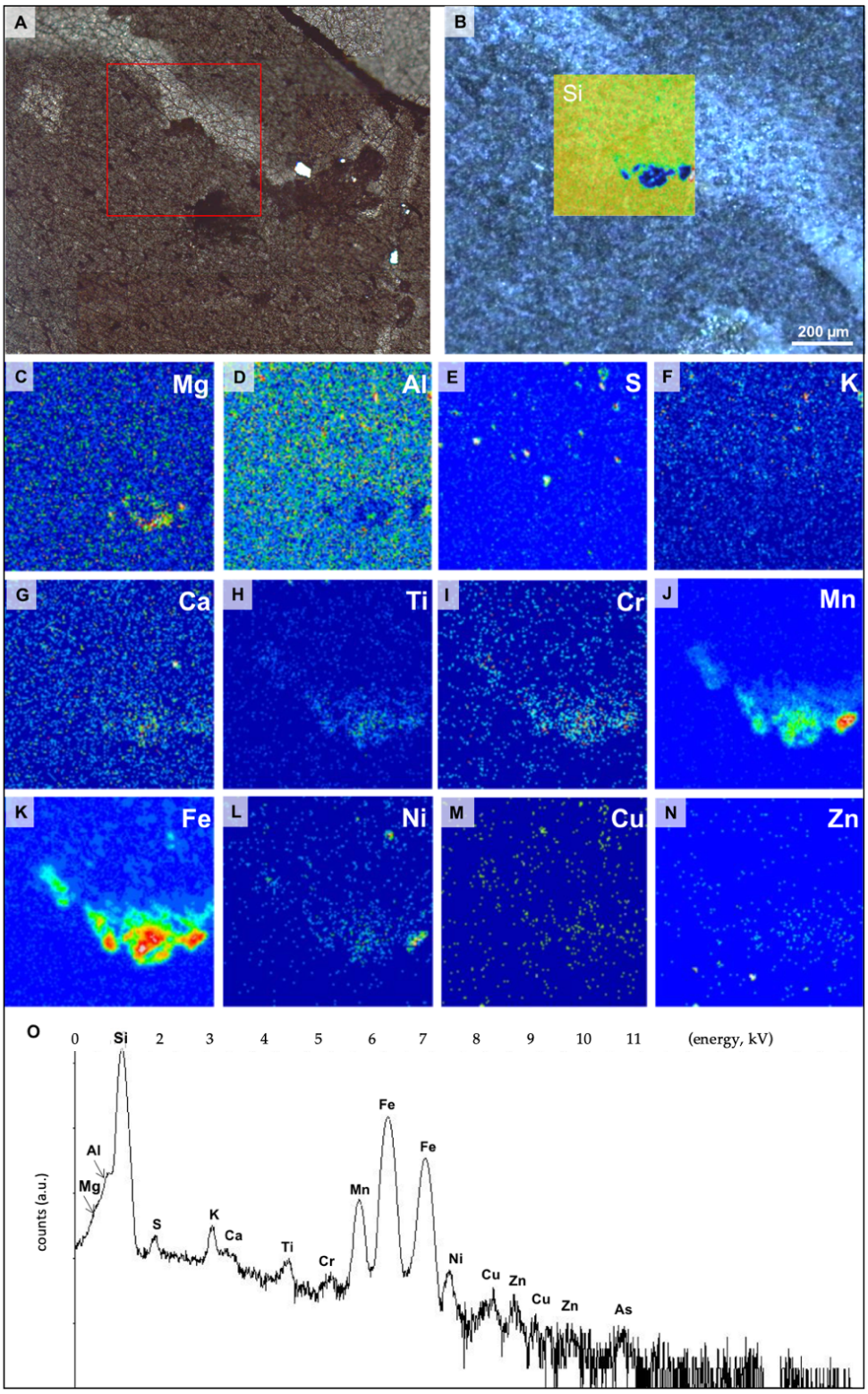

Fig. 13. PIXE analysis of one matrix zone (sample 12SA34). **A**) Transmitted light photomicraph mosaic of the matrix. Red box indicates the region of B. **B**) Optical image of the matrix, superimposed with silica map, demonstrating the anti-correlation with the siderite-rhodochrosite crystals. **C**) Elemental maps of major and trace elements within the matrix: Mg, Ca, Ti, Cr, Mn, Fe, Ni, Cu and Zn are concentrated within the siderite-rhodochrosite crystal aggregate, Al is anti-correlated with the crystals. Fe, Ni, Cu and Zn are further concentrated in micron-scale particles elsewhere in the matrix. **D**) Corresponding PIXE spectrum.

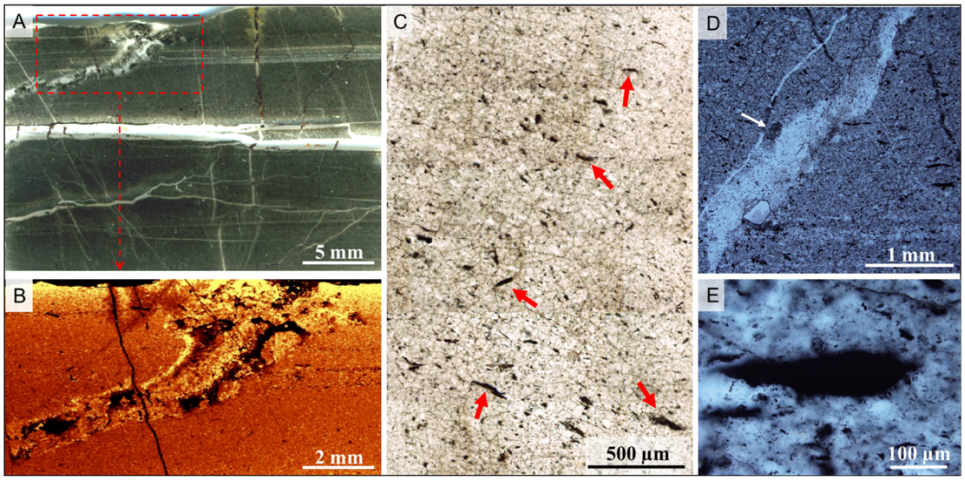

Fig. 14. Geological setting of carbonaceous flakes in hydrothermally permeated sediment. **A**) Thin section scan of sample 12SA34, through which pass vertical and stratiform veins of hydrothermal origin. The red box denotes a miniature vent mapped by Raman spectroscopy in B. **B**) Raman map of carbon, wherein brightness corresponds to occurrence of carbonaceous material. Note therefore that carbon is greatly enriched within the fluids in the vent relative to the surrounding sediment. **C**) Carbonaceous flakes (arrowed) and disaggregated carbonaceous material distributed throughout the matrix. **D**) PIXE instrument's optical image of the matrix, which includes frequent siderite particles (arrowed). **E**) PIXE instrument's optical image of a carbonaceous flake with tapered margins.

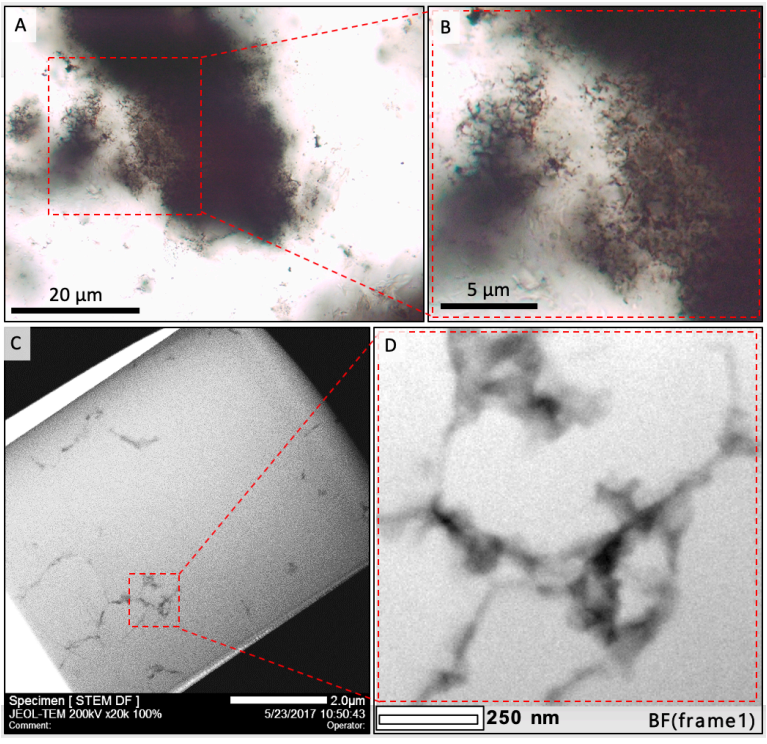

Fig. 15. Petrographic and transmission electron microscopy (TEM) characterisation of CM comprising irregular clots (sample 99SA07). **A-B**) Optical photomicrographs showing the edge of an irregular clot. The 'blackness' of the clot is an optical effect, as demonstrated by the high-magnification view shown in B. Here, where the CM is less dense, one can appreciate that the clot is composed of CM interleaved between micro-crystals of quartz, forming a web-like arrangement. **C-D**) TEM micrographs showing the high-resolution spatial relationships between CM (dark grey-black phase) and quartz (light grey phase). Note that the CM itself is near-pure carbon and does not incorporate nanoscopic mineral particles.

3.2.1. Irregular clots

Irregular, scalloped clots exhibit significant (>150%) enrichments in nine of the sixteen elements analysed relative to the matrix: P, S, Ti, V, Fe, Co, Ni and As (Figs. 16-17; Table 1, Table 2). Modest enrichments (100-150%) are present in Mn, Cu, Zr and Mo, although all of these and Zn occur at concentrations below the limit of detection appropriate for quantification (Table 1). Ca and Cr are depleted (<100%) relative to the matrix. Although P is depleted relative to the matrix in two analyses, there are high densities of apatite (Ca-phosphate) crystals in the matrices of these two analyses, and P concentrations within CM are of the same order of magnitude as in analyses where CM is enriched. Considering this, the 370% enrichment reported is an accurate average value for true P concentrations within clotted CM. Therefore, concentrations in these elements follow the pattern: K > Ti > Fe, P > V > Ni > Cr > As, S > Co > Cu > Zn > Zr, Mo, Mn (Figs. 16-17, Table 1).

Anomalously high S within clotted CM is attributed to microscopic Fe-Ni sulphide crystals which are absent in the matrix (Figs. 5-7, Table 1). Fe is enriched by up to over 100,000 ppm in some analyses of iron sulphide or oxide crystals, but taking into account the 'mineral effect' yields lower enrichments of around 280% within CM. PIXE analyses of sulphides imply that they are also point sources of As (up to 3,000-11,500 ppm), Cu and Ni (Figs. 16-17), although these elements are nonetheless enriched throughout CM. There is a general trend in decreasing absolute concentration of trace elements with atomic mass, whereas enrichment relative to the matrix is element-dependent, following no specific trend (Fig. 22).

3.2.2. Carbonaceous coatings

Carbonaceous coatings on volcanic particles show similar elemental enrichments to irregular clots, although P is inconsistently distributed (Fig. 18; Table 1, Table 2). Coatings are significantly enriched in nine elements: S, V, Ni, Cu, Zn, As and Zr (Table 1), although Zn concentrations are below the limit of detection appropriate for quantification. K, Fe and Co are modestly enriched. Depletions in P, Ca, Ti, Cr and Mo are noted, however, Mo is present at a calculated value far below the limit of detection for reliable quantification. Anomalously high Ti and Cu values are ascribed to the unavoidable concomitant quantification of microscopic ilmenite, titanomagnetite and anatase crystals, which have been identified within this volcanogenic material *via* SEM-EDS and Raman spectroscopy (Figs. 8-9). These are present regularly throughout carbonaceous matter. Overall, elemental concentrations follow the pattern: K, Ni > Cu, Fe > V > S > As > P, Ti > Co > Zr > Ca > Zn, Mo, Mn (Table 1). There is again a trend in decreasing absolute concentration of trace elements with atomic mass, whereas enrichment relative to the matrix is element-dependent (Fig. 22).

3.2.3. Other carbonaceous material in the JC sediments

As a negative control, we also measured the elemental composition of a third CM morphology, 'flakes' (Fig. 14), which are elongate objects often lying parallel to bedding planes. There is again a decreasing absolute enrichment with atomic mass, which is also characteristic of the matrix, however, enrichments in all elements are minor or inexistent, and μ-PIXE mapping of elemental abundances shows that the distribution of trace metals is very different to that seen in irregular clots and particle coatings: most enrichment can be ascribed to mineral grains within flaky CM (Figs. 19-20). Removal of the 'mineral effect' therefore

results in concentrations within CM closely matching those of the matrix (Fig. 22; Table 1, Table 2), and distinguishes the type of signature seen in flakes from those of clots and coatings.

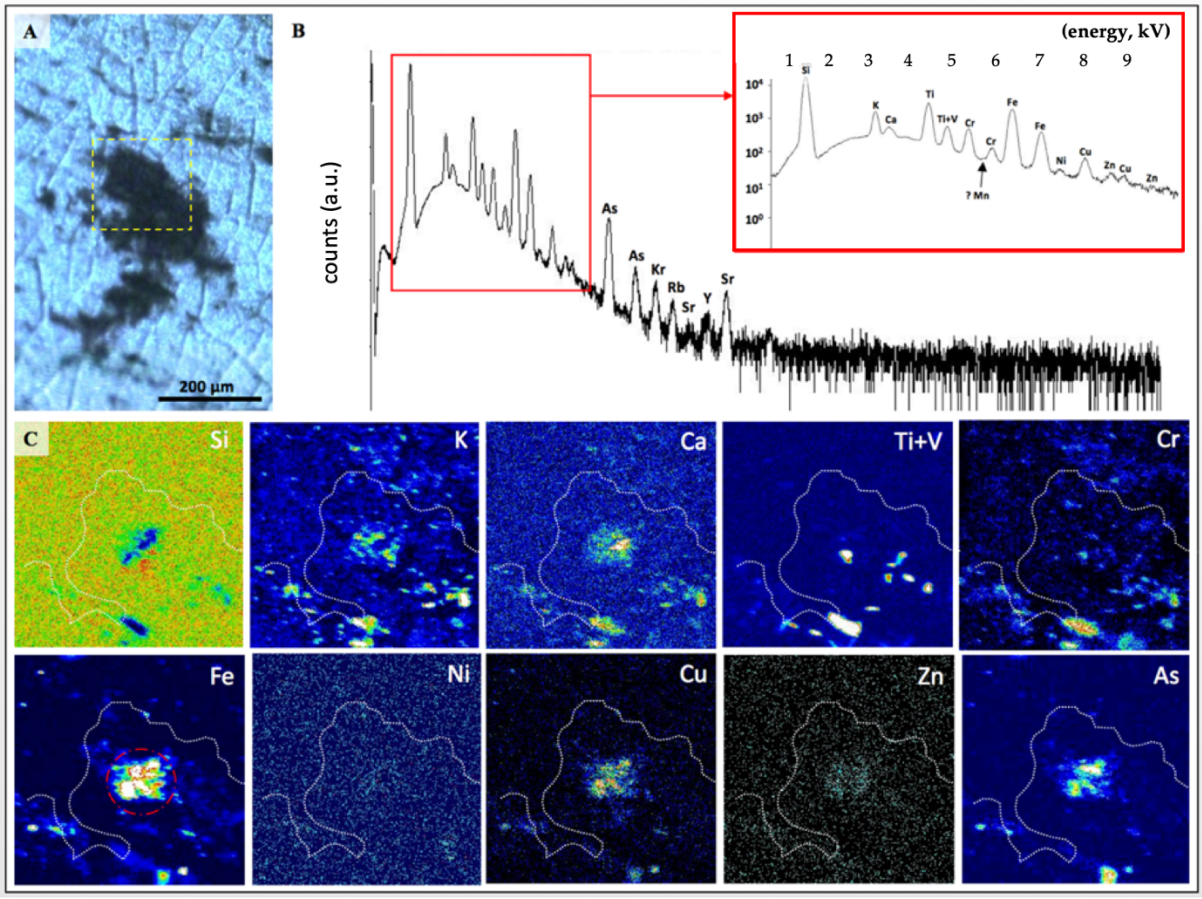

Fig. 16. Example particle-induced X-ray emission (PIXE) analysis of irregular carbonaceous clots (sample 99SA07). **A**) Optical photomicrograph of irregular clot analysed; boxed area indicates the region of PIXE analysis. **B**) Spectra from within the carbonaceous material, excluding the central crystal (excluded zone within red circle in Fe map), demonstrating the enrichment in numerous bio-functional elements. **C**) Elemental maps for silica, potassium, arsenic, calcium, titanium, chromium, iron, nickel, copper and zinc. Although many transition metals are concentrated within the metallic complex at the centre, there is a notable distributed enrichment in As, Cr, Fe, Ni and Cu within the carbonaceous matter surrounding the complex with respect to the matrix. Correlated high concentrations of Fe and Ti likely indicate a micron-scale ilmenite or titanomagnetite mineral phase. Boundary between carbon and matrix highlighted.

3.2.4. Comparison between trace element composition of clots and coatings

Similar magnitudes of enrichment in major and trace elements are present within both irregular, scalloped clots and carbonaceous coatings on volcanic particles. This is coupled with similar magnitudes of carbon isotope fractionation, albeit with slightly more negative, and more constrained, values in the coating morphology. Both CM morphologies are associated with volcanogenic particles: coatings are in direct contact with volcanic particles, and irregular clots are also templated by microscopic (1-50 µm) volcanic particles, largely altered to K- and Cr-bearing aluminosilicates – montmorillonite and fuchsite – and the Ti-bearing mineral anatase (Figs. 5-9). Unsilicified Cr-spinel is present throughout (e.g. Fig. 5). K concentration is broadly constant throughout most analyses (Table 1).

The difference in the ratio of CM to the interfacial area of volcanic material between these two CM morphologies makes it highly unlikely that the variable concentration of major and trace elements (i.e. the enrichments indicated by the grey trend-lines in Fig. 22) is entirely the result of either passive diffusion from volcanic particles or passive enrichment from the ambient fluid, but is rather a directional and facilitated diffusion process. If passive diffusion were the mechanism by which the accumulation of elements took place, the concentrations reported in the coatings should be higher and more heterogeneously distributed than in the irregular clots as a result of both metal ion availability and mineralogical variation in the volcanogenic 'substrate'. The diffuse trace element signature in both CM morphologies is therefore primary and indigenous to CM. Since regions of interest were not selected from secondary veins or obvious deformational features (Fig. 10), and indeed that such remobilisation is not at all evidenced in our samples, no later migration of geochemical signatures could have occurred in these cherts.

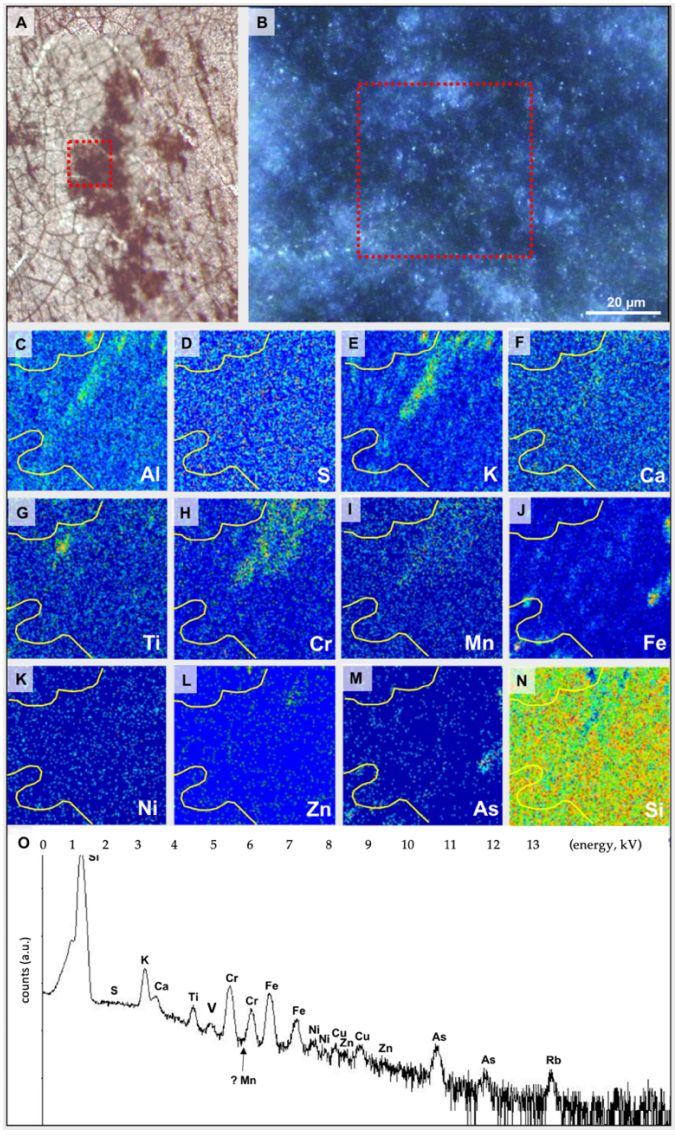

Fig. 17. PIXE analysis of irregular clot (sample 99SA07). **A**) Transmission light photomicrograph mosaic of the studied clot. Red box indicates the region of B. **B**) Optical image of the clot. Red box indicates the region mapped.

C) Elemental maps of major and trace elements within the clotted material and adjacent matrix (yellow lines denote the edge of the carbon). Note that, aside from enrichment in the linear crystal mass at the upper centre of the image (and other minor minerals), Al, S, K, Cr, Mn, Fe, Ni, Zn and As are broadly enriched within the carbonaceous matter relative to the matrix (compare matrix zone at upper left). Ca and Ti are uniformly enriched throughout both clot and matrix. Si is depleted within the clotted carbon. **D**) Spectrum from the zone of carbonaceous material. Although Mn is mapped, its presence is difficult to determine, since it occurs on the shoulder of the Cr K_{beta} peak. X and Y axes are energy channel (instrumental) and counts per channel, respectively.

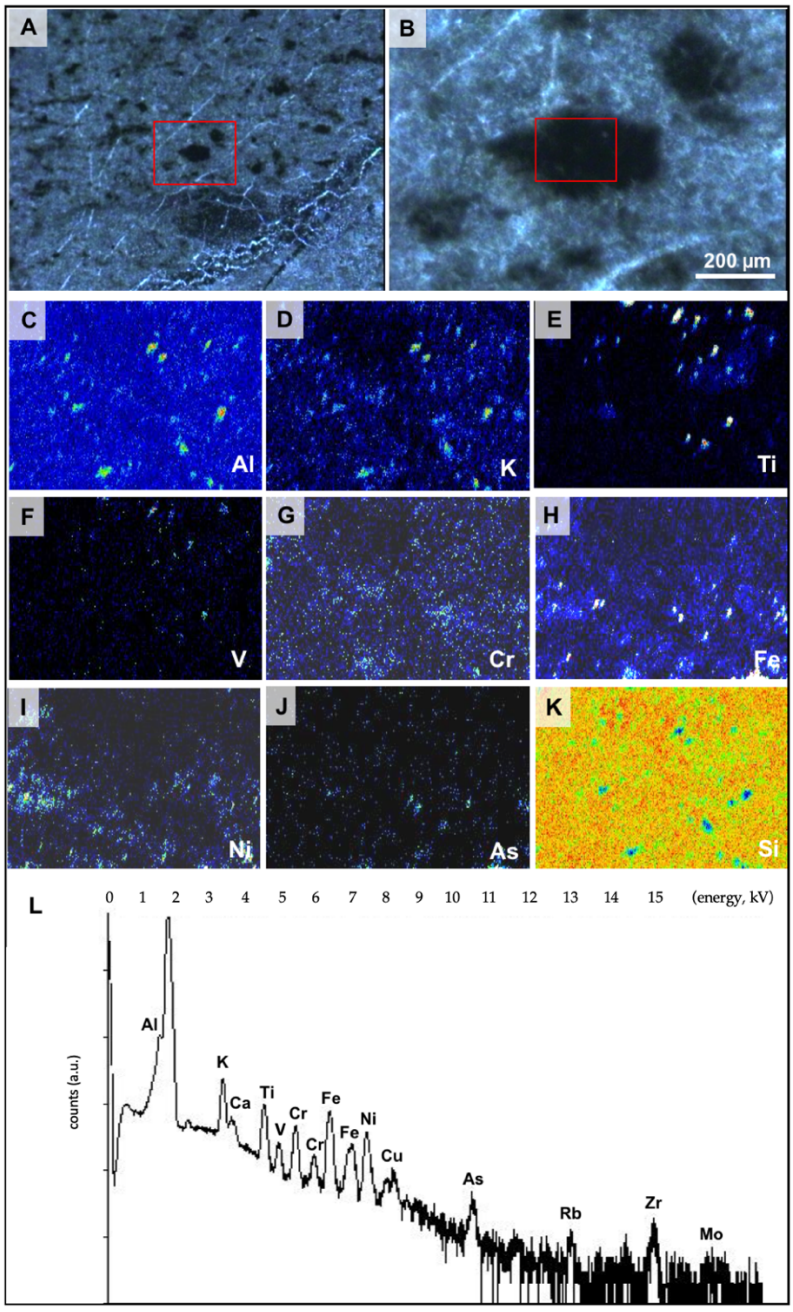

Fig. 18. PIXE analysis of carbon-coated volcanic particle (sample 14SA01). **A**) Optical image of the sample. Red box indicates the region of B. **B**) Optical image of the particle. Red box indicates the region mapped. **C**) Elemental maps of major and trace elements within the carbonaceous material. **D**) Spectrum from the zone of carbonaceous material. X and Y axes are energy channel (instrumental) and counts per channel, respectively.

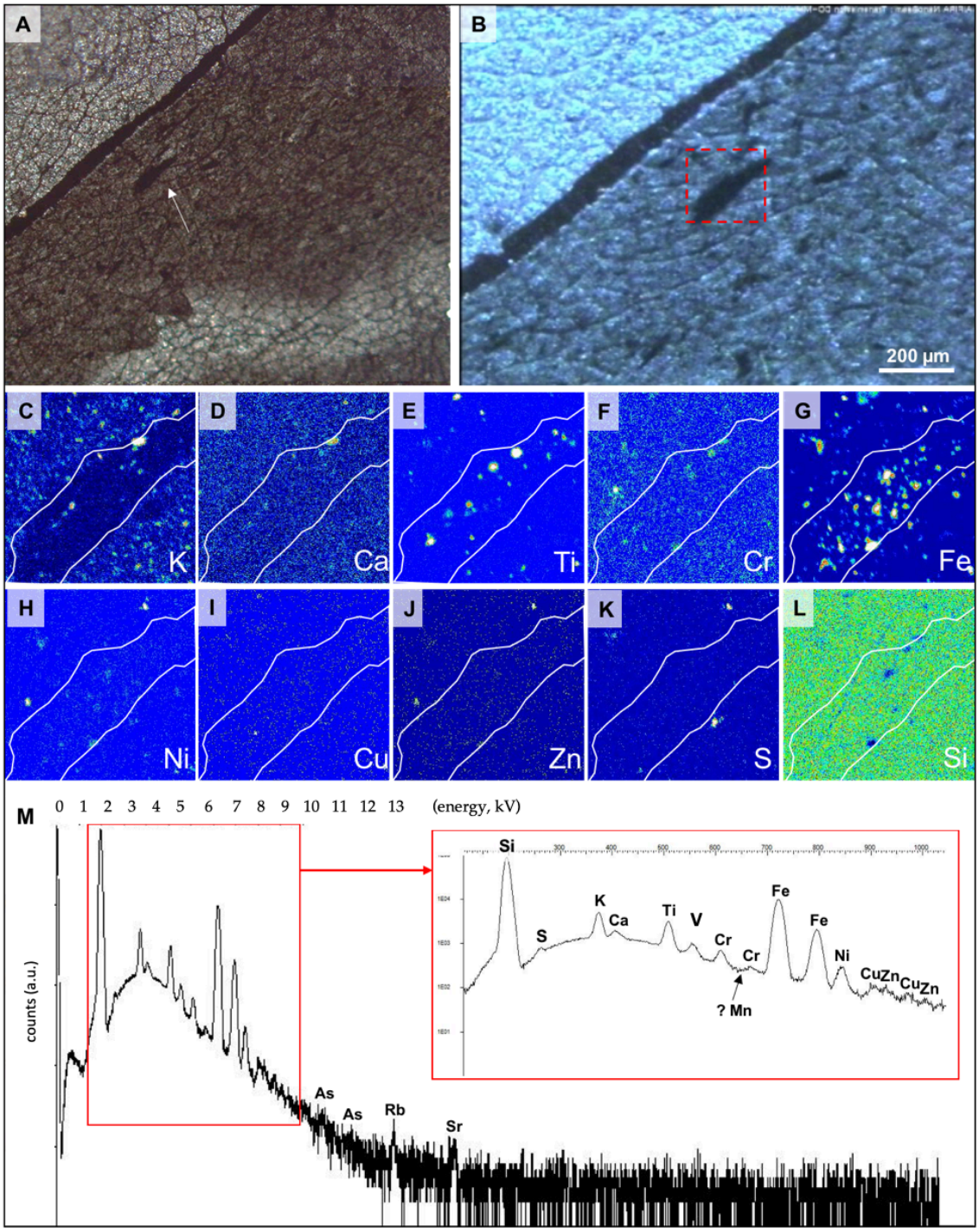

Fig. 19. PIXE elemental mapping of flake (sample 12SA34). **A**) Petrographic image mosaic of the studied flake. **B**) PIXE instrument's optical image of the clot. Red box indicates the region mapped. **C**) PIXE spectroscopy mapping of major and trace elements within the flake and adjacent matrix (yellow lines denote the edge of the carbon). K, Ti, Cr, Fe, Ni and Cu are enriched specifically in micron-scale mineral particles within the flake and matrix. Zn and S are enriched specifically in particles dispersed throughout the matrix. Ca is uniformly enriched throughout both flake and matrix. **D**) PIXE spectra from the zone of carbonaceous material. The presence of Mn in the spectra is difficult to determine, since it occurs on the shoulder of the minor Cr K_{beta} peak.

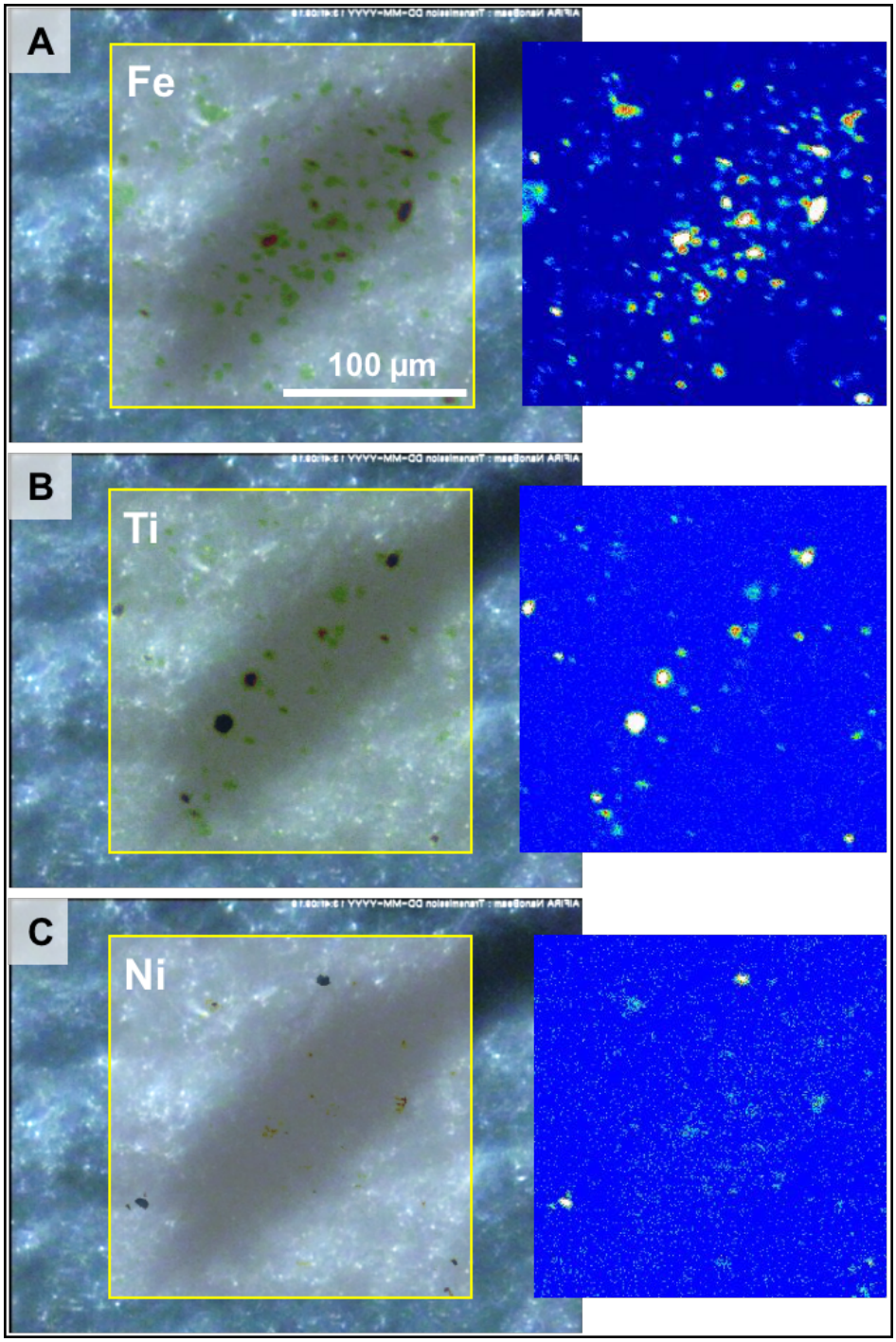

Fig. 20. PIXE elemental mapping of **A**) Fe, **B**) Ti and **C**) Ni within carbonaceous flake (sample 12SA34). These maps (comparable in the case of each flake studies) demonstrate beyond doubt that the enrichment within this morphology of carbonaceous material is not due to trace metals being distributed throughout the carbon, but rather localised within equant microcrystals.

3.3. Carbon isotopic compositions

In situ carbon isotope fractionations were measured for a representative population of irregular clots within a finely laminated sediment and a representative population of carbonaceous particle coatings (identical to microstructures shown in Fig. 1). In irregular clots,

$\delta^{13}C$ varied between –19.5 ±3.4 ‰ and +38.1 ±2.4‰, although the majority of the values lie between 0‰ and –21‰, with a relative probability maximum around –15.5‰ (Fig. 21A). The extremely high value of +38.1‰ is an isolated outlier. The $\delta^{13}C$ values of carbonaceous coatings are typically more negative than those recorded in irregular clots, ranging between –41.8 ± 9.3‰ and +7.3 ±2.4‰, although all but one of these measurements are negative. The relative probability curve of these analyses reaches two maxima between $\delta^{13}C$ values of –10‰ and –21‰ (Fig. 22B). Other CM (i.e., not morphology-specific) throughout the Josefsdal Chert samples studied ranges more widely between of –47.4 ±8.3‰ and +24.0 ±2.4‰, and has its probability maximum between –8‰ and –12‰. All of these values, with the exception of the single outlier point at +38.1‰, (i.e., 97.7% of the reported values) lie within the accepted range of fractionations possible for biology and are particularly consistent with multiple anaerobic metabolisms (Schidlowski, 1984, 1988).

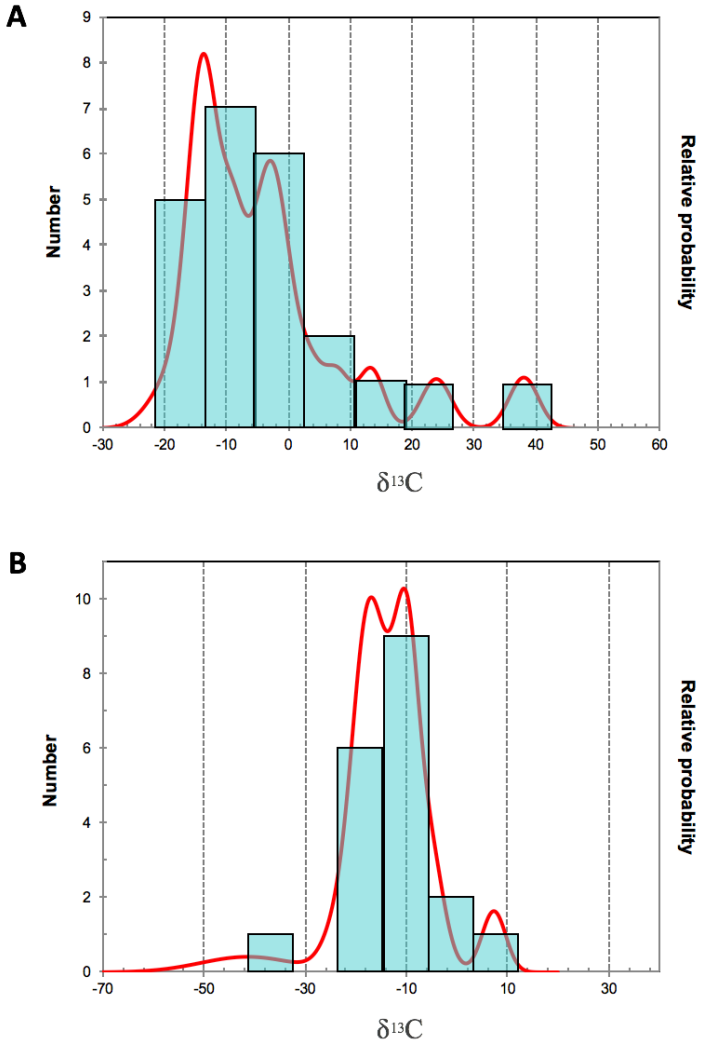

Fig. 21. *In situ* carbon isotope ratio mass spectrometry for **A**) irregular clots and **B**) carbonaceous coatings on volcanic particles. Both exhibit dominantly negative $\delta^{13}C$ values, with those for clots mostly ranging between 0‰ and –21‰, and those of coatings ranging between –5‰ and –27‰ (i.e., values consistent with fractionation by microbial metabolism). Blue bars represent the total number of measurements falling within the indicated range, which yield the red relative probability curves as shown.

Table 1 - Elemental concentrations within carbonaceous microstructures (ppm)

Element	Irregular clot 1	Irregular clot 2	Irregular clot 3	Irregular clot 4	Irregular clot 5	Volcanic particle 1	Volcanic particle 2	Volcanic particle 3	Volcanic particle 4	Flake 1	Flake 2	Flake 3	Flake 4	Flake 5	Flake 6
P	1654.43	304.8±121	207.25	71.2	45	0	60.6±41.3	0	0	253.3	244.3	74.6	32.4	3131.9	1490
S	603.60	0	48.35	3.7	0	0	222.5±20.0	40.8±17.4	0	23.5	67.4	286.8	17.3	63.5	64.6
K	2030.37	30.2±0.7	218.25	81.9	175.8	0	429.9±43.0	338.8±50.7	0	364.9	17.05	796.3	55.9	101	518.6
Ca	84.10	2.1±0.4	4.85	0	8.6	0	0	0	0	14.6	78.5	39.2	155.9	159.8	239.5
Ti	62195.70	160.4±90	198.70	48.35	55.9	0	20.6±4.2	0	0	1085.7	7206	533.5	116.8	58.6	354.9
V	1059.43	337.2±37	228.35	0	1.7	38.5	5±3.1	35.6±4.6	244.6	75.3	239.8	157.6	134.3	0	111.5
Cr	1906.47	169.2±20	157.55	57	0	0	50.6±4.4	35.2±4.2	0	8.8	212.85	17.4	0	0	36.5
Mn	12.00	0	2.05	0	0	0	0	0	0	5.8	62.6	0	14.8	0	645.3
Fe	5120.90	243.6±10	186.10	263	184.8	163.1	0	67±16.5	223.1	4161.1	41101.8	1459.1	632	1651.9	3490.5
Co	3.17	8.6±1.5	11.85	79.85	4.3	0	34.6±11.2	0	0	0	0	28.8	0	46.4	0
Ni	14.67	44±4	37.05	392.1	31.7	1.1	873.7±50.1	6.7±2.5	17.9	50.4	451.1	80.9	17.5	23.4	48.9
Cu	102.57	7.5±2.6	1.55	0	3.7	0	604.7±36.282	0	25.9	18.9	4.4	7.2	12.2	11.4	0
Zn	23.07	6.2±0.6	3.60	0	1.2	0	4.5±3.2	0	0	2.6	20.55	9.7	0	7.3	7.3
As	139.97	7.2±2.4	18.85	1.55	47.6	0	88.9±7.12	0	0	0	0	8.4	0	0	0
Zr	108.90	0	1.40	0	1.9	0	0	25.1±12.3	0	28.8	104.9	0	0	0	19
Mo	1.20	0	1.05	0	0	0	0	0	0	0	0	0	0	0	0

Table 1 – Element concentrations within carbonaceous material, obtained by μPIXE.

Table 2 - Elemental concentrations within matrix adjacent to carbonaceous microstructures in Table S1 (ppm)													
Element	Irregular clot 1	Irregular clot 2	Irregular clot 3	Irregular clot 4	Irregular clot 5	Volcanic particle 1	Volcanic particle 2	Volcanic particle 3	Volcanic particle 4	Flake 1	Flake 2	Flake 3	Flake 4	Flake 5	Flake 6
P	0	246.2	184.5	1137.4	21.7	21.7	66.7	21.7	21.7	179.4	406.4	0	576.9	1376.7	0
S	0	0	0	49.9	0	0	41.3	0	0	12.7	33.9	0	167.5	40.1	67.9
K	711.5	22.4	194.9	1423.9	98.6	98.6	299.3	98.6	98.6	868.1	129	826.8	211.4	1042.9	461
Ca	72.9	1582	23.1	165.8	15	15	5.5	15	15	28.3	40.8	47.4	6.7	74.3	384.6
Ti	80.1	21	89.6	277.8	4	4	57.8	4	4	136.8	171.1	220.5	30.9	342.4	127.5
V	94.7	64.3	191.6	786.3	1.4	1.4	1.7	1.4	1.4	7.8	28.1	32.7	24.6	309.1	206.8
Cr	213.1	54.6	239.9	488.1	3.2	3.2	58.1	3.2	3.2	81.7	10.2	23.9	8	80.4	22.7
Mn	0	0	1.6	0	0	0	0	0	0	2.3	2.5	310.2	0	0	0
Fe	250.4	99.1	71.1	228.9	41.9	41.9	116.2	41.9	41.9	1166.9	2098.8	2293.5	401.3	1468.5	1596.2
Co	0	0	0	10.1	0	0	15.9	0	0	4.6	4.6	0	0	23.5	0
Ni	6.8	1.4	16.8	76.5	4.7	4.7	53.8	4.7	4.7	26.5	35.7	36.1	18	20.6	101.8
Cu	8.8	0	4	0	0	0	12.3	0	0	10	13.2	4.6	1.8	8.4	30.3
Zn	7.5	1.2	1.4	2.9	0	0	1.1	0	0	3.2	8.1	6.5	3.2	14.1	4.8
As	8.9	3.4	0	0	12	12	7.4	12	12	2.2	1.4	2.1	1.3	0	0
Zr	1.2	0	0	0	0	0	3.7	0	0	2.6	20.4	5.7	0	0	0
Mo	0	0	0	0	0	0	1.4	0	0	0	0	0	0	0	0

Table 2 – Elemental concentrations in the matrices surrounding CM microstructures, obtained by μPIXE.

3.4. Abiotic *versus* biotic origins of the CM

Despite the case for the biogenicity of the clotted and coating structures outlined in the Introduction, it has become necessary to fully evaluate the origin of CM in Archaean meta-sediments in terms of its mode of occurrence within the parameters of the environment, especially in light of previous controversies concerning the origin of putatively biogenic CM in similar rocks (Brasier et al., 2002, 2006; Lindsay et al., 2005; Wacey et al., 2016, 2018), Brasier et al. (2002, 2006) and Lindsay et al. (2005) suggested that the Fischer-Tropsch-type reactions, known to occur in natural hydrothermal settings and generate large volumes of hydrocarbons, are potential sources of the CM constituting putative biosignatures. The hydrothermal inputs to the environment of deposition of the Josefsdal Chert require that this potential abiotic CM reservoir be considered. Similar abiotic aggregations of CM may occur as tephra with morphological resemblance to putatively fossiliferous material (Wacey et al., 2018). Due to the strong volcanic inputs to the Josefsdal Chert (Hofmann et al., 2013; Westall et al., 2015), this possibility of carbon accumulation by abiotic means must also therefore be evaluated.

There are several potential abiotic means of accumulating CM in volcano-hydrothermal environments as seen in the studied samples that deserve consideration:

- Fischer-Tropsch-type organic matter synthesised within the hydrothermal system, extruded together with hydrothermal fluid and sequestered within a gel-like chemical sediment (Lindsay et al., 2005) or adhered to mineral phases (cf. Wacey et al., 2016);
- Detrital organic matter of unknown origin aggregated in the water column, falling out of suspension and accumulating within the sediment;
- Detrital organic matter of mixed origins that re-enters into the hydrothermal system, is assimilated within the hydrothermal fluid and redeposited into a chemical sediment with a direct genetic link to the hydrothermal system (the hydrothermal pump hypothesis; Duda et al., 2018);
- Pyrobitumen inclusions generated either during hydrocarbon migration during subsequent metamorphic processes (cf. Buick et al., 1998; Rasmussen and Buick, 2000);
- Carbon-rich volcanic clasts or tephra that strongly resemble microfossils (Wacey et al., 2018) or rip-up clasts of microbialites;
- Meteoritic carbon exogenously delivered and sequestered in shallow-water depositional environment (Westall et al., 2018).

Fischer-Tropsch-type products of relevance are liquid hydrocarbons including alkanes, alkenes and alcohols. Such CM may aggregate in the vicinity of hydrothermal vents since these reactions are observed to occur in natural hydrothermal settings (McCollum et al., 1999; Sherwood Lollar et al., 2002). The $\delta^{13}C$ of naturally produced liquid hydrocarbons ranges between +40‰ and –80‰, depending upon the source of the material and the reaction series followed (McCollum and Seewald, 2006; Taran et al., 2007). The majority of FTT products recorded in this literature exhibit strongly negative $\delta^{13}C$ between –40 and –70‰. The probability maxima of the datasets in these publications would form a broadly continuous maximum throughout the values from +40 to –80‰, with striking maxima at highly depleted values, corresponding to the abiogenic production of methane by a suite of the FTT reactions

(McCollum and Seewald, 2006). The FTT reactions would not yield the relatively restricted range of $\delta^{13}C$ values between –10 and –21‰ seen in the carbon isotope fractionations reported herein. It is also unknown for the FTT processes to produce CM with recurrent morphologies. Abiotic CM would be expected to take the appearance of unremarkable and nondescript aggregations of material disseminated throughout the matrix, since it has no morphogenetic growth framework. It is highly unlikely that CM originating from the FTT reactions would form either particle-specific, non-isopachous carbonaceous coatings or recognisable irregular, stellate clots in multiple sedimentary layers. For these reasons, both isotopic and morphogenetic, we consider it entirely unlikely that the CM herein is the result of FTT hydrocarbon production. It is possible that the disseminated CM in our samples derives from FTT processes, although the $\delta^{13}C$ values and Raman spectral characteristics of this material are also more readily explained as metamorphosed biological material (see van Zuilen et al., 2007). The highly positive $\delta^{13}C$ value in sample 99SA07, also a candidate for having an abiotic origin, was derived from a measurement at the edge of the rastered area. These spots could be the result of instrumental bias due to beam centring, which may generate a concomitant bias in isotopic values. Such values should be considered outliers.

Detrital organic matter falling out of suspension after autotrophic-heterotrophic production and consumption in the water column may be the source of some CM-rich layers in Archaean cherts. Sub-rounded, 'fluffy' particles of CM – superficially similar to the clots described herein – have been identified in the stratiform 'Apex chert' (Brasier et al., 2011; Hickman-Lewis et al., 2016) and the Dresser Formation (Wacey et al., 2018; Duda et al., 2018). In the latter case, a contribution from water column productivity has been implied. In modern seafloor sediments, analogous 'marine snow' occurs as blanket-like deposits over large areas of the seafloor. This is not the case of the irregular clotted morphologies in the Josefsdal Chert since these occur within spatially restricted facies confined to regions of higher hydrothermal flux (Westall et al., 2015). Furthermore, this could not possibly be the case for the coating morphologies, which are particle-specific within individual sedimentary layers. Increased CM-rich layers in the vicinity of the outflow of hydrothermal material is, however, consistent with an origin as biomass associated with hydrothermal effluent (flocs, cf. Juniper et al., 1995; Crowell et al., 2008). For these sedimentological reasons, it is impossible to interpret either the clotted or coating morphologies as detrital organic matter.

Detrital organic matter reworked and sequestered within hydrothermal veins (Duda et al., 2018) is a further possible interpretation of the origin of this carbon. We do not consider that the clotted or coating morphologies could be reworked material since they occur within primary rock fabrics and far from obvious field- and petrographic-scale remobilisation of material. Their morphologies are not consistent with having undergone transport or mechanical erosion. It is thus not possible to explain the petrography of these features in terms of detrital CM inputs.

Oil droplets in the form of bitumen globules have been reported from Archaean successions (Buick et al., 1998). Optical microscopy and SEM and HRTEM images of the CM studied herein, however, show that they lack both the regular, smooth shapes of reported bitumen globules and the enrichment of radioactive minerals in their cores. Consequently, the organic material constituting these clots is unequivocally not thermally matured bitumen.

Wacey et al. (2018) provided a compelling account of carbonaceous, entirely abiogenic, volcanic pseudofossils from the Dresser Formation. Observations of carbonaceous laminae and

accumulations within and onto shards of altered volcanic glass is a potential origin for the microstructures herein given the notable volcanogenic inputs evidenced by SEM-EDS and Raman spectroscopy observations (Figs. 4-9). It is not possible to compare our findings with the pseudocellular morphologies reported by Wacey et al. (2018) since no such morphologies exist in our samples. The irregular clots bear no morphological similarity to the tephra pseudofossil morphologies shown in Wacey et al. (2018). It is more challenging to overcome the possibility that the particle coatings may originate from accumulation on altered volcanic glass and other minerals and we cannot unambiguously discount this possibility. Nonetheless, since the colonisation of volcanic and other particle surfaces in contemporaneous cherts has been noted (Westall et al., 2011; Wacey et al., 2011), it appears that both biotic and abiotic possibilities exist for this fabric, and should be explored in more detail in individual cases.

Meteoritic carbon is the final plausible alternative origin for the accumulation of CM seen in the Josefsdal Chert. The volume of CM exogenously delivered to the early Earth was vastly greater than at present due to increased impactor flux early in the history of the solar system (Maurette and Brack, 2006; Koeberl, 2006; Gourier et al., 2019), and may have been ongoing throughout the first ~1.2 Ga of Earth history (Zellner, 2017). Impactor events by carbonaceous chondrites would result in blanket-like carbon deposition and major geochemical signatures on local scales. Examples include the Ir and Pt-group element enrichments seen together with microkrystites in the Marble Bar chert, Pilbara (Glikson et al., 2016), the impact spherule layers observed throughout the BGB (Lowe and Byerly, 2003), and CM with the distinct EPR characteristics of the carbonaceous fraction of carbonaceous chondrites (Gourier et al., 2019). Since no large-scale blanket-like aggregations of CM or other geochemical and petrological signatures have been noted in the Josefsdal Chert, there is no evidence for the clot and coating microstructures to be explained in terms of any known morphology relating to meteoritic impact. While there was likely a meteoritic input of carbon to the Josefsdal Chert and other Archaean environments, its input to these microstructures was negligible.

Therefore, no plausible abiological interpretation for either the irregular clot or particle coating CM morphologies described herein is sustained under scrutiny. In all but one case – the possibility that particle coatings may reflect non-biological accumulation of carbon on volcanogenic particles – an abiological interpretation is impossible. Since the CM described is present as recognisable microstructures encapsulated rapidly within silica representing the primary deposition of these meta-sediments, and since demonstrable biogenic interpretations exist for carbonaceous accumulations on or in volcanic substrates (Westall et al., 2006, 2011; Furnes et al., 2007), all abiotic null hypotheses are overcome and an alternative explanation is required to assess the origin of all CM described herein.

Having considered and negated abiotic mechanisms of CM accumulation, the biogenic interpretative frameworks are as follows:

- Detrital biogenic material sequestered into a gel-like sediment with a direct genetic link to the adjacent hydrothermal system, and rapidly silicified, but not necessarily a primary fabric;
- Cellular material from a mixed community and its extracellular products that developed *in situ* and was preserved in a manner reflecting the mode of growth (a primary imprint) by virtue of the rapidity of their silicification.

Addressing these biological possibilities in turn:

As noted above, there is no evidence for the detrital origin of the CM described in this study. Both the fact that the CM morphologies occur as facies-specific and, within that, particle-specific, features is unequivocally diagnostic of their origin as a primary textural element. We therefore discount this interpretation as unsupported by our detailed field and petrographic assessment of these rocks.

The second biological interpretation, that the CM represents the rapidly preserved primary imprint of a community that developed *in situ* within certain horizons, requires several key pieces of evidence. Firstly, it requires that the structures, being rapidly silicified, should be preserved in three dimensions with no preferential axis. The carbonaceous matter forming both irregular clots and particle coatings is indeed preserved in three dimensions, as demonstrated by thin sections cut both parallel and perpendicular to the faint bedding present in these samples. Furthermore, the clots are associated with micron-scale minerals which may or may not occur within the CM, and do not contribute to grain-supported fabrics in the cherts. Secondly, the microstructures should be facies-specific, diagnosing ecological functionality, and should not be ubiquitous throughout the varied Josefsdal Chert sediments. Both CM microstructures are indeed lithofacies-specific, occurring only in near-pure hydrothermally influenced chert for irregular clots, and within hydrothermally influenced, shoreface volcaniclastic sediments for the particle coatings. The first of these is not a common lithofacies of the Josefsdal Chert (see the stratigraphic column in Westall et al., 2015), and this is compelling evidence for clots being an palaeoenvironmentally constrained phenomenon. Biological community constraint due to facies has been noted in younger sediments from the Moodies Group of South Africa (Homann et al., 2015). Palaeoenvironmental or facies restriction for detrital carbonaceous matter of either biogenic or abiotic origin is not favoured, further arguing for the rejection of such hypotheses.

If the clotted carbon reflects a community signature as seen in modern-day microbe-mineral clots and flocs (see Juniper et al., 1995; Crowell et al., 2008), and not a monospecific entity, the carbon isotopic fractionation should be varied and centre around values that are negative. Most common anoxygenic photosynthetic bacteria produce carbon isotope fractionations between –8 and –22‰ (Schidlowski et al., 1984, 1988). This almost exactly matches the isotopic fractionation seen in our samples (with strong probability maxima between –10 and –21‰. These values are consistent with the expected biomes and metabolic pathways present on the anoxic early Earth (Nisbet, 2000; Nisbet and Sleep, 2001; Arndt and Nisbet, 2012). Values that significantly deviate from these probability maxima are not common; the overwhelming majority of analyses lie within the region of 0 to –25‰, which is consistent with reported values from anoxygenic photosynthesisers, and sulphur- and methane-metabolising organisms. Thus, although the fractionations are slightly light relative to some previous reports of Archaean carbon isotope fractionations (e.g. Lepot et al., 2013; Morag et al., 2016), they are nonetheless entirely supportive of a biological origin. Indeed, they are in fact more consistent with the estimated metabolic pathways of primitive prokaryotes in shallow-water sediments than previously reported, more negative estimates are.

We are therefore able to both refute potential abiological and biological hypotheses on the origin of these microstructures and arrive at a conclusion for their origin that satisfies two- and three-dimensional petrographic observations and geochemical data from isotope ratio mass spectrometry. This conclusion is consistent with expected biomes in the palaeoenvironment

determined for these cherts based on stratigraphy, trace and rare earth element geochemistry (Section 1.1) and Archaean ecosystem theory (e.g. Nisbet, 2000).

Consequently, it is acceptable, and indeed only logical, to assess the metal enrichments observed by μ-PIXE in a biological framework. These metal-rich signatures plausibly represent the metallome of the precursor biomass of clotted and coating CM morphologies. In the following section, we assess the metal signature in terms of its origin by bio-accumulation.

4. The palaeo-metallomic biosignature

4.1. Validation: authenticity of the palaeo-metallomic signature in Archaean cherts

Metals are bio-essential to all life in various concentrations and fractional contributions, and have widespread utility in metalloproteins, enzymatic co-factors, polysaccharides and heteropolymers, among many other molecules (Williams, 1981, 2001; Fraústo da Silva and Williams, 2001; Williams and Fraústo da Silva, 2003; Moore et al., 2017). This metal composition is termed the metallome (after Williams, 2001), and can be considered the inorganic third element of cell expression alongside the organic genome and proteome. Of the three, the metallome is the only likely candidate for preservation throughout deep time, since even biomarkers indicative of the proteome have been shown not to preserve in ancient sediments as previously thought (French et al., 2015). In deducing the palaeo-metallome, it is necessary to account for the lack of continuity of the metal-rich signature, which is a function of cellular and biopolymer preservation. The distribution of elements within μ-PIXE maps is inconsistent throughout CM (i.e., over micrometric scales). This is an authentic representation of the micrometric distribution of the CM, which is dispersed as interleaved fragments between silica crystals after Ostwald ripening under lower greenschist facies metamorphic pressures and temperatures (van Zuilen et al., 2012; Hickman-Lewis et al., 2017). This distribution is further evident from the spatial distribution of point enrichments in carbon obtained by isotope ratio mass spectrometry (instrumental maps, not shown). High-resolution transmission electron microscopy observations have confirmed that this distribution of carbon is responsible for the diffuse appearance of clots when observed at high magnification in thin section (Fig. 15). Raman spectroscopy indicates that the CM studied herein has undergone some limited graphitisation (Fig. 4), likely during the metamorphic events leading to the formation and crystallisation of micro-quartz crystals that displace CM (Fig. 15).

The occurrence of CM as fragments interleaved between microquartz crystals is sustained by the patterns of observation of elemental concentration seen in μ-PIXE mapping, i.e., a diffuse enrichment (Figs. 16-18). Regions that are strongly enriched in CM are also those in which metals are enriched relative to the matrix. Generally, higher concentrations of elements are seen in regions of visually elevated concentration of CM. Although the detection of some elements is below the theoretical detection limit of PIXE (~100 ppm for most elements), the ability to map their occurrence in discrete energy channels is consistent with their occurrence at low concentration as shown in the individual element maps (Halden et al., 1995; Campbell et al., 1995).

We have deduced that the metal signature reported in the study is neither due to nanoscopic mineral phases nor to micron-scale mineral phases, because these are, respectively, not present and mitigated by the ‘mineral effect’. Reported metal enrichments are demonstrably

indigenous to the carbonaceous matter. Two key points are then important in the assessment of the signature as a palaeo-metallomic signature:

i) Biological carbonaceous matter readily scavenges metals from the environment during its life processes (this is a fundamental process in all metabolism and cellular catalysis), and has been demonstrated to considerably outcompete non-biological material in the retention of heavy metals (Schultz-Lam et al., 1993, 1996; Loaec et al., 1998). Bacterial surfaces (both Gram negative and Gram positive) provide loci for the sorption of metals due to the overall anionic charges of the electronegative macromolecules that constitute their cell walls.

ii) Thereafter, post-diagenetic leaching, if it occurs, acts following the death of the organism, i.e., the two processes are not acting at the same time (Orange et al., 2009, 2011). Since biological molecules are rich in carboxylate groups, peptidoglycan, teichuronic acid and other heteropolymeric polysaccharides, they are likely to retain metals accumulated during life even after death (Schultz-Lam et al., 1993; Orange et al., 2011). Rapid silicification of CM provides a 'time capsule' of preservation that assures the survival of the palaeo-metallomic signature.

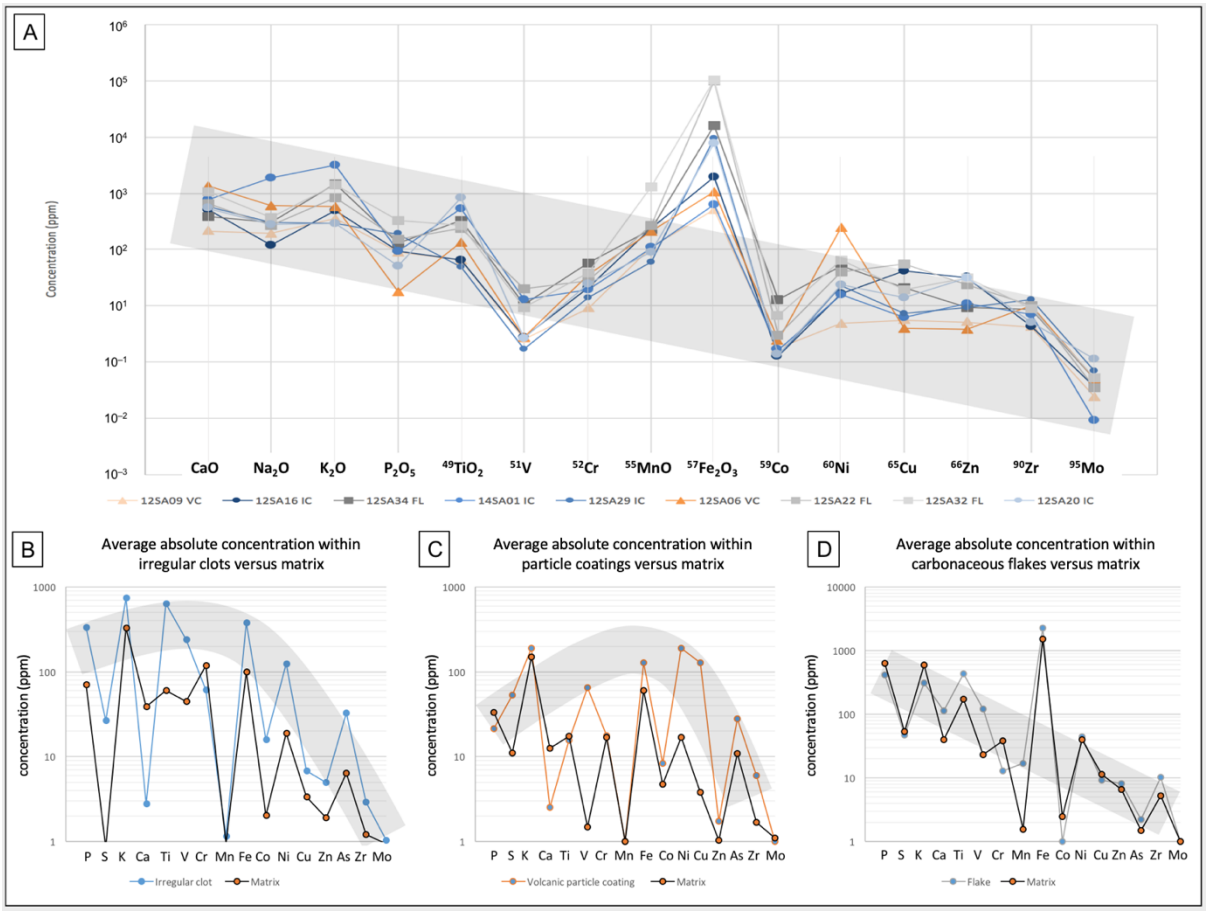

Fig. 22. Comparison of concentrations of the elements of interest by inductively coupled plasma-mass spectrometry (ICP-MS) bulk sample analysis and particle induced X-ray emission (PIXE) area-specific analysis within carbonaceous material (averaged for each morphology). Grey trend-lines indicate a qualitative ideal signature that might constitute elemental concentrations corresponding to the enrichment within the structure (the average values of each element measured, see Table 1). If biological, a recurrent fit to a trend line such as this

could constitute a trace element biosignature. **A**) ICP-MS bulk measurements from studied samples, indicating the relatively constant concentrations of elements which may be taken to represent their concentrations in the bulk matrix, herein estimated to reflect the ambient, hydrothermally influenced, fluid environment. **B-D**) Concentrations determined from within irregular clots (**B**), coatings on volcanic particles (**C**) and flakes (**D**). The trend-lines of enrichment in the bulk matrix (ICP-MS results in **A**) and flakes are almost indistinguishable, suggesting that there are no directional processes of enrichment in the flake morphology. By contrast, the trend-lines of irregular clots and volcanic particle coatings show enrichments that significantly deviate from the matrix values in certain elements (i.e. values which are modestly or significantly enriched relative to the ambient environment).

4.2. Context: the chemical oceanographic and biochemical environments of early life

In the Archaean oceans, soluble Fe^{II}, Ni^{II}, Co^{II} and Mn^{II} were more bio-available, whereas insoluble Cu^{II}, Zn^{II} and Mo^{II} were less so (Saito et al., 2003). Our findings corroborate these models: in the ambient environment, Cu, Zn and Mo are present in low concentrations, whereas Fe, Ni and Co are relatively enriched. Mo, Mn, Cu and Zn were probably later additions to the metallome (Dupont et al., 2010). Phylogenomic analyses of prokaryotes suggest metal requirements consistent with the ferro-sulphidic environment, for instance an absolute requirement of Co (Moore et al., 2018) and lacking requirement of Zn (Saito et al., 2002), high Cu sensitivity and low metal tolerance in the absence of ferro-sulphidic conditions (Saito et al., 2003). Thus, early metabolic evolution in a ferro-sulphidic ocean is sustained by phylogenomics and geomicrobiology. Moreover, these expectations of the ferro-sulphidic model are supported by the trace elemental concentrations presented herein: almost all metallic elements are enriched relative to the modern oceans (Table 1). Putatively biogenic CM further concentrates this range of trace elements (Figs. 16-18). This is consistent with expected relative elemental dependencies in the prokaryotic metallome (Zerkle et al., 2005; Liermann et al., 2007; Cameron et al., 2012), raising the hypothesis that this clear pattern of enrichment in enigmatic CM reflects the degraded metallomic complement of former biomass, exceptionally preserved within 3.33 Ga chert.

This enrichment is consistent with a metallomic scenario in which coordination chemistry involving metalloproteins yields an ion enrichment within biomass (Wang et al., 2014). Hard and soft Lewis acid and base (HSAB) theory predicts that hard Lewis acids (K, Ti, Fe, V, Cr, Mo, Mn) and soft Lewis acids (Ni, Co, Cu), together with Lewis bases, e.g., hard bases (P, probably associated with PO_4^{3-} and H_2PO^{4-}) and S, a hard base in SO_4^{2-} and soft base in ROH, R_2S and $S_2O_3^{2-}$ would be associated with ligands including H_2O, ROH, RCO^{2-}, CO_3^{2-}, NO_3^-, PO_4^{3-}, SO_4^{2-} and NH_3, which are present in hydrothermal effluent and complex readily therein (Konhauser 2007) (although note that SO_4^{2-} and NO_3^- are present at low concentrations in hydrothermal fluids). Clots are enriched in both hard and soft metals, and the elevated presence of ions within this CM is consistent with bioaccumulation. It is improbable that the identified elemental complement could be entrapped by abiotic CM (*cf*. Wang et al., 2014). Coordination complexes formed from hard acids require hard bases. The presence of either carboxylate groups or phosphates is thus necessary, e.g. EPS in biomass (Martins et al., 2008). Coordination by aliphatic compounds or highly cyclised abiotic carbon produced by Fischer Tropsch-type and other wet hydrothermal reactions is, from the point of view of coordination, distinctly less favourable.

The elemental enrichments reported herein may result from either syngenetic environmental and architect organismal effects (i.e. different metallomic situations related to biomolecules and bioaccumulation) or diagenetic and taphonomic histories related to

secondary alteration (Raven, 1988; Williams, 2001; Zerkle et al., 2005; Lepot et al., 2013). The CM likely consists of intermixed cellular material and biomolecules such as EPS and metal-chelating proteins, both of which contain anions (cell proteins and aspartic and glutamic acids, respectively) which would have chelated the metal cations contributing to this elemental signature (Martins et al., 2008). EPS, including metal-chelating proteins, such as siderophores, are able to strongly chelate ferric iron and other metals with variable affinities (Schalk et al., 2011; Leventhal et al., 2019). Notwithstanding, significant metal accumulation associated with siderophores would likely be represented by the extremely high concentrations on the micron scale that are removed by the 'mineral effect'. These would not affect the analyses of metal accumulation within CM, however, the effects of metal-chelating proteins in biological systems remains an area of active research (Leventhal et al., 2019) that is yet to be explored for fossil biomass.

4.3. Interpretation: trace element data as a palaeo-metallomic biosignature

For the above reasons, together with the case for the biogenicity of these CM fabrics described in the Introduction, it is plausible to consider that the trace element signature within this enigmatic CM represents a degraded metallomic biosignature, *i.e.* an elemental relic of the systematic functional interaction between cell components and the immediate environmental compartment. If true, this reflects bioaccumulated material flow between environment and organism by virtue of the essentiality of individual elements to cellular function (Williams, 1981, 2001; Lobinski et al., 2010) and yields a novel and unexplored biosignature.

It is probable that the signal acquired in this putative biomass represents a community of organisms, which makes direct comparison with the previously reported single organism datasets (e.g., Zerkle et al., 2005; Liermann et al., 2007; Cameron et al., 2012) challenging, and suggests that a more appropriate comparison would be made with the broad metallomic patterns of trophic levels. Certain metabolisms show specific requirements: hyperthermophile methanogens such as *Methanocaldococcus jannaschii* show metabolomic fractional requirements of Zn and Mn which are notably reduced relative to other microbial strains, whereas Ni, Co, Cu and V are required at substantially higher fractional contributions, a pattern which could conceivably be used as a biosignature. For comparison with these metabolomic requirements, reported concentrations herein have been calculated as percentage contributions to the hypothesised metallome following the approach of Zerkle et al. (2005) and show strong similarities in the fractional requirements of certain trace elements (Fig. 22).

Fe, Na, Mg, P, S, K and Ca are bio-essential (Zerkle et al., 2005; Robbins et al., 2016) and, with the exception of Ca, are distributed throughout JC CM. S is localised in micron-scale sulphide particles, which are of size ranges and morphologies compatible with their origination during sulphur-reducing metabolism, but also throughout the CM as organo-sulphur. V is considered either bio-essential or bio-functional (Zerkle et al., 2005; Robbins et al., 2016) and has recently been deemed bio-indicative when occurring throughout CM (Marshall et al., 2017). The very high fractional contribution of V in clots and coatings may stem from this preferential retention or enrichment, and is therefore likely an overestimate relative to the enrichments present in other elements. Modern microbial etching structures, however, also show enrichments of V (together with P, Ti, C, Mn, Y and Zr) (Banerjee et al., 2010). Although V is generally a minor component of the metallome, it is nonetheless essential to methanotrophic and some diazotrophic bacteria and archaea (Zerkle et al., 2005). These

primitive, anaerobic metabolisms are most compatible with thermophilic hydrothermal biomes (evidenced by REE+Y pattern in Fig. 3). Comparison of data from PIXE (Table 1) and ICP-MS (Figs. 12-13, 22) shows essentially no detection of V in the latter; this can be explained by the fact that the V is concentrated within organic matter which, though somewhat abundant in the regions of interest, is negligible in bulk sample. Cu, by contrast, is not likely to have been incorporated into the metallome until after the Great Oxygenation Event (Dupont et al., 2010). Cu incorporation into particle coatings could be due in part to a non-specificity of uptake where elements are micro-toxic to the consortium (Hickman-Lewis et al., 2019), given that some of the carbonaceous material is likely to represent EPS or other lipopolysaccharides.

Co, Ni, Zn and As are considered either bio-essential or bio-functional. Co, Ni and As are enriched especially within individual sulphide grains and more diffusely within CM. The modelled metallomes of chemoautotrophic methanogens and, more broadly, (hyper)thermophiles, demonstrate an enrichment of Ni to a fractional contribution twice that of other metabolisms (Zerkle et al., 2005). Ni is also an important component of the proteometallome of chemolithotrophs (Friedrich and Schwartz, 1993). This pattern of enriched Ni (together with V) is present in our data (Figs. 16-18) and is compatible with expected metabolisms in this hydrothermal-lithotrophic microcosm. Other bio-functional elements, including Ba, W, Cd and Sn, were not detected during our analyses. These elements are either not present in this CM, or are present in vanishingly small concentrations well below the limit of detection of PIXE. In either case, they do not form an integral part of the palaeo-metallome of any biomass analysed.

4.4. Implications: the prokaryotic metallome as a novel Precambrian biosignature

Metallomic – according to the definition of Williams (2001) – biosignatures could conceivably withstand diagenesis and be imprinted into preserved CM after more than three billion years. This is possible in chert which, due to its rapid lithification and subsequent impermeability, prevents mobilisation of preserved components after silicification, and thus creates a preservational 'time capsule'. For a thermophilic, hydrothermally influenced biome in the Archaean oceans, a biologically indicative metallome would consist of the bio-essential elements together with metabolism-specific V, Cr, Co, Ni, As, Mo and W, and possibly others (Robbins et al., 2016). Due to bio-availability constraints in anoxic environments, Mn and Zn should not have played a major metallomic role on the Earth prior to the Great Oxygenation Event (Moore et al., 2017), whereas the internally heat-driven, anaerobic conditions were plausibly more clement to thermophiles demanding metallomic V, Co, Ni, As and W, evident from qualitative trophic-level comparisons with reported metallomes (Zerkle et al., 2005; Liermann et al., 2007; Cameron et al., 2012). Our results are further consistent with many of the expected ion concentrations in the Archaean oceans (Saito et al., 2003; Westall et al., 2018). The trace element enrichments in CM (both irregular clots and particle coatings) from this 3.33 Ga material thus carry a strong resemblance to those expected for anaerobic, methanogenic or diazotrophic, thermophiles (and likely a combination of the two) in terms of both absolute and relative enrichments and fractional contributions to the metallome. We suggest that this represents a bioaccumulation effect driven by biomolecules of cellular origin (after Orange et al., 2011; Edwards et al., 2014; Wang et al., 2014). The reported *in situ* carbon isotope fractionation corroborate such an interpretation: values centred around relative probability maxima lighter than –10‰ are consistent with fractionation by nitrogen-cycling, sulphur-

cycling, methanogenic and/or anoxygenic phototrophic bacteria, although slightly heavy to infer methanotrophic biomass.

Moreover, a trace element enrichment pattern that is similar, but not identical, between different microstructures, yet recurrent between examples of a specific morphology across multiple samples (Fig. 22; Table 1), argues strongly against the preserved signal being dominated by either palaeoenvironmental imprinting or diagenetic overprinting. We therefore suggest that a directional force of concentration leads to enrichments in elements which are not necessarily pre-enriched beyond others in the ambient environment (V, Ni, Cu(?), As) and that this directional force is biological. The lack of cellular preservation indicates that any original cellular tissue was disaggregated before as a consequence of silicification (see discussion in Hickman-Lewis et al., 2017). This rapidity of silicification precludes late diagenetic and subsequent enrichment, since relict functional groups that could potentially have chelated ambient ions were already occupied by Si groups (Orange et al., 2011). Metal- and nutrient-rich hydrothermal fluids, which were replete in this volcano-sedimentary environment (Hofmann and Bolhar, 2007; Westall et al., 2011, 2015; Fig. 3), were likely an important source of the metals associated with this CM. The imprint of these nutrient-rich conditions, key to the evolutionary aspect of the theory of the biological chemistry of the elements (Fraústo da Silva and Williams, 2001), is preserved throughout both the CM and the matrix.

We suggest that the microstructure-specificity of these trace element patterns, together with a lack of proportionality between absolute concentrations of trace elements within CM characterised by a δ13C signature consistent with biological fractionation (Fig. 21) and that of the ambient fluid (the agent of preservation) further exclude diagenetic enrichment; diagenesis has lithological implications on a scale greater than that appraised in an individual analysis and should present either a trendless trace element continuum across both objects and samples or homogeneity in elemental enrichment. We therefore interpret the origin of CM clotted and coating morphologies to be biogenic. The complementary case of CM in the form of flakes supports another standpoint: that some CM simply scavenges metals according to their ambient concentrations and without directional effects. In non-biological organic matter, no specific intracellular elemental requirements exist and, as such, no concentration factor is present. The uptake of metals by such organic matter should be sieve-like, non-directional, and directly mirror concentrations recorded in matrix measurements, since cell-specific sites of metal uptake are not present. This non-specific, non-biological uptake is shown by the analysed flakes, which show trend lines of elemental concentration indistinguishable from those of the matrix (Fig. 22). The trend lines of irregular clots and particle coatings show enrichments that significantly deviate from the matrix values. It is thus likely that flakes do not stem from a biological precursor.

5. Conclusions

Two conclusions can be made:

i) Elements must be bio-available in their ambient chemical environment (reflected by the rock matrix) to become an integral part of the metallome. Our results provide an estimation of the trace element complement present in Archaean ocean biomes,

and support that hydrothermal habitats were rich in many of the elements required by the prokaryotic metallome;

ii) Trace element signatures associated within CM of demonstrable antiquity, perhaps including V, Co, Ni, Cu and As together with a complement of the CHNOPS elements, may indicate bioaccumulation of these elements and be used as a biosignature (*cf*. Liermann et al., 2007; Cameron et al., 2012). Not all bio-functional metallic elements are present (e.g. W and Sn), and thus the metallome may have undergone degradation as a function of cell death and taphonomy, or these elements may simply have played no role in metabolisms of the original biomass. The preservation of metallomic biosignatures is likely a function of both original cellular concentrations and the preservation potential of the intra- and extra-cellular components with which the element was associated and is most accurately assessed as a community signal;

Concentrations of bio-essential and bio-functional elements (C, N, P, S, K, V, Fe, Co, Ni, Zn and As) within carbonaceous material in 3.33 Ga cherts from the Josefsdal Chert (Kromberg Formation) strongly supports that such morphologies are derived from common precursors, which may be chemosynthetic biomass. These carbonaceous microstructures have antiquities and thermal histories concurrent with the age of the host rock and have predominantly negative carbon isotope fractionations (largely distributed within the range of –10‰ to –21‰) consistent with biological fractionation.

The preserved trace element concentrations in carbonaceous material from these cherts resemble the expected metallomic trends for anaerobic, perhaps lithotrophic, thermophiles utilising methane- and nitrogen-based metabolisms. Microstructure-specific differences between the elemental concentrations in irregular clotted and particle-coating structures of interest suggest that they are not pseudo-biomass formed by the aggregation of organic debris, but are *bona fide* carbonaceous biosignatures. This approach could open new avenues of life detection in geological materials of any age and would provide an unexplored opportunity to re-interrogate certain contentious putative biosignatures, particularly in the absence of obvious cellular preservation.

Most significantly, our findings empirically support that the hypothesis of Frausto da Silva and Williams (2001) – that modern biological dependency on trace elements was influenced by the environments in which early life evolved – is correct. On a thermophile early Earth, hydrothermally influenced oceans were the environments relevant to the evolution of the prokaryotic metallome. Since the early aeons accounted for a large portion of microbial evolutionary history (Nisbet and Fowler, 1999; Brasier et al., 2011; Knoll et al., 2016), it is perhaps unsurprising that these elemental legacies have endured.

Chapter IV – Geological-geochemical-geobiological testing of the ExoMars 2020 rover payload instrumentation

This chapter comprises the following manuscripts:

Hickman-Lewis, K., Foucher, F., Pelletier, S., Messori, F., Westall, F. Geological appraisals using the ExoMars 2020 rover imaging instrumentation: challenges inherent in the interpretation of core samples. Under review, *Planetary and Space Science*.

Hickman-Lewis, K., Baumann, E., Foucher, F., Westall, F., et al. A sol in the life of the ExoMars 2020 "*Rosalind Franklin*" rover: distinguishing biosignatures, bio-indicators and abiotic matter using the Pasteur payload strategy. Manuscript in preparation for *Astrobiology*.

Introduction

The previous two chapters have demonstrated geological-geochemical-geobiological appraisals of fossiliferous horizons from the Palaeoarchaean using a range of instrumentation that is relevant both to *in situ* Mars exploration and the analysis of samples brought back to Earth during Mars Sample Return. In this final chapter, the case is tested wherein the ExoMars 2020 rover instrumentation alone is used to make analyses and interpretations of Mars analogue samples. Science testing of rover instrumentation is the keystone to determining the network of analyses required during rover operations to maximise the scientific return of the mission.

The first manuscript presents a test of the abilities of the ExoMars 2020 rover instrumentation, particularly the imaging instrumentation (CLUPI and HRC), to make geological assessments and preliminary biosignature identification based on core samples alone. CLUPI and HRC images of core samples will likely be the highest-resolution images obtained of the sampled subsurface material, however, constraints relating to sample dimensions and morphologies, together with sample preparation artefacts created during the drilling process, can hinder the interpretation of this material. This study reports the process of obtaining optimal, mission-representative images of Mars-analogue natural samples, followed by a blind test using these samples. Although some misidentifications were made, particularly relating to features at the millimetre to centimetre scale, it was found that most of the diverse sample suite analysed could be classified with at least reasonable accuracy using imaging alone. Mineralogical data (Raman or otherwise) nonetheless significantly enhanced the accuracy of petrological interpretations, particularly in the case of aphanitic sediments and certain igneous rocks. This strongly argues for the value of inter-instrument collaboration during the progressive learning process at each analysed outcrop.

A second outcome of this first manuscript was the definition of the scientific protocol to be followed by the ExoMars 2020 mission, and how this differs from the geological fieldwork protocol on Earth. This protocol determines those data that could/should be obtained at each step in the mission and at which points it is necessary to cross-correlate data from the analyses of each instrument.

In the second manuscript, the synthesis and characterisation of artificial Mars-analogue sediments of specific astrobiological relevance is described. Although incomplete at the time of writing this thesis, the current version of this manuscript describes in full the relevance of the lithologies and biosignatures chosen for the artificial sediments, how the combinations chosen allow for biosignature-relevant testing of the payload instrumentation, and their incorporation into the samples. The preparation of each of the samples for testing is also outlined, and preliminary results from four instruments (ISEM, Ma_MISS, RLS and MOMA) are presented with interpretations.

These two manuscripts provide an outline and demonstration of the portions of the ExoMars 2020 science protocols relevant to biosignature detection, and how the methods of proposing biosignatures on Mars differ from those conducted on Earth.

Manuscript 1 – Geological appraisals of core samples using the ExoMars 2020 rover instrumentation

Abstract

The ExoMars 2020 mission will characterise a Martian locality with potential former habitability – Oxia Planum – and attempt to identify preserved physical and chemical biosignatures. The payload will include a drill retrieving cores from the subsurface (up to 2 m depth), which will be imaged at high resolution by two instruments: the Panoramic Camera High Resolution Camera (PanCam HRC) and CLose UP Imager (CLUPI). These instruments will provide guiding interpretation and govern the approach used by the analytical instruments, which will conduct their analyses after crushing of the core sample. Blind tests using Mars-analogue lithological samples provide valuable mission training in terms of maximising scientific return. Previous blind tests evaluating the abilities of ExoMars 2020 payload to conduct geological approaches used solid rock hand samples as test specimens. Here, we prepared samples of ExoMars mission-equivalent shapes and dimensions (3 x 1 cm cores). Imaging these samples using mission-equivalent original resolutions to avoid image processing artefacts, we found that the difficulty inherent in making definitive geological conclusions using traditional 'field petrography' approaches is increased when only limited amounts of core sample are available for observation. Issues inherent in interpreting core samples include scale-representativeness, distinction between layer-specific characteristics at the sub-centimetre to centimetre scale, mechanical effects, such as drill marks and dust covering, and correlation between analyses of the outcrop and the core. These issues vary depending upon the rock type and change as a function of the mechanical properties (and thus composition) of the sample. Despite these challenges, we find that CLUPI and PanCam HRC images alone allow many accurate and detailed geological observations; however, confidence and detail of interpretation are notably increased when additional geochemical data are provided, in this case, Raman spectra reflecting the contribution of the Raman Laser Spectrometer (RLS) instrument. Our results argue for the importance of core imaging during the experimental phase of the rover mission despite the challenges involved in interpretation, since HRC and CLUPI images offer a great degree of synergy. Inter-instrumental collaboration will be essential during the ExoMars 2020 rover mission (and indeed in any rover mission), since no single payload instrument is able to perform a comprehensive assessment of a putative biosignature within its geological context, and since the instrument suite provides highly complementary data at multiple scales that are key to maximising scientific return.

1) Introduction

1.1. The geological context of Martian astrobiology

The planetary-scale geodynamic decay responsible for the decline in Martian habitability since the Noachian period implies that missions aimed at the detection of traces of life should focus on geologically complex ancient terranes (Westall et al., 2015; Vago et al., 2017; Cabrol, 2018). If life emerged on Mars, it would likely have been restricted to the Noachian and early Hesperian, when conditions may have been broadly similar to those of the early Earth (Nisbet and Sleep, 2001; Westall et al., 2015). Much evidence supporting the long-

term habitability of the surface Martian hydrosphere throughout the early history of the planet has been identified both from geomorphology and mineralogy. Geomorphological evidence is most apparent in the widespread dendritic river valley networks that extend across Noachian terranes (e.g., Malin and Edgett, 2003; Bhattacharya et al., 2005). Meandering channels indicate that Martian rivers were characterised by significant flows and long courses. Large bodies of standing water are indicated by the deltas impinging upon lakes and seas into which palaeo-rivers flowed (e.g. Pondrelli et al., 2005), although isolated lakes may have formed from meteoric water alone. Furthermore, a diversity in surface water states on the Noachian Mars is denoted by potential glacial deposits, including moraines and lobate debris aprons (e.g. Garvin et al., 2006), lineated valley floor deposits (Head et al., 2006) and ridges many kilometres in length interpreted as eskers (Butcher et al., 2017). Sedimentological and mineralogical evidence for aqueous episodes is abundant, the best-studied example being the kilometres of sediments observed by the MSL Curiosity rover at Gale Crater (e.g. Williams et al., 2013; Grotzinger et al., 2014; Eigenbrode et al., 2018). Deposits of hydrated minerals, including silica and hydrous phyllosilicates, are also common in many of the sedimentary deposits associated with the Martian hydrosphere (e.g., Wang et al., 2006; Chevrier and Mathé, 2007; Carter et al., 2013; Ehlmann and Edwards, 2014; Michalski et al., 2017). Enclaves for life associated with this hydrosphere would, under a trajectory of planetary-scale habitability degradation, have rapidly decreased early in Mars' history (Cockell, 2014), although recurrent periods of moisture may have occurred since the Hesperian (Kite, 2019). Identifying traces of ancient life fossilised billions of years previously poses a range of challenges. The unambiguous distinction of such traces of life in terrestrial rocks demands multi-technique investigations (e.g. Westall et al., 2011; Brasier et al., 2015; Wacey et al., 2016), which are more challenging on Mars given the inherent limitations of rover instrumentation. Thus, in order to maximise the chance of biosignatures detection at the landing site, several pre-requisites were necessitated:

i) the landing site must contain ancient strata with high habitability;
ii) studied samples should be taken from depth, avoiding surface degradative effects; and
iii) instrumentation should conduct an integrative, multi-scalar petrological, mineralogical and geochemical study at each studied locality.

1.2. Martian astrobiology in the Age of Rovers

The upcoming ExoMars 2020 (ESA-Roscosmos) and Mars2020 (NASA) rover missions ensure that the next decade will be formative in Martian astrobiology, both missions having objectives to search for extinct or extant traces of life (biosignatures) on Mars (Vago et al., 2006, 2017; Mustard et al., 2013; Hays et al., 2017). The instrumental payloads carried by both rovers are oriented toward the *in situ* analysis of biosignatures, and are capable of conducting petrological and organogeochemical assessments of biosignatures in their evolving geological environment (Vago et al., 2017; Cabrol, 2018). For technical reasons, the geological investigations on Mars do not follow the classical Earth protocol. There are no hammers permitting the observation of unaltered rocks, there are no possibilities for thin section preparation for mineralogy and micropaleontology, and many of the analyses will be carried out on crushed samples. These differences must be taken into account when interpreting the data collected on Mars (Foucher et al., 2013; Mangold et al., 2017). Emulations of mission

operations – accounting for the constraints of space instrumentation and protocols – are therefore essential for training and learning processes in preparation for mission experimental cycles. Such training may use experimental setups mimicking the predicted environment (Martins et al., 2017) or the process of measurement (Foucher et al., 2013; Bost et al., 2015; this study).

Among the key targets of interest, microorganisms and organic molecules of unambiguous biological origin are of foremost importance (e.g., pigments, peptides). Organics have already been identified on Mars in Gale Crater sediments by the Mars Science Laboratory (MSL) *Curiosity* rover, firstly in the Sheepbed Mudstone at Yellowknife Bay (Freissinet et al., 2015) and later at the base of the Murray Formation at Pahrump Hills (Eigenbrode et al. 2018). Freissinet et al. (2015) identified hydrocarbons – 150-300 ppb by weight chlorobenzene and 70 ppb by weight dichloroalkanes – that were determined to originate from the reaction of chlorine with organic carbon, whereas Eigenbrode et al. (2018) later identified thiophenic, aromatic, and aliphatic compounds with ~50 nanomoles of organic carbon, the preservation of which may have been aided by sulphurisation. Nevertheless, although organic matter is evidently present at the surface of Mars, environmental, UV and ionising radiation has been shown to degrade most biological matter, as demonstrated by multiple experiments in laboratory and low Earth orbit, for example the experiments on-board the EXPOSE-E, EXPOSE-R and EXPOSE-R2 missions (Rabbow et al, 2012, 2015, 2017; de Vera et al. 2019 and references therein). Other authors have demonstrated that ionising irradiation may lead to the degradation of organics even at depth using laboratory setups (Kminek and Bada, 2006; Dartnell et al. 2012), and by numerical models (Pavlov et al., 2012). These studies concluded that, after several million years, a large proportion of the organic molecules of astrobiological interest would be degraded throughout the first tens of centimetres (down to more than 1.5 metres depth depending on the study). Thus, Kminek and Bada (2016) recommended drilling to at least 1 m to increase the potential of detecting biological remains dating to the Noachian-Hesperian period. On the other hand, geological processes may lead to the exhumation of rocks previously protected from irradiation by erosion, exposing well-preserved organic molecules at the surface. In light of this, Pavlov et al. (2012) advocated analysing rocks "freshly" exposed at the surface, in accordance with the sampling strategy used for the MSL mission. With the disappearance of liquid water activity at the surface of Mars, however, weathering and erosional processes have been very limited since the early Hesperian. Wind erosion and transport are also minor due to the low atmospheric pressure; therefore, very ancient geological structures can be observed at the surface (e.g. dried rivers dating back from the Noachian). Consequently, freshly exposed surfaces may be uncommon. Conversely, exposed rocks may have been "recently" covered by tens of centimetres of sand and dust, meaning that even if they are deeper than 1 m from the surface, the organics molecules they contain may have been destroyed before burial. To circumvent these issues, the ExoMars 2020 rover has the unique ability to drill down to 2 m in depth to collect samples, maximising the potential for the detection of well-preserved organic molecules (Vago et al., 2017). This method of collecting samples demands a unique investigative protocol that must be considered in the training for the mission.

2) ExoMars scientific workflow and the importance of imaging systems

2.1. The ExoMars 2020 exploration protocol and scientific workflow

The ExoMars 2020 rover is equipped with several external instruments: a high-resolution imaging system, PanCam (Panoramic Camera) and an infrared spectrometer, ISEM (Infrared Spectrometer for ExoMars), located on the mast, a high resolution camera, CLUPI (Close-UP Imager), fixed on the drill box, and a neutron radiation detector, ADRON (Autonomous Detector of Radiation Of Neutrons), and radar for water detection and density and interface characterisation in the subsurface, WISDOM (Water Ice Subsurface Deposit Observation on Mars), both fixed on the body of the rover. The drill is equipped with a visible-near-infrared spectrometer, Ma_MISS (Mars_Multispectral Imager for Subsurface Studies), that will analyse the borehole wall. The drill will collect cores of 3 x 1 cm that will be crushed (250 µm grain size) prior to analysis by the instruments of the internal analytical laboratory: the Vis-IR spectro-imager MicrOmega, the Raman Laser Spectrometer (RLS), and a mass spectrometer, MOMA (Mars Organic Molecule Analyser). The positions of the instruments on the rover are indicated in Figure 1A. These instruments will enable the rover to carry out the exploration procedure described in Vago et al. (2017, pp. 496):

1- Landing site characterisation
2- Outcrop localisation, approach and study
3- Surface sampling (using the drill) and analyses
4- Subsurface characterisation to decide where to drill
5- Subsurface sampling and analyses

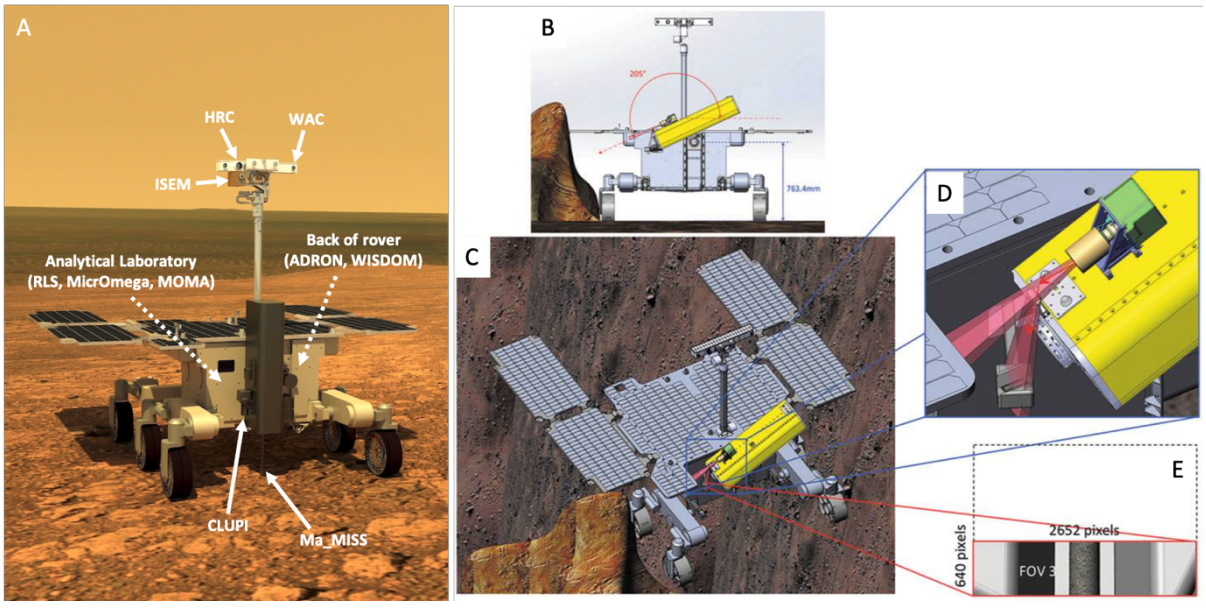

Fig. 1. ExoMars 2020 rover and aspects of its experimental cycle. A) Rendering of the ExoMars 2020 river showing the positions of the payload instruments (see main text for details). Credit: European Space Agency. B) Outcrop imaging configuration, drill arm shown in yellow. C) Top view of the outcrop imaging configuration with CLUPI shown in green mounted on the drill arm. D) Two CLUPI viewing modes, fields of view (FOVs) shown in red, CLUPI in green and the drill arm in yellow. FOV enables the imaging of core samples in the transport mechanism. E) Example image taken in CLUPI FOV3 mode. B-E adapted from Josset et al. (2017).

Accordingly, scientific data will be obtained following the specific workflow shown in Figure 2, involving progressively increasing resolution and a concomitant decrease in the scale of analysis. The findings of each step form a governing framework for the interpretation made in the next step (consistency). Similarly, at each step, there will be the opportunity to refine and/or reinterpreted the conclusions of the previous steps. This progressive learning approach is equivalent to that of MSL, described by Mangold et al. (2017). The interpretation of subsurface samples is, however, more complex due to the possible differences between surface and subsurface lithologies. Inconsistency between outcrop and subsurface samples must be considered and high-resolution data obtained from core analyses are limited in their utility for the refinement of surface data.

2.2. The importance of imaging for Mars exploration

Imaging is crucial for planetary exploration and all rovers and landers sent to Mars have been equipped with several imaging systems and cameras aimed at characterising the geological context and guiding the investigations (from punctual spectroscopic analyses to sampling and moving). High-resolution imaging systems are used to appraise the mineralogy, texture and structure of rocks and soils, similarly to field geologists using a magnifying hand lens. The MAHLI (Mars Hand Lens Imager) instrument on the *Curiosity* rover, for example, continues to play a major role in petrographic and mineralogical descriptions at Gale Crater (Grotzinger et al., 2014, 2015).

PanCam and CLUPI are the two external imaging systems onboard the ExoMars rover. PanCam, mounted on the rover mast (Fig. 1A), consists of two wide-angle cameras (WAC) for multi-spectral spectroscopic imaging and the High Resolution Camera (HRC) for detailed colour images. PanCam is the instrument primarily responsible for characterising the locality of the rover at outcrop scale, providing the 2D and 3D geological and mineralogical context for outcrops and the drilling site, in addition to navigation and strategic target identification along the rover traverses (Coates et al., 2017). Mast-mounted cameras have provided essential sedimentological and structural information in previous Mars missions, most recently the Mars Science Laboratory mission (Grotzinger et al., 2014, 2015; Rubin et al., 2017; Schieber et al., 2017). In addition to outcrop characterisation, HRC is also tasked with fine-scale outcrop characterisation, the monitoring of drilling operations and imaging the core during the short time that it is deposited in the core sample transport mechanism. CLUPI is a miniaturised, highly adaptive camera for high-resolution colour imaging (Josset et al., 2017), and is accommodated on the rover drill appendage (Fig. 1A-D). Two mirrors permit three fields of view (FOV): one for forward-facing observations of the geological environment and two for observation of the drilling area and drilled products (Fig. 1D-E). The first mirror provides an image of 2652 x 1768 pixels (FOV 1). The second mirror separates the field of vision and yields FOV 2, an image of 2652 x 1128 pixels in the direction of the optical axis of CLUPI, and FOV 3, 2652 x 640 pixels, oriented toward the drill tip. Thus, in addition to inspecting the local geological environment, CLUPI will provide the highest resolution images of drill core samples – before their subsequent crushing and ingestion into the body of the rover – using FOV 3 (Fig. 1E). In this configuration, CLUPI observes the core at a distance of 28.5 cm at an angle of incidence of 7.5˚, ergo at a resolution of 22 μm/pixel (Josset et al., 2017), capturing 1.42 x 1 cm of the 3 x 1 cm core sample. These images will provide a means of estimating rock type, mineral associations, context stratigraphy, grain size and shape parameters and

distributions, material properties such as hardness, induration and friability, and secondary alteration phenomena (fractures, veins and voids). Sedimentary and igneous rocks are commonly characterised according to their grain size (Udden, 1914; Wentworth, 1922; Le Maitre, 2002). Figure 3 displays the type of rocks that could by identified by PanCam and CLUPI with respect to the working distance, considering that a resolution of at least 3x3 pixels/grain is required to determine the grain size. Sediment transport agents may also be determined, assisting in palaeoenvironmental reconstruction . A detailed study of grain morphology in CLUPI-representative images by Kapui et al. (2018) demonstrated the possibility to differentiate aeolian from fluvial sediments if the resolution is sufficiently high (approx. 30 x 30 pixel/grain).

Textural biosignatures down to the the millimetre- to micron-scale may also be imaged and, through appraising them concomitantly with secondary alteration phenomena, one may build a context scenario for signs of life. FOV 2 and FOV 3 will provide complementary information on rover activities, imaging the drilled area and the resulting deposits at the surface. A comprehensive description of the role of CLUPI in rover operations may be found in Josset et al. (2017) and Vago et al. (2017).

Fossilised terrestrial biosignatures are most easily identified using optical microscopy, however, on Mars, observations able to detect morphological biosignatures (e.g., biofilm stacks and microfossil colonies/aggregations) are conducted only during the imaging of outcrops and samples. Thus, for ExoMars, microscopic observations of core samples represent probably the only opportunity for *in situ* imaging of potential biosignatures. Since this contact phase of imaging (terminology of Vago et al., 2017) at scales between regional and mineral-molecule is designed to establish a large range of characteristic geological parameters for each sample, including habitability potential, the imaging phase of ExoMars operations – in which the notably synergistic approaches of the Close UP Imager (CLUPI) and Panoramic Camera High Resolution Camera (PanCam HRC) will be employed – would provide both guidance and context for fine-scale analytical studies (Vago et al., 2017; Josset et al., 2017; Coates et al., 2017). In this contribution, we simulate this synergy, applying a protocol through which we aim to:

i) determine the crucial observations made on core samples by coupling HRC and CLUPI imaging;
ii) assure confidence in these observations by coupling imaging data to mineralogical data (Raman spectra using a wavelength and data acquisition strategy comparable to that of the Raman Laser Spectrometer (RLS) instrument; Rull et al., 2017); and
iii) identify shortcomings in the observations made, thus evaluating the role of core imaging in the ExoMars 2020 imaging and experimental cycle protocols through a blind test.

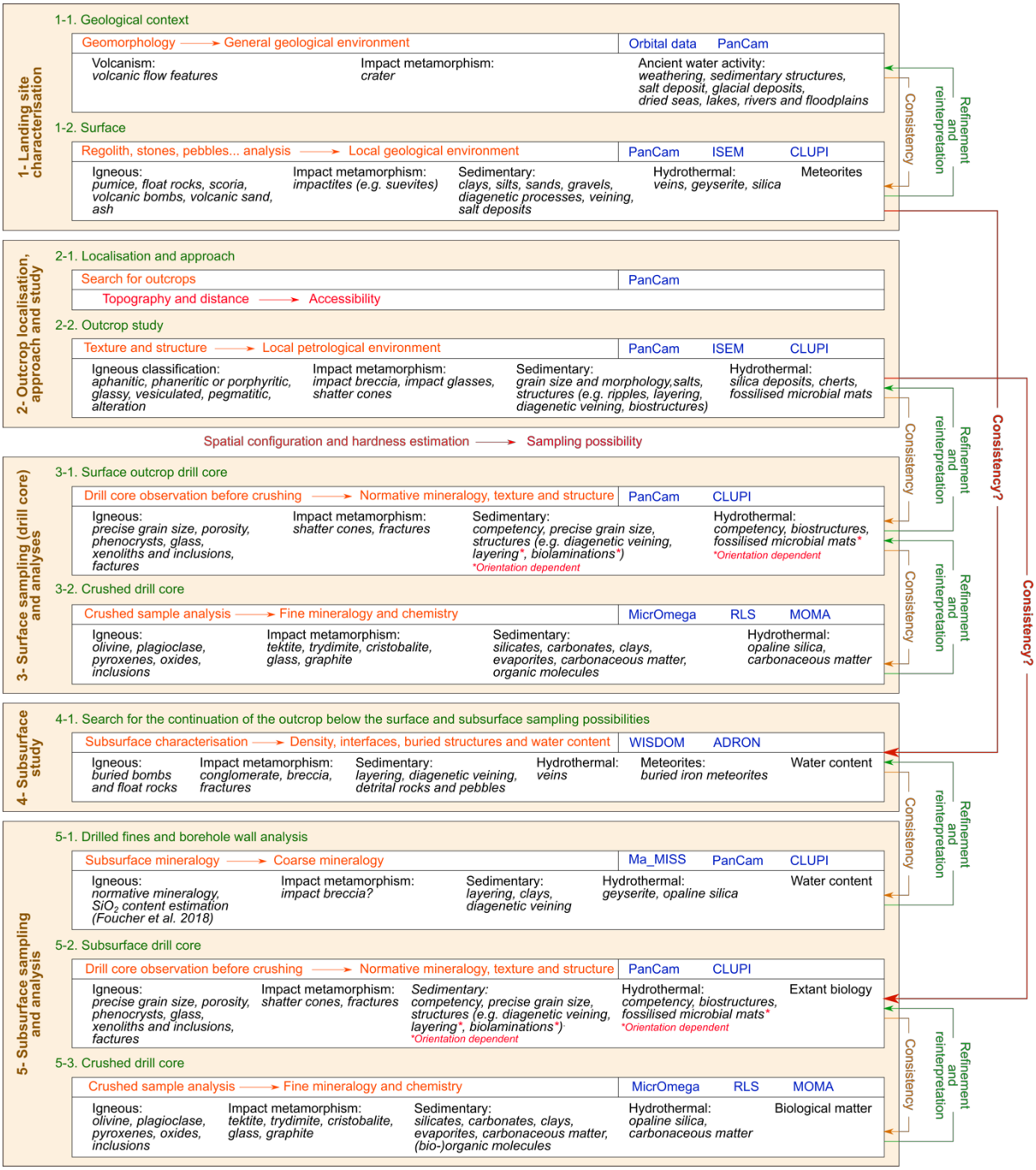

Fig. 2. ExoMars 2020 exploration procedure and scientific workflow. Comprehensive analysis of a locality involves three steps if only surface outcrops are studied, and five steps if subsurface samples are collected and analysed. Information in orange at each step describes the scope of analysis and the objective. Instruments performing these analyses are indicated at each step. Consistency of interpretation can be repeatedly checked after each stage of analysis, and reinterpretation made if necessary. Consistency between outcrop and subsurface analyses must be determined on a case-by-case basis, and requires detailed imaging of core samples.

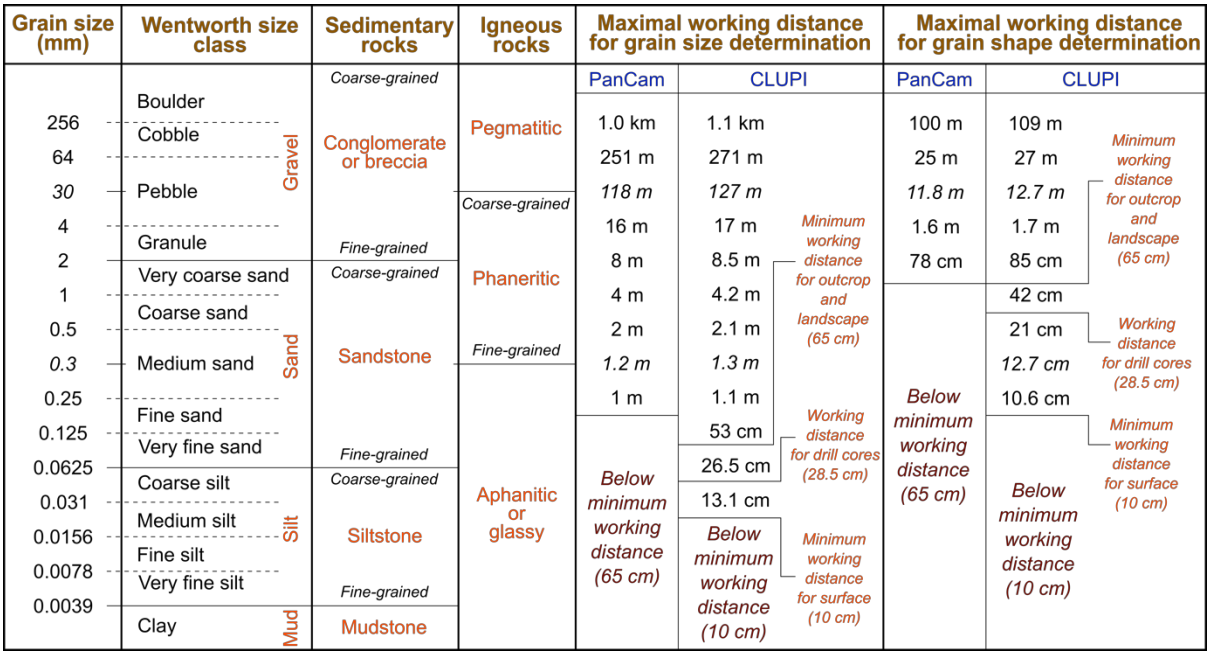

Fig. 3. Scales of sedimentary and igneous textures relevant to Martian geology, and the maximal working distance required to accurately identify them using PanCam or CLUPI. Working distances were obtained based on the fact that the ratio between the working distance and the resolution is equal to approximately 12,720 for CLUPI (Josset et al., 2017) and equal to 11,765 for PanCam (Coates et al., 2017), and considering that 3 x 3 pixels per grain are required to estimate grain size and that 30 x 30 pixels per grain are required to determine grain shape.

2.3. Scientific and technical training using blind tests

Bost et al. (2015) presented a first blind test using ExoMars 2020 instrumentation, studying two well-characterised samples from the International Space Analogue Rockstore (ISAR; Bost et al., 2013), a curated selection of astrobiologically relevant specimens. These were provided to imaging instrument teams as solid rock hand specimens with cut faces and to spectroscopy teams as powders, following which these teams were asked to attempt interpretation. Combining measurements acquired with CLUPI, Ma_MISS, MicrOmega and RLS emulator systems, it was found that comprehensive geological characterisation of outcrops could be achieved when combined with PanCam-representative context information from outcrops (of which the samples were representative). This was possible from optical images of hand samples alone, although much useful complementary information related to alteration features indicative of small scale habitability and potential biosignature preservation was added by the cross-correlation of data from the analytical geochemistry instruments. Nevertheless, the hand samples used by Bost et al. (2015) were around 10 cm in size and representative of the outcrop. Although this approach is relevant for drill cores taken at the surface of Mars, it is not necessarily the case for subsurface samples (see Fig 2., stage 5.2). For the test described herein, core samples of ExoMars 2020 dimensions (3 x 1 cm) were prepared, and no outcrop information was provided. Consequently, all scientific interpretation presented in the blind test conducted herein is based entirely on the interpretation of core samples as imaged by HRC and CLUPI emulators, complemented by RLS-representative data. This approach more accurately evaluates the difficulties in interpretation resulting from limited sample volume and area of imaging, which may be sample- or lithology-specific. The objective of this blind test is therefore to assess – using mission-representative emulation of the core

imaging process – to what extent geological observations can be made in the challenging scenario that core samples alone are available to characterise of the petrological context of putative biosignatures.

3) Materials and Methods

3.1. Core samples

Core samples were produced using specimens from the ISAR collection (Bost et al., 2013). Whereas the cores collected by ExoMars 2020 will be produced slowly and continuously, over a number of sols, without the use of water, our core samples were produced using water, the implications for which we outline in Section 4. Eight cores were produced, including volcanogenic, volcaniclastic, detrital sedimentary and biochemically precipitated rocks (Fig. 4; Table 1). Complete details of all samples are provided in Table 1. Cores measured 3 cm in length and 1 cm in diameter, i.e., they are dimensionally identical to those that will be produced during the mission.

Volcanogenic rocks (99SA13, 09SV17 and 17NZ14) were chosen to reflect some of the diversity in volcanic lithology identified on Mars (Bandfield et al., 2000; McSween et al., 2009). Detrital rocks (19AQ01, 11SP01, 17NZ05) were selected to reflect Martian sedimentary basin fills under erosive regimes. Oxia Planum, the chosen landing site for ExoMars 2020, is a phyllosilicate-rich terrain of volcanogenic and volcaniclastic materials sourced from volcanic terranes north of the ExoMars 2020 landing ellipse and their alteration products (Quantin et al., 2016). Due to the use of water in the coring process, the poorly indurated detrital rocks did not maintain cohesion; consequently, they were cut and shaped by manually grinding samples into the required dimensions in dry conditions. Two additional laminated sedimentary samples were chosen in order to test the ability of the imaging instrumentation to resolve millimetre-scale stratification, sedimentary structure and organic-rich strata. Using these dimensionally relevant samples, we performed the test using the following protocol, elaborated upon in Sections 3.2-3.5, which simulates the core imaging phase and fundamental mineralogical characterisation by the analytical laboratory drawer.

i) Produce a FOV3 image of part of the core (identical resolution to CLUPI core imaging, e.g. Fig. 5) and conduct a preliminary lithological appraisal, noting any missing or indeterminable characteristics;
ii) Produce two HRC images at identical resolution to HRC core images (Fig. 6) in different lighting conditions.
iii) Acquire systematic Raman spectra to emulate RLS measurements. Re-appraise the sample and note any complementary information;
iv) Produce a high-resolution (CLUPI FOV3) image of the entire core sample (Fig. 4) and identify any further complementary information, i.e. the missing characteristics after mission-relevant steps i) and ii).

3.2. CLUPI imaging

CLUPI-representative images were acquired with a CLUPI emulator equipped with the same FOVEON detector as the flight instrument (SIGMA SD15 camera). CLUPI FOV3 is 5.90 x 1.42 cm (2652 x 640 pixels, where each pixel is 22 μm), within which the core sample

accounts for 450 x 640 pixels (Fig. 5). Focal length, aperture and working distance were set according to the objective used in order to obtain images of similar native resolution, i.e. meaning that no further image processing was applied to the photographs.

3.3. PanCam HRC imaging

The same SIGMA SD15 camera was used as an emulator for the HRC instrument. The HRC core images will be 1024 x 1024 pixels, where each pixel is 0.17 mm, within which the core sample accounts for 177 x 59 pixels (Fig. 6). As for the CLUPI images, focal length, aperture and working distance were set according to the objective used in order to obtain images of similar native resolution, i.e. meaning that no further image processing was applied to the photographs.

3.4. Raman spectroscopy

The RLS instrument aboard ExoMars 2020 will use a 532 nm wavelength green laser to detect mineral phases in the crushed sample ingested into the rover analytical laboratory (Rull et al., 2017). RLS may use either an automatic (focussed on the RLS instrument) or cooperative (focussed on collaboration with MicrOmega and MOMA) operation mode. We simulated the automatic mode, acquiring twenty Raman spectra at consecutive, equally spaced intervals along the core samples. The system used was a WITec Alpha500 RA equipped with a frequency doubled Nd:YAG 532 nm green laser (similar to that of RLS) but using a spot size of 1.6 μm diameter (i.e. smaller than the 50 μm spot size diameter of RLS). Nevertheless, mineral identification using this system has been demonstrated to be representative of that conducted using the RLS system after data processing, spectral demixing and petrological considerations (Foucher et al., 2013).

3.5. Method of questioning

The protocol outlined in Section 2.1. was followed by a team of five geologists and one individual geologist, all of whom were involved in neither this project nor the ExoMars 2020 mission. The first step of the protocol determines whether core images taken by CLUPI (Fig. 5) alone are sufficient to identify the sample and, if not possible, at minimum to define certain characteristics (Table 2). The second step determines whether the various functions of PanCam HRC (Fig. 6) and RLS (identified minerals given in Table 1) can add critical information to validate and augment CLUPI information. This step also determines whether any identified characteristics are unreliable, not useful or whether further information is still needed (Table 3). The third step – high-resolution images of the full drill core (Fig. 4) – confirms whether misidentifications are due to instrumental, material/dimensional or lithological factors (Table 3). The six geologists to whom we set this challenge – with expertise in approaches and techniques relevant to sedimentology, igneous petrology, geochemistry, geomorphology and palaeontology – were required to return the information pertinent to each step before being sent the data for the next step, such that interpretations were successively built on receiving more data, as during a mission. Subjects were asked not to make interpretations unless confident in so doing, determining which characteristics could be most accurately ascertained using specific instrumentation, and which would be unidentifiable without specific instrumentation.

4) Results

4.1. 99SA13

The CLUPI core image (Fig. 5A) allowed the geologists to describe 99SA13 (silicified volcaniclastics) as grey-blue, fine-grained and generally homogeneous, although no specific minerals were identifiable. The sample was correctly determined as well-indurated, with low porosity and high hardness. The presence of faint laminations independent of coring striations was noted, but the sedimentological character of these laminations could not be described in detail (simply described as depositional layers). Secondary fractures were noted. The geologists suggested that the rock was sedimentary (pelite). Small, reflective grains, scattered throughout the sample, were not identified, nor was the blotchy texture of the upper region of the image. HRC core images provided little complementary information, although they confirmed that the sample was well-indurated, not fragmented, and weakly stratified throughout (Fig. 6A). Raman spectra identified quartz, albite, orthoclase, epidote, muscovite and potentially titanite (Table 1), a mineral assemblage consistent with a metapelite of volcanogenic origin. This identification was accurate, and crucial observations were granulometry, stratification and mineralogy from both imaging and mineralogical data.

4.2. 09SV17

From the CLUPI core image (Fig. 5B), the sample appears green-yellow, mineralogically heterogeneous and granular. Suggested mineralogies included peridotitic minerals and their alteration products, and inclusions/xenoliths were identified (arrowed in Fig. 4B). The sample was deemed massive, non-porous, well-indurated, hard, and of magmatic origin. A preliminary identification suggested peridotite or serpentinite based on granulometry and estimated mineralogy. The addition of HRC core images did not add any complementary information, as the rock colour was too uniformly dark in tested lighting conditions to discern individual mineral phases (Fig. 6B). Raman data, however, proved extremely useful; a mineral assemblage of augite-diopside, enstatite, labradorite, forsterite, carbonaceous material and possible magnetite (Table 1) clearly suggest that this is a mafic (basaltic-gabbroic) rock. Full core images confirmed that the green mineralogy corresponded only to a coarse-grained xenolith, although the geologists did not identify the porphyritic fabric of the rock, leaving its petrogenetic history incompletely appraised; the rock is in fact a porphyritic basalt. The eventual interpretation was very accurate, in spite of some initial error, and colour, texture, xenoliths and mineralogy were deemed the key characters enabling the description of the sample (Table 1).

4.3. 17NZ14

The CLUPI core image (Fig. 5C) enabled the immediate identification of a bipartite mineral assemblage: darker grey-black and lighter white-pink phases, which the geologists correctly suggested were mafic minerals and quartz/feldspars, respectively. The sample was also correctly characterised as coherent, hard, and rich in inclusions. The occurrence of stratification was mistakenly identified, since horizontal striations from the coring process sometimes coincided with zones of changing mineralogy. The geologists failed to identify the circular vesicles present throughout the sample (arrowed in Fig. 4C), as their depth was not obvious from the CLUPI image. Granulometry and the misidentification of stratification and

vesicles resulted in the sample being incorrectly interpreted as a sedimentary conglomerate. HRC images did not assist the identification (Fig. 6C), since at their lower resolution, mineralogical zonation, which is broadly laminated in some parts of the rock, was misinterpreted as metamorphic foliation. Raman spectra again proved very useful for lithological interpretation: a pyroxene-rich mineralogy of mostly labradorite, some augite-diopside, and minor anorthoclase feldspar and forsterite can only reflect a pyroxenite (Table 1). Thus, although the misindentification of foliation led to a final interpretation of metamorphosed pyroxenite, this revised interpretation is considerably more accurate than the preliminary suggestion of conglomerate. Mineralogical data enabled identification, however, the ambiguity of mineralogy in darker areas (vesicles) was a limiting factor to overall interpretation.

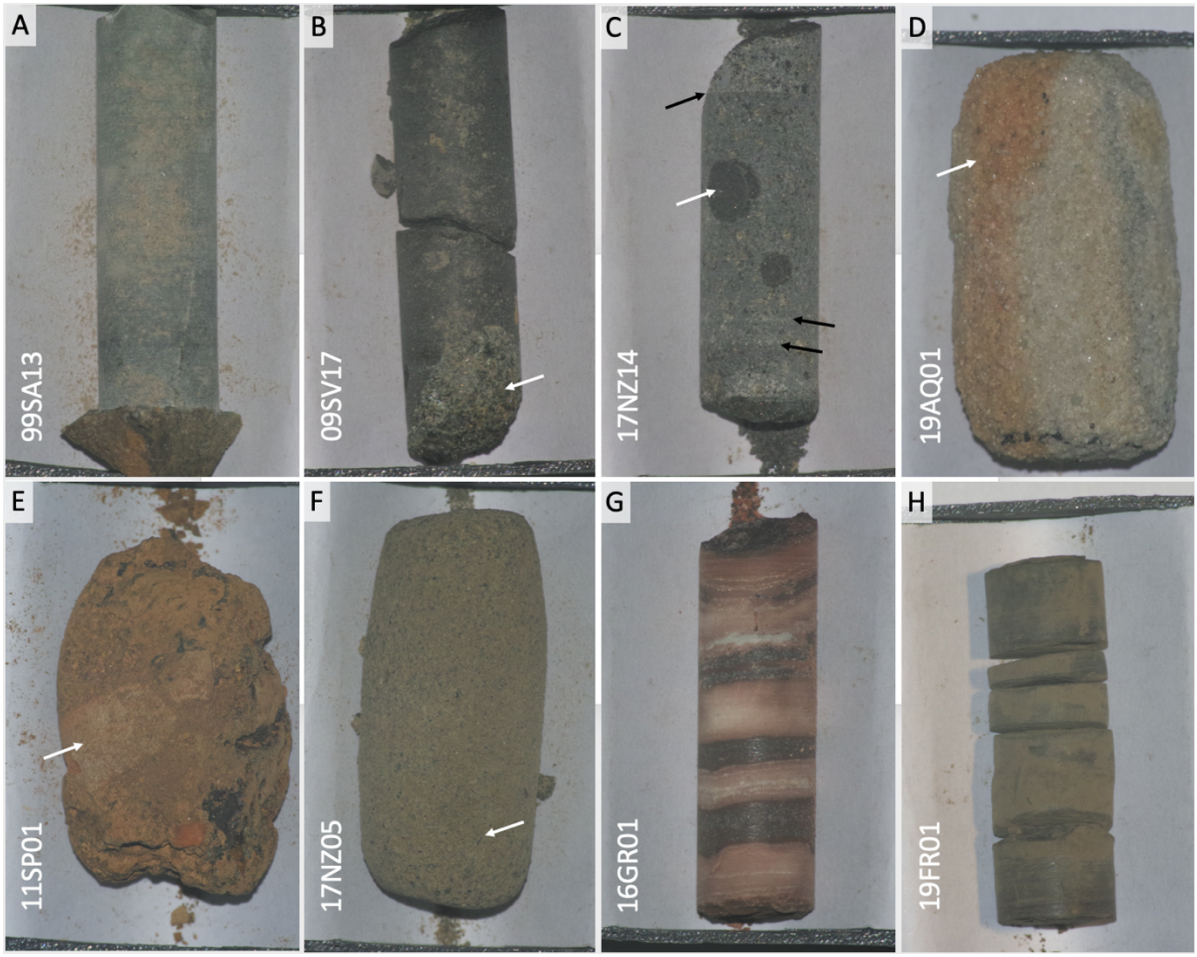

Fig. 4. Photographs (at maximal CLUPI resolution) of whole core samples, which are approximately 3 cm by 1cm in size. A) Sample 99SA13, metapelite with carbonate. B) Sample 09SV17, tholeiitic basalt with copious large olivine-rich xenoliths (white arrow). C) Sample 17NZ14, basalt-pyroxenite featuring large spherical vesicles (white arrow). Damage during the coring process is reflected in surficial striations (black arrows). D) Sample 19AQ01, calcitic quartz arenite. White arrow indicates region of chemical alteration. E) Sample 11SP01, conglomerate with angular and sub-angular pale clasts (e.g., white arrow). F) Sample 17NZ05, coarse volcanogenic sandstone. White arrow indicates chevron-like black mineral. G) Sample 16GR01, ferruginous chert with alternately Fe- and Mn-rich layers. H) Sample 19FR01, finely laminated, organic-rich mudstone. The significance of the arrowed objects – causing difficulties in the interpretation – is given in the main text.

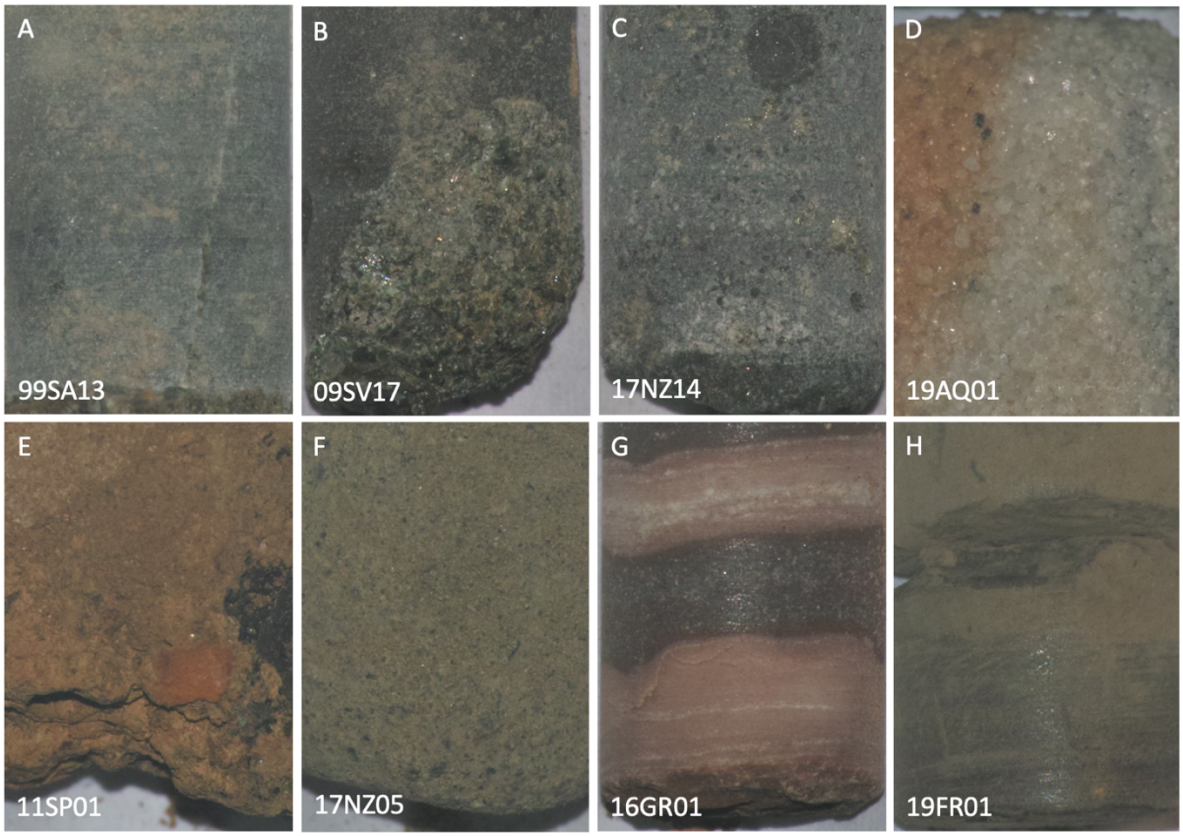

Fig. 5. Step 1 of the protocol: core samples of selected ISAR specimens imaged with emulated CLUPI FOV 3 (only core region shown) at maximal resolution of 22 µm/pixel. Field of view is equivalent to that planned for CLUPI FOV 3 observations (1.42 x 1cm). A) Sample 99SA13, metapelite with carbonate. B) Sample 09SV17, tholeiitic basalt. C) Sample 17NZ14, basalt-pyroxenite. D) Sample 19AQ01, calcitic quartz arenite. E) Sample 11SP01, conglomerate. F) Sample 17NZ05, coarse volcanogenic sandstone. G) Sample 16GR01, ferruginous chert. H) Sample 19FR01, finely laminated, organic-rich mudstone. See Table 1 for full lithological descriptions.

4.4. 19AQ01

The CLUPI core image (Fig. 5D) alone permitted a thorough examination of this coarse-grained quartz arenite. The geologists described the sample as orange, pink, white and bluish, coarsely granular, lightly porous, quite well-indurated and broadly homogeneous in terms of mineralogy (quartz) despite colour alterations. The rock was easily identified at this first step as a quartz-rich sandstone. HRC images and Raman spectra showing quartz, haematite, calcite and unidentifiable fluorescent minerals (Table 1) added no essential information but confirmed and added further detail to the identification (Fig. 6D). The sole remaining cryptic aspect was the vertical colour zoning (arrowed in Fig. 4D), although this was most easily explained as chemical weathering. The geologists did not comment on other characteristics of the grains (e.g. roundness, sphericity, kurtosis, skewness, Corey Shape Factors), despite the apparent ease of making these morphometric distinctions from the CLUPI core image. This sample was interpreted very accurately, with both granulometry from PanCam and CLUPI images, and mineralogy from Raman spectra providing all necessary information.

4.5. 11SP01

Although the CLUPI core image (Fig. 5E) of this iron-rich conglomerate allowed a number of sedimentary observations to be made, several crucial characteristics could not be

confidently interpreted: hardness, stratification, porosity and mineralogy. The ochrous and black colouration of various zones of the sample were noted, as was the fine grain size and heterogeneity of the matrix. Comparison with other samples suggested that this was a more friable, poorly cemented lithology. Since no clasts were visible in the CLUPI image, an identification as a matrix-supported conglomerate was not possible. HRC images (Fig. 6E) showed the conglomeratic characteristics of the sample (large entrained particles in a fine matrix), however, large, angular, pale grains (arrowed in Fig. 4E) were misinterpreted as secondary alteration features. Raman data, identifying haematite (the surface alteration), quartz, the zeolite chabazite, carbonaceous material and possible magnesiochromite (Table 1), led to an eventual inaccurate and incomplete identification as a detrital iron-rich sediment, tentatively a ferruginous laterite.

4.6. 17NZ05

From the CLUPI core image (Fig. 5F), the geologists described a green-grey, heterogeneous, granular rock, both well-indurated and cohesive, with no distinct sedimentary features. Elongate, prismatic black minerals were interpreted as amphiboles. Lighter, reflective minerals (oxides) were not noted, but chevron-like black minerals were identified throughout the sample. At this stage, the geologists were not confident in making an identification. HRC images (Fig. 6F) showed the mineralogical diversity at different scales of observation: whereas at the scale of tens of microns (step one), the sample is heterogeneous, at the scale of millimetres, the sample is homogeneous (step two) and structureless. In HRC images, the sample appears brown, as opposed to green-grey (Fig. 6F). Only two Raman spectra were obtained, corresponding to leucite/labradorite and anorthoclase/labradorite, i.e., the rock contains calcium feldspar (Table 1). All other spectra were masked by high fluorescence, but a magmatic origin was suspected based on these two measurements. Without identification of the clay mineral cementing phase (achievable using Ma_MISS and MicrOmega), and in the absence of visible sedimentary structures, the logical steps leading to an identification as volcanogenic sandstone could not be made. The eventual interpretation was therefore broadly accurate, but lacked many important details. The geologists noted that colour and certain unidentifiable phases (the matrix and numerous chevron-like minerals; arrowed in Fig. 4F) made the appraisal particularly challenging.

4.7. 16GR01

The CLUPI and HRC core images (Figs. 5G and 6G) allowed an equally comprehensive petrographic and petrological description of this banded ferruginous chert. Heterogeneous laminations alternate between grey-black and pink-orange-white colouration and exhibit differential coarseness, dark laminations being coarser. The rock is evidently hard and well-indurated, with pressure solution fronts (stylolites) at lamination boundaries. In this first step, the geologists speculated that evaporite minerals might constitute the darker layers, and that the rock itself may be a biochemical precipitate. HRC permitted observations on the millimetre scale and aiding the visualisation of vertical variation in lamination. Raman data identified almost exclusively haematite, with minor orthoclase and microcline (Table 1). Although the composition of the dark bands remained difficult to interpret, having apparently not been measured during the Raman analyses, comparison with similar strata from the geological

record allowed accurate determination that this is a banded ferruginous chert, and therefore reflects (bio-)chemical deposition.

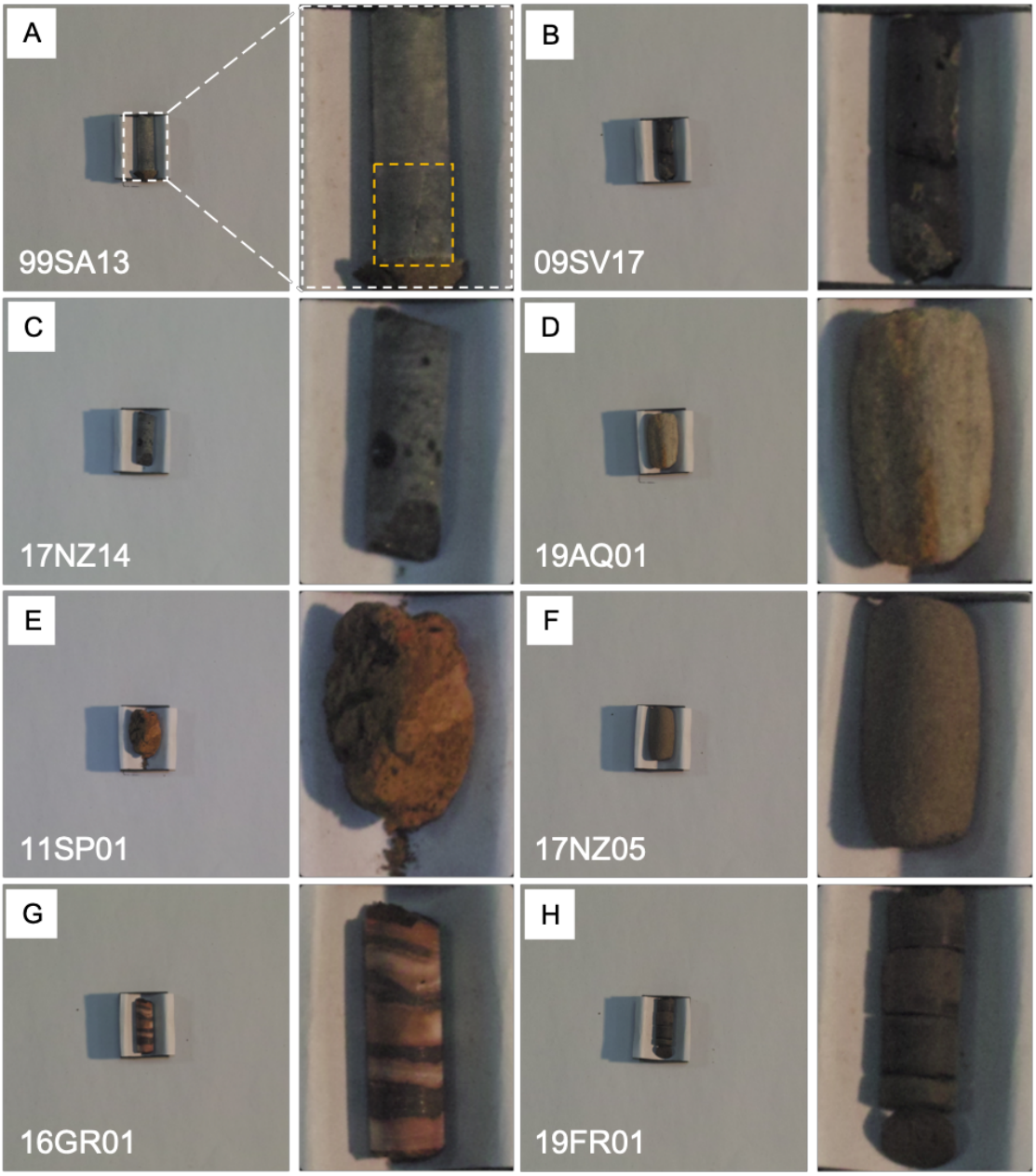

Fig. 6. Step 2: selected core samples imaged with HRC emulator conditions at a resolution of 17 mm/pixel. Samples were each imaged in two light conditions. Field of view is equivalent to that planned for HRC images (17.4 x 17.4 cm). Yellow box in A indicates size of the FOV3 of CLUPI (cf. Fig. 3A). A) Sample 99SA13, metapelite with carbonate. B) Sample 09SV17, tholeiitic basalt. C) Sample 17NZ14, basalt-pyroxenite. D) Sample 19AQ01, calcitic quartz arenite. E) Sample 11SP01, conglomerate. F) Sample 17NZ05, coarse volcanogenic sandstone. G) Sample 16GR01, ferruginous chert. H) Sample 19FR01, finely laminated, organic-rich mudstone.

4.8. 19FR01

The CLUPI and HRC core images (Figs. 5H, 6H) both show a brown-grey-yellow, fine-grained, heterogeneous sample, which is cohesive but soft relative to the other studied samples. Stratification was identified independent of striations left by the coring mechanism, however,

porosity was mistakenly inferred where none exists. Dust from the fragmentation of the sample further hindered observation of the upper part of the image; nonetheless, this sample was correctly identified as a fine-grained, organic-rich, laminated sediment (mud- or silt-grade) from CLUPI and HRC images alone. The sole difference between the two images is that the colour variation seen in the CLUPI image is an artefact of the small area of observation; the wider scale of observation of the HRC image demonstrates that the sample is colourimetrically and compositionally repetitive. Raman measurements identify mostly carbonaceous material, often associated with quartz and brookite (TiO_2), together with minor haematite and zircon, i.e. a siliciclastic composition (Table 1). The geologists made an accurate identification of the sample and deemed that the fine grain size, regular, fine-scale stratification and compositional information were equally important characteristics for successful interpretation.

5) Discussion

5.1. Differences inherent in the study of samples on Earth and Mars

Although all reasonable effort was made to ensure the mission-representativeness of our experiments, a small number of technical process differences between the study of samples in Earth and Mars conditions are unavoidable:

- During the ExoMars 2020 mission, no water will be used for drilling. This will increase dust production, which may hinder the visual interpretation of samples.
- On Mars, drilling will be conducted very slowly and smoothly leading to fewer and less distinct striations, which reduces the risk of misinterpretation of such features.
- Martian light conditions have not been considered in the test. The difference in light colour and intensity may change the apparent colour of samples and influence interpretation. In light of this, image calibration methods permitting the correction of sample colour on Mars are presently under development (Josset et al., 2017; Foucher et al., 2018).
- No liquid water is expected in the exhumed samples. In rocks which exhibit cementation as a function of water content, e.g. sandstones, this may alter competency and increase friability.
- The exhumation of core samples at the Martian surface could induce the sublimation of water ice, causing the cracking and disaggregation of samples with closed porosity, thus the core samples may emerge with their stratigraphy disturbed.

Table 1. Geological and petrological descriptions of the eight samples used in the blind test.

Table 1 – Sample Characterisation (hand sample)								
Sample	99SA13	09SV17	17NZ14	19AQ01	11SP01	17NZ05	16GR01	19FR01
Colour	Grey-white	Grey, green, black	Black-grey, green	White, light grey, orange (chemical alteration)	Red-orange (oxidation), white-grey-black-red (clasts)	Brown-grey-black	Dark red-orange and black interbeds	Black-brown
Granulometry	Fine-grained	Porphyritic; phenocrysts up to 1.5 mm, aphanitic matrix	Coarse (0.5-1 mm), sub-angular grains (phaneritic texture) in an aphanitic groundmass	Coarse sand (< 1 mm)	Coarse (0.1-1 cm) particles suspended in fine-medium sand matrix	Sand-grade with clay-rich matrix, angular/sub-angular grains	Fine-grained (<0.5 mm)	Very fine-grained
Homogeneity	Homogeneous	Heterogeneous	Heterogeneous	Homogeneous	Heterogeneous	Broadly homogeneous at centimetre scale, heterogeneous at millimetre scale	Heterogeneous at centimetre scale, homogeneous at millimetre scale	Broadly homogeneous; heterogeneities at the millimetre scale
Mineralogy	Quartz, albite, orthoclase, epidote, muscovite, carbonate phases, minor oxides including titanite and magnetite	Dominant: augite, enstatite, labradorite, forsterite. Minor: carbonaceous material, magnetite, rutile, other oxide phases	Labradorite, augite-diopside (pyroxenes), anorthoclase feldspar, minor forsterite	Quartz, haematite, calcite, clay minerals, carbonaceous material	Haematite, quartz, augite, magnetite, chabazite, some carbonaceous material	Clay mineral matrix, alkali feldspar, amphiboles	Red layers: haematite, orthoclase, microcline, quartz. Black layers: quartz, manganese oxides.	Clay minerals, carbonaceous material, quartz, iron and titanium oxides, numerous siliciclastic detrital phases
Coherence	Coherent	Coherent	Coherent	Somewhat cohesive, but not well-cemented	Low coherency	Coherent	Coherent	Coherent
Inclusions		Large (< 1.5 cm) olivine-rich xenocrysts	No	No	Large (0.1-1 mm) xenoliths	No	No	No
Hardness	Hard (5-7)	Hard (6-7)	Medium (3 < x < 5)	Hard (~7)	Matrix soft (< 3), clasts variable	Medium (3 < x < 5)	Hard (5-7)	Soft (< 3)
Schistosity	No	No	No	No	No	No	No	No
Stratification	Some, poorly defined	No	Some poorly demarcated compositional layering	Massive	No	Massive	Yes, well-stratified in sub-centimetric layers	Yes, well-stratified in millimetric layers
Fractures	Yes	Yes	No	No	No	No	No	No
Veins	Yes	No	No	No	No	No	No	No
Porosity	No	No	Some (vesicles)	Yes	Some	Low	No	No
Biosignatures	No	No	No	No	No	No	Yes – biochemical sediment	Yes – rich in organic carbon of biological origin
Rock type	**Igneous/sedimentary**	**Igneous**	**Igneous**	**Sedimentary**	**Sedimentary**	**Igneous/sedimentary**	**Sedimentary**	**Sedimentary**
Rock name	**Metapelite with carbonate**	**Tholeiitic basalt**	**Basalt-pyroxenite**	**Calcitic quartz arenite**	**Conglomerate**	**Coarse volcanogenic sandstone**	**Ferruginous chert**	**Mudstone**

Table 2. Responses of the subjects after step 1 of the protocol described in Section 2.1.

Table 2 – Blind Test Results, Step 1 (core sample)								
Sample	99SA13	09SV17	17NZ14	19AQ01	11SP01	17NZ05	16GR01	19FR01
Colour	Grey-blue	Grey, green, yellow	Dark and white/pink regions	Orange, pink, white, grey	Ochre, blackish	Dark grey-green	Dark blue, green, pink, white	Yellow, brown
Granulometry	Fine-grained	Visibly granular	Visibly coarse-grained	Coarse-grained	Fine-grained	Medium-coarse grained	Variable; finer in upper and lower layers	Fine-grained
Homogeneity	Homogeneous	Heterogeneous	Heterogeneous	Homogeneous	Heterogeneous	Heterogeneous	Heterogeneous	Heterogeneous
Mineralogy	None identified	Peridotite and its alteration phases	Quartz, feldspar	Quartz	None identified; likely oxides	Amphiboles (black crystals)	? salts	None identified; likely clay minerals
Coherence	Coherent	Coherent	Coherent	Lightly cohesive	Friable	Coherent	Coherent	Lightly cohesive
Inclusions	No	Yes	Yes	No	No	No	No	No
Hardness	Hard	Hard	Hard	Hard (~7)	Soft	Hard	Hard	Soft
Schistosity	No	No	No	No	Some	No	No	No
Stratification	Yes	No	Yes	No	Some	No	Yes	Yes
Fractures	Yes	No	No	No	No	No	Yes	Yes
Veins	No	No	No	No	No	No	No	No
Porosity	No	No	No	Some	No	No	No	No
Visible biosignatures	No	No	No	No	No	No	No	No
Rock type	**Sedimentary**	**Igneous**	**Sedimentary**	**Sedimentary**	**–**	**–**	**Sedimentary**	**Sedimentary**
Rock name	**Pelite**	**Peridotite or serpentinite**	**Conglomerate**	**–**	**–**	**–**	**Biochemical sediment, metachert, evaporative salts?**	**Clay-rich mudstone**
Further observations	**Horizontal deposition**	**Massive texture**		**Homogeneous mineralogy; different colours due to chemical alteration**		**Difficult to identify chevron-like minerals**	**Dark fronts between layers**	
Accuracy of identification	**Accurate**	**Broadly accurate**	**Inaccurate**	**Very accurate**	**Inaccurate**	**Inaccurate**	**Accurate**	**Very accurate**

Table 3 – Blind Test Results, Steps 2-3 (core sample)									
Sample	**99SA13**	**09SV17**	**17NZ14**	**19AQ01**	**11SP01**	**17NZ05**	**16GR01**	**19FR01**
Colour	–	Dark, no colour distinctions	Green, blue, grey, black	–	Reddish, ochre	Brown	–	Less colour variation than suggested by CLUPI image
Granulometry	–	–	–	–	–	Visible, thus granular or microgranular	–	–
Homogeneity	–	–	–	–	–	Homogeneous	–	–
Mineralogy	Quartz, albite, orthoclase, epidote, muscovite, titanite(?)	Augite-diopside, enstatite, labradorite, forsterite, carbonaceous material, possible magnetite	Labradorite, augite-diopside, anorthoclase feldspar, forsterite	Quartz, haematite, calcite, unidentified fluorescent minerals	Haematite, quartz, chabazite, carbonaceous material, possible magnesiochromite	Only two spectra obtained: leucite/labradorite and anorthoclase/labradorite	Haematite, minor orthoclase and microcline, one spectra of arzakite(?)	Carbonaceous material, associated with quartz and brookite, minor haematite and zircon
Coherence	–	–	–	–	–	–	–	–
Inclusions	–	–	–	–	–	–	–	–
Hardness	–	–	–	–	–	–	–	–
Schistosity	–	–	Foliation	–	–	–	–	–
Stratification	–	–	–	–	–	–	–	–
Fractures	–	–	–	–	–	–	–	–
Veins	–	–	–	–	Yes, white zone in centre of core (alteration)	–	–	–
Porosity	–	–	–	–	–	–	–	–
Biosignatures	–	–	–	–	–	–	–	–
Rock type	**Sedimentary**	**Igneous**	**Meta-igneous**	**Sedimentary**	**Detrital sedimentary**	**Igneous**	**Sedimentary**	**Sedimentary**
Rock name	**Pelite of volcanogenic origin**	**Mafic rock (basaltic-gabbroic)**	**Pyroxenite**	**Quartz-rich sandstone**	**Ferruginous laterite**	–	**Biochemical sediment, metachert, evaporative salts?**	**Organic-rich mudstone**
Further observations	**No further optical information obtained**	**No further optical information obtained**	–	–	–	**Mineralogy: rich in calcium feldspar**	**No further optical information obtained**	–
Accuracy of identification	**Accurate**	**Very accurate**	**Very accurate**	**Very accurate**	**Inaccurate**	**Broadly accurate, but unspecific**	**Accurate**	**Very accurate**
Useful identifying characteristics	**Mineralogy, grain size, stratification**	**Colour, texture, presence of inclusions, mineralogy**	**Mineralogy, texture as seen in PanCam images**	**Granularity, visible mineralogy**	**Colour, texture, some mineralogy**	**Mineralogy, texture**	–	**Stratigraphy, fine grain size, mineralogy (presence of carbonaceous matter)**
Ambiguous characteristics	–	–	**Lacks visible mineralogy, dark regions (vesicles)**	**Vertical colour zoning**	–	**Colour, chevron-like minerals**	–	–
Missing characteristics	–	–	–	–	**Mineralogy; few distinct spectra obtained**	**Mineralogy; few spectra obtained**	–	–

Table 3. Responses of the subjects after steps 2-3 of the protocol outlined in the Section 2.1. Where '-' is indicated, no further conclusions could be made with respect to those already made after step 1, i.e. CLUPI alone offered as much information as was possible or necessary.

5.2. Challenges of interpreting limited samples

5.2.1. Misidentification and misinterpretation

The principal challenge inherent in the interpretation of core samples is the possibility of misinterpretation of features at the sub-centimetre to centimetre scale. Although these features are within the range observable by the ExoMars 2020 imaging instrumentation (see Fig. 3), their interpretation is more difficult in practice, particularly given the limited field of view possible for core samples. CLUPI images only 1.42 cm of the length of the core at 22 µm/pixel (Josset et al., 2017). Using HRC, the whole core is imaged with a resolution 0.17 mm/pixel (Coates et al., 2017), thus the sample accounts for only 177 x 59 pixels (the full image being 1024 x 1024 pixels, corresponding to 17.4 x 17.4 cm). Consequently, sedimentary structures (e.g. stratification, deformation) and igneous features (e.g. xenoliths, phenocrysts) close to this size may be either given undue importance or neglected. For example, the fine lamination in sample 19FR01 (Fig. 4H) was under-recognised by virtue of both the fragmentation of the sample and its covering by dust, requiring both CLUPI and HRC images to delineate the character and consistency of lamination. Contrastingly, the large olivine-rich xenolith in sample 09SV17 (Fig. 4B) was attributed over-importance by the geologists due to its accounting for a large portion of the core sample (particularly in the CLUPI image) which was not representative of the hand sample. Consequently, interpretations focussed on the mineralogy of this xenolith, and the porphyritic texture of the groundmass was ignored. In the third case, the large (0.1-1 cm) conglomeratic clasts in sample 11SP01 (Fig. 4E), were misidentified as alteration features due to the fact that they did not feature in the CLUPI image and were coarsely pixelated in the HRC image. The point of caution raised here is that neither CLUPI nor HRC is ideally adapted to imaging core characteristics in the sub-centimetre to centimetre range, and the identification of textural heterogeneity at these scales may be limited. Smaller and larger features and structures are more easily recognised, having constituent features that fall within the optimal resolution range of either CLUPI or PanCam at the contact operation working distance (see also Fig. 3). At this scale, determinations of granulometry are, in addition to being a function of resolution, also contrast-dependent: diverse mineralogies with distinct colour are easier to appraise in detail than homogeneous mineralogies in CLUPI and HRC images alone.

A second potential fabric misidentification involves the potential interpretation of damage resulting from the coring process as primary sedimentary features. Striations in sample 17NZ14 (Fig. 4C) were interpreted as primary bedding whereas, conversely, vesicles were thought to be mechanical erosion effects. Of note is that these features largely fall in the range of sub-centimetre to centimetre as discussed above. Striations are enhanced by the irregular drilling required to let the water flow along the core to evacuate fines, however, and would probably be less visible on ExoMars 2020 drill cores by virtue of its continuous drilling. Mineralogical data from Raman analyses can be used to revise interpretation, but this is nonetheless an important consideration since the imaging data have an inherent guiding value for geological interpretation. The fact that the numerous vesicles in sample 17NZ14 were not identified resulted in misinterpretation of its petrogenesis. The misidentification of conglomeratic clasts in sample 11SP01 (Fig. 4E) as alteration phenomena presents similar issues, however, atlases of texture at multiple scales (e.g. Schieber et al., 2007) may provide

invaluable references for the interpretation of unusual or unexpected textures and microstructure in such cases.

5.2.2. Analytical uncertainties

Both of the above challenges imply that caution should be taken when determining lithology from core samples exhumed by ExoMars 2020, as neither analysed regions nor the core sample itself is necessarily representative of the bulk lithology. Although many units in Martian stratigraphy are relatively homogeneous on the metre-scale in mineralogical and sedimentological terms (McSween et al., 2009; Grotzinger et al., 2014; Quantin et al., 2016), this should not be assumed and small scale specificities have been key to palaeoenvironmental interpretation. *In situ* rover-based studies of Martian sediments in Gale Crater using ChemCam have identified, for example, centimetre-scale veins of light-toned, fracture-filling material determined to be the calcium sulphates gypsum and bassanite (Nachon et al., 2017). Rubin et al. (2017) also identified decimetre-scale cylindrical, pipe-like structures interpreted as fluidised sediment pipes in photographs taken by the *Curiosity* rover. Single analyses yielding either indicative or, conversely, unrepresentative data, for example the zircon identified using Raman spectroscopy in sample 19FR01, and suites of analyses failing to identify the characteristics of large portions of a sample, such as the dark laminations in the banded ferruginous chert 16GR01, introduce analytical uncertainties to lithological interpretations and therefore to estimations of the palaeoenvironment. For example, the calcium sulphate veins observed in Gale Crater, although volumetrically minor, have been critical in the proposition of post-depositional micro-environments (Kronyak et al., 2019) that may contribute to the alteration of biosignature preservation potential. Cross-correlation of imaging and compositional data at both the outcrop and core scale is necessary and will rely on the multi-stage experimental cycle outlined in Figure 2 (outcrop study and core study) planned for the ExoMars rover mission (Vago et al., 2017). The PanCam wide-angle cameras and CLUPI in the FOV1 operating mode will provide decisive complementary information at the surface. Further mitigation of residual issues in geochemical interpretation may be achieved through the combined approach of MicrOmega and RLS during the analytical stage, since MicrOmega will map the crushed grain surfaces and identify points of interest for further analysis by RLS (Bibring et al., 2017; Rull et al., 2017).

Among the most challenging mineralogies to identify, whether petrographically or spectroscopically, are clay minerals. This is evident from sample 17NZ05, in which the clay mineral matrix was not identified by any of the imagery and Raman spectroscopy conducted. Mineral phases immersed in clay mineral matrices tend to have their signals masked; indeed, even the identified minerals (leucite/labradorite and laboradorite/anorthoclase) exhibited either weak spectral signals or were identified only by certain unmasked peaks. This masking effect will be greater during the mission since the RLS instrument uses a 50 μm laser and will likely incorporate multiple minerals into each analysis. At the outcrop scale and at the working distance from the mast-mounted instruments to the core sample, the Infrared Spectrometer for ExoMars (ISEM) instrument (Korablev et al., 2017) may be able to acquire compositional data relating to these phases both in the core and in the surrounding exposures. Axiomatic identifications of clay minerals will likely be achieved after MicrOmega analyses of crushed samples (Bibring et al., 2017). Furthermore, although a clay-rich core sample would lose its cohesion at the surface, its stratigraphy may nonetheless be inferred by Ma_MISS images

within the borehole (De Sanctis et al., 2017) together with PanCam spectral images of the surrounding outcrops, before MicrOmega analyses.

The above considerations highlight that, since core samples may be neither wholly nor partly representative of their local and regional geological environments, the merging and integrative interpretation of data from all instruments of the ExoMars 2020 rover payload is necessary (Fig. 2). On Earth, the geological settings for ancient biosignatures are appraised on scales between regional and atomic (Wacey, 2009; Westall et al., 2015), and this can be achieved to some extent using the ExoMars 2020 instrumentation (Vago et al., 2017, 2018), which is split into panoramic, contact and analytical scales of observation. Within one stage of this protocol, for instance the contact analyses conducted herein, multiple complementary analyses of the same features or object may permit interpretation.

5.2.3. Life detection

A third category of challenges relates to biosignature detection. Macroscopic biosignatures, despite some controversies, are widely considered convincing evidence for life (Wacey, 2009), however, the range of biosignatures possible for Mars is expected to be subtler than that on Earth in terms of both morphology and geochemistry (Mustard et al., 2013; Westall et al., 2015; Hays et al., 2017). The challenge of life detection for ancient biosignatures on Earth (Westall et al., 2015; Hays et al., 2017), widely considered informative for the potential Martian biosphere, will be compounded on Mars by virtue of the reduced capabilities of rover instrumentation relative to Earth-based instrumentation. Microbial biosignatures were present in three of the samples studied: carbonaceous material in silicified volcaniclastic sediment 99SA13, biologically induced ferruginous precipitates in 16GR01, and organic-rich layers in 19FR01. In two cases (16GR01 and 19FR01), the presence of biology was correctly inferred, however, it was not explicitly identified, but rather implied from comparison to known rocks of similar origin with biological influences. Implication of biology in this manner could prove to be a significant drawback during the mission. Since even macroscopic traces of life are not wholly unambiguous, we suggest that some combination of optically identifiable biostructure and molecular characterisation is necessary to impute an unambiguous, *in situ* biosignature. We did not consider, however, in this blind test, the MicrOmega and MOMA data that will likely provide further important information on the composition of organic material in the samples. Were the crushed sample to contain bio-indicative molecules (e.g., Fig. 2, stage 2), closer analysis of the sample and locality in question would be necessitated. In the absence of either optically identifiable and/or molecular characterisation, the classification of putative biosignature or possible biosignature (*sensu* Buick, 1990) should be used. Such a potential biosignature might be appraised by Mars sample return.

5.3. Complementarity of the ExoMars 2020 instrumentation

Our blind test demonstrated that rover imaging instrumentation alone can, in many instances, make a reasonably comprehensive geological analysis of samples of limited size, such as the ExoMars 2020 core samples (3 x 1 cm). Accurate identifications were made for four of the tested samples, and many informative characteristics noted for two others. Two samples (17NZ14 and 11SP01) were inaccurately identified, although, even in these cases, informative observations were made. In all cases, confidence in interpretation was significantly increased when mineralogical data (Raman spectra) were added. Mineralogical data can

confirm interpretations based on optical imagery and, where petrographic mineral identification is ambiguous, add key information that allows the lithology to be characterised. The combination of HRC and CLUPI core images identified material properties (e.g., friability, hardness, cohesion) that inform lithological interpretation even in the absence of mineralogical data. In most cases, the combination of optical and mineralogical data led to an accurate estimation of the identity of the sample. Instrumental collaboration is therefore of fundamental and decisive importance in the success of the ExoMars 2020 mission (Figs. 2-3), since the mission is constrained by the small sample sizes inherent to its innovative approach. The interrelationship of rover instrumentation, and the possibility to ascertain consistency between observations during the panoramic, contact and analytical stages, will provide guidance and validation for all ExoMars 2020 findings (Vago et al., 2017). Such progressive learning has been key to the interpretation of samples taking into account the strengths and shortcomings of previous rover instrumentation suites (Mangold et al., 2017). In the case of ExoMars 2020 rover operations, petrographic studies using PanCam, HRC, ISEM, and CLUPI images in their panoramic and contact operating modes should guide the selection of samples for analytical study. Any indication of deleterious secondary alteration, for instance veining, fracturing, oxidation or other chemical weathering (even if misidentified as in the case of 11SP01), might constitute a case against further assessment of a potentially biosignature-bearing sample. Contextualising information at each sampling site by the ExoMars 2020 panoramic operations should be the primary safeguard against incorrect interpretation.

5.4. Strategies for geological appraisal of core samples

Our protocol involved a *checklist* of lithological characteristics (Tables 2-3), and largely achieved its goals by guiding the questioned geologists in their answers, however, a reluctance to offer additional comments on the samples in an open space on the response form meant that many sample-specific characteristics were ignored, for example grain morphologies indicating potential transport agents, and sedimentary observations beyond stratification. Since it is known that grain morphology can be an indicator of transportation mode (Williams et al., 2013; Kapui et al., 2018), and since this can be determined in medium-coarse sandstones at CLUPI resolutions (Fig. 3), such sedimentary characters may assist palaeoenvironmental reconstructions. Sedimentology has proven invaluable in the reconstruction of other Martian localities, most notably the varied deposits of Gale Crater (Grotzinger et al., 2014; Schieber et al., 2017; Banham et al., 2018) and across Meridiani Planum (Squyres et al., 2005; Grotzinger et al., 2005; McLennan et al., 2005). Although methods of calculating the probability of biosignature detection and biogenicity on Mars have been extensively proposed (Westall et al., 2015; Vago et al., 2017; Neveu et al., 2018), these methods usually do not explicitly characterise habitability in its geological context. Westall et al. (2015) considered the processes from origination to transportation in trajectories of biosignature evolution, a key parameter of which is the geological setting of the primary biosignature, defined by sedimentological and igneous characteristics that, during the ExoMars 2020 mission, will be evaluated. Vago et al. (2017) 'scored' aqueous and hydrothermal habitats within their biosignature calculator, the evidence for which will come from individual morphological and geochemical datapoints. The framework for biosignature plausibility, detection and proof must evidently encompass geospheric and potential biospheric notions, an approach considered in terms of the co-evolution of Martian habitats and biotopes by Westall et al. (2015) and Cabrol (2018).

In this blind test, surface geological context, i.e., whether the core sample is representative of the outcrop sample, was not considered. We therefore focussed on the critical importance of steps 3-5 in the ExoMars 2020-specific workflow shown in Figure 2. This represents a worst-case scenario for sample identification since, although this challenging situation is entirely possible on Mars, it is more likely that at least some informative guidance will be provided by surface lithology and characteristics of the landscape.

Our protocol explicitly requested that no speculative interpretation be made in the absence of data. Mineralogical data were generally able to overturn incorrect interpretations made based on imaging data alone, however, the combination of HRC and CLUPI core imaging, together with outcrop data gathered in the initial stages of mission experimental cycles, would likely place firm constraints on local geological conditions and suggest the likelihood of habitability. The progressive arrival of data from the panoramic, contact and analytical stages of ExoMars 2020 rover operations has many advantages. As shown in this blind test, increasing the amount of data available to scientists generally resulted in continually more accurate interpretations. From a geological standpoint, the progressive arrival of data closely aligns the process of interpretation with the traditional 'terrestrial' approach. Panoramic observations are approximately equivalent to the planning and preliminary stages of fieldwork in a new location. Contact operations reflect the main stage of fieldwork: outcrop examination and sampling. The analytical stage of operations is analogous to laboratory work when the field campaign is complete. We consider that the progressive arrival of data, although potentially demanding repeated reinterpretation, should not be considered as a negative aspect of the protocol, but rather an opportunity for the construction of hypotheses and their evaluation and modification in light of increasingly specific datasets.

6) Conclusions

In this contribution, we have sought to demonstrate and evaluate the challenges that will be faced in the interpretation of the 3 x 1 cm core samples exhumed by the ExoMars 2020 rover. Cores should be imaged by the PanCam HRC and CLUPI during the brief period before their ingestion and crushing within the body of the rover. Geological appraisals of these cores will provide fine-scale context information for potential organic signatures detected within. Core samples may not be representative of surface lithology and, in this worst-case scenario, accurate geological descriptions of core samples will be required to provide fine-scale characterisation for the petrological context of putative biosignatures. Our findings and recommendations are as follows:

- Detailed, accurate petrology – and by extension a potential estimate of habitability – is often possible using CLUPI and HRC images alone. Since different resolutions and scales of observation are encountered in HRC and CLUPI images, there are often opportunities to rectify misinterpretations based on scale-representativeness.
- Compositional data from the analytical laboratory instruments alone are not sufficient to characterise the petrogenesis and petrology of a rock; we therefore recommend that imaging cores using both HRC and CLUPI should form an integral part of the contact operations of the ExoMars rover and form a framework for the interpretation of analytical data. Furthermore, our results confirm the necessity of multi-scalar, multi-instrument

analyses during the rover mission and the opportunities for progressive learning that they permit.

- It is more challenging to determine petrological character from a core sample than from a hand sample or from direct outcrop data. Core sample interpretation has a number of shortcomings, which vary between rock types. Sample heterogeneity, distinguishing sub-centimetric to centimetric structures, and the unambiguous identification of biosignatures are amongst the challenges most often faced due to the limited information available in high-resolution images. Shape-relevant challenges to sample interpretation should be taken into account when conducting image analysis.
- Mineralogical (compositional) data improved confidence in, and accuracy of, petrogenetic interpretations, and a synergistic approach advocating the collaboration of the panoramic, contact and analytical onboard instrumentation will be essential to achieve the scientific goals of the mission.

Manuscript 2 – A sol in the life of the ExoMars 2020 "Rosalind Franklin" rover: distinguishing biosignatures, bio-indicators and abiotic matter using the Pasteur payload strategy

Abstract

The ExoMars 2020 rover "Rosalind Franklin" will be delivered to Mars by the landing module "Kazachok" at Oxia Planum in early March 2021. The rover has the objectives of understanding the geology and potential habitability of its landing site and distinguishing, if present, biosignatures of extinct or extant life, whether as bioconstructions or as molecules of unambiguous biogenic origin. When compared to previous rovers, *Rosalind Franklin* has the unique ability to exhume samples from up to 2 m depth for analysis, thus hopefully circumventing the issues of oxidative and radiative degradation that challenge sample analysis at the surface of Mars. In order to maximise the scientific return of the mission, it is necessary to i) calibrate the rover instrumentation using known samples of relevance to Martian geology, and ii) test the ability of the rover to identify the astrobiological potential of samples with characteristics that may mirror those of the landing site. In this contribution, we seek to conduct tests that challenge the latter objective. Using an ESA-NHM Mars analogue basalt as a compositional base, we constructed a suite of Mars analogue sediments by artificial sedimentation. Some of these samples were doped with artificially mineralised hyperthermophilic chemotrophic organisms considered candidates for potential Martian life under the assumption that surface habitability on Mars would have favoured polyextremophilic organisms in restricted niches. Other samples were doped with molecules (nucleobases, amino acids and sugars) of relevance to prebiotic chemistry. Some samples were doped with a mixture of the two in order to determine the potential for their distinction by rover instrumentation. A final set of samples were devoid of all biosignatures. Following the construction of these finely laminated sediments over the course of several months and the confirmation of their elemental and mineralogical relevance to presumably habitable Martian localities, they were prepared as sample of mission-relevant shapes, i.e., hand samples for PanCam and ISEM, core samples for HRC and CLUPI, cored hand samples for Ma_MISS, and powder for RLS, μOMEGA and MOMA. A suite of samples was sent to each instrument team in a blind test, and their interpretations were requested. These samples are the first set of astrobiologically relevant materials able to be tested under mission-specific conditions by a complete rover payload.

At the time of writing this chapter, the test is not yet complete. We present herein the synthesis and characterisation of the samples (using SEM and TEM), and their preparation for analysis by the instrument teams. At the time of writing, we have received very preliminary characterisation and interpretaton from ISEM, Ma_MISS, RLS and MOMA.

1. Introduction

1.1. ExoMars and habitability on the Noachian Mars

The ESA-Roscosmos ExoMars 2020 rover, named *Rosalind Franklin*, is expected to land on Oxia Planum – a potentially habitable Noachian terrane on Mars – in early March 2021. It will be delivered by the *Kazachok* landing module. Upon soft landing, the rover has the

objectives of characterising the geological context, habitability and potentially preserved biosignatures in the stratigraphy of Oxia Planum (Vago et al., 2017).

Oxia Planum, a phyllosilicate-rich region of Mars dating to the Noachian, has been determined to meet all necessary criteria for the landing site of the rover. Since habitability on the ancient Mars is likely to have been punctuated both spatially and temporally (Westall et al., 2015; Cabrol, 2018), the choice of landing site at the local scale is very important. First and foremost, it is scientifically compelling, comprising lithologies that evidence palaeo-hydrospheric activity and potential associated habitability (e.g., Quantin et al., 2016; Bishop et al., 2018; Quantin-Nataf et al., 2018, 2019) together with the potential for the preservation of biosignatures (e.g. Westall et al., 2015; Hays et al., 2017; Pan et al., 2019). Further to this, it has been adjudged safe for landing and surface operations and to conform to regulations on planetary protection, i.e., it is not a Mars special region. Oxia Planum meets the key criterion of being an ancient terrane (~4 Ga), dating to the period between the Noachian and Early Hesperian, during which the planet was shaped by an active hydrosphere (Quantin et al., 2016), and it exhibits abundant morphological and mineralogical evidence for widespread and continuous aqueous activity within outcrops throughout the region spanned by the ExoMars 2020 landing ellipse (Carter et al., 2013; Quantin-Nataf et al., 2018). The units comprising Oxia Planum are the Early to Late Noachian highland units, together with Hesperian transition units (Tanaka, 2014). This temporal longevity affords the potential for a larger and potentially evolved biosphere to have developed. The site also seems to have relatively limited dust coverage (Vago et al., 2017). The sediments of Oxia Planum were deposited during the period of Mars history in which the planet was most geodynamically active, and it is thus unequivocal that volcanogenic and pyroclastic material would have been a major input to the sediments (Vago et al., 2017), even if no obvious volcanic effusions are detected in the surrounding landscape (Pan et al., 2019).

The type of biosphere relevant to the Noachian Mars remains a subject of debate. In spite of extensive evidence for a diverse hydrosphere throughout Martian history (Malin and Edgett, 2003; Bhattacharya et al., 2005; Williams et al., 2013; Grotzinger et al., 2014; Butcher et al., 2017), the globality of the hydrosphere remains under question (Head et al., 2019, and references therein) and thus the potential for a globally connected biosphere as exists on Earth is similarly uncertain and probably unlikely. Most current research focusses on subsurface lithoautotrophic microbial ecosystems (e.g., Westall et al., 2013, 2015; Tarnas et al., 2018), especially since this is the only niche that could possibly have remained habitable after the early Hesperian (Boston et al., 1992; Michalski et al., 2013; Kite et al., 2019). Furthermore, since Mars would likely have received limited solar energy under the remote gaze of the Faint Young Sun (Sagan and Mullen, 1972), and since surface habitability may have degraded to inclement conditions within only 700 Ma (Jakosky et al., 2017), the widespread photosynthetic communities that dominated the Archaean (Tice and Lowe, 2006; Westall and Southam, 2006; Knoll et al., 2016) may not have developed during the approximately time-equivalent Noachian. Des Marais et al. (2008), considering that Martian habitability may have moved further into the subsurface over time and Cabrol (2018), raising the highly interesting concept of Martian ecotones, however, highlight that habitability is a spatially dynamic and evolving factor in a geological environment, and may have varied significantly over small lengthscales and timescales. If we conceptualise ecotones in temporal terms and assume that life is a possible consequence of habitability, it is likely that, in spite of ecophysiological challenges,

photosynthetic ecosystems were also a part of any Martian biosphere. This justifies the fact that they form the basis for much research into microstructural and compositional mapping of relevance to rover operations at the Martian surface (Allwood et al., 2015; Douglas et al., 2015; Kose et al., 2016; Tice et al., 2017; Williford et al., 2018), and that they rank highly in biosignature calculators (Vago et al., 2017).

Chemosynthetic biological communities tend to leave more subtle traces of their presence in the fossil record, and these putative biosignatures are often controversial (e.g., Rasmussen, 2000; Furnes et al., 2004; Banerjee et al., 2006). Nonetheless, since the fossilisation of their constituent carbonaceous material is made possible by the rapidly mineralising hydrothermal and geothermal systems with which they are usually associated (Jones and Renaut, 2004; Campbell et al., 2015), they remain critical targets for Martian astrobiology. Indeed, microbes of many metabolic affinities are shown to preserve well under rapid mineralisation, e.g. localised silicification (Schultze-Lam et al., 1995; Toporski et al., 2004; Orange et al., 2009) that may have analogue mineralising environments on Mars (Squyres et al., 2008; Ruff and Farmer, 2016; Michalski et al., 2017). Any organism, either at the surface or within the subsurface of Mars most likely had to be extremotolerant to multiple stressors (Cavalazzi et al., 2019), especially as the atmosphere-hydrosphere system was lost and habitability became increasingly restricted to minor, polyextremophilic niches (Fairén et al., 2010; Cockell, 2014; Vago et al., 2017). This again highlights the necessity to characterise, at at multiple scales both before and during any mission, the geological, mineralogical and geochemical characteristics of the chosen Martian study site.

1.2. Astrobiologically oriented samples designed to challenge the abilities of the ExoMars 2020 Pasteur payload

It is frequently stated that the perfect Mars analogue does not exist on Earth. Moreover, since the use of an analogue is highly dependent upon the questions asked of it for the experiment in which it is applied (Foucher et al., 2017), it is inevitable that most analogues, in spite of all best intentions in their selection, reflect considerable oversimplifications with respect to reality. In this study, we sought to produce and characterise Mars-analogue sediments with specific relevance to the geological and astrobiological objectives of the ExoMars 2020 mission. These samples, produced by artificial sedimentation and including organic material of both biological and abiotic origins, pose a number of challenges to the Pasteur payload instruments. Our experiment was designed to answer the following questions: i) to what degree of completeness can the Pasteur payload instruments identify the mineralogy (both major and accessory phases), macrostructure and microstructure of the samples?; ii) at what stage of the exploration protocol, i.e., contact or analytical stage, can the payload make a first detection of carbonaceous material of putative biological origin, and can its occurrence be tied to the microstratigraphy of the sample?; iii) can the payload distinguish between biological and abiotic (magmatic or extraterrestrial, where present) carbonaceous material?; iv) what combination of measurements is necessary for the characterisation of the occurrence, nature and organic geochemistry of biosignatures in Mars analogue sediments?

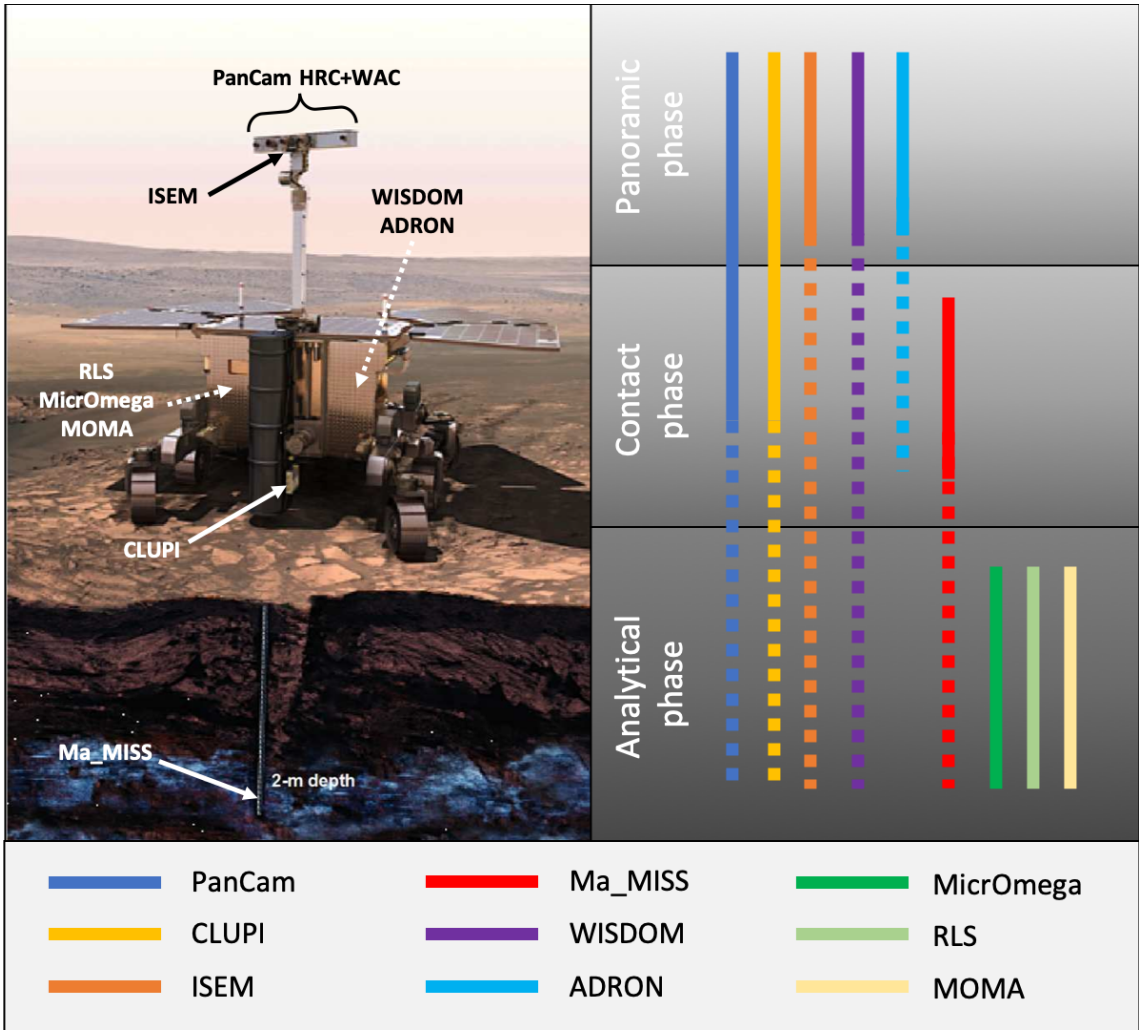

Fig. 1. The highly interconnected instrumental suite aboard the ExoMars 2020 *Rosalind Franklin* rover. The locations of the instruments on the rover are indicated, and their roles throughout the scientific protocol of ExoMars 2020 (see Vago et al., 2017; Hickman-Lewis et al., in revision) are shown. Solid lines indicate that the instrument is directly used at the corresponding stage of analysis; dotted lines indicate that the results obtained by the instrument are crucial in governing the process of analysis at a subsequent phase of analysis.

1.3. Studying unknown samples by the ExoMars scientific workflow

Vago et al. (2017) described the protocol for landing site exploration using the Rosalind Franklin rover, which consists of three phases: the panoramic phase includes characterisation of outcrops and the surrounding landscape at low resolution and provides preliminary stratigraphic, textural and compositional appraisals that guide all subsequent steps; the contact phase characterises outcrops and exhumed core samples at high resolutions and provides the first measurements of micro-scale stratigraphy and compositional variation, in addition to detecting morphologically identifiable putative biosignatures; the analytical phase uses crushed samples to determine the nature and organic (bio)chemistry of carbonaceous material, molecules and individual mineral phases (see Fig. 1). As noted in the scientific workflow for the *Rosalind Franklin* rover described in Hickman-Lewis et al. (in revision), this three-step protocol has similarities and differences to the standard geological fieldwork approaches used on Earth. The key difference is the limitation imposed by reduced sample volume and fixed sample shape, usually requiring correlation and corroboration between the results of multiple

instruments to confirm the consistency of interpretations and rectify potential mistaken conclusions (Hickman-Lewis et al., 2018). A further challenge that, to the best of our knowledge, has yet to be simulated in scientifically motivated blind tests, is the use of exclusively instrument-specific sample preparation for each tested part of the payload. This has been incorporated into the test described herein: hand samples of our Mars-analogue sediments were prepared for PanCam and ISEM, core samples for PanCam and CLUPI, cored hand samples to simulate the drilled borehole for Ma_MISS, and powders for RLS, μOMEGA and MOMA. During missions, data arrives progressively (Mangold et al., 2017), but fully refined data and complete interpretations from the previous stage may not be available at the time of data acquisition during the subsequent stage due to transmission limitations (both in terms of scheduling and duration, and in terms of volume). As such, we asked the instrument teams to make a first interpretation of their measurements in the absence of the interpretations of the other instrument teams before making any final refinements using all available data. The progressive amelioration of interpretations should not be restricted to the period of data acquisition, however, but be continually revisited by calibration exercises and laboratory experimentation throughout and after the mission.

2. Materials and Methods

2.1. Composition of artificial sediments

We selected a sample from the ESA-NHM Collection (ESA01-E; County Antrim, Northern Ireland) as the basis for our artificial sediments. This material, considered by ESA to be suitable bulk Mars analogue for instrumental testing, is an olivine-bearing, low-SiO_2 basanite-basalt (~tholeiite, cf. McSween et al., 2009) with high Fe and Mg content and is thus highly representative of igneous rocks previously identified at Gusev and Gale craters and Meridiani Planum (Rogers and Aharonson, 2008; Vaniman et al., 2014; Buz et al., 2017). ICP-MS analyses of ESA01-E determined that it contained 44.18% SiO_2, 16.03% Al_2O_3, 14.46% Fe_2O_3, 0.19% MnO, 7.71% MgO, 8.72% CaO, 2.75% Na_2O, 0.18% K_2O and 1.66% TiO_2. Relative to most terrestrial basalts, with the exception of komatiites and boninites, this basalt is very rich in Fe and Mg. Although some evidence for evolved igneous compositions have been identified on Mars, amongst which are high-Si andesites, dacites and trachytes, mafic basalts are an accurate bulk representation of the average mineralogy across much of the Martian surface, particularly the Noachian terranes (Bandfield et al., 2000; McSween et al., 2009; McSween, 2015). The elemental composition is therefore appropriate for inclusion in artificial volcanogenic Martian sediments.

2.1.1. Optical microscopy, SEM-EDS and TEM characterisation

The ESA01-E basalt was prepared both as a thin section for optical microscopy observation and as granules of various size fractions (< 100 μm, 100-250 μm and > 250 μm) for granulometric and compositional characterisation using SEM-EDS. Optical microscopy was conducted using an Olympus BX-51 microscope equipped with a CCD camera (CNRS-CBM, Orléans). SEM was conducted using a Hitachi S-4500 instrument equipped with an Oxford Instruments 6853 EDS unit.

Artificially fossilised cellular material was studied by optical microscopy (Gram-stained sections) and by TEM. Samples were prepared for TEM as 80-100 nm ultramicrotome-

cut resin-fixed slices and observed using a Philips CM20 instrument. Uranyl acetate was added during preparation to render the biological material visible in brightfield observation.

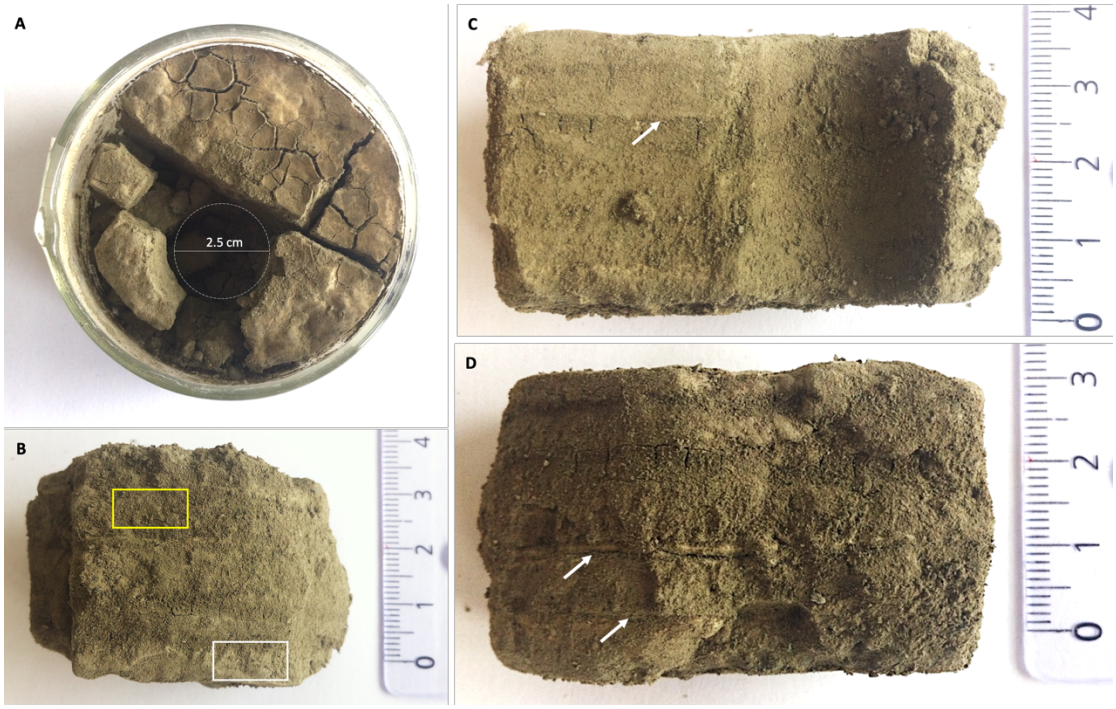

Fig. 2. Artificial Martian sediments. **A**) Sample from which a core of 2.5 cm diameter (identical to ExoMars 2020 drilling conditions) has been extracted. **B**) Fragment of layered Mars analogue sediment showing coarser (yellow box) and finer (white box) layers. **C-D**) Fragment of sediment sample with fine, clay-rich layers (white arrows). In C, a core has been taken from the right hand side; note that layering can still be detecting within the 'borehole'.

2.1.2. Additional phases for astrobiological relevance

Although the sample ESA01-E meets many requirements for a Mars analogue sediment, preliminary optical observations showed that it was limited in clay mineral composition relative to most Martian sedimentary sequences. Montmorillonite, one of the most common clay minerals at the Martian surface (Clark et al., 2007), and of high significance to astrobiology (Craig et al., 2017), was added in varying quantity from 20-70 wt% in certain layers of the synthesised samples (Fig. 2).

Finally, in order to test the payload potential for the identification of biosignatures and molecules relevant to prebiotic chemistry, a range of organics were added to several of the samples. Artificially mineralised *Geobacillus stearothermophilus* and *Methanocaldococcus jannaschii*, two thermophilic, extremotolerant organisms favouring excellent preservation of cellular structure in the case of *Geobacillus* and abundant cell-related EPS in the case of *Methanocaldococcus* (Orange et al., 2009, 2011), were chosen as the added biomass. Molecules of relevance to prebiotic chemistry (see Dass et al., 2016) and the origin of primitive metabolisms were chosen as chemical biosignatures, specifically the sugars ribose and glucose, the amino acids alanine, tryptophan, glycine, cysteine, histidine and aspartic acid, and the nucleobases uracil and adenine. Glucose and ribose were selected for their potential as energy sources for multiple metabolic pathways, and for the role of the latter in the structure of RNA. The nucleobases uracil and adenine are N-containing compounds, respectively a pyramidine and a purine, and are associated in RNA. The selection of amino acids includes an apolar

aliphatic hydrophobe (alanine), a non-polar aromatic hydrophobe (tryptophan), the sole achiral hydrophile (glycine), a hydrophile with an organosulphur side chain (cysteine), and positively and negatively charged polar compounds (histidine and aspartic acid, respectively).

2.2. Synthesis and preparation of artificial sediments

Artificial sediments were synthesised in 10 cm diameter by 5 cm depth sterilised glass cylindrical vessels (Fig. 2A). For each sedimentary layer, a mixture of ground ESA01-E basalt and montmorillonite was added together with Si-enriched (6.95 g/L) fluid to ensure cementation. The mixture was allowed to settle and the excess fluid was permitted to evaporate under gentle heating (< 50˚C) for two days. When dry, but before desiccation, the next layer was added following the same procedure. Certain layers were doped with the organic material described above. Chemical biosignatures were added in quantities of 10 mL per layer at concentrations of 1 mM/L in order to ensure their detectability by laboratory and rover instrumentation (T. Georgelin, personal communication, 2019). The artificial sedimentation procedure was continued until the samples had reached a height of between 4-5 cm (Fig. 2), i.e., of a scale relevant to the analyses of PanCam and ISEM, the instruments playing a key role in the panoramic phase of operations. Four samples were prepared: a control sample with no added organic matter (sample 1), a sample with molecules of prebiotic relevance (sample 2), a sample with artificially fossilised microbes (sample 3), and a sample with mixed molecules and microbes (sample 4).

When the samples had dried, they were apportioned according to the requirements of the payload instrumentation: the whole samples were used for characterisation by PanCam and ISEM, core samples of approximately 3 x 1 cm were extracted from the whole samples for analysis by CLUPI and HRC (see Fig. 2A), and powdered samples with a median grain size of 250 μm (equivalent to mission conditions; Vago et al., 2017) were prepared for each of the analytical laboratory instruments.

Our approach therefore presents the first wholly mission-representative test of the ExoMars 2020 rover payload. We have taken into consideration both the analogy of the samples with expected lithologies at Oxia Planum and the sample morphologies that will be available during the mission due to the unique drilling and crushing process of the rover.

3. Results

3.1. Fundamental geological and biosignature characterisation

The mineralogical and petrological characteristics of the ESA01-E basalt were determined using optical microscopy and SEM-EDS. In thin section, the basalt is porphyritic, with mostly plagioclase and some olivine (forsterite) phenocrysts within an aphanitic pyroxene-plagioclase groundmass. Rare, equant, opaque crystals are evidence of oxide phases. SEM-EDS measurements on individual particles confirmed this petrographic characterisation. Four dominant phases were observed, namely plagioclase feldspar, pyroxene, olivine and aluminous phyllosilicates (smectites). Plagioclase ranged mostly from oligoclase (10-30% Ca) to bytownite (70-90% Ca), with labradorite being the most common composition (Fig. 3A). Pyroxenes plotted mostly within augite-pigeonite compositions, although Al-containing pyroxenes exhibited compositions between aegirine-augite and omphacite, i.e. there are both Mg-Fe-Ca and Al-Ca-Na pyroxenes (Fig. 3B-C). Olivine was forsteritic in composition (Mg >

Fe). Aluminosilicates were present throughout all size fractions. In addition to these materials, titanomagnetite and alkali feldspar (anorthose) were found in minor quantities as accessory phases.

Artificially fossilised microbes, both *Geobacillus stearothermophilus* and *Methanocaldococcus jannaschii*, were preliminarily studied by optical microscopy and found to have a sufficiently high cell count for detection (several hundred cells per mL). Using TEM, it was observed that the fossilisation process had resulted in the silicification of the cellular material such that identifiable organic fragments were preserved (Fig. 4).

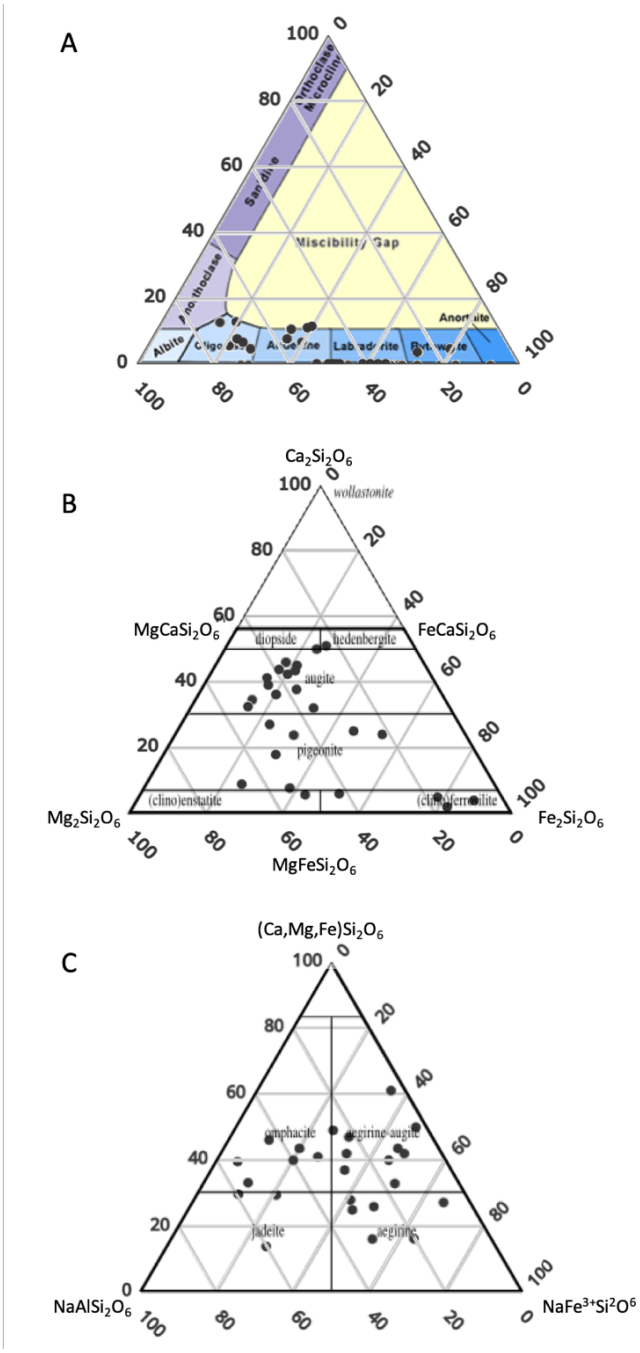

Fig. 3. SEM-EDS mineralogical analyses of feldspar and pyroxene grains identified. Feldspars were dominantly laboradorite, but ranged in composition from oligoclase (10-30% Ca) to bytownite (70-90% Ca). Pyroxenes plotted mostly within augite-pigeonite compositions, with less common aegirine-augite and omphacite phases.

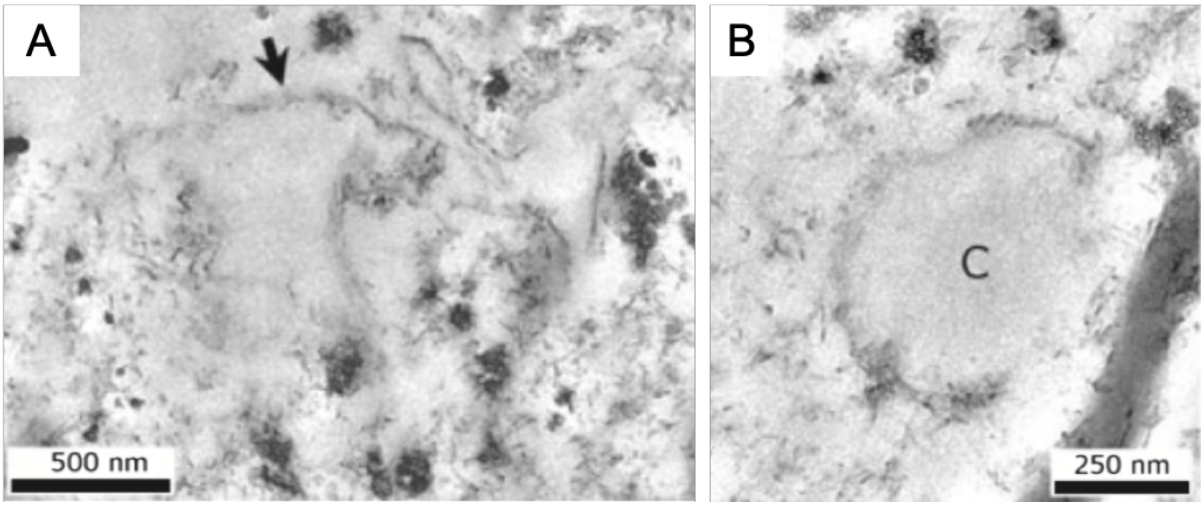

Fig. 4. Characterisation of Methanocaldococcus jannaschii cells and associated EPS after long-term fossiliaation (1 year) in a 500 ppm silica solution, i.e., a selection of the organisms included in these samples. **A**) Delicate relics of cells (arrowed) and fibrous remains ascribed to EPS. **B**) Significantly deformed cell (indicated as C) surrounded by fibrous material.

3.2. Characterisation by the Rosalind Franklin payload instrumentation

3.2.1. ISEM

Four hand samples were analysed using the ISEM science simulator at the Space Research Institute of the Russian Academy of Sciences, Moscow (Korablev et al., 2017). Spectra were smoothed and multiplied by five on the y-axis for clarity and features were identified (Fig. 5) for comparison with the CRISM (Compact Reconnaissance Imaging Spectrometer for Mars) spectral library (Viviano-Beck et al., 2014). Comparisons shown are against the spectra of phyllosilicates, carbonates and sulphates from the CRISM library (Fig. 6). Montmorillonite, kaolinite, calcite, siderite and gypsum were identified in sample 1. Montmorillonite, alunite, calcite, dolomite and siderite were identified in sample 2. Only montmorillonite, jarosite (~ alunite) and gypsum were delineated in sample 3. Montmorillonite, jarosite, gypsum and calcite were identified in sample 4. The carbonates may have precipitated during the drying process, although all other identifications were consistent with expectations.

3.2.2. Ma_MISS

Four hand samples were analysed using the Ma_MISS breadboard at the Istituto di Astrofisica e Planetologia Spaziali, Rome. Unlike the Ma_MISS flight model, the breadboard does not image the borehole itself, and therefore a cut sample was prepared for analysis (Fig. 7A-B). All other experimental parameters were mission-specific (De Sanctis et al., 2017).

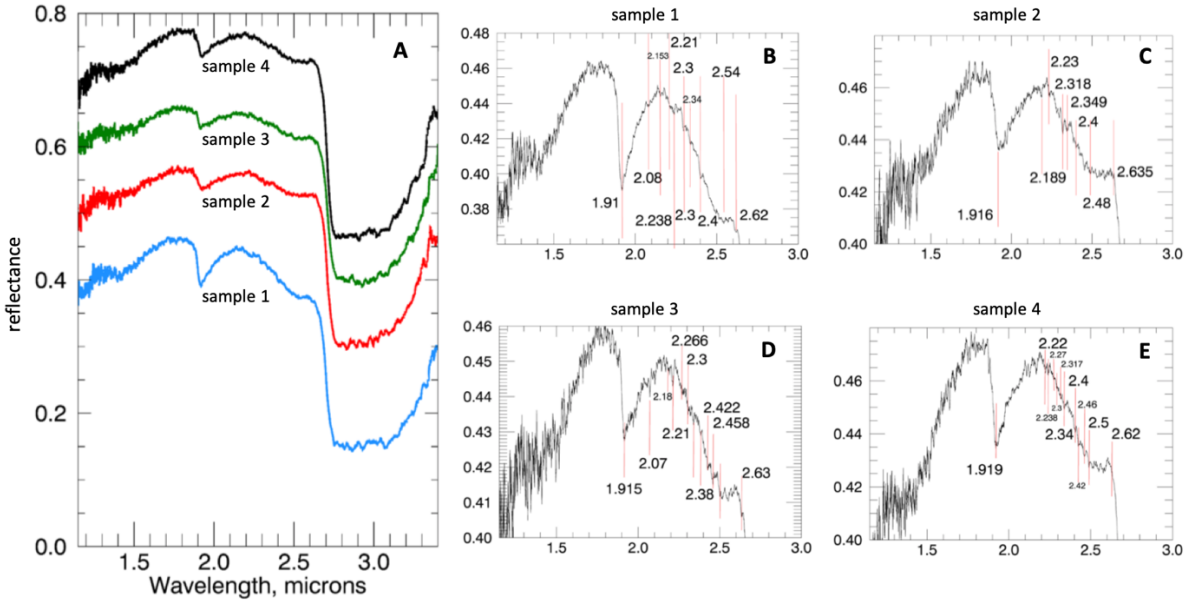

Fig. 5. ISEM spectral acquisitions. **A**) Comparison of the four spectra obtained. **B-D**) Details of each spectra with prominent spectral features identified from which mineral identifications were made (compare with CRISM library spectra in Figure 6).

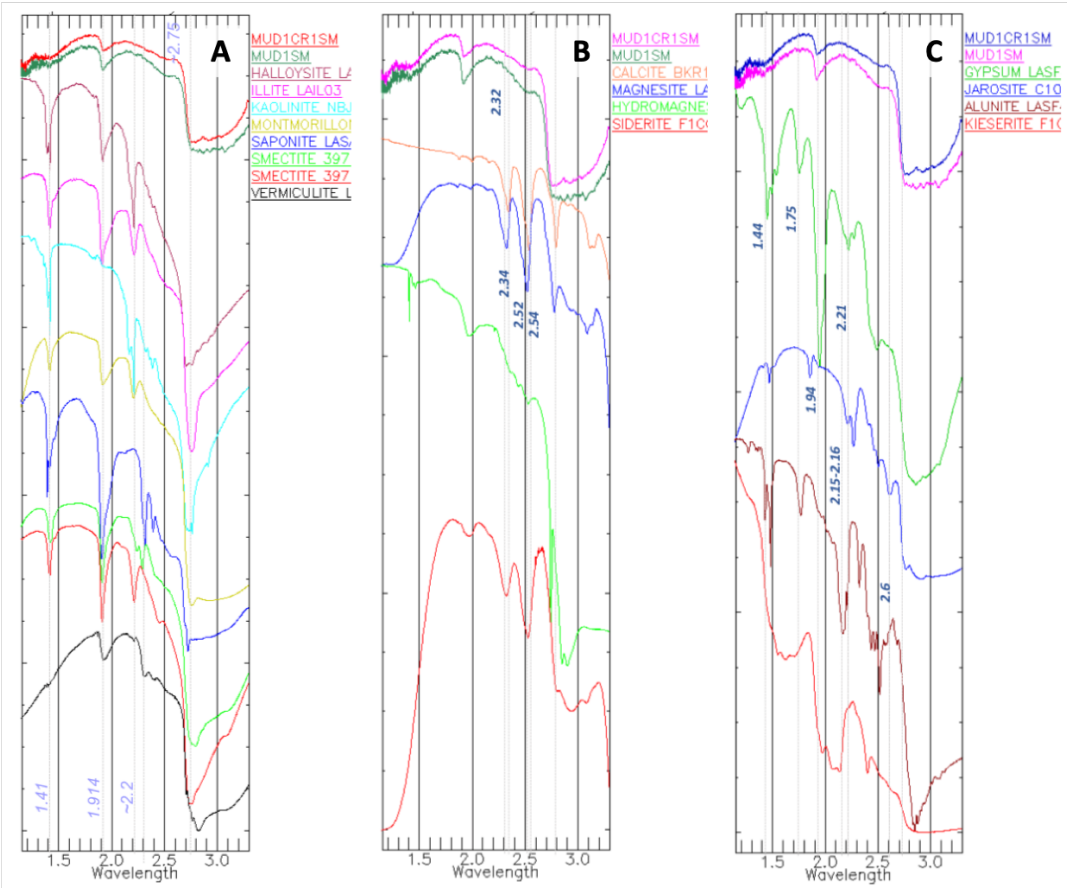

Fig. 6. Comparison of ISEM spectra (raw, MUD1CRISM; smoothed, MUD1SM) with selected CRISM spectra for phyllosilicates (A), carbonates (B) and sulphates (C). Results for sample 1 shown.

The Ma_MISS breadboard is equipped with an ASD FieldSpec 4 operated at a spectral range between 0.5 and 2.3 µm, i.e., identical to the flight model. 48 spectra were acquired through the stratigraphy of the sample with a step of 0.5 mm (Fig. 7C). Layers within the sample were distinghuished visually and end-member spectra were obtained for each (Fig. 7D). Spectral types determined from these end-members are given in Figure 7. Although further analyses are required, clear hydration bands at 1.4 and 1.9 µm were identified in layers B and D (montmorillonite-rich), and a single hydration band at 1.9 µm was noted in layers C and E (plagioclase-rich). Further spectral features at 1.7 and 2.1-2.2 µm were identified in layer D. Layers A, B, F and G exhibited variably strong 0.7 µm features attributed to Fe^{3+}, i.e., haematite or magnetite.

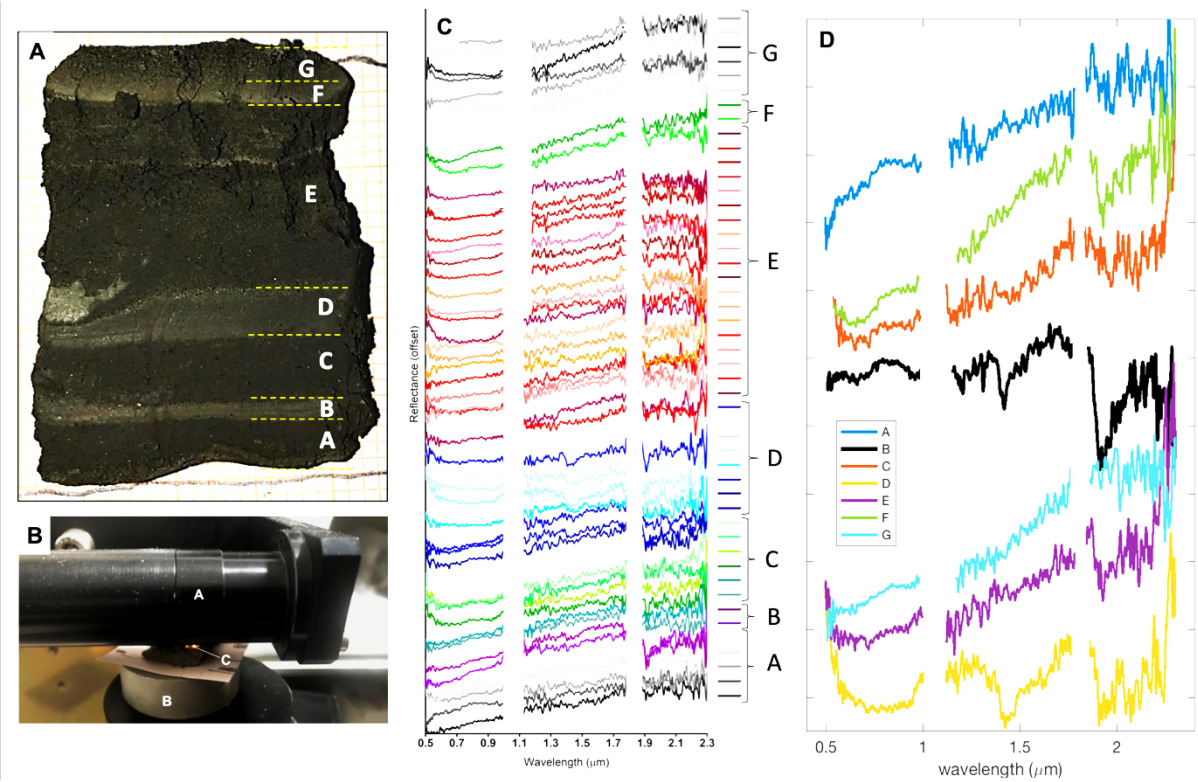

Fig. 7. Ma_MISS spectral acquisition. **A**) Cut sample showing designation of layering. **B**) Ma_MISS breadboard setup showing the Ma_MISS tip (A), the sample holder containing sample 1 (B), and the illumination spot focussed on sample 1. **C**) All spectra obtained, assigned to layers in the sample. **D**) End-member spectra for each layer, derived from the spectra in C.

3.2.3. *RLS*

Four powdered samples were analysed using the RLS science simulator at the Department of Condensed Matter Physics, Crystallography and Mineralogy, Universidad de Valladolid. The procedure was fully automatic following the operation methodology that the RLS flght model will use in Mars during ExoMars sample analysis operations (Rull et al., 2017). Up to 39 points were observed at regular intervals at the surface of the powder of each sample using a 50 µm spot and a laser power of ~17 mW. Autofocus and automatic spectral acquisition parameters (integration time and number of accumulations) were used. Manual spectra were also obtained for particular grains in order to confirm mineral identification performed on the basis of the automatic simulator results.

Raman spectra obtained on sample 1 (Fig. 8) show that the mineralogy is dominated by plagioclase (Pg) with some olivine (O), pyroxene (Px), calcite (Ca), haematite, and probably amorphous carbonaceous material (C), mostly corresponding to the G-band. Additional analysis is required to characterise the carbonaceous material. The majority of plagioclase spectra could be compositionally constrained to labradorite (example spectra given in Fig. 8B), although anorthite and bytownite were also present in some spots. Most pyroxene spectra aligned most closely with augite. Olivine was forsteritic in composition and often associated with haematite, identified by a 1310 cm^{-1} band (e.g., Fig. 8C). Bands at 1310 and 1570 cm^{-1} cannot therefore be entirely explained as carbonaceous material, since a strong contribution from haematite is present in the former. Phyllosilicates were also identified, and tentatively interpreted as trioctahedral, potentially montmorillonite.

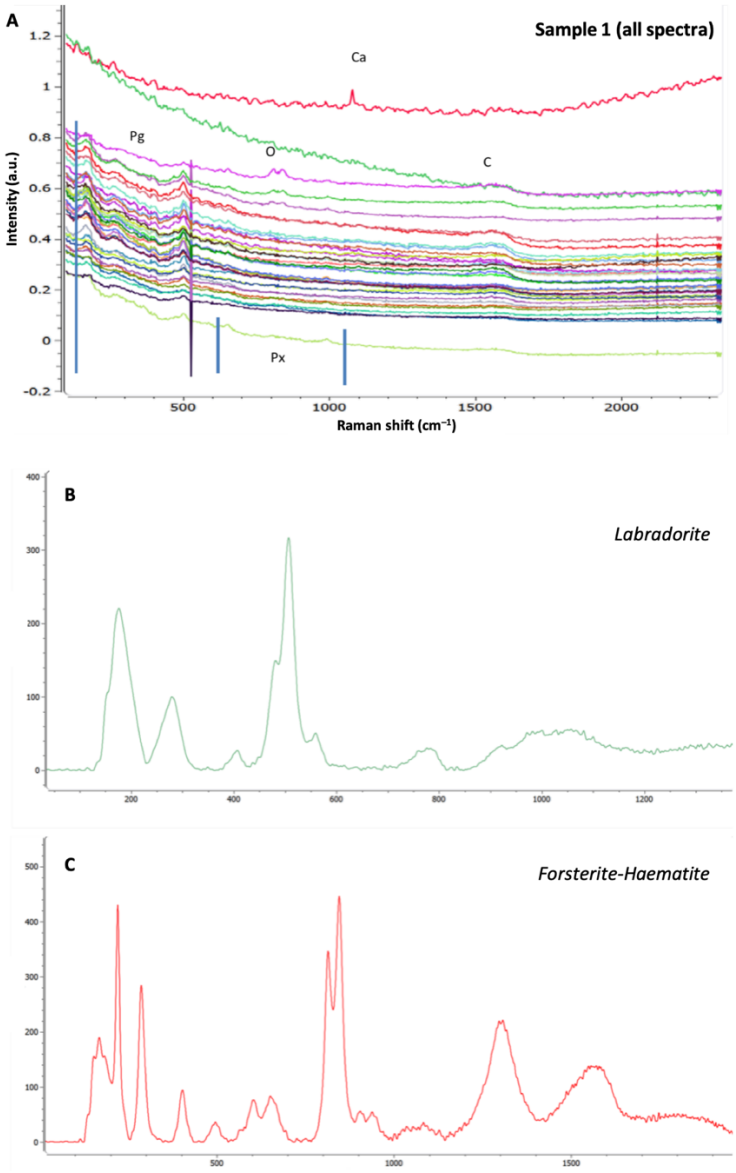

Fig. 8. RLS characterisation of sample 1. **A**) All spectra obtained using the automatic procedure. **B**) Extracted spectra corresponding to labradorite, the dominant mineral phase. **C**) Spectra corresponding to forsterite and haematite potentially associated with carbonaceous material.

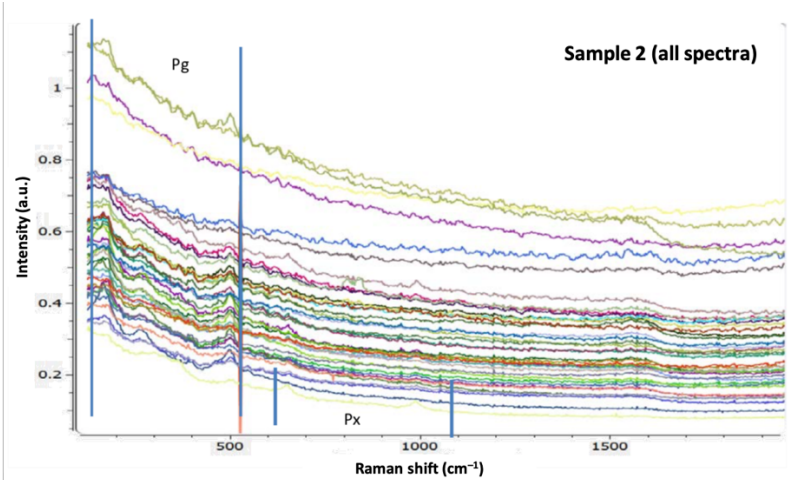

Fig. 9. All RLS spectra obtained for sample 2.

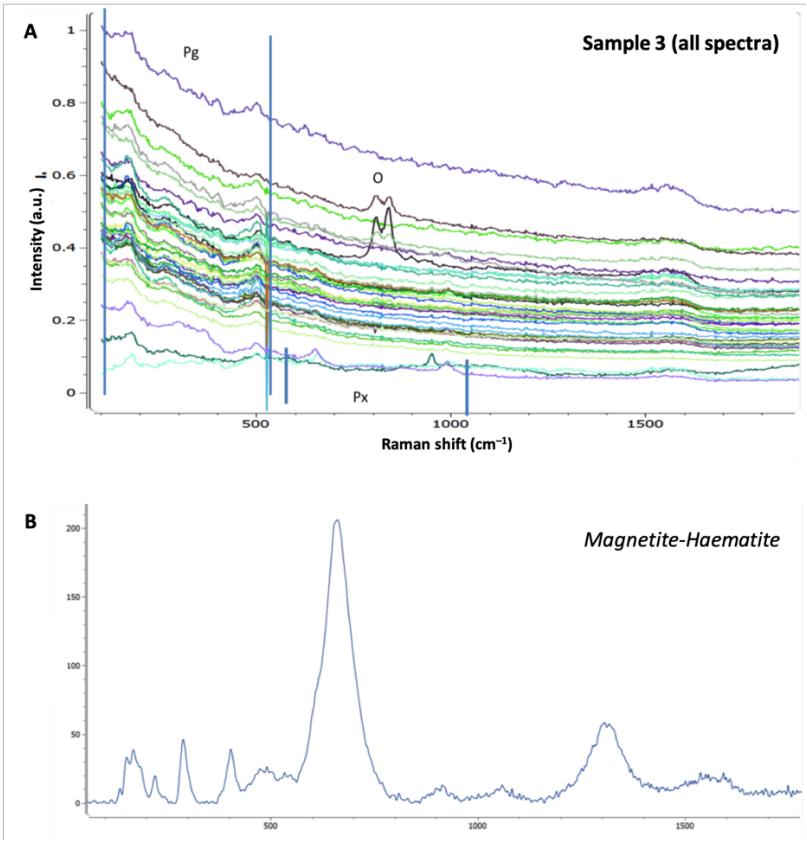

Fig. 10. RLS characterisation of sample 3. **A**) All spectra obtained using the automatic procedure. **B**) Extracted spectra corresponding to magnetite and haematite.

In sample 2, a similar bulk mineralogy was identified, in which phyllosilicates and pyroxenes were strongly spatially correlated (Fig. 9). Since calcite was not identified, the broad spectral feature around 1570 cm^{-1} was attributed to the G-band of carbonaceous material.

Sample 3 showed a similar bulk mineralogy (Fig. 10A), although small shifts in the pyroxene doublet imply modification to pyroxene composition. Plagioclase ranges in composition from andesine to bytownite (30-90 An%). Forsterite is again present, although in

this case it is not associated with haematite, which is instead found to occur spatially with magnetite (Fig. 10B). Apatite, calcite and amorphous carbon were also detected.

Sample 4 showed a similar bulk mineralogy, again with variations in plagioclase and pyroxene chemistry (Fig. 11). In this sample, magnetite, haematite and carbonaceous material were shown to co-occur. Carbonaceous material exhibited both D- and G-bands.

Ongoing detailed studies will seek to clarify ambiguous mineralogical detections and more fully characterise the carbonaceous material. This further study comprises a methodology based on fitting the bands of the primary identified phases, intensity normalisation and subtraction of the fitted spectrum, and further analysis of the remaining spectral features over several iterations until the whole spectrum is assigned.

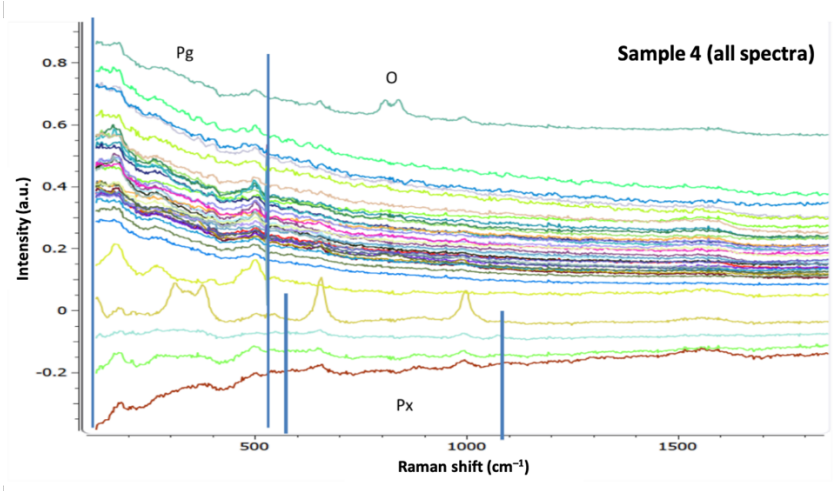

Fig. 11. All RLS spectra obtained for sample 2.

3.2.4. MOMA

Partial MOMA analyses were conducted: Laser Desorption Mass Spectrometry (LDMS; Fig. 12) mode to provide an initial indication of higher-molecular-weight (hundreds of atomic mass units) nonvolatile organics, and pyrolysis Gas Chromatography–Mass Spectrometry (GC-MS; Fig. 13). LDMS analyses were conducted at the NASA Goddard Space Flight Center, Maryland using a MOMA flight analogue system simulator. GC-MS was conducted at the Max-Planck-Institut für Sonnensystemforschung, Göttingen, using a MOMA flight analog system (Goesmann et al., 2017) consisting of a MOMA oven, manually operated tapping station and an adsorption trap (filled with Tenax® GR). The the flight analogue system used was connected to a commercial gas chromatograph–mass spectrometer (GC-MS; Varian CP-3800 GC, Varian 240-MS/4000MS). During analysis, the oven was heated to 700 °C (held for 10 s), the trap to 160°C. FAS transfer line temperatures were no higher than 110°C. GC parameters were as follows: Varian factor Four VF-5ms column (30 m length, 0.25 mm inner diameter, 0.25µm film thickness); helium flow rate = 2 mL/min; injector T = 250°C; GC T-program started at 30°C (held for 1 min) and heated to 250°C (held for 5 min; heating rate 10 °C/min). MS parameters were as follows: full-scan mode (scan range of m/z 35 to 1000), scan time = 0.58 s, internal ionisation (filament on after 1 min). Around 10 mg of sample material, respectively, were pyrolysed (11.33 mg of sample 1, 13.55 mg of sample 2, 10.53 mg of sample 3, 11.33 mg of sample 4). Blank runs were performed before each pyrolysis and the system

was regularly cleaned afterwards. An analytical standard (n-octadecane, 100 ng) was used to estimate compound concentrations. Four samples were observed, and no obvious compositional differences were observed.

In LDMS results (sample 1 shown; Fig. 12A), a clear series of peaks was observed. Peaks at 189, 245, 301 (the strongest peak in the spectra), 357 and 413 showed a spacing of Δm (mass difference) of 56, which may be ascribed to CaO. Other peaks with Δm=16 correspond to O addition or loss, and the peak at ~189 shows involvement of water in the cluster. Comparison with a natural sample (Cretaceous pillow lava from Biscay Province, Spain; Fig. 12B) similar peaks were deemed to arise from calcite, quartz, anatase, chlorite and kaolinite, thus these new LDMS data may be linked to CaO-related clusters from calcite.

Pyrolysis of samples 1–4 released (alkyl) benzenes, (alkyl) naphthalenes, benzonitrile, short-chain n-alkenes (*n*-$C_{5:1–8:1}$), medium-chain n-alkenes (*n*-$C_{14:1–16:1}$) and medium-chain *n*-alkanes (*n*-$C_{14–17}$) (Fig. 13). Although all four samples contained the same compounds, the absolute amounts varied between the samples (e.g., benzene varies between 16.5 and 37.7 µg/g sample; Table 1). Reduced concentrations of carbon-bearing molecules in sample 3 is consistent with expectations, since this sample contains only mineralised bacteria with limited preservation of carbonaceous material. Blanks did not contain any compounds released during pyrolysis of samples 1–4. Although (alkyl) benzenes, (alkyl) naphthalenes and short-chain *n*-alkenes may be artificially produced by pyrosynthesis reactions, n-alkene/n-alkane homologues (medium-chain in the samples) may indicate the pyrolysis of sample-indigenous macromolecular organic matter. The decrease in abundance from *n*-C_{14} to *n*-C_{17} may be explained by condensation effects caused by the maximum temperatures of the system trap and transfer lines (160 and 110°C, respectively). These temperatures are too low to mobilise molecules with higher boiling points (Reinhardt et al., accepted).

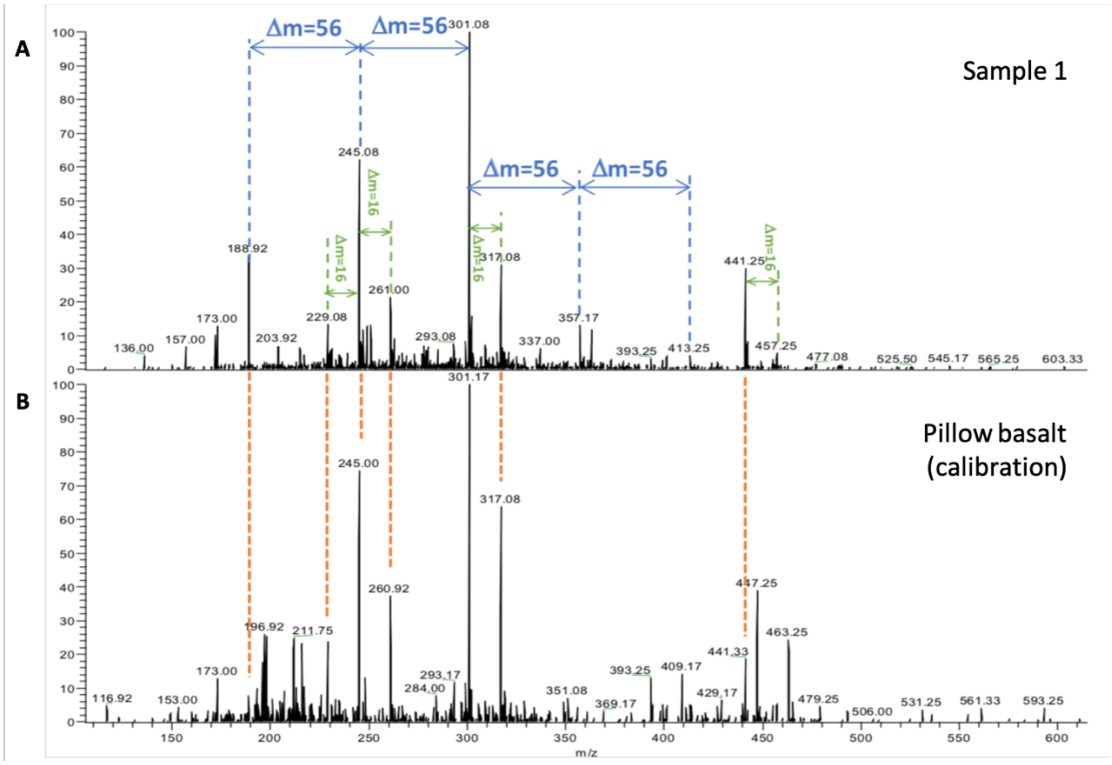

Fig. 12. Results of LDMS analyses of sample 1 compared with a pre-characterised Cretaceous igneous sample.

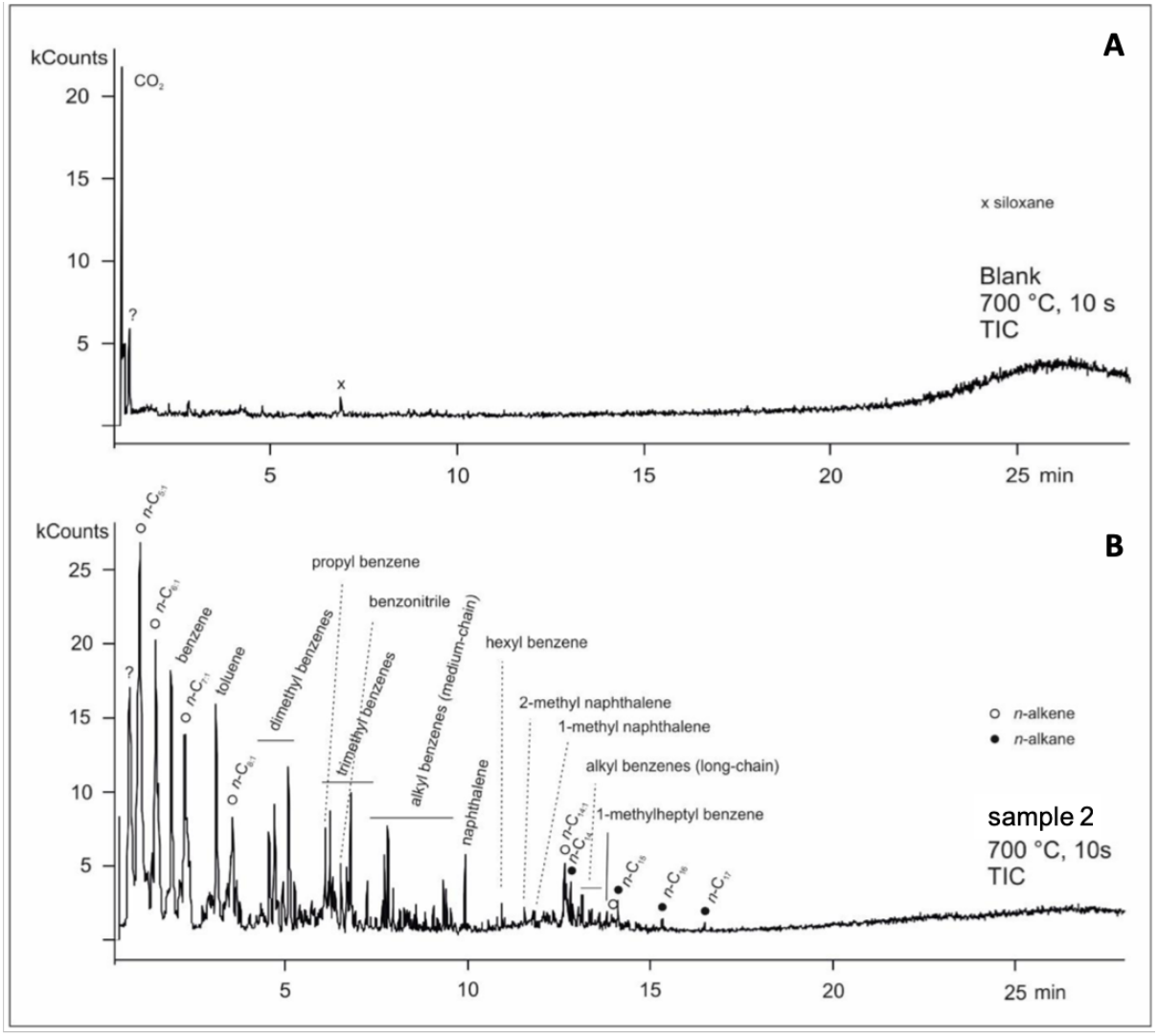

	n-$C_{5:1}$	benzene	toluene	Na	2-Me Na	1-Me Na	*n*-$C_{14:1}$	*n*-C_{14}
1 (control)	84.2	37.7	32.2	5.0	0.6	0.4	1.1	1.3
2 (molecules)	43.2	23.5	21.4	3.9	1.3	0.6	2.8	2.5
3 (bacteria)	13.4	16.5	9.0	2.5	0.7	0.3	1.1	0.6
4 (both OMs)	31.4	23.4	15.2	3.0	0.4	0.4	0.7	1.3

Me = methyl, Na = naphthalene

Fig. 13. Gas chromatograms (total ion currents, TICs) from MOMA emulator pyrolysis GC-MS at 700°C (10 s) of a blank (A) and sample 2 (B). The blank shows CO_2, a siloxane and an unknown (?) component. Sample 2 contains various (alkyl) benzenes, (alkyl) naphthalenes, short- and medium-chain *n*-alkenes, as well as medium-chain *n*-alkanes.

4. Conclusions

At the time of writing this chapter, we have yet to receive all of the results of the analyses of the artificial samples from the instrument teams. At present the following conclusions and perspectives can be made:

- We have synthesised the first astrobiologically relevant samples to be tested by a complete rover payload. Understanding the interrelationships of the data provided by each of the rover instruments, together with the combinations of data required to make accurate interpretations of both the geology and organic geochemistry of these samples, should be highly illuminating for mission protocols.
- The ESA01-E basalt was an excellent choice for Mars analogy, both in terms of elemental composition and mineralogy. It matches the volcanogenic material determined in many Noachian-Hesperian Martian terranes, including Arabia Terra and Meridiani Planum. The addition of clay minerals has made the sample a more suitable analogue for the phyllosilicate-rich lithologies of Oxia Planum that are of interest the ExoMars 2020 mission.
- The results thus far obtained from the instrument teams (ISEM, Ma_MISS, RLS, MOMA) show that the bulk mineralogy of the samples is accurately determined by the payload instrumentation, although phyllosilicates and carbonaceous material detected by RLS and MOMA, i.e., the two phases of highest astrobiological importance, require further detailed characterisation that has yet to be performed. Nonetheless, the detection of carbonaceous material at low concentration in these samples is highly encouraging.
- Differences in the concentrations of carbon-bearing molecules detected by the MOMA GC-MS emulator are consistent with expectations according to the astrobiologically relevant material added: reduced concentrations were present in sample 3 relative to sample 2. The origin of the high concentrations of carbon-bearing molecules in sample 1 (the control) remains unclear at this time.

Chapter V – Concluding Remarks and Perspectives

The objectives of this thesis were the application of multi-scalar, multi-modal approaches in instrumentation and methodology to the study of some of the earliest traces of life on Earth, and the integration of these approaches into the search for life on Mars. A range of samples, mostly from the chert horizons of the Barberton greenstone belt, were studied in terms of their petrography, petrology, morphology and inorganic and organic geochemistry. It was found that this approach provided a network of evidence and a nested combinatorial analytical framework within which considerable interpretation and, indeed, re-interpretation of the co-evolution of life and the palaeoenvironment in Early Archaean sediments was possible. Nonetheless, deducing Early Archaean palaeobiology remains contentious and open to ambiguity without the use of high-resolution correlative microscopy and biogeochemistry. In relation to the second axis of the thesis – the search for life on Mars – it appears that while the identification of samples with high fossiliferous potential and well-preserved biosynthetic indicators is possible using ExoMars 2020 rover instrumentation, the study of less well-preserved samples within their geological contexts at biome and ecosystem scales may demand Mars Sample Return.

Chapter II, Manuscript I provided an up-to-date review of potential traces of life in the Barberton greenstone belt, finding that well-described biosignatures were concentrated in chertified volcaniclastic horizons throughout the Onverwacht Group and silicified sandstones throughout the Moodies Group. In the Palaeoarchaean Onverwacht Group, particularly diverse biosignatures have been noted in the 3.42 Ga Buck Reef Chert and the 3.33 Ga Josefsdal Chert, both of which are interpreted as hydrothermally influenced marine settings. The totality of biosignatures in the Barberton region is comparable to that of the East Pilbara, implying that both terranes reflect a time by which life was already metabolically and ecologically diverse.

In Chapter II, Manuscript II, the oldest traces of life in the Barberton greenstone belt were described: microbial mats and their associated features from the 3.472 Ga Middle Marker horizon. Several morphologies of microbial mats were identified, included undulating, flat-laminated mats and crinkly mats featuring locally micro-tufted topographies. The mats were found to meet many biogenicity criteria: i) they are formed of wavy to crinkly kerogenous lamina sets that are continuous on the centimetre scale but discontinuous on the sub-millimetre scale; ii) they alternate between layers of film- or filament-like organic material with syndepositional sediment layers as in modern microbial mats; iii) deformed and torn structures demonstrably indigenous to the mats indicate their originally plastic and cohesive nature; iv) they mantle primary sedimentary structures, but are non-isopachous and evidence ecophysiological behaviour, forming micro-tufts; and v) they entrain and bind oriented sediment particles, denoting biostabilisation. These anoxygenic photosynthetic communities exhibit significant similarities to other Palaeoarchaean microbial mat-rich horizons, for example the 3.46 Ga stratiform ‘Apex chert’, ~3.45 Ga Hooggenoeg Formation cherts, 3.42 Ga Buck Reef Chert, ~3.33 Ga Josefsdal Chert, and ~3.26 Ga Mendon Formation cherts. In the Discussion of Chapter II, Manuscript II, it was proposed that the Middle Marker horizon represented the oldest example of a regionally, or even globally, significant microbial biome or biocoenosis, and that detailed palaeoenvironmental reconstructions of such fossiliferous horizons across the Palaeoarchaean may evaluate this hypothesis.

Chapter II, Manuscript III tested this hypothesis, selecting well-preserved fossiliferous horizons from throughout the 150 Ma of Palaeoarchaean stratigraphy in the Barberton region

for analysis by bulk ICP-MS and *in situ* LA ICP-MS through microbial horizons. This multi-scale appraisal sought to reconstruct the palaeoenvironments of early life – identified as well-preserved photosynthetic biofilms – at regional, local and biome scales. Selected samples included well-preserved photosynthetic microbial mat fabrics, and were sourced from the 3.472 Ga Middle Marker horizon, the 3.45 Ga Hooggenoeg H5c chert, the 3.334 Ga Footbridge Chert, and the 3.33 Ga Josefsdal Chert. Using combined trace and REE+Y systematics, it was demonstrated that the palaeodepositional environments of these cherts bore many similarities. Firstly, all showed the combined influences of marine, hydrothermal and terrigenous (riverine) aqueous chemistries both in bulk and *in situ*, however, the inputs from marine and hydrothermal sources were shown to be greatly reduced during periods of phototrophic microbial colonisation, whereas continental influences were significantly increased. Trace element patterns and concentrations indicated that heightened microbial productivity was associated with mixed mafic and felsic contributions, which correlate with lower Y/Ho ratios consistent with exposed continental landmasses, i.e., input of nutrients forming the loci of microbial colonisation. Nonetheless, when considering LA ICP-MS transect analyses through microbial horizons, it was found that resurgences of marine characteristics (particularly increased Y/Ho ratios and more strongly positive La and Y anomalies) featured. This led to the suggestion that the geomorphology of the regions of the Palaeoarchaean Earth represented by the Barberton greenstone belt were characterised by systems of epicontinental basins teeming with microbial life as a result of the complex chemical disequilibrium resulting from the interplay between marine and terrestrial influences. Whether these habitable basins formed a globally extensive "Gaian" biosphere is perhaps a question that cannot be answered by the available Early Archaean rock record. In conducting this fossil-calibrated study, it became apparent that previous "broad brushstroke" approaches to characterising Archaean habitable palaeoenvironments had likely suffered from a lack of comparison between bulk and *in situ* analyses. Viewing the Archaean Earth as a hydrothermally dominated ocean world is seemingly an oversimplification. The geomorphology of the Archaean habitable realm was more complex, supported by analyses presented herein showing repeated similarities between qualitatively similar biomes throughout 150 Ma of the stratigraphy of the Barberton greenstone belt. Previous trace and rare earth element studies of these cherts have, by virtue of their not being linked to individual structures or horizons in the studies samples and sequences, failed to note the fine-scale changes in environment that accompany the rise of fall of microbial biomes. Bulk analyses can dilute the signals of fluctuations in geochemistry and lead to interpretations of palaeoenvironment that, although accurate on a broad (superficial?) level, lack potentially crucial details and elemental excursions within the microstratigraphy.

When compiling the range of traces of early life from both the Barberton and Pilbara regions, one can thus conclude that the Palaeoarchaean was a time of surprising biological diversity, but is poorly understood at either an ecosystem or biome level. The coupled ICP-MS and LA ICP-MS analyses conducting during this thesis have aimed to open the discussion on biome reconstruction in the Archaean. Biome networks and their constituent ecosystems are among the fundamental tenets of the success of life, and the manuscripts in Chapter II sought to unravel such relationships, where possible, between the geosphere-hydrosphere and the biosphere – i.e., the dynamic environmental container and its living contents – since the two systems necessarily interact and co-evolve on timescales relevant both to momentary (short-

lived, on the order of days to months) microbial ecosystems and biospheric trajectories over hundreds of millions of years. Although the original research presented herein has gone some way toward appraising this, there remains much scope for advancing fossil-calibrated palaeoenvironmental reconstructions in deep time. Two immediately apparent perspectives are the extension of this deep time record beyond the Palaeoarchaean and the distinction of REE+Y patterns in microbialite sediments that are related to or controlled by bio-accumulation.

The extension of the record of biosphere-geosphere interactions preserved in photosynthetic microbial mat-rich horizons may be conducted over two timescales. The first, and possibly the more meaningful, would involve repeating the studies in Chapter II, Manuscripts II and III, for the available microbial mat-rich horizons through the Palaeoarchaean, Mesoarchaean and Neoarchaean of the Kaapvaal and Pilbara cratons, thus spanning the period between 3.5 and ~2.5 Ga, at which point the effects of the Great Oxygenation Event change the dynamics of certain isotopic and REE+Y systematics. This billion-year period is associated with the development of modern-style plate tectonics and the formation of most of the continental crust. These events opened a large number of palaeoenvironmental niches that seem to not exist in the Palaeoarchaean, specifically wide-reaching river networks and freshwater lacustrine systems isolated from marine influence. Understanding the changing predominant aqueous chemistries associated with these microbial horizons, together with delineating the changing characteristics of the microbial communities themselves, could distinguish the evolution of the ecosystems responsible for primary productivity at the Earth surface over hundreds of millions of years. Concomitantly, the trace and REE+Y compositions of these microbial horizons should record the changing terrigenous inputs and the progressive oxygenation of the surface of the surface ocean. To the best of my knowledge, datapoints charting the co-evolution of the Earth and Life during this crucial period of Earth history are astonishingly few in number.

Defining the compositions of microbialite sediments as a function of the scavenging of trace and REE+Y by microbial organic matter would both place further constraints on biogeochemical processes active in ancient fossiliferous sediments (i.e., the balance between environmentally and organochemically controlled REE+Y patterns) and potentially define a new biosignature. At present, organic matter interactions with REE+Y have been conducted only on recent and sub-fossil sedimentary organic matter but have shown that strong MREE and HREE enrichments can be linked to the binding of REE+Y by carboxylate and phosphate groups in microbial mat biomass. If these patterns could be extended into deeper time, they would serve as a biogenicity indicator for more ancient carbonaceous laminations interpreted as photosynthetic microbial mats. Furthermore, if such patterns are detected in bulk analyses, they may provide an initial survey of samples that are rich in biogenic organic material.

In Chapter II, Manuscript IV, in light of the knowledge that the palaeoenvironment can detectably modulate the development of microbial ecosystems, it was sought to determine whether morphologically complex microbialites (organo-sedimentary structures of biological origin) could be explained in terms of their morphogenesis, i.e., the processes of biogenesis that lead to their eventual morphologies. Using experimentally grown microbial mats from previous experiments (the ANR-ARCHAEMAT project) and complex Archaean organo-sedimentary structures including stromatolites of the 3.481 Ga Dresser Formation and the 3.472 Ga Middle Marker horizon. It was demonstrated that 3D morphogenetic similarities between

microbial mats grown under geochemically stressed conditions and the stromatolites of the Dresser Formation could enable the interpretation of the morphogenesis of the latter, and thus advocate its biogenicity, in light of the former. More significantly, this idea of a morphogenetic biosignature overcomes the principal constraint inherent in determining biogenicity based on morphology. Although descriptive morphologies may not yield unambiguous indications of biogenicity, a proof of the mechanistic processes involved in the generation of morphologies (morphogenesis) is able to do so. The 3D comparative morphogenetic approach pioneered in this manuscript is a complex correlative microscopy protocol and should form the means of assessing biogenicity only for complex but replicable biological systems.

The furthest-reaching perspective of 3D comparative morphogenesis is that it could form a framework within which organo-sedimentary structures – which account for most of the Archaean fossil record and are among the prime targets for Martian astrobiology – can be quantified and predicted. A range of physical models exist to predict these morphologies and further calibrated experimentation may elucidate the magnitude of the response to certain stressors and define a scale of response that enables the interpretation of biogenesis in such structures. Whether in early Archaean or Noachian sequences, degraded organo-sedimentary structures of controversial origin may be explicable through laboratory simulation of their conditions of formation, and mathematically reproduced by applying experimental parameters estimated by approaches that quantify the characteristics of the palaeodepositional environment, such as those presented in Chapter II, Manuscript III.

The manuscripts presented in Chapter II are an interlinked body of work that concerns defining the earliest traces of life within their environments and evaluating the regulation of Archaean biomes by prevailing geological and hydrological characteristics. These principles are relevant to the evaluation of the co-evolution of Life and the environment on any rocky planet upon which it might have emerged.

Chapter III, Manuscripts I and II presented complementary analytical approaches to enigmatic carbonaceous material in the form of clotted textures. Previous studies have hypothesised that this material derives from biomass and may represent non-photosynthetic biosignatures that are of especial relevance to the sporadic and restricted habitable environments characterising the early Mars. Clotted carbonaceous cherts are a common lithology throughout the stratigraphy of the Barberton greenstone belt, and have also been identified in some Pilbara sequences, thus ascertaining their origin(s) would aid the understanding of organic matter synthesis on the early Earth. If originating from non-photosynthetic biomass, demonstrating the metabolisms responsible for generating these textures would help to fill some of the gaps in the biomes represented, particularly where microbial mats and carbonaceous clots occur together. Previous appraisals of clots suffered from two major shortcomings: most studies conducted only low-resolution petrographic descriptions of this material, from which the conclusions were ambiguous and, where higher resolution analytical approaches were used, the approach adopted usually focussed on only one such technique, typically carbon isotopes, which are generally considered unable to prove biological origins without complementary data. As such, at the time of conducting the studies presented herein, the significance of clotted textures had not been satisfactorily addressed.

In Chapter III, Manuscript I, the nanostructure and bonding state of the carbonaceous matter were assessed using a combinatorial approach of optical microscopy, TEM, STEM-EDS, HRTEM coupled to EELS, and NanoSIMS. Studying material from three horizons – the 3.472 Ga Middle Marker horizon, 3.45 Ga Hooggenoeg Chert H5c and 3.33 Ga Josefsdal Chert – two morphologies of clot were identified, forming a structured framework for their characterisation that was lacking in previous research. Large (up to 2 mm), irregular, stellate, scalloped clots in matrix-supported chemical sediments were defined as Type 1 clots and were identified in the three studied horizons. Smaller (not exceeding 800 μm), sub-spheroidal clots occurring between the laminations of microbialite sediments were defined as Type 2 clots, and were identified only in the Hooggenoeg H5c and Josefsdal cherts. TEM and STEM-EDS showed that carbonaceous material in clots occurred as a dominantly interstitial phase, although Type 2 clots also included a portion of carbon that occurred as globules associated with nanosulphide crystals. Both interstitial and globular carbon were analysed by HRTEM. This demonstrated that much of the carbon was amorphous, however, some weak ordering (graphitisation) of the carbon consistent with the thermal history of the samples had occurred. In HRTEM micrographs, poorly ordered turbostratic carbon with graphene layer spacing up to 0.385 nm, more highly stacked swirling, curled and ribbon-like graphitic carbon with graphene layer spacing of 0.35-0.36 nm, and rare well-ordered linear fragments of graphite with interlayer spacing of 0.334-0.34 nm were identified, suggesting that clots originated from heterogeneous carbonaceous precursors with differing potential for graphitisation. Comparison with younger material from Palaeoproterozoic sequences suggests that this carbonaceous material is kerogenous material comprising mostly pyrolysed organic material of biological origin. This is supported by NanoSIMS ion mapping indicating the co-occurrence of C, N and S within carbonaceous material, the latter both as organo-sulphur distributed throughout the clots and in sulphides associated with globules, where present. Negative carbon isotope ratios are further consistent with biology, most of the measured values corresponding to multiple potential metabolic pathways (–8.6 to –28.0‰), but extremely negative values (–77.3 to –126.0‰) being explicable only by methanotrophic metabolisms and biogenic methane release and perhaps associated exclusively with globule formation.

Combining these findings with those of Chapter III, Manuscript II, one finds the strength for the case of the biogenicity of clotted microstructures significantly strengthened. μPIXE element mapping shows enrichments of Fe, V, Ni, Cu, As and Co, a range of elements of significance to the cellular machinery of lithotrophic and organotrophic methane- and nitrogen-cycling organisms. In this manuscript, the *palaeo-metallome*, a trace element biosignature based on the inorganic complement of the cell, was developed as a tool to determine the metabolic origin of potentially biogenic carbonaceous material. The palaeo-metallome was defined in terms of the fractional contribution of various elements to the total inorganic elemental complement, and combinations of elements, for example Fe, Ni and Co in the metallome of methanogens, and Fe and V in nitrogen fixation, may indicate the metabolic machinery, i.e., the intra- and extra-cellular processes responsible for biosynthesis producing the carbonaceous material in question.

The two manuscripts in Chapter III provide a number of advances relative to Chapter II. Firstly, they provide strong support for the idea that biogenicity, and perhaps even

metabolism, can be identified in the absence of obvious cellular preservation. This idea has not been studied to fruition in previous research, although enigmatic and generic carbonaceous matter has often been described as being of probable biogenic origin. Chapter III proposes that a network of analyses combining petrography with carbon nanostructure, bonding state, isotopic and trace element composition may prove this hypothesis. The manuscripts also suggest that trace element data in the form of a palaeo-metallomic biosignature may sustain and develop hypotheses on the biosynthetic processes responsible for generating specific morphologies of organic carbon, even where the metabolic pathway is ambiguous after carbon isotope measurements. By way of proof, the interpretation of μPIXE data on Type 1 clots in Manuscript II are consistent with the interpretation made on the basis of carbon isotope data coupled with STEM-EDS identification of nanosulphides in Manuscript I, i.e., that a contribution from methane-cycling organisms was important. Finally, from the viewpoint of theoretical evolutionary biology, Chapter III could be considered to provide the first empirical support for the hypothesis of the "biological chemistry of the elements", proposed by Williams and Fraústo da Silva to explain the dependency of modern organisms on elements that are now trace in their environments. If clots are indeed biological as proposed in Manuscript I, and if the trace element signatures described in Manuscript II reflect their palaeo-metallomes, then it is likely true that certain elements – such as Fe, V, Ni, Co and As – were incorporated into cells as a function of their abundances in early Earth environments and have remained bio-essential over the billions of years that followed.

Chapter IV moved the discussions in this thesis away from Earth and to Mars, the extraterrestrial body upon which it is considered most likely that life could have emerged, flourished and left a detectable imprint (fossil) for analysis and identification by space missions. In the two manuscripts of Chapter IV, the differences and limitations inherent in space exploration designed to detect features that require a highly nested network of evidence were evaluated. In Chapter IV, Manuscript I, a scientific workflow for ExoMars 2020 rover operations was defined and, within this, the importance of the core imaging phase, when the highest-resolution images of the microstructure and microstratigraphy of subsurface samples will be obtained, was simulated using Mars-analogue igneous and sedimentary rocks, some of which contained biosignatures. The importance of mission scientific calibration using experimental setups and sample morphologies and dimensions identical to those of the mission is clear. A range of restrictions in interpretation emerge, most notably the limited detection of microstructures of millimetre-centimetre scale using the imaging instrumentation, and the potential misinterpretation of features arising from the drilling procedure.

For Chapter IV, Manuscript II, complex artificial samples were synthesised using Mars-analogue igneous material augmented with clay minerals, molecules of relevance to prebiotic chemistry and mineralised organisms that may resemble the constituents of a putative Martian biosphere. Fundamental characterisation of these samples showed that they meet all of the requirements of Mars analogy from a geological perspective (mineralogical and elemental) and are uniquely analogues of astrobiological relevance to the ExoMars 2020 mission. Having been prepared as instrument-specific morphologies (hand samples, cores or powders), it is intended that the analysis of these samples by the instruments of the Pasteur payload will enable the distinction of instrumental collaborations required to identify specific biosignatures and place them within their geological context at macroscopic and microscopic scales. The preliminary

characterisation conducted by some of the instrument teams (ISEM, Ma_MISS, RLS and MOMA) indicate accurate characterisation of the mineralogy and presence of organic material and an excellent degree of consistency between the instruments. Integrating these findings into the scientific workflow proposed in Manuscript I would provide valuable pre-mission training for the identification of biosignatures or their microenvironments during actual mission operations.

This thesis has presented a number of new ways of looking at ancient life, and these couplings between instrumentation, methodology and hypothesis have demonstrated several previously unrecognised aspects of the earliest known fossils. The manuscripts herein have shown how multi-modal approaches between the macroscale and nanoscale, coupling morphology in two and three dimensions with mineralogy, palaeodepositional signatures, major and trace elemental composition, and carbon chemistry, can link fossils to their environments and build an ecosystem- or biome-level understanding of life on the early Earth that may be used as part of a framework for decoding Gaian biospheres on any geologically dynamic rocky planet.

Keyron Hickman-Lewis
August 2019

Acknowledgements

I am immensely grateful to a large number of people for their support, collaboration and friendship throughout the course of this thesis, and these final few words will try and surely fail to do justice to this.

Frances Westall welcomed me into her group and 2016 and has been a constant source of support, scientific discussion, and encouragement to undertake a number of challenging projects and be part of many highly interesting endeavours. Through this I have been exposed to so many new ideas and opportunities to extend my learning that there truly never has been a quiet moment here! I have appreciated very much also having been trusted to present and represent the group on many occasions and at many meetings and conferences that have given me as good an introduction to both the science and the scientific community as I could possibly have asked for. Away from the lab, I am glad that we could also enjoy a shared enthusiasm for classical music, culture, good wine and hearty doses of philosophy.

I am similar grateful to Barbara Cavalazzi for involving me in so many of the research projects in her group, introducing me to a range of cutting-edge techniques (and indeed to the highly interesting field of nanoscopic geosciences), and for a great deal of useful advice in navigating the multitude of challenges in the scientific community. In addition to this, a number of highly enjoyable and highly productive missions – in Italy, France, Romania and the UK – have given us plenty of opportunities to dicsuss and develop ideas and approaches and truly test some new ways of looking at ancient life (in the last instance, naturally accompanied by the wonders of British cuisine…).

Frédéric Foucher has also been a constant friend and good colleague over the course of the thesis, and I have especially enjoyed our long discussions about the philosophies involved in the approach to science, which I very much hope will form the basis of a number of projects in the very near future. Further to this, we have a shared love of music of many diverse forms!

A special acknowledgement goes to Avinash Dass, whose presence in my daily life I have greatly missed over this last year. Avinash has been a consistent source of entertainment and good-natured banter both in the lab and outside, and I could not be more glad that we were both able to obtain places to study in Orléans. Particular instances are naturally too numerous to mention, but involve some uniquely excellent evenings out in Athens and Berlin…

I am, of course, deeply indebted to the members of the jury – Jean-Gabriel Bréhéret, Andrew Czaja, Jorge Vago and Michel Viso – who agreed to read and evaluate this work, particularly Andrew and Jorge for accepting to undertake the task of being the rapporteurs.

Amongst the many people outside the CBM with whom I have had the pleasure to work, I am especially grateful for the continually harmonious and productive collaborations with Pascale Gautret and Sylvain Janiec at ISTO, Stéphanie Soreiul at AIFIRA, Blandine Gourcerol at the BRGM, Jean-Gabriel Bréhéret at the Université de Tours, and Lara Maldanis at the Brazilian Synchrotron. Their considerable involvement of the topics of this thesis and beyond, and their readiness to discuss widely have been most appreciated, and from this I have learnt a lot. I am especially grateful to Sylvain for his always being ready to prepare the often unusal(!) preparations of samples I have requested at little more than a moment's notice, to Jean for a number of very pleasant days spent in the field in South Africa that transpired to become an excellent course in field sedimentology, and to Pascale for many fruitful hours of discussion over the geobiological content of this thesis.

Further collaborations with a number of people have also opened and a range of scientifically interesting avenues to me, all of which are reported in this thesis: André Brack, Daniela Manzini, Laurent Arbaret, Annie Richard, Giorgio Gasparotto, Martin Whitehouse, Heejin Jeon, Raluca Negrea, Corneliu Ghica, Adrian Maraloiu, Xuchao Zhao, Ian Franchi, Rutger De Wit, Elisa Miccinilli, Elisabeth Baumann, Steven Pelletier, Fabio Messori, Charles Cockell and Thomas Georgelin.

Ongoing collaborations that have not yet reached fruition (but hopefully will in the near future) owe a great thanks to: Pierre Gueriau, Andy King, Andrea Somogyi, Sara Russell, Jens Najorka, Brook Clark and Amin Garbout.

A number of good friends in the departments both in Orléans and Bologna deserve mention here: Isabelle Simon and Barnabé Cherville (and of course Dubaï), Mateja Seničar, Francesco Greco, Barbara Marchesini and Mariateresa Balzano.

Outside of the lab, I wish to especially acknowledge my close friendship with JJ Heaney (and to the bank clerk who introduced us with: “he is also English!” [neither of us are]). Further sources of good humour and continual friendship across the globe include Nina Kopacz, Andi Sai, Kathryn Pillidge, Kamila Godzińska, Guy Paxman, Patrick Sugden, Matthew Jerram, Branwen Snelling, Felix Tennie and Iris Kramberger Tennie, Mabel Wong and Philomena Yuqian Gan.

On a personal note: when I arrived in Orléans, I was for the first time without a piano in my home, and those of you who know me well know that this posed a unique challenge. I owe many thanks to the people who assured me ready access to various pianos (and in so doing, assured my sanity outside of work), in particular Michel and Olivier at Club 15 (which consequently became a centre of my social life here), Mme Bonnemaison, who allowed me to play on the wonderful piano in her home, and the good people of the conservatoire, who although initially confused by my request for access to a piano (“but we already have enough teachers”), were kindly grant me exceptional access to their pianos in my first few months here.

Finally, of course, my parents and grandparents, who I know are only ever a phone call away.

On a concluding note, I cannot resist to say that I will never acknowledge Reviewer 3 and hope that, for the sake of his or her own longevity (and structural integrity), their identity remains forever a mystery to me…

References

Alibo, D.S., Nozaki, Y., 1999. Rare earth elements in seawater: particle association, shale-normalization, and Ce oxidation. *Geochimica et Cosmochimica Acta* **63**, 363–372.

Allwood, A.C., Walter, M.R., Kamber, B.S., Marshall, C.P., Burch, I.W., 2006. Stromatolite reef from the early Archean era of Australia. *Nature* **441**, 713–718.

Allwood, A.C., Walter, M.R., Burch, I.W., Kamber, B.S., 2007. 3.43 billion-year-old stromatolite reef from the Pilbara Craton of western Australia: Ecosystem-scale insights to early life on Earth. *Precambrian Research* **158**, 198–227.

Allwood, A.C., Grotzinger, J.P., Knoll, A.H., Burch, I.W., Anderson, M.S., Coleman, M.L., Kanik, I., 2009. Controls on development and diversity of Archean stromatolites. *Proceedings of the National Academy of Sciences USA* **106**, 9548–9555.

Allwood, A.C., Kamber, B.S., Walter, M.R., Burch, I.W., Kanik, I., 2010. Trace element record depositional history of an Early Archean stromatolitic carbonate platform. *Chemical Geology* **270**, 148–163.

Allwood, A.C., Clark, B., Flannery, D.T., Hurowitz, J.A., Wade, L.A., Elam, T., Foote, M.C., Knowles, E.C., 2015. Texture-specific elemental analysis of rocks and soils with PIXL: The Planetary Instrument for X-ray Lithochemistry on Mars 2020. *IEEE Aerospace Conference Proceedings* 2015, 15215581.

Altermann, W., 2001. The oldest fossils of Africa – a brief reappraisal of reports from the Archean. *Journal of African Earth Sciences* **33**, 427–436.

Altermann, W., 2002. The evolution of life and its impact on sedimentation. In Altermann, W., Corcoran, P.L. (Eds.) Precambrian Sedimentary Environments: A Modern Approach to Ancient Depositional Systems. Wiley-Blackwell, pp. 15–32.

Altermann, W., Kazmierczak, J., 2003. Archean microfossils: a reappraisal of early life on Earth. *Research in Microbiology* **154**, 611–617.

Armstrong, R.L., 1981. Radiogenic isotopes: The case for crustal recycling on a steady-state no-continental-growth Earth. *Philosophical Transactions of the Royal Society of London A*, *Mathematical and Physical Sciences* **301**, 443–472.

Armstrong, R.A., Compston, W., de Wit, M.J., Williams, I.S., 1990. The stratigraphy of 3.5-3.2 Ga Barberton Greenstone Belt revisited: a single zircon microprobe study. *Earth and Planetary Science Letters* **101**, 90–106.

Anhaeusser, C.R., 1973. The evolution of the early Precambrian crust of southern Africa. *Philosophical Transactions of the Royal Society of London A, Mathematical and Physical Sciences* **273**, 359–388.

Anhaeusser, C.R., 1978. The geology and geochemistry of the Muldersdrif Complex and surrounding area, Krugersdorp District. *Transactions of the Geological Society of South Africa* **81**, 193–203.

Armendariz, A.L., Talano, M.A., Wevar Oller, A.L., Medina, M.I., Agostini, E., 2015. Effect of arsenic on tolerance mechanisms of two plant growth-promoting bacteria used as biological inoculants. *Journal of Environmental Science* **33**, 203–210.

Arndt, N.T., Nisbet, E.G., 2012. Processes on the young Earth and the habitats of early life. *Annual Review of Earth and Planetary Sciences* **40**, 521–549.

Arvidson, R.E., Anderson, R.V., Bartlett, P. et al., 2004. Localization and physical properties experiments conducted by Spirit at Gusev Crater. *Science* **305**, 821–824.

Awramik, S.M., Grey, K., 2005. Stromatolites: Biogenicity, biosignatures, and bioconfusion. *Proceedings of SPIE, 5906, Astrobiology and Planetary Missions; International Society for Optics and Photonics*, Bellingham, WA, USA, p. 5906.

Bailey, J., Orphan, V., Joye, S., Corsetti, F., 2009. Chemotrophic microbial mats and their potential for preservation in the rock record. *Astrobiology* **9**, 843–859.

Baker, D.R., Mancini, L., Polacci, M., Higgins, M.D., Gualda, G.A.R., Hill, R.J., Rivers, M.L., 2012. An introduction to the application of X-ray microtomography to the three-dimensional study of igneous rocks. *Lithos* **148**, 262–276.

Bandfield, J.L., Hamilton, V.E., Christensen, P.R., 2000. A global view of Martian surface compositions from MGS-TES. *Science* **287**, 1626–1630.

Banerjee, N.R., Furnes, H., Muehlenbachs, K., Staudigel, H., de Wit, M., 2006. Preservation of ~3.4–3.5 Ga microbial biomarkers in pillow lavas and hyaloclastites from the Barberton Greenstone Belt, South Africa. *Earth and Planetary Science Letters* **241**, 707–722.

Banerjee, N.R., Izawa, M.R.M., Sapers, H.M., Whitehouse, M.J., 2010. Geochemical biosignatures preserved in microbially altered basaltic glass. *Surface and Interface Analysis* **43**, 452–457.

Banham, S.G., Gupta, S., Rubin, D.M., Watkins, J.A., Sumner, D.Y., Edgett, K.S., Grotzinger, J.P., Lewis, K.W., Edgar, L.A., Stack-Morgan, K.M., Barnes, R., Bell, J.F., Day, M.D., Ewing, R.C., Lapotre, M.G.A., Stein, N.T., Rivera-Hernandez, F., Vasavada, A.R., 2018. Ancient Martian aeolian processes and palaeomorphology reconstructed from the Stimson formation on the lower slope of Aeolis Mons, Gale crater, Mars. *Sedimentology* **65**, 993–1042.

Barbieri., R., Cavalazzi, B., 2014. How do modern extreme hydrothermal environments inform the identification of Martian habitability? The case of the El Tatio geyser field. *Challenges* **5**, 430–443.

Barghoorn, E.S., Schopf, J.W., 1966. Microorganisms three billion years old from the Precambrian of South Africa. *Science* **152**, 758–763.

Batchelor, M.T., Burne, R.V., Henry, B.I., Watt, S.D. Deterministic KPZ model for stromatolite laminae. *Physica A* **282**, 123–136.

Batchelor, M.T., Burne, R.V., Henry, B.I., Watt, S.D., 2003. Mathematical and image analysis of stromatolite morphogenesis. *Mathematical Geology* **35**, 789–803.

Batchelor, M.T., Burne, R.V., Henry, B.I., Jackson, M.J., 2004. A case for biotic morphogenesis of coniform stromatolites. *Physica A* **337**, 319–326.

Batustuzzi, F.A., Feijao, A., Blair Hedges, S., 2004. A genomic timescale of prokaryote evolution: insights into the origin of methanogenesis, phototrophy, and the colonization of land. *BMC Evolutionary Biology* **4**, 44.

Bau, M., 1999. Scavenging of dissolved yttrium and rare earths by precipitating iron oxyhydroxide: experimental evidence for Ce oxidation, Y-Ho fractionation, and lanthanide tetrad effect. *Geochimica et Cosmochimica Acta* **63**, 67–77.

Bau, M., Dulski, P., 1996. Distribution of yttrium and rare-earth elements in the Penge and Kuruman iron-formations, Transvaal Supergroup, South Africa. *Precambrian Research* **79**, 37–55.

Betts, H.C., Puttick, M.N., Clark, J.W., Willliams, T.A., Donoghue, P.C.J., Pisani, D., 2018. Integrated genomic and fossil evidence illuminates life's early evolution and eukaryote origin. *Nature Ecology and Evolution* **2**, 1556–1562.

Berhault, G., Mehta, A., Pavel, A.C., Yang, J., Rendon, L., Yácaman, M.J., Araiza, L.C., Moller, A.D., Chianelli, R.R., 2001. The role of structural carbon in transition metal sulfides hydrotreating catalysts. *Journal of Catalysis* **198**, 9–19.

Beyssac, O., Goffé, B., Chopin, C., Rouzaud, J.-N., 2002. Raman spectra of carbonaceous material in metasediments: a new geothermometer. *Journal of Metamorphic Geology* **20**, 859–871.

Bhattacharya, J.P., Payenberg, T.H.D., Lang, S.C., Bourke, M., 2005. Dynamic river channels suggest a long-lived Noachian crater lake on Mars. *Geophysical Research Letters* **32**, L10201.

Bibring, J.-P., Hamm, V., Pilorget, C., Vago, J.L., MicrOmega Team, 2017. The MicrOmga investigation onboard ExoMars. *Astrobiology* **17**, 621–626.

Bishop, J.L., Fairén, A.G., Michalski, J.R., Gago-Duport, L., Baker, L.L., Velbel, M.A., Gross, C., Rampe, E.B., 2018. Surface clay formation during short-term warmer and wetter conditions on a largely cold ancient Mars. *Nature Astronomy* **2**, 206–213.

Blake, R.E., Chang, S.J., Lepland, A., 2010. Phosphate oxygen isotope evidence for a temperate and biologically active Archean ocean. *Nature* **464**, 1029–1033.

Bolhar, R., Van Kranendonk, M.J., 2007. A non-marine depositional setting for the northern Fortescue Group, Pilbara Craton, inferred from trace element geochemistry of stromatolitic carbonates. *Precambrian Research* **155**, 229–250.

Bolhar, R., Kamber, B.S., Moorbath, S., Fedo, C.M., Whitehouse, M.J., 2004. Characterisation of early Archaean chemical sediments by trace element signatures. *Earth and Planetary Science Letters* **222**, 43–60.

Bolhar, R., Van Kranendonk, M.J., Kamber, B.S., 2005. A trace element study of siderite-jasper banded iron formation in the 3.45 Ga Warrawoona Group, Pilbara Craton-Formation from hydrothermal fluids and shallow seawater. *Precambrian Research* **137**, 93–114.

Bolhar, R., Hofmann, A., Siahi, M., Feng, Y.-X., Delvigne, C., 2015. A trace element and Pb isotopic investigation into the provenance and deposition of stromatolitic carbonates, ironstones and associated shales of the ~3.0 Ga Pongola Supergroup, Kaapvaal Craton. *Geochimica et Cosmochimica Acta* **158**, 57–78.

Bontognali, T.R.R., Session, A.L., Allwood, A.C., Fischer, W.W., Grotzinger, J.P., Summons, R.E., Eiler, J.M., 2012. Sulfur isotopes of organic matter preserved in 3.45-billion-year-old stromatolites reveal microbial metabolism. *Proceedings of the National Academy of Sciences U.S.A.* **109**, 15146–15151.

Bosak, T., Greene, S., Newman, D.K., 2007. A likely role for anoxygenic photosynthetic microbes in the formation of ancient stromatolites. *Geobiology* **5**, 119–126.

Bosak, T., Liang, G., Sim, M.S., Petroff, A.P., 2009. Morphological record of oxygenic photosynthesis in conical stromatolites. *Proceedings of the National Academy of Sciences U.S.A*. **106**, 10939–10943.

Bosak, T., Bush, J.W.M., Flynn, M.R., Liang, B., Ono, S., Petroff, A.P., Sim, M.S., 2010. Formation and stability of oxygen-rich bubbles that shape photosynthetic mats. *Geobiology* **8**, 45–55.

Bosak, T., Knoll, A.H., Petroff, A.P., 2013. The meaning of stromatolites. *Annual Review of Earth and Planetary Sciences* **41**, 21–44.

Bost, N., Westall, F., Ramboz, C., Foucher, F., Pullan, D., Meunier, A., Petit, S., Fleischer, I., Klingelhöfer, G., Vago, J.L., 2013. Mission to Mars: characterisation of Mars analogue rocks for the International Space Analogue Rockstore (ISAR). *Planetary and Space Science* **82–83**, 113–127.

Bost, N., Ramboz, C., LeBreton, N., Foucher, F., Lopez-Reyes, G., De Angelis, S., Josset, M., Venegas, G., Sanz-Arranz, A., Rull, F., Medina, J., Josset, J.-L., Souchon, A., Ammannito, E., De Sanctis, M.C., Di Iorio, T., Carli, C., Vago, J.L., Westall, F., 2015. Testing the ability of the ExoMars 2018 payload to document geological context and potential habitability on Mars. *Planetary and Space Science* **108**, 87–97.

Boston, P.J., Ivanov, M.V., McKay, C.P., 1992. On the possibility of chemosynthetic ecosystems in subsurface habitats on Mars. *Icarus* **95**, 300–308.

Bottke, W.F., Vokrouhlicky, D., Minton, D., Nesvorny, D., Morbidelli, A., Brasser, R., Simonson, B., Levison, H.F., 2012. An Archaean heavy bombardment from a destabilized extension of the asteroid belt. *Nature* **485**, 78–81.

Bourbin, M., Gourier, D., Derenne, S., Binet, L., Le Du, Y., Westall, F., Kremer, B., Gautret, P., 2013. Dating carbonaceous matter in Archean cherts by electron paramagnetic resonance. *Astrobiology* **13**, 151–162.

Brasier, M.D., Green, O.R., Jephcoat, A.P., Kleppe, A.K., Van Kranendonk, M.J., Lindsay, J.F., Steele, A., Grassineau, N.V., 2002. Questioning the evidence for Earth's oldest fossils. *Nature* **416**, 78–81.

Brasier, M.D., Green, O., Lindsay, J.F., Steele, A., 2004. Earth's oldest (> 3.5 Ga) fossils and the 'early Eden hypothesis': questioning the evidence. *Origins of Life and Evolution of Biospheres* **34**, 257–269.

Brasier, M.D., Green, O.R., McLoughlin, N., 2004. Characterization and critical testing of potential microfossils from the early Earth: the Apex 'microfossil debate' and its lessons for Mars sample return. *International Journal of Astrobiology* **3**, 139–150.

Brasier, M.D., Green, O.R., Lindsay, J.F., McLoughlin, N., Steele, A., Stoakes, C., 2005. Critical testing of Earth's oldest putative fossil assemblage from the 3.5 Ga Apex chert, Chinaman Creek Western Australia. *Precambrian Research* **140**, 55–102.

Brasier, M.D., McLoughlin, N., Green, O.R., Wacey, D., 2006. A fresh look at the fossil evidence for early Archaean cellular life. *Philosophical Transactions of the Royal Society B* **361**, 887–902.

Brasier, M.D., Wacey, D., McLoughlin, N., 2011. Taphonomy in temporally unique settings: an environmental traverse in search of the earliest life on Earth. In: Allison, P.A., Bottjer, D.J. (Eds.), Taphonomy: Process and Bias Through Time, Topics in Geobiology. Springer, pp. 487.

Brasier, M.D., Antcliffe, J., Saunders, M., Wacey, D., 2015. Earth's earliest fossils (3.5-1.9 Ga): changing the picture with new approaches and new discoveries. *Proceedings of the National Academy of Sciences* **112**, 4859–4864.

Buick, R., 1984. Carbonaceous filaments from North Pole, Western Australia: are they fossil bacteria in Archean stromatolites? *Precambrian Research* **24**, 157–172.

Buick, R., 1990. Microfossil recognition in Archaean rocks: an appraisal of spheroids and filaments from 3500 M.Y. old chert-barite at North Pole, Western Australia. *Palaios* **5**, 441–459.

Buick, R., 2008. When did oxygenic photosynthesis evolve? *Philosophical Transactions of the Royal Society of London B* **363**, 2731–2743.

Buick, R., Dunlop, J., Groves, D., 1981. Stromatolite recognition in ancient rocks: an appraisal of irregularly laminated structures in an Early Archean chert-barite unit from North Pole, Western Australia. *Alcheringa* **5**, 161–181.

Buick, R., Rasmussen, B., Krapez, B., 1998. Archean Oil: Evidence for Extensive Hydrocarbon Generation and Migration 2.5-3.5 Ga. *AAPG Bulletin* **82**, 50–69.

Burne, R.V., Moore, L.S., 1987. Microbialites: Organosedimentary deposits of benthic microbial communities. *Palaios* **2**, 241–254.

Burnham, A.D., Berry, A.J., 2017. Formation of Hadean granites by melting of igneous crust. *Nature Geoscience* **10**, 457–461.

Buseck, P.J., Huang, B.-J., 1985. Conversion of carbonaceous material to graphite during metamorphism. *Geochimica et Cosmochimica Acta* **49**, 2003–2016.

Buseck, P.R., Huang, B.-J., Miner, B., 1988. Structural order and disorder in Precambrian kerogens. *Organic Geochemistry* **12**, 221–234.

Busscher, H.J., van der Mei, H.C., 2000. Initial microbial adhesion events: mechanisms and implications. In: Allison, D.G., Gilbert, P., Lappin-Scott, H.M., Wilson, M. (Eds.), Community Structure and Co-operation in Biofilms. Cambridge University Press, Cambridge, pp. 25–36.

Butcher, F.E.G., Conway, S.J., Arnold, N.S., 2017. Are the Dorsa Argentea on Mars eskers? *Icarus* **275**, 65–84.

Buz, J., Ehlmann, B.L., Grotzinger, J.P., 2017. Mineralogy and stratigraphy of the Gale crater rim, wall, and floor units. *JGR Planets*, E005163.

Byerly, G.R., Palmer, M.R., 1991. Tourmaline mineralization in the Barberton greenstone belt, South Africa: early Archean metasomatism by evaporite-derived boron. *Contributions to Mineralogy and Petrology* **107**, 387–402.

Byerly, G.R., Lowe, D.R., Walsh, M.M., 1986. Stromatolites from the 3300-3500-Myr Swaziland Supergroup, Barberton Mountain Land, South Africa. *Nature* **319**, 489–491.

Byerly, G.R., Kröner, A., Lowe, D.R., Todt, W., Walsh, M.M., 1996. Prolonged magmatism and time constraints for sediment deposition in the early Archean Barberton greenstone belt: evidence from the Upper Onverwacht and Fig Tree groups. *Precambrian Research* **78**, 125–138.

Cabrol, N.A., 2018. The coevolution of life and environment on Mars: An ecosystem perspective on the robotic exploration of biosignatures. *Astrobiology* **18**, 1–27.

Cameron, V., House, C.H., Brantley, S.L., 2012. A first analysis of metallome biosignatures of hyperthermophilic archaea. *Archaea*, Article ID 789278.

Campbell, J.L., Teesdale, W.J., Halden, N.M., 1995. Theory, practice and application of PIXE microanalysis and SPM element mapping. *Canadian Mineralogist* **33**, 279–292.

Campbell, K.A., Guido, D.M., Gautret, P., Foucher, F., Ramboz, C., Westall, F., 2015. Geyserite in hot-spring siliceous sinter: window on Earth's hottest terrestrial (paleo)environment and its extreme life. *Earth-Science Reviews* **148**, 44–64.

Canfield, D.E., 1998. A new model for Proterozoic ocean chemistry. *Nature* **396**, 450–453.

Canfield, D.E., Rosing, M.T., Bjerrum, C., 2006. Early anaerobic metabolisms. *Philosophical Transactions of the Royal Society B* **361**, 1819–1836.

Carr, M.H., Head, J.W., 2010. Geologic history of Mars. *Earth and Planetary Science Letters* **294**, 185–203.

Carter, J., Poulet, F., Bibring, J.-P., Mangold, N., Murchie, S., 2013. Hydrous minerals on Mars as seen by the CRISM and OMEGA imaging spectrometers: Updated global view. *Journal of Geophysical Research Planets* **118**, 831–858.

Cavalazzi, B., 2007. Chemotrophic filamentous microfossils from the Hollard Mound (Devonian, Morocco) as investigated by focused ion beam. *Astrobiology* **7**, 402–415.

Cavalazzi, B., Barbieri, R., Ori, G.G., 2007. Chemosynthetic microbialites in the Devonian carbonate mounds of Hamar Laghdad (Anti-Atlas, Morocco). *Sedimentary Geology* **200**, 73–88.

Cavalazzi, B., Westall, F., Barbieri, R., Foucher, F., Cady, S., 2011. Potential fossil endoliths in vesicular pillow basalt, Coral Patch Seamount, eastern North Atlantic Ocean. *Astrobiology* **11**, 619–632.

Cavalazzi, B., Barbieri, R., Gómez, F., Capaccioni, B., Olsson-Francis, K., Pondrelli, M., Rossi, A.P., Hickman-Lewis, K., Agangi, A., Gasparotto, G., Glamoclija, M., Ori, G.G., Rodriguez, N., Hagos, M., 2019. The Dallol Geothermal Area, Northern Afar (Ethiopia)—An Exceptional Planetary Field Analog on Earth. *Astrobiology* **19**, 553–578.

Cawood, P.A., Hawkesworth, C.J., Pisarevsky, S.A., Dhuime, B., Capitanio, F.A., Nebel, O., 2018. Geological archive of the onset of plate tectonics. *Philosophical Transactions of the Royal Society of London A* **376**, 20170405.

Censi, P., Cangemi, M., Brusca, L., Madonia, P., Saiano, F., Zuddas, P., 2013. The behavior of rare-earth elements, Zr and Hf during biologically-mediated deposition of silica-stromatolites and carbonate-rich microbial mats. *Gondwana Research* **27**, 209–215.

Charnay, B., Le Hir, G., Fluteau, F., Forget, F., Catling, D.C., 2017. A warm or a cold early Earth? New insights from a 3-D climate-carbon model. *Earth and Planetary Science Letters* **474**, 97–109.

Chevrier, V., Mathé, P.E., 2007. Mineralogy and evolution of the surface of Mars: A review. *Planetary and Space Science* **55**, 289–314.

Clark, B.C., Arvidson, R.E., Gellert, R., Morris, R.V., Ming, D.W., Richter, L., Ruff, S.W., Michalski, J.R., Farrand, W.H., Yen, A., Herkenhoff, K.E., Squyres, S.W., Schröder, C., Klingelhöfer, G., Bell, J.F., 2007. Evidence for montmorillonite or its compositional equivalent in Columbia Hills, Mars. *JGR Planets* 112 E6.

Cnossen, I., Sanz-Forcada, J., Favata, F., Witasse, O., Zegers, Z., Arnold, N.F., 2007. Habitat of early life: solar X-ray and UV radiation at Earth's surface 4–3.5 billion years ago. *Journal of Geophysical Research* **112**, E02008.

Coates, A.J., Jaumann, R., Griffiths, A.D., Leff, C.E., Schmitz, N., Josset, J.-L., Paar, G., Gunn, M., Hauber, E., Cousins, C.R., Cross, R.E., Grindrod, P., Bridges, J.C., Balme, M., Gupta, S., Crawford, I.A., Irwin, P., Stabbins, R., Tirsch, D., Vago, J.L., Theodorou, T., Caballo-Perucha, M., Osinski, G.R., PanCam team, 2017. The PanCam instrument for the ExoMars rover. *Astrobiology* **17**, 511–541.

Cockell, C.S., 2014. Trajectories of Martian habitability. *Astrobiology* **14**, 182–203.

Cockell, C.S., Raven, J.A., 2004. Zones of photosynthetic potential on Mars and the early Earth. *Icarus* **169**, 300–310.

Cockell, C.S., Balme, M., Bridges, J.C., Davila, A., Schwenzer, S.P., 2012. Uninhabited habitats on Mars. *Icarus* **217**, 184–193.

Condie, K.C., 1981. Archean Greenstone Belts. Elsevier, Amsterdam, pp. 433p.

Craig, P.I., Mickol, R.L., Archer, P.D., Kral, T.A., 2017. Nontronite and Montmorillonite as Nutrient Sources for Life on Mars. *LPSC XLVIII, #1997*.

Crowell, B.W., Lowell, R.P., Von Damm, K.L., 2008. A model for the production of sulfur floc and "snowblower" events at mid-ocean ridges. *Geochemistry, Geophysics, Geosystems* **9**, GC002103.

Cuerno, R., Escudero, C., García-Ruiz, J.-M., Herrero, M.A., 2012. Pattern formation in stromatolites: Insights from mathematical modelling. *Journal of the Royal Society: Interface* **9**, 1051–1062.

Danielson, A., Möller, P., Dulski, P., 1992. The europium anomalies in banded iron formations and the thermal history of the oceanic crust. *Chemical Geology* **97**, 89–100.

Dann, J.C., Grove, T.L., 2007. Volcanology of the Barberton Greenstone Belt, South Africa: inflation and evolution of flow fields. In: Van Kranendonk, M.J., Smithies, R.H., Bennett, V. (Eds.), Earth's Oldest Rocks. Developments in Precambrian Geology. Elsevier, Amsterdam, pp. 527–570.

Dartnell, L.R., Page, K., Jorge-Villar, S.E., Wright, G., Munshi, T., Scowen, I.J., Ward, J.M., Edwards, H.G.M., 2012. Destruction of Raman biosignatures by ionising radiation and the implications for life detection on Mars. *Analytical and Bioanalytical Chemistry* **403**, 131–144.

Dass, A.V., Hickman-Lewis, K., Brack, A., Kee, T.P., Westall, F., 2016. Stochastic prebiotic chemistry within realistic geological systems. *ChemistrySelect* **1**, 2096-2126.

De Carlo, E.H., Green, W.J., 2002. Rare earth elements in the water column of Lake Vanda, McMurdo Dry Valleys, Antarctica. *Geochimica et Cosmochimica Acta* **66**, 1323–1333.

de Duve, C., 1991. Blueprint for a Cell: The Nature and Origin of Life. Neil Patterson Publishers, p. 275.

de Duve, C., 1995. Vital dust: Life as a cosmic imperative. BasicBooks, New York, p. 384.

De Gregorio, B.T., Sharp, T.G., 2003. Determining the Biogenicity of Microfossils in the Apex Chert, Western Australia, Using Transmission Electron Microscopy. *LPSC XXXIV, #1267*.

De Gregorio B. T., Sharp T.G., 2006. The structure and distribution of carbon in the 3.5 Ga Apex chert: implications for the biogenicity of Earth's oldest putative microfossils. *American Mineralogist* **91**, 784-789.

De Gregorio, B.T., Sharp, T.G., Rushdi, A.I., and Simoneit, B.R.T., 2011. Bugs or Gunk? Nanoscale Methods for Assessing the Biogenicity of Ancient Microfossils and Organic Matter. In Early Life on Earth: Habitats, Environments and Methods of Detection. Golding, S.D., Glikson, M. (Eds.) Springer, 239-289.

de Oliveira Martins, P.S., de Almeida, N.F., Leite, S.G.F., 2008. Application of a bacterial extracellular polymeric substance in heavy metal adsorption in a co-contaminated aqueous system. *Brazilian Journal of Microbiology* **39**, 780–786.

De Sanctis, M.C., Altieri, F., Ammannito, E., Biondi, D., De Angelis, S., Meini, M., Mondello, G., Novi, S., Paolinetti, R., Soldani, M., Mugnuolo, R., Pirrotta, S., Vago, J.L., Ma_MISS team, 2017. Ma_MISS on ExoMars: Mineralogical Characterization of the Martian Subsurface. *Astrobiology* **17**, 612–620.

de Vera, J.-P., Alawi, M., Backhaus, T., Baqué, M., Billi, D., Böttger, U., Berger, T., Bohmeier, M., Cockell, C., Demets, R., la Torre Noetzel, R., Edwards, H., Elsaesser, A., Fagliarone, C., Fiedler, A., Foing, B., Foucher, F., Fritz, J., Hanke, F., Herzog, T., Horneck, G., Hübers, H.-W., Huwe, B., Joshi, J., Kozyrovska, N., Kruchten, M., Lasch, P., Lee, N., Leuko, S., Leya, T., Lorek, A., Martinez-Frias, J., Meessen, J., Moritz, S., Moeller, R., Olsson-Francis, K., Onofri, S., Ott, S., Pacelli, C., Podolich, O., Rabbow, E., Reitz, G., Rettberg, P., Reva, O., Rothschild, L., Sancho, L.G., Schulze-Makuch, D., Selbmann, L., Serrano, P., Szewzyk, U., Verseux, C., Wadsworth, J., Wagner, D., Westall, F., Wolter, D., Zucconi, L., 2019. Limits of Life and the Habitability of Mars: The ESA Space Experiment BIOMEX on the ISS, *Astrobiology* **19**, 145-157.

de Vries, S.T., 2004. Early Archaean sedimentary basins: depositional environment and hydrothermal systems. *Geologica Ultraiectina* **244**, 1–160.

de Vries, S.T., Nijman, W., de Boer, P.L., 2010. Sedimentary geology of the Palaeoarchaean Buck Ridge (South Africa) and Kittys Gap (Western Australia) volcano-sedimentary complexes. *Precambrian Research* **183**, 749–769.

de Wit, M.J., Hart, R.A., 1993. Earth's earliest continental lithosphere, hydrothermal flux and crustal recycling. *Lithos* **30**, 309–335.

de Wit, M., Hart, R., Martin, A., Abbott, P., 1982. Archean abiogenic and probable biogenic structures associated with mineralized hydrothermal vent systems and regional metasomatism, with implications for greenstone belt studies. *Economic Geology* **77**, 1783–1802.

de Wit, M.J., Furnes, H., 2016. 3.5-Ga hydrothermal fields and diamictites in the Barberton Greenstone Belt—Paleoarchean crust in cold environments. *Science Advances* **2**, e1500368.

Debaille, V., O'Neill, C., Brandon, A.D., Haenecour, P., Yin, Q.Z., Mattielli, N., Treiman, A.H., 2013. Stagnant-lid tectonics in early Earth revealed by Nd-142 variations in late Archean rocks. *Earth and Planetary Science Letters* **373**, 83–92.

Des Marais, D.J., Jakosky, B.M., Hynek, B.M., 2008. Astrobiological implications of Mars surface composition and properties. In The Martian Surface: Composition, Mineralogy and Physical Properties, J.A. Bell (Ed.), Cambridge Planetary Science Series 9, Cambridge University Press, New York, pp. 599–623.

Decho, A.W., 1990. Microbial exopolymer secretions in ocean environments: their role(s) in food webs and marine processes. *Oceanography and Marine Science Annual Review* **28**, 73153.

Decho, A.W., 2000. Microbial biofilms in intertidal systems: An overview. *Continental Shelf Research* **20**, 1257–1273.

Decho, A.W., Kawaguchi, T., 2003. Extracellular polymers (EPS) and calcification within modern marine stromatolites. In: Krumbein, W.E., Paterson, D.M., Zavarzin, G.A. (Eds.), Fossil and Recent Biofilms. Kluwer, Dordrecht, pp. 227–240.

Decho, A.W., Frey, R., Ferry, J., 2011. Chemical challenges to bacterial AHL signaling in the environment. *Chemical Reviews* **111**, 86–99.

Decker, N.B., Byerly, G.R., Stiegler, M.T., Lowe, D.R., Stefurak, E., 2015. High resolution tephra and U/Pb chronology of the 3.33e3.26 Ga Mendon formation, Barberton Greenstone Belt, South Africa. *Precambrian Research* **261**, 54–74.

Delarue, F., Rouzaud, J.-N., Derenne, S., Bourbin, M., Westall, F., Kremer, B., Sugitani, K., Deldicque, D., Robert, F., 2016. The Raman-derived carbonization continuum: a tool to select the best preserved molecular structures in Archean kerogens. *Astrobiology* **16**, 407–417.

Dhuime, D., Wuestefeld, A., Hawkesworth, C.J., 2015. Emergence of modern continental crust about 3 billion years ago. *Nature Geoscience* **8**, 552–555.

Douglas, S., Perry, M.E., Abbey, W.J., Tanaka, Z., Chen, B., McKay, C.P., 2015. The structure and chemical layering of Proterozoic stromatolites in the Mojave Desert. *International Journal of Astrobiology* **14**, 517–526.

Drabon, N., Lowe, D.R., Byerly, G.R., Harrington, J.A., 2017. Detrital zircon geochronology of sandstones of the 3.6–3.2 Ga Barberton greenstone belt: no evidence for older continental crust. *Geology* **45**, 803–806.

Djokic, T., Van Kranendonk, M.J., Campbell, K.A., Walter, M.R., Ward, C.R., 2017. Earliest signs of life on land preserved in c. 3.5 Ga hot spring deposits. *Nature Communications* **8**, 15263.

Doemel, W.N., Brock, T.D., 1977. Structure, growth and decomposition of laminated algal-bacterial mats in alkaline hot springs. *Appied Environmental Microbiology* **34**, 433–452.

Duda, J.-P., Thiel, V., Bauersachs, T., Mißbach, H., Reinhardt, M., Schäfer, N., Van Kranendonk, M.J., Reitner, J., 2018. Ideas and perspectives: hydrothermally driven redistribution and sequestration of early Archean biomass – the "hydrothermal pump hypothesis". *Biogeosciences* **15**, 1535–1548.

Dumas, S., Arnott, R.W.C., 2006. Origin of hummocky and swaley cross-stratification d the controlling influence of unidirectional current strength and aggradation rate. *Geology* **34**, 1073–1076.

Dupraz, C., Pattisina, R., Verrecchia, E., 2006. Translation of energy into morphology: Simulation of stromatolite morphospace using a stochastic model. *Sedimentary Geology* **185**, 185–203.

Dziggel, A., Stevens, G., Poujol, M., Anhaesser, C.R., Armstrong, R.A., 2002. Metamorphism of the granite-greenstone terrane south of the Barberton greenstone belt, South Africa: an insight into the tectono-thermal evolution of the 'lower' portions of the Onverwacht Group. *Precambrian Research* **114**, 221–247.

Dziggel, A., Stevens, G., Poujol, M., Armstrong, R.A., 2006. Contrasting source compositions of clastic metasedimentary rocks in the lowermost formations of the Barberton greenstone belt. In: Reimold, W.U., Gibson, R.L. (Eds.), Processes on the Early Earth. *Geological Society of America Special Paper* **405**, 157–172.

Edwards, N.P., Manning, P.L., Bergmann, U., Larson, P.L., van Dongen, B.E., Sellers, W.I., Webb, S.M., Sokaras, D., Alonso-Mori, R., Ignatyev, K., Barden, H.E., van Veelen, A., Anné, J., Egerton, V.M., Wogelius, R.A., 2014. Leaf metallome preserved over 50 million years. *Metallomics* **6**, 774–782.

Ehlmann, B.L., Edwards, C.S., 2014. Mineralogy of the Martian surface. *Annual Review of Earth and Planetary Sciences* **42**, 291–315.

Eigenbrode, J.L., Summons, R.E., Steele, A., Freissinet, C.,, Millan, M., Navarro-González, R., Sutter, B., McAdam, A.C., Franz, H.B., Glavin, D.P., Archer Jr., P.D., Mahaffy, P.R., Conrad, P.G., Hurowitz, J.A., Grotzinger, J.P., Gupta, S., Ming, D.W., Sumner, D.Y., Szopa, C., Malespin, C., Buch, A., Coll, P., 2018. Organic matter preserved in 3-billion-year-old mudstones at Gale crater, Mars. *Science* **360**, 1096–1101.

Elderfield, H., Upstill-Goddard, R., Sholkovitz, E.R., 1990. The rare earth elements in rivers, estuaries, and coastal seas and their significance to the composition of ocean waters. *Geochimica et Cosmochimica Acta* **54**, 971–991.

Engel, A.E.J., Nagy, B., Nagy, L.A., Engel, C.G., Kremp, G.O.W., Drew, C.M., 1968. Alga-like forms in Onverwacht Series, South Africa: oldest recognized lifelike forms on earth. *Science* **161**, 1005–1008.

Eriksson, K.A., 1978. Alluvial and destructive beach facies from the Archean Moodies Group, barberton mountain land, South Africa and Swaziland. In: Miall, A.D. (Ed.), Fluvial Sedimentology. *Canadian Society of Petroleum Geologists Memoir* **5**, 287–311.

Ernst, W.G., Sleep, N.H., Tsujimori, T., 2016. Plate-tectonic evolution of the earth: bottom-up and top-down mantle circulation. *Canadian Journal of Earth Sciences* **53**, 1103–1120.

Fairén, A.G., Davila, A.F., Lim, D., Bramall, N., Bonaccorsi, R., Zavaleta, J., Uceda, E.R., Stoker, C., Wierzchos, J., Dohm, J.M., Amils, R., Andersen, D., McKay, C.P., 2010. Astrobiology through the ages of Mars: the study of terrestrial analogues to understand the habitability of Mars. *Astrobiology* **10**, 821–843.

Fedo, C.M., Whitehouse, M.J., 2002. Metasomatic origin of quartz-pyroxene rock, Akilia, Greenland, and implications for Earth's earliest life. *Science* **296**, 1448–1452.

Fetisova, Z.G., Freiberg, A.M., Timpmann, K.E., 1988. Long-range molecular order as an efficient strategy for light harvesting in photosynthesis. *Nature* **334**, 633–634.

Flannery, D.T., Walter, M.R., 2011. Archean tufted microbial mats and the Great Oxidation Event: new insights into an ancient problem. *Australian Journal of Earth Sciences* **59**, 1–11.

Foing, B.H., Lillo, A., Jonglez, C., Offringa, M., Kamps, O., Guinet, V., Monnerie, M., Jehannin, B., Cowley, A., Kolodziejczyk, A., Harasymczuk, M., Stoker, C., Authier, L., Blanc, A., Chahla, C., Evellin, P., Neklesa, A., Preusterink, J., Tomic, A., Mirino, M., Hettrich, S., Lousada, J.L., Fonseka, M., Martinez, B., Decadi, A., 2011. EuroMoonMars Extreme Field Analogue Campaigns. https://www.cosmos.esa.int/documents/1566003/1643649/eslab2017-abstract+Foing+et+al+1.pdf/65ed88f6-43ea-a3b2-c2d8-9c708da840da

Foucher, F., Lopez-Reyes, G., Bost, N., Rull-Perez, F., Rüßmann, P., Westall, F., 2013. Effect of grain size distribution on Raman analyses and the consequences for in situ planetary missions. *Journal of Raman Spectroscopy* **44**, 916–925.

Foucher, F., Westall, F., Zipfel, J., Bost, N., and the EURO-CARES Team, 2017. General reflections on the definition of analogues and consequences for the EURO-CARES Project. *LPI contribution #3245*.

Foucher, F., Guimbretière, G., Bost, N., Westall, F., 2017. Petrographical and mineralogical applications of Raman mapping. In Raman Spectroscopy and Applications; Maaz, K., Ed.; Pakistan Institute of Nuclear Science and Technology: Nilore, Pakistan.

Foucher, F., Guimbretière, G., Bost, N., Courtois, A., Luengo, L., Marceau, E., Messori, F., Pelletier, S., Hickman-Lewis, K., Westall, F., 2018. CaliPhoto: an optical method to help identification of rocks during the ExoMars 2020 mission, 42nd Committee On Space Research Scientific Assembly Abstracts, B4.2-0006-18, 464-465.

Fraústo da Silva, J.J.R., Williams, R.J.P., 2001. The Biological Chemistry of the Elements; Oxford University Press, Oxford, UK, 2011, p. 600.

Freissinet, C., Glavin, D.P., Mahaffy, P.R., Miller, K.E., Eigenbrode, J.L., Summons, R.E., Brunner, A.E., Buch, A., Szopa, C., Archer, P.D., Franz, H.B., 2015. Organic molecules in the Sheepbed Mudstone, Gale Crater, Mars. *Journal of Geophysical Research Planets* **120**, 95–514.

Freslon, N., Bayon, G., Toucanne, S., Bermell, S., Bollinger, C., Chéron, S., Etoubleau, J., Germain, Y., Khripounoff, A., Ponzevera, E., Rouget, M.-L., 2014. Rare earth elements and neodymium isotopes in sedimentary organic matter. *Geochimica et Cosmochimica Acta* **140**, 177–198.

Friedrich, B., Schwartz, E., 1993. Molecular biology of hydrogen utilization in aerobic chemolithotrophs. *Annual Review of Microbiology* **47**, 351-383.

Furnes, H., Staudigel, H., 1999. Biological mediation in ocean crust alteration: how deep is the deep biosphere? *Earth and Planetary Science Letters* **166**, 97–103.

Furnes, H., Muehlenbachs, K., Tumyr, O., Torsvik, T., Thorseth, I.H., 1999. Depth of active bio-alteration in the ocean crust: Costa Rica Rift (Hole 504B). *Terra Nova* **11**, 228–233.

Furnes, H., Staudigel, H., Thorseth, I.H., Torsvik, T., Muehlenbachs, K., Tumyr, O., 2001. Bioalteration of basaltic glass in the oceanic crust. *Geochemistry Geophysics Geosystems* **2**. https://doi.org/10.1029/2000GC000150.

Furnes, H., Banerjee, N.R., Muehlenbachs, K., Staudigel, H., de Wit, M., 2004. Early life recorded in Archean pillow lavas. *Science* **304**, 578–581.

Furnes, H., Banerjee, N.R., Staudigel, H., Muehlenbachs, K., McLoughlin, N., de Wit, M., Van Kranendonk, M., 2007. Comparing petrographic signatures of bioalteration in recent to Mesoarchean pillow lavas: tracing subsurface life in oceanic igneous rocks. *Precambrian Research* **158**, 156–176.

Gamper, A., Heubeck, C., Demskec, D., 2012. Composition and microfacies of Archean microbial mats (Moodies Group, ca. 3.22 Ga, South Africa). In: Noffke, N., Chafetz, H. (Eds.), Microbial Mats in Siliciclastic Depositional Systems through Time. *SEPM Special Publication* **101**, 65–74.

Gao, S., Wedepohl, K.H., 1995. The negative Eu anomaly in Archean sedimentary rocks: Implications for decomposition, age and importance of their granitic sources. *Earth and Planetary Science Letters* **133**, 81–94.

Garvin, J.B., Head, J.W., Marchant, D.R., Kreslavsky, M.A., 2006. High-latitude cold-based glacial deposits on Mars: Multiple superposed drop moraines in a crater interior at 70°N latitude. *Meteoritics and Planetary Science* **41**, 1659–1674.

Gaucher, E.A.J.T., Kratzer, J.T., Randall, R.N., 2010. Deep Phylogeny—How a Tree Can Help Characterize Early Life on Earth. *Cold Spring Harbor Perspectives Biology* **2**, a002238.

Gautret, P., De Wit, R., Camoin, G., Golubic, S., 2006. Are environmental conditions recorded by the organic matrices associated with precipitated calcium carbonate in cyanobacterial microbialites? *Geobiology* **4**, 93–107.

Geesey, G.G., Jang, L., 1989. Interactions between metal ions and capsular polymers. In Metal Ions and Bacteria; Beveridge, T.J., Doyle, R.J. (Eds.), John Wiley and Sons: New York, NY, USA, 1989; pp. 325–358.

Gerdes, G., 2007. Structures left by modern microbial mats in their host sediments. In: Schieber, J., Bose, P.K., Eriksson, P.G., Banerjee, S., Sarkar, S., Altermann, W., Catuneanu, O. (Eds.), Atlas of Microbial Mat Features Preserved within the Siliciclastic Rock Record. Elsevier, Amsterdam, pp. 5–38.

Gerdes, G., Krumbein, W., 1987. Biolaminated Deposits. Springer-Verlag, Berlin.

Gerdes, G., Krumbein, W.E., Reineck, H.E., 1991. Biolaminations – ecological versus depositional dynamics. In: Einsele, G., Ricken, W., Seilacher, A. (Eds.), Cycles and events in stratigraphy. Springer, Berlin, pp. 592–607.

Gerdes, G., Klenke, T., 2007. States of biogenic bedding as records of the interplay of ecologic time and environment (a case study of modern siliciclastic sediments, Mellum Island, southern North Sea). *Senckenbergana Maritima* **37**, 129–144.

Gerdes, G., Noffke, N., Klenke, Th., 2000. Microbial biosignatures in peritidal siliciclastic sediments: a catalogue. *Sedimentology* **47**, 279–308.

Gíslason, S.R., Oelkers, E.H., 2003. Mechanism, rates and consequences of basaltic glass dissolution: II. An experimental study of the dissolution rates of basaltic glass as a function of pH and temperature. *Geochimica et Cosmochimica Acta* **67**, 3817–3832.

Glikson, M., Duck, L.J., Golding, S.D., Hofmann, A., Bolhar, R., Webb, R., Baiano, J.C.F., Sly, L.I., 2008. Microbial remains in some earliest Earth rocks: comparison with a potential modern analogue. *Precambrian Research* **164**, 187–200.

Goesmann, F., Brinckerhoff, W.B., Raulin, F., Goetz, W., Danell, R.M., Getty, S. A., Siljeström, S., Mißbach, H., Steininger, H., Arevalo Jr., R.D., Buch, A., Freissinet, C., Grubisic, A., Meierhenrich, U.J., Pinnick, V.T., Stalport, F., Szopa, C., Vago, J.L., Lindner, R., Schulte, M., Brucato, J.R., Glavin, D.P., Grand, N., Li, X., van Amerom, F.H.W., and the MOMA Science Team, 2017. The Mars Organic Molecule Analyzer (MOMA) Instrument: Characterization of Organic Material in Martian Sediments. *Astrobiology* **17**, 655–685.

Golombek, M., Grant, J., Kipp, D. et al., 2012. Selection of the Mars Science Laboratory landing site. *Space Science Reviews* **170**, 641–737.

Golubic, S., 1976. Organisms that build stromatolites. In: Walter, M.R. (Ed.), Stromatolites. Elsevier, Amsterdam, pp. 113–126.

Gorbunov, M.Y., Falkowski, P.G., 2004. Fluorescence induction and relaxation (FIRe) technique and instrumentation for monitoring photosynthetic processes and primary production in aquatic ecosystems. In Photosynthesis: Fundamental Aspects to Global Perspectives; Van der Est, A., Bruce, D., (Eds.), Alliance Communications Group: Lawrence, KS, USA; pp. 1029–1031.

Gourcerol, B., Thurston, P.C., Kontak, D.J., Côté-Mantha, O., 2015. Interpretations and implications of LA ICP-MS analysis of chert for the origin of geochemical signatures in banded iron formations (BIFs) from the Meadowbank gold deposit, Western Churchill Province, Nunavut. *Chemical Geology* **410**, 89–107.

Gourcerol, B., Thurston, P.C., Kontak, D., Côté-Mantha, O., Biczok, J., 2016. Depositional setting of Algoma-type banded iron formation. *Precambrian Research* **281**, 47–79.

Gourier, D., Binet, L., Calligaro, T., Capelli, S., Vezin, H., Bréhéret, J.G., Hickman-Lewis, K., Gautret, P., Foucher, F., Campbell, K.A., Westall, F. Extraterrestrial organic matter preserved in 3.33 Ga sediments from Barberton, South Africa. *Geochimica et Cosmochimica Acta* **258**, 207–225.

Grassineau, N.V., Nisbet, E.G., Fowler, C.M.R., Bickle, M.J., Lowry, D., Chapman, H.J., Mattey, D.P., Abell, P., Yong, J., Martin, A., 2002. Stable isotopes in the Archaean Belingwe belt, Zimbabwe: evidence for a diverse microbial mat ecology. *Geological Society, of London Special Publication* **199**, 309–328.

Grassineau, N.V., Appel, P.W.U., Fowler, C.M.R., Nisbet, E.G., 2005. Distinguishing biological from hydrothermal signatures via sulphur and carbon isotopes in Archaean mineralizations at 3.8 and 2.7 Ga. In McDonald, I., Boyce, A.J., Butler, I.B., Herrington, R.J., Polya, D.A. (Eds.) Mineral Deposits and Earth Evolution, *Geological Society of London Special Publication* **248**, 195–212.

Greco, F., Cavalazzi, B., Hofmann, A., Hickman-Lewis, K. Raman spectroscopy in palaeontology: a case study from Archaean biostructures. *Bollettino della Società Paleontologica Italiana* **57**, 59–74.

Grey, K., Sugitani, K., 2009. Palynology of Archean microfossils (c. 3.0 Ga) from the Mount Grant area, Pilbara Craton, Western Australia: further evidence of biogenicity. *Precambrian Research* **173**, 60–69.

Griffin, W.L., Belousova, E.A., O'Neill, C., O'Reilly, S.Y., Malkovets, V., Pearson, N.J., Spetsius, S., Wilde, S.A., 2014. The world turns over: Hadean–Archean crust–mantle evolution. *Lithos* **189**, 2–15.

Grosch, E.G., McLoughlin, N., 2014. Reassessing the biogenicity of Earth's oldest trace fossil with implications for biosignatures in the search for early life. *Proceedings of the National Academy of Sciences U.S.A.* **111**, 8380–8385.

Grosch, E.G., McLoughlin, N., 2015. Questioning the biogenicity of titanite mineral trace fossils in Archean pillow lavas. *Proceedings of the National Academy U.S.A.* 112, E3090-E3091.

Grosch, E.G., Hazen, R.M., 2015. Microbes, mineral evolution, and the rise of micro-continents—origin and coevolution of life with early earth. *Astrobiology* **15**, 922–939.

Grosch, E.G., Munõz, M., Mathon, O., McLoughlin, N., 2016. Earliest microbial trace fossils in Archaean pillow lavas under scrutiny: new micro-X-ray absorption near-edge spectroscopy, metamorphic and morphological constraints. *Geological Society London Special Publication* **448**, 57–70.

Grotzinger, J.P.; Rothman, D.H., 1996. An abiotic model for stromatolite morphogenesis. *Nature* **383**, 423–425.

Grotzinger, J.P., Knoll, A.H., 1999. Stromatolites in Precambrian carbonates: Evolutionary mileposts or environmental dipsticks? *Annual Review of Earth and Planetary Sciences* **27**, 313–358.

Grotzinger, J.P., Arvidson, R.E., Bell, J.F., Calvin, W., Clark, B.C., Fike, D.A., Golombek, M., Greeley, R., Haldemann, A., Herkenhoff, K.E., Jolliff, B.L., Knoll, A.H., Malin, M., McLennan, S.M., Parker, T., Soderblom, L., Sohl-Dickstein, J.N., Squyres, S.W., Tosca, N.J., Watters, W.A., 2005. Stratigraphy and sedimentology of a dry to wet eolian depositional system, Burns formation, Meridiani Planum, Mars. *Earth and Planetary Science Letters* **240**, 11–72.

Grotzinger, J.P., Sumner, D.Y., Kah, L.C., Stack, K., Gupta, S., Edgar, L., Rubin, D., Lewis, K., Schieber, J., Mangold, N., Milliken, R., Conrad, P.G., DesMarais, D., Farmer, J., Siebach, K., Calef, F., Hurowitz, J., McLennan, S.M., Ming, D., Vaniman, D., Crisp, J., Vasavada, A., Edgett, K.S., Malin, M., Blake, D., Gellert, R., Mahaffy, P., Wiens, R.C., Maurice, S., Grant, J.A., Wilson, S., Anderson, R.C., Beegle, L.W., Arvidson, R.E., Hallet, B., Sletten, R.S., Rice, M., Bell, J.F., III, Griffes, J., Ehlmann, B., Anderson, R.B., Bristow, T.F., Dietrich, W.E., Dromart, G., Eigenbrode, J., Fraeman, A., Hardgrove, C., Herkenhoff, K., Jandura, L., Kocurek, G., Lee, S., Leshin, L.A., Leveille, R., Limonadi, D., Maki, J., McCloskey, S., Meyer, M., Minitti, M., Newsom, H., Oehler, D., Okon, A., Palucis, M., Parker, T., Rowland, S., Schmidt, M., Squyres, S., Steele, A., Stolper, E., Summons, R., Treiman, A., Williams, R., Yingst, A., and the MSL Science Team, 2014. A habitable fluvio-lacustrine environment at Yellowknife Bay, Gale crater, Mars. *Science* **343**, 1242777.

Grotzinger, J.P., Gupta, S., Malin, M.C., Rubin, D.M., Schieber, J., Siebach, K., Sumner, D.Y., Stack, K.M., Vasavada, A.R., Arvidson, R.E., Calef, F., III, Edgar, L., Fischer, W.F., Grant, J.A., Griffes, J., Kah, L.C., Lamb, M.P., Lewis, K.W., Mangold, N., Minitti, M.E., Palucis, M., Rice, M., Williams, R.M.E., Yingst, R.A., Blake, D., Blaney, D., Conrad, P., Cirsp, J., Dietrich, W.E., Dromart, G., Edgett, K.S., Ewing, R.C., Gellert, R., Hurowitz, J.A., Kocurek, G., Mahaffy, P., McBride, M.J., McLennan, S.M., Mischna, M., Ming, D., Milliken, R., Newsom, H., Oehler, D., Parker, T.J., Vaniman, D., Wiens, R.C., Wilson, S.A., 2015. Deposition, exhumation, and paleoclimate of an ancient lake deposit, Gale Crater, Mars. *Science* **350**, 177–188.

Gupta, P., Diwan, B., 2017. Bacterial Exopolysaccharide mediated heavy metal removal: a review on biosynthesis, mechanism and remediation strategies. *Biotechnology Reports* **13**, 58–71.

Halden, N.M., Campbell, J.L., Teesdale, W.J., 1995. PIXE microanalysis in mineralogy and petrology. *Canadian Mineralogist* **33**, 293–302.

Hamon, A.-L., Verbeeck, J., Schryvers, D., Benedikt, J., van der Sanden, R.M.C.M., 2004. ELNES study of carbon K-edge spectra of plasma deposited carbon films. *Journal of Materials Chemistry* **13**, 2030–2035.

Hanor, J.S., Duchac, K.C., 1990. Isovolumetric silicification of early Archean komatiites; geochemical mass balances and constraints on origin. *Journal of Geology* **98**, 863–877.

Harazim, D., Callow, R.H.T., McIlroy, D., 2013. Microbial mats implicated in the generation of intrastratal shrinkage (synaeresis) cracks. *Sedimentology* **60**, 1621–1638.

Harwood, C.L., Sumner, D.Y., 2012. Origins of microbial microstructures in the Neoproterozoic Back Spring Dolomite: Variations in microbial community and timing of lithification. *Journal of Sedimentary Research* **82**, 709–722.

Harrison, T.M., 2009. The Hadean crust: Evidence from >4 Ga zircons. *Annual Review of Earth and Planetary Sciences* **37**, 479–505.

Hays, L.E., Graham, H.V., Des Marais, D.J., Hausrath, E.M., Horgan, B., McCollom, T.M., Parenteau, M.N., Potter-McIntyre, S.L., Williams, A.J., Lynch, K.L., 2017. Biosignature preservation and detection in Mars analog environments. *Astrobiology* **17**, 363–400.

Head, J.W., Marchant, D.R., Agnew, M.C., Fassett, C.I., Kreslavsky, M.A., 2006. Extensive valley glacier deposits in the northern mid-latitudes of Mars: evidence for Late Amazonian obliquity-driven climate change. *Earth and Planetary Science Letters* **241**, 663–671.

Head, J., Forget, F., Wordsworth, R., Turbet, M., Cassanelli, J., Palumbo, A., 2019. Oceans on Mars: history, evidence, problems and prospects. *LPI Contribution #6108*.

Hessler, A.M., Lowe, D.R., Jones, R.L., Bird, D.K., 2004. A lower limit for atmospheric carbon dioxide levels 3.2 billion years ago. *Nature* **428**, 736–738.

Heubeck, C., 2009. An early ecosystem of Archean tidal microbial mats (Moodies Group, South Africa, ca. 3.2 Ga. *Geology* **37**, 931–934.

Heubeck, C., Lowe, D.R., 1994. Late syndepositional deformation and detachment tectonics in the Barberton Greenstone Belt, South Africa. *Tectonics* **13**, 1514–1536.

Heubeck, C., Lowe, D.R., 1994. Depositional and tectonic setting of the Archean Moodies Group, Barberton Greenstone Belt, South Africa. *Precambrian Research* **68**, 257–290.

Hickman, A.H., 2012, Review of the Pilbara Craton and Fortescue Basin: crustal evolution providing environments for early life. *Island Arc* **21**, 1–31.

Hickman-Lewis, K., Garwood, R.J., Brasier, M.D., Goral, T., Jiang, H., McLoughlin, N., Wacey, D., 2016. Carbonaceous microstructures of the 3.46 Ga stratiform 'Apex chert', Chinaman Creek locality, Pilbara, Western Australia. *Precambrian Research* **278**, 161–178.

Hickman-Lewis, K., Garwood, R.J., Withers, P.J., Wacey, D., 2016. X-ray microtomography as a tool for investigating the petrological context of Precambrian cellular remains. In: Brasier, A.T., McIlroy, D., McLoughlin, N. (Eds.), Earth System Evolution and Early Life: A Celebration of the Work of Martin Brasier, *Geological Society of London Special Publication* **448**, 33–56.

Hickman-Lewis, K., Cavalazzi, B., Foucher, F., Westall, F., 2018. Most Ancient Evidence for Life in the Barberton Greenstone Belt: Microbial Mats and Biofabrics of the ~3.47 Ga Middle Marker Horizon. *Precambrian Research* **312**, 45–67.

Hickman-Lewis, K., Westall, F., Cavalazzi, B., 2018. Trace of Early Life in the Barberton Greenstone Belt. In Earth's Oldest Rocks, Second Edition (Eds. Van Kranendonk, M.J., Bennett, V.C., Hofmann, J.E.), pp. 1029–1058.

Hickman-Lewis, K., Gautret, P., Arbaret, L., Sorieul, S., De Wit, R., Foucher, F., Cavalazzi, B., Westall, F., 2019. Mechanistic morphogenesis of organo-sedimentary structures growing under geochemically stressed conditions: keystone to the interpretation of some Archaean stromatolites? *Geosciences* **9**, 359.

Hofmann, H.J., 1973. Stromatolites: Characteristics and utility. *Earth-Science Reviews* **9**, 339–373.

Hofmann, H.J. Grey, K. Hickman, A.H. Thorpe, R.I., 1999. Origin of 3.45 Ga coniform stromatolites in Warrawoona Group, Western Australia. *GSA Bulletin* **111**, 1256–1262.

Hofmann, A., 2005. The geochemistry of sedimentary rocks from the Fig Tree Group, Barberton greenstone belt: implications for tectonic, hydrothermal and surface processes during mid-Archaean times. *Precambrian Research* **143**, 23–49.

Hofmann, A., 2011. Archaean hydrothermal systems in the Barberton greenstone belt and their significance as a habitat for early life. In: Golding, S.D., Glikson, M. (Eds.), Earliest Life on Earth: Habitats, Environments and Methods of Detection. Springer, pp. 51–78.

Hofmann, A., Bolhar, R., 2007. The origin of carbonaceous cherts in the Barberton Greenstone Belt and their significance for the study of early life in mid-Archaean rocks. *Astrobiology* **7**, 355–388.

Hofmann, A., Wilson, A.H., 2007. Silicified basalts, bedded cherts and other sea floor alteration phenomena of the 3.4 Ga Nondweni greenstone belt, South Africa. In: Van Kranendonk, M.J., Smithies, R.H., Bennett, V.H. (Eds.), Earth's Oldest Rocks. Elsevier (Developments in Precambrian Geology), Amsterdam, pp. 570–605.

Hofmann, A., Harris, C., 2008. Stratiform alteration zones in the Barberton greenstone belt: a window into subseafloor processes 3.5 to 3.3 Ga ago. *Chemical Geology* **257**, 224–242.

Hofmann, A., Bolhar, R., Orberger, B., Foucher, F., 2013. Cherts of the Barberton greenstone belt, South Africa: petrology and trace-element geochemistry of 3.5 to 3.3 Ga old silicified volcaniclastic sediments. *South African Journal of Geology* **116**, 297–322.

Homann, M., Heubeck, C., Airo, A., Tice, M.M., 2015. Morphological adaptations of 3.22 Ga-old tufted microbial mats to Archean coastal habitats (Moodies Group, Barberton Greenstone Belt, South Africa). *Precambrian Research* **266**, 47–64.

Homann, M., Heubeck, C., Bontognali, T.R.R., Bouvier, A.-S., Baumgartner, L.P., Airo, A., 2016. Evidence for cavity-dwelling microbial life in 3.22 Ga tidal deposits. *Geology* **44**, 51–54.

Homann, M., Sansjofre, P., van Zuilen, M., Heubeck, C., Gong, J., Killingsworth, B., Foster, I.S., Airo, A., Van Kranendonk, M.J., Ader, M., Lalonde, S.V., 2018. Microbial life and biogeochemical cycling on land 3,220 million years ago. *Nature Geoscience* **11**, 665–671.

House, C.H., Oehler, D.Z., Sugitani, K., Mimura, K., 2013. Carbon isotopic analyses of ca. 3.0 Ga microstructures imply planktonic autotrophs inhabited Earth's early oceans. *Geology* **41**, 651–654.

Hoyle, J., Elderfield, H., Gledhill, A., Greaves, M., 1984. The behavior of the rare earth elements during mixing of river and sea waters. *Geochimica et Cosmochimica Acta* **48**, 143–149.

Hren, M.T., Tice, M.M., Chamberlain, C.P., 2009. Oxygen and hydrogen isotope evidence for a temperate climate 3.42 billion years ago. *Nature* **205**, 205–208.

Hubert, A., 2015. Chemical and mineralogical signatures of oxygenic photosynthesis in Archean and Paleoproterozoic sediments. Ph.D. Thesis, University of Orléans, pp. 333.

Hurley, P.M., Pinson Jr., W.H., Nagy, B., Teska, T.M., 1972. Ancient age of the Middle Marker horizon, Onverwacht Group, Swaziland Sequence, South Africa. *Earth and Planetary Science Letters* **14**, 360–366.

Igisu, M., Ueno, Y., Takai, K., 2018. FTIR microspectroscopy of carbonaceous matter in ~ 3.5 Ga seafloor hydrothermal deposits in the North Pole area, Western Australia. *Progress in Earth and Planetary Science* 5, 85.

Jakosky, B.M., Grebowsky, J.M., Luhmann, J.G., Brain, D.A., 2015. Initial results from the MAVEN mission to Mars. *Geophysical Research Letters* **42**, 8791–8802.

Jakosky, B.M., Slipski, M., Benna, M., Mahaffy, P., Elrod, M., Yelle, R., Stone, S., Alsaeed, N., 2017. Mars' atmospheric history derived from upper-atmosphere measurements of $^{38}Ar/^{36}Ar$. *Science* **355**, 1408–1410.

Javaux, E.J., Marshall, C.P., Bekker, A., 2010. Organic-walled microfossils in 3.2-billion-year-old shallow-marine siliciclastic deposits. *Nature* **463**, 934–938.

Jeandel, C., Oelkers, E.H., 2015. The influence of terrigenous particulate material dissolution on ocean chemistry and global element cycles. *Chemical Geology* **395**, 50–66.

Jones, B., Renaut, R.W., 2004. Hot spring and geyser sinters: the integrated product of precipitation, replacement, and deposition. *Canadian Journal of Earth Sciences* **40**, 1549–1569.

Josset, J.-L., Westall, F., Hofmann, B.A., Spray, J., Cockell, C.S., Kempe, S., Griffiths, A.D., De Sanctis, M.C., Colangeli, L., Koschny, D., Föllmi, K., Verrecchia, E., Diamond, L., Josset, M., Javaux, E.J., Esposito, F., Gunn, M., Souchon-Leitner, A.L., Bontognali, T.R.R., Korablev, O., Erkman, S., Paar, G., Ulamec, S., Foucher, F., Martin, P., Verhaeghe, A., Tanevski, M., Vago J.L., 2017. The Close-Up Imager onboard the ESA ExoMars rover: Objectives, description, operations, and science validation activities. *Astrobiology* **17**, 595–611.

Juniper, S.K., Martineu, P., Sarrazin, J., Gélinas, Y., 1995. Microbial-mineral floc associated with nascent hydrothermal activity on CoAxial Segment, Juan de Fuca Ridge. *Geophysical Research Letters* **22**, 179–182.

Kamber, B.S., Webb, G.E., 2001. The geochemistry of late Archean microbial carbonate: implications for ocean chemistry and continental erosion history. *Geochimica et Cosmochimica Acta* **65**, 2509–2525.

Kamber, B.S., Collerson, K.D., Moorbath, S., Whitehouse, M.J., 2003. Inheritance of early Archaean Pb-isotope variability from long-lived Hadean protocrust. *Contributions to Mineralogy and Petrology* **145**, 25–46.

Kamber, B.S., Bolhar, R., Webb, G.E., 2004. Geochemistry of late Archaean stromatolites from Zimbabwe: evidence for microbial life in restricted epicontinental seas. *Precambrian Research* **132**, 379–399.

Kamber, B.S., Greig, A., Collerson, K.D., 2005. A new estimate for the composition of weathered young upper continental crust from alluvial sediments, Queensland, Australia. *Geochimica et Cosmochimica Acta* **69**, 1041–1058.

Kamber B.S, 2015. The evolving nature of terrestrial crust from the Hadean, through the Archaean, into the Proterozoic. *Precambrian Research* **258**, 48–82.

Kamekura, M., 1998. Diversity of extremely halophilic bacteria. *Extremophiles* **2**, 289–295.

Kapui, Zs., Kereszturi, A., Kiss, K., Szalai, Z., Újvári, G., Hickman-Lewis, K., Foucher, F., Westall, F., 2018. Fluvial or aeolian grains? Separation of transport agents on Mars using earth analogue observations. *Planetary and Space Science* **163**, 56–76.

Karatan, E., Watnick, P., 2009. Signals, regulatory networks, and materials that build and break bacterial biofilms. *Microbiology and Molecular Biology Reviews* **72**, 310–347.

Kardar, M., Parisi, G., Zhang, Y.-C., 1986. Dynamic scaling of growing interfaces. *Physical Review Letters* **56**, 889.

Kasting, J.F., 1993. Earth's early atmosphere. *Science* **259**, 920–926.

Kazmierczak, J., Kempe, S., 2006. Genuine modern analogues of Precambrian stromatolites from caldera lakes of Niuafo'ou Island, Tonga. *Naturwissenschaften* **93**, 119–126.

Kelly, L.C., Cockell, C.S., Thorsteinsson, T., Marteinsson, V., Stevenson, J., 2014. Pioneer microbial communities of the Fimmvörðuháls lava flow, Eyjafjallajökull, Iceland. *Microbial Ecology* **68**, 504–518.

Kemp, A.I.S., Wilde, S.A., Hawkesworth, C.J., Coath, C.D., Nemchin, A., Pidgeon, R.T., Vervoort, J.D., and DuFrane, S.A., 2010. Hadean crustal evolution revisited: new constraints from Pb–Hf isotope systematics of the Jack Hills zircons. *Earth and Planetary Science Letters* **296**, 45–56.

Kempe, S., Degens, E.T., 1985. An early soda ocean? *Chemical Geology* **53**, 95–108.

Kempe, A., Wirth, R., Altermann, W., Stark, R.W., Schopf, J.W., Heckl, W.M., 2005. Focussed ion beam preparation and in situ nanoscopic study of Precambrian acritarchs. *Precambrian Research* **140**, 36–54.

Kerrich, R., Said, N., Manikyamba, C., Wyman, D., 2013. Sampling oxygenated Archean hydrosphere: Implication from fractionations of Th/U and Ce/Ce* in hydrothermally altered volcanic sequences. *Gondwana Research* **23**, 506–525.

Ketcham, R.A., Carlson, W.D., 2011. Acquisition, optimization and interpretation of X-ray computed tomographic imagery: Applications to the geosciences. *Computers & Geosciences* **27**, 381–400.

Kite, E.S., 2019. Geologic constraints on Early Mars climate. *Space Science Reviews* **215**, 10.

Klinkhammer, G.P., Elderfield, H., Edmond, J.M., Mitra, A., 1994. Geochemical implications of rare earth element patterns in hydrothermal fluids from mid-ocean ridges. *Geochimica et Cosmochimica Acta* **58**, 5105–5103.

Kminek, G., Bada, J.L., 2006. The effect of ionizing radiation on the preservation of amino acids on Mars. *Earth and Planetary Science Letters* **245**, 1–5.

Knauth, L.P., 2005. Temperature and salinity history of the Precambrian ocean: Implications for the course of microbial evolution. *Palaeogeography Palaeoclimatology Palaeoecology* **219**, 53–69.

Knoll, A.H., Barghoorn, E.S., 1977. Archean microfossils showing cell division from the Swaziland system of South Africa. *Science* **198**, 396–398.

Knoll, A.H., Strother, P.K., Rossi, S., 1988. Distribution and diagenesis of microfossils from the Lower Proterozoic Duck Creek Dolomite, Western Australia. *Precambrian Research* **38**, 257–279.

Knoll, A.H., Bergmann, K.D., Strauss, J.V., 2016. Life: The first two billion years. *Philosophical Transaction of the Royal Society of London B*, **371**.

Koeberl, C., 2006. The record of impact processes on the early Earth—a review of the first 2.5 billion years. In Processes of the Early Earth. In Reimold, W.U., Gibson, R.L., *Geological Society of America Special Paper* **405**, 1–22.

Konhauser, K.O., 2007. Introduction to Geomicrobiology. Wiley, pp. 440.

Konhauser, K.O., Jones, B., Reysenbach, A.-L., Renaut, R.W., 2003. Hot spring sinters: keys to understanding Earth's earliest life forms. *Canadian Journal of Earth Sciences* **40**, 1713–1724.

Korablev, O.I., Dobrolensky, Y., Evdokimova, N., Fedorova, A.A., Kuzmin, R.O., Mantsevich, S.N., Cloutis, E.A., Carter, J., Poulet, F., Flahaut, J., Griffiths, A., Gunn, M., Schmitz, N., Martín-Torres, J., Zorzano, M.-P., Rodionov, D.S., Vago, J.L., Stepanov, A.V., Titov, A.Y., Vyazovetsky, N.A., Trokhimovskiy, A.Y., Sapgir, A.G., Kalinnikov, Y.K., Ivanov, Y.S., Shapkin, A.I., Ivanov, A.Y., 2017. Infrared Spectrometer for ExoMars: A mast-mounted instrument for the rover. *Astrobiology* **17**, 542–564.

Kose, S.H., George, S.C., Lau, I.C., 2016. Distinguishing in situ stromatolite biosignatures from silicification and dolomitisation using short wave, visible-near and thermal infrared spectroscopy: a Mars analogue study. *Vibrational Spectroscopy* **87**, 67–80.

Kremer, B., Kazmierczak, J., 2017. Cellularly preserved microbial fossils from ~3.4 Ga deposits of South Africa: a testimony of early appearance of oxygenic life? *Precambrian Research* **295**, 117–129.

Kröner, A., Byerly, G.R., Lowe, D.R., 1991. Chronology of early Archaean granite-greenstone evolution in the Barberton Mountain Land, South Africa, based on precise dating by single zircon evaporation. *Earth and Planetary Science Letters* **103**, 41–54.

Kröner, A., Hegner, E., Wendt, J.I., Byerly, G.R., 1996. The oldest part of the Barberton granitoid-greenstone terrain, South Africa: evidence for crust formation between 3.5 and 3.7 Ga. *Precambrian Research* **78**, 105–124.

Kronyak, R.E., Kah, L.C., Edgett, K.S., VanBommel, S.J.,Thompson, L.M., Wiens, R.C., Sun, V.Z., Nachon, M., 2019. Mineral-filled fractures as indicators of multigenerational fluid flow in the Pahrump Hills Member of the Murray Formation, Gale Crater, Mars. *Earth and Space Science* **6**, 238–265.

Lammer, H., Bredehöft, J.H. Coustenis, A. Khodachenko, M.L. Kaltenegger, L. Grasset, O. Prieur, D. Raulin, F. Ehrenfreund, P. Yamauchi, M. Wahlund, J.-E. Grießmeier, J.-M. Stangl, G. Cockell, C.S. Kulikov, Yu.N. Grenfell, J.L. Rauer, H., 2009. What makes a planet habitable? *Astronomy and Astrophysics Reviews* **17**, 181–249.

Langenhorst, F., Solozhenko, V.L., 2002. ATEM-EELS study of new diamond-like phases in the B–C–N system. *Physical Chemistry Chemical Physics* **20**, 5183–5188.

Lanier, W.P., 1986. Approximate growth rates of Early Proterozoic Microstromatolites as deduced by biomass productivity. *Palaios* **1**, 525–542.

Lanier, W.P., Lowe, D.R., 1982. Sedimentology of the middle marker (3.4 Ga), Onverwacht Group, Transvaal, South Africa. *Precambrian Research* **18**, 237–260.

Lawrence, M.G., Kamber, B.S., 2006. The behavior of the rare earth elements during estuarine mixing — revisited. *Marine Chemistry* **100**, 147–161.

Lawrence, M.G., Grieg, A., Collerson, K.D., Kamber, B.S., 2006. Rare earth element and yttrium variability in South East Queensland waterways. *Aquatic Geochemistry* **12**, 39–72.

Le Guillou, C., Rouzaud, J.-N., Bonal, L., Quirico, E., Derenne, S., Remusat, L., 2012. High resolution TEM of chondritic carbonaceous matter: Metamorphic evolution and heterogeneity. *Meteoritics and Planetary Science* **47**, 345–362.

Le Maitre, R.W., 2002. Igneous Rocks: A classification and glossary of terms. Recommendations of the International Union of Geological Sciences Subcommission on the Systematics of Igneous Rocks, 2nd Edition, 236 pp. Cambridge.

Ledevin, M., 2018. Archean cherts: Formation processes and paleoenvironments. In Earth's Oldest Rocks, Second Edition (Eds. Van Kranendonk, M.J., Bennett, V.C., Hofmann, J.E.), pp. 913–944.

Ledevin, M., Arndt, N., Simionovici, A., Jaillard, E., Ulrich, M., 2014. Silica precipitation triggered by clastic sedimentation in the Archean: new petrographic evidence from cherts of the Kromberg type section, South Africa. *Precambrian Research* **255**, 316–334.

Lemelle, L., Labrot, P., Salomé, M., Simionovici, A., Viso, M., Westall, F., 2008. In situ imaging of organic sulfur in 700-800 My-old Neoproterozoic microfossils by X-ray spectromicroscopy at the S K-edge. *Organic Geochemistry* **39**, 188-202.

Lenton, T.M., Daines, S.J., 2016. Matworld – the biogeochemical effects of early life on land. *New Phytologist*, doi: 10.1111/nph.14338

Lepot, K., Williford, K.H., Ushikubo, T., Sugitani, K., Mimura, K., Spicuzza, M.J., Valley, J.W., 2013. Texture-specific isotopic compositions in 3.4 Gyr old organic matter support selective preservation in cell-like structures. *Geochimica et Cosmochimica Acta* **112**, 66–86.

Lespade, P., Al-Jishi, R., Dresselhaus, M.S., 1982. Model for Raman scattering from incompletely graphitized carbons. *Carbon* **20**, 427–431.

Liermann, L.J., Hausrath, E.M., Anbar, A.D., Brantley, S.L., 2007. Assimilatory and dissimilatory processes of microorganisms affecting metals in the environment. *Journal of Analytical Atomic Spectrometry* **22**, 867–877.

Lin, Q., Wang, J., Algeo, T.J., Sun, F., Lin, R., 2016. Enhanced framboidal pyrite formation related to anaerobic oxidation of methane in the sulfate-methane transition zone of the northern South China Sea. *Marine Geology* **379**, 100–108.

Lindsay, J.F., Brasier, M.D., McLoughlin, N., Green, O.R., Fogel, M.L., Steele, A., Mertzman, S.A., 2005. The problem of deep carbon—An Archean paradox. *Precambrian Research* **143**, 1–22.

Loaëc, M., Olier, R., Guezennec, J., 1998. Chelating properties of bacterial exopolysaccharides from deep-sea hydrothermal vents. *Carbohydrate Polymers* **35**, 65–70.

Lobinski, R., Becker, J.S., Haraguchi, H., Sarkar, B., 2010. Metallomics: Guidelines for terminology and critical evaluation of analytical chemistry approaches (IUPAC Technical Report). *Pure and Applied Chemistry* **82**, 493–504.

Londry, K.L., Des Marais, D.J., 2003. Stable carbon isotope fractionation by sulfate-reducing bacteria. *Applied and Environmental Microbiology* **69**, 2942–2949.

Lowe, D.R., Abiological origin of described stromatolites older than 3.2 Ga. *Geology* **22**, 387–390.

Lowe, D.R., 1999. Petrology and sedimentology of cherts and related silicified sedimentary rocks in the Swaziland Supergroup. In: Lowe, D.R., Byerly, G.R. (Eds.), Geologic Evolution of the Barberton Greenstone Belt, South Africa. *Geological Society of America Special Paper* **329**, pp. 83–114.

Lowe D.R., 1999. Geologic evolution of the Barberton Greenstone Belt and vicinity. In Lowe, D.R., Byerly, G.R. (Eds.) Geologic evolution of the Barberton Greenstone Belt, South Africa. *Geological Society of America Special Paper* **329**, pp. 287–312.

Lowe, D.R., Knauth, L.P., 1977. Sedimentology of the Onverwacht Group (3.4 billion years), Transvaal, South Africa, and its bearing on the characteristics and evolution of the early Earth. *Journal of Geology* **85**, 699–723.

Lowe, D.R., Knauth, L.P., 1978. The oldest marine carbonate ooids reinterpreted as volcanic accretionary lapilli: Onverwacht Group, South Africa. *Journal of Sedimentary Petrology* **48**, 709–722.

Lowe, D.R., Byerly, G.R., 1999. Stratigraphy of the west-central part of the Barberton Greenstone Belt, South Africa. In: Lowe, D.R., Byerly, G.R. (Eds.), Geologic Evolution of the Barberton Greenstone Belt, South Africa. *Geological Society of America Special Paper 329*, pp. 1–36.

Lowe, D.R., Fisher Worrell, G., 1999. Sedimentology, mineralogy, and implications of silicified evaporites in the Kromberg Formation, Barberton Greenstone Belt, South Africa. In: Lowe, D.R., Byerly, G.R. (Eds.), Geologic Evolution of the Barberton Greenstone Belt, South Africa. *Geological Society of America Special Paper* **329**, pp 167–188.

Lowe, D.R., Nocita, B.W., 1999. Foreland basin sedimentation in the Mapepe formation, southern-facies Fig Tree Group. In: Lowe, D.R., Byerly, G.R. (Eds.), Geologic Evolution of the Barberton Greenstone Belt, South Africa, *Geological Society of America Special Paper* **329**, pp. 233–258.

Lowe, D.R., Byerly, G.R., 2007. An overview of the geology of the Barberton Greenstone Belt and vicinity: implications for early crustal development. In: Van Kranendonk, M.J., Smithies, R.H., Bennett, V.H. (Eds.), Earth's Oldest Rocks. Elsevier (Developments in Precambrian Geology), Amsterdam, pp. 481–526.

Lowe, D.R., Tice, M.M., 2007. Tectonic controls on atmospheric, climatic, and biological evolution 3.5–2.4 Ga. *Precambrian Research* **158**, 177–197.

Lowe, D.R., Byerly, G.R., 2015. Geologic record of partial ocean evaporation triggered by giant asteroid impacts, 3.29-3.23 billion years ago. *Geology* **43**, 535–538.

Lowe, D.R., Byerly, G.R., Kyte, F.T., Shukolyukov, A., Asaro, F., Krull, A., 2003. Spherule beds 3.47–3.24 billion years old in the Barberton Greenstone Belt South Africa: a record of large meteorite impacts and their influence on early crustal and biological evolution. *Astrobiology* **3**, 7–48.

Lowe, B.R., Byerly, G.R., Heubeck, C., 2012. Geologic map of the west-central Barberton Greenstone Belt. In: Geological Society of America Map and Chart Series MCH103, 1 Sheet, Scale 1:25,000.

Malin, M.C., Edgett, K.S., 2003. Evidence for persistent flow and aqueous sedimentation on Early Mars. *Science* **302**, 1931–1934.

Maliva, R.G., Knoll, A.H., Simonson, B.M., 2005. Secular change in the Precambrian silica cycle: insights from chert petrology. *Geological Society of America Bulletin* **117**, 835–845.

Mangold, N., Schmidt, M.E., Fick, M.R., Forni, O., McLennan, S.M., Ming, D.W., Sautter, V., Sumner, D., Williams, J.A., Clegg, S.M., Cousin, A., Gasnault, O., Gelleter, R., Grotzinger, J.P., Wiens, R.C., 2017. Classification scheme for sedimentary and igneous rocks in Gale crater, Mars. *Icarus* **284**, 1–17.

Marchi, S., Bottke, W.F., Elkins-Tanton, L.T., Bierhaus, M., Wuennemann, K., Morbidelli, A., Kring, D.A., 2014. Widespread mixing and burial of Earth's Hadean crust by asteroid impacts. *Nature* **511**, 578–582.

Margulis, L., Barghoorn, E.S., Ashendorf, D., Banerjee, S., Chase, D., Francis, S., Giovannoni, S., Stolz, J., 1983. The microbial community in the layered sediments at Laguna Fugueroa, Baja California, Mexico: does it have Precambrian analogues? *Precambrian Research* **11**, 93–123.

Margulis, L., Grosovsky, B.D.D., Stolz, J.F., Gong-Collins, E.J., Lenk, S., 1983. Distinctive microbial structures and the pre-Phanerozoic fossil record. *Precambrian Research* **20**, 443–477.

Marin-Carbonne, J., Robert, F., Chaussidon, M., 2014. The silicon and oxygen isotope compositions of Precambrian cherts: a record of oceanic paleo-temperatures? *Precambrian Research* **247**, 223–234.

Marshall, C.P., Love, G.D., Snape, C.E., Hill, A.C., Allwood, A.C., Walter, M.R., Van Kranendonk, M.J., Bowden, S.A., Sylva, S.P., Summons, R.E., 2007. Structural characterization of kerogen in 3.4 Ga Archaean cherts from the Pilbara Craton, Western Australia. *Precambrian Research* **155**, 1–23.

Marshall, C.P., Olcott Marshall, A., Aitken, J.B., Lai, B., Vogt, S., Breuer, P., Steemans, P., Lay, P.A., 2017. Imaging of vanadium in microfossils: a new potential biosignature. *Astrobiology* **17**, 1069–1076.

Maurette, M. Brack, A., 2006. Cometary petroleum in Hadean time? *Meteoritics and Planetary Science* **41**, 5247.

Martins, Z., Cottin, H., Kotler, J.M., Carrasco, N., Cockell, C.S. et al., 2017. Earth as a Tool for Astrobiology - A European Perspective. *Space Science Reviews* **209**, 43-81.

Maxwell, J.A., Teesdale, W.J., Campbell, J.L., 1995. The Gupix PIXE software package II. *Nuclear Instruments and Methods in Physics Research B* **95**, 407–421.

Mayer, M., 1999. SIMNRA, a simulation program for the analysis of NRA, RBS and ERDA. *AIP Conference Proceedings* **475**, 541.

McCollum, T.M., Amend, J.P., 2005. A thermodynamic assessment of energy requirements for biomass synthesis by chemolithoautotrophic micro-organisms in oxic and anoxic environments. *Geobiology* **3**, 135–144.

McCollum, T.M., Seewald, J.S., 2006. Carbon isotope composition of organic compounds produced by abiotic synthesis under hydrothermal conditions. *Earth and Planetary Science Letters* **243**, 74–84.

McKay, D.S., Gibson, E.K. Jr, Thomas-Keprta, K.L., Vali, H., Romanek, C.S., Clemett, S.J., Chillier, X.D.F., Maechling, C.R., Zare, R.N., 1996. Search for past life on Mars: possible relic biogenic activity in Martian meteorite ALH84001. *Science* **273**, 924–930.

McLennan, S.M., Bell, J.F., Calvin, W.M., Christensen, P.R., Clark, B.C., de Souza, P.A., Farmer, J., Farrand, W.H., Fike, D.A., Gellert, R., Ghosh, A., Glotch, T.G., Grotzinger, J.P., Hahn, B., Herkenhoff, K.E., Hurowitz, J.A., Johnson, J.R., Johnson, S.S., Jolliff, B., Klingelhöfer, G., Knoll, A.H., Learner, Z., Malin, M.C., McSween, H.Y., Pocock, J., Ruff, S.W., Soderblom, L.A., Squyres, S.W., Tosca, N.J., Watters, W.A., Wyatt, M.B., Yen, A., 2005. Provenance and diagenesis of the evaporite-bearing Burns formation, Meridiani Planum, Mars. *Earth and Planetary Science Letters* **240**, 95–121.

McLoughlin, N., Wilson, L.A., Brasier, M.D., 2008. Growth of synthetic stromatolites and wrinkle structures in the absence of microbes – Implications for the early fossil record. *Geobiology* **6**, 95–105.

McLoughlin, N., Grosch, E.G., 2014. A hierarchical system for evaluating the biogenicity of metavolcanic- and ultramafic-hosted microalteration textures in the search for extraterrestrial life. *Astrobiology* **15**, 901–921.

McLoughlin, N., Staudigel, H., Furnes, H., Eickmann, B., Ivarsson, M., 2010. Mechanisms of microtunneling in rock substrates: distinguishing endolithic biosignatures from abiotic microtunnels. *Geobiology* **8**, 245–255.

McLoughlin, N., Grosch, E.G., Kilburn, M.R., Wacey, D., 2012. Sulfur isotope evidence for a Paleoarchean subseafloor biosphere, Barberton, South Africa. *Geology* **40**, 1031–1034.

McMahon, S., Hood, A.v.S., McIlroy, D., 2016. The origin and occurrence of subaqueous sedimentary cracks. In: Brasier, A.T., McIlroy, D., McLoughlin, N. (Eds.), Earth System Evolution and Early Life: A Celebration of the Work of Martin Brasier. *Geological Society of London Special Publication* **448**, *285–309.*

McSween, H.Y., 2015. Petrology on Mars. *American Mineralogist* **100**, 2380-2395.

McSween, H.Y., Taylor, G.J., Wyatt, M.B., 2009. Elemental composition of the Martian crust. *Science* **324**, 736–739.

McSween, H.Y., Arvidson, R.E., Bell, J.F. et al., 2004. Basaltic rocks analyzed by the Spirit Rover in Gusev Crater. *Science* **305**, 842–845.

Michalski, J.R., Cuadros, J., Niles, P.B., Parnell, J., Rogers, A.D., Wright, S.P., 2013. Groundwater activity on Mars and implications for a deep biosphere. *Nature Geoscience* **6**, 133–138.

Michalski, J.R., Noe Dobrea, E.Z., Niles, P.B., Cuadros, J., 2017. Ancient hydrothermal seafloor deposits in Eridania basin on Mars. *Nature Communications* **8**, 15978.

Miner, B., 1988. Poorly graphitized kerogens: a high resolution transmission electron microscope study. Ph.D. Dissertation, Arizona State University, Tempe.

Ming, D.W., Mittlefehldt, D.W., Morris, R.V. et al., 2006. Geochemical and mineralogical indicators for aqueous processes in the Columbia Hills of Gusev crater, Mars. *Journal of Geophysical Research* **111**, E02S12.

Monty, C.L.V., 1976. The origin and development of cryptalgal fabrics. In: Walter, M.R. (Ed.), Stromatolites. Elsevier, Amsterdam, pp. 193–249.

Moore, E.K., Jelen, B.I., Giovannelli, D., Raanan, H., Falkowski, P.G., 2017. Metal availability and the expanding network of microbial metabolisms in the Archaean eon. *Nature Geoscience* **10**, 629–636.

Morag, N., Williford, K.H., Kitajima, K., Philippot, P., Van Kranendonk, M.J., Lepot, K., Thomazo, C., Valley, J.W., 2016. Microstructure-specific carbon isotopic signatures of organic matter from ~3.5 Ga cherts of the Pilbara Craton support a biologic origin. *Precambrian Research* **275**, 429–449.

Moreau, J.W., Sharp, T.G., 2004. A transmission electron microscopy study of silica and kerogen biosignatures in ~1.9 Ga Gunflint microfossils. *Astrobiology* **4**, 96–210.

Morowitz, H.J., 2002. The emergence of everything. Oxford University Press, p. 209.

Muir, M.D., Grant, P.R., 1976. Micropalaeontological evidence from the Onverwacht Group, South Africa. In: Windley, B.F. (Ed.), The Early History of the Earth. Wiley/Interscience, London, pp. 595–608.

Mustard, J.F., Adler, M., Allwood, A.C., Bass, D.S., Beaty, D.W., Bell, J.F., Brinckerhoff, W.B., Carr, M., Des Marais, D.J., Drake, B., Edgett, K.S., Eigenbrode, J., Elkins-Tanton, L.T., Grant, J.A., Milkovich, S.M., Ming, D., Moore, C., Murchie, S., Onstott, T.C., Ruff, S.W., Sephton, M.A., Steele, A., Treiman, A., 2013. Report of the Mars 2020 Science Definition Team, 154 pp., posted July, 2013, by the Mars Exploration Program Analysis Group (MEPAG) at http://mepag.jpl.nasa.gov/reports/MEP/Mars_2020_SDT_Report_Final.pdf.

Nachon, M., Mangold, N., Forni, O., Kah, L.C., Cousin, A., Wiens, R.C., Anderson, R., Blaney, D., Blank, J.G., Calef, F., Clegg, S.M., Fabre, C., Fisk, M.R., Gasnault, O., Grotzinger, J.P., Kronyak, R., Lanza, N.L., Lasue, J., Le Deit, L., Le Mouélic,S., Maurice, S., Meslin, P.-Y., Oehler, D.Z., Payré, V., Rapin, W., Schröder, S., Stack, K., Sumner, D., 2017. Chemistry of diagenetic features analyzed by ChemCam at Pahrump Hills, Gale crater, Mars. *Icarus* **281**, 121–126.

Nagy, B., Nagy, L.A., 1969. Early Precambrian Onverwacht microstructures: possibly the oldest fossils on earth? *Nature* **223**, 1226–1229.

Neu, T.R., Eitner, A., Paje, M.L., 2003. Development and architecture of complex environmental biofilms. In: Krumbein, W.E., Paterson, D.M., Zavarzin, G.A. (Eds.), Fossil and Recent Biofilms. Kluwer, Dordrecht, pp. 29–45.

Neveu, M., Hays, L.E., Voytek, M.A., New, M.H., Schulte, M.D., 2018. The Ladder of Life Detection. *Astrobiology* **18**, 1375–1402.

Nijman, W., De Vries, S.T., 2009. Geological map of the lower Archaean Buck Ridge volcano-sedimentary complex. In: Barberton Greenstone Belt, Republic of South Africa. Faculty of Geosciences, Utrecht University, The Netherlands, 3 map sheets and explanatory note.

Nijman, W., Kloppenburg, A., de Vries, S.T., 2017. Archaean basin margin geology and crustal evolution: an East Pilbara traverse. *Journal of the Geological Society of London* **174**, 1090–1112.

Nisbet, E.G., 1995. Archaean ecology: a review of evidence for the early development of bacterial biomes, and speculations on the development of a global-scale biosphere. *Geological Society of London Special Publication* **95**, 27–55.

Nisbet, E.G., 2000. The realms of Archaean life. *Nature* **405**, 625–626.

Nisbet, E.G., Fowler, C.M.R., 1999. Archaean metabolic evolution of microbial mats. Proceedings of the Royal Society of London B, 266, 2375–2382.

Nisbet, E.G., Fowler, C.M.R., 2003. The early history of life. In Schlesinger, W.H. (Ed.) Treatise on Geochemistry, Volume 8. Elsevier, Amsterdam, pp. 1–39.

Nisbet, E.G., Sleep, N.H., 2001. The habitat and nature of early life. *Nature* **409**, 1083–1091.

Nocelli, N., Bogino, P.C., Banchio, E., Giordano, W., 2016. Roles of Extracellular polysaccharides and biofilm formation in heavy metal resistance of Rhizobia. *Materials* **9**, 418.

Noffke, N., 2003. Epibenthic cyanobacterial communities interacting with sedimentary processes in siliciclastic depositional systems (present and past). In: Krumbein, W.E., Paterson, D.M., Zavarzin, G.A. (Eds.), Fossil and Recent Biofilms. Kluwer, Dordrecht, pp. 265–280.

Noffke, N., 2009. The criteria for the biogenicity of microbially induced sedimentary structures (MISS) in Archean and younger, sandy deposits. *Earth-Science Reviews* **96**, 173–180.

Noffke, N., 2010. Microbial Mats in Sandy Deposits from the Archean Era to Today. Springer, New York, 175 p.

Noffke, N., 2015. Ancient sedimentary structures in the <3.7 Ga Gillespie Lake Member, Mars, that resemble macroscopic morphology, spatial associations, and temporal succession in terrestrial microbialites. *Astrobiology* **15**, 169–192.

Noffke, N., Awramik, S.M., 2013. Stromatolites and MISS e differences between relatives. *GSA Today* **23**, 4–9.

Noffke, N., Gerdes, G., Klenke, T., Krumbein, W.E., 2001. Microbially induced sedimentary structures e a new category within the classification of primary sedimentary structures: perspectives. *Journal of Sedimentary Research* **71**, 649–656.

Noffke, N., Hazen, R.M., Nhleko, N., 2003. Earth's earliest microbial mats in a siliciclastic marine environment (2.9 Ga Mozaan Group, South Africa). *Geology* **31**, 673–676.

Noffke, N., Eriksson, K.A., Hazen, R.M., Simpson, E.L., 2006. A new window into Archean life: microbial mats in Earth's oldest siliciclastic tidal deposits (3.2 Ga Moodies Group, South Africa). *Geology* **34**, 253–256.

Noffke, N., Beukes, N., Gutzmer, J., Hazen, R.M., 2006. Spatial and temporal distribution of microbially induced sedimentary structures: a case study from siliciclastic storm deposits of the 2.9 Ga Witwatersrand Supergroup South Africa. *Precambrian Research* **146**, 35–44.

Noffke, N., Christian, D., Wacey, D., Hazen, R.M., 2013. Microbially induced sedimentary structures recording an ancient ecosystem in the ca. 3.48 billion-year-old Dresser Formation, Pilbara, Western Australia. *Astrobiology* **13**, 1103–1124.

Oberlin, A., Oberlin, M., 1983. Graphitizability of carbonaceous materials as studied by TEM and X-ray diffraction. *Journal of Microscopy* **132**, 353–363.

Oberlin, A., Boulmier, J.L., Durand, B., 1974. Electron microscope investigation of the structure of naturally and artificially metamorphosed kerogen. *Geochimica et Cosmochimica Acta* **38**, 647–650.

Oberlin, A., Boulmier, J.U., Villey, M., 1980. Electron microscopic study of kerogen microtexture. Selected criteria for determining the evolution path and evolution stage of kerogen. In Kerogen (Ed: Durand, B.), pp. 191–204. Editions Technip, Paris.

Oehler, D.Z., Robert, F., Walter, M.R., Sugitani, K., Allwood, A., Meibom, A., Mostefaoui, S., Selo, M., Thomen, A., Gibson, E.K., 2009. NanoSIMS: insights to biogenicity and syngeneity of Archaean carbonaceous structures. *Precambrian Research* **173**, 70–78.

Oehler, D.Z., Walsh, M.M., Sugitani, K., Liu, M.-C., House, C.H., 2017. Large and robust lenticular microorganisms on the young Earth. *Precambrian Research* **296**, 112–119.

Ohmoto, H., Kakegawa, T., Lowe, D.R., 1993. 3.4-billion-year-old pyrites from Barberton, South Africa: sulphur isotope evidence. *Science* **262**, 555–557.

Ohtomo, Y., Kakegawa, T., Ishida, A., Nagase, T., Rosing, M.T., 2014. Evidence for biogenic graphite in early Archaean Isua metasedimentary rocks. *Nature Geoscience* **7**, 25–28.

Oelkers, E.H., Gíslaison, S.R., 2001. The mechanism, rates, and consequences of basaltic glass dissolution: I. An experimental study of the dissolution rates of basaltic glass as a function of aqueous Al, Si, and oxalic acid concentration at 25°C and pH = 3 and 11. *Geochimica et Cosmochimica Acta* **65**, 3671–3681.

Orange, F., Westall, F., Disnar, J.-R., Prieur, D., Bienvenu, N., Le Romancer, M., Défarge, C., 2009. Experimental silicification of the extremophilic Archaea Pyroccus abyssi and Methanocaldococcus jannaschii. Applications in the search for evidence of life in early Earth and extraterrestrial rocks. *Geobiology* **7**, 403–418.

Orange, F., Chabin, A., Gorlas, A., Lucas-Staat, S., Geslin, C., Le Romancer, M., Prangishvili, D., Forterre, P., Westall, F., 2011. Experimental fossilisation of viruses from extremophilic Archaea. *Biogeosciences* **8**, 1465–1475.

Orange, F., Disnar, J.-R., Gautret, P., Westall, F., Bienvenu, N., Lottier, N., Prieur, D., 2012. Preservation and Evolution of organic matter during experimental fossilisation of the hyperthermophilic Archaea Methanocaldococcus jannaschii. *Origins of Life and Evolution of Biospheres* **42**, 587–609.

Orberger, B., Rouchon, V., Westall, F., de Vries, S., Pinti, D., Wagner, C., Wirth, R., Gallien, J.-P., Hashizume, K., 2006. Microfacies and origin of some Archean Cherts (Pilbara, Australia). In: Reimold, W.U., Gibson, R.L. (Eds.), Processes on the Early Earth. *Geological Society of America Special Paper* **405**, pp. 133–156.

Oschmann, W., 2000. Microbes and black shales. In: Riding, R.E., Awramik, S.M. (Eds.), Microbial Sediments. Springer-Verlag, Berlin Heidelberg, pp. 137–148.

Pan, L., Carter, J., Quantin-Nataf, C., 2019. Hydrated silica in Martian alluvial fans and deltas. *LPI Contribution #6239*.

Papineau, D., Walker, J.J., Mojzsis, S.J., Pace, N.R., 2005. Composition and structure of microbial communities from stromatolites of Hamelin Pool in Shark Bay, Western Australia. *Applied and Environmental Microbiology* **71**, 4822–4832.

Paris, I., 1985. The Geology of the Farms Josefsdal, Dunbar and Part of Diepgeziet in the Barberton Greenstone Belt. Ph.D. thesis, Univ. Witwatersrand, 239 p.

Paris, I., Stanistreet, I.G., Hughes, M.J., 1985. Cherts of the Barberton greenstone belt interpreted as products of submarine exhalative activity. *Journal of Geology* **93**, 111–129.

Parkes, R.J., Cragg, B., Roussel, E., Webster, G., Weightman, A., Sass, H., 2014. A review of prokaryotic populations and processes in sub-seafloor sediments, including biosphere:geosphere interactions. *Marine Geology* **352**, 409–425.

Paterson, D.M., Yates, M.G., Wiltshire, K.H., McGrorty, S., Miles, A., Eastwood, J.E.A., Blackburn, J., Davidson, I., 1998. Microbial mediation of spectral reflectance from intertidal cohesive sediments. *Limnology and Oceanography* **43**, 1207–1221.

Paterson, D.M., Perkins, R., Consalvey, M., Underwood, G.J.C., 2003. Ecosystem function, cell microcycling and the structure of transient biofilms. In: Krumbein, W.E., Paterson, D.M., Zavarzin, G.A. (Eds.), Fossil and Recent Biofilms: A Natural History of Life on Earth. Kluwer, Dodrecht, pp. 47–63.

Pavlov, A.A., Vasilyev, G., Ostryakov, V.M., Pavlov, A.K., Mahaffy, P., 2012. Degradation of the organic molecules in the shallow subsurface of Mars due to irradiation by cosmic rays. *Geophysical Research Letters* **39**, L052166.

Pearce, B.K.D., Tupper, A.S., Pudritz, R.E., Higgs, P.G., 2018. Constraining the time interval for the Origin of Life on Earth. *Astrobiology* **18**, 343–364.

Petroff, A.P., Sim, M.S., Maslov, A., Krupenin, M., Rothman, D.H., Bosak, T., 2010. Biophysical basis for the geometry of conical stromatolites. *Proceedings of the National Academy of Sciences U.S.A.* **107**, 9956–9961.

Petroff, A.P., Beukes, N.J., Rothman, D.H., Bosak, T., 2013. Biofilm growth and fossil form. *Physical Review X* **3**, 041012.

Pflug, H.D., 1966. Organic Remains from the Fig Tree Series of the Barberton Mountain Land. *University of the Witwatersrand Economic Geology Research Unit, Information Circular* **28**, Johannesburg, 36 p.

Pflug, H.D., Jaeschke-Boyer, H., 1979. Combined structural and chemical analysis of 3,800-Myr-old microfossils. *Nature* **280**, 483–486.

Picioreanu, C., van Loosdrecht, M.C.M., Heijnen, J.J., 1998. Mathematical modeling of biofilm structure with a hybrid differential-discrete cellular automaton approach. *Biotechnology and Bioengineering* **58**, 101–116.

Pinti, D., 2005. The origin and evolution of the oceans. In Gargaud, M., Barbier, B., Martin, H., Reisse, J. (Eds.), Lectures in Astrobiology Volume I, Springer, pp. 83–112.

Pondrelli, M., Baliva, A., Di Lorenzo, S., Marinangeli, L., Rossi, A.P., 2005. Complex evolution of paleolacustrine systems on Mars: An example from the Holden crater. *Journal of Geophysical Research* **110**, E04016.

Pope, M.C., Grotzinger, J.P., 2000. Controls on fabric development and morphology of tufa and stromatolites, uppermost Pethei Group (1.8 Ga), Great Slave Lake, northwest Canada. In Grotzinger, J., James, N. (Eds.), Carbonate Sedimentation and Diagenesis in the Evolving Precambrian World. *SEPM Special Publication* **67**, 103–122.

Pope, M.C., Grotzinger, J.P., Schreiber, B.C., 2000. Evaporitic subtidal stromatolites produced by in situ precipitation: textures, facies associations, and temporal significance. *Journal of Sedimentary Research* **70**, 1139–1151.

Proskurowski, G., 2009. Abiogenic hydrocarbon production at the geosphere-biosphere interface via serpentinization reactions. In Timmis, K. (Ed.). Handbook of Hydrocarbon and Lipid Microbiology, Springer, Heidelberg, pp. 215-231.

Qu, Y., Zhu, S., Whitehouse, M.J., Engdahl, A., McLoughlin, N., 2018. Carbonaceous biosignatures of the earliest putative macroscopic multicellular eukaryotes from 1630 Ma Tuanshanzi Formation, north China. *Precambrian Research* **304**, 99–109.

Quantin, C., Carter, J., Thollot, P., Broyer, J., Lozach, L., Davis, J., Grindrod, P., Pajola, M.,.Baratti, E., Rossato, S., Bultel, B., Leyrat, C., Fernando, J., Ody, A., 2016. Oxia Planum, the landing site for ExoMars 2018. *LPI Contribution #2863*.

Quantin-Nataf, C., Thollot, P., Carter, J., Mandon, L., Dehouck, E., 2018. The unique and diverse record of Noachian aqueous activity in Oxia Planum, Mars. 49th Lunar and Planetary Science Conference, *LPI Contribution #2562*.

Quantin-Nataf, C., Carter, J., Mandon, L., Balme, M., Fawdon, P., Davis, J., Thollot, P., Dehouck, E., Pan, L., Volat, M., Millot, C., Breton, S., Loizeau, D., Vago, J.L., 2019. ExoMars at Oxia Planum, probing the aqueous-related Noachian environments. Ninth International Conference on Mars, *LPI Contribution #6317*.

Rabbow, E., Rettberg, P., Barczyk, S., Bohmeier, M., Parpart, A. Panitz, C., Horneck, G., von Heise-Rotenburg, R., Hoppenbrouwers, T., Willlnecker, R., Baglioni, P., Demets, R., Dettmann, J., Reitz, G., 2012. EXPOSE-E: an ESA astrobiology mission 1.5 years in space. *Astrobiology* **12**, 374–386.

Rabbow, E., Rettberg, P., Barczyk, S., Bohmeier, M., Parpart, A. Panitz, C., Horneck, G., Burfeindt, J., Molter, F., Jaramillo, E., Pereira, C., Weiß, P., Willlnecker, R., Demets, R., Dettmann, J., Reitz, G., 2015. The astrobiological mission EXPOSE-R on board of the International Space Station. *International Journal of Astrobiology* **14**, 3–16.

Rabbow, E., Rettberg, P., Parpart, A., Panitz, C., Schulte, W., Molter, F., Jaramillo, E., Demets, R., Weiß, P., Willnecker, R., 2017. EXPOSE-R2: The Astrobiological ESA Mission on Board of the International Space Station, *Frontiers in Microbiology* **8**, 1533, pp.14

Rasmussen, B., 2000. Filamentous microfossils in a 3,235-million-year-old volcanogenic massive sulphide deposit. *Nature* **405**, 676–679.

Rasmussen, B., Buick, R., 2000. Oily old ores: evidence for hydrothermal petroleum generation in an Archean volcanogenic massive sulfide deposit. *Geology* **28**, 731-734.

Raven, J. A., 1988, The iron and molybdenum use efficiencies of plant growth with different energy, carbon and nitrogen sources. *New Phytologist* **109**, 279–287.

Reid, R.P., James, N.P., Macintyre, I.G., Dupraz, C.P., Burne, R.V., 2003. Shark Bay stromatolites: Microfabrics and reinterpretations of origins. *Facies* **9**, 243–270.

Reineck, H.E., 1967. Layered sediments of tidal flats, beaches, and shelf bottoms of the North Sea. In: G.H. Lauff (Ed.), Estuaries. *American Association for the Advancement of Science Publication* **83**, 191–206.

Reinhardt, M., Goetz, W. Thiel, V. Testing flight-like pyrolysis GC-MS as performed by MOMA onboard the ExoMars 2020 rover on Oxia Planum analog samples (iron-rich shale and opaline chert). Accepted, *Astrobiology*.

Reitner, J., 2010. Architecture of archaeal-dominated microbial mats from cold seeps in the Black Sea (Dnjepr Canyon, Lower Crimean Shelf). In: Seckbach, J., Oren, A. (Eds.), Microbial Mats: Modern and Ancient Microorganisms in Stratified Systems. Springer Verlag, Heidelberg, pp. 207–220.

Revsbech, N.P., 1989. Microsensors: spatial gradients in biofilms. In Characklis, W.G., Wilderer, P.A. (Eds.) Structure and Function of Biofilms. John G. Wiley and Sons Ltd., Dahlem Konferenzen 1989, Chichester, New York, pp. 129–144.

Robbins, L.J., Lalonde, S.V., Planavsky, N.J., Partin, C.A., Reinhard, C.T., Kendall, B., Scott, C., Hardisty, D.S., Gill, B.C., Alessi, D.S., Dupont, C.L., Saito, M.A., Crowe, S.A., Poulton, S.W., Bekker, A., Lyons, T.W., Konhauser, K., 2016. Trace elements at the intersection of marine biological and geochemical evolution. *Earth-Science Reviews* **163**, 323–348.

Rogers, A.D., Aharonson, O., 2008. Mineralogical composition of sands in Meridiani Planum determined from Mars Exploration Rover data and comparison to orbital measurements. *JGR Planets* **113**, JE002995.

Rosing, M.T., 1999. ^{13}C-depleted carbon microparticles in >3700-Ma sea-floor sedimentary rocks from west Greenland. *Science* **283**, 674–676.

Rosing, M.T, Bird, D.K., Sleep, N.H., Bjerrum, C.J., 2010. No climate paradox under the faint Sun. *Nature* **464**, 744–747.

Rubin, D.M., Fairén, A.G., Martínas-Frías, J., Frydenvang, J., Gasnault, O., Gelfenbaum, G., Goetz, W., Grotzinger, J.P., Le Mouélic, S., Mangold, N., Newsom, H., Oehler, D.Z., Rapin, W., Schieber, J., Wiens, R.C., 2017. Fluidized-sediment pipes in Gale crater, Mars, and possible Earth analogs. *Geology* **45**, 7–10.

Ruff, S.W., Farmer, J.D., 2016. Silica deposits on Mars with features resembling hot spring biosignatures at El Tatio in Chile. *Nature Communications* **7**, 13554.

Rull, F., Maurice, S., Hutchinson, I., Moral, A., Perez, C., Diaz, C., Colombo, M., Belenguer, T., Lopez-Reyes, G., Sansano, A., Forni, O., Parot, Y., Striebig, N., Woodward, S., Howe, C., Tarcea, N., Rodriguez, P., Seoane, L., Santiago, A., Rodriguez-Prieto, J.-A., Medina, J., Gallego, P., Canchal, R., Santamaría,P., Ramos, G. , Vago, J.L., 2017. The Raman Laser Spectrometer for the ExoMars Rover Mission to Mars. *Astrobiology* **17**, 627–654.

Russell, M.J., Hall, A.J., Martin, W., 2010 Serpentinization as a source of energy at the origin of life. *Geobiology* **8**, 355–371.

Sadezky, A., Muckenhuber, H., Grothe, H., Niessner, R., Poschl, U., 2005. Raman microspectroscopy of soot and related carbonaceous materials: Spectral analysis and structural information. *Carbon* **43**, 1731–1742.

Sagan, C., Mullen, G., 1972. Earth and Mars: evolution of atmospheres and surface temperatures. *Science* **177**, 52–56.

Saito, M.A., Moffett, J.W., Chisholm, S.W., Waterbury, J.B., 2002. Cobalt limitation and uptake in Prochlorococcus. *Limnology and Oceanography* **47**, 1629–1636.

Saito, M.A., Sigman, D.M., Morel, F.M.M., 2003. The bioinorganic chemistry of the ancient ocean: the co-evolution of cyanobacterial metal requirements and biogeochemical cycles at the Archean-Proterozoic boundary. *Inorganica Chimica Acta* **356**, 308–318.

Sánchez-Román, M., Fernández-Remolar, D., Amils, R., Sánchez-Nava, A., Schmid, T., Martin-Uriz, P.S., Rodríguez, N., McKenzie, J.A., Vasconcelos, C., 2014. Microbial mediated formation of Fe-carbonate minerals under extreme acidic conditions. *Scientific Reports* **4**, 4767.

Schidlowski, M., 1984. Biological modulation of the terrestrial carbon cycle: Isotope clues to early organic evolution. *Advances in Space Research* **4**, 183–193.

Schidlowski, M., 1988. A 3,800-million-year isotopic record of life from carbon in sedimentary rocks. *Nature* **333**, 313–318.

Schieber, J., 1986. The possible role of benthic microbial mats during the formation of carbonaceous shales in shallow Mid-Proterozoic basins. *Sedimentology* **33**, 521–536.

Schieber, J., 1998. Possible indicators of microbial mats deposits in shales and sandstones: examples from the Mid-Proterozoic Belt Supergroup, Montana, U.S.A. *Sedimenatry Geology* **120**, 105 124.

Schieber, J., Bose, P.K., Eriksson, P.G., Banerjee, S., Sarkar, S., Altermann, W., Catuneanu, O. (Eds.), 2007. Atlas of Microbial Mat Features Preserved within the Siliciclastic Rock Record. Elsevier, Amsterdam, p. 324.

Schieber, J., Southard, J.B., Schimmelmann, A., 2012. Lenticular shale fabrics resulting from intermittent erosion of water-rich muds – interpreting the rock record in the light of recent flume experiments. *Journal of Sedimentary Research* **80**, 119–128.

Schieber, J., Bish, D., Coleman, M., Reed, M., Hausrath, E.M., Cosgrove, J., Gupta, S., Minitti, M.E., Edgett, K.S., Malin, M., 2017. Encounters with an unearthly mudstone: Understanding the first mudstone found on Mars. *Sedimentology* **64**, 311–358.

Schopf, J.W., Barghoorn, E.S., 1967. Alga-like fossils from the early Precambrian of South Africa. *Science* **156**, 508–512.

Schopf, J.W., 1992. Paleobiology of the Archean. In: Schopf, J.W., Klein, C. (Eds.), The Proterozoic Biosphere: A Multidisciplinary Study. Cambridge University Press, New York, 1348 p.

Schopf, J.W., 1993. Microfossils of the early Archean Apex Chert e new evidence of the antiquity of life. *Science* **260**, 640–646.

Schopf, J.W., 2006. Fossil evidence of Archaean life. *Philosophical Transactions of the Royal Society B* **361**, 869–885.

Schopf, J.W., Walter, M.R., 1983. Archean microfossils: new evidence of ancient microbes. In: Schopf, J.W. (Ed.), Earth's Earliest Biosphere: Its Origin and Evolution. Princeton University Press, Princeton, pp. 214–239.

Schopf, J.W., Packer, B.M., 1987. Early Archean (3.3-billion to 3.5-billion-year-old) microfossils from Warrawoona Group, Australia. *Science* **237**, 70–73.

Schopf, J.W., Kudryavtsev, A.B., Osterhout, J.T., Williford, K.H., Kitajima, K., Valley, J.W., Sugitani, K., 2017. An anaerobic ~3400 Ma shallow-water microbial consortium: Presumptive evidence of Earth's Paleoarchean anoxic atmosphere. *Precambrian Research* **299**, 309–318.

Schultze-Lam, S., Fortin, D., Davis, B.S., Beveridge, T.J., 1993. Mineralization of bacterial surfaces. *Chemical Geology* **132**, 171–181.

Schultze-Lam, S., Ferris, F.G., Konhauser, K., Wiese, R.G., 1995. In situ silicification of an Icelandic hot spring microbial mat: implications for microfossil formation. *Canadian Journal of Earth Sciences* **32**, 2021–2026.

Segarra, K.E.A., Schubotz, F., Samarkin, V., Yoshinaga, M.Y., Hinrichs, K.-U., Joye, S.B., 2015. High rates of anaerobic methane oxidation in freshwater wetlands reduce potential atmospheric methane emissions. *Nature Communications* **6**, 7477.

Sforna, M.C., van Zuilen, M.A., Philippot, P., 2014. Structural characterization by Raman hyperspectral mapping of organic carbon in the 3.46 billion-year-old Apex chert Western Australia. *Geochimica et Cosmochimica Acta* **124**, 18–33.

Sforna, M.C., Philippot, P., Somogyi, A., van Zuilen, M.A., Medjoubi, K., Schoepp-Cothenet, B., Nitschke, W., Visscher, P.T., 2014. Evidence for arsenic metabolism and cycling by organisms 2.7 billion years ago. *Nature Geoscience* **7**, 811–815.

Shaw, G.H., 2014. Earth's Early Atmosphere and Surface Environment. *GSA Special Paper* **504**.

Shepard, R.N., Sumner, D.Y., 2010. Undirected motility of filamentous cyanobacteria produces reticulate mats. *Geobiology* **8**, 179–190.

Shibuya, T., Komiya, T., Nakamura, K., Takai, K., Maruyama, S., 2010. Highly alkaline, high-temperature hydrothermal fluids in the early Archean ocean. *Precambrian Research* **182**, 230–238.

Shields, G., Webb, G., 2004. Has the REE Composition of Seawater Changed Over Geological Time? *Chemical Geology* **204**, 103–107.

Siegesmund, M.A., Johansen, J.R., Karsten, U., Friedl, T., 2008. Coleofasciculus gen. nov. (cyanobacteria): Morphological and molecular criteria for revision of the genus Microcoleus Gomont. *Journal of Phycology* **44**, 1572–1585.

Siesser, W.G., Rogers, J., 1976. Authigenic pyrite and gypsum in south-west African Continental slope sediments. *Sedimentology* **23**, 567–577.

Siever, R., 1992. The silica cycle in the Precambrian. *Geochimica et Cosmochimica Acta* **56**, 3265–3272.

Sim, M.S., Liang, B., Petroff, A.P., Evans, A., Klepac-Ceraj, V., Flannery, D.T., Walter, M.R., Bosak, T., 2012. Oxygen-dependent morphogenesis of modern clumped photosynthetic mats and implications for the Archean stromatolite record. *Geosciences* **2**, 235–529.

Simonson, B.M., Schubel, K.A., Hassler, S.W., 1993. Carbonate sedimentology of the early Precambrian Hamersley Basin Group of western Australia. *Precambrian Research* **60**, 287–335.

Sleep, N.H., 2016. Asteroid bombardment and the core of Theia as possible sources for the Earth's late veneer component. *Geochemistry Geophysics Geosystems* **17**, 2623-2642.

Sleep, N.H., 2018. Geological and geochemical constraints on the origin and evolution of life. *Astrobiology* **18**, 1199–1219.

Sleep, N.H., Zahnle, K., Neuhoff, P.S., 2001. Initiation of clement surface conditions on the earliest Earth. *Proceedings of the National Academy of Sciences U.S.A.* **98**, 3666–3672.

Sorieul, S., Alfaurt, Ph., Daudin, L., Serani, L., Moretto, Ph., 2014. Aifira: an ion beam facility for multidisciplinary research. *Nuclear Instruments and Methods in Physics Research Section B: Beam Interactions with Material and Atoms* **332**, 68–73.

Spangenberg, J.E., Frimmel, H.E., 2001. Basin-internal derivation of hydrocarbons in the Witwatersrand Basin, South Africa: evidence from bulk and molecular $\delta^{13}C$ data. *Chemical Geology* **173**, 339–355.

Squyres, S.W., Grotzinger, J.P., Arvidson, R.E., Bell, J., Calvin, W., Christensen, P., Clark, B.C., Crisp, J.A., Farrand, W.H., Herkenhoff, K.E., Johnson, J.R., Klingelhöfer, G., Knoll, A.H., McLennan, S.M., McSween, H.Y., Morris, R.V., Rice, J.W., Rieder, R., Soderblom, L.A., 2005. In situ evidence for an ancient aqueous environment at Meridiani Planum, Mars. *Science* **306**, 1709–1714.

Squyres, S.W., Arvidson, R.E., Ruff, S.W., Gellert, R., Morris, R.V., Ming, D.W., Crumpler, L., Farmer, J.D., Des Marais, D.J., Yen, A., McLennan, S.M., Calvin, W., Bell, J.F., Clark, B.C., Wang, A., McCoy, T.J., Schmidt, M.E., de Souza, P.A., 2008. Detection of silica-rich deposits on Mars. *Science* **320**, 1063–1067.

Staudigel, H., Furnes, H., de Wit, M., 2015. Paleoarchean trace fossils in altered volcanic glass. *Proceedings of the National Academy of Sciences U.S.A.* **112**, 6892–6897.

Strullu-Derrien, C., Bernard, S., Spencer, A.R.T., Remusat, L., Kenrick, P., Derrien, D., 2019. On the structure and chemistry of fossils of the earliest woody plant. *Palaeontology*.

Stüeken, E.E., Buick, R., 2018. Environmental control on microbial diversity and methane production in the Mesoarchean. *Precambrian Research* **304**, 64–72.

Stüeken, E.E., Anderson, R.E., Bowman, J.S., Brazleton, W.J., Colangelo-Lillis, J., Goldman, A.D., Som, S.M., Baross, J.A., 2013. Did life originate from a global chemical reactor? *Geobiology* **11**, 101–126.

Stüeken, E.E., Buick, R., Anderson, R.E., Baross, J.A. Planavsky, N.J., Lyons, T.W., 2017. Environmental niches and metabolic diversity in Neoarchean lakes. *Geobiology* **15**, 767–783.

Sugahara, H., Sugitani, K., Mimura, K., Yamashita, F., Yamamoto, K., 2010. A systematic rare-earth elements and yttrium study of Archean cherts at the Mount Goldsworthy greenstone belt in the Pilbara Craton: Implications for the origin of microfossil-bearing black cherts. *Precambrian Research* **177**, 73–87.

Sugitani, K., 2018. Early Archaean (pre-3.0 Ga) cellularly preserved microfossils and microfossil-like structures frm the Pilbara craton, Western Australia–a review. In Earth's Oldest Rocks, Second Edition (Eds. Van Kranendonk, M.J., Bennett, V.C., Hofmann, J.E.), pp. 1007–1028.

Sugitani, K., Grey, K., Allwood, A., Nagaoka, T., Mimura, K., Minami, M., Marshall, C.P., Van Kranendonk, M.J., Walter, M.R., 2007. Diverse microstructures from Archean chert from the Mount Goldsworthy-Mount Grant area, Pilbara Craton, Western Australia: microfossils, dubiofossils, or pseudofossils? *Precambrian Research* **158**, 228–262.

Sugitani, K., Grey, K., Nagaoka, T., Mimura, K., 2009. Three-dimensional morphological and textural complexity of Archean putative microfossils form the northeastern Pilbara Craton: indications of biogenicity of large (> 15mm) spheroidal and spindle-like structures. *Astrobiology* **9**, 603–615.

Sugitani, K., Lepot, K., Nagaoka, T., Mimura, K., Van Kranendonk, M.J., Oehler, D.Z., Walter, M.R., 2010. Biogenicity of morphologically diverse carbonaceous microstructures from the ca. 3,400 Ma Strelley Pool formation, in the Pilbara Craton, Western Australia. *Astrobiology* **10**, 899–920.

Sugitani, K., Mimura, K., Takeuchi, M., Yamaguchi, T., Suzuki, K., Senda, R., Asahara, Y., Wallis, S., Van Kranendonk, M.J., 2015. A Paleoarchean coastal hydrothermal field inhabited by diverse microbial communities: the Strelley Pool Formation, Pilbara Craton, Western Australia. *Geobiology* **13**, 522–545.

Sumner, D.Y., 1997. Late Archean calcite-microbe interactions: two morphologically distinct microbial communities that affects calcite nucleation differently. *Palaios* **12**, 302–318.

Sutherland, I.W., 2001. The biofilm matrix – an immobile but dynamic microbial environment. *Trends in Microbiology* **9**, 222–227.

Sutton, M., Rahman, I., Garwood, R.J., 2014. Techniques for Virtual Palaeontology; Wiley-Blackwell: Hoboken, NJ, USA, p. 208.

Takahashi, Y., Châtellier, X., Hattori, K.H., Kato, K., Fortin, D., 2005. Adsorption of rare earth elements onto bacterial cell walls and its implication for REE sorption onto natural microbial mat. *Chemical Geology* **219**, 53–67.

Tanaka, K.L., 2014. The new geologic map of Mars: guiding research and education. *EOS* **95**, 341–342.

Tankard, A.J., Jackson, M.P.A., Eriksson, K.A., Hobday, D.K., Hunter, D.R., Minter, W.E.L., 1982. Crustal Evolution of Southern Africa, 3.8 Billion Years of Earth History. Springer-Verlag, New York, Heidelberg and Berlin.

Tarnas, J.D., Mustard, J.F., Sherwood-Lollar, B., Bramble, M.S., Cannon, K.M., Palumbo, A.M., Plesa, A.-C., 2018. Radiolytic H_2 production on Noachian Mars: Implications for habitability and atmospheric warming. *Earth and Planetary Science Letters* **502**, 133–145

Tartèse, R., Chaussidon, M., Gurenko, A., Delarue, F., Robert, F., 2017. Warm Archean oceans reconstructed from oxygen isotope composition of early-life remnants. *Geochemical Perspective Letters* **3**, 55–65.

Thorseth, I.H., Torsvik, T., Furnes, H., Muehlenbachs, K., 1995. Microbes play an important role in the alteration of oceanic crust. *Chemical Geology* **126**, 137–146.

Thurston, P.C., Kamber, B.S., Whitehouse, M., 2012. Archean cherts in banded iron formation: insight into Neoarchean ocean chemistry and depositional processes. *Precambrian Research* **214-215**, 227–257.

Tice, M.M., 2009. Environmental controls on photosynthetic microbial mat distribution on and morphogenesis on a 3.42 Ga clastic-starved platform. *Astrobiology* **9**, 989–1000.

Tice, M.M., Lowe, D.R., 2004. Photosynthetic microbial mats in the 3416-Myr-old ocean. *Nature* **431**, 549–552.

Tice, M.M., Lowe, D.R., 2006. Hydrogen-based carbon fixation in the earliest known photosynthetic organisms. *Geology* **34**, 37–40.

Tice, M.M., Lowe, D.R., 2006. The origin of carbonaceous matter in pre-3.0 Ga greenstone terrains: a review and new evidence from the 3.42 Ga Buck Reef Chert. *Earth-Science Reviews* **76**, 259–300.

Tice, M.M., Bostick, B.C., Lowe, D.R., 2004. Thermal history of the 3.5-3.2 Ga Onverwacht and Fig Tree Groups, Barberton greenstone belt, South Africa, inferred by Raman microspectroscopy of carbonaceous material. *Geology* **32**, 37–40.

Tice, M.M., Thornton, D.C.O., Pope, M.C., Olszewsku, T.D., Gong, J., 2011. Archean microbial mat communities. *Annual Review of Earth and Planetary Sciences* **39**, 297–319.

Tice, M.M., Quezergue, K., Pope, M.C., 2017. Microbialite biosignature analysis by mesoscale X-ray fluorescence (μXRF) mapping. *Astrobiology* **17**, 1161–1172.

Toporski, J.K., Steele, A., Westall, F., Thomas-Keprta, K.L., McKay, D.S., 2004. The simulated silicification of bacteria--new clues to the modes and timing of bacterial preservation and implications for the search for extraterrestrial microfossils. *Astrobiology* **2**, 1–26.

Tostevin R.E., Shields, G.A., Tarbuck, G.M., He, T., Clarkson, M.O., Wood, R.A., 2016. Effective use of Ce anomalies as a redox proxy in carbonate-dominated marine settings. *Chemical Geology* **438**, 146–162.

Trower, E.J. Lowe, D.R., 2016. Sedimentology of the ~3.3 Ga upper Mendon Formation, Barberton Greenstone Belt, South Africa. *Precambrian Research* **281**, 473-494.

Turcotte, D.L., Pflugrath, J.C., 1985. XV Lunar and Planetary Science Conference. *Journal of Geophysical Research, Supplement* **90**, C541-C544.

Udden, J.A., 1914. Mechanical composition of clastic sediments. *Geological Society of America Bulletin* **25**, 655-744.

Ueno, Y., Maruyama, S., Isozaki, Y., Yurimoto, H., 2001. Early Archean (ca. 3.5 Ga) microfossils and ^{13}C-depleted carbonaceous matter in the North Pole area, Western Australia: Field occurrence and geochemistry. In Geochemistry and the Origin of Life; Nakashima, S., Maruyama, S., Brack, A., Windley, B.F., (Eds.), Universal Academy Press Inc.: Tokyo, Japan, 2001, pp. 201–236.

Vago, J.L., Gardini, B., Kminek, G., Baglioni, P., Gianfiglio, G., Santovincenzo, A., Bayon, S., Van Winnendael, M., 2006. ExoMars—searching for life on the red planet. *ESA Bulletin, European Space Agency* **126**, 16–23.

Vago, J.L., Westall, F., Pasteur Instrument Teams, ExoMars Landing Site Selection Group, Other Contributors, 2017. Habitability on early Mars and the search for biosignatures with the ExoMars rover. *Astrobiology* **17**, 471–510.

Vago, J.L., Westall, F., Cavalazzi, B., ExoMars Science Working Team, 2018. Searching for signs of life on other planets: Mars a case study. In Cavalazzi, B., Westall, F. (Eds.), Biosignatures for Astrobiology, Springer, pp. 283–300.

Vai, G.B., Ricci Lucchi, F., 1977. Algal crusts, autochthonous and clastic gypsum in a cannibalistic evaporitic basin: a case history from the Messinian of Northern Appenines. *Sedimentology* **24**, 211–244.

van den Boorn, S.H.J.M., van Bergen, M., Nijman, W., Vroon, P., 2007. Dual role of seawater and hydrothermal fluids in Early Archean chert formation: evidence from silicon isotopes. *Geology* **35**, 939–942.

van den Boorn, S.H.J.M., van Bergen, M.J., Vroon, P.Z., de Vries, S.T., Nijman, W., 2010. Silicon isotope and trace element constraints on the origin of ~3.5 Ga cherts: implications for Early Archaean marine environments. *Geochimica et Cosmochimica Acta* **74**, 1077–1103.

Van Kranendonk, M.J., 2006. Volcanic degassing, hydrothermal circulation and the flourishing of early life on Earth: new evidence from the Warrawoona Group, Pilbara Craton, Western Australia. *Earth-Science Reviews* **74**, 197–240.

Van Kranendonk, M.J., 2007. A review of the evidence for putative Paleoarchean life in the Pilbara craton, Western Australia. In: Van Kranendonk, M.J., Smithies, R.H., Bennett, V.H. (Eds.), Earth's Oldest Rocks. Elsevier (Developments in Precambrian Geology), Amsterdam, pp. 855–877.

Van Kranendonk, M.J., 2011. Stromatolite morphology as an indicator of biogenicity for Earth's oldest fossils from the 3.5-3.4 Ga Pilbara Craton, Western Australia. In: Reitner, J., Queric, N.-V., Arp, G. (Eds.), Advances in Stromatolite Geobiology. Springer, Germany. *Lecture Notes in Earth Sciences* **131**, 517–534.

Van Kranendonk, M.J., Smithies, R.H., Griffin, W.L., Huston, D.L., Hickman, A.H., Champion, D.C., Anhaeusser, C.R., Pirajno, F., 2015. Making it thick: a volcanic plateau origin of Palaeoarchean continental lithosphere of the Pilbara and Kaapvaal cratons. *Geological Society of London Special Publication* **389**, 83–111.

van Zuilen, M.A., 2018. The significance of carbonaceous matter to understanding life processes on early Earth. In Van Kranendonk, M.J., Bennett, V.C., Hofmann, J.E. (Eds.) Earth's Oldest Rocks, Elsevier, pp. 945–963.

van Zuilen, M.A., Chaussidon, M., Rollion-Bard, C., Marty, B., 2007. Carbonaceous cherts of the Barberton Greenstone Belt, South Africa: isotopic, chemical and structural characteristics of individual microstructures. *Geochimica et Cosmochimica Acta* **71**, 655–669.

van Zuilen, M.A., Fliegel, D., Wirth, R., Lepland, A., Qu, Y., Schreiber, A., Romashkin, A.E., Philippot, P., 2012. Mineral-templated growth of natural graphite films. *Geochimica et Cosmochimica Acta* **83**, 252–262.

Vaniman, D.T., Bish, D.L., Ming, D.W., Bristow, T.F., Morris, R.V., Blake, D.F., Chipera, S.J., Morrison, S.M., Treiman, A.H., Rampe, E.B., Rice, M., Achilles, C.N., Grotzinger, J., McLennan, S.M., Williams, J., Bell, J., Newsom, H., Downs, R.T., Maurice, S., Sarrazin, P., Yen, A.S., Morookian, J.M., Farmer, J.D., Stack, K., Milliken, R.E., Ehlmann, B., Sumner, D.Y., Berger, G., Crisp, J.A., Hurowitz, J.A., Anderson, R., Des Marais, D., Stolper, E.M., Edgett, K.S., Gupta, S., Spanovich, N., 2014. Mineralogy of a mudstone at Yellowknife Bay, Gale Crater, Mars. *Science* **343**, 1243480.

Verrecchia, E.P., 1996. Morphometry of microstromatolites in calcrete laminar crusts and a fractal model of their growth. *Mathematical Geology* **28**, 87–109.

Vieth, A., Wilkes, H., 2009. Stable isotopes in understanding origin and degradation processes of petroleum. In Timmis, K. (Ed.). Handbook of Hydrocarbon and Lipid Microbiology, Springer, Heidelberg, pp. 97–111.

Wacey, D., 2009. Early life on earth, a practical guide. In: Topics in Geobiology, 31. Springer, Heidelberg, p. 274.

Wacey, D., 2010. Stromatolites in the ~3400 Ma Strelley Pool Formation, Western Australia: examining biogenicity from the macro- to the nano-scale. *Astrobiology* **10**, 381–395.

Wacey, D., McLoughlin, N., Brasier, M.D., 2009. Looking through windows onto the earliest evidence for life on Earth and Mars. In: Seckbach, J., Walsh, M.M. (Eds.), From Fossils to Astrobiology. Springer, pp. 39–68.

Wacey, D., Kilburn, M.R., Saunders, M., Cliff, J., Brasier, M.D., 2011. Microfossils of sulphur-metabolizing cells in 3.4-billion-year-old rocks of Western Australia. *Nature Geoscience* **4**, 698–702.

Wacey, D., Menon, S., Green, L., Gerstmann, D., Kong, C., McLoughlin, N., Saunders, M., Brasier, M.D., 2012. Taphonomy of very ancient microfossils from the ~3400 Ma Strelley Pool Formation and ~1900 Ma Gunflint Formation: New insights using a focused ion beam. *Precambrian Research* **220–221**, 234–250.

Wacey, D., McLouglin, N., Kilburn, M.R., Saunders, M., Cliff, J.B., Kong, C., Barley, M.E., Brasier, M.D., 2013. Nanoscale analysis of pyritized microfossils reveals differential heterotrophic consumption in the ~1.9-Ga Gunflint chert. *Proceedings of the National Academy of Sciences U.S.A.* **110**, 8020–8024.

Wacey, D., Battison, L., Garwood, R.J., Hickman-Lewis, K., Brasier, M.D., 2016. High-resolution techniques for the study of the morphology and chemistry of Proterozoic microfossils. In: Brasier, A.T., McIlroy, D., McLoughlin, N. (Eds.), Earth System Evolution and Early Life: A Celebration of the Work of Martin Brasier. *Geological Society of London Special Publication* **448**, 81–104.

Wacey, D., Saunders, M., Kong, C., Brasier, A.T., Brasier, M.D., 2016. 3.46 Ga Apex chert 'microfossils' reinterpreted as mineral artefacts produced during phyllosilicate exfoliation. *Gondwana Research* **36**, 296–313.

Wacey, D., Fisk, M., Saunders, M., Eiloart, K., Kong, C., 2017. Critical testing of potential cellular structures within microtubes in 145 Ma volcanic glass from the Argo Abyssal Plain. *Chemical Geology* **466**, 575–587.

Walker, J.C.G., 1985. Carbon dioxide on the early Earth. *Origins of Life and Evolution of Biospheres* **16**, 117–127.

Walsh, M.M., 1992. Microfossils and possible microfossils from the early Archean Onverwacht group, Barberton mountain land, South Africa. *Precambrian Research* **54**, 271–293.

Walsh, M.M., Lowe, D.R., 1985. Filamentous microfossils from the 3,500-Myr-old Onverwacht Group, Barberton Mountain Land, South Africa. *Nature* **314**, 530–532.

Walsh, M.M., Lowe, D.R., 1999. Modes of accumulation of carbonaceous matter in the early Archaean: a petrographic and geochemical study of the carbonaceous cherts of the Swaziland Supergroup. In: Lowe, D.R., Byerly, G.R. (Eds.), Geologic Evolution of the Barberton Greenstone Belt, South Africa. *Geological Society of America Special Paper* **329**, 115-132.

Walsh, M.M., Westall, F., 2003. Archean biofilms preserved in the Swaziland Supergroup, South Africa. In: Krumbein, W.E., Paterson, D.M., Zavarin, G.A. (Eds.), Fossil and Recent Biofilms. Springer, Netherlands, pp. 307–316.

Walter, M.R., Buick, R., Dunlop, J., 1980. Stromatolites, 3400–3500 Myr old from the North Pole area, Western Australia. *Nature* **284**, 443–445.

Wang, A., Freeman, J.J., Jolliff, B.L., Chou, I.-M., 2006. Sulfates on Mars: A systematic Raman spectroscopic study of hydration states of magnesium sulfates. *Geochimica et Cosmochimica Acta* **70**, 6118–6135.

Wang, S., Shi, X., Sun, H., Chen, Y., Pan, H., Yang, X., Rafiq, T., 2014. Variations in Metal Tolerance and Accumulation in Three Hydroponically Cultivated Varieties of Salix integra Treated with Lead. *PLoS ONE* **9**, e108568.

Way, M.J., Del Genio, A.D., Kiang, N.Y., Sohl, L.E., Grinspoon, D.H., Aleinov, I., Kelley, M., Clune, T., 2016. Was Venus the first habitable world of our solar system? *Geophysical Research Letters* **43**, 8376-8383.

Welz, S., McNallan, M.J., Gogotsi, Y., 2006. Carbon structures in silicon carbide derived carbon. *Journal of Materials Processing Technology* **179**, 11–22.

Wentworth, C.K., 1922. A scale of grade and class terms for clastic sediments. *The Journal of Geology* **30**, 377–392.

Westall, F., 2016. Microbial palaeontology and the origin of life: a personal approach. *Bollettino della Società Paleontologica Italiana* **55**, 85–103.

Westall, F., Gernecke, D., 1998. Electron microscope methods in the search for the earliest life on Earth (in 3.5–3.3 Ga cherts from the Barberton greenstone belt, South Africa): applications for extraterrestrial life studies. *Proceedings of SPIE: The International Society for Optical Engineering* **3114**, 158–169.

Westall, F., Folk, R.L., 2003. Exogenous carbonaceous microstructures in Early Archaean cherts and BIFs from the Isua Greenstone Belt: implications for the search for life in ancient rocks. *Precambrian Research* **126**, 313-330.

Westall, F., Southam, G., 2006. Early life on earth. In: Benn, K., Mareschal, J.-C., Condie, K.C. (Eds.), Archean Geodynamics and Environments. AGU Geophysical Monograph 164. American Geophysical Union, Washington, DC, pp. 283–304.

Westall, F., Cavalazzi, B., 2011. Biosignatures in rocks. In: Thiel, V. (Ed.), Encyclopedia of Geobiology. Springer, Berlin, pp. 189–201.

Westall, F., de Wit, M.J., Dann, J., van der Gaast, S., de Ronde, C.E.J., Gerneke, D., 2001. Early Archaean fossil bacteria and biofilms in hydrothermally-influenced sediments from the Barberton greenstone belt, South Africa. *Precambrian Research* **106**, 93–116.

Westall, F., de Ronde, C.E.J., Southam, G., Grassineau, N., Colas, M., Cockell, C.S., Lammer, H., 2006. Implications of a 3.472-3.333 Gyr-old subaerial microbial mat from the Barberton Greenstone Belt, South Africa for the UV environmental conditions on the early Earth. *Philosophical Transactions of the Royal Society* B **361**, 1857–1875.

Westall, F., de Vries, S.T., Nijman, W., Rouchon, V., Orberger, B., Pearson, V., Watson, J., Verchovsky, A., Wright, I., Rouzaud, J.-N., Marchesini, D., Anne, S., 2006. The 3.466Ga Kitty's Gap chert, an Early Archean microbial ecosystem. In Processes on the Early Earth, Reimold, W.U., Gibson R.L. (Eds.). *Geological Society of America Special Paper* **405**, 105–131.

Westall, F., Cavalazzi, B., Lemelle, L., Marocchi, Y., Rouzaud, J.-N., Simionovici, A., Salomé, M., Mostefaoui, S., Andreazza, C., Foucher, F., Toporski, J., Jauss, A., Thiel, V., Southam, G., MacLean, L., Wirick, S., Hofmann, A., Meibom, A., Robert, F., Défarge, C., 2011. Implications of in situ calcification for photosynthesis in a w3.3 Ga-old microbial biofilm from the Barberton greenstone belt, South Africa. *Earth and Planetary Science Letters* **310**, 468–479.

Westall, F., Foucher, F., Cavalazzi, B., de Vries, S., Nijman, W., Pearson, V., Watson, J., Verchovsky, A., Wright, I., Rouzaud, J.-N., Marchesini, D., Anne, S., 2011. Volcaniclastic habitats for early life on Earth and Mars: a case study from c.3.5 Ga-old rocks from the Pilbara, Australia. *Planetary and Space Science* **59**, 1093–1106.

Westall, F., Loizeau, D., Foucher, F., Bost, N., Bertrand, M., Vago, J.L., Kminek, G., 2013. Habitability on Mars from a microbial point of view. *Astrobiology* **13**, 887–897.

Westall, F., Campbell, K.A., Bréhéret, F.G., Foucher, F., Gautret, P., Hubert, A., Sorieul, S., Grassineau, N., Guido, D.M., 2015. Complex microbe-sediment systems are ancient (3.33 Ga) and flourished in a hydrothermal context. *Geology* **43**, 615–618.

Westall, F., Foucher, F., Bost, N., Bertrand, M., Loizeau, D., Vago, J.L., Kminek, G., Gaboyer, F., Campbell, K.A., Bréhéret, J.-G., Gautret, P., Cockell, C.S., 2015. Biosignatures on Mars: what, where, and How? Implications for the search for Martian life. *Astrobiology* **15**, 998–1029.

Westall, F., Hickman-Lewis, K., Hinman, N., Gautret, P., Campbell, K.A., Bréhéret, J.-G., Foucher, F., Hubert, A., Sorieul, S., Kee, T.P., Dass, A.V., Georgelin, T., Brack, A., 2018. A hydrothermal-sedimentary context for the origin for life. *Astrobiology* **18**, 259–293.

Wheat, C.G., Mottl, M.J., Rudnicki, M., 2002. Trace element and REE composition of a low-temperature ridge-flank hydrothermal spring. *Geochimica et Cosmochimica Acta* **66**, 3683–3705.

Wilde, S.A., Valley, J.W., Peck, W.H., and Graham, C.M. (2001) Evidence from detrital zircons for the existence of continental crust and oceans on the Earth 4.4 Gyr ago. *Nature* **409**, 175–178.

Williams, R.J.P., 2001. Chemical selection of elements by cells. *Coordination Chemistry Reviews* **216–217**, 583–595.

Williams, L.A., Reimers, C., 1982. Recognizing organic mats in deep water environments. *Geological Society of America Abstracts Program* **14**, 647.

Williams, R.J.P., Fraústo da Silva, J.J.R., 2003. Evolution was chemically constrained. *Journal of Theoretical Biology* **220**, 323–343.

Williams, R.M.E., Grotzinger, J.P., Dietrich, W.E., Gupta, S., Sumner, D.Y., Wiens, R.C., Mangold, N., Malin, M.C., Edgett, K.S., Mauice, S., Forni, O., Gasnault, O., Ollila, A., Newsom, H.E., Dromart, G., Palucis, M.C., Yingst, R.A., Anderson, R.B., Herkenhoff, K.E., Le Mouélic, S., Goetz, W., Madsen, M.B., Koefoed, A., Jensen, J.K., Bridges, J.C., Schwenzer, S.P., Lewis, K.W., Stack, K.M., Rubin, D., Kah, L.C., Bell, J.F., Farmer, J.D., Sullivan, R., Van Beek, T., Blaney, D.L., Pariser, O., Deen, R.G., MSL Science Team, 2013. Martian fluvial conglomerates at Gale Crater. *Science* **340**, 1068–1072.

Williford, K.H., Farley, K.A., Stack, K.M., Allwood, A.C., Beaty, D., Beegle, L.W., Bhartia, R., Brown, A.J., de la Torre Juarez, M., Hamran, S.-E., Hecht, M.H., Hurowitz, J.A., Rodriguez-Manfredi, J.A., Maurice, S., Milkovich, S., Wiens, R.C., 2018. The NASA Mars 2020 rover mission and the search for extraterrestrial life. In Cabrol, N.A., Grin, E.A. (Eds.), From habitability to life on Mars. Elsevier, Amsterdam, pp. 275–308.

Wogelius, R.A., Manning, P.L., Barden, H.E., Edwards, N.P., Webb, S.M., Sellers, W.I., Taylor, K.G., Larson, P.L., Dodson, P., You, H., Da-Qing, L., Bergmann, U., 2011. *Science* **333**, 1622–1626.

Wolff-Boenisch, D., Gíslason, S.R., Oelkers, E.H., 2006. The effect of crystallinity on dissolution rates and CO_2 consumption capacity of silicates. *Geochimica et Cosmochimica Acta* **70**, 858–870.

Zavarzin, G.A., 1981. The genus Metallogenium. In Starr, M.P. et al. (Eds.), The Prokaryotes: A Handbook on Habitats, Isolation, and Identification of Bacteria, pp. 524-528. Springer-Verlag, Berlin.

Zellner, N.E.B., 2017. Cataclysm no more: new views on the timing and delivery of lunar impactors. *Origins of Life and Evolution of Biospheres* **47**, 261–280.

Zerkle, A.L., House, C.H., Brantley, S.L., 2005. Biogeochemical signatures through time as inferred from whole microbial genomes. *American Journal of Science* **305**, 467–502.

Zhang, M., Konishi, H., Xu, H., Sun, X., Lu, H., Wu, D., Wu, N., 2014. Morphology and formation mechanism of pyrite induced by the anaerobic oxidation of methane from the continental slope of the NE South China Sea. *Journal of Asian Earth Sciences* **92**, 293–301.

Zonneveld, K.A.F., Versteegh, G.J.M., Kasten, S., Eglinton, T.I., Emeis, K.-C., Huguet, C., Koch, B.P., de Lange, G.J., de Leeuw, J.W., Middelburg, J.J., Mollenhauer, G., Prahl, F.G., Rethemeyer, J., Wakeham, S.G., 2010. Selective preservation of organic matter in marine environments; processes and impact on the sedimentary record. *Biogeosciences* **7**, 483-511